



HAL
open science

Optimizing the in vivo monitoring of female workers using in vivo measurements and Monte Carlo calculations: method for the management of complex contaminations

Jad Farah

► **To cite this version:**

Jad Farah. Optimizing the in vivo monitoring of female workers using in vivo measurements and Monte Carlo calculations: method for the management of complex contaminations. Other [cond-mat.other]. Université Paris Sud - Paris XI, 2011. English. NNT : 2011PA112183 . tel-00638153

HAL Id: tel-00638153

<https://theses.hal.science/tel-00638153>

Submitted on 4 Nov 2011

HAL is a multi-disciplinary open access archive for the deposit and dissemination of scientific research documents, whether they are published or not. The documents may come from teaching and research institutions in France or abroad, or from public or private research centers.

L'archive ouverte pluridisciplinaire **HAL**, est destinée au dépôt et à la diffusion de documents scientifiques de niveau recherche, publiés ou non, émanant des établissements d'enseignement et de recherche français ou étrangers, des laboratoires publics ou privés.

UNIVERSITE PARIS-SUD 11

ÉCOLE DOCTORALE : *Modélisation et Instrumentation en Physique,
Energies, Géosciences et Environnement (MIPEGE)*

THÈSE DE DOCTORAT DE PHYSIQUE

soutenue le 06/10/2011

par

Jad FARAH

Amélioration des mesures
anthroporadiométriques personnalisées assistées
par calcul Monte Carlo :
optimisation des temps de calculs
et méthodologie de mesure pour l'établissement
de la répartition d'activité

Directeur de thèse : Dr. Didier FRANCK

Chef du LEDI (IRSN)

Composition du jury :

Président du jury :

Pr. Costel PETRACHE

Directeur Recherche (IPN)

Rapporteurs :

Dr. Maria Antonia LOPEZ-PONTE

Directeur Recherche (CIEMAT)

Dr. Gianfranco GUALDRINI

Directeur Recherche (ENEA)

Examineurs :

Pr. Libor MAKOVICKA

Directeur Recherche (Univ. Franche
Comté)

Membre invité :

M. Xavier LECHAFTOIS

Technicien principal (AREVA NC)

Dr. David BROGGIO

Ingénieur-Chercheur (IRSN)

Recherches effectuées à l'IRSN/DRPH/SDI/LEDI, BP 17, 92262 Fontenay-aux-Roses Cedex

Remerciements - Acknowledgements

Je remercie la Direction de la Radioprotection de l'Homme, Monsieur Patrick GOURMELON et Madame Jocelyne AIGUEPERSE, pour m'avoir donné l'occasion de réaliser ce travail de thèse à l'IRSN. Je souhaite également remercier particulièrement Madame Michèle AGARANDE, Chef du Service de Dosimétrie Interne, pour m'avoir accueilli et avoir mis à disposition les moyens de mener à bien ce projet de thèse dans les meilleures conditions.

Je tiens à remercier tout particulièrement les responsables AREVA du Programme d'intérêt Commun en Dosimétrie Interne pour m'avoir fait confiance et avoir suivi mon travail tout au long de ces trois années : le Docteur Alain ACKER et le Docteur Stéphane HENRY de la Direction Médicale d'AREVA, Madame Inès V. de LAGUERIE de la Direction des Technologies, de la Recherche et de l'Innovation d'AREVA ainsi que Madame Bernadette PELEAU et l'ensemble de l'équipe du Secteur Analyses Médicales du centre AREVA NC de La Hague.

Je remercie également Monsieur Bernard BERTHIER pour m'avoir accueilli au sein de l'école doctorale Rayonnements et Environnement devenue l'école doctorale MIPEGE sous la direction de Monsieur Xavier QUIDELEUR et Monsieur Bruno ESPAGNON.

Je tiens à remercier vivement Monsieur Costel PETRACHE, Professeur à l'Université Paris-Sud 11 et Directeur de Recherche à l'Institut de Physique Nucléaire d'Orsay, pour avoir accepté de présider le jury de cette thèse.

I really want to thank Dr Maria Antonia LOPEZ-PONTE, head of internal dosimetry group at CIEMAT, and Dr Gianfranco GUALDRINI, first researcher at the ENEA-Radiation Protection Institute, for their review of this manuscript. I am sincerely grateful for your valuable input to this work by your extensive knowledge of *in vivo* measurements and your lifelong experience of Monte Carlo simulations and computational dosimetry.

Je voudrais exprimer ma grande reconnaissance à Monsieur Libor MAKOVICKA, Professeur à l'Université de Franche Comté et responsable de l'équipe Interaction Rayonnement-Matière, pour avoir accepté de faire partie de ce jury. Sa présence est pour moi un grand honneur.

Je remercie vivement Monsieur Xavier LECHAFTOIS, technicien principal du Secteur Analyses Médicales du centre AREVA NC de La Hague pour avoir accepté de participer à ce jury et surtout pour avoir soutenu et suivi avec intérêt ce travail pendant ces trois ans.

Mes plus sincères remerciements vont à mon Directeur de thèse, Monsieur Didier FRANCK, Chef du Laboratoire d'Evaluation de la Dose Interne, pour m'avoir accueilli, pour m'avoir accordé toute sa confiance et son aide précieuse dans le domaine de la dosimétrie interne. Merci Didier de m'avoir considéré, dès le premier jour, comme un vrai chercheur dans ton équipe, de m'avoir tout de suite mis à l'aise et appris à tirer le meilleur de moi même.

Je remercie également mon responsable et tuteur Monsieur David BROGGIO pour m'avoir transmis son expérience et ses conseils en anthroporadiométrie, en modélisation et en calcul Monte Carlo. David, merci pour la qualité de l'encadrement, pour ton investissement sans

faillie dans ce projet, pour m'avoir tant soutenu et encouragé. Merci également pour tous nos échanges, pour ta disponibilité, ton écoute, ta confiance en moi et ton soutien inconditionnel. Tu as été pour moi, à la fois, un référent sûr, un chercheur modèle et un ami fiable je t'exprime ici toute ma gratitude.

I would also like to thank Dr Patrick MIN (formerly at Princeton University), for his efficient and friendly collaboration in using and improving the Binvox program.

Je tiens aussi à remercier tout particulièrement Monsieur Julien HENRIET, chercheur à l'Université de Franche Comté, et l'ensemble de l'équipe IRMA pour la très fructueuse collaboration dans le développement de la plateforme EquiVox et les différentes publications et présentations qu'on a faites ensemble.

I am extremely thankful to the CIEMAT (Madrid) and KIT (Karlsruhe) teams, especially Dr Maria Antonia LOPEZ-PONTE and Dr Bastian BREUSTDET, for hosting me in their units and for giving me the opportunity to carry out *in vivo* measurements with their equipments. All my gratitude goes to Mrs Begoña PEREZ-LOPEZ and Mr Juan Francisco NAVARRO-AMARO for their warm welcome and sympathy. I am also grateful to Dr Debora LEONE and to Dr Olaf MARZOCCHI for their precious contribution to this work and for the helpful discussions and brainstorming.

Je tiens à remercier sincèrement l'équipe du LEDI pour le soutien et la sympathie qu'elle m'a témoignée durant ces trois ans. Aurélie, Cécile, Estelle, Lama, Eric, Mouhamad ainsi que les collègues du LEDI/VES merci ! Que tout le monde trouve ici ma profonde gratitude pour avoir eu à mes côtés des personnes avec qui j'ai eu le plaisir de travailler et d'échanger. Grand merci à Monsieur Raphaël BÔ, technicien au LEDI, pour son aide notamment dans les mesures et pour avoir été un voisin de bureau très aimable, toujours souriant et disponible. Merci également aux membres du Laboratoire de Radiochimie pour leur sympathie, leur soutien et leur amitié. Je voudrais enfin remercier Mme Juliette AMBROISE, secrétaire du Service de Dosimétrie Interne pour sa bonne humeur quotidienne, sa disponibilité et son aide.

Je voudrais remercier la communauté des Frères des Ecoles Chrétiennes, et tout particulièrement F. Noel BOIS, pour avoir été pour moi une vraie famille avec un accueil toujours chaleureux et un soutien moral et spirituel infaillible.

Enfin, je souhaite remercier infiniment mes parents pour m'avoir permis de réaliser les études que j'avais choisies, mes proches pour leur soutien moral et matériel, mes amis pour leur sympathie. Tout le monde le sait : il y a des personnes qui ne s'oublient jamais. Joelle, chérie, je pense particulièrement à toi. Merci d'avoir été toujours là pour moi, merci pour ta foi et ta confiance en moi, merci également pour ton écoute et ton encouragement infini. Tu es le soldat inconnu de cette thèse, tu l'as si patiemment relue, corrigée et imprégnée de ton amour ici je t'exprime toute ma gratitude, mon estime et mon affection.

Abstract

To optimize the monitoring of female workers using *in vivo* spectrometry measurements, it is necessary to correct the typical calibration coefficients obtained with the Livermore male physical phantom. To do so, numerical calibrations based on the use of Monte Carlo simulations combined with anthropomorphic 3D phantoms were used. Such computational calibrations require on the one hand the development of representative female phantoms of different size and morphologies and on the other hand rapid and reliable Monte Carlo calculations. A library of female torso models was hence developed by fitting the weight of internal organs and breasts according to the body height and to relevant plastic surgery recommendations. This library was next used to realize a numerical calibration of the AREVA NC La Hague *in vivo* counting installation. Moreover, the morphology-induced counting efficiency variations with energy were put into equation and recommendations were given to correct the typical calibration coefficients for any monitored female worker as a function of body height and breast size. Meanwhile, variance reduction techniques and geometry simplification operations were considered to accelerate simulations.

Furthermore, to determine the activity mapping in the case of complex contaminations, a method that combines Monte Carlo simulations with *in vivo* measurements was developed. This method consists of realizing several spectrometry measurements with different detector positioning. Next, the contribution of each contaminated organ to the count is assessed from Monte Carlo calculations. The *in vivo* measurements realized at LEDI, CIEMAT and KIT have demonstrated the effectiveness of the method and highlighted the valuable contribution of Monte Carlo simulations for a more detailed analysis of spectrometry measurements. Thus, a more precise estimate of the activity distribution is given in the case of an internal contamination.

Key-words: *in vivo* monitoring, numerical calibrations, deformable phantoms, variance reduction, activity mapping.

Contents

Résumé de la thèse/French summary of the thesis.....	I
List of notations.....	XXV
List of figures.....	XXVI
List of tables.....	XXX
General introduction.....	1
Chapter 1 Issues and challenges of <i>in vivo</i> measurements.....	4
I. Overview of internal dosimetry	5
I.1. Internal contamination of nuclear workers	5
I.1.1. Radionuclides involved in internal contamination situations.....	5
I.1.2. Incorporation pathways.....	5
I.2. Biokinetics of radionuclides	6
I.2.1. Transfer in the systemic circulation.....	7
I.2.2. Biokinetic models.....	7
I.3. Internal dose definition, principles and calculation	8
I.3.1. Dose definition.....	8
I.3.2. Dosimetry models.....	10
I.3.3. Internal dose calculation.....	10
I.4. Radiological protection and individual monitoring of workers	11
I.4.1. Radiological protection.....	11
I.4.2. Monitoring and measurement techniques.....	12
I.4.3. Decision threshold and detection limits.....	14
II. State of the art of <i>in vivo</i> measurements	16
II.1. Choice of the counting system	16
II.2. Positioning of the counting system	16
II.3. Calibrating the counting system	17
II.4. Measurement uncertainties	19
III. Basis of the numerical calibration	20
III.1. Monte Carlo approach for particles transport	20
III.1.1. The Monte Carlo method.....	21
III.1.2. The MCNPX code.....	21
III.1.3. Monte Carlo precision and efficiency.....	22
III.1.4. Application of MC simulation for <i>in vivo</i> measurements.....	23
III.2. Tools for Monte Carlo numerical calibrations	24
III.2.1. The OEDIPE software.....	24
III.2.2. Voxelization process.....	25
IV. Anthropomorphic human models	27
IV.1. Constructive Solid Geometry representations	27
IV.1.1. Phantoms developed using the CSG format.....	28
IV.1.2. Applications of CSG phantoms.....	31
IV.2. Boundary representations	32
IV.2.1. Phantoms developed using the BREP format.....	33
IV.2.2. Applications of BREP phantoms.....	35
IV.2. Discussion of the 3D representations	36

V. Female workers and <i>in vivo</i> monitoring	37
Chapter 2 Development of a Mesh and NURBS-based female torso library...40	
I. Generating 3D graphic phantoms	41
I.1. Tools for 3D models generations	41
I.1.1. Isogray.....	41
I.1.2. IDL.....	42
I.1.3. Rhinoceros 3D.....	42
I.1.4. The Binvox program.....	43
I.2. Protocols for 3D models generation	44
I.2.1. Medical images available.....	44
I.2.2. Medical images unavailable.....	45
II. Female body type, morphology and size designation	45
II.1. Chest girth designation and evaluation	45
II.2. Cup size designation and evaluation	46
III. Creation of a deformable female torso core model	47
III.1. Geometry creation	47
III.2. Tissue composition and density	48
III.2.1. Case of the breasts.....	48
III.2.2. Case of the internal organs.....	49
III.2.3. Case of the residual tissue.....	50
III.3. Validation of the torso core model	51
III.3.1. Volume of the created organs.....	51
III.3.2. Simulation of <i>in vivo</i> counting efficiency.....	52
IV. Phantom geometry modification	53
IV.1. Target values for geometry modification	53
IV.1.1. Chest girth modification.....	53
IV.1.2. Cup size modification.....	54
IV.1.3. Internal organs volume variation.....	55
IV.2. Creating the library	56
IV.3. Tissue composition and density attribution	57
IV.3.1. Case of the breasts.....	58
IV.3.2. Case of the internal organs.....	58
IV.3.3. Case of the residual tissue.....	59
IV.4. Validation of the generated models	60
V. Discussion and conclusion	61
V.1. Choice of the creation method	61
V.2. Choice of tissue composition and density	62
V.3. Comparison to existing models	62
Chapter 3 Numerical calibration of the AREVA NC <i>in vivo</i> monitoring installation.....	64
I. Monte Carlo simulation of an <i>in vivo</i> measurement	65
I.1. Reproducing the <i>in vivo</i> measurement with OEDIPE	65
I.1.1. Choice and distribution of the source.....	65
I.1.2. Choice and positioning of the detectors.....	65
I.1.3. Generating the MCNPX input file.....	66
I.2. Simulated counting efficiency calculation	67
I.2.1. From a simulated spectrum to a calibration curve.....	67
I.2.2. Uncertainty assessment.....	67

II. Numerical calibration using the developed female library and Monte Carlo simulations	68
II.1. Cup size effect	68
II.2. Chest girth and internal organ volume effects	70
II.3. Comparison to published data	73
III. Parameterization of morphology-induced variations of counting efficiency ...74	
III.1. Modeling the morphological effect	74
III.1.1. Chest wall thickness effect.....	74
III.1.2. Internal organ volume effect.....	76
III.2. Development of a morphological equation	78
III.3. Validating the developed equation	79
III.3.1. Reproducing MC simulations with the developed equation.....	79
III.3.2. Reproducing measurements with the developed equation.....	82
III.3.3. Reproducing published data with the developed equation.....	86
III.4. Study of the introduced parameters	88
III.4.1. C1 correlation with lung volume.....	88
III.4.2. C2 correlation with chest wall thickness.....	89
III.5. Generalizing the use of the developed equation	90
IV. Practical recommendations	91
V. Discussion and conclusion	93
IV.1. Choice and distribution of the source	94
IV.2. Alternative positioning of the detectors	95
IV.3. Improving the morphological equation	96
Chapter 4 Accelerating MC simulations using Variance Reduction techniques and geometry simplification operations	98
I. In vivo simulation: problem statement, methods and objectives	99
II. Overview of the MCNPX Pulse Height Tally	99
II.1. General functioning of a PHT	100
II.2. Variance Reduction and PHT	100
II.2.1. Variance Reduction aim.....	100
II.2.2. Functioning of a PHT with VR.....	101
II.3. The available VR methods for PHT	101
II.4. Previous experience with VR and PHT	102
III. Accelerating MC simulations with Variance Reduction techniques	102
III.1. Problem identification	102
III.2. Population control VR methods	104
III.2.1. IMP card: Geometry splitting and Russian roulette.....	104
III.2.2. WW card: weight windows to control weight fluctuations.....	106
III.3. Modified Sampling Methods	108
III.3.1. SB card: biasing the distribution of particles.....	108
III.3.2. VEC card: biasing the emission direction.....	110
III.3.3. FCL card: forcing the collisions.....	112
III.3.4. EXT card: increasing the mean free path.....	113
III.4. Results of the VR methods	114
III.4.1. IMP card effect.....	114
III.4.2. WW card effect.....	115
III.4.3. SB card effect.....	116
III.4.4. Vec card effect.....	116
III.4.5. FCL card effect.....	117
III.4.6. EXT card effect.....	118

III.4.7. Combining different VR cards.....	119
III.5. VR methods discussion.....	121
III.5.1. Simulation time.....	121
III.5.2. Statistical relative error.....	122
III.5.3. Counting efficiency values and uncertainties.....	122
III.5.4. Implementation for routine use.....	123
IV. Accelerating MC simulations with geometry simplification operations.....	124
IV.1. Void plans.....	124
IV.1.1. Generalities and functioning.....	124
IV.1.2. Application to the numerical calibration.....	124
IV.2. Phantom geometry simplification.....	125
IV.2.1. Voxel grid reduction.....	125
IV.2.2. Validation of the simplified phantom.....	126
IV.2.3. Application to the numerical calibration.....	127
V. Accelerating MC output file treatment.....	127
V.1. Development of a Unix/Linux shell script.....	128
V.1.1. Objective.....	128
V.1.2. Functioning.....	128
V.1.3. Polynomial equation.....	128
V.2. Script use and validation.....	129
VI. Discussion and conclusion.....	131
VI.1. A one hour calibration process.....	131
VI.2. Statistical checks and FOM analyses.....	132
VI.3. Enhancing efficiency calculation with VR methods.....	133
Chapter 5 Activity mapping using in vivo spectrometry measurements and MC simulations.....	134
I. Management of complex contaminations.....	135
I.1. Activity distribution in complex scenarios.....	135
I.2. Separation method.....	136
I.3. Tools.....	137
I.3.1. ICRP biokinetic models.....	137
I.3.2. Counting system and positioning.....	138
I.3.3. Physical phantom and radioactive sources.....	139
I.3.4. Monte Carlo calculation tools.....	139
I.4. Work plan and investigation limits.....	139
I.4.1. Detector positioning.....	139
I.4.2. Biokinetic distribution.....	139
I.4.3. Presence of a perturbation source.....	140
II. Feasibility study using the Livermore phantom.....	140
II.1. Method validation with measurements.....	140
II.2. Parameters investigation.....	141
II.2.1. Effect of the detector positioning.....	141
II.2.2. Effect of the contamination hypothesis.....	142
II.2.3. Effect of a perturbation point source.....	143
III. Method validation with MC simulations.....	145
III.1. Reproducing in vivo measurements.....	146
III.2. Activity estimation from simulations.....	147
III.2.1. Optimizing the detector positioning.....	147
III.2.2. Improving the MCNPX model of detectors.....	148
IV. Applying the method for different counting systems.....	149
IV.1. Feasibility study with the CIEMAT counting system.....	149

IV.1.1.	Tools and methods: phantom, source and detectors.....	149
IV.1.2.	Measurement data and linearity check.....	150
IV.1.3.	Activity estimation from measurements.....	150
IV.1.4.	Activity estimation from Monte Carlo simulations.....	151
IV.1.5.	Investigating the effect of a perturbation source.....	153
IV.1.5.	Activity estimate from other energy lines.....	156
IV.2.	Feasibility study with the KIT counting system.....	157
IV.2.1.	Tools and methods: phantom, source and detectors.....	157
IV.2.2.	Measurement data and linearity check.....	157
IV.2.3.	Activity estimation from measurements.....	158
IV.2.4.	Activity estimation from Monte Carlo simulations.....	158
IV.2.5.	Investigating the effect of a perturbation source.....	159
IV.2.6.	Alternative detector positioning.....	160
IV.	Discussion and Conclusion.....	161
IV.1.	Measurements and MC simulations.....	162
IV.2.	Choice of the detector and positioning.....	163
IV.3.	Choice of the point source positioning.....	163
Chapter 6	Synthesis, Discussion and Perspectives.....	164
I.	Synthesis.....	165
I.1.	Treatment chain for numerical calibration.....	165
I.2.	Management of complex contaminations.....	166
II.	Discussion and improvements.....	167
II.1.	Library of female phantoms and numerical calibration.....	167
II.2.	Variance reduction techniques for in vivo simulations.....	169
II.3.	Contamination mapping procedure.....	170
III.	Perspectives.....	171
III.1.	Numerical calibration of a mobile in vivo unit.....	171
III.1.1.	The IRSN in vivo mobile unit.....	172
III.1.2.	MCNPX modeling of the in vivo mobile unit detectors.....	172
III.1.3.	Numerical calibration using a whole body male library.....	173
III.1.4.	Conclusion.....	174
III.2.	A CBR-Based platform for dosimetry in emergency situations.....	175
III.2.1.	Aim and methods.....	175
III.2.2.	Case-Based reasoning principles.....	175
III.2.3.	Artificial neuronal network methods.....	176
III.2.4.	Preliminary results of the platform.....	176
III.2.5.	Conclusion.....	177
	General Conclusion.....	179
	References.....	181
	Publications and oral presentations.....	194
	Appendix.....	196

Résumé de la thèse

Introduction

L'anthroporadiamétrie (mesures *in vivo*) est une méthode de surveillance des travailleurs exposés à des risques de contamination interne qui permet une estimation rapide et fiable de l'étendue, la nature et l'activité des radionucléides incorporés afin d'optimiser le traitement de décontamination. Dans le cas des mesures *in vivo*, il s'agit d'optimiser l'étalonnage des systèmes de comptage qui, dans la pratique, se fait à l'aide de fantômes physiques d'un réalisme anatomique limité. En effet, ces mannequins sont dotés d'un nombre restreint d'organes pouvant être chargés et ne permettent pas de reproduire la distribution souvent hétérogène des radionucléides incorporés. De plus, pour le personnel féminin, à ce jour aucun fantôme physique féminin n'a été développé pour les étalonnages anthroporadiamétriques. Pourtant, l'atténuation supplémentaire des radiations par les poitrines est l'un des facteurs majeurs à prendre en compte lors du calcul des coefficients d'étalonnage. Ainsi les étalonnages numériques, basés sur les simulations Monte Carlo et l'utilisation de fantômes anthropomorphes numériques, ont été proposés pour améliorer la surveillance des travailleuses du nucléaire.

Par ailleurs, les simulations Monte Carlo nécessitent une puissance de calcul importante. Des clusters dédiés aux simulations Monte Carlo sont couramment utilisés pour réaliser le calcul. Cependant, dans certaines conditions d'urgence, le résultat du calcul peut être nécessaire dans les plus brefs délais pour effectuer le geste approprié d'intervention ou de décontamination. Des simulations rapides et fiables sont donc requises tout en maintenant des résultats statistiquement corrects.

Enfin, la gestion des cas complexes de contamination interne reste délicate pour les plaies contaminées et pour les cas où très peu d'informations sont disponibles sur le nombre, la nature et la distribution des radionucléides incorporés. Ainsi, l'efficacité des mesures anthroporadiamétriques reste limitée pour déterminer la répartition précise de l'activité. Les modèles biocinétiques apportent une réponse partielle à ce problème puisqu'ils sont très difficilement vérifiables et parce qu'ils ne tiennent en aucun cas compte des particularités et du métabolisme de l'individu concerné. La mise en œuvre des calculs Monte Carlo associés aux mesures *in vivo* représente une méthode très prometteuse pour déterminer la cartographie d'activité à la suite d'une contamination interne.

Ce travail de thèse a été entrepris avec les objectifs suivants :

- Développer une librairie de fantômes féminins en utilisant des formats 3D flexibles telles que les Mesh et les NURBS,
- Réaliser un étalonnage numérique des installations anthroporadiamétrie d'AREVA NC pour le personnel féminin et ainsi corriger les coefficients d'étalonnage typiques obtenus avec le fantôme physique masculin Livermore,
- Établir une équation décrivant les variations de l'efficacité de comptage en fonction de la morphologie féminine et formuler une méthode, simple à mettre en place en pratique, pour une correction systématique des coefficients d'étalonnage pour chaque personne surveillée par le service médical d'AREVA NC,
- Améliorer l'efficacité des simulations Monte Carlo par le biais des méthodes de réduction de variance et par la simplification de la géométrie du fantôme,

- Associer le calcul Monte Carlo aux mesures anthroporadiométriques pour améliorer la prise en charge de cas de contaminations complexes et une détermination précise de la répartition d'activité dans le corps.

1. Création d'une librairie de fantômes thoraciques féminins déformables

La création de fantômes numériques anthropomorphes, dédiés aux applications dosimétriques, fait appel à deux types de représentations. La « Constructive Solid Geometry » (CSG) comprend les modèles mathématiques et voxelisés. Ces derniers sont directement dérivés d'images médicales et sont donc d'un grand réalisme anatomique. Cependant, la construction de fantômes voxelisés est coûteuse en temps et le modèle final est difficilement modifiable. Ainsi, les formats 3D graphiques utilisant la représentation « Boundary Representation » (BREP) ont été introduits pour leur grande flexibilité permettant ainsi la production de fantômes anthropomorphes adaptés à une dosimétrie personnalisée. Un modèle féminin déformable de base a ainsi été modélisé selon la représentation BREP. Ensuite, à partir de ce modèle, le développement d'une librairie de fantômes féminins a été réalisé par la déformation des surfaces Mesh et NURBS.

1.1. Création d'un fantôme féminin de base en géométrie BREP

Pour ce travail, un modèle 3D féminin déformable a été créé à partir du nouveau fantôme voxelisé de référence de la CIPR 110 (ICRP 2010) représentant la femme adulte de référence (Figure 1 (a)). Ainsi, une procédure écrite en langage Interactive Data Language (IDL) a été utilisée pour transformer les grilles de voxels, représentant un organe donné, en surfaces Mesh de ce même organe (Figure 1 (b)). Les surfaces des seins et du contour externe du thorax ont été par la suite importées dans le logiciel Rhinocéros 3D pour être transformées en surfaces NURBS (Figure 1 (c)).

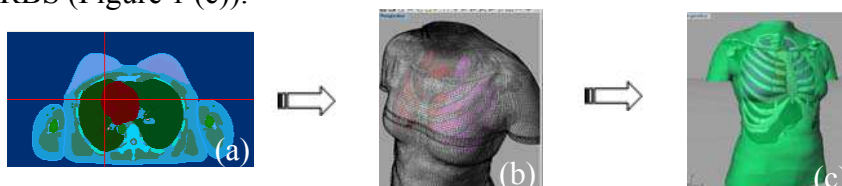


Figure 1. Etapes de création d'un fantôme au format BREP à partir de modèles voxelisés.

1.2. Variation de la taille et de la morphologie des modèles

Le fantôme féminin de base a été ensuite déformé afin de varier sa morphologie pour couvrir une population étendue de travailleuses à travers une librairie de 24 thorax féminins développée aux formats Mesh (les organes internes) et NURBS (seins et contour externe). Les variations morphologiques comprennent la variation du bonnet, du tour de poitrine et des organes internes.

1.2.1. Variation du bonnet

Lors de la création de la librairie de fantômes, la masse des seins a été reliée au tour de thorax et au bonnet en suivant les recommandations de spécialistes de la chirurgie plastique (Regnault et al. 1972, Berger and Lane 1985, Smith et al. 1986, Pechter 1998, Warren et al. 2007). La méthode consiste à déplacer manuellement les points de contrôle des surfaces NURBS afin de faire varier la taille et la morphologie de la poitrine (cf. Figure 2). Pour un tour de thorax donné, la taille de poitrine a été modifiée par l'ajout de la même quantité de tissu adipeux pour chaque changement de bonnet comme recommandé par Turner et Dujon (2005). La morphologie des seins a été modélisée en position couchée, position des mesures

anthroporadiométriques, et a été adaptée pour simuler le positionnement des seins sur le thorax sous l'effet de la pesanteur. Plus la taille des poitrines est grande, plus il est difficile de les modéliser et de les positionner correctement sur le thorax en position couchée de sorte que le réalisme anatomique peut être biaisé. Cependant, la forme des seins peut devenir encore plus complexe quand la position (assis/debout), l'âge ou l'origine sont pris en considération (Fabié et al. 2006).

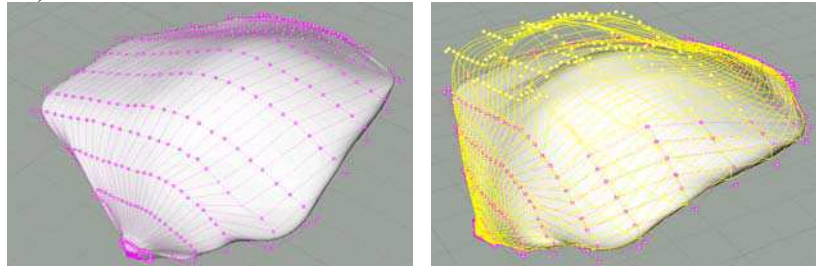


Figure 2. Visualisation sous Rhino 3D de la variation de la taille et de la morphologie des poitrines à travers l'utilisation des points de contrôle des surfaces NURBS.

1.2.2. Variation du tour de poitrine

Le tour de poitrine, tel qu'il est défini par le Comité Européen de Normalisation (CEN 2004), est calculé par la mesure de la circonférence du thorax juste en dessous de la poitrine. Il est désigné par des nombres clés représentant des intervalles de 4 cm centrés en 70, 75, 85, 95 et 105 cm pour respectivement un tour de poitrine de 85, 90, 100, 110 et 120. La modification du tour de poitrine a été réalisée en considérant ces intervalles et en utilisant le logiciel Rhinocéros de modélisation 3D (tridimensionnel). Par exemple, pour passer d'un tour de poitrine de 90 à un autre de 85, une contraction 2D (droite-gauche et antérieur-postérieur) avec un coefficient de 0,93 (70/75) a été appliquée.

1.2.3. Variation des organes internes

Une étude bibliographique a été réalisée pour modifier la taille des organes internes en identifiant les corrélations existantes entre le volume de ces organes et certains paramètres externes comme le sexe, l'âge, la taille, l'indice de masse corporelle, etc. (Clairand et al. 2000, de La Grandmaison et al. 2001). La corrélation linéaire entre la masse pulmonaire et la taille totale du sujet, identifiée par Clairand et al. (2000), a été retenue pour cette étude. Pour les fantômes de tour de poitrine de 85 et 90, le volume des organes internes est le même que dans le modèle féminin thoracique de base (90B) puisque ces modèles représentent des femmes de même taille. Pour les fantômes de tour de poitrine de 100, 110 et 120, cependant, la taille du modèle a été considérée comme représentant un sujet de 1,82 m. Par conséquent, un coefficient d'augmentation de masse de 1,3 a été considéré pour le cœur, le foie, les poumons et les os suivant les recommandations de Clairand et al. (2000). Le volume des organes internes a été modifié en utilisant le logiciel Rhinocéros 3D et des opérations de dilatation dans les trois directions. La dilatation de tous les organes a été effectuée en choisissant la même origine afin de conserver le recalage des organes les uns par rapport aux autres.

2. Etalonnage numérique du système de mesure d'AREVA NC

La librairie de fantômes développée et le calcul Monte Carlo ont permis la correction des coefficients d'étalonnage et la prise en compte de la morphologie et de son effet sur un comptage pulmonaire.

2.1. Préparation des calculs Monte Carlo

2.1.1. Voxelisation

Le code MCNP(X) de transport des particules (Pelowitz 2008) ne permet pas d'utiliser directement les surfaces Mesh et NURBS mais seulement les géométries au format voxel. Le logiciel Binvox développé par Dr. P. Min (<http://www.cs.princeton.edu/~min/binvox/>) a donc été utilisé pour voxeliser les fantômes de la librairie. La taille des voxels, générés sous Binvox, est choisie par l'utilisateur selon le degré de précision (résolution spatiale) requis pour son calcul.

2.1.2. Création du fichier d'entrée sous OEDIPE

Une fois les modèles voxelisés prêts, ils sont chargés dans le logiciel OEDIPE¹ (Franck et al. 2007). Ce dernier permet de modéliser rapidement l'expérience réalisée et de générer un fichier d'entrée pour le code MCNPX. Les étapes réalisées sous OEDIPE comprennent le choix de la source radioactive et sa répartition dans le fantôme ainsi que le choix du système de détection et de son positionnement vis-à-vis du modèle.

Pour les simulations réalisées dans ce travail, une source émettant des rayonnements gamma d'énergie entre 15 keV et 1,4 MeV a été créée pour représenter les éléments les plus communément utilisés pour les étalonnages anthroporadiométriques. De plus 1 Bq de cette source a été uniformément distribué dans les poumons des fantômes créés.

Par ailleurs, le système de 4 détecteurs germanium de l'usine d'Areva NC à la Hague a été utilisé pour les simulations MC et positionné pour couvrir au mieux les poumons (organes chargés en activité). Plus précisément, les détecteurs ont été placés à 2 cm de la peau au niveau de la clavicule et une inclinaison de 35° dans la direction tête-pieds a été opérée pour éviter une collision des détecteurs avec les seins et permettre les simulations MC. Ce positionnement, bien que significativement différent de celui utilisé dans la pratique (détecteurs quasiment au contact de la peau), est facilement reproductible d'une simulation à l'autre. Ainsi, la différence d'efficacité observée pour chaque fantôme pourra être attribuée à la variation de la morphologie et ne sera pas affectée par le positionnement des détecteurs.

2.2. Etude de l'effet de la morphologie

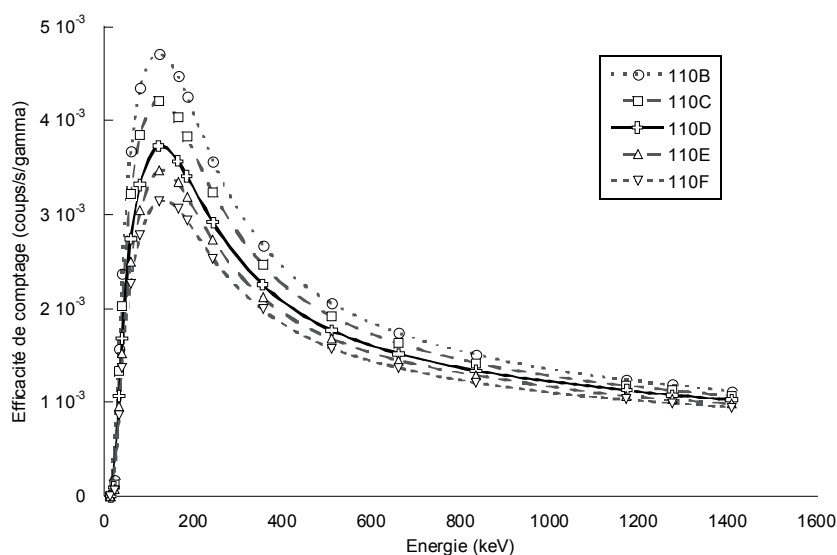
2.2.1. Effet du bonnet

Le Tableau I présente les valeurs simulées d'efficacité de comptage pour les fantômes de tour de poitrine de 100 et tous les bonnets créés et pour des radionucléides d'intérêt. Ces valeurs montrent que l'efficacité de comptage diminue avec l'augmentation de la taille de poitrine. Ceci peut s'expliquer par le fait que l'augmentation du bonnet implique une augmentation d'épaisseur de tissu, résultant en une atténuation supplémentaire des photons émis par les poumons en direction des détecteurs. Plus l'énergie du photon diminue, plus l'atténuation est importante, ce qui résulte en une perte significative de l'efficacité de comptage. En effet, l'efficacité de comptage de la raie du ¹⁰⁹Cd à 22 keV subit une perte de l'ordre de 59% entre le modèle doté du bonnet F et celui avec le bonnet B. La Figure 3 représente cette variation d'efficacité de comptage avec l'énergie pour le tour 110 et les bonnets B à F.

¹ Outil d'Evaluation de la Dose Interne PErsonnalis e

Tableau I. Valeurs de l'efficacité de comptage simulée pour les fantômes de tour 100 et les bonnets B à F et les radionucléides ^{109}Cd , ^{241}Am , ^{235}U , ^{137}Cs et ^{60}Co .

Radionucléide	Efficacité de comptage (coups/s/gamma)	fantôme				
		100B	100C	100D	100E	100F
^{109}Cd 22,2 keV		8,66E-04	6,86E-04	5,32E-04	4,53E-04	3,57E-04
^{241}Am 59,5 keV		8,57E-03	7,69E-03	6,85E-03	6,38E-03	5,56E-03
^{235}U 185,7 keV		8,58E-03	7,94E-03	7,28E-03	6,87E-03	6,14E-03
^{137}Cs 661,7 keV		3,04E-03	2,88E-03	2,73E-03	2,63E-03	2,44E-03
^{60}Co 1173,2 keV		2,06E-03	1,99E-03	1,88E-03	1,84E-03	1,76E-03


Figure 3. Variation de l'efficacité de comptage en fonction de l'énergie pour le tour 110 et tous les bonnets créés (B-F).

Pour les modèles de tour de poitrine de 85 et 90, l'épaisseur extra thoracique (seins + épaisseur de thorax) est la seule différence existant entre ces deux ensembles de fantômes. La différence d'efficacité de comptage la plus significative est obtenue pour la plus basse énergie (15,31 keV raie de ^{238}U), où une perte d'un facteur 1,15 est observée entre le modèle 85D et le modèle 90D. Pour les photons de haute énergie émis par le ^{60}Co (1,17 MeV), ce facteur d'atténuation n'est que de 1,04. Pour les modèles de tour de poitrine de 100, 110 et 120, le même phénomène de perte de l'efficacité de comptage avec l'épaisseur de tissu est observé. Toutefois, l'atténuation est significativement plus importante puisque la dilatation du thorax rajoute de l'épaisseur de tissu à celle de la poitrine. Ainsi, pour la raie du ^{109}Cd à 22,16 keV, l'atténuation supplémentaire s'élève à un facteur 5,74 entre le modèle 110D et le modèle 100D et un facteur 4,17 entre le 120D et le 110D. Pour les raies de haute énergie (^{60}Co à 1,17 MeV), l'atténuation reste relativement constante avec l'augmentation du bonnet comme observé pour les tours 85-90. Des facteurs de l'ordre de 1,67 et 1,81 sont obtenus entre les modèles 100D-110D et 110D -120D respectivement.

2.2.2. Effet du tour de poitrine et des organes internes

Le Tableau II présente les résultats des simulations Monte Carlo pour tous les tours de poitrines et tous les bonnets créés dans le cas de ^{241}Am . Les mêmes effets de perte d'efficacité de comptage avec l'augmentation de l'épaisseur atténuante, résultant de la variation du tour de thorax, ont été observés. De plus, l'effet du volume pulmonaire s'est avéré être prépondérant par rapport à l'effet du bonnet. En effet, la perte d'efficacité de comptage entre le 100D et le 90D à 511 keV est de l'ordre de 38% et est principalement due à la variation du volume pulmonaire, la taille des poitrines étant sensiblement similaire.

Tableau II. Efficacité de comptage pour l'Américium 241 à 59,54 keV pour tous les tours et bonnets créés.

	Efficacité de comptage (coups/s/gamma)	Bonnets					
		A	B	C	D	E	F
Tour	85	1,60E-02	1,36E-02	1,24E-02	1,19E-02	1,06E-02	-
	90	1,43E-02	1,26E-02	1,20E-02	1,13E-02	1,03E-02	-
	100	-	8,57E-03	7,69E-03	6,85E-03	6,38E-03	5,56E-03
	110	-	3,67E-03	3,22E-03	2,74E-03	2,50E-03	2,27E-03
	120	-	-	1,27E-03	1,13E-03	9,96E-04	7,99E-04

Par ailleurs, l'augmentation du tour de poitrine entraîne une perte de l'efficacité de comptage comme le montre clairement le Tableau II. La perte sensible d'efficacité entre les tours 85-90 et les tours 100-110-120 s'explique de la façon suivante. Les trois plus grands tours de poitrines ont un volume pulmonaire chargé significativement plus grand (30%) que celui des tours 85-90. Les détecteurs étant toujours positionnés identiquement, ils couvrent ainsi le même angle solide et donc le même volume pulmonaire quelque soit le fantôme et la taille des poumons. Mais, puisqu'une distribution volumique de la source a été réalisée dans les poumons, la concentration en activité est sensiblement inférieure dans les poumons de plus grande taille impliquant une réduction dans le nombre de coups détectés. De plus, l'épaisseur extra thoracique provenant des seins et de l'épaisseur du thorax est responsable d'une atténuation supplémentaire des rayonnements accentuée aux basses énergies et explique la perte d'efficacité de comptage entre les modèles 85 et les modèles 90.

3. Mise en équation de la variation de l'efficacité de comptage en fonction de l'énergie et de la morphologie

L'efficacité de comptage dépend fortement de la morphologie de la personne surveillée, de la distribution de l'activité, de la sensibilité des détecteurs et de leur positionnement. Elle est directement liée à l'atténuation des rayonnements par le tissu, qui varie avec la morphologie du sujet. Par conséquent, il est possible d'établir une relation entre deux efficacités simulées impliquant deux contaminations identiques et le même système de comptage mais des sujets de morphologies différentes. Une équation décrivant la variation de l'efficacité de comptage (en fonction de l'énergie) avec la morphologie du fantôme a été développée afin d'estimer l'efficacité de comptage pour toute personne surveillée.

3.1. Développement d'une équation analytique

Dans le cas de la librairie de fantômes développée dans ce travail, les variations de morphologie se limitent à la différence d'épaisseur extra thoracique (seins et tour de thorax) et à la modification du volume des organes internes pour le cas des trois plus grands tours de

poitrine (100-110-120). Pour une différence de volume pulmonaire, il a été démontré que l'efficacité de comptage des détecteurs varie avec l'inverse du volume pulmonaire si une distribution uniforme de l'activité est impliquée (Farah et al. 2010b). Ainsi, un premier paramètre (c_1) a été introduit pour représenter le rapport entre le volume de référence et le nouveau volume pulmonaire. Dans le cas d'une différence d'épaisseur extra thoracique, un second paramètre a été introduit (c_2) pour représenter l'atténuation exponentielle des rayonnements qui dépend de l'épaisseur des tissus traversés et de leur coefficient massique d'atténuation. De ces deux considérations, une équation simplifiée reliant deux efficacités de comptage peut être formulée de la sorte :

$$\varepsilon_2(E) = \varepsilon_1(E)c_1e^{-c_2\mu(E)} \quad (1)$$

Où ε_1 représente l'efficacité de comptage de référence, ε_2 l'efficacité inconnue, E l'énergie, et c_1, c_2 les paramètres à calculer qui reproduisent la variation de l'efficacité de comptage avec la morphologie du fantôme. La fonction $\mu(E)$ est le coefficient massique d'atténuation de l'ICRU-44 (ICRU 1989) pour le tissu adipeux (7 composantes) obtenu en ligne à l'aide de la base de données XCOM du NIST (Berger et al. 2005) pour la source de photons considérée. Cette valeur simplifiée de $\mu(E)$ reste réaliste puisque les trois principales structures présentes dans la région thoracique (graisse, muscle et glande) ont des coefficients massiques d'atténuation similaires aux énergies considérées.

3.2. Utilisation de l'équation développée

Pour utiliser l'équation développée, les paramètres de morphologie c_1 et c_2 doivent être déterminés et une courbe de référence doit être sélectionnée. L'équation a été testée pour reproduire les données simulées, d'abord à partir d'une courbe de référence obtenues par calcul Monte Carlo puis à partir d'une courbe mesurée avec le fantôme Livermore.

3.2.1. Application aux données simulées

L'équation (1) est appliquée aux courbes d'efficacité de comptage simulées (ε_{phant}) en prenant l'efficacité obtenue avec le modèle 85A comme courbe de référence (ε_{ref}). Les paramètres c_1 et c_2 sont obtenus en traçant la variation linéaire de la fonction $Y = \ln(c_1) - c_2 X$ où $Y = \ln\left(\frac{\varepsilon_{phant}}{\varepsilon_{ref}}\right)$ et $X = \mu(E)$. Quand cette équation est appliquée aux modèles de tour de poitrine 85 et 90, le paramètre c_1 est directement pris égal à 1 puisque le volume pulmonaire chargé est le même pour ces fantômes et identique à celui de référence (85A). Une fois obtenu, le paramètre c_2 est utilisé dans l'équation (1) et l'efficacité de comptage est calculée et comparée à la valeur obtenue par simulation MC. La différence maximale observée (i.e. écart relatif) entre les valeurs simulées par MC et celles obtenues par l'équation (1) est un indicateur pratique de la validité du modèle proposé. Cependant, ce paramètre ne donne qu'une indication locale, i.e. pour une énergie donnée, de l'efficacité de l'équation à reproduire les données simulées. Un meilleur indicateur de la qualité de la régression donnant c_2 , peut être calculé avec l'indicateur suivant :

$$\chi^2 = \frac{1}{N-n} \sum_{i=1}^N \left(\frac{\varepsilon_{MC} - \varepsilon_{cal}}{\varepsilon_{MC}} \right)^2 \quad \text{où } N \text{ est le nombre de données simulées (i.e. nombre d'énergies}$$

simulées), n le nombre de paramètres qui varient dans l'équation, ε_{cal} représente les efficacités de comptage calculées par l'équation et ε_{MC} représente celles simulées par Monte Carlo. Ce paramètre donne une indication globale de la pertinence de l'équation puisque la variance est additionnée sur toutes les énergies simulées.

Le tableau III compare les valeurs des efficacités de comptage simulées MC à celles obtenues avec l'équation (1) pour le fantôme 85E, en utilisant le paramètre c_2 et la courbe de référence du 85A. Pour le modèle 85E, la valeur estimée pour le paramètre c_2 , qui représente l'épaisseur de tissu additionnelle, est de l'ordre de 1,87 g/cm². En utilisant cette valeur et l'équation (1), une différence maximale sur les valeurs d'efficacité de comptage de l'ordre de 6,4% est obtenue à l'énergie la plus basse (15 keV). Pour le tour de poitrine 90 et tous les bonnets associés, la différence maximale a été observée à 15 keV et pour le modèle E, avec une valeur de l'ordre de 6% entre l'efficacité simulée et celle donnée par l'équation (1).

Tableau III. Valeurs de c_2 pour les modèles de tour de poitrine 85 et 90 et valeurs associées des paramètres R^2 et χ^2 (gauche). Comparaison des valeurs d'efficacité simulées par MC et calculées avec l'équation (1) pour le modèle 90E à différentes énergies (droite).

Fantôme	c_2 (g/cm ²)	R^2	χ^2	Energie (keV)	Efficacité MC (coups/s/γ)	Efficacité calculée (coups/s/γ)	Ecart Relatif (%)	
85	B	0,86	0,9982	0,8E-4	15,31	1,72E-05	1,61E-05	6,42
	C	1,18	0,9967	2,5E-4	22,16	1,02E-03	1,04E-03	-1,41
	D	1,47	0,9995	0,6E-4	59,54	1,06E-02	1,10E-02	-4,00
	E	1,87	0,9928	13E-4	122,06	1,26E-02	1,31E-02	-3,76
90	A	0,60	0,9875	2,5E-4	185,72	1,10E-02	1,12E-02	-1,93
	B	1,26	0,9964	3,2E-4	356,01	6,46E-03	6,64E-03	-2,69
	C	1,40	0,9943	6 ^E -4	661,66	3,98E-03	4,13E-03	-3,89
	D	1,64	0,9936	9,3E-4	1173,23	2,68E-03	2,78E-03	-3,57
	E	2,05	0,9944	13E-4	1408,01	2,40E-03	2,47E-03	-3,07

Le tableau IV compare les valeurs simulées MC d'efficacité de comptage et celles obtenues avec l'équation (1) pour le fantôme 120F, en utilisant les paramètres c_1 et c_2 et la courbe de référence du 85A. Puisque les modèles 100, 110 et 120 ont le même volume pulmonaire, mais que celui-ci est différent de celui du 85A, le paramètre c_1 doit être utilisé. Pour les fantômes de plus grand tour de poitrine et de différents bonnets (B à F), les efficacités de comptage simulées et celles calculées par l'équation (1) ne diffèrent pas de plus de 5%. Ces résultats valident l'équation développée puisque des différences acceptables (<10%) entre les valeurs simulées d'efficacité de comptage et celles calculées par l'équation (1) ont été obtenues. La Figure 4 compare les courbes d'efficacité de comptage simulées et calculées par l'équation pour les modèles suivants : 85C, 90D, 100E, 110F et 120F.

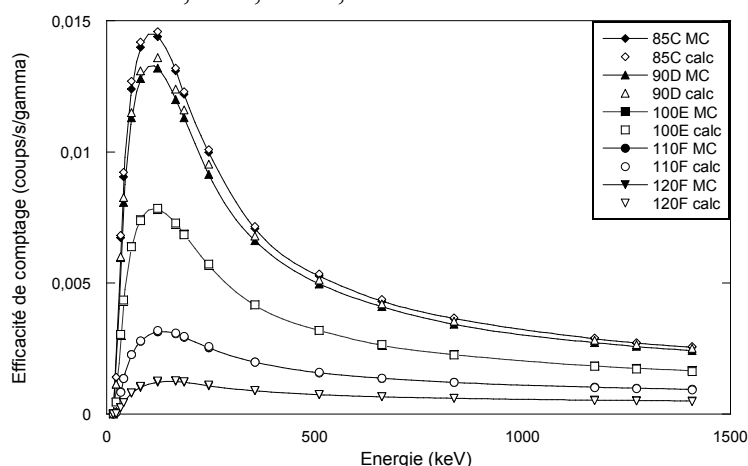


Figure 4. Variation de l'efficacité de comptage (coups/s/gamma) avec l'énergie (keV) : comparaison des valeurs simulées MC (symboles noirs et courbes pleines) et celles calculées par l'équation (1) (symboles blancs) pour les modèles : 85C (diamants), 90D (triangles), 100E (carrés), 110F (cercles) et 120F (triangles inversés). La courbe du 85A étant la référence pour l'équation.

Tableau IV. Valeurs de c_1 et c_2 pour les modèles de tour de poitrine 100, 110 et 120 et valeurs associées des paramètres R^2 et χ^2 (gauche). Comparaison des valeurs d'efficacité simulées par MC et calculées avec l'équation (1) pour le modèle 120F à différentes énergies (droite).

Fantôme	Paramètres				Energie (keV)	Efficacité MC (coups/s/ γ)	Efficacité calculée (coups/s/ γ)	Ecart Relatif (%)	
	c_1	c_2 (g/cm ²)	R^2	χ^2					
100	B	0,73	1,63	0,9986	2E-4	22,16	1,28E-05	1,25E-05	2,42
	C	0,72	2,01	0,9997	1E-4	33,44	2,54E-04	2,47E-04	2,63
	D	0,70	2,51	0,9998	1E-4	40,12	4,42E-04	4,37E-04	1,06
	E	0,71	2,81	0,9996	1E-4	59,54	7,99E-04	8,15E-04	-2,04
	F	0,66	3,17	0,987	7E-4	81	1,02E-03	1,06E-03	-3,47
	110	B	0,53	4,31	0,9985	3E-4	122,06	1,22E-03	1,27E-03
C		0,52	4,87	0,9992	2E-4	165,86	1,25E-03	1,28E-03	-2,64
D		0,51	5,65	0,9993	3E-4	244,7	1,08E-03	1,12E-03	-3,00
E		0,50	5,91	0,9996	1E-4	356,01	8,93E-04	9,00E-04	-0,78
F		0,49	6,20	0,9995	2E-4	511	7,42E-04	7,54E-04	-1,50
120		C	0,34	7,40	0,9994	4E-4	661,66	6,62E-04	6,68E-04
	D	0,33	7,78	0,9996	3E-4	835,84	6,06E-04	5,99E-04	1,17
	E	0,31	8,11	0,9995	4E-4	1173,23	5,37E-04	5,18E-04	3,45
	F	0,29	8,86	0,9990	9E-4	1408,01	5,03E-04	4,81E-04	4,44

3.2.2. Application aux mesures expérimentales

Le modèle donné par l'équation (1) permet une estimation rapide et fiable de l'efficacité de comptage en partant d'une courbe de référence simulée. Cependant, cette courbe de référence n'est pas en pratique disponible. Ainsi, une nouvelle référence a été utilisée : une courbe d'étalonnage expérimental obtenue avec le Livermore. Cette dernière a été transformée pour reproduire les valeurs simulées d'efficacité de comptage avec les 24 fantômes de la librairie.

Dans un premier temps, les valeurs d'efficacité de comptage mesurées avec le mannequin physique Livermore doté de différentes plaques (P0 – P4) sur les installations du Laboratoire d'Analyse Médicale d'AREVA NC de La Hague ont été directement comparées à celles simulées pour les fantômes féminins. Ainsi, il a été observé que les valeurs simulées avec le fantôme 85A sont équivalentes à celles des mesures Livermore associées à la plaque 1 comme le montre le Tableau V. L'écart relatif donné dans ce tableau montre des différences <5 % pour des énergies supérieures à 59,5 keV mais sensiblement plus importantes pour les photons de 22, 33 et 40 keV. Ces valeurs restent cependant acceptables puisque la composition des tissus du modèle 85A et celle du mannequin du Livermore sont loin d'être les mêmes. De cette comparaison ressort la conclusion suivante : le fantôme physique du Livermore associé à la plaque P1 est équivalent à une femme de taille de poitrine 85A en prenant en compte les différents positionnements des détecteurs réalisés.

Tableau V. Valeurs des efficacités de comptage pour la mesure Livermore associée à la plaque P1 et comparaison aux valeurs simulées (MC) pour le modèle 85A

Energie (keV)	P1 efficacité mesurée (coups/s/γ)	Efficacité MC du 85A (coups/s/γ)	Ecart Relatif (%)
15,3	1,21E-04	1,10E-04	8,6
22,2	3,29E-03	2,43E-03	25,9
33,7	1,16E-02	9,41E-03	18,6
40,5	1,44E-02	1,22E-02	15,4
59,5	1,72E-02	1,60E-02	7
81,2	1,76E-02	1,75E-02	0,5
122,1	1,68E-02	1,76E-02	-4,9
165,9	1,51E-02	1,57E-02	-4,2
185,7	1,42E-02	1,46E-02	-2,5
245,0	1,17E-02	1,18E-02	-0,3
356,0	8,36E-03	8,16E-03	2,4
511,13	5,90E-03	5,99E-03	-1,6
661,7	4,75E-03	4,85E-03	-2,2
834,8	4,05E-03	4,03E-03	0,6
1173,2	3,29E-03	3,14E-03	4,5
1274,5	3,08E-03	2,95E-03	4,1
1408,0	2,79E-03	2,76E-03	0,9

Dans un second temps, l'équation (1) a été testée pour transformer une courbe mesurée avec le Livermore (et différentes combinaisons de plaques) en une courbe simulée d'abord à celle du modèle 85A puis aux 23 autres modèles. Les valeurs obtenues pour les paramètres $c_1 - c_2$ sont données dans le Tableau VI avec le coefficient de régression (R^2) associé définissant la qualité de l'interpolation. De ce tableau, il ressort que la meilleure interpolation pour reproduire la valeur de l'efficacité de comptage du 85A est obtenue avec le fantôme Livermore associé à la plaque P4 (de 4,3 cm d'épaisseur) avec un coefficient de régression $R^2 = 0,99$. Ce résultat semble contredire le précédent (équivalence entre mesure P1 et simulation 85A) mais s'explique par une grande dispersion des efficacités mesurées P1 et simulées 85A pour les basses énergies et un très bon accord à partir de 59 keV (cf. Tableau V). Par contre, en utilisant la courbe de référence mesurée avec la plaque P4, une meilleure régression linéaire est obtenue puisque la dispersion des résultats est homogène sur l'ensemble du spectre ; les écarts entre mesure et simulation étant cependant plus importants qu'avec la P1. En utilisant les paramètres c_1-c_2 donnés pour la plaque P4, la valeur simulée de l'efficacité de comptage du modèle 85A est retrouvée avec un écart relatif maximal égal à 8,7 % pour la raie de ^{152}Eu à 40 keV (cf. Tableau VII). La Figure 5 compare les courbes d'efficacité de comptage obtenues par simulations MC et celles calculées par l'équation 1, à partir de la mesure P4, et en utilisant les données des Tableaux V et VI et ce pour les modèles suivants : 85B, 90C, 100D, 110E et 120F. Pour ces exemples, l'écart relatif maximal entre les simulations et les valeurs calculées par l'équation est inférieur à 10%.

Tableau VI. Valeurs de c_1 et c_2 pour les différentes mesures Livermore associées aux différentes plaques et valeurs du coefficient de détermination obtenu par l'interpolation linéaire.

Plaque mesure référence	c_1	c_2 (g/cm ²)	R ²
P0	0,96	1,19	0,964
P1	0,99	0,18	0,206
P2	1,05	-0,14	0,192
P3	1,20	-1,00	0,982
P4	1,30	-1,91	0,990

Tableau VII. Comparaison des efficacités de comptage simulées pour le modèle 85A (MC) et celles estimées par l'équation à partir de la mesure Livermore associée à la plaque P4 à différentes énergies.

Energie (keV)	efficacité calculée à partir de P4 (coups/s/g)	efficacité MC du 85A (coups/s/g)	Ecart Relatif (%)
22,2	2,48E-03	2,43E-03	-2,1
40,5	1,33E-02	1,22E-02	8,7
122,1	1,67E-02	1,76E-02	5,2
356,0	8,16E-03	8,16E-03	0,05
1173,2	3,24E-02	3,14E-03	-3,4

En conclusion, il est possible d'estimer l'efficacité de comptage de tout sujet féminin en utilisant l'équation 1 et la mesure Livermore avec la plaque P4 comme référence. Cependant, cette référence nécessite le recours aux paramètres c_1 et c_2 du Tableau VI pour corriger les différences morphologiques existantes entre le Livermore et le sujet féminin concerné. Par ailleurs, l'utilisation de la plaque P1 comme référence reste possible et ne requiert aucune correction de morphologie intermédiaire ($c_1=1$ et $c_2=0$) mais induit forcément une erreur sur les basses énergies (cf. Tableau V).

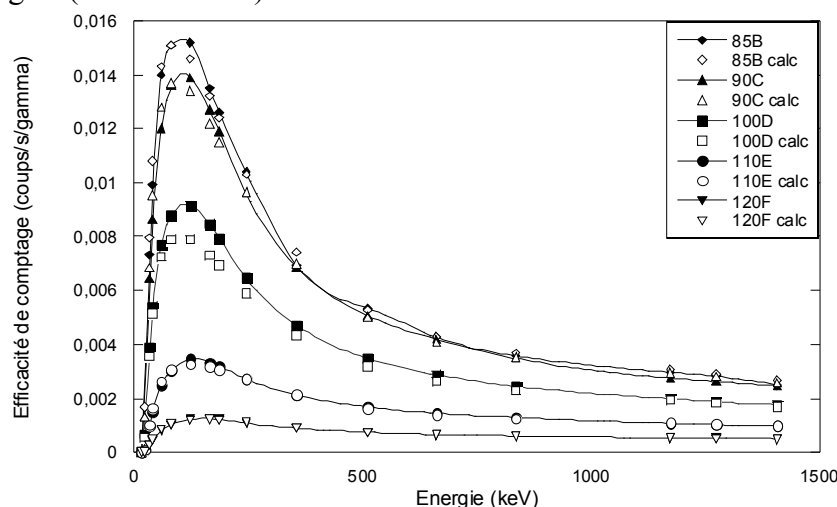


Figure 5. Variation de l'efficacité de comptage (coups/s/gamma) avec l'énergie (keV) : comparaison avec les valeurs simulées MC (symboles noirs et courbes pleines) et celles calculées par l'équation (1) (symboles blancs) pour les modèles : 85B (diamants), 90C (triangles), 100D (carrés), 110E (cercles) et 120F (triangles inversés). La courbe mesurée du Livermore associé à la plaque 4 étant la référence pour l'équation.

3.3. Discussion : corrélation des paramètres avec la morphologie

Dans cette partie, il s'agit de donner une validation supplémentaire de l'équation développée par l'étude de la corrélation des paramètres introduits (c_1 et c_2) avec la morphologie et ce à partir des données simulées ainsi que des mesures Livermore. Cette étude vise aussi à développer une méthode pratique pour le choix des paramètres c_1 et c_2 et pour utiliser

l'équation développée afin d'estimer l'efficacité de comptage en l'absence de modèle numérique représentant le sujet surveillé.

La corrélation de c_1 avec le volume pulmonaire a été étudiée à partir des données simulées MC et des trois plus grands tours de poitrine. Pour les modèles de tour 100, 110 et 120, c_1 est supposé représenter le rapport entre le volume pulmonaire de référence (2,3 L) et celui modifié (2,99 L). Puisque les trois plus grands tours ont le même volume pulmonaire, ils doivent avoir le même paramètre c_1 , quel que soit le bonnet, et avec une valeur de 0,77. Bien que cette valeur de c_1 soit plutôt acceptable pour le tour de poitrine 100 (cf. Tableau IV), c'est loin d'être le cas pour les fantômes de tour 110 et 120 ($c_1 \sim 0,5$ et $0,3$ respectivement). Toutefois, pour un tour de poitrine donné, le coefficient c_1 reste constant pour tous les bonnets conformément aux hypothèses formulées. En réalité, dans les simulations, la distance peau-détecteurs a été modifiée avec la variation du tour de poitrine pour éviter toute collision des détecteurs avec les seins. Ainsi, l'angle solide des détecteurs couvrant les poumons est modifié et le paramètre c_1 ne peut représenter le rapport exact des volumes pulmonaires. De plus, quand la régression linéaire est utilisée, c_1 et c_2 sont simplement les meilleures approximations permettant l'ajustement des données simulées. Les changements du volume des poumons, du tour de poitrine, du bonnet, et de l'angle solide des détecteurs sont naturellement regroupés dans les paramètres c_1 et c_2 . Par ailleurs, la corrélation de c_2 avec l'épaisseur extra thoracique est étudiée pour tous les fantômes et toutes les données simulées. Pour ces modèles, le paramètre c_2 est supposé reproduire une épaisseur moyenne d'atténuation directement reliée à la variation de la taille de poitrine. Puisque cette épaisseur absorbante ne peut pas être exactement définie, il est raisonnable d'étudier la corrélation de c_2 avec la variation de la masse de poitrine entre le modèle de référence (85A) et les autres modèles. La Figure 6 montre que la variation de c_2 avec l'augmentation de la masse des seins suit une tendance linéaire, et ce pour tous les tours créés. Cependant la forme exacte, et en particulier la pente de l'interpolation linéaire, dépend entièrement du tour de poitrine.

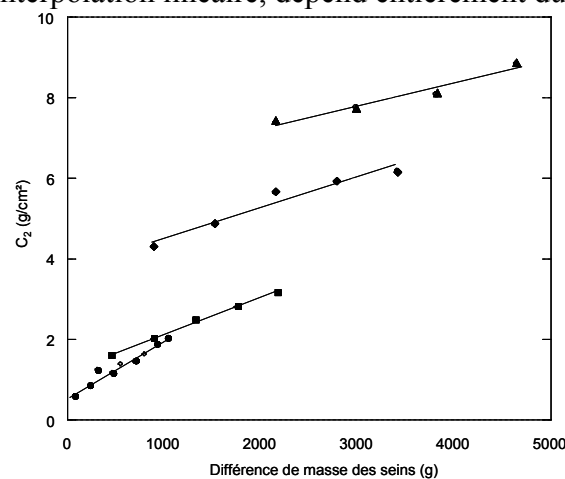


Figure 6. Variation du paramètre c_2 (g/cm²) avec la différence de la masse des seins (g) pour les tours de poitrines 85 -90 (cercles), 100 (carrés), 110 (diamants) et 120 (triangles); Interpolation linéaire effectuée par Microsoft Excel 2008TM: **85-90**: $y = 0.0016x + 0.4034$, $R^2 = 0.952$. **100**: $y = 0.0009x + 1.2424$, $R^2 = 0.994$. **110**: $y = 0.0008x + 3.7414$, $R^2 = 0.955$. **120**: $y = 0.0006x + 6.1098$, $R^2 = 0.961$.

Les mêmes corrélations ont été observées pour les paramètres c_1 et c_2 avec une courbe mesurée Livermore comme référence (P1 ou P4 transformée). En effet, c_2 a montré une variation linéaire avec l'épaisseur de plaque, conformément aux attentes, avec un coefficient de régression (R^2) égal à 0,992. Par ailleurs, c_1 a montré une variation linéaire avec la distance poumons-détecteurs, corrélation étudiée dans le cas où le volume pulmonaire reste inchangé.

Enfin, pour donner une relation pratique pour le choix de c_1 et c_2 , on peut examiner l'existence d'une corrélation entre ces paramètres pour les tours 100, 110 et 120. D'après la Figure 7, une tendance linéaire qui montre la variation de c_1 en fonction de c_2 est observée. Cette corrélation est d'un intérêt particulier puisqu'elle permet le calcul des efficacités de comptage en fonction de la morphologie de la personne surveillée. Quand une bonne estimation de c_2 existe, *i.e.* une estimation de la variation du bonnet, une valeur réaliste de c_1 peut être calculée. A titre d'exemple, cette équation peut être utilisée pour estimer l'efficacité de comptage pour une personne de tour de poitrine 95C pour laquelle aucun modèle numérique n'a été développé. Dans la publication de Turner et Dujon (2005), les auteurs ont estimé que le rajout de masse de tissu pour faire varier le bonnet d'une personne d'un tel tour de poitrine (95) serait le même que celui d'une personne de tour de poitrine 100. En utilisant l'association 95C/100B (ou 100C/110B, 115D/120C) suggérée par Wood et al. (2008), la valeur $c_2 = 1,63$ est tirée du Tableau IV et l'équation donnée dans la Figure 7 est utilisée. Pour ce cas, la valeur estimée du paramètre c_1 est de 0,75. En utilisant ces paramètres et l'équation (1), l'efficacité de comptage obtenue pour le sujet de tour de poitrine 95 et un bonnet C est de $8,7 \cdot 10^{-3}$ coups/s/gamma pour la raie de ^{241}Am à 59,54 keV. Cette valeur d'efficacité de comptage est raisonnablement correcte puisqu'elle est inférieure à celle du modèle 90D ($1,13 \cdot 10^{-2}$ coups/s/gamma) mais supérieure à celle du 100B ($8,57 \cdot 10^{-3}$ coups/s/gamma). Il est suggéré d'utiliser cette méthode pour les tours de poitrine entre 95 et 120 pour lesquels aucun fantôme n'a été développé. Pour les tours entre 80 et 90 il est proposé de simplifier l'utilisation des valeurs de c_2 donnés dans le Tableau III, et ce en utilisant les valeurs obtenues pour le tour 85 quand une personne de tour 80 se présente.

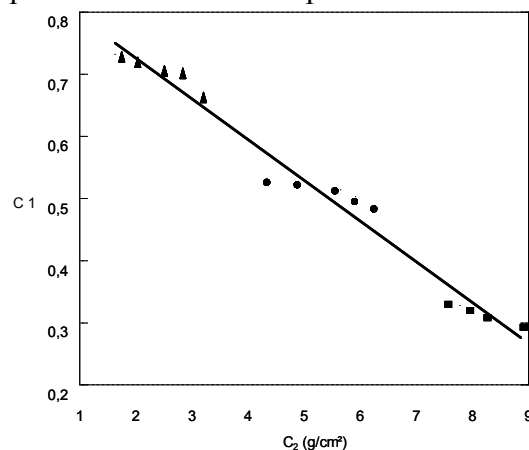


Figure 7. Variation du paramètre c_1 en fonction du paramètre c_2 (g/cm^2) pour les tours de poitrine 100 (triangles), 110 (cercles) et 120 (carrés), chaque point représente un bonnet pour un tour donné; Interpolation linéaire effectuée par Microsoft Excel 2008TM: $y = -0.0656 x + 0.8574$, $R^2=0.9728$.

3.4. Recommandation pratique

L'utilisation de l'équation développée a été étendue, à travers l'étude des corrélations des facteurs morphologiques, pour déterminer les efficacités de comptage pour les femmes pour lesquelles aucun fantôme n'est disponible parmi les modèles de la librairie. Cependant, cette équation reste peu adaptée à une utilisation pratique, qui se veut être rapide et simple, pour corriger les coefficients d'étalonnage en fonction de la morphologie de la travailleuse surveillée. Ainsi des facteurs de correction ont été tabulés, et fournis à AREVA NC, pour une utilisation directe décrivant la perte d'efficacité entre le fantôme physique masculin et le sujet féminin surveillé. Il suffit donc de diviser l'efficacité de comptage obtenue à une énergie donnée avec le mannequin Livermore et la plaque P1 par le coefficient adéquat du Tableau 3.10 (cf. Chapitre 3 Section IV) pour corriger l'effet de la morphologie.

4. Accélération des simulations Monte Carlo par le biais des méthodes de réduction de variance et par la simplification de la géométrie du fantôme

L'optimisation des étalonnages numériques nécessite, en plus d'un fantôme réaliste et personnalisé, des simulations MC fiables et rapides. Le travail réalisé a donc porté sur la réduction du temps de calcul par l'application de méthodes de réduction de variance ou par la simplification de la géométrie du fantôme.

4.1 Problématique et objectifs

La variation de l'efficacité de comptage en fonction de l'énergie, représentée dans la Figure 5 par exemple, montre une dépendance directe entre l'énergie du photon et le comptage. En effet, on distingue sur cette figure trois régions différentes : les très basses énergies (< 30 keV) où l'efficacité est minimale, les moyennes énergies (30 à 356 keV) où l'efficacité est maximale et les très hautes énergies (> 356 keV) où l'efficacité de comptage observée décroît à nouveau. Cette variation de l'efficacité de comptage est particulièrement due à l'atténuation significative des rayonnements de plus basse énergie contre un pouvoir de pénétration trop important pour ceux de très haute énergie.

Dans ce travail, des méthodes de réduction de variance sont utilisées afin d'augmenter le pouvoir de pénétration des photons de basse énergie et pour favoriser les interactions des photons de haute énergie dans les détecteurs. Ceci se traduit par une amélioration de la statistique aux énergies considérées. Par ailleurs, pour les photons dont l'énergie varie entre 30 et 356 keV, les techniques de réduction de variance ont été introduites afin de limiter le nombre de particules simulées à ces énergies et par conséquent réduire le temps de calcul. Cependant, l'introduction des techniques de réduction de variance (RV) ne doit en aucun cas biaiser les résultats et conduire à de fausses convergences. Pour cela, le résultat des simulations avec RV sera comparé à celui de référence pour chacune des méthodes utilisées. Enfin, il s'agit d'identifier les méthodes de RV les plus simples à mettre en place pour une utilisation en routine et de tester leur efficacité avec deux fantômes différents en termes de nombre de structures et d'organes mais aussi avec un nombre de voxels et une taille de voxels bien différents. Dans cette partie, on a comparé l'efficacité des méthodes de RV à accélérer le calcul pour un modèle voxelisé du fantôme physique Livermore et le nouveau fantôme féminin de référence de la CIPR.

4.2 Principe et fonctionnement des méthodes de réduction de variance

La réduction de variance a pour objectif de favoriser la propagation des particules ayant la plus grande probabilité de participer au résultat. Deux catégories de techniques ont été utilisées les « Modified Sampling Methods » parmi lesquelles la « cell importance card » et les « Weight Windows » et les « Population Control Methods » dont les cartes de biaisage de la nature et de la direction de l'émission de la source, la carte de collision forcée et la carte « exponential transform ».

4.2.1. Cell Importance (IMP)

Une importance est systématiquement associée à chaque cellule et est utilisée lors de la propagation des particules. Le devenir d'une particule dépend du rapport entre la cellule où elle entre et celle qu'elle quitte. Si ce rapport est supérieur à 1, la particule initiale est divisée suivant la fonction de division appelée « Splitting » à autant de particules fille que la valeur du rapport d'importance de cellules. Le poids des particules filles engendrée par cette division est égale au poids de la particule mère divisé par le nombre de particules filles créées. Par

ailleurs, si le rapport des importances entre les cellules est inférieur à 1, une fusion à l'aide de la fonction « Russian Roulette » est opérée afin de regrouper plusieurs particules de même énergie et le poids est aussi ajustée.

Pour ces simulations, l'importance associée aux différentes cellules a été triplée dans la direction des détecteurs. En effet, l'importance des cellules poumons (organe source) a été fixée à 1, celle du tissu résiduel du thorax a été fixée à 3, pour la plaque thoracique (cas du Livermore) et pour les poitrines (cas du fantôme féminin) l'importance des cellules était de 9 et celle de la fenêtre d'entrée du cristal détecteur était de 18. Pour le fantôme féminin, l'utilisation de cette carte reste plus délicate du fait de la présence de 198 cellules dans le fichier MCNPX pour lesquelles l'importance à associer doit être minutieusement choisie.

4.2.2. Weight Windows (WW)

Pour contrôler les fluctuations du poids des particules à la suite des différentes interactions, les fenêtres de poids ont été utilisées. La gestion des fluctuations utilise également les processus de Splitting et de Russian Roulette. Dans le premier cas, il s'agit de diviser des particules dont le poids dépasse la limite haute de la WW, les particules fils se partagent le poids de la particule mère. Dans le second cas, l'objectif est de fusionner des particules dont le poids est inférieur à la limite basse de la WW, ainsi le poids des particules résultantes représente la somme des poids des particules primaires. Ces WW sont générées d'abord d'une façon aléatoire par le code MCNPX en utilisant un tally f6 puis plusieurs itérations sont répétées afin de les optimiser pour le tally f8 et la géométrie considérée. Pour cette étude, les WW ont été créées en utilisant des maillages sphériques ou rectangulaires couvrant le fantôme (spherical or cylindrical mesh-based weight windows).

4.2.3. Source biasing (SB & VEC)

Cette carte est l'une des premières méthodes de réduction de variance mise en place pour le code MCNPX. Elle est simple d'utilisation et permet de modifier la nature et la direction d'émission de la source. En effet, grâce à l'utilisation de cette carte, il est possible d'augmenter la proportion de particules émises à une énergie donnée (notée SB) ou de favoriser les émissions vers les détecteurs (notée VEC). Ainsi, avec la SB, le nombre de particules de très basse énergie, particulièrement celles émises à 15 keV, a été multiplié pour augmenter la probabilité d'en collecter à la sortie du fantôme. Par ailleurs, le nombre de particules simulées de moyenne énergie (30 à 356 keV) a été sensiblement réduit pour gagner du temps tout en conservant une très bonne efficacité de comptage. De plus, avec VEC, les particules simulées ont toutes été émises dans le plan contenant les détecteurs ; celles allant vers le dos du fantôme ayant une très faible probabilité de diffuser et revenir aux détecteurs.

4.2.4. Forced collision (FCL)

Les photons de très haute énergie (>356 keV) ont un pouvoir de pénétration très important et traversent tout le corps et même les détecteurs avec très peu d'interactions. Pour favoriser la collecte des photons de ces énergies, la collision a donc été forcée dans les cellules sensibles des détecteurs. L'utilisation de cette carte est également très simple puisqu'il suffit d'identifier les cellules concernées par la collision forcée (cellules actives en germanium) et de changer la probabilité de collision des photons qui y rentrent.

4.2.5. Exponential transform (EXT)

Cette carte permet de faire varier le libre parcours moyen des particules et a été implémentée pour favoriser la pénétration des structures denses telle que les os par les photons de faible énergie. Pour appliquer cette méthode, il s'agit d'identifier les cellules concernées puis de

définir une direction vers laquelle les particules doivent être favorisées (généralement vers le centre des détecteurs) ainsi qu'un facteur d'augmentation du libre parcours moyen. L'utilisation de cette carte aboutit cependant à une forte fluctuation du poids des particules d'où la nécessité de lui associer des WW. Enfin, il est à noter que cette carte est d'une utilisation plus difficile à mettre en place en pratique.

4.3 Résultats des méthodes de réduction de variance

Les différentes méthodes de RV ont été testées individuellement pour étudier leur effet sur le temps de calcul, l'efficacité de comptage et l'erreur statistique associée. De plus, les cartes ont été combinées afin de vérifier qu'il est possible de bénéficier de l'apport de chacune des méthodes et que ces dernières restent compatibles et ne biaisent pas le résultat quand elles sont combinées entre elles.

Les différentes méthodes de RV appliquées ont influencé le temps de calcul, l'incertitude statistique et l'efficacité de comptage. Certaines méthodes, comme le biaisage de la nature de la source ainsi que le biaisage de la direction d'émission, ont sensiblement réduit le temps de simulation (jusqu'à un facteur 20). D'autres méthodes, comme la carte de collision forcée et la carte d'augmentation du libre parcours moyen, ont surtout amélioré l'erreur statistique associée au calcul. Enfin, quelques méthodes comme les WW et l'importance des cellules ont montré des résultats plutôt décevants. Le Tableau VIII résume les différentes grandeurs d'intérêt obtenues avec le fantôme féminin de la CIPR et les combinaisons de méthodes de RV. Ces résultats sont donnés uniquement pour les photons de 15 keV, ces derniers étant les plus difficiles à simuler. Pour toutes les autres énergies, l'écart relatif maximal observé entre l'efficacité de comptage sans et avec RV reste <5% quelle que soit la méthode utilisée.

Tableau VIII. Résumé des valeurs obtenues, en combinant les différentes méthodes de réduction de variance, pour le fantôme CIPR féminin et les photons de 15 keV. (L'étoile indique une combinaison par exemple, FCL* = SB + FCL)

Méthode	Efficacité comptage (coups/s/gamma)	Erreur relative statistique (%)	Ecart à la référence (%)	Facteur réduction temps
SB	4.68E-05	3.31	-3.53	10.6
FCL*	4.63E-05	2.95	-2.51	10.6
VEC*	4.35E-05	3.03	3.84	19.8
IMP*	4.04E-05	2.34	10.72	7.3

La combinaison des méthodes de réduction de variance a permis de bénéficier de l'apport de chacune des cartes pour optimiser les simulations. Les méthodes les plus faciles à mettre en place pour une utilisation en routine sont celles relatives au biaisage de la source (nature et direction d'émission) et la collision forcée. Les autres cartes utilisées sont plus difficiles à mettre en œuvre et restent d'un intérêt limité. En effet, le recours à des itérations multiples pour générer les meilleurs WW réduit l'intérêt pour cette carte surtout que l'on cherche à réduire le temps de simulation. Cette observation concerne également l'utilisation de la carte EXT qui fait aussi appel aux WW. Pour la carte IMP, le choix manuel de l'importance des cellules reste délicat et la complexité augmente avec le nombre de cellules concernées.

Enfin, une version parallélisée du code MCNPX a été implémentée et les calculs sont désormais lancés sur 32 processeurs en parallèle. Ainsi un calcul Monte Carlo comprenant l'utilisation de différentes combinaisons de méthodes de RV et parallélisé sur les 32 processeurs nécessite seulement 1 à 2 h de simulations quand, auparavant, 7 jours de calculs étaient nécessaires pour obtenir le résultat requis.

4.4 Simplification de la géométrie du fantôme

En plus des facteurs liés au code de calcul Monte Carlo, des facteurs liés aux détecteurs et au fantôme peuvent être considérés pour réduire le temps de calcul. En effet, le fantôme voxelisé Livermore est beaucoup plus simple que celui de la CIPR et contient moins d'organes et de structures, mais le nombre de voxels contenus dans le Livermore est beaucoup plus élevé. Pourtant, le temps de simulation reste relativement similaire avec les deux fantômes. En conséquence, le gain de temps dû à la simplicité du Livermore est malheureusement compensé avec le temps perdu à cause du nombre de voxels du fantôme. Ainsi, l'accélération des simulations par la simplification de la géométrie du fantôme a été envisagée. Les opérations de simplification comprennent le rajout de plans d'importance nulle et la réduction du nombre de voxels du fantôme à l'aide de la fonction rebin.

4.4.1. Plans d'importance nulle

Les particules allant vers la tête, vers les pieds et dans le dos du fantôme ont peu de probabilité de revenir par diffusion aux détecteurs. Ainsi, afin de gagner du temps en évitant de propager de telles particules, des plans d'importance nulle ont été rajoutés. Ces derniers arrêtent toute particule le traversant. L'introduction de ces plans est très simple et très facile à mettre en place. Les résultats ont montré une réduction du temps de simulation d'un facteur 1.3 et sans impact sur l'efficacité de comptage. Ces plans peuvent également être utilisés en association avec les méthodes de réduction de variance pour une réduction supplémentaire du temps de calcul. Cependant, il faut noter que cette méthode annule toute possibilité de diffusion des particules vers les détecteurs et ne tient pas compte de l'ensemble des murs et de tout objet « diffusant » présent dans la cellule de mesure.

4.2.4. Fusion de voxels

Cette étude cherche à minimiser le temps de simulation par la réduction du nombre de voxels contenus dans le fantôme. Pour cela, une procédure a été développée, sous IDL, qui utilise la fonction « rebin » pour fusionner les voxels et réduire la taille de la grille de moitié. Pour maintenir un volume d'organe correct, la taille du voxel élémentaire est nécessairement doublée. De plus, l'option « /sample » de la fonction « rebin » a été utilisée afin que la fusion de voxels ne résulte pas en la création d'une nouvelle couleur. La fonction rebin a été appliquée au fantôme voxelisé Livermore et à celui de la CIPR et les fantômes fusionnés résultants ont été validés par la comparaison des volumes de toutes leurs structures avec les modèles initiaux. Les résultats montrent que l'opération de fusion de voxels n'a pas induit des différences de volume de plus de 1% sur la plupart des organes des deux modèles. Seules quelques différences significatives (> 5%) ont été observées pour les petites structures du fantôme féminin (la partie corticale du sternum par exemple) mais ces dernières ont un impact limité sur la simulation des mesures anthroporadiométriques. Les résultats observés montrent une réduction du temps de calcul d'un facteur 2, pour une réduction du nombre de voxels de moitié. Les simulations avec les fantômes fusionnés et les méthodes de réduction de variance ont confirmés l'intérêt et la cohérence des opérations sur la géométrie et sur le code lui même. Cependant, il faut noter que l'utilisation de la fonction « rebin » réduit sensiblement le nombre de voxels du fantôme et résulte par une perte significative de résolution spatiale.

4.5 Traitement des fichiers de sortie MCNPX

Par ailleurs, un algorithme de traitement des fichiers de sortie a été développé (Linux/Unix) pour automatiser l'extraction des valeurs des efficacités de comptage. En effet, le résultat des simulations Monte Carlo, donnés dans le tally f8, représente un nombre de coups collectés par les détecteurs pendant une seconde et pour une particule source émise (efficacité en coups/s/gamma). Cependant, il est nécessaire de traiter cette valeur d'efficacité de comptage afin d'en déduire la contribution du Compton. Ceci est particulièrement important dans le cas où plusieurs photons sources de différentes énergies sont simulés dans un même fichier. L'algorithme développé commence le traitement du fichier de sortie par la recherche des raies simulées puis calcule pour chacune des raies l'efficacité de comptage et l'incertitude associée. Cet algorithme fournit également l'équation polynomiale d'ordre 6 régissant la variation de l'efficacité de comptage en fonction de l'énergie. En sortie, l'algorithme de traitement écrit deux fichiers, le premier présentant les valeurs numériques simulées et calculées (fichier .txt) alors que le second fichier présente la variation en fonction de l'énergie en comparant les données simulées à celle de l'équation polynomiale développée (cf. Figure 8).

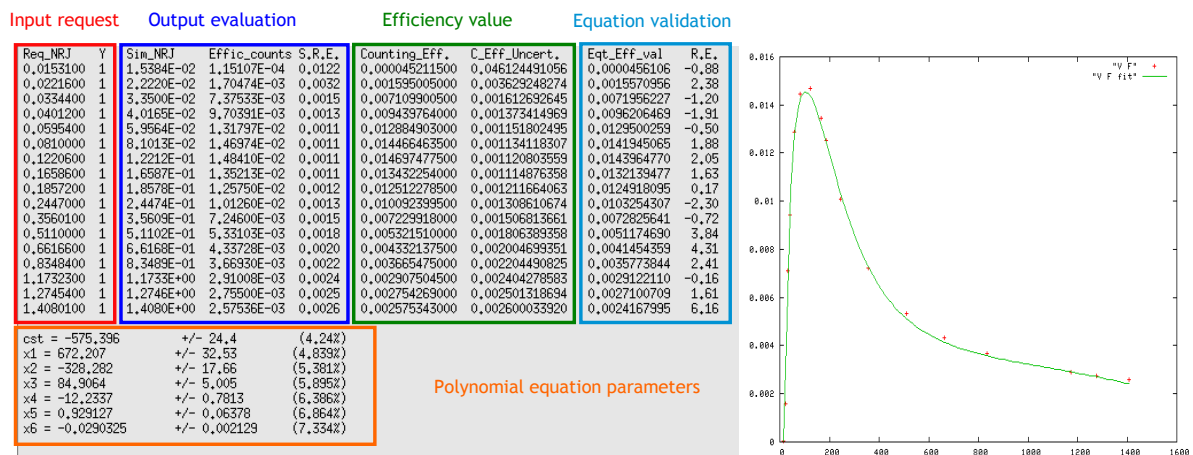


Figure 8. Les deux fichiers de sortie fournis par l'algorithme de traitement des fichiers MC.

5. Prise en charge des contaminations complexe et méthodologie de mesure pour la cartographie d'activité dans le corps

La troisième partie de la thèse porte sur l'étude des cas complexes de contamination où très peu d'informations sont présentes sur la localisation et la nature de la contamination. Dans ce cas, il est très difficile d'estimer l'activité incorporée par de simples mesures spectrométriques comme par exemple dans le cas d'une vieille contamination. Ici, il est proposé de remonter à la cartographie d'activité dans chaque organe par l'utilisation des calculs Monte Carlo couplées à des mesures expérimentales.

5.1. Méthode pour déterminer la répartition de l'activité

La méthode consiste à séparer la contribution au comptage total, de chacun des organes potentiellement contaminés. En effet, pour une mesure pulmonaire par exemple, les détecteurs collectent l'ensemble des radiations émises par les poumons, les côtes, le foie ou tout autre organe chargé. Pour déterminer correctement l'activité présente dans chaque organe, il faut absolument séparer le nombre de coups en provenance de chacun. Dans ce cas, le taux de comptage total n'est autre que la somme des comptages réalisés quand chacune des sources est présente seule suivant la formule ci-dessous :

$$\tau_{\text{exp}} = y_i \sum_{\text{organ}} .A_{\text{organ}} .\varepsilon_{\text{organ}}^{\text{det.ector. position}} \quad (\text{Equation 2})$$

Où τ_{exp} est donné en coups/s, le rendement de la raie (y_i) en γ /désintégration nucléaire, l'activité en Bq et l'efficacité de comptage, i.e. coefficient de contribution au comptage, en coups/s/ γ .

Pour deux organes chargés et deux positions de comptage, cette relation s'écrit :

$$\begin{pmatrix} \tau_{\text{exp}}^{\text{det.pos.1}} \\ \tau_{\text{exp}}^{\text{det.pos.2}} \end{pmatrix} = y_i \begin{pmatrix} \varepsilon_{\text{poumon.droit}}^{\text{det.pos.1}} & \varepsilon_{\text{poumon.gauche}}^{\text{det.pos.1}} \\ \varepsilon_{\text{poumon.droit}}^{\text{det.pos.2}} & \varepsilon_{\text{poumon.gauche}}^{\text{det.pos.2}} \end{pmatrix} \times \begin{pmatrix} A_{\text{poumon.droit}} \\ A_{\text{poumon.gauche}} \end{pmatrix} \quad (\text{Equation 3})$$

La résolution de ce système nécessite donc autant de mesures que d'organes potentiellement contaminés. Les mesures donnent le taux expérimental de comptage qui intègre l'ensemble des coups collectés par les détecteurs et issus des organes chargés. Par ailleurs, les simulations MC fournissent les coefficients de la matrice des contributions. Ensuite, le système de l'Equation 3 est inversé pour déterminer la répartition de la contamination. Pour cette méthode, il faut donc, au départ, identifier les organes de rétention plausibles.

5.2. Etude de faisabilité et mesures expérimentales

Pour valider la méthode de séparation, des mesures ont été effectuées à l'IRSN en utilisant le fantôme Livermore et des poumons radioactifs chargés avec de l'américium. Le Livermore permet une séparation physique de la contribution de chaque organe puisqu'il suffit d'utiliser séparément chacun des poumons pour déterminer le nombre de coups qui en provient au détecteur. L'activité des poumons américium utilisés était de 34,6 kBq pour le poumon droit et de 25,7 kBq pour le gauche. Par ailleurs, pour ces mesures, un détecteur de type LOAX dédié pour les mesures spectrométriques basses énergies a été utilisé. Ce détecteur a été positionné à 2 cm de la peau de façon à couvrir au mieux le poumon chargé. Un temps de mesure de 40 min a été considéré afin de garantir une erreur statistique sur la mesure $< 1\%$. Pour une position donnée du détecteur (en face du poumon droit par exemple) les deux poumons ont d'abord été chargés simultanément et la mesure réalisée. Ensuite, deux mesures ont été effectuées pour le même positionnement mais avec cette fois un seul poumon. Le Tableau IX présente le résultat des mesures pour les différentes positions du détecteur et les différentes configurations de poumons chargés.

Tableau IX. Taux de comptage (coups/s) mesuré avec le LOAX à deux positions distinctes et différentes configurations de poumon chargé.

Organe chargé	2 poumons	Poumon droit seul	Poumon gauche seul
Détecteur droit	97,84	91,04	4,46
Détecteur gauche	45,86	10,57	35,65

Les valeurs de ce tableau sont ensuite reportées dans l'Equation 3. Le comptage obtenu quand les 2 poumons ont été chargés à la fois représente le taux expérimental. Les configurations où un seul poumon est chargé à la fois déterminent la matrice des coefficients de contribution après normalisation par l'activité du poumon en question (contribution en coups/s/Bq). Ensuite le système est inversé et l'activité dans chaque poumon est estimée. Dans ce cas, la méthode donne une activité de 35,54 kBq pour le poumon droit et 25,26 kBq pour le poumon gauche. Ces valeurs sont à moins de -2,7% d'écart par rapport aux valeurs réelles ce qui démontre l'efficacité de la méthode pour déterminer la répartition de l'activité.

Par la suite, l'influence du positionnement du détecteur sur l'estimation de la répartition de l'activité a été étudiée. Les résultats ont démontré que l'activité peut être sous estimée avec 22% d'erreur du fait d'un mauvais choix de positionnement des détecteurs. De même, des sources ponctuelles perturbatrices ont été insérées dans le fantôme afin de représenter par exemple des ganglions lymphatiques contaminés ou une vieille contamination dans l'os. Les résultats ont montré que de telles sources perturbatrices biaisent sensiblement les mesures et faussent l'estimation de l'activité. Cependant, la méthode a démontré des capacités limitées à identifier la présence de telles sources uniquement dans certaines configurations (source très proche du détecteur). Enfin, l'adéquation des modèles biocinétiques qui déterminent la répartition de la contamination a été étudiée. Il s'agit dans ce cas, d'étudier l'effet sur l'estimation de l'activité, d'un organe potentiellement chargé non pris en compte dans les hypothèses sur la répartition de la contamination. Les résultats ont clairement montré que de telles erreurs faussent complètement l'estimation de l'activité mais restent facilement identifiables.

5.3. Simulations Monte Carlo et test de la méthode

Séparer les contributions de chaque organe reste cependant impossible quand il s'agit d'une personne contaminée puisque l'on ne peut isoler un organe à l'intérieur du corps et le compter seul. D'où l'intérêt des simulations Monte Carlo qui permettent le calcul des coefficients de contribution en utilisant un modèle voxelisé de la personne concernée créé à partir d'images médicales. Pour appliquer cette méthode, cependant, une reproduction exacte des conditions de mesure est nécessaire et la modélisation des détecteurs utilisés doit être aussi bonne que possible.

Pour valider la méthode Monte Carlo du calcul des contributions, les mesures réalisées avec le Livermore ont été simulées. Dans ce cas, un fantôme voxelisé Livermore a été créé à partir d'images tomodensitométriques du mannequin physique. Ensuite, l'activité a été chargée successivement dans chacun des poumons et les détecteurs ont été positionnés conformément aux mesures expérimentales. Le Tableau X présente les coefficients de contribution obtenus par simulation ainsi que l'écart par rapport aux valeurs expérimentales. L'utilisation de ces coefficients dans l'Equation 3 a pour résultat de fausser l'estimation de l'activité des poumons puisque des différences allant jusqu'à 16% ont été observées. Ces erreurs sur l'estimation de l'activité proviennent essentiellement des valeurs obtenues pour les simulations avec des tirs croisés, i.e. dans le cas où le détecteur est en face du poumon non chargé, et remettent en cause la modélisation du détecteur. Un travail de repositionnement des détecteurs lors des simulations et de correction de l'épaisseur de la couche morte périphérique du détecteur ont été réalisées. Le modèle amélioré réduit les erreurs sur l'estimation de l'activité à moins de 5% et permet de démontrer la faisabilité de la méthode même quand des matrices calculées de contribution sont utilisées.

Tableau X. Matrice des efficacités de comptage (coups/s/ γ) déterminée par calcul Monte Carlo et représentant la contribution de chaque organe pour une position donnée du détecteur.

Organe chargé	Poumon droit seul		Poumon gauche seul	
	Coeff.	Diff. (%)	Coeff.	Diff. (%)
Détecteur droit	2,73E-03	-3,7	1,96E-04	-13,3
Détecteur gauche	5,17E-04	-69,2	1,38E-03	0,8

5.4. Application à d'autres systèmes de comptage et d'autres protocoles de mesure

Deux études supplémentaires ont été réalisées par la suite afin de tester l'efficacité de la méthode avec d'autres sources (europium, uranium etc.), différents organes radioactifs (poumons, foie etc.), mais aussi divers systèmes de comptage avec différents positionnements. Ainsi, une première série de mesures a été effectuée au CIEMAT (Madrid) avec des poumons chargés simultanément avec de l'euporium et de l'américium ainsi qu'un système de 4 détecteurs germanium. De même, des mesures ont été réalisées au KIT (Karlsruhe) en utilisant des poumons et un foie chargés avec de l'américium et un détecteur germanium haute pureté afin de valider la méthode pour trois organes simultanément chargés.

Les résultats obtenus ont démontré l'efficacité de la méthode quelque soit le système de mesure utilisé, le radionucléide concerné et le nombre d'organes chargés pourvu que des mesures adaptées soient réalisées. Bien que l'utilisation des simulations Monte Carlo pour la détermination des matrices de contribution montre des limites (mauvaise gestion des tirs croisés, reproduction du positionnement des détecteurs), les résultats obtenus ont démontré l'intérêt de la méthode pour déterminer la cartographie de l'activité incorporée.

6. Conclusions et perspectives

6.1. Chaîne de traitement pour les étalonnages numériques

Dans ce travail, 24 fantômes thoraciques féminins ont été créés aux formats 3D flexibles Mesh et NURBS pour représenter les mensurations les plus communes. Ces modèles combinent différents tours de poitrines (85-120), bonnets (A-F), organes internes et morphologies et compensent l'absence des modèles physiques féminins pour l'étalonnage des installations d'anthroporadiamétrie.

Les simulations MC ont été réalisées pour les énergies les plus communément utilisés pour les étalonnages anthroporadiamétriques. De plus, un système de comptage typique formé de 4 détecteurs germanium a été utilisé. La réduction de l'efficacité de comptage de ces détecteurs avec l'augmentation de la taille du bonnet et du tour de poitrine a ainsi pu être quantifiée. Par la suite, la mise en équation de la variation de l'efficacité de comptage en fonction de la morphologie a été réalisée. L'influence de la variation de l'épaisseur extra thoracique et du volume de l'organe chargé sur le comptage a été déterminée. Enfin, l'équation établie a été reliée aux mesures obtenues avec le fantôme Livermore et des recommandations ont été données pour généraliser son utilisation à toute personne surveillée.

Les étalonnages numériques étant directement liés à la fiabilité et la rapidité des simulations Monte Carlo, la suite du travail a donc porté sur l'accélération des calculs par le biais des méthodes de réduction de variance ainsi que par la simplification de la géométrie du fantôme.

La réduction de variance a pour objectif de favoriser la propagation des particules ayant la plus grande probabilité de participer au résultat. Les cartes de biaisage de la nature et de la direction de l'émission de la source, la carte de collision forcée et les cartes de « fenêtres de poids » (Weight Window) couplées à la carte « exponential transform » ont été testées. Celles-ci ont permis d'augmenter le nombre de coups dans les détecteurs en biaisant l'émission, en favorisant les interactions des photons de haute énergie dans les cellules des détecteurs et/ou en augmentant le pouvoir de pénétration des photons de basse énergie pour atteindre les cellules actives des détecteurs. Les méthodes appliquées ont permis une réduction totale du temps de simulation d'un facteur 20 avec des valeurs d'efficacité de

comptage en accord avec les situations de référence (sans RV) puisque l'écart relatif maximal observé reste <5% quelle que soit l'énergie du radionucléide simulé. La simplification du fantôme, quand à elle, a compris l'introduction de plans d'importance nulle qui arrêtent la propagation de particules qui y arrivent et la réduction du nombre de voxels par l'utilisation de la fonction de fusion « rebin ». La première opération a donné un facteur 1.3 de réduction du temps de calcul alors que la fusion des voxels a réduit de moitié le temps. Cependant, ces opérations restent d'un intérêt limité puisque dans le premier cas aucune particule diffusée n'est collectée et dans le second, la résolution du fantôme est sensiblement perdue.

Enfin, les mêmes gains en temps de calcul ont été obtenus pour le fantôme voxel équivalent Livermore et le modèle beaucoup plus complexe du thorax de la femme de référence de la CIPR. Par ailleurs, un algorithme de traitement des fichiers de sortie a été développé (Linux/Unix) pour automatiser l'extraction des valeurs des efficacités de comptage et pour fournir l'équation polynomiale de degré 6 donnant la variation de l'efficacité de comptage avec l'énergie. De plus, une version parallélisée du code MCNPX a été implémentée et les calculs sont désormais lancés sur 32 processeurs en parallèle, ainsi un facteur de réduction de temps de 20 à 30 a été obtenu selon la complexité du fichier d'entrée.

6.2. Prise en charge de contaminations complexes

Les mesures anthroporadiométriques sont souvent effectuées sous des hypothèses d'une distribution connue de l'activité. Cependant, les cas complexes de contamination impliquant plusieurs voies d'incorporations avec un mélange d'éléments radioactifs de différents types et solubilités sont particulièrement difficiles à gérer. De plus, quand on ne connaît pas précisément la date d'incorporation le positionnement des détecteurs reste délicat. Dans ce cas, il est proposé de remonter à la cartographie d'activité dans chaque organe par l'utilisation des calculs Monte Carlo couplées à des mesures expérimentales. La méthode consiste à séparer la contribution au comptage total, de chacun des organes potentiellement contaminés.

Pour valider la méthode, une série de mesure a été effectuée au LEDI avec le fantôme Livermore qui permet la séparation physique de la contribution de chaque organe. Les premiers résultats démontrent la faisabilité de cette méthode puisque les activités des poumons ont été estimées avec seulement 3% d'écart en utilisant les mesures Livermore. Des cas plus complexes de répartition d'activités ont été réalisés par l'utilisation d'un foie chargé et de différents types de poumons radioactifs (Europium, Uranium etc.). Ces travaux ont été réalisés en collaboration avec le KIT à Karlsruhe et le CIEMAT à Madrid. Les mesures réalisées ont permis de valider la méthode pour d'autres systèmes de comptage et avec un positionnement différent des détecteurs. De même, cette méthode a montré une grande efficacité à gérer des situations comprenant 3 organes radioactifs simultanément chargés. Ainsi, la méthode a été considérée valable quelque soit le nombre d'organes contaminés pourvu que les mesures adaptées soient réalisées.

Par ailleurs, quand le calcul Monte Carlo a été utilisé pour estimer l'activité des poumons, les simulations ont donné un écart inacceptable (> 10%). Cette erreur sur l'estimation de l'activité provient essentiellement des valeurs obtenues pour les simulations avec des tirs croisés, dans le cas où le détecteur est en face du poumon non chargé, et remet en cause la modélisation du détecteur. Plusieurs mesures correctives ont été envisagées comprenant la correction du positionnement des détecteurs, la variation des inclinaisons des détecteurs et la modification de la taille de l'épaisseur de la zone morte du cristal. Lors de toute nouvelle modélisation de détecteurs, il a été décidé de réaliser des expériences avec des sources ponctuelles excentrées afin de modéliser correctement les tirs croisés.

6.3. Perspectives

Pour aller plus loin dans la démarche de personnalisation de la mesure *in vivo*, un projet en cours vise au développement d'une plateforme de raisonnements à partir de cas qui permet de sélectionner dans une base de données (la librairie développée), le fantôme le plus similaire pour chaque sujet surveillé (Bopp et al. 2009, Farah et al. 2011, Henriot et al. 2010). Le choix du fantôme le plus similaire se base sur la comparaison des caractéristiques de chaque fantôme (taille, poids, âge, volume pulmonaire etc.) à celles du sujet surveillé. Ce modèle est par la suite adapté à la morphologie de la personne à l'aide des réseaux de neurones (Makovicka et al. 2009). Pour ce faire, l'algorithme apprend les coordonnées de points caractéristiques définissant chaque organe et propage ensuite, à travers les réseaux de neurones, l'information relative aux caractéristiques du sujet surveillé (taille, morphologie etc.) afin d'ajuster ces coordonnées.

L'efficacité du raisonnement à partir de cas dans le choix du fantôme le plus similaire a atteint les 85% quand le fantôme équivalent personne existait selon les critères de choix retenus. Par ailleurs, l'adaptation via les réseaux de neurones s'est avéré être un processus très efficace puisque le code a réussi à reproduire correctement le volume cible (erreur <1%) pour les 8 fantômes utilisés (Laurent et al. 2010). De plus, l'adaptation est très rapide puisque la position de plus de 2400 points caractéristiques est calculée en quelques dizaines de millisecondes en utilisant un processeur double cœur très commun (2.1 GHz).

Enfin, l'IRSN a développé des moyens mobiles d'intervention en cas de crise dont le Laboratoire Mobile d'Anthroporadiométrie (LMA). Afin d'optimiser le suivi des travailleurs surveillés par le LMA, la modélisation du système de comptage a été entreprise pour réaliser des étalonnages numériques. En effet, grâce aux calculs Monte Carlo, des facteurs correctifs seront donnés pour une meilleure prise en charge de la morphologie du travailleur. Ceci est d'autant plus stratégique que l'IRSN a été amené à effectuer plusieurs expertises et mesures anthroporadiométriques avec le LMA pour des travailleurs de différents services hospitaliers de médecine nucléaire. Ainsi, une estimation des plus réalistes de l'activité incorporée pourrait être donnée par le LMA quand les mesures *in vitro* classiques (urines, selles) restent peu efficaces dans la détection de la contamination.

List of notations

AF-RCP	Adult Female Reference Computational Phantom
ANN	Artificial Neural Network
CBR	Case Based Reasoning
CT	Computed Tomography
CWT	Chest Wall Thickness
DICOM	Digital Imaging and Communications in Medicine
EXT	Exponential transform
FCC	Forced Collision Control
FCL	Forced Collision
HPGe	High Purity Germanium
ICRU	International Commission on Radiation Units and measurements
ICRP	International Commission on Radiological Protection
IDL	Interactive Data Language
IRSN	French Institute for Radiological Protection and Nuclear Safety
IMP	Cell Importance
MRI	Magnetic Resonance Imaging
LANL	Los Alamos National Laboratory
LEDI	Internal Dose Assessment Laboratory
MC	Monte Carlo
MCNP(X)	Monte Carlo N-Particle (eXtended)
Mesh	Triangular Mesh geometries
MIRD	Committee on Medical Internal Radiation Dose
NPS	Number of Starting Particles
NURBS	Non Uniform Rational B-Splines
OEDIPE	Tool for personalized internal dosimetry evaluation
PHT	Pulse Height Tally
Rhino 3D	Rhinoceros 3D modeling software
RR	Russian Roulette
SAM	Medical Analyses Department at AREVA NC La Hague
SB	Source Biasing card
SI	Source Information card
SP	Source Probability card
Tally	MCNP(X) simulation result
TPS	Treatment Planning System
Vec	Emission direction vector
Voxel	VOLUME X ELEMENT (the three dimensional equivalent of pixel)
VR	Variance Reduction
WW	Weight Windows
WWG	Weight Window Generator
WWP	Weight Window Parameters

List of figures

- Figure 1.1.** Summary of the main routes of intake, transfers and excretion (Davesne 2010).
- Figure 1.2.** Typical *in vitro* urine sample measurement.
- Figure 1.3.** Typical *in vivo* whole body counting (left). Measured spectrum visualized using Genie 2000 (right).
- Figure 1.4.** The SCHMIER bottle phantom used for whole body calibrations representing a 90 kg adult male subject.
- Figure 1.5.** The IGOR bricks used for whole body calibrations of a typical counting system (left); Different configurations of the IGOR bricks representing respectively a 70 kg, 24 kg and 12 kg subject (right).
- Figure 1.6.** The Livermore physical torso phantom with its core chest plates.
- Figure 1.7.** Visualisation of the Monte Carlo simulation chain and of the OEDIPE software components and functionalities (Lamart 2008)
- Figure 1.8.** Left: MIRDA adult mathematical model developed at ORNL. Middle: Adam and Eva mathematical adult developed at HMGU. Right: the mathematical 9 month pregnant female developed at ORNL.
- Figure 1.9.** Examples of voxelized models developed at different institutes starting from CT scan or MRI medical images (taken from a presentation by M. Zankl 2010; <http://www.enea.it/com/web/convegna/ComputationalDosimetry081007/Zankl.pdf>).
- Figure 1.10.** The new ICRP AM-RCP (left) and AF-RCP (right).
- Figure 1.11.** BREP representation of a sphere using NURBS (left) and Mesh geometries (right); Visualisation using the Rhino 3D modeling software.
- Figure 1.12.** Comparison between three models of the gastro-intestinal tract for the new-born: (left) Stylized phantom or mathematical (ORNL); (middle) Voxelized phantom (UF); (right) Hybrid Phantom (UF). (Lee et al. 2007a)
- Figure 1.13.** Frontal views of the UFH-NURBS female newborn phantom (Lee et al. 2007b).
- Figure 1.14.** Models of the pregnant woman at 3, 6 and 9 months of pregnancy respectively and visualization of the fetus' Mesh polygons (Xu et al. 2007).
- Figure 1.15.** Left: RPI Mesh-based adult male and female phantoms (Zhang et al. 2009); Right: FASH and MASH Mesh models of the FAX and MAX voxel phantoms (Cassola et al. 2010).
- Figure 2.1.** IDL[®] plotting of the Livermore lungs using the xvolume function.
- Figure 2.2.** Visualization of the Rhino 3D software and the available surface modification tools.
- Figure 2.3.** Viewvox visualization of voxelized ribs obtained using the Binvox program.
- Figure 2.4.** The Binvox program input and output functions, example of using the ignore function when three structures are present in the input file to be voxelized.
- Figure 2.5.** 3D phantom creation from medical images
- Figure 2.6.** 3D phantom creation from voxel model
- Figure 2.7.** Rhino 3D steps for the generation of NURBS surfaces starting from Mesh triangulations and using the loft tool.
- Figure 2.8.** Rhino 3D visualisation of Mesh surface intersections between ribs (grey) and lungs (red).
- Figure 2.9.** Variation of the counting efficiency (counts/s/gamma) with energy (keV), for the ICRP AF-RCP reference model (black symbols) and the female torso core model (white symbols).
- Figure 2.10.** Rhino 3D visualization of the operated manual shifting of the Splines control vertices to realize cup size change.
- Figure 2.11.** i) position up: Rhino 3D visualisation of the 90B (left), 100C (middle) and 110 D (right) created models; ii) position down: OEDIPE visualization of the voxelized models of chest girth 90 and of cup size ranging from A to E.
- Figure 2.12.** Steps for the generation of the library of female models starting from the deformable core model.
- Figure 3.1.** OEDIPE visualization of the detectors' positioning for phantoms of cup size C and a chest girth of 90, 100 and 110.
- Figure 3.2.** Schematic method to switch from a simulated spectrum to a calibration curve.

Figure 3.3. Counting efficiency (counts/s/gamma) variation with energy (keV) for the chest girth of 90 and all cup sizes: **A** (dots), **B** (squares), **C** (diamonds), **D** (triangles), **E** (inverted triangles).

Figure 3.4. Example of two different breast shapes created to represent a female subject having a chest girth of 90 and a C cup size breast; visualization using OEDIPE.

Figure 3.5. Counting efficiency (counts/s/gamma) variation with energy (keV) for the phantoms of cup size D and various chest girths (85-120) normalized to the 85 chest girth: **85** (dots), **90** (squares), **100** (diamonds), **110** (triangles), **120** (inverted triangles).

Figure 3.6. Counting efficiency (counts/gamma) variation with plate thickness (cm) for the Livermore mesh model. Linear fit calculated using Microsoft Excel 2008TM: $y=0.0077026*\exp(-0.2116x)$.

Figure 3.7. Counting efficiency of the three different detector arrays (50, 70 and 85 mm diameter) at 60 keV as a function of lung volume (both lungs) (Kramer and Capello, 2005).

Figure 3.8. Counting efficiency (counts/gamma) variation with energy (keV) for the different Mesh models: 0.85 contracted (black diamonds), contracted (black triangles), 0.95 contracted (black inverted triangles), reference (black squares), 1.05 dilated (white inverted triangles), 1.1 dilated (white triangles), 1.15 dilated (white diamonds). Values above 800 keV not shown in this plot.

Figure 3.9. Counting efficiency (counts/gamma) variation with the inverse of lungs volume (L^{-1}) for photons of 30 keV (dots), 60 keV (diamonds) and 250 keV (triangles). Linear fit calculated using Microsoft Excel 2008TM: **30 keV**: $y = 0.0026807 x - 0.000649$, $R^2 = 0.98552$; **60 keV**: $y = 0.0053597 x + 0.00010445$, $R^2 = 0.99726$; **250 keV**: $y = 0.0031493 x + 0.00014296$, $R^2 = 0.99634$.

Figure 3.10. Linear regression giving the c_2 parameter for the 90 chest girth phantom; simulations normalized to the 85A phantom values. Linear fit calculated using Microsoft Excel 2008TM: **90A** (diamonds) $y = -0.6025x$, $R^2 = 0.9875$; **90B** (triangles) $y = -1.2576x$, $R^2 = 0.9964$; **90C** (squares) $y = -1.3966x$, $R^2 = 0.9943$; **90D** (circles) $y = -1.6433x$, $R^2 = 0.9936$; **90E** (inverted triangles) $y = -2.0526x$, $R^2 = 0.9944$.

Figure 3.11. Counting efficiency (counts/s/gamma) variation with energy (keV): Comparison between MC simulated values (black symbols and solid lines) and the estimated ones (white symbols) for the models: 85B (diamonds), 90C (triangles), 100D (squares), 110E (dots) and 120F (inverted triangles). 85A being the reference for calculation.

Figure 3.12. Variation of the natural logarithm of efficiency ratio as a function of the mass attenuation coefficient (cm^2/g) for plate P1 (black diamonds) and plate P4 (white diamonds).

Figure 3.13. Variation of counting efficiency (counts/s/gamma) as a function of energy (keV): comparison between MC simulated values (black symbols and solid lines) and the calculated values (white symbols) for the 85A model (diamonds), 90B (triangles), 100C (squares), 110D (dots) and 120E (inverted triangles). The Livermore phantom with plate P4 is the calculation reference.

Figure 3.14. Variation of the natural logarithm of the ratio of the 105D efficiencies to the 105AA values (white diamonds) and those of the ratio of the 105D efficiencies to the 105A values (black diamonds) as a function of the mass attenuation coefficient (cm^2/g). Linear fit calculated using Microsoft Excel 2008TM: **105AA reference**: $y = x +$, $R^2=0.9$; **105A reference**: $y = x +$, $R^2=0.98$.

Figure 3.15. Variation of c_2 (g/cm^2) as a function of breast weight difference (g) for chest girths from 85 to 90 (dots), 100 chest girth (squares), 110 chest girth (diamonds) and 120 chest girth (triangles). Linear fit calculated using Microsoft Excel 2008TM: **85-90**: $y = 0.0016 x + 0.4034$, $R^2 = 0.952$. **100**: $y = 0.0009x + 1.2424$, $R^2 = 0.994$. **110**: $y = 0.0008x + 3.7414$, $R^2 = 0.955$. **120**: $y = 0.0006x + 6.1098$, $R^2 = 0.961$.

Figure 3.16. Variation of c_2 (g/cm^2) as a function of chest wall thickness variation (cm) for the Livermore measured data and the 85A simulation as reference. Linear fit calculated using Microsoft Excel 2008TM: $y = -1.2084 x + 1.0658$; $R^2 = 0.99217$.

Figure 3.17. Variation of c_2 (g/cm^2) as a function of breast weight difference (g) for the Hegenbart et al. (2008) data and the AA reference breasts. Linear fit calculated using Microsoft Excel 2008TM: **85-90**: $y = 0.029094 x + 13.65$; $R^2 = 0.955$.

Figure 3.18. Variation of c_1 as a function of c_2 (g/cm^2) for chest girths of 100 (triangles), 110 (dots) and 120 (squares), with all cup sizes represented. Linear fit calculated using Microsoft Excel 2008TM: $y = -0.0656 x + 0.8574$, $R^2=0.9728$.

Figure 3.19. Counting efficiency (counts/s/gamma) variation with energy (keV) with the source distributed: (i) following the volumetric proportion of each compound (black diamonds), (ii) uniformly in the four compounds (white diamonds).

Figure 3.20. Counting efficiency (counts/s/gamma) variation with energy (keV) with the detectors positioned: (i) facing the breasts (black diamonds), (ii) at the sides (white triangles), (iii) in the back of the phantom (inverted triangles).

Figure 4.1. Representation of the analog random walk of an MCNPX particle (Booth 1992).

Figure 4.2. Representation of the random walk of an MCNPX particle with VR splitting (Hendricks and McKinney 2005).

Figure 4.3. MCNPX plotter of a lung counting in vivo simulation with: (1) a point source located near the detectors and with small attenuation; (2) a point source located far from the detectors and suffering consequent attenuation (Lamart 2008).

Figure 4.4. MCNPX plot of the energy spectrum obtained for different VR methods; (1) in black: analogue calculation; (2) in green: biasing at 100% probability towards a fictitious sphere around one detector; (3) in red: biasing towards a fictitious sphere around the four detectors; (4) in blue: biasing towards a fictitious sphere around the four detectors with weight windows (Lamart 2008).

Figure 4.5. Variation of simulated counting efficiency (counts/gamma) with energy (keV) for the ICRP reference female.

Figure 4.6. Principles of splitting (1) and Russian roulette (2) (Breismeister 2000).

Figure 4.7. Input parameters of cell importance card (right) and schematic representation of the Livermore phantom (left).

Figure 4.8. Weight window principles: particules are represented by spheres as their size is proportional to their statistical weight (Lamart 2008).

Figure 4.9. MCNPX code for a rectangular WW (left) and MCNPX plotter visualisation of the defined rectangular WW (right).

Figure 4.10. MCNPX code for a spherical WW (left) and MCNPX plotter visualisation of the defined spherical WW (right).

Figure 4.11. Comparison of the variation with photon energy of: (1) the inverse of counting efficiency and of (2) the germanium energy-dependant mass attenuation coefficient.

Figure 4.12. Two examples of the Source Biasing cards used to favor low energy photon emissions. In the first case (left), 15/51 photons start at 15 keV while in the second case (right) this proportion is equal to 15/37.5.

Figure 4.13. MCNPX command of the source Vec card for direction emission biasing (left) and visualization of the particles tracks with a 180° cone directional biasing (right).

Figure 4.14. MCNPX command of the source Vec card for direction emission biasing (left) and visualization of the particles tracks with the continuous exponential biasing (right).

Figure 4.15. The FCL input parameters for the ICRP female phantom.

Figure 4.16. EXT input parameters for the Livermore phantom when applied to the chest plate only.

Figure 4.17. EXT input parameters for the Livermore phantom when applied to all internal organs and to the front dead layers of the used detectors.

Figure 4.18. Counting efficiency ratio of the values obtained with the VR methods to the reference values obtained without VR and associated uncertainties; results at 15 keV (left) and 59.5 keV (right) and the ICRP female phantom.

Figure 4.19. MCNPX plotter of a typical sphere of work inside of which the transport of particles is followed (right) and introduced void plans kill particles going in undesired directions (right).

Figure 4.20. Schematic visualization of the rebin functioning when two adjacent voxels with similar (left) and different (right) colors are fused together.

Figure 4.21. Errors on the organ volume caused by the rebin voxel fusion.

Figure 4.22. Example of an MCNPX input file and highlighted steps of the inputs identified by the script.

Figure 4.23. Visualisation of the “txt” output file of the script summarizing the requested inputs, the simulated outputs, the processed counting efficiency values and the polynomial equation parameters as well as validation for the ICRP female reference simulation.

- Figure 4.24.** Visualisation of the “png” script output file representing the counting efficiency (counts/gamma) variation with energy (keV) and comparing the simulated values (red) to those given by the polynomial equation (green) for the ICRP female reference simulation.
- Figure 5.1.** Visualization of a typical *in vivo* pulmonary measurement and schematic representation of the possible organ sources which contribute to the detectors’ count.
- Figure 5.2.** ²⁴¹Am biokinetics and retention organs days after a contamination by inhalation (Lamart 2008).
- Figure 5.3.** Photos of the three different germanium counting systems used for this study: IRSN’s LOAX (left), CIEMAT’s 4-LEGe (middle) and KIT’s HPGe (right).
- Figure 5.4.** Visualization of the LOAX experimental positioning (left) and of the MCNPX simulated one (right).
- Figure 5.5.** Visualization and designation of the detectors and their positioning with various angulations to cover at best the lungs.
- Figure 5.6.** MCNPX translation card and visualization of the lower pair positioning (shielding in yellow).
- Figure 5.7.** Operated positioning of the ¹⁵²Eu point source on the left and right side of the phantom at the level of the liver.
- Figure 5.8.** Plot of particles tracks with the ParaView software representing different organ contribution curves: Left: Liver and right lung with 80-15% proportion; Right: Liver, right lung and left lung with 80-15-5% proportion.
- Figure 5.9.** Positioning of the point perturbation source operated at KIT. Left: simulated tracks to determine the position for which there is an equal contribution of each organ; Right: positioning within the Livermore phantom.
- Figure 5.10.** Detectors positioning operated at KIT.
- Figure 6.1.** Photos of the IRSN LMA *in vivo* mobile unit and of the two installed germanium detectors.
- Figure 6.2.** Visualization of the experimental measurements done with point sources (left) and with the IGOR phantom (right).
- Figure 6.3.** MCNPX visualization of the activity distributions in the ICRP male reference phantom for the ¹³⁷Cs (left) and ^{99m}Tc (right). (red = 95% activity, blue = 5% activity).
- Figure 6.4.** MCNPX counting efficiency values for the ten phantoms. Inset: Example of several phantoms representing adult male individuals of different height and weight.
- Figure 6.5.** The CBR cycle: problem definition (new case), retrieve (most similar case from the database), reuse (previous solution), revise (adaptation) and retain (storage in the CBR database).
- Figure 6.6.** The EquiVox graphical comparison of the CAESER female with case-base model 85A (left) and model 120F (right).

List of tables

- Table 1.1.** Reference values for the radiation weighting factors (ICRP 2007).
- Table 1.2.** Reference values for tissue weighting factors (ICRP 2007)
- Table 1.3.** Typical detection limits according to ICRP (1997).
- Table 1.4.** Uncertainties involved in the calibration of *in vivo* counting systems for ^{239}Pu (Razafindralambo 1995).
- Table 2.1.** Chest girth designation according to the European committee for standardization.
- Table 2.2.** Bra size designation according to the European committee for standardization
- Table 2.3.** Composition of the deformable female core model's breasts.
- Table 2.4.** Densities of the deformable female core model's breasts, compounds are named according to their designation in the ICRP AF-RCP.
- Table 2.5.** Composition of the deformable female core model's internal organs.
- Table 2.6.** Densities of the deformable female core model's internal organs, compounds are named according to their designation in the ICRP AF-RCP.
- Table 2.7.** Composition and density of the deformable female core model's residual tissue.
- Table 2.8.** Organ volume of the reference ICRP female and the deformable core model and associated relative error.
- Table 2.9.** Tissue weight adding per cup size change according to Turner and Dujon (2005).
- Table 2.10.** Weight, density and composition of the created breasts.
- Table 2.11.** Weight factor applied to the organs and tissues of the created models, 90B model taken as reference.
- Table 2.12.** Residual tissue's composition and density for the female library phantoms as a function of chest girth.
- Table 2.13.** General features of the created models.
- Table 2.14.** Volumetric comparison of the created breasts.
- Table 3.1.** Counting efficiency and associated statistical error obtained with the MC simulations for the 85 chest girth and the different cup sizes for radionuclides of particular interest.
- Table 3.2.** Counting efficiency and associated statistical error obtained with the MC simulations for the different breast morphologies of the 90C phantom and the radionuclides of particular interest.
- Table 3.3.** Counting efficiency and associated statistical error obtained with the MC simulations for the C cup size and the 5 different chest girths; values given for the following radionuclides: ^{238}U , ^{241}Am , ^{57}Co , ^{137}Cs and ^{60}Co .
- Table 3.4.** Values of the parameter c_2 for the 85 and 90 chest girths and associated R^2 and χ^2 (left). Comparison of the MC and calculated efficiencies for the 90E model at various energies (right).
- Table 3.5.** Values of the parameters c_1 and c_2 for the 100, 110 and 120 chest girths and associated R^2 and χ^2 (left). Comparison of the MC and calculated efficiencies for the 120F model at various energies (right).
- Table 3.6.** Parameters of the sixth-order polynomial equation describing the counting efficiency variation with energy, measured for the Livermore phantom and the associated plates.
- Table 3.7.** Comparison of simulated counting efficiencies for the 85A female model and measured values obtained for the Livermore with plate P1 and associated difference (relative error).
- Table 3.8.** Values of the c_1 and c_2 parameters for the different Livermore plates and associated determination coefficient obtained from linear regression.
- Table 3.9.** Values of c_1 and c_2 parameters for all cup sizes (A to G) with the associated R^2 and χ^2 values (left). Comparison of published and calculated values of counting efficiency with the associated difference (%) for the Am-241 photons at 59.54 keV (right).
- Table 3.10.** Conversion factors to correct the Livermore P1 measurement as a function of female size ($E_{\text{ff}} = E_{\text{ff Livermore}} / \text{factor}$).
- Table 3.11.** Comparison of simulated counting efficiencies obtained for the photons at 59.54 keV with the artificial 17 photon source and the natural Am-241 source; results for the ICRP female torso.
- Table 4.1.** Study of the impact of the WWP on the simulation time and on the counting efficiency values at 15 keV when spherical WW are used and the Livermore phantom.

Table 4.2. Number of collisions obtained for three different FCC values and the ICRP female torso phantom.

Table 4.3. Statistical relative error (%) obtained for three different FCC values and the ICRP female torso phantom.

Table 4.4. Number of simulated particles for the applied VR techniques to save time and guarantee reliable MC values.

Table 4.5. Statistical relative error on the photoelectric peak at 15 keV obtained for the applied VR techniques and both phantoms.

Table 4.6. Comparison of the reference organ volumes and the resized phantom and associated relative error.

Table 4.7. Comparison of the reference organ volumes with the resized phantom and associated relative error.

Table 4.8. The FOM value obtained for the applied VR techniques and both phantoms.

Table 4.9. Counting efficiency values and associated statistical relative error obtained for the 110 chest girth phantoms and the combination of Vec, EXT and WW VR cards.

Table 5.1. Experimental counting rate of the LOAX detector obtained for the Livermore phantom and different configurations of loaded americium lungs.

Table 5.2. Experimental counting rate (counts/s) obtained for the Livermore phantom and different configurations of loaded Americium lungs with the LOAX detector positioned over the heart and liver.

Table 5.3. Experimental counting rate of the LOAX detector obtained for the Livermore phantom and different configurations of loaded americium lungs by adding a perturbation point source at the level of the heart.

Table 5.4. Experimental counting rate of the LOAX detector obtained for the Livermore phantom and different configurations of loaded americium lungs by adding a point source at the level of the liver.

Table 5.5. Simulated counting efficiencies (counts/Bq) for the considered detector positioning and the two configurations of loaded Americium lungs.

Table 5.6. Effect of the errors in the detector positioning on the simulated counting efficiency for cross fire situations.

Table 5.7. Effect of an increase in the side dead layer thickness on the simulated counting efficiency for cross fire situations.

Table 5.8. Experimental counting rate (counts/s) obtained for the CIEMAT four-germanium counting system and different sets of loaded lungs.

Table 5.9. Linearity check for the CIEMAT system and the operated detector positioning.

Table 5.10. Activity estimates and differences to reference values for various combinations of detectors' counts.

Table 5.11. Simulated counting efficiency for the CIEMAT detectors and difference to reference values.

Table 5.12. Experimental counting rate (counts/s) obtained for the CIEMAT four-germanium counting system and different sets of loaded lungs with the adding of the point source on the left side of the phantom.

Table 5.13. Experimental counting rate (counts/s) obtained for the CIEMAT four-germanium counting system and different sets of loaded lungs with the adding of the point source on the right side of the phantom.

Table 5.14. Impact of different possible combinations of detectors on the activity estimates and on their differences to the reference values when a point source was added on the left side of the phantom.

Table 5.15. Impact of different possible combinations of detectors on the activity estimates and on their differences to the reference values when a point source was added on the right side of the phantom.

Table 5.16. Experimental counting rate (counts/s) obtained at KIT for different detector positioning and various organ configurations.

Table 5.17. Linearity check for the KIT system and the operated detector positioning.

Table 5.18. Simulated counting efficiencies (counts/Bq) obtained at KIT for different detector positioning and various organ configurations.

Table 5.19. Experimental counting rate (counts/s) obtained at KIT for various organ configurations when the point source was added.

Table 5.20. Experimental counting rate (counts/s) obtained at KIT for the new detector positioning and the various configurations of loaded organs.

General introduction

In the nuclear industry, the exposition to ionizing radiation can be either by external irradiation or by internal contamination after inhalation, ingestion or wound. The occupational exposure is assessed using collective or individual measurements to demonstrate the compliance with regulatory requirements and to design an adapted monitoring program. Individual measurements include *in vivo* counting and bioassays that enable the assessment of the retained activity. The typical calibration of *in vivo* counting systems often relies on the use of physical phantoms that remain of limited anatomical realism. Moreover, no physical female phantom has been developed for the calibration of *in vivo* counting installations. An alternative to the use of physical phantoms consists in computing the calibration coefficients using a 3D model of the monitored subject and Monte Carlo calculations.

Voxel phantoms, created from CT scan or MRI medical images, were first introduced to realize Monte Carlo calculations. The construction of voxel phantoms is however significantly time consuming and the final model's flexibility is considerably limited. New 3D formats, developed for computer graphics and design, were thus introduced to create an extended library of female torsos. The models were carefully designed to represent the most common female morphologies based on plastic surgery and relevant recommendations. The library was next used to realize the numerical calibration of a typical four-germanium-detector counting system for which the effect of breast size and chest girth was quantified.

Furthermore, numerical calibrations require rapid and reliable calculations in addition to realistic anthropomorphic phantoms. The MCNPX Monte Carlo code, used for these simulations, enables the calculation of the calibration coefficients through the use of pulse height tally. For this latter, several new features were implemented in the newest versions of the code to improve the efficiency of the calculation and to reduce the simulation time. Thus, the work investigated the use of the developed variance reduction methods and some geometry simplification operations to accelerate Monte Carlo calculations.

Finally, the know-how and developed tools were put into application to improve the management of complex contaminations. In this case, a method was developed to enable the activity mapping by associating Monte Carlo simulations to *in vivo* measurements. The method is based on separating the different contributions to an experimental count through the use of Monte Carlo calculations. The feasibility of this method was investigated by using experimental measurements with the Livermore phantom and 3 different counting systems.

Chapter 1 starts with an overview of internal dosimetry and presents the principles of *in vivo* monitoring. Next, the basics of numerical calibrations and the available formats for anthropomorphic human phantoms are presented with an extensive study of the features and applications of each of the available formats.

In the second chapter, the development of a Mesh and NURBS-based female torso library is presented. A special attention is paid to the criteria and target values for the design of the female morphologies. All these topics are investigated along with a discussion of the possible improvements to be done.

The aim of chapter 3 is to realize a numerical calibration of the AREVA NC *in vivo* monitoring installation using the designed library. The work also includes a careful study of the morphological parameters and mainly cup size and chest girth. This led to the

parameterization of the morphology-induced variation of counting efficiency from which practical recommendations were given to correct the typical calibration coefficients to fit the morphology of any female worker monitored with the AREVA *in vivo* counting system.

Chapter 4 deals with optimizing the efficiency of Monte Carlo calculations when assessing the calibration coefficients with the use of variance reduction techniques and some geometry simplification operations. The work introduces the different methods available for the pulse height tally, the aim and mean of each of the methods and the use for this particular application. This work highlights the methods most appropriate and easy to use for routine calibration of *in vivo* installations. In this chapter, an algorithm was also developed to automatically treat the MCNPX output file and plot the simulated calibration curve.

In chapter 5, Monte Carlo simulations are introduced as a mean to improve the activity mapping in the case of complex contaminations. In this chapter, the developed method is first introduced along with the available tools. Next, a feasibility study is conducted using measurements with the Livermore physical phantom, followed by a validation of the method when using Monte Carlo simulations. At last, the method's validity is demonstrated for different counting systems, measurement protocols and contamination scenarios.

Finally, chapter 6 summarizes the obtained results, discusses the methods and improvements to be done and introduces the perspectives and future steps following this work which include the development of a case-based reasoning platform.

Chapter 1

Issues and challenges of *in vivo* measurements

In vivo spectrometry measurements is a very efficient method, used for the monitoring of workers with internal contamination risks, that enables the assessment of incorporated activity and, in some cases, its distribution inside the body. Typical calibration of the counting systems relies on the use of physical phantoms that are of limited anatomical realism.

This chapter introduces the principles of internal dosimetry, the generalities of *in vivo* monitoring and focuses on the female monitoring problematic. Moreover, the tools used in this work are introduced; these include numerical Monte Carlo calculations and 3D anthropomorphic phantoms.

I. Overview of internal dosimetry

Internal dosimetry involves situations where radioactive materials are present inside the body. This section presents first, the different contamination scenarios in the nuclear industry, then, the biokinetic models established to describe the transfer of radionuclides once incorporated. Next, the dose definition and calculation are given along with the radiological protection and individual monitoring principles.

I.1. Internal contamination of nuclear workers

I.1.1. Radionuclides involved in internal contamination situations

Several radionuclides can be involved in accidental internal contaminations in the nuclear industry and in the nuclear medicine medical departments.

In the nuclear industry, fission reactions inducing the production of electric power result in the generation of a big number of radionuclides with various physical and chemical characteristics. These radionuclides are divided to three categories depending on the modality and nature of production (Ecole Joliot Curie 2006). These include actinides that are generated when atoms of important weight are bombarded with neutrons or accelerated charged particles, fission products generated by decay chains of the primal ^{235}U nuclei and activation products created when stable nuclei capture neutrons.

In nuclear medicine medical departments, various radioactive elements are daily manipulated by medical staff for therapeutic or medical imaging purposes. These elements can be generated on site or provided by an external institution. The most commonly used radioelements include ^{131}I for therapeutic purposes and ^{201}Tl and $^{99\text{m}}\text{Tc}$ for medical imaging.

I.1.2. Incorporation pathways

Handling uranium, transuranic elements, fission or activation products, cleaning or dismantling facilities can lead to irradiation or contamination at the workplace. External irradiation is caused by a radioactive source lying outside the body while contamination is the incorporation of a radionuclide through inhalation, ingestion or wound.

For workers in nuclear medicine or medical imaging departments, the same incorporation routes are identified and may occur while preparing the radiopharmaceutical, i.e. associating the radioactive element to a vector, or even when administrating the radiopharmaceutical to the patient.

- **Inhalation**

In the nuclear industry, the fabrication of radioactive fuel implicates the manipulation of oxide powders and solutions of nitrate or uranium fluoride and other transuranian solutions. From these powders and solutions, fine particles, i.e. aerosols, can be suspended in the air. The inhalation of such aerosols is considered to be the most probable incorporation pathway for actinides in radioactive fuel processing laboratories (Bhattacharyya et al. 1995). For nuclear medicine medical departments, inhalation of radioactive elements constitutes an evident risk for the primary work chain implicating the association of the element to a vector.

In both cases, radionuclides are always manipulated in enclosed glove box. However, a confinement breach can occur and lead to an air contamination. Nevertheless, the activities that can be inhaled remain low thanks to the installed protection system including the enclosed depressurization systems, the radioactive particles detection system and the operator breathing masks (Métivier 1997).

Finally, for public, a contamination by inhalation can occur following the dispersion of radionuclides in the atmosphere.

- **Ingestion**

For the workers, the incorporation by the digestive tract can occur following the egestion of inhaled particles. For the public, the principle internal contamination pathway is through the ingestion of soiled food alimentary or beverages.

- **Wound**

For worker, a wound can accidentally occur in many cases as for example following a bad manipulation of sharp/cutting objects containing actinides like uranium, plutonium or americium. It can also occur when the worker is operating near the reactor circuit involving the incorporation of fission and activation products such as cobalt, chrome or ruthenium (Bhattacharyya et al. 1995).

Wounds are mostly found on hands. In these cases, the skin does not play its role as a natural barrier limiting the transcutaneous penetration of radionuclides into the organism. Wounds are very rare when compared to inhalation contamination cases, but can nevertheless induce more significative incorporations (Métivier 1997).

I.2. Biokinetics of radionuclides

Incorporated radionuclides are transferred throughout the body organs and tissue following biokinetic mechanisms. This section introduces the different biokinetic models developed to describe the becoming of radionuclides after their incorporation.

1.2.1. Transfer in the systemic circulation

Following the incorporation by inhalation, ingestion or due to a wound, a part of the activity is stopped by the tissue of the input pathway or directly eliminated by the organism; whereas a second part is transferred through the blood. The systemic circulation distributes next, the radionuclides in different body tissues where it can be retained for a period depending on the element. The radionuclide retention is highly dependent on the organ's metabolism and the similarity of the radionuclide to a natural element usually drained by the organ from the blood. For example, ^{241}Am is preferably retained by the liver and the skeleton whereas ^{137}Cs is mainly retained in the muscles (ICRP 1995; Legget et al. 2003).

The radionuclide is progressively eliminated by the organism through desintegration or excretion (urine or feces). The incorporation of radionuclides has been studied thoroughly by the International Commission on Radiological Protection (ICRP) who has defined different models for each incorporation pathway. After its transfer to the blood, the becoming of the radionuclide and its elimination are highly dependent on the considered element itself, on its radioactive period and its chemical composition. To take into account all these parameters, the ICRP has defined a biokinetic systemic model for each element or group of elements of similar chemical properties. These models describe the exchange between blood and tissues, the retention of activity in organs and the excretion in urine and feces as functions of time (cf. Figure 1.1).

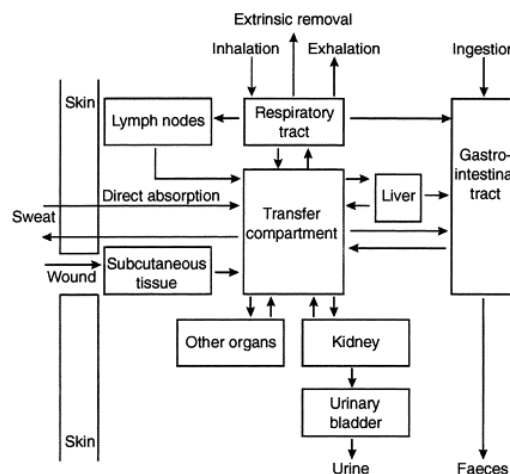


Figure 1.1. Summary of the main routes of intake, transfers and excretion (Davesne 2010).

1.2.2. Biokinetic models

The behaviour of radionuclides from intake to elimination is described by biokinetic models. These are made of compartments corresponding to organs, tissues, metabolic states or fractions of activity within a tissue. Activity transfer between compartments is governed by first order kinetics with constant rates estimated from animal experiments or follow-up of human contamination cases. They allow predicting from a given intake, the retention of activity in organs and the excretion in urine and feces as functions of time.

Specific models are recommended by ICRP to describe the movement of radionuclides in the site of entry following inhalation, ingestion or due to a wound, its entry into the blood, the element-specific systemic kinetics of exchange between blood and tissues and the excretion process. The main biokinetic models include the human respiratory tract model, the gastro-intestinal tract model, the human alimentary tract model, the wound model and the systemic model.

These models give the user a fairly realistic and precise mean to determine the received dose from the product of the dose coefficient (e_{50}) and the intake. The dose coefficient, deduced from biokinetics, is highly dependent on the solubility of the radioactive element (Fast, Medium or Slow), its size (Activity Median Aerodynamic Diameter for aerosols) and concentration.

I.3. Internal dose definition, principles and calculation

Radiological protection of workers aims at preventing and managing the internal and external exposure to ionizing radiation to guarantee the safety of each worker. Ionizing radiations are responsible for the destructive biological effects as most of the damage caused to the cells is assumed to be through the alteration of DNA (Métivier 2006). Moreover, radionuclides have different radiotoxicity depending on their physical half-life, the nature of the emitted radiations and the retention/clearance of the element in the organism (ICRP 2008). However, repair processes come into play to reduce the DNA damage.

Specific values, based on the absorbed dose definition and calculation, were thus introduced to determine the risks and radiation effects. These were divided to deterministic effects that are recorded within a few hours or months after irradiation and to stochastic effects that appear randomly after a few years or few decades with frequencies depending on the exposure. It is believed that the risk of stochastic effects is proportional to the dose down to the slightest irradiation: this is known as the linear-non-threshold model (ICRP 2007).

I.3.1. Dose definition

The exposure to ionizing radiation is defined by the dose concept (ICRP 2007). The International Commission on Radiation Units and measurements (ICRU 1998) also introduces the concept of absorbed dose.

- **Absorbed dose**

Ionizing radiations interact with matter and deposit energy. The absorbed dose is defined as the quantity of imparted energy by unit of mass and is given in J.kg^{-1} ; generally known as gray (Gy). It is an average of deposited energy by point interactions over a defined volume and time per unit mass. For radiation protection purposes, the absorbed dose is averaged over an organ (liver), a tissue (muscle) or sensitive target cells within a tissue (endosteal surfaces of skeleton) when those are identified.

- **Equivalent dose**

When considering the relative biological effectiveness of different types of radiations, some are found to be more harmful than other. Indeed, α particles are particularly toxic due to the high Linear Energy Transfer rate (LET). Their toxicity is to be considered only in the case of internal contamination since such particles have very small range (few centimeters in the air and about 40 microns in water). Moreover, β emitters have a smaller LET but a higher range of about few metres in the air and a few millimetres in water. For γ particles however, a very high penetrating power is observed with a small local energy deposition in material along the particle path. Therefore, the concept of equivalent dose (H_T) in an organ or tissue is defined as follows:

$$H_T = \sum_R w_R D_{T,R} \quad \text{Equation 1.1}$$

where $D_{T,R}$ is the average absorbed dose in the target organ or tissue T, due to radiation of type R. w_R is the radiation weighting factor for radiation R (cf. Table 1.1) representing the biological damage caused by the latter. The unit of equivalent dose is the sievert (Sv). w_R is equal to 1 for photons and β while its value is set to 20 for α particles.

Table 1.1. Reference values for the radiation weighting factors (ICRP 2007).

Radiation type	Radiation weighting factor (w_R)
Photons	1
Electrons and muons	1
Protons and charged pions	2
Alpha particles, fission fragments, heavy ions	20
Neutrons	Energy dependent

- **Effective dose**

In order to account for the fact that some tissues are more radiosensitive than others, the concept of effective dose is used. The effective dose E is defined as a weighted average of equivalent doses to radiosensitive tissues of the body as follows:

$$E = \sum_T w_T H_T = \sum_T \sum_R w_T w_R D_{T,R} \quad \text{Equation 1.2}$$

where w_T is the tissue weighting factor for T, with the sum of w_T being 1 (cf. Table 1.2). The values of w_T are set on the basis of epidemiological data of Hiroshima-Nagasaki survivors considering the frequency of stochastic effects and their severity in the different tissues at a given level of exposure.

Table 1.2. Reference values for tissue weighting factors (ICRP 2007)

Tissue	Tissue weighting factor (w_T)
Bone marrow (red), colon, lungs, stomach, breast, remainder tissue*	0.12
gonads	0.08
Bladder, oesophagus, liver, thyroid	0.04
Bone surface, brain, salivary glands, skin	0.01

*Adrenals, extrathoracic region, gall bladder, heart, kidneys, lymphatic nodes, muscle, oral mucosa, pancreas, small intestine, spleen, thymus, uterus

Moreover, the concept of committed equivalent dose $H_T(\tau)$ (akin to committed effective dose) was introduced since incorporated radionuclides may irradiate the tissues for days, months or years depending on their physical half-life and their biological retention. The committed equivalent dose $H_T(\tau)$ is defined as the total dose delivered in a tissue over the time period τ following intake of a radionuclide. The time period τ is usually set to 50 years for adults; whereas, for children, the equivalent dose is summed until the child reaches the age of 70 to cover life-long irradiation. Committed effective dose is calculated from committed equivalent doses accounting for intakes occurring over the years.

It should be noticed however that equivalent and effective doses are related to the risk of stochastic effects for a reference person after low-dose irradiation (ICRP 2002). These doses are defined for radiological protection purposes and to enable the comparison of different sources of exposure. Effective dose is defined for a reference person, by taking into account the conditions of exposure but not the characteristics of a specific exposed individual, such as sex, age or health status. Therefore, it cannot be used for individual risk assessment. Instead, the effective dose is a tool used in the management of radiation protection for prospective dose assessment in order to plan and optimize protection, and for retrospective dose assessment in order to demonstrate compliance with dose constraints and limits.

I.3.2. Dosimetry models

When an internal contamination occurs, each loaded organ constitutes a source of radiations that irradiates the body compounds. In order to assess effective dose, dosimetric models are used to calculate the absorbed doses in each tissue. The absorbed dose $D_{r_T,R}$, in the target region r_T due to radiation type R, is calculated using the MIRD formalism (Bolch et al. 2009):

$$D_{r_T,R} = \sum_{r_s} \tilde{A}(r_s, T_D) S(r_T \leftarrow r_s) \quad \text{Equation 1.3}$$

where $\tilde{A}(r_s, T_D)$ is the time-integrated activity (or total number of nuclear transformations) in the source region r_s over commitment period T_D . $\tilde{A}(r_s, T_D)$ is calculated by integrating over T_D the activity in r_s predicted by the biokinetic models. Moreover, $S(r_T \leftarrow r_s)$ represents the mean absorbed dose, specific for each radionuclide, due to radiations of type R in the target region (r_T) per nuclear transformation in the source region (r_s). $S(r_T \leftarrow r_s)$ is evaluated by:

$$S(r_T \leftarrow r_s) = \sum_i \frac{Y_{R,i} \times E_{R,i} \times \phi(r_T \leftarrow r_s, E_{R,i})}{M(r_T)} \quad \text{Equation 1.4}$$

where $E_{R,i}$ and $Y_{R,i}$ are respectively the energy and yield of the i^{th} radiation of type R, $\phi(r_T \leftarrow r_s, E_{R,i})$ is the absorbed fraction, $M(r_T)$ is the mass of target region r_T in the reference individual. The absorbed fraction is the fraction of energy $E_{R,i}$ emitted within r_s that is deposited in r_T (ICRP 2008). For penetrating radiations, it is calculated by applying Monte Carlo radiation transport codes to anthropomorphic computational phantoms representing reference individuals for which organ sizes and densities are representative of the adult population (ICRP 2002).

I.3.3. Internal dose calculation

Biokinetic and dosimetric models enable the calculation at a given moment of the activity retention and excretion. In order to quantify the exposure of workers, the measurement of retained or excreted activity must be interpreted in terms of committed effective dose.

Practically, the dose is assessed in two steps:

- the intake I is estimated by dividing the value of activity M measured t days after incorporation by the retention or excretion function $m(t)$:

$$I = \frac{M}{m(t)} \quad \text{Equations 1.5}$$

- the committed effective dose E is calculated by multiplying the intake by the dose coefficient e_{50} :

$$E = I \times e_{50} \quad \text{Equations 1.6}$$

The dose coefficient is the committed effective dose received by the reference man for a unit intake. The retention and excretion functions and the dose coefficient depend on:

- radionuclide(s),
- isotopic composition,
- intake time(s) and type: chronic or severe,
- intake route(s): inhalation, ingestion, wound,
- physico-chemical properties of the radioactive material: absorption type, AMAD for an aerosol.

These parameters are often unavailable; therefore, the ICRP recommends reference values corresponding to a mean of the literature observations. For example, for ^{241}Am , the reference absorption type is M and the recommended AMAD is of $5 \mu\text{m}$ (ICRP 1998).

To each combination of parameters a series of retention and excretion functions is available at a given time following the incorporation (ICRP 1998). The DCAL software (Eckerman et al. 2006) enables the calculation of these functions for more operator-specific input parameters.

I.4. Radiological protection and individual monitoring of workers

For situations in which there is a risk of radionuclide intake by workers, the occupational exposure must be assessed to demonstrate the compliance with regulatory requirements. Workplace studies are carried out to determine the overall radiation protection program, to assess, identify and quantify the likely intake of radioactive material and the resulting committed effective dose received. From this workplace study, an adapted monitoring program can be designed based on collective or individual measurements.

This section introduces first, the principles of radiological protection and then, presents the available monitoring techniques. Next, the use of such techniques to estimate incorporation is discussed with the definition of the decision threshold and detection limits.

I.4.1. Radiological protection

A system of radiological protection was developed by the ICRP in order to limit the exposure of workers and members of the public to ionizing radiation. However, the benefit from practices involving ionizing radiation should not be unnecessarily limited. Planned exposure to ionizing radiation should follow the three principles of justification, optimisation and limitation (ICRP 2007).

- **Justification**

Only useful or needed practices involving exposure should be performed. Furthermore, these should achieve sufficient individual or societal benefit to offset the detriment they cause.

- **Optimisation**

Exposure should be kept As Low As Reasonably Achievable (ALARA), taking into account economic and societal factors. The individual dose resulting from exposure to a given source should be restricted below a dose constraint by undertaking actions such as shielding, reduction of exposure time or confinement of radionuclides.

- **Limitation**

The total dose should not exceed a dose limit fixed to ensure that occurrences of stochastic effects are below unacceptable levels and that tissue reactions are avoided. The annual effective dose limit for workers is 20 mSv (Code du travail 2008) while it is of 1 mSv for members of the public.

Radiological protection policies have been developed since the 1920's to protect people against health effects of ionizing radiation. The ICRP publishes recommendations based on the available scientific knowledge. National authorities, Autorité de Sûreté Nucléaire in France, ensure that radiological protection programs, defining the dose limits and constraints, are respected.

I.4.2. Monitoring and measurement techniques

Monitoring the exposure and the intake risks involve collective and individual measurements. Workplace monitoring evaluates exposure for a group of workers assuming identical working conditions. It uses measurements made in the working environment such as air monitoring to assess the air contamination and surface activities. Individual monitoring gives information needed to assess the exposure of a single worker by measuring individual body activities, excretion rates or inhaled activity (using personal air samplers). *In vivo* counting enables the assessment of the activity retained in the body at the time of measurement. Meanwhile, *in vitro* bioassay permits the determination of the activity in excreta (ICRP 1988). Below is a summary of the principles of each method.

- ***In vitro* bioassay analyses**

In vitro (or indirect) measurement is the analysis of excreta or another biological sample (nose blow, nasal smear, blood or biopsy) during a sampling period (on a monthly basis for example). It is the most adapted measurement approach for radionuclides which emit nonpenetrating radiation (mainly alpha and beta emitters but rarely photons). Urine and feces measurements are widely used because of their high sensitivity and applicability to any radionuclide (cf. Figure 1.2).



Figure 1.2. Typical *in vitro* urine sample measurement.

For X and γ emitters, High Purity Germanium (Ge-HP) detectors are often used to realize the spectrometry measurements. Moreover, for β particles, proportional counters or scintillation detectors are more appropriate than Ge detectors. Finally, α spectrometry usually focuses on measuring the activity of the sample using a proportional or a scintillator detector or by alpha spectrometry using silicon semi-conductors preceded by a radiochemical purification process. This technique requires a one-week-long chemical process and sample counting for several days.

For actinides, the sample weight can be determined by elementary techniques like the Kinetic Analysis of Phosphorescence (KAP) and Mass Spectrometry using Inductive Coupled Plasma (ICP-MS). This latter technique is very sensitive, rapid and particularly adapted for the monitoring of uranium isotopes (Bouvier-Capely et al. 2004).

Even if α spectrometry is highly sensible and enables a very low detection limit (as good as 1 mBq.L^{-1}), the protocols to use this technique are complex and time consuming (6 days are required to prepare and measure one sample of urine).

Moreover, estimating the initial incorporation with spectroscopy is highly dependent on the biokinetic models used. These can have large uncertainties depending on the variability of excreta and the sampling procedure. New protocols are being developed based on the use of calyx-6-arene extraction molecules to reduce the time required for the chemical preparation of the sample (Boulet et al. 2007).

- ***In vivo* spectrometry measurements**

In vivo measurement is the direct measurement of the body content of radionuclides thanks to detectors set outside the body (Figure 1.3). It provides a quick (20-30 minutes) estimate of activity in the body or in a specific organ. However, this technique is only feasible for radionuclides emitting radiation that can escape the body such as X, γ or energetic β particles.

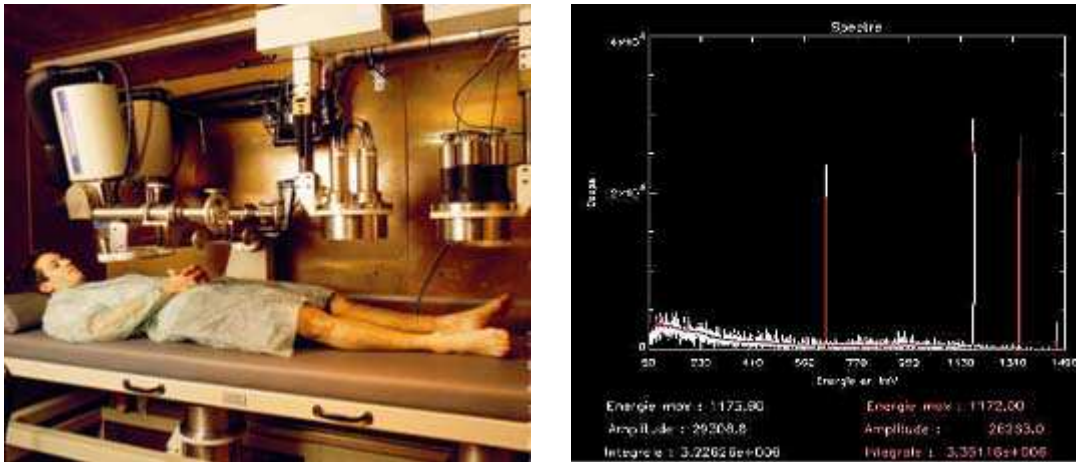


Figure 1.3. Typical *in vivo* whole body counting (left). Measured spectrum visualized using Genie 2000™ (right).

When the measured spectrum is analysed, this technique enables:

- the identification of the radionuclides involved in the contamination through the energy of the photoelectric peaks,
- the quantification of the retained activity in a particular organ or in whole body through the intensity of the peaks and its height.

From the spectrum presented in Figure 1.3 for example, the user can easily identify ^{137}Cs and ^{60}Co emissions at 661.6 keV and 1.17 MeV and 1.33 MeV. The area of these peaks is used to calculate the activity of the radionuclide detected in the monitored region. *In vivo* measurements are often conducted in sealed chambers in order to reduce the background generated by natural radiation.

1.4.3. Decision threshold and detection limits

The main challenge of both *in vitro* and *in vivo* monitoring techniques is to identify if a peak on the measured spectrum refers to a true contamination or not. Indeed, the difficulty in any radioactivity measurement is the presence of natural background radiation caused by cosmic and telluric radiation for the most part. The objective is thus, to separate between natural radiations and those resulting from an internal contamination. In addition, the natural radioactive elements present in each monitored subject introduce noise to the measurement.

To limit the contribution of the background, cosmic radiation can be reduced, for example, by shielding. Still, the sensitivity of the measurement techniques depends on the remaining background. Two situations are therefore considered separately.

First, since the background is variable, a measured low but positive count may be the consequence of a simple fluctuation of the background rather than the presence of an activity of interest. Therefore, a Decision Threshold (DT) was introduced to give a clear and decisive indication if the sample or the body contains a radionuclide. It is calculated under the hypothesis of a Poisson background by:

$$DT = K_{1-\alpha} \times \sqrt{R_0 \left(\frac{1}{t_0} + \frac{1}{t_s} \right)} \quad \text{Equation 1.8}$$

Where $K_{1-\alpha}$ is the desired $1-\alpha$ percentile of the Poisson distribution, R_0 the background effect counting rate, t_0 the duration of the background measurement and t_s is the duration of the gross-effect measurement. This means that if the number of counts is higher than DT , a wrong decision occurs with the probability α that there is a sample or body contribution when, in fact, only a background effect exists (ISO 2010). DT is the highest number of counts which would be interpreted as an absence of the activity of interest.

In the second situation, a true contamination could be interpreted as being part of the noise because of the overall variability of the counting. In this case, it is erroneously deduced that the radionuclide of interest is absent (β risk of false negative). A Detection Limit (DL) was hence defined to specify the minimum sample or body contribution which can be detected with a given probability β of error using the measuring procedure in question. Under assumption of Poisson background, DL is given using:

$$DL = (K_{1-\alpha} + K_{1-\beta}) \times \sqrt{R_0 \left(\frac{1}{t_0} + \frac{1}{t_s} \right)} \quad \text{Equation 1.9}$$

This allows a decision to be made as to whether a measuring method satisfies certain requirements and is consequently suitable for the given purpose of measurement or not (ISO 2010). The DL refers to the smallest expectation of the net counting rate for which a wrong decision occurs with a probability β that there is no sample contribution but only a background effect.

DL is directly dependent on the measurement time which does not exceed 30 min as it should remain reasonable for both the monitored subject and for the availability of the monitoring installation. Typical DL for *in vivo* and *in vitro* measurements of various radionuclides can be found in Table 1.3 (ICRP 1997).

The decision threshold and the detection limits characterize each counting system for a given counting geometry and a particular photon energy and help give a reliable indication on the existence of any contamination.

Table 1.3. Typical detection limits according to ICRP (1997).

Radionuclide	Method of measurement		Typical DL
^{137}Cs	γ -ray spectrometry in vivo	Whole body	50 Bq
	Radiochemical separation and α -ray spectrometry	Urine	1 Bq.L ⁻¹
^{241}Am	γ -ray spectrometry in vivo	Lung	20 Bq
		Skeleton	20 Bq
	Radiochemical separation and α -ray spectrometry	Urine	1 mBq.L ⁻¹
		Faeces	1 mBq
^{239}Pu	γ -ray spectrometry in vivo	Lung	2000 Bq
	Radiochemical separation and α -ray spectrometry	Urine	1 mBq.L ⁻¹
		Faeces	1 mBq

II. State of the art of *in vivo* measurements

The speed and simplicity of X and gamma spectrometry analyses as well as the direct and efficient access to the incorporation make *in vivo* measurements a more convenient individual monitoring technique when compared to *in vitro* bioassay analyses.

However, *in vivo* measurements require a careful choice of the most appropriate detectors and of their positioning while the calibration process with physical phantoms remains delicate.

II.1. Choice of the counting system

Spectrometry detectors are based on scintillation and ionization phenomena. The choice of the counting system, adapted for a particular radionuclide, is highly dependent on the energy of the emitted X and gamma radiations.

For high energy emitters such as ^{137}Cs and ^{60}Co , the sensitivity of the detectors should be localized at the high energy range. Thallium doped Sodium Iodide NaI(Tl) scintillation crystals are often used for such radionuclides. However, such detectors are of limited interest for low energy X and gamma emitters because of their poor energy resolution. This makes them unable to differentiate between the characteristic energy lines of actinides for example.

For actinides, the main emissions are alpha particles with a mean energy of 5 MeV. However, as such particles have a limited transport (few microns) external spectrometry measurements detect only low energy X and photons associated to the alpha desintegrations. Therefore, detectors with semi conductor crystals were developed to improve the detection of low energy photon emissions for actinides. The most common semi conductor detectors are those involving germanium (Ge) crystals. The detection technique is based on the ionization phenomenon which separates low energy X photons thanks to an excellent energy resolution within few keV. These crystals are however continuously cooled with liquid azote and require thus expensive support systems.

New series of semi-conductor counting systems functioning at room temperature such as silicium (Si) and cadmium-telluride (CdTe) are being developed in order to prevent the use of the cooling systems (Franck et al. 1997). Moreover, silicium crystal has a higher sensibility (up to three times) when compared to germanium crystal. This enables a better distinction of the low energy photons emitted by ^{239}Pu and ^{241}Am for example. Finally, detectors equipped with electric cryostats are being developed to replace liquid azot cooling systems.

II.2. Positioning of the counting system

The positioning of the detectors is chosen depending on the incorporation pathway, the nature and biokinetics of the incorporated radionuclide and the incorporation date.

For high energy gamma emitters (> 200 keV), the attenuation is of poor effect on the photons. Therefore, the activity estimate can be given with a very good precision using *in vivo* spectrometry measurements. In this case, a whole body counting is privileged as the detectors can be positioned within few centimetres away from the skin at the level of the thorax or facing the abdomen. These are the typical positions used when monitoring ^{137}Cs and ^{60}Co involved contaminations.

Since inhalation is the most common way of internal contamination for workers, lower photon emitters, such as actinides, are often involved in the accidental incorporation. In general, *in vivo* lung counting measurements are conducted in this case using Ge detectors positioned touching the thorax. Nevertheless, this positioning is often only appropriate in the early days following the incorporation since actinides are transported with time to the bones and skeleton (long term retention organs). Therefore, more adequate *in vivo* counting of bone can be operated at the level of the knee or the head for example in the case of an old contamination.

Finally, in the case of a wound, the retention remains local in the early stages and can be measured with the detectors positioned directly facing the wound and the closest possible to the skin.

II.3. Calibrating the counting system

To correctly relate the number of counts in the detectors to the incorporated activity (cf. Figure 1.3), the used detectors must be calibrated. Calibration is defined by detectors' counting efficiency which represents the ratio between the number of particles collected in the detectors at a given energy and the number of particles emitted from the source. Counting efficiency depends on the energy and number of emitted particles, on the source distribution in the body, on the geometry of the measurement (position of the detectors) and on the counting time. It is given by the following equation:

$$\varepsilon(E) = \frac{N_{\text{counts}}}{A \times Y \times T} \quad \text{Equation 1.7.}$$

where N_{counts} is the number of counts collected in the detectors at the photoelectric peak; A is the retained activity (Bq); Y is the yield of the X or gamma emission (photon/nuclear disintegration) and T is the measurement time (s). The efficiency of detection, or calibration coefficient, is evaluated for one or multiple detectors and should be assessed for each photon energy and each counting geometry.

The calibration procedure consists in reproducing, with the maximum realism, the geometry of the actual measurement. For *in vivo* measurements, calibration is done using physical anthropomorphic phantoms similar in composition and morphology to the human body and containing sources of known activity and distribution.

There are various physical phantoms dedicated for the calibration of *in vivo* counting systems. The bottle phantom SCHMIER has long been used to realize whole body calibrations (Schlagbauer 2006). It consists of cylindrical 1-L and 2-L polyethylene bottles filled with a radioactive solution including ^{40}K , ^{137}Cs , and ^{60}Co with ten different possible configurations representing persons of various weights and heights (cf. Figure 1.4).



Figure 1.4. The SCHMIER bottle phantom used for whole body calibrations representing a 90 kg adult male subject.

The IGOR phantom was introduced to further improve the whole body calibrations (Kovtun et al. 2000). It consists of several parallelepipedic tissue-equivalent bricks of two sizes ($16.5 \times 11 \times 55$ and $16.5 \times 11 \times 25$ cm³) in which cylindrical sources (16.3 cm long and 0.3 cm radius) can be introduced (cf. Figure 1.5).

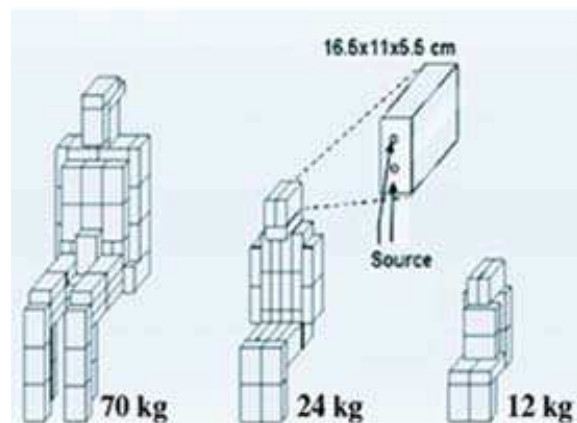


Figure 1.5. The IGOR bricks used for whole body calibrations of a typical counting system (left); Different configurations of the IGOR bricks representing respectively a 70 kg, 24 kg and 12 kg subject (right).

For *in vivo* lung counting studies, the counting system is calibrated using the Livermore physical phantom (Griffith et al. 1978, Newton et al. 1984). This is a male-equivalent torso phantom including several organs and compounds such as the lungs, the liver, the heart, the ribs and the sternum. The activity is uniformly distributed in the lungs and the liver, which can be separately used depending on the study. This phantom is also given with several thoracic plates that can be used to represent different chest wall thicknesses (cf. Figure 1.6). Indeed, as photon attenuation is directly dependent on the tissue thickness, several combinations of chest plates are used to obtain calibration curves for different chest wall thicknesses. When a real measurement is done, the chest wall thickness of the monitored subject is estimated as a function of body height and weight using biometric equations (Pierrat 2005). The calibration curve to be used for the activity estimate is then chosen when comparing the individual's chest thickness to a Livermore-equivalent chest thickness. Other phantoms including head and neck phantoms (with thyroid gland as a main organ) and leg

phantoms (USTUR) were developed and used for the calibration of *in vivo* counting systems (Gualdrini et al. 2000; Lopez-Ponte et al. 2011).



Figure 1.6. The Livermore physical torso phantom with its core chest plates.

II.4. Measurement uncertainties

Radioactivity measurement is subject to different sources of uncertainty which will impact the activity estimate and consequently the determination of the contamination.

The first uncertainty comes from the random transformation of radionuclides according to a Poisson distribution (ISO 2010). Moreover, the biological excretion of trace elements fluctuates randomly around a log-normal distribution (Usuda et al. 2002).

For *in vitro* countings, the chemical preparation of samples required to evaluate the quantity of radionuclide in the original sample, also introduces an uncertainty since a precise determination of the yields is required (Hurtgen and Cossonet 2003). Furthermore, the normalisation of a measurement of the bioassay sample to the daily excretion rate also introduces a substantial uncertainty (Davesne 2010).

In the case of *in vivo* measurements, the counting system calibration involves several sources of uncertainty. Indeed, calibration is carried out using physical phantoms which can have important morphological differences when compared to the measured person. Moreover, only few organs can be uniformly loaded with radionuclides. Many studies have proven that measurement geometry is critical (Lopez-Ponte and Navarro 2003; de Carlan et al. 2007). For instance, the uncertainty on the thoracic thickness (combination of muscular and adipous tissue) attenuating radiation can lead to uncertainties as high as 80% on lung measurement (Franck et al. 1997). Moreover, the source distribution has also shown to be responsible for uncertainties as high as 66% (Kramer and Burns 1995). The work by Razafindralambo (1995) has distinguished between two categories of uncertainties: those related to the measurement called metrological errors (due to calibration or to the geometry of the counting system) and those related to the person (due mainly to the biokinetics and the heterogeneous distribution of the contamination) (cf. Table 1.4).

Table 1.4. Uncertainties involved in the calibration of *in vivo* counting systems for ^{239}Pu (Razafindralambo 1995).

Source of uncertainty	Relative standard deviation (% at 1σ)*	
Detectors' positioning	9	
Variation of the loaded organ volume	4	
Chest wall thickness determination from:	- biometric equations	19
	- ultrasound measurements	11
	- magnetic resonance imaging	3
Variation of the adipose tissue percentage	13	
Distribution of the contamination (biokinetics)	33	
Global uncertainty	41 (1σ) / 82 (2σ)	

* σ is the standard deviation, estimated using gaussian distribution, quantifying the dispersion of measurements around the true value.

To minimize these uncertainties, the Monte Carlo method has been successfully introduced to realize numerical calibrations of typical *in vivo* counting installations (Franck et al. 2003; Kramer et al. 2003a). These include a statistical approach for particles transport and the development of anthropomorphic human phantoms of greater anatomical realism when compared to physical phantoms; these are introduced in the following sections.

III. Basis of the numerical calibration

Transport phenomena such as heat transfer, mass transfer, fluid dynamics etc. are generally described by a generic scalar transport equation (Kuzmin 2010). To solve such transport problems numerical methods were developed such as the Finite Volume Method (FVM) (LeVeque 2002) and the Discrete Ordinates Method (DOM) (Lathrop and Carlson 1965). These methods offer a good compromise between accuracy and computational requirements.

However, deterministic algorithms are sometimes inefficient to compute an exact result or to even modelize complex problems. The Monte Carlo method was thus introduced to bring an answer to such transport problems.

III.1. Monte Carlo approach for particles transport

Monte Carlo methods are a class of computational algorithms that rely on repeated random sampling to compute their results and are most suited when the deterministic methods fail to give reliable results (Metropolis and Ulam 1949).

The following subsections explain how the Monte Carlo method can efficiently resolve the transport equation. Next, the MCNPX code, used in this study, is presented and its precision and uncertainties are discussed. Finally, the implementation of the Monte Carlo method to simulate *in vivo* measurements is reviewed.

III.1.1. The Monte Carlo method

Radioactive transformations and inherent nuclear disintegrations and rearrangements involve statistical processes. This is also the case for the radiation interactions with materials and the inherent parameters such as the absorbed dose in an organ or the measured energy spectrum by a detector. The value of interest, the energy deposit in a given cell for example, can be written as a theoretical mean of random variables and its estimation is equivalent to solving a statistical problem that requires computing an integral calculation. For a big sample (N high enough), the central limit theorem indicates that an integral can be calculated by a numerical method, the Monte Carlo calculation.

The Monte Carlo method is a statistical approach for the interaction of radiation with matter that can efficiently resolve the transport equation by simulating histories of particle. To resolve the transport equation, the Monte Carlo method simulates individual particles and records their average behavior. It uses then the central limit theorem to determine the behavior of particles in the physical system.

Different Monte Carlo codes have been developed to simulate the particles transport. The main existing differences between the available codes are on the source data used (cross sections mainly) and on approximations (on the physics of interactions) realized to transport the particles. The most famous MC codes used in internal dosimetry are:

- MCNP (Briesmeister 2000) and MCNPX (Hendricks 2004),
- EGS4 (Nelson et al. 1985) and EGSnrc (Kawrakow and Rogers 2001),
- PENELOPE (Salvat et al. 2006),
- GEANT4 (Agostinelli et al. 2003).

III.1.2. The MCNPX code

For its internal dosimetry-related research activities, the LEDI has privileged since 1998 the use of the Monte Carlo N-Particles code (MCNP) and its eXtended version MCNPX developed at the Los Alamos National Laboratory (USA). MCNPX can simulate the transport of 34 different types of particles including neutrons, photons, electrons and charged alpha particles. This code enables:

- Modeling all elements included in any experimental *in vivo* measurement (person, detector, seat etc.),
- Simulating a wide variety of sources (photons, electrons, neutrons, charged particles etc.) which distribution can be extremely heterogeneous and covers an energy range from 10 keV to 100 GeV,
- Simulating the particles transport in different media (air, tissue, water, detector etc.),
- Obtaining multiple outputs and simulation results (including the energy deposit spectrum, the dose cartography or particles' fluence etc.)

MCNPX also presents new geometry representations called lattice (3D mesh grids) particularly adapted for the description of voxelized phantoms (Hendricks 2004). The latest versions of the code enable also variance reduction schemes that could be applied for the simulation of *in vivo* measurements (Hendricks and McKinney 2005). In this work, the MCNPX 2.6c and 2.6f versions of the code were used.

III.1.3. Monte Carlo precision and efficiency

Monte Carlo is designed to solve complicated three-dimensional, time-dependent problems and allows detailed representation of all aspects of physical data. When resolving the transport equation, the Monte Carlo method's precision and efficiency should be discussed. Since the MCNPX code was used in this study, the discussion involves the output parameters of this particular code.

- **Precision of the MCNPX code**

The MCNPX results, also called tallies, represent records of the average behavior of simulated individual particles. These records cover various quantities such as the surface current, the flux of particles at a given point, the energy distribution of pulses in a detector etc. and are normalized to be per starting particle. Tally results are printed in the output accompanied by a second number R, which is the estimated relative error defined as:

$$R = \frac{S_{\bar{x}}}{\bar{x}} \quad \text{Equation 1.10}$$

Where $S_{\bar{x}}$ is the standard deviation of the mean (\bar{x}). R represents the estimated relative error at the 1st level. For a well-behaved tally, R will be proportional to $1/\sqrt{N}$ where N is the number of histories. Thus, to halve R, the total number of histories must be increased by a factor four. For a poorly behaved tally, R may increase as the number of histories increases. An R value below 0.1 is necessary but insufficient to prove that the Central Limit theorem is fulfilled.

The estimated relative error can be used to define confidence intervals around the estimated mean, allowing one to make a statement about what the true result is. The Central Limit Theorem states that, as N approaches infinity, there is:

- a 68% chance that the true result will be in the range $\bar{x}(1 \pm R)$ i.e. within one standard deviation of the mean (\bar{x}),
- a 95% chance that the true result will be in the range $\bar{x}(1 \pm 2R)$ i.e. within two standard deviations of the mean (\bar{x}),
- and a 99% chance that the true result will be in the range $\bar{x}(1 \pm 3R)$ i.e. within three standard deviations of the mean (\bar{x}).

Therefore, to increase the precision of a MC calculation (R), the standard deviation of the mean should be decreased ($S_{\bar{x}}$), this is equivalent to:

- increasing the number of stochastic histories in the sample (N) which would increase drastically the simulation time,
- reducing the distribution of the samples (S), which is equivalent to reducing the variance of the sample. This is typically done using Variance Reduction (VR) techniques.

Finally, it is extremely important to highlight that these confidence statements refer only to the precision of the Monte Carlo calculation itself and not to the accuracy of the result compared to the true physical value (Breismeister 2000). A statement regarding accuracy

requires a detailed analysis of the uncertainties in the physical data, modeling, sampling techniques, and approximations used in a calculation.

- **Efficiency of the MCNPX code**

At the end of each MCNPX output file, 10 statistical checks are made on the Tally Fluctuation Charts (TFC) to identify the statistical properties of Monte Carlo solutions. The quantities involved in these checks are the estimated mean, the statistical relative error (R), the Variance Of the Variance (VOV), the Figure Of Merit (FOM), and the large history score behavior of the slope. The results of these checks provide the user with more information about the statistical behavior of the result in the TFC bin of each tally (Breisemeister 2000).

Among the quantities implicated in the 10 statistical checks, the FOM is considered to be a tally reliability indicator in the sense that if the tally is well behaved, the FOM should be approximately a constant as a function of the number of histories (N). FOM is defined as follows:

$$FOM = \frac{1}{R^2T} \quad \text{Equation 1.11}$$

Therefore, as the estimated relative error squared (R^2) is proportional to $1/N$ and since the computer time (T) is directly proportional to N; the FOM should be approximately a constant within any Monte Carlo run.

The FOM is also used to optimize the efficiency of the Monte Carlo calculation with variance reduction (selecting the method with the largest FOM). A third use for the FOM is to estimate the computer time required to reach a desired value of R (by using $T \sim 1/R^2FOM$). The more efficient a Monte Carlo calculation is, the lesser the computer time required to reach a given value of R becomes and thus the larger the FOM will be.

III.1.4. Application of MC simulation for *in vivo* measurements

The MC method is a statistical approach that simulates the transport of particles throughout a three dimensional (3D) geometry taking into account all possible interactions with matter.

Basic nuclear and anatomic data such as interaction cross sections, interaction type and location, energy loss or exchange, secondary generated particles etc. are often taken from available libraries to determine the probability density function of a random variable which characterizes a history, a particle or a track (Roger 2008).

Starting from this basic data, the transport of particles is treated differently depending on the case in which:

- A charged particle is followed (electron, positron, ion etc.).
- A non-charged particle is followed (neutron, photon).

In the first case, the physical phenomena involved are rather complex. For example, electron can interact: 1) by elastic collision with the nucleus and changes its propagation direction; 2) by inelastic collision with the electronic cloud surrounding the nucleus which slows it down;

3) by acceleration when interacting with the nucleus. These three interactions generate either charged or non-charged daughter particles. The transport is thus realized using approximations relative to both diffusion and slowing down processes.

For non-charged particles, however, the Boltzmann equation is used to simulate the transport of such particles in matter. Neutrons interact mostly with nuclei by elastic or non elastic diffusion, by radiative capture, by fission and absorption. Photons however interact mainly with the electronic cloud following photoelectric absorption, coherent diffusion process, Compton scattering or pair production.

Applying the MC method for *in vivo* counting measurements consists of:

- Modeling the nature and distribution of the internal contamination in a numerical anthropomorphic phantom,
- Positioning the MC model of the used counting system according to real measurement procedures,
- Generating with MC calculations the pulse height spectra (in the detectors).

Considering the simulated source activity, the counting efficiency coefficient is assessed from the simulated spectrum. The MC method enables thus a numerical calibration of *in vivo* counting installations where experimental values are difficult to assess or even inexistant.

III.2. Tools for Monte Carlo numerical calibrations

To generate the MCNPX input file and realize a numerical calibration of a given *in vivo* installation, the OEDIPE software was used with voxelized anthropomorphic phantoms. A brief overview of the OEDIPE software and of the voxelization principles are given here.

III.2.1. The OEDIPE software

At first, a graphical interface called ANTHROPO was developed to optimize the calibration of *in vivo* counting systems (Borisov et al. 2002). The functions and tools of this interface were next enlarged to estimate the internal dose and the software was renamed OEDIPE (Outil d'Evaluation de la Dose Interne Personnalisée), a tool for personalized internal dosimetry evaluation.

OEDIPE offers a graphic interface that enables the modeling of an internal contamination which includes the choice of the phantom, the source(s), the detector(s) and the counting geometry (for *in vivo* measurements). OEDIPE contains three main fonctionnalités:

- the creation of a numeric voxelized phantom starting from medical images,
- the creation of an MCNPX input file for Monte Carlo simulations,
- and the processing of the MCNPX output file.

Using OEDIPE, it is possible not only to load any voxelized phantom but also to generate anthropomorphic personalized models starting from available CT scan or MRI medical images. This can be done either by loading the DICOM medical images and segmenting the organs inside OEDIPE or by loading the organ contours with a manual segmentation using any Treatment Planing System. Two applications are next possible with OEDIPE. Indeed,

the user may select to simulate an *in vivo* spectrometry measurement and in this case the detectors are loaded from a predefined library and positioned to cover at best the monitored organ. While in the second application, the operator may choose to calculate the delivered organ or tissue-doses by selecting a radiopharmaceutical of interest and distributing it inside the phantom. In addition, OEDIPE automatically generates the MCNPX input file for Monte Carlo calculations. Finally, using OEDIPE it is possible to process the Monte Carlo output files in order to visualize the simulated energy spectrum of the detectors or the organ-dose delivery. Figure 1.7 resumes the whole Monte Carlo simulation chain and highlights the OEDIPE contribution through the modeling of the internal contamination, the automatic generation of the MCNPX input file and the processing of the simulation results.

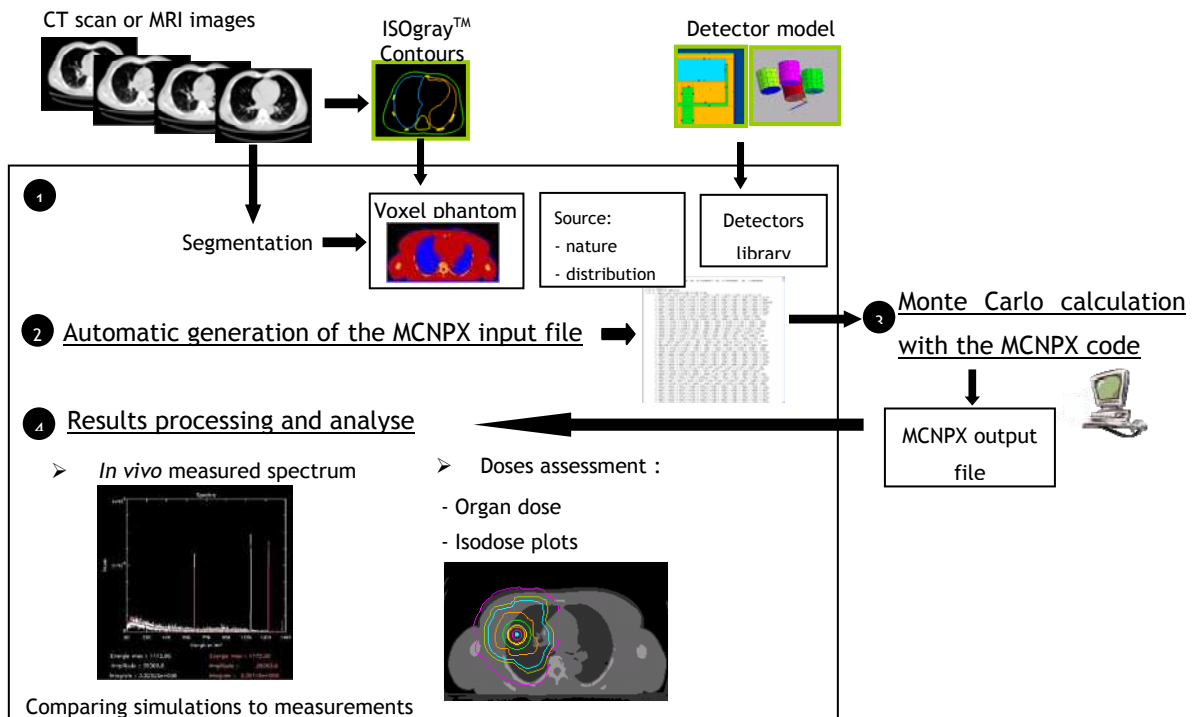


Figure 1.7. Visualization of the Monte Carlo simulation chain and of the OEDIPE software components and functionalities (Lamart 2008).

OEDIPE has proven to be an efficient tool for the simulation of *in vivo* measurements, for the improvement of calibrations (Franck et al. 2003; 2007) and for the calculation of organ-specific doses following accidental or therapeutic internal incorporation of radionuclides (de Carlan et al. 2003; Chiavassa 2005).

Multiple improvements have been achieved in OEDIPE to generate MCNPX input files in the “repeated structures” format (Chiavassa 2005; Pierrat 2005) that has proven to be faster for MC simulations. Work has also focused on simplifying the source definition (especially for those of multiple radionuclides) and reproducing the biokinetic distributions of radionuclides to further optimize the numerical calibration process (Lamart 2008).

III.2.2. Voxelization process

The available Monte Carlo calculation codes, including MCNPX, recognize voxel geometries as the main format for geometry representations and particle transport. Therefore,

anthropomorphic human phantoms used for numerical calibrations are often voxelized before running Monte Carlo simulations. A voxel (volumetric pixel or volumetric picture element) is a volume element, representing a value on a regular grid in three dimensional space. This is analogous to a pixel, which represents 2D image data in a bitmap. Similarly to 2D images, a voxel representation of a model is a regular grid of cells (elementary cubes or parallelepipeds) in which each elementary volume or voxel contains a density value of 0 for an unoccupied space or of 1 for a filled space. Moreover, as with pixels, voxels do not typically have their position (their coordinates) explicitly encoded along with their values. Instead, the position of a voxel is inferred based upon its position relative to other voxels. Thus, voxels are good at representing regularly sampled spaces. Common uses of voxels include volumetric imaging in medicine and representation of terrain in games and simulations.

Meanwhile, the voxelization process consists in converting geometric objects from their continuous geometric representation into a set of voxels that best approximates the continuous object. More specifically, voxelizing a 3D element consists in differentiating between a coding voxel and a non coding voxel i.e. differentiating between an elementary volume inside the element's volume or outside of it. A commonly used algorithm called the "Thin Shelled Voxelization" attributes to each voxel on the surface edge a non null value and then eliminates all the other voxels. Thin-shelled voxelization is performed by finding the distance between a given voxel and the nearest polygon (Nooruddin and Turk 2003). A thin-shelled representation of a sphere, for instance, would contain nonzero voxels only near the sphere's surface. Such a sphere would have a large region of zero-valued voxels inside its boundary. Another surface classification method called the "Parity Count Method" looks for the number of times a ray, starting from the center of the voxel to be classified, intersect with the polygonal model. An odd intersections number means that the voxel is inside the model while a pair number of intersections means the voxel is on the outside surface. The parity count method was also upgraded to work well for polygonal models having various degeneracies such as cracks or holes in the surface. To voxelize such models, the parity count method was extended by using k different directions (typically 13) of orthographic projection and by scan-converting the model once for each direction. Each of the k projections votes on the classification of a voxel (interior or exterior), and the majority vote is the voxel's final classification (Nooruddin and Turk 2003). Last, the "Ray Stabbing Method" is used for polygonal models that are double-walled or that have intersecting surfaces or several interpenetrating subparts. For instance, an upper arm might be placed so that portions of its surface are inside the torso. This is not a problem if we are just rendering such a model. The parity count method, however, would incorrectly classify the overlapped portions of the arm and torso as being outside of the model. The ray stabbing method consists in cutting/stabbing the surface in two opposite directions and all voxels present deep between two opposite rays are considered to be inside the model (Nooruddin and Turk 2003). In addition, rays of different projection directions are used to reduce the classification errors (up to 13 directions). The algorithm choice depends on the required precision when eliminating non coding voxels, on the nature and characteristics of the surface or the object to be voxelized (a clean and error free model where no leaks or holes are available on the surfaces). More details on the voxelization algorithms can be found in (Nooruddin and Turk 2003).

Different voxelizing software were considered among which the "Voxelizer" program (<http://techhouse.org/~dmorris/projects/voxelizer/>) and the "Binvox" program by Dr. Patrick Min (<http://www.cs.princeton.edu/~min/binvox/>). Binvox showed to be of simple functioning and handling with satisfying output voxel definition and was privileged in this study.

IV. Anthropomorphic human models

To reduce the systematic uncertainties inherent to the typical calibration process, numerical phantoms were introduced to give a realistic and personalized representation of the monitored subject (Kramer and Burns 1995; Pierrat 2005).

This section introduces the two available categories of 3D representations and gives examples of the most famous anthropomorphic phantoms developed using each representation along with some of their applications.

IV.1. Constructive Solid Geometry representations

Constructive solid geometry (CSG) is a procedural modeling technique used in 3D infography and in Computer Aided Design (CAD) that enables the creation of surfaces or complex objects by combining easier shapes with Boolean operators.

The simplest solid objects used for the representation of CSG are called primitives. These objects have typically a very simple shape such as: cubes, cylinders, prisms, pyramids, spheres, cones etc. Each primitive can be described by a “procedure” which involves certain parameters. For instance, a sphere can be described thanks to the coordinate of its center and the value of its radius. These primitives can be combined, using Boolean operations such as union, intersection or difference, to form the structures of objects. Therefore, starting from very simple shapes (or primitives), it is possible to create structures and very complex objects. The user can modify these complex shapes either by adjusting the position of the primitives or by modifying the Boolean operations used on the latter.

CSG methods are particularly interesting when a simple organ geometry is desired and when the exactitude of mathematical structures is required. The most important advantage of CSG is that the user can easily check if the defined object is a solid and that it does not contain any defaults or holes in the model. This is particularly important in the case of organ modeling for dosimetric studies. Moreover, with CSG, it is easy to classify the position of points relative to the object and to check if a point is interior or exterior to the CSG solid. This represents a major asset for surface voxelisation or for the detection of surface collisions for example.

IV.1.1. Phantoms developed using the CSG format

Many research groups have been working on designing and developing CSG phantoms. The ICRU report 48 (ICRU 1992) distinguishes mathematical phantoms from voxelized ones. The following paragraphs first introduce the mathematical phantoms and some of the most famous voxelized models with a brief overview of their applications.

- **Mathematical phantoms**

Mathematical phantoms, also called stylized phantoms, use simple geometric figures to describe the organs such as spheres, cones or ellipses. The first mathematical phantoms were primarily developed (Snyder et al. 1978) for dosimetry studies mainly by the Medical Internal Radiation Dose committee (MIRD). The aim was to approximate the main organ characteristics (shape, size, localization) with easy to use equations to minimize the

calculation time. Most of nowadays mathematical phantoms are based on Snyder's phantoms presented in Figure 1.8 which represent a hermaphrodite Caucasian adult. The Oak Ridge National Laboratory (ORNL) developed mathematical phantoms representing children of different age (Cristy 1980). Male and female adult phantoms called Adam and Eva of the Helmholtz Zentrum München (HMGU) have been elaborated from the MIRD model (Kramer et al. 1982). Body height and weight as well as the organ masses of these MIRD-type phantoms are in accordance with the Reference Man data (ICRP 1975). Stabin et al. (1995) developed a Caucasian pregnant female adult phantom at three different gestational stages (3, 6 and 9 months). Clairand (1999) also defined three male and three female phantoms with different dimensions. In addition to all these phantoms which represent Caucasian human being, a Korean adult male phantom was developed by Park et al. (2006) and a Japanese phantom was elaborated for Hiroshima survivors' dosimetry studies (Saito et al. 2001). Finally, a 4D Mathematical Cardiac Torso (MCAT) phantom was developed to model respiratory mechanisms and organ motion (Pretorius et al. 1997, Segars et al. 2001). Nevertheless, these mathematical descriptions remain very simplified and approximate (Lemosquet et al. 2002).

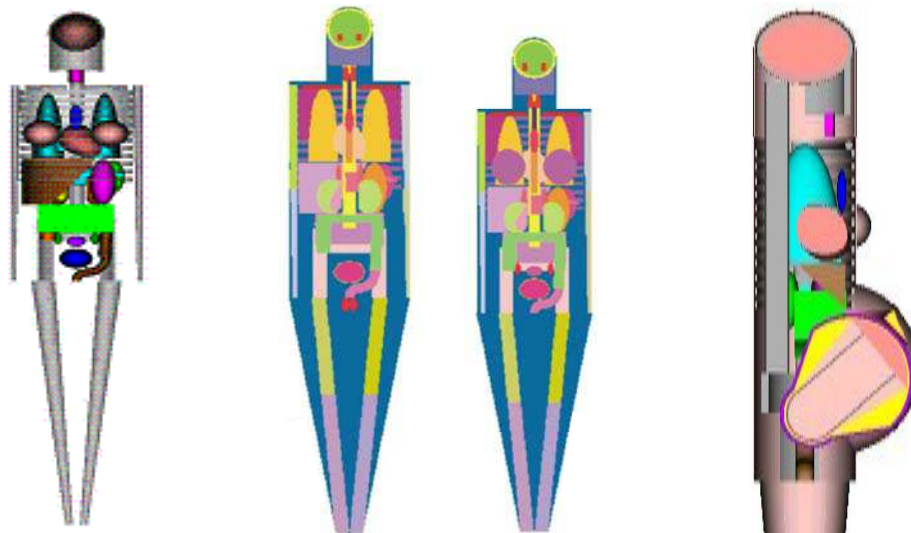


Figure 1.8. Left: MIRD adult mathematical model developed at ORNL. Middle: Adam and Eva mathematical adult developed at HMGU. Right: the mathematical 9 month pregnant female developed at ORNL.

- **Voxelized phantoms**

Due to the advances in computer technology, it was possible to create more complex figures representing realistic 3D organs by the mean of voxelized geometries. Such models are elaborated using medical images like the Computed Tomography (CT scan) images or the Magnetic Resonance Images (MRI) ones and using parallelepipedic or cubic basic elements.

Tomographic or voxel phantoms were first introduced by Gibbs et al. (1984) to determine patient dose from dental radiography. This work was next extended by the development of two children voxel models: one representing an eight-week-old subject called BABY, and the other one a seven-year-old subject called CHILD (Williams et al. 1986; Zankl et al. 1988; Veit et al. 1989).

Zubal et al. (1994) created a model called VOXELMAN starting from thoracic and head CT scan images of a 35-year-old patient having a height of 178 cm and a weight of 70 kg (4 mm length cubic voxels). This phantom was next upgraded by adding arms and legs derived from the “Visible Human” project (Spitzer and Whitlock 1998). The model was then made to fit the ICRP89 (ICRP 2002) recommendations regarding organ weights and a new phantom call MAX was generated (Kramer et al. 2003b). MAX, for example, has the following characteristics: 175 cm height, 75 kg weight, 22 different organs. It contains 487 axial slices with a resolution of 196*96 voxels and a voxel size of 0.36*0.36*0.36 mm³. A female model of the MAX phantom was also developed at the Brazilian Department of Nuclear Energy and was baptized FAX (Kramer et al. 2004). FAX, however, was created from CT scan images of a 37-year-old female individual of 165 cm and 63.4 kg. MAX and FAX were long considered to be representative of the reference individual.

Other phantoms were developed at the Health Protection Agency, NORMAN (for NORmal MAN) (Dimbylow 1995) and NAOMI (aNAtoMical model) (Dimbylow 2005), starting from MRI images of healthy volunteers. The voxel dimensions of the male model have been scaled to match the body height and weight of the Reference Man (ICRP 1975), that is a body weight of 70 kg and a body height of 170 cm. Jones (1997) later modified the NORMAN phantom to match the newer referential (ICRP 2002) body height and weight (176 cm, 73 kg). The ADELAIDE voxel phantom represents a 14-year-old girl, used to determine the absorbed organ doses from computed tomography examinations (Caon et al. 1999).

The VIP-Man (VIsible Photographic MAN), part of the “Visible Human” project (Spitzer and Whitlock 1998), was created at the Rensselaer Polytechnic Institute (Xu et al. 2000) starting from colored photographic images obtained after the dissection of a human donor. The HMGU digitized a male Golem segmented from whole-body medical image data of a 38-year-old living person who had external dimensions close to those of the ICRP Reference Man (Zankl and Wittmann 2001). Other voxel female models were developed at HMGU including Helga, Donna, Irene and Regina which were next upgraded to represent the ICRP reference female phantom (ICRP 2009). Finally, Shi and Xu (2004) developed a 30-week-pregnant female voxel phantom from CT images. Several of these voxelized phantoms are shown in Figure 1.9 and information is shared online at the Consortium of Computational Human Phantoms (<http://www.virtualphantoms.org/>).

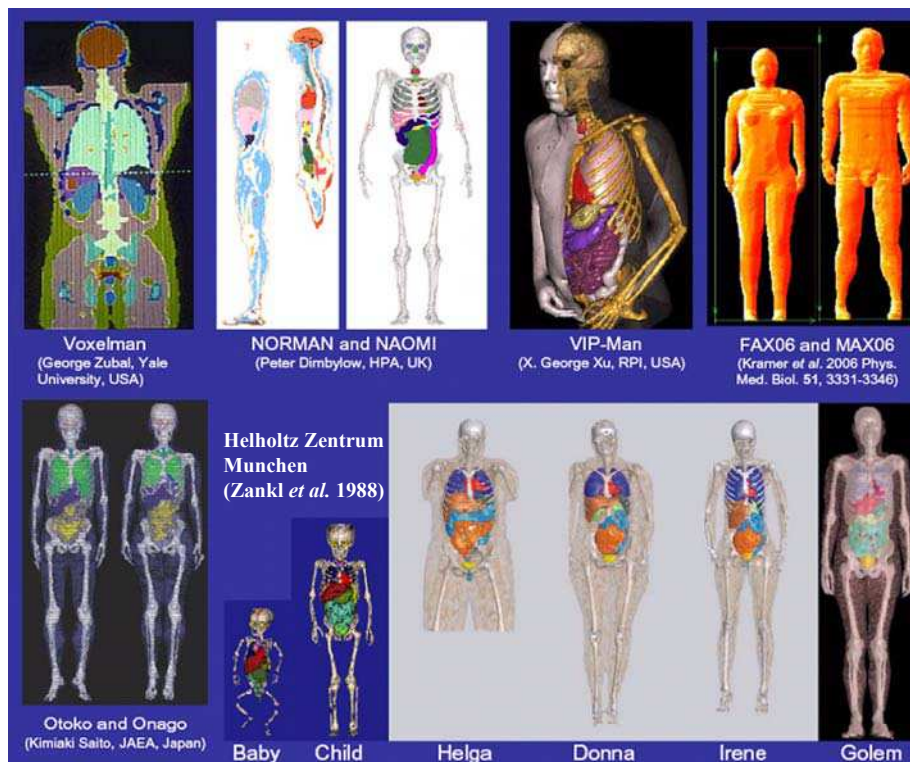


Figure 1.9. Examples of voxelized models developed at different institutes starting from CT scan or MRI medical images (taken from a presentation by M. Zankl 2010; <http://www.enea.it/com/web/convegna/ComputationalDosimetry081007/Zankl.pdf>).

Voxelized anthropomorphic phantoms were also designed to fit subjects of various ethnic origins and not only Caucasian individuals. These were also modeled starting from medical and anatomical images of Asiatic subjects. CNMAN is a voxelized phantom developed at the Chinese Radiation Protection Institute (Zhang et al. 2007) starting from available photographic images of a Chinese adult male cadaver (170 cm, 65 kg). In this model, 29 different tissues and structures were segmented separately and the voxel resolution of $0.16 \times 0.16 \times 1 \text{ mm}^3$ was considered. Other Japanese and Korean phantoms were also designed to fit the Asiatic population and its particular body type and morphology (Saito et al. 2001; Sato et al. 2007). These were created from whole-body CT data of patients with external dimensions (height and weight) close to the Japanese Reference Man (Saito et al. 2001).

The ICRP has developed new voxelized models to fit reference anatomical measurements (ICRP 2002) and represent the standard adult male and female subjects (ICRP 2009). These were created from CT scan images of a 38-year-old male leukemia patient and from CT images of a 43-year-old female patient. The voxelized phantoms were created at the HMGU starting from CT scan images of individuals having the characteristics of the standard individual. In these phantoms, over 140 different structures were defined to fit, with maximum realism, the reference individual. Figure 1.10 presents the new ICRP reference male and female phantoms respectively named Adult Male/Female Reference Computational Phantom. These phantoms match the human subject, not only in terms of organ geometries and shapes, but also in regards of different materials, densities and chemical composition to create correct organ weights and simulate realistic radiation interaction with matter.

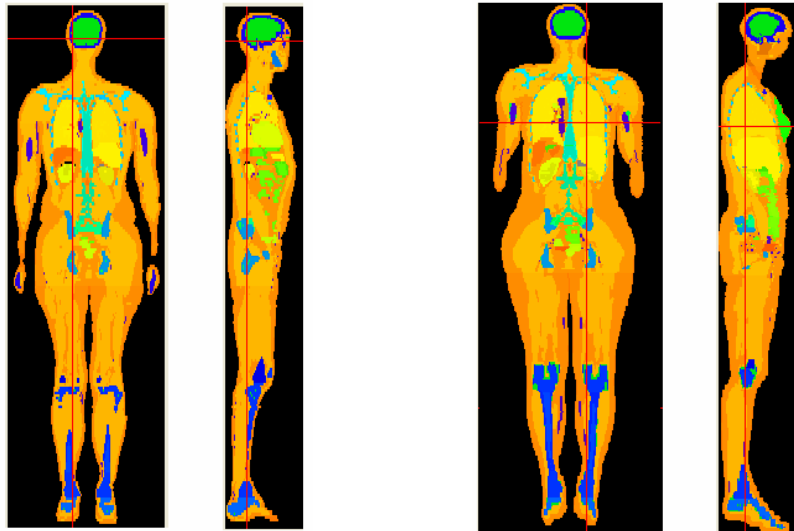


Figure 1.10. The new ICRP AM-RCP (left) and AF-RCP (right).

Other research groups focused on the development of animal voxelized phantoms for environmental dosimetry studies among which the Canine Anatomic Phantom designed by Padilla et al. (2008). More details about the characteristics and availability of voxel phantoms can be found in the reviews by A. Lemosquet and H. Zaidi (Lemosquet et al. 2003; Zaidi et al. 2007).

IV.1.2. Applications of CSG phantoms

Mathematical phantoms, introduced in the early 60s, gave first approximations for the human anatomy and enabled dosimetric studies for ionizing and non-ionizing radiation applications. For internal dosimetry studies, the MIRD phantom was used to calculate the dose distribution in the body from a gamma-emitter organ (Fish and Snyder 1967) and to estimate the specific absorbed fractions for monoenergetic photon sources distributed inside the body (Snyder et al. 1978). Mathematical phantoms have also been used for external dosimetry studies to determine the effective dose in the case of external exposures in nuclear power plants (Xu et al. 2006). Moreover, stylized phantoms were adopted for nuclear medicine research activities (Tsui et al. 1993; 1994) specifically Single Photon Emission Computed Tomography (SPECT) and Positron Emission Tomography (PET). The software OLINDA, based on MIRD-5 Mathematical phantoms, remains widely used for Nuclear Medicine applications mainly for internal dose calculations for radiopharmaceuticals (Stabin and Siegel 2003).

Voxelized phantoms, introduced in the early 80s, have proven to significantly improve internal and external dosimetry when combined with MC simulations (Lemosquet et al. 2003). The reliability and interest of such representations in radiation protection have been extensively shown in many studies. Frank et al. (2003) and Kramer et al. (2003a) have used voxel geometries to improve the *in vivo* monitoring of nuclear workers. Meanwhile, Petoussi-Hens and Zankl (1998) have used such phantoms as a tool for internal dosimetry, radiology and radiation protection (Zankl et al. 1988) and for environmental exposure applications (Petoussi-Hens et al. 1991). The new ICRP reference voxelized phantoms were used to review the previous dose coefficients established on the use of mathematical phantoms. Important and relevant differences were noticed for some specific organs (ICRP 2009) and for the fetus (Taranenko and Xu 2008), newborn (Staton et al. 2006) or pediatric cases (Lee et al. 2006a). The radiation protection consequences of the body type difference between Asian

models and their ICRP or Caucasian counterparts have been illustrated (Saito et al. 2001, Kinase et al. 2003, Lee et al. 2006b, Zhang et al. 2007). Finally, voxel geometries were also used in accidental dosimetry reconstruction situations to improve the dose delivery estimation by the means of a personalized phantom and a correct positioning of the source (Lataillade et al. 2007; Courageot et al. 2010).

Although such models have great anatomical realism, they continue to represent one particular morphology, and thus, should not be systematically used for all human subjects. Moreover, the construction of the voxelized phantoms requires a careful segmentation of medical images, which is significantly time consuming depending on the desired accuracy and the image modality and quality. Nevertheless, it is clear that accuracy in calculations is increased when personalized and realistic phantoms are used. Hence, additional phantom adjustment is required to further match a given human victim. This is made possible with the Boundary representations approach.

IV.2. Boundary representations

Recent studies cover another possible tridimensional description of the anatomy: the Boundary REPresentation (BREP) which was introduced to replace rigid voxel grids with flexible structures (Stroud 2006).

BREP phantoms, like voxel phantoms, are created from medical images and allow accurate representations of complex volumes. However, surface modeling with boundaries allows an easy modification of these volumes. BREP has been developed in the beginning of the 1970's by Ian Braid (1973) and Baumgart (1975). This method is based on the fact that a solid divides the space in two continuous sets separated by a surface boundary. The BREP model describes the boundary as a juxtaposition of several oriented surfaces, bounded by summits and interconnected to reconstruct the desired volume. Advanced BREP models include Non Uniform Rational B-Spline (NURBS) and polygonal Mesh surfaces. NURBS surfaces are defined by spline curves smooth tridimensional surfaces, and their shape is determined by control points, parameters and equations defining the relation between these control points (Xu et al. 2007). Control points are always either connected directly to the curve/surface, or act as if they were connected by a rubber band (cf. Figure 1.11 left). Modeling the NURBS can thus be extremely easy by acting on the control points. Meanwhile, a polygon Mesh is a collection of vertices, edges and faces that define the shape of an object (cf. Figure 1.11 right). The faces usually consist of triangles, quadrilaterals or other simple convex polygons. Various operations can be performed on meshes including Boolean logic, smoothing, simplification, ray tracing, collision detection etc. Mesh models are commonly used to represent complex geometries.

However, Mesh modeling remains more delicate when compared to NURBS representations and the management of Mesh geometries is heavier since it requires all data regarding the coordinates, connectivities of the triangulations and their normal vectors. Moreover, surface deformation with NURBS geometries is much easier than with Mesh surfaces thanks to the presence of control points (too important deformations can destroy the topology of Mesh). Meanwhile, thanks to the high density of triangulations, Mesh models reproduce complex geometries better than NURBS curves. Besides, when comparing the Mesh and NURBS performances against voxel geometries, it is noticed that BREP representations outperform

voxels when modeling geometry deformations. Indeed, when representing geometries with high gradient and curvatures, voxel geometries lead to step functions and discontinuities especially when considering the voxel size and limited resolution. This is not the case for Mesh and NURBS analytical formats.

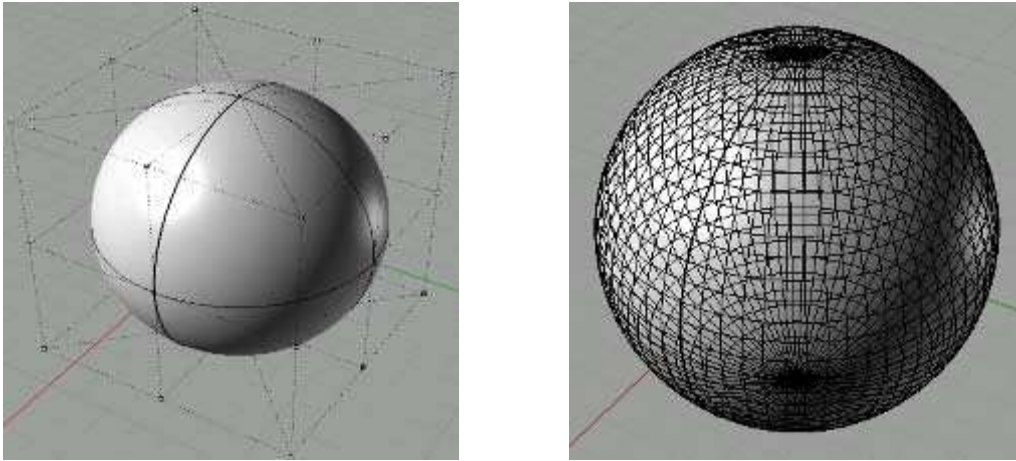


Figure 1.11. BREP representation of a sphere using NURBS (left) and Mesh geometries (right); Visualisation using the Rhino 3D modeling software.

IV.2.1. Phantoms developed using the BREP format

- **NURBS phantoms**

The NURBS-based numerical phantoms are called hybrid because these have concurrently the advantages of the mathematical phantoms and those of the voxelized phantoms. As with stylized phantoms, these models are defined by mathematical equations which render a very smooth shape for tissues and allow an easy modification of the morphology. However, contrary to the mathematical phantoms, the shape and position of the organs and tissues are modeled in a realist way, similarly to voxelized phantoms (Figure 1.12).

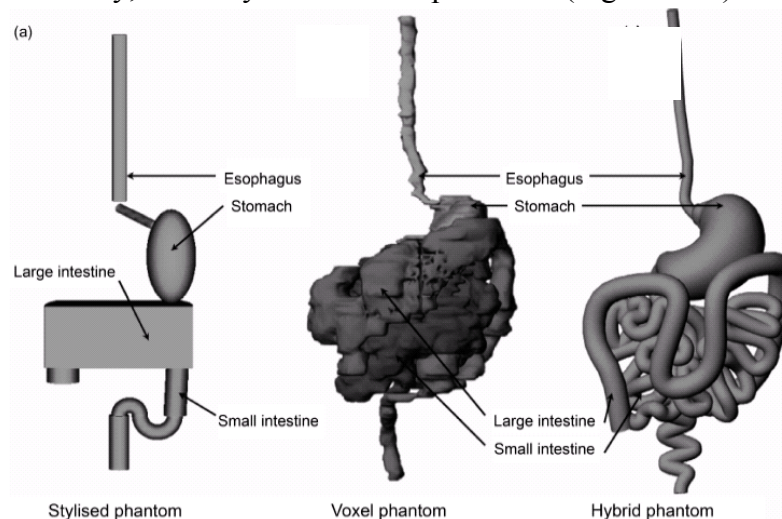


Figure 1.12. Comparison between three models of the gastro-intestinal tract for the new-born: (left) Stylized phantom or mathematical (ORNL); (middle) Voxelized phantom (UF); (right) Hybrid Phantom (UF). (Lee et al. 2007a)

Segars (2001) was the first to demonstrate the feasibility of this type of advanced phantoms with the development of the 4D NURBS-based cardiac-torso (NCAT later upgraded to XCAT) phantom for nuclear medicine imaging using the Visible Human Project CT data set. This phantom was developed using a set of medical images including gated MRI images and 3D angiogram data to accurately represent human lungs and heart during the different stages of respiration and heart beat. Segars et al. (2004) have also developed a NURBS-based 4D digital mouse phantom called MOBY for molecular imaging research.

At the University of Florida (Lee et al. 2007a, Lee et al. 2007b), NURBS geometries have been applied for the creation of new-born phantoms whose anatomy has been adjusted to the reference morphology defined by the ICRP 89 publication (ICRP 2002). By design, the NURBS surfaces in the UFH-NURBS newborn phantom yield improved continuity and smoothness in the abdominal anatomy, especially the small intestine and colon as shown in Figure 1.13. This figure also highlights the flexibility of this BREP representation when modifying the morphology and posture of the phantom. More details about the characteristics and availability of Mesh and NURBS phantoms can be found in the Handbook by Xu and Eckarman (2009).

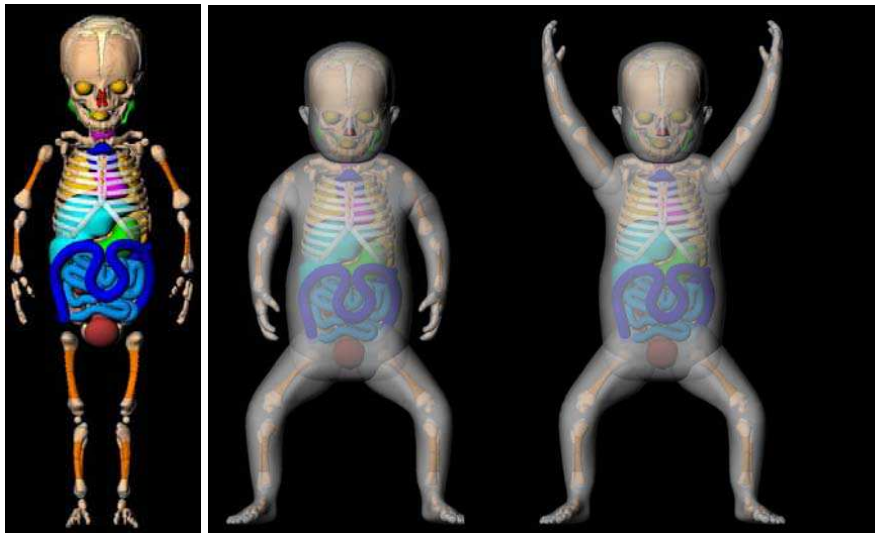


Figure 1.13. Frontal views of the UFH-NURBS female newborn phantom (Lee et al. 2007b).

- **Mesh phantoms**

Mesh triangulations were found to yield better anatomical accuracy than NURBS geometries and were particularly introduced to represent organs of complex topology such as the skeleton, lungs and liver (Xu et al. 2008).

The Ressenlear Institute has constructed several numerical phantoms using this representation. First, the VIP-Man chest phantom was extended to 4D with respiratory motion simulation using mesh modeling techniques (Xu and Shi 2005). Next, three models were created representing a pregnant woman at 3, 6 and 9 months of pregnancy (Figure 1.14). These were called RPI-P3, RPI-P6 and RPI-P9 which used concurrently NURBS surfaces (female body) and Mesh polygons (fetus). Organs of the mother and the fetus were adjusted to match ICRP-89 recommendations (ICRP 2002).

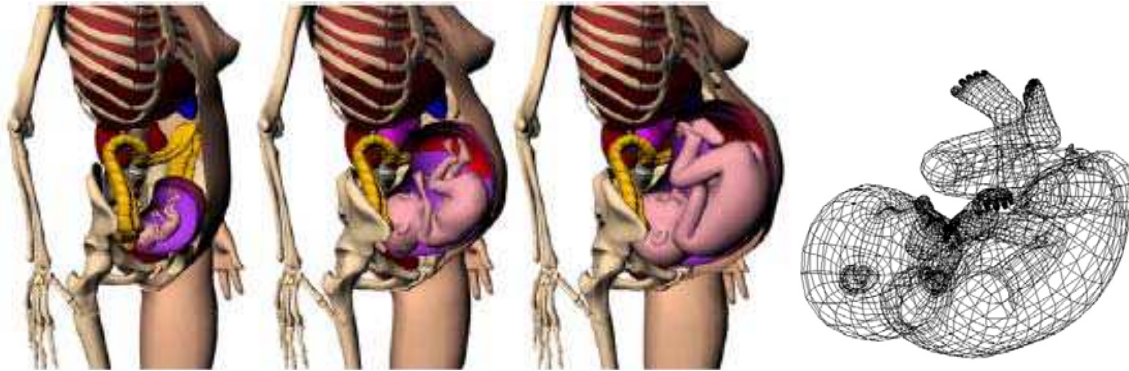


Figure 1.14. Models of the pregnant woman at 3, 6 and 9 months of pregnancy respectively and visualization of the fetus' Mesh polygons (Xu et al. 2007).

Also at Ressenlear Institute, Zhang et al. (2009) have developed a pair of mesh-based, size-adjustable, adult male and female computational phantoms called RPI-AM and RPI-AF (cf. Figure 1.15). These were created from mesh anatomical models (Anatomium™ 3D www.anatomium.com) that were adjusted to match the ICRP-89 recommendations on organ weight and size (ICRP 2002). Finally, using a combination of 3D modeling software (MakeHuman, Blender, Bivox and ImageJ), Cassola et al. (2010) have developed two adult Mesh phantoms called FASH (Female Adult meSH) and MASH (Male Adult meSH) starting from anatomical atlases to be equivalent to the FAX and MAX voxelized phantoms (cf. Figure 1.15).

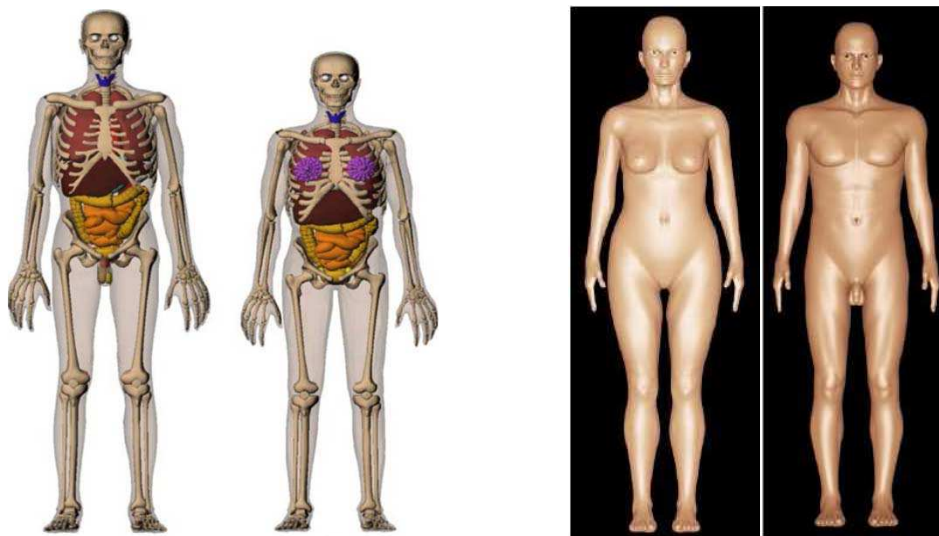


Figure 1.15. Left: RPI Mesh-based adult mal and female phantoms (Zhang et al. 2009); Right: FASH and MASH Mesh models of the FAX and MAX voxel phantoms (Cassola et al. 2010).

IV.2.2. Applications of BREP phantoms

The application of BREP geometries goes beyond the limits of mathematical and voxelized phantoms of CSG type in modeling the anatomy in the human body. Organs or tissues are precisely represented with smooth surfaces and their shape can be easily modified to adapt the desired morphology. Using BREP representations, it is possible to create numerical phantoms for several morphologies starting from a simple and unique MRI or CT acquisition. However, for radiation transport simulations, transforming BREP surfaces into voxel grids remains mandatory since, until now, the MCNPX code supports only voxel geometries.

A few examples of the applications of NURBS and Mesh phantoms are given here. The NCAT phantom with beating heart and breathing lungs and the MOBY mouse were used to optimize nuclear medicine imaging and dosimetry (Segars 2001, Segars et al. 2004). The UFH-NURBS newborn phantoms were used to evaluate radiation dose distributions in human anatomy (Lee et al. 2007b). RPI mesh phantoms were used for organ dose calculation from monoenergetic photon beams (Zhang et al. 2009). The 4D VIP-Man (Xu and Shi 2005) was used to study external-beam treatment planning for a lung cancer patient (Zhang et al. 2008). Finally, Badal et al. (2008) have introduced Mesh geometries for brachytherapy imaging studies.

Mesh and NURBS geometries have applications in various fields other than radiation dosimetry. Several projects, such as the Virtual Family Project, have been developing phantoms used for the non-ionizing radiation community (Christ et al. 2010). For example, BREP models have proven to be very useful to improve the knowledge of the electrical fields' distribution in the human body (Sachse et al. 2000). Such models are also extensively used for computer-aided design in automobile or aeronautic industry, in mechanical studies (Behr et al. 2003) or thermal effect applications (Wainwright 2000).

The actual work focuses on the creation of reference libraries representing a wider population using Mesh and NURBS techniques (when compared to ICRP reference individuals). Johnson et al. (2009) have recently released 25 adult male models and 15 pediatric female models corresponding to percentile individuals. Na et al. (2010) have also developed morphing algorithms to create percentile individuals of different height and weight.

IV.3. Discussion of the 3D representations

Computer graphic designers have defined two types of representations, CSG and BREP, which are commonly used to realize modeling and design studies. However, it is not always easy to distinguish between these representations. This is particularly the case when comparing a mathematical phantom to a Mesh or NURBS model since these representations are based on mathematical equations. The key point differentiating between CSG and BREP lies in the definition of each representation. Indeed, “solid” volumes are used for CSG while “empty” surfaces are considered for BREP. However, surface and volume definitions are very similar and connected. The main and most obvious difference comes from the format and style in which the data is encoded. Triangular Mesh geometries are written in virtual reality modeling language (.vrm) or polygon file format (ply). NURBS models are written as wavefront objects (.obj) while voxel geometries are mostly raw (.raw) type files.

Various modeling software have been developed to generate 3D representations. The Rhinoceros 3D modeling software (<http://www.rhino3d.com/>) remains one of the most commonly used software with a set of deformation and geometry modification tools. RPI Mesh phantoms, FASH and MASH phantoms, NCAT and MOBY are examples of phantoms created with this software. Other modeling tools such as Blender (<http://www.blender.org/>) and 3D-Doctor™ (<http://www.ablesw.com/>) have also been used by the radiation dosimetry community to develop anthropomorphic 3D phantoms such as the UF newborn phantoms.

When compared to CSG representations, BREP representations are more flexible and allow a wider set of morphing operations which makes them more appropriate for CAD.

Nevertheless, these still suffer from a major limitation rising from the voxelization process to

comply with Monte Carlo simulation requirements of geometry definition. Indeed, each model generated with Mesh and NURBS geometries should be transformed into voxel grids before running the MCNPX simulations. Some Monte Carlo transport codes such as Geant 4 (geant4.slac.stanford.edu/SLACTutorial07/Geometry1.ppt) and Penelope (Badal et al. 2008) were upgraded to handle Mesh representations. However, the simulation time with these geometries is sensitively increased, up to orders of magnitude, which makes the feature of limited interest.

Finally, Mesh and NURBS geometries offer definitely more appropriate definitions of 3D surfaces when compared to voxel representations. However, it should be noticed that the visualized images of 3D models, presented in Figure 1.13 for example, do not faithfully represent the quality of the phantom. Indeed, such images are obtained with surface rendering software that produce 2D images from 3D representations by adding lights, texture and bump mapping, shadows etc. The produced image looks realistic and even ideal as would an “artist” picture a scene. Therefore, the data contained in the primal file is often improved with the rendering process showing the Mesh and NURBS geometries far more “perfect” than what they really are.

V. Female workers and *in vivo* monitoring

One of the main drawbacks in the calibration of counting systems is the use of physical phantoms of limited realism in regards to the human anatomy. For *in vivo* lung monitoring of female workers, no physical female phantom dedicated for the calibration of *in vivo* installations exists. The use of the typical male-based calibration coefficients results in high uncertainties on the activity estimate, and consequently on the dose calculation for female workers. Therefore, numerical calibrations based on MC calculations are needed to optimize the monitoring of female workers using *in vivo* spectrometry measurements.

Moreover, simulating an *in vivo* counting requires massive and performing calculation potential and significant time. Clusters dedicated for Monte Carlo simulations are often needed to run the statistical calculations and compute the result. However, the simulation result may sometimes be required, in emergency situations for example, to take the correct decontamination action. Accurate and rapid Monte Carlo simulations are thus required while maintaining statistically reliable results.

Finally, the management of complex internal contamination situations remains critical particularly when very few information is available on the number, nature and distribution of the incorporated radionuclides. In this situation, *in vivo* measurements remain of limited efficiency when determining the activity distribution because of the multiple contributions of several organs to the counting. Biokinetic models remain up to now the only mean to establish the distribution of radionuclides inside the body. These models were however built from animal experiments and can difficultly be verified in practice. Moreover, these models do not account for the metabolism of each individual. Putting MC simulations into benefit represents thus a promising solution to accurately determine the activity mapping.

This PhD thesis has thus been undertaken with the following objectives:

- to develop of a library of female phantoms using Mesh and NURBS geometries,

- to realize the numerical calibration of the AREVA NC *in vivo* counting system and to correct the typical calibration coefficients obtained with the male torso phantom,
- to establish an equation describing the morphological dependence of lung counting calibration coefficients to give the AREVA NC medical staff, responsible for the monitoring program, a mean to correct the calibration for any female morphology,
- to improve the efficiency of MC simulations through the use of variance reduction techniques and by simplifying the phantom geometry,
- to use *in vivo* spectrometry measurements coupled with Monte Carlo simulations to handle complex internal contaminations and to determine the activity distribution.

Chapter 2

Development of a Mesh and NURBS-based female torso library

To correct the typical calibration coefficients obtained with the Livermore male mannequin, numerical calibrations using Mesh and NURBS representations and Monte Carlo calculations were required. This chapter focuses on the development of an extended library of 24 thoracic female phantoms, derived from the torso of the ICRP adult female reference computational phantom, created to represent the most common female morphologies.

This chapter is divided into five main sections. The first section introduces the available tools used for the generation of 3D numerical phantoms and the protocols established for the cases in which medical images are available or not. The second section discusses the female body type, measurement and definition. The third section presents the method used for the creation of a deformable female torso core model from which a library of female models was derived by varying the cup size, the chest girth and the internal organ volume as shown in the fourth section. The last section discussed the creation methods and characteristics of the library and compares it to existing models.

I. Generating 3D graphic phantoms

The following paragraphs introduce the tools used for the creation of 3D anthropomorphic phantoms based on Mesh and NURBS representations. Next, the protocols established for the creation of anthropomorphic phantoms using these tools and starting from medical images or from a voxelized model are discussed.

I.1. Tools for 3D models generations

I.1.1. Isogray

The Isogray Treatment Planning System (TPS) was developed in collaboration between the “Institut Curie” and the “Institut Gustave Roussy” and commercialized by DosiSoft since 2002 (<http://www.dosisoft.com/index.html>). In this study, Isogray was considered for its image treatment capacities mainly organ delineation and segmentation that are essential for the simulation process. This software supports both CT scan images and MRI images and enables automatic and manual organ delineation. Image segmentation using Isogray was validated in a previous study (Pierrat 2002) by comparing numerical phantoms, reconstructed from Isogray image segmentations, to experimental measurements.

The first step in image segmentation is the automatic delineation of the body surface. Some organs such as the lungs are also automatically adjusted since they have a sensitively different Hounsfield number, i.e. a density of about 0.3 g/cm^3 , which makes their differentiation easier when compared to other tissue. Manual adjustments are, however, often required to further improve the segmentation of such structures. Meanwhile, most internal organs have similar densities and require thus manual segmentation. Nevertheless, the manual segmentation is highly dependant on the image quality, contrast, modality, and above all on the user experience and knowledge of the human anatomy. Isogray also enables a three-dimensional visualisation of the segmented structures which gives a rough representation of the phantom.

The more realistic the required phantom is, the higher the number of segmented structures is and thus the more the segmentation time increases.

I.1.2. IDL

The IDL[®] (Interactive Data Language) is an object oriented language used since 2005 at LEDI for data treatment and visualisation (<http://www.itvis.com/ProductServices/IDL.aspx>). The IDL[®] executable (extension “.sav”) can be run using the IDL[®] Virtual Machine (VM) with free online access. With the VM, it is possible to make any IDL[®] program accessible to all interested parties without diffusing the source code and without requiring an IDL[®] licence.

In this study, IDL[®] was introduced for its excellent 3D visualisation tools and options (cf. Figure 2.1). Indeed, IDL enables the plot of various input data formats among which the “.raw” files and the DICOM files (Digital Imaging and COmmunications in Medicine). Dozens of routines were developed using the IDL[®] tool kits and functions that were essential at different levels of the female library development. Among these routines, the most important ones are relative to the visualisation of voxelized organs (cf. Section I.1.4), the generation of an OEDIPE input file format (cf. Section I.1.4), the calculation of vertices and connectivities of 3D surfaces (cf. Section III.1 and Appendix A.1) the correction of intersections and voxelization errors (cf. Section III.1 and Appendix A.2), the addition of a voxel layer representing the skin (cf. Section III.1 and Appendix A.3).



Figure 2.1. IDL[®] plotting of the Livermore voxelized lungs using the xvolume function.

I.1.3. Rhinoceros 3D

Rhinoceros 3D (Rhino 3D) modeling software (<http://www.fr.rhino3d.com/>) is a tool that is widely used for computer graphics and design. Rhino 3D has also been used to design realistic and personalized anthropomorphic phantoms for dosimetry studies (Segars 2001; Zhang et al. 2008; Lee et al. 2009).

Rhino 3D supports multiple input and output data types among which the Mesh (.wrl) and NURBS geometries (.obj). It allows various surface modifications and transformations including Boolean operations, rotations, dilation/contraction operations, surface fusion/subtraction etc. (cf. Figure 2.2).

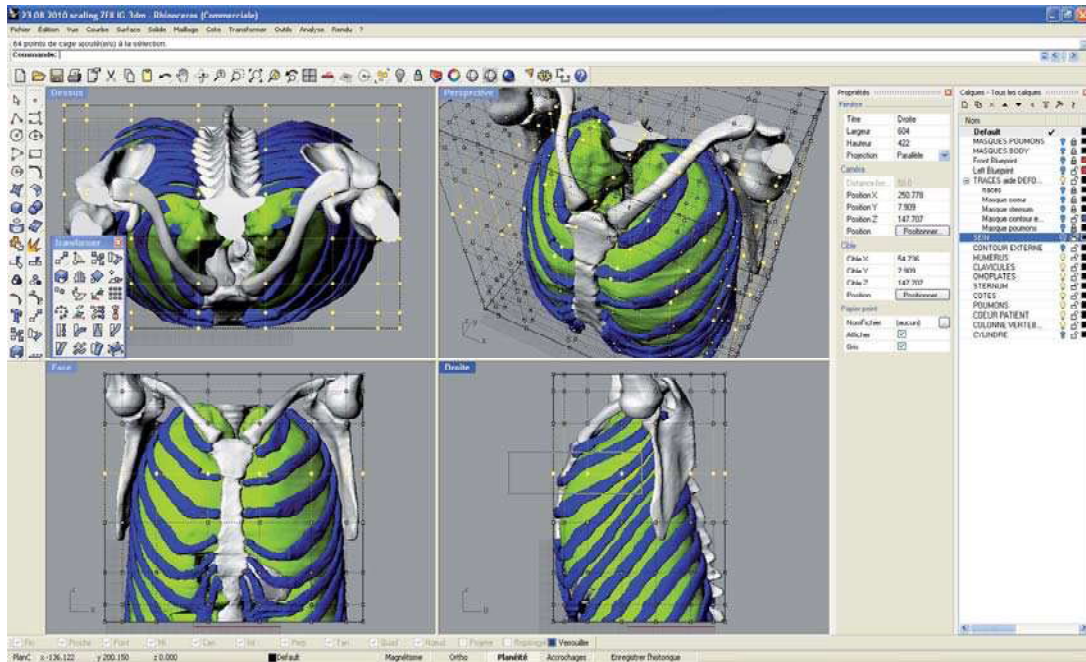


Figure 2.2. Visualization of the Rhino 3D software and the available surface modification tools.

1.1.4. The Binvox program

Mesh and NURBS surface voxelization was done using the Binvox program. Once launched (using Dos command), Binvox requires the user to specify the voxel grid dimension (default 128*128*128), the output file format (default .binvox), the voxelization algorithm (default both Ray Stabbing and Parity Count). Binvox supports various input formats among which the VRML2.0 (.wrl) obtained with Rhino 3D and representing Mesh triangulations and the Object (.obj) format representing the NURBS splines (when polygons are used). Visualizing the output files is possible with the Viewvox program, also developed by Dr. Patrick Min (<http://www.cs.princeton.edu/~min/binvox/>), for the “.binvox” format files (cf. Figure 2.3).

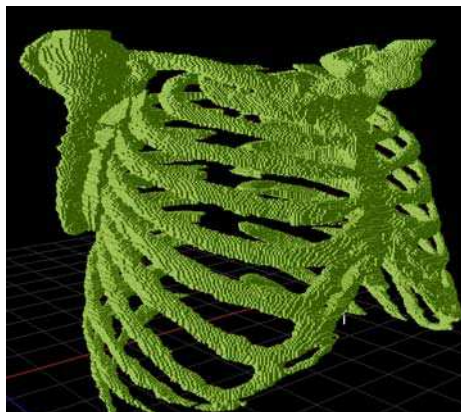


Figure 2.3. Viewvox visualization of voxelized ribs obtained using the Binvox program.

Before voxelizing, Binvox normalizes the Mesh such that it fits inside a 0.95x0.95x0.95 cube ensuring an empty "shell" around the voxel model in the unit cube. As a consequence, each voxel in the model has coordinates inside the unit cube. Nevertheless, the normalization in the unit cube is independent from the real size of the structure. In other words, the Binvox voxelization of a car and of the miniature of this car give identical representations having the

same number of coding voxels. Thus, in order to ensure a realistic representation of the voxelized object, the elementary voxel dimension is assigned to meet with the real dimensions of the object. Moreover, in the case where multiple structures/organs are present in the input file to be voxelized, Binvox transforms the surfaces to voxel grids while conserving the relative positioning of each organ. However, Binvox attributes to all coding voxels the same value (one). This is a limiting factor since no direct distinction between the voxelized structures/organs is possible. In order to separate the structures using Binvox, Dr. Min has agreed to modify the source code of Binvox by adding an “ignore” function that enables the user to isolate a particular structure/organ and voxelize it separately from the compounds of the Binvox input file. An example of the use of Binvox with the ignore function is given in Figure 2.4 where three structures are available and only the third being voxelized.

```
D:\semaine_5>binvox0.37.exe
--- [binvox] mesh voxelizer, version 0.37, build #150 on 2008/02/14 17:10:57
--- written by Patrick Min, 2004-2006

Error: missing model filename

Usage: binvox [-d <voxel dimension>] [-t <voxel file type>] [-c] [-v] <model file
spec>
  -d: specify voxel grid size (default 128, max 1024)
  -t: specify voxel file type (default binvox, also supported: hips, mira, vtk,
raw)
  -c: z-buffer based carving method only
  -v: z-buffer based parity voting method only (default is both -c and -v)
Supported 3D model file formats:
URML U2.0: almost fully supported
UG, OBJ, OFF, DXF, XGL, POJ, BREP, PLY, JOT: only polygons supported
Example:
binvox -c -d 200 -t mira plane.wrl

D:\semaine_5>binvox0.37.exe -ignore 1 -ignore 2 -c -d 256 -t raw input.wrl
```

Figure 2.4. The Binvox program input and output functions, example of using the ignore function when three structures are present in the input file to be voxelized.

Thus, the voxelization of an input file is repeated as many times as the number of available structures in the file and, as a consequence, the number of output files collected is equal to the number of times Binvox was used with the ignore function. Each of these Binvox output files is imported to an IDL[®] routine that assigns a density value to the coding voxels. The output of the routine is thus a voxelized version of the 3D model with contrasted structures. The used IDL[®] routine is given in detail in Appendix A.2.

I.2. Protocols for 3D models generation

Using the 3D tools introduced above, numerical anthropomorphic phantoms were generated following two protocols starting from medical images, if such images are available, or starting from a reference voxelized model, if not.

I.2.1. Medical images available

The creation of 3D Mesh and NURBS personalized phantoms starts with DICOM medical images, mainly CT scan and MRI, from which anatomical data can be extracted (Figure 2.5(a)). This guarantees a high degree of realism and fidelity in the modeling of the human anatomy. Hence, the Isogray TPS was used to delineate the organs of interest influencing the

count (Figure 2.5(b)). Organ contours were then imported to the Rhino 3D modeling software that enables the creation of Mesh and NURBS 3D models (Figure 2.5(c)). Finally, the Binvex program was used to transform 3D geometries into voxel grids (Figure 2.5(d)).

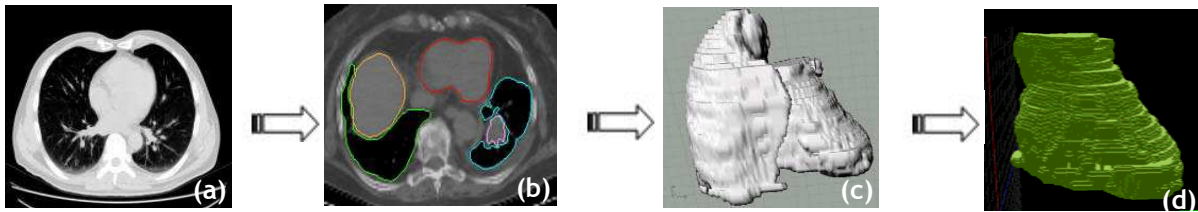


Figure 2.5. 3D phantom creation from medical images

I.2.2. Medical images unavailable

For the female phantom creation, a second protocol was used since no medical images of a female subject were available. In this case, voxel grids of the ICRP Adult Female Reference Computational Phantom (AF-RCP) (Figure 2.6(a)) were transformed to Mesh surfaces using a routine developed in the IDL code (Figure 2.6(b)). Next, NURBS surfaces were created from Mesh geometries using the Rhino 3D “loft tools” (Figure 2.6(c)). Once the geometries created, the Binvex program was again used to voxelize the phantom (Figure 2.6(d)).

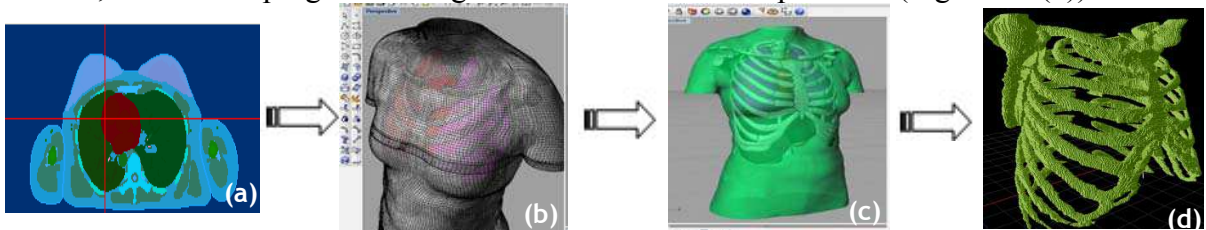


Figure 2.6. 3D phantom creation from voxel model

II. Female body type, morphology and size designation

The aim of this work was to optimize the calibration of *in vivo* counting systems to improve the monitoring of female workers. Thus, it was necessary to generate a library of female phantoms representing the most common female body types and measurements. The first step in the library creation is to identify the measurements most likely to efficiently represent the female workers’ community. These include the chest girth and cup size designation and evaluation. The second step, however, consists in identifying the methods to be used to modify each parameter in order to create realistic and representative female models.

II.1. Chest girth designation and evaluation

The size designation norm of clothes published by the European Committee for Standardization (CEN 2001) defines two dimensions to measure women’s breast size: the bust girth (BG), which is the maximum horizontal girth, and the underbust girth (UBG), which is the horizontal girth just below the breast. Chest girth is designated by numbers and appended to the UBG (cf. Table 2.1). For example, if the UBG is between 68 and 72 cm, the chest girth

code is 85. Following the brassiere industry practice, the chest girth code number is given without units. These measurements (BG and UBG) are taken for female subjects in a standing position and have been used by the fashion industry to create their brassiere models.

Table 2.1. Chest girth designation according to the European committee for standardization.

Code	85	90	100	105	110	120
UBG range (cm)	68-72	73-77	83-87	88-92	93-97	103-107

For the created models, band size was calculated at the base of the breasts as recommended by the European norms cited above. This was done by counting the elementary voxels on the outer periphery of the bust and calculating their length. For the ICRP AF-RCP for example, the estimated band size was about 73 cm, so the phantom reasonably corresponds to a small 90 chest girth (European Standard Clothing Units code).

II.2. Cup size designation and evaluation

The ICRP, in its latest publication (ICRP 2009), has specified the anthropometric data for the average female breast organs in terms of dimension, total weight, tissue composition, and density. The size designation norm of clothes established by the European Committee for Standardization has also defined a secondary dimension to measure women's breast size. The introduced parameter, called cup size (CS), characterizes the difference between BG and UBG (CEN 2002, 2004). According to this committee, bras are labeled compactly using a letter code cf. Table 2.2.

Table 2.2. Bra size designation according to the European committee for standardization

Code	A	B	C	D	E	F
CS range (cm)	12-14	14-16	16-18	18-20	20-22	22-24

However, breast structures vary widely depending on multiple criteria like age, ethnic origin, hormonal activity, corpulence, musculature, etc. Many studies (Berger and Lane 1985; Lee et al. 2004) tried to identify reliable anthropometrical marks to quantify and describe breast dimensions or even to develop empirical equations to determine breast shapes. Moreover, the definition of relevant parameters or landmarks that allow a precise determination of breast shape is still debated. As reported in the literature, traditional brassiere-industry measurements of breast size and chest girth are somewhat insufficient for correct and realistic design of breast shapes. Brown et al. (1999) identified 12 key landmarks for subjects sitting upright. Vandeput and Nelissen (2002) used only 6 landmarks while Sigurdson and Kirkland (2006) introduced 11 anthropomorphic measurements to assess the breast volumes for a standing person. The design of breast shapes can become even more complex when position (supine versus prone), age or ethnic origin are considered (Fabié et al. 2006). The brassiere industry organizes measurement campaigns in order to produce the most representative bras fitting the most common sizes. Such statistics provide a reasonable estimate of the female breast size distribution of a population and were thus considered to identify the library models to be created.

For the considered routine *in vivo* lung counting measurements, the monitored female is in a supine position. Thus, depending on their weight and elasticity, breasts take different shapes over the chest. This makes the CS classification method of little help to design breast models in supine position. To overcome this difficulty, working over breast volumes and weights to estimate the correct cup size was considered. For cup size calculation, the breast volume measurements of different female populations were considered (Loughry et al. 1989; Smith et al. 1986; Warren et al. 2007). It was found that the average woman having breast weights ranging from 350 to 650 g would represent a B cup size subject. In this study, the ICRP reference female model has a total breast weight of about 500 g, thus it fitted a B cup breast.

III. Creation of a deformable female torso core model

The creation of a female torso library starts with the generation of a deformable core model whose geometry can be easily modified to cover a wide range of female body type and morphology. The Mesh and NURBS torso core phantom was created from the ICRP reference voxelized female. The creation of a torso core model dedicated for numerical calibration requires the creation of a realistic geometry, the attribution of a correct tissue composition and density. The created model was then compared to the reference ICRP female to validate its organ volume and MC simulation results.

III.1. Geometry creation

First, an IDL routine was developed to transform the voxel data of the ICRP AF-RCP to surfaces in order to generate a Mesh model using the `shade_volume` function (cf. Appendix A.1). This step includes the selection of the thoracic region, the organ grouping, the Mesh building (vertex, connectivity, normal vectors calculation) and the VRML writing. For this study, the internal organs that were included in the model are the ribs, sternum, spin, shoulder blades, lungs, liver, heart and breasts. Next, the breast and thorax contours were transformed to NURBS surfaces to enable higher flexibility and deformation potential; this was done under Rhino 3D loft tools. This is a four steps method that consists first in isolating the Mesh model of the organ of interest (Figure 2.7(a)) projecting the surface to have the optimal view of the outer curvature (Figure 2.7(b)), cutting sections in the Mesh model to generate as many slices as necessary to reproduce, with the maximum realism, the organ shape (Figure 2.7(c)) and finally creating NURBS surfaces by linking the generated slices (Figure 2.7(d)) with the loft tool. This method is particularly interesting since the user can specify the number of control vertices on each slice, i.e. Spline curve, that can be very helpful in the deformation steps cf. Section IV.1.

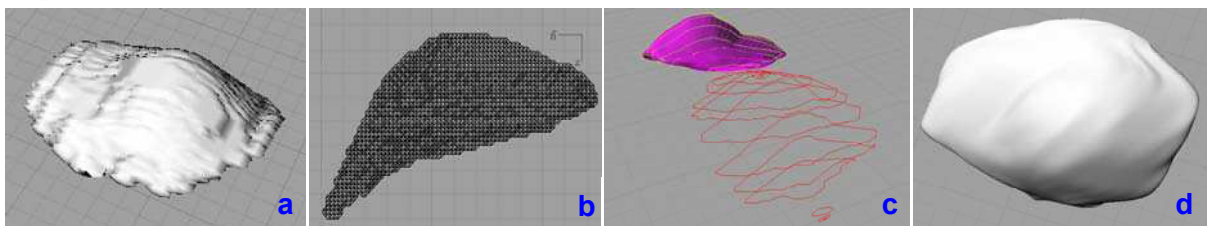


Figure 2.7. Rhino 3D steps for the generation of NURBS surfaces starting from Mesh triangulations and using the loft tool.

This generation method requires however two additional operations to complete the model: correcting the surface intersections and adding the skin. Indeed, for the generated 3D Mesh surfaces, organ intersections were observed under Rhino 3D (cf. Figure 2.8). To correct these intersections, an IDL routine was used to fuse the merging areas to one of the intersecting organs using the voxelized model of the phantom (cf. Appendix A.2). Nevertheless, the observed intersections did not involve a volumetric overlapping of more than 3% (case of the sternum). Moreover, the skin is defined in ICRP voxelized model by one voxel layer surrounding the residual tissue of the trunk. Thus, an IDL routine was developed to generate a voxel layer surrounding the trunk in order to complete the skin adding (cf. Appendix A.3).

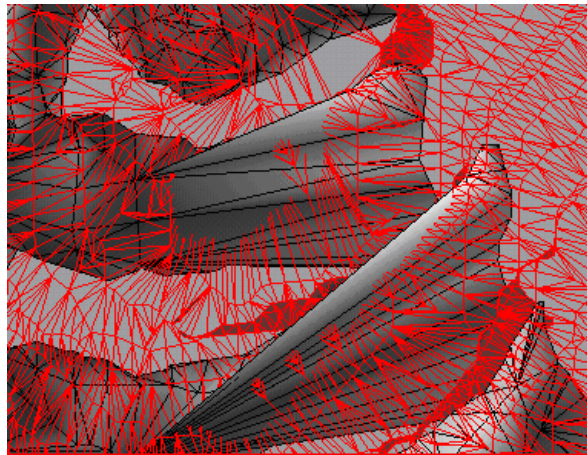


Figure 2.8. Rhino 3D visualisation of Mesh surface intersections between ribs (grey) and lungs (red).

III.2. Tissue composition and density

To assign a correct and realistic tissue composition and density to the created organs, the method used for the generation of each organ was reviewed. Tissue composition was attributed by considering the different compounds fused together to form the organ while the density was fixed so that the created volume meets with the ICRP reference weight. In this particular study, the breasts, the internal organs and the residual tissue are considered separately. The elemental compositions were taken from the ICRP 110 (ICRP 2009).

III.2.1. Case of the breasts

For the breasts, the only involved structures that were fused to generate the 3D model of the organ are the ICRP breast adipose and glandular tissues. Since the glandular and adipose tissues were fused, the tissue composition and density were attributed to the whole breast volume and no regional considerations whatsoever was done.

As in ICRP AF-RCP, the weight proportion for the breasts of the core model was maintained. Namely, 40% of the breast tissue was of glandular nature and 60% was of adipose tissue nature. This proportion affected the tissue composition assigned for the generated breast structure *cf.* Table 2.3.

Table 2.3. Composition of the deformable female core model's breasts.

Model	H	C	N	O	Na	S	Cl
Core phant.	11.40	53.78	0.62	34.02	0.06	0.06	0.06

After voxelization, the breast density was fixed so that the weight of the created breasts equals that of the ICRP model (ICRP 2002). Namely, the ICRP breast compounds -adipose and glandular tissue- have a respective weight of 150 and 100 g, meaning a total breast weight of 500 g *cf.* Table 2.4. The density was hence fixed at 0.99 g/cm³ so that the created breast volume corresponds to this exact weight. For the ICRP AF-RCP, the densities of adipose and glandular tissue are respectively 0.95 and 1.05 g/cm³. The fixed breast density value (0.99 g/cm³) seems reasonable since it is fairly equal to the mean of the theoretical tissue densities.

Table 2.4. Densities of the deformable female core model's breasts, compounds are named according to their designation in the ICRP AF-RCP.

Created organ	Compounds	Compound weight (g)	Total organ weight (g)	Density ^a (g/cm ³)
Breasts	Breast left adipose	150	500	0.990
	Breast left glandular	100		
	Breast right adipose	150		
	Breast right glandular	100		

III.2.2. Case of the internal organs

The first step concerns the created “organs of interest” considered to have a potential influence on the *in vivo* counting efficiency simulation including the ribs, sternum, spin, shoulder blades, lungs, liver, heart, breasts and skin. To choose the right composition and density, the method used to create each organ was again taken into account as most organs were created as a mixture of different compounds of various composition and densities. For example, the spine was created as the sum of 6 compounds: thoracic spine cortical, thoracic spine spongiosa, lumbar spine cortical, lumbar spine spongiosa, spinal cord and cartilage. Hence, this organs' final composition was defined as the mass contribution of each compound to the final weight of the structure (*cf.* Table 2.5). This method was considered for all internal organs involved in this study.

Table 2.5. Composition of the deformable female core model's internal organs.

Model	H	C	N	O	Na	Mg	P	S	Cl	K	Ca	Fe
Heart	10.28	12.13	3.14	73.45	0.10	0.00	0.14	0.20	0.26	0.24	0.00	0.06
Liver	10.20	13.10	3.10	72.40	0.20	0.00	0.20	0.30	0.20	0.30	0.00	0.00
Lungs	10.29	10.73	3.21	74.59	0.19	0.00	0.19	0.29	0.30	0.20	0.00	0.01
Ribs	7.58	27.54	3.22	47.67	0.21	0.07	4.24	0.31	0.14	0.06	8.90	0.06
Shoulder blades	6.73	27.41	3.17	44.42	0.24	0.12	5.52	0.31	0.07	0.05	11.97	0.00
Skin	10.00	19.50	4.20	64.50	0.20	0.00	1.00	0.20	0.30	0.10	0.00	0.00
Spine	7.18	26.52	3.35	47.13	0.20	0.10	4.76	0.31	0.11	0.06	10.25	0.03
Sternum	9.66	29.48	2.64	53.48	0.23	0.00	1.70	0.42	0.23	0.07	2.02	0.07

Meanwhile, the mass proportion contribution cannot be considered for densities calculation. As a consequence, densities were again calculated so that the created structures have the exact organ weight as in the ICRP AF-RCP. Table 2.6 resumes the tissue compounds fused to create each internal organ and documents the densities assigned.

Table 2.6. Densities of the deformable female core model's internal organs, compounds are named according to their designation in the ICRP AF-RCP.

Created organ	Compounds	Compound weight (g)	Total organ weight (g)	Density (g/cm ³)
Heart	Heart wall	250	620	1.046
	Heart content	370		
Liver	Liver	1400	1400	1.048
	Left lung blood	59		
Lungs	Left lung tissue	377	951	0.413
	Right lung blood	42		
	Right lung tissue	472		
Ribs	Ribs cortical	162	470	1.283
	Ribs spongiosa	259		
	Cartilage	50		
	Clavicles cortical	23		
	Clavicles spongiosa	28		
Shoulder blades	Humeri upper half cortical	56	420	1.391
	Humeri upper half spongiosa	106		
	Humeri medullary	7		
	Scapulae cortical	102		
	Scapulae spongiosa	77		
Skin	Cartilage	21	553	1.120
	Skin trunk	553		
	Thoracic spine cortical	204		
Spine	Thoracic spine spongiosa	253	752	1.309
	Lumbar spine cortical	90		
	Lumbar spine spongiosa	142		
	Spinal cord	12		
	Cartilage	52		
Sternum	Sternum cortical	2	70	1.095
	Sternum spongiosa	47		
	Cartilage	21		

III.2.3. Case of the residual tissue

In this study, when creating the deformable torso core model, Mesh surfaces were generated only for the organs having a significant influence on the *in vivo* count. As a consequence, all internal organs that were not used in this study were fused all together to generate a structure representing the residual tissue of the core model. The residual tissue composition and density

were again defined taking into account the mixture of the ICRP merged body compounds. The composition was defined as the mass contributions of the ICRP phantom gathered organs whereas the density was fixed so that the generated volume has the correct mass.

Table 2.7. Composition and density of the deformable female core model's residual tissue.

Model	Composition												Density (g/cm ³)
	H	C	N	O	Na	P	S	Cl	K	Ca	Fe	I	
Core phant.	10.8	34.7	2.0	51.7	0.1	0.1	0.2	0.1	0.2	0.0	0.0	0.0	1.017

III.3. Validation of the torso core model

Once the core phantom was completed, it was validated by comparing the created organ volumes to those of the ICRP model and the MC simulation results with both models.

III.3.1. Volume of the created organs

For the volume comparison, the ICRP AF-RCP was taken as the reference model against which the voxel version of the core model was checked for each organ. The maximum relative error in volume, around 3.3%, was observed for the sternum structure. All internal organ volumes matched reference values with less than 1.5% deviation (cf. Table 2.8). It should be noticed however that, in this case, the trunk cartilage was associated to the generated bone structures. Namely, one third of the trunk cartilage was added to the ribs, another third was fused with the spine while the last third was equally distributed between the sternum and the shoulder blades. The cartilage adding represented 10% of the total weight of the ribs, while this proportion was of 7% for the spine, 30% for the sternum and 5% for the shoulder blades.

Table 2.8. Organ volume of the reference ICRP female and the deformable core model and associated relative error.

organ	ICRP AF-RCP reference volume (cm ³)	Deformable core phant. volume (cm ³)	Relative Error (%)
Breasts	511.9	505.0	1.35
Heart	587.2	592.5	-0.91
Liver	1333.3	1336.4	-0.23
Lungs	2301.1	2301.7	-0.03
Ribs	366.3	364.6	0.46
Shoulder blades	304.4	302.3	0.71
Sternum	67.5	65.3	3.31
Spine	563.8	562.3	0.26
Skin	507.7	495.4	2.43
Residual tissue	10697.9	10530.4	1.57

III.3.2. Simulation of *in vivo* counting efficiency

Monte Carlo simulations of *in vivo* counting were also used to validate the created torso core model. Indeed, radiation interactions with matter are directly related, through the mass attenuation coefficient, to the tissue composition and density. Bone structures of high densities have a sensitive attenuation effect on low energy photons while adipose tissue is of lesser effect. Thus, in order to validate the assigned tissue composition and density, MC simulations were conducted with the ICRP reference model and with the simplified female deformable core model.

These simulations were carried out for radionuclides of interest (^{241}Am , ^{238}U , ^{60}Co , ^{137}Cs etc.). The detectors that were used are typical germanium detectors dedicated for *in vivo* lung counting studies that were positioned identically in both simulations. The OEDIPE software (Franck et al. 2007) was used to create the source and distribute it uniformly in the lungs and to position the detectors. Counting efficiency values similar to those obtained for the ICRP phantom were thus expected in order to validate the female deformable torso core model and particularly the attributed tissue composition and density.

Figure 2.9 represents the counting efficiency variation with energy for the ICRP AF-RCP torso and for the flexible female torso core model. For all energies greater than 40 keV the difference in counting efficiency was less than 5%. For lower energies, the maximum difference was as high as 35% at 15 keV. This difference at low energy is presumably due to the different types of materials used in the two phantoms. In fact, the ICRP AF-RCP torso is made up of 67 organs or tissues, while the flexible female torso model contains just ten organs. The average tissue considered for the flexible model is most likely responsible for the observed differences. Nevertheless, these differences remain acceptable and validate the choice of tissue composition and density.

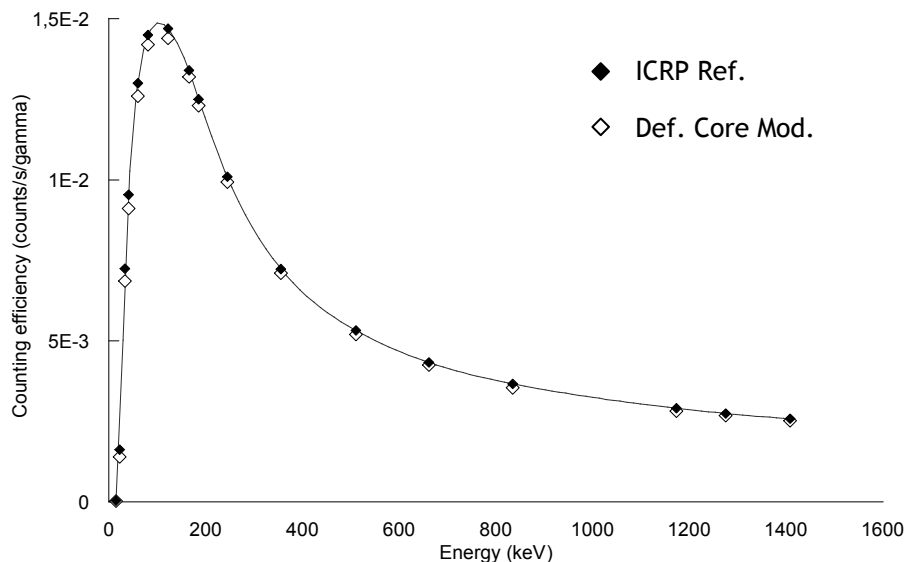


Figure 2.9. Variation of the counting efficiency (counts/s/gamma) with energy (keV), for the ICRP AF-RCP reference model (black symbols) and the female torso core model (white symbols).

IV. Phantom geometry modification

A library of 24 torso models representing most common breast morphologies was derived from the validated flexible female torso core model. This section resumes how the target values for geometry modification were chosen. Then, the method used to generate the various morphologies and to attribute the correct tissue composition and density are presented.

IV.1. Target values for geometry modification

The steps involved in the creation of the female torso library are those relative to the variation of cup size, chest girth and internal organ volume.

IV.1.1. Chest girth modification

To realize chest girth modification, the targeted chest circumferences were fixed at the middle of the UBG intervals indicated in Table 2.1. Namely, to create the 85, 100, 110 and 120 chest girths, final models' band size was chosen to be equal to 70, 85, 95 and 105 cm respectively.

Starting from the reference 90 chest girth, simple contraction and dilation operations were applied over the Mesh phantom to create the 85 and 100 chest girths. For example, to switch from a chest girth of 90 to another of 85, a two-dimensional (left-right and posterior-anterior) contraction coefficient of 0.93 (70/75) was applied. This transformation induced a total thoracic weight reduction by only about 2.3 kg, hence the Body Mass Index (BMI) was not significantly changed. For the 100 chest girth, a 3 directional dilation was applied in order to create a realistic phantom. Indeed, it is more plausible to have a 182 cm person with a chest circumference of 85 cm (i.e. 100 chest girth cf. Table 1) than a 163 cm person with such chest girth. The change in phantom's height was also realized to maintain the same BMI as for the ICRP AF-RCP. More precisely, the thorax of the ICRP model represented around 27.5% of the total body weight. This weight proportion was maintained for the 100B chest girth phantom. The operated 3D dilation of the 90B torso resulted thus in a 74.7 kg and 182 cm female subject having a chest girth of 100 and a BMI of about 22.6.

For the 110 and 120 chest girths, 3D dilation operations would generate a 205 and 220 cm height person to maintain a "normal" BMI. These are rather rare measurements in reality, so the Mesh surfaces were replaced by NURBS ones. Modifying the NURBS surfaces for the creation of the two biggest chest girths was particularly advantageous since it enabled the use of local and controllable deformation over the volume, leading to realistic shapes. Starting from the 100 chest girth Mesh model, a NURBS model was created using Rhino 3D loft tools and then the control vertices of the splines, mainly those over the stomach, were manually shifted in the correct direction to create the targeted chest girths (110 and 120). Phantom's height, however, was not changed and the 100, 110 and 120 chest girth models have the same total height but different BMI. Indeed, about 5 kg of adipose tissue were added to increase the chest girth from 100 to 110 (respectively about 11 kg to generate the 120 chest girth model). Therefore, the models represented an 80 kg female with a BMI of about 24.4 (respectively 86 kg and a BMI of 25.6).

IV.1.2. Cup size modification

To realize cup size modification, breast weight variation was considered following plastic and reconstructive surgery recommendations. It was found that surgeons count mostly on their personal experience to choose the right implant nature and volume. Regnault et al. (1972) considered an addition of 100 cm^3 to increase chest circumference by 1 inch and brassiere cup size by one letter designation. While Pechter (1998) found that the volume needed would be around 300 cm^3 . Yet others indicate that it depends significantly on the implant location: if the implant is under the muscles, an additional implant volume of 75 cm^3 is needed per cup size change. To realize cup size change, the recommendations by Turner and Dujon (2005) were followed especially since the authors quantified tissue adding not only as a function of cup size but also with respect to chest girth (cf. Table 2.9).

Table 2.9. Tissue weight adding per cup size change according to Turner and Dujon (2005).

Chest Girth	Tissue weight to be added (g) per cup size change
85 - 90	2×115
95 - 100	2×215
105 - 110	2×315
115 - 120	2×415

• 90 chest girth models

Starting from the reference 90B NURBS breasts (i.e. deformable core model), and to create a 90C model, $2 \times 115 \text{ g}$ of tissue were added. For a given chest girth, cup size was modified by adding the same amount of adipose tissue for each increase in cup size as recommended by Turner and Dujon (2005). The additional tissue was considered to be of adipose nature only to simplify and ease phantom's creation. The equivalent volume (of the $2 \times 115 \text{ g}$ amount of adipose tissue) was then calculated. This volume was added to the primary breast volume (511.88 cm^3 cf. Table 2.8) and the final targeted volume was fixed to about 754 cm^3 . Using Rhino 3D, the NURBS breasts surfaces were then modified by manual shifting of the control vertices in the posterior-anterior direction to reach the target breast volume cf. Figure 2.10. For greater realism, a left-right translation was applied to simulate how breasts fall naturally over the chest as the morphology of the breasts was modelled in the supine position, i.e. *in vivo* counting position. The larger the breasts, the more difficult they are to model and position correctly on the bust in the supine position, and realism may be affected as a result. This manual morphology modeling technique was used to create all the considered cup sizes.

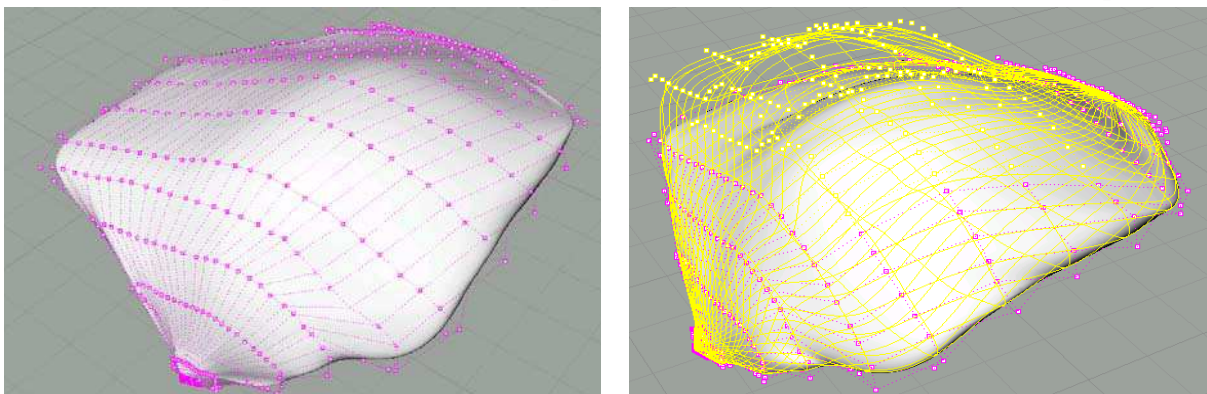


Figure 2.10. Rhino 3D visualization of the operated manual shifting of the Splines control vertices to realize cup size change.

- **Other chest girth models**

At this point, methods for varying cup size and modifying chest girth are clearly defined. The remaining problem is to fix a reference mass for one cup size of each chest girth. As highlighted by Young et al. (1994), cup size varies with band size, e.g., the cup of a 95C bra is slightly larger than the cup of a 90C bra. Hence, to create the new reference cup size for each chest girth, breast's weight was fixed considering statistical data, plastic surgery recommendations and the creation method used. On the one hand, for the 85 chest girth models (respectively for the 100 chest girth model), a simple contraction (respectively dilation) operation was used to vary band size starting from the 90B phantom. Therefore, the created cup volumes were considered to be the new reference ones representing respectively an 85B and a 100B models. On the other hand, for the 110-120 chest girth phantoms, manual operations were also required when varying band size, therefore the reference cup size was chosen differently. Indeed, in this case a simple empirical equivalence was used that relates one combination of a letter (for cup size) and a chest girth to the next letter and the previous chest girth, for example a 100E model has the same breast volume of a 110D subject which is also equivalent to a 120C breast size (Wood et al. 2008). Particularly, while creating the 110B cup size (resp. 120C), the 100C cup (resp. 110D) was used as a morphology model; hence, they were considered to have the same breast weight. The created reference cup sizes for each chest girth are thus the 85B, 90B, 100B, 110B and the 120C. They were used as a basis for the creation of the other cup sizes with the recommended additional tissue of Turner and Dujon (2005) given in Table 2.9.

For greater realism, we considered changing breasts morphology since it changes from one person to another and even for the same person. Thus 10 additional big cup sizes were created. For example, three different breast models, representing a 90C female subject, were created. The method used to create the first morphology (90C1) was to translate the vertices of the 90B breast Mesh in their normal vector direction. The second morphology (90C2) was created from the 90B by a 3D dilation. The final morphology (90C3), retained for the simulations, was created by manual positioning of the NURBS control vertices. The three simulations were then compared to assess the morphology effect on counting efficiency.

IV.1.3. Internal organs volume variation

Standard anatomical tables of organ weights have been developed (Ludwig 1972). Recent studies aimed to update these tables, to formulate standard reference values and to provide a range of organ weight values (de la Grandmaison et al. 2001). Other studies also investigate existing correlations between organ weight/volume and external parameters such as sex, age, height, Body Mass Index (BMI) etc. (Clairand et al. 2000). For example, it was reported that organ weight decreases with age, except for the heart and thyroid, and increases in relation to body height and/or BMI (de la Grandmaison et al. 2001). Moreover, except for the heart, the organ weight showed a better statistical correlation with body height than BMI (Clairand et al. 2000). In this study, internal organs weight correlations to height were considered.

For the 85 and 90 chest girth, the total height of the phantom was preserved so no internal organs resizing was necessary. However, for the three biggest chest girths, modifications in the head-feet direction were applied modifying thus the total height of the phantom. Hence, internal organs were resized to meet a minimum realism with a person of 100, 110 or 120 band size chest. Recommendations from Clairand et al. (2000) were partially followed for internal organ adjustment. Indeed, the published linear equations, correlating internal organs

mass and total body height, were considered and particularly the one for the lungs. Those experimental equations were adjusted to meet internal organ weights of the ICRP AF-RCP. The new equations were then applied to the set of created phantoms to estimate the correct internal volumes to be inserted into the 100, 110 and 120 bust phantoms. As for bones, the work by Heymsfield et al. (2007) has proven that similar scaling factors were identified. Thus, in order to remain realistic and simplify internal organ relative positioning, the lungs formula was applied by simple 3D dilations under Rhino 3D to resize all internal organs.

Specifically, for the 100, 110 and 120 chest girth phantoms, the height of the model was considered to represent a 182 cm woman. The choice of this height insures a body mass index estimate roughly within the limits of a normal subject (BMI between 18-25 kg/m²). As a consequence, a mass scaling factor of 1.3 was considered for the heart, liver, lungs, bones (ribs, sternum, spine, shoulder blades). Figure 2.11 shows examples of different phantoms with various cup sizes, chest girths and internal organs (cf. Table 2.10 and Table 2.11).

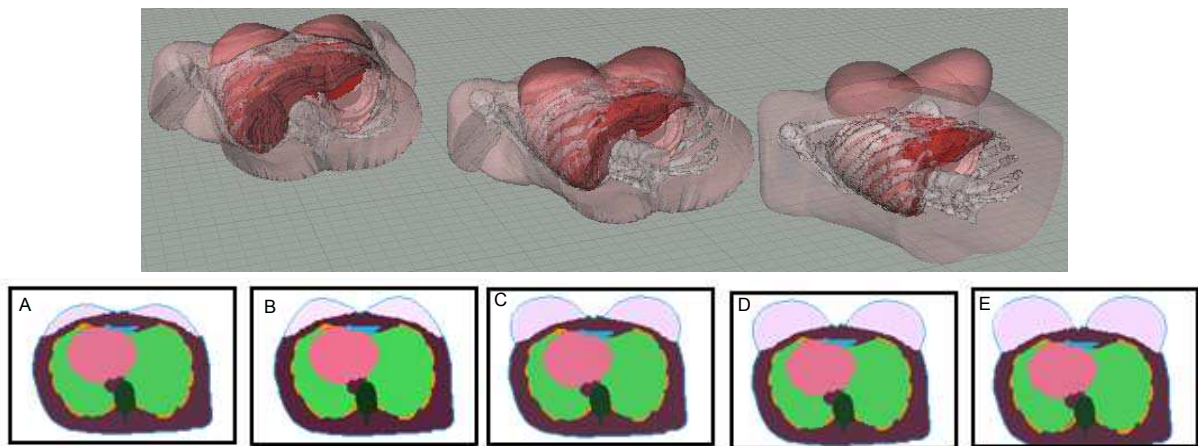


Figure 2.11. i) position up: Rhino 3D visualisation of the 90B (left), 100C (middle) and 110 D (right) created models; ii) position down: OEDIPE visualization of the voxelized models of chest girth 90 and of cup size ranging from A to E.

IV.2. Creating the library

Figure 2.12 recapitulates the steps taken to create each phantom starting from the deformable torso core phantom. Three essential steps in the Library creation are outlined in this figure. By the end of each step a test is done to evaluate the resulting phantom progressing.

- Step one is the elementary step where the target values are designated: chest girth, cup size, internal organ volume and body shape.
- Step two is the manipulation step where the basic Mesh and NURBS phantoms are modeled, using the Rhinoceros 3D software, to generate different morphologies. Other transformations were considered as related to the internal organ volume, thoracic thickness, band size and shape and finally organs positioning in the bust and over the chest for the breasts. The output format resulting from this step is a VRML2.0 file supporting Mesh geometries.
- Step three is the phantom's finalization step where Mesh and NURBS formats are transformed to voxel grids, using the Binvox program, to enable the MCNPX calculations. An IDL routine is then used to test the voxel 3D matrix, verify and correct any possible voxelization error and attribute the dimension to each elementary

voxel cube. By the end of this step, a temporary voxel phantom is generated. This phantom is submitted to the final test where organ volumes and dimensions are checked and validated in comparison to the theoretically targeted one. If any significant difference ($>5\%$) is noticed, the return to step two is mandatory. Otherwise, the phantom can be imported into the OEDIPE software to finalize the preparation to Monte Carlo simulations with the source distribution and the detector positioning. It should be noticed that, while creating the breast structures, any volumetric difference exceeding 2% was rejected and the NURBS construction was restarted.

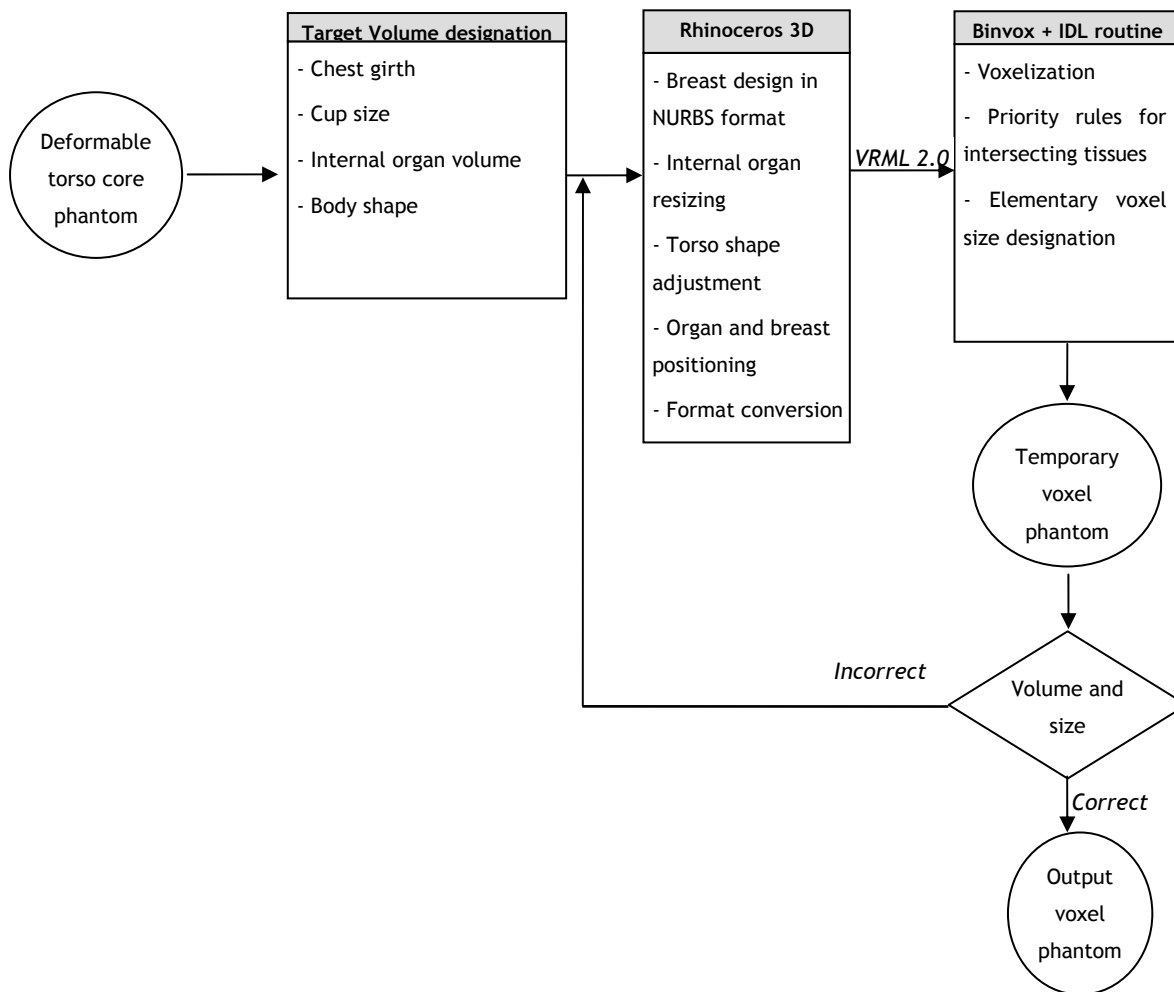


Figure 2.12. Steps for the generation of the library of female models starting from the deformable core model.

IV.3. Tissue composition and density attribution

For each organ, the tissue composition and densities were again taken from the ICRP 110 (ICRP 2009) according to the weight proportion of each structure fused to create the organ.

IV.3.1. Case of the breasts

For breast organs, the ICRP reference female voxel phantom has a 60-40 % adipose-glandular breasts composition as shown in Table 2.10. The additional adipose tissue, used for cup size change, was taken into account to fix the breast composition. Breast tissue density was fixed so that the final volume of the voxel model has the exact targeted weight (original weight + added adipose tissue weight). When the chest girth was changed, new reference cup sizes were fixed and the composition of those breasts was considered to be equal to the one of the 90B voxel phantom. Namely the 85B, 100B, 110B and the 120C models have a 60-40 % adipose-glandular breasts composition. Table 2.10 summarizes chest girth, cup size, breast weight, density and breast composition for the 24 different 3D female phantoms.

Table 2.10. Weight, density and composition of the created breasts.

Chest Girth	Cup Size	Breast weight (g)	Density	Composition	
				Adipose tissue (%)	Glandular tissue (%)
85	A	197	1.015	13.5	86.5
	B	427	0.967	60.0	40.0
	C	657	0.968	74.0	26.0
	D	887	0.961	80.7	19.3
	E	1117	0.965	84.7	15.3
90	A	270	1.008	25.9	74.1
	B	500	0.990	60.0	40.0
	C	730	0.982	72.6	27.4
	D	960	0.970	79.2	20.8
	E	1190	0.958	83.2	16.8
100	B	651	0.976	60.0	40.0
	C	1081	0.973	75.9	24.1
	D	1511	0.972	82.8	17.2
	E	1941	0.969	86.6	13.4
	F	2371	0.950	89.0	11.0
110	B	1081	0.964	60.0	40.0
	C	1711	0.965	74.7	25.3
	D	2341	0.959	81.5	18.5
	E	2971	0.961	85.4	14.6
	F	3601	0.959	88.0	12.0
120	C	2341	0.961	60.0	40.0
	D	3171	0.959	70.5	29.5
	E	4001	0.951	76.6	23.4
	F	4831	0.957	80.6	19.4

IV.3.2. Case of the internal organs

Internal organs' composition and density were considered to remain the same regardless of any volume change as only 3D dilation operations were applied on these organs. Table 2.11 gives the mass scaling factors for internal organs of all created models considering the 90B phantom as a reference.

Table 2.11. Weight factor applied to the organs and tissues of the created models, 90B model taken as reference.

Organ	Weight (g)	Phantom weight factor				
		85	90	100	110	120
Breasts ^a	500	0.85	1	1.30	2.16	4.68
Heart	620	1	1	1.30	1.30	1.30
Liver	1400	1	1	1.30	1.30	1.30
Lungs	951	1	1	1.30	1.30	1.30
Ribs	470	1	1	1.30	1.30	1.30
Shoulder blades	420	1	1	1.30	1.30	1.30
Skin	553	0.85	1	1.30	1.47	1.69
Spine	752	1	1	1.30	1.30	1.30
Sternum	70	1	1	1.30	1.30	1.30
Soft tissue	10600	0.85	1	1.30	1.85	2.41

^a The breast weight in this table is the weight of the reference cup size created for each chest girth.

IV.3.3. Case of the residual tissue

For the 85, 90 and 100 chest girths the composition was considered to be the same since they were all created from the voxelized phantom with simple transformations that preserve the mass proportion of the different compounds. For the 110 and 120 chest girths, the designed band size augmentation was reasonably attributed to a fat increase. Thus new compositions were calculated for the two biggest chest girths since adipose tissue percentile changed cf. Table 2.12. For each of the 24 generated phantoms, and according to chest girth, Table 2.12 resumes the different dimensions and particularly the thoracic height and weight, the considered soft tissue composition and the lungs volume.

Table 2.12. Residual tissue's composition and density for the female library phantoms as a function of chest girth.

Model	Composition												Density (g/cm ³)
	H	C	N	O	Na	P	S	Cl	K	Ca	Fe	I	
85 90 100	10.8	34.7	2.0	51.7	0.1	0.1	0.2	0.1	0.2	0.0	0.0	0.0	1.017
110	11.0	41.9	1.6	44.9	0.1	0.1	0.2	0.1	0.1	0.0	0.0	0.0	0.986
120	11.1	45.8	1.4	41.1	0.1	0.1	0.1	0.1	0.1	0.0	0.0	0.0	0.977

Table 2.13. General features of the created models.

Phantom	Thoracic height (cm)	Thoracic weight ^a (kg)	Residual tissue composition			Lungs volume (L)
			Adipose tissue (%)	Muscular tissue (%)	Other tissue (%)	
85	37.3	14.7	45.5	38.2	16.3	2.3
90	37.3	16.3	45.5	38.2	16.3	2.3
100	40.7	21.3	45.5	38.2	16.3	2.9
110	40.7	27.5	61.6	26.8	11.6	2.9
120	40.7	34.8	70.5	20.6	8.9	2.9

^a for the 85B, 90B, 100B, 110B and 120C models only.

IV.4. Validation of the generated models

To validate the generated models, the comparison of the generated organ volumes to the targeted values was done (cf. Table 2.14). This comparison particularly involves the breasts that were manually modelled using Rhino 3D. As for the chest girth, the created volume agreed within 1% with the targeted one as automatic and operations (3D dilation, contraction, shifting) were realized using Rhino 3D to reach the targeted volumes. The target volume validation was conducted with the voxel version of the breasts since such geometry is used to run Monte Carlo simulations.

Table 2.14. Volumetric comparison of the created breasts.

Chest Girth	Cup Size	Targeted volume (cm ³)	Created volume (cm ³)	Relative Error (%)
85	A	195.87	194.82	0.5
	B	437.98	442.44	-1.0
	C	680.08	679.63	0.1
	D	922.19	923.55	-0.1
	E	1164.29	1157.87	0.6
90	A	269.77	267.81	0.7
	B	511.88	504.97	1.3
	C	753.98	743.64	1.4
	D	996.09	989.23	0.7
	E	1238.19	1241.62	-0.3
100	B	666.55	666.90	-0.1
	C	1119.18	1111.51	0.7
	D	1571.82	1555.09	1.1
	E	2024.45	2002.17	1.1
	F	2477.08	2470.50	0.3
110	B	1119.18	1121.57	-0.2
	C	1782.34	1772.64	0.5
	D	2445.50	2440.77	0.2
	E	3108.66	3092.76	0.5
	F	3771.82	3766.43	0.1
120	C	2445.50	2435.27	0.4
	D	3319.18	3306.99	0.4
	E	4192.87	4207.29	-0.3
	F	5066.55	5046.68	0.4

Regarding the attributed tissue compositions and densities, MC simulations could not be used to validate the considered hypothesis, as it was the case for the core model since no reference model existed. Thus, a general observation was made on the variation of the organ densities with the evolution of the adipose tissue proportion. As expected, the attributed density

decreased with increasing adipose tissue proportion for all the breasts and chest girths (cf. Table 2.10 and Table 2.12).

V. Discussion and conclusion

The library of female models developed in this study compensates for the lack of female physical phantoms for the routine calibration of *in vivo* counting installations. This work used the Mesh and NURBS 3D formats to create a flexible female thoracic phantom from the ICRP Adult Female Reference Computational Phantom. Using the deformable model, a library of 34 different thoracic female phantoms was created combining different chest girths, cup sizes and morphologies. The method consisted in fixing first a target value for organ volume and modifying next the geometry to reach the desired volume. Next, the model is voxelized to prepare MC simulations and validated by comparing volumes to the targeted values. The newly created phantoms represent the most common breast measurements; their design is based on the brassiere industry statistics, plastic surgery recommendations and other relevant considerations to define internal organs volume variation with morphology.

To discuss the realism of this library of deformable female torso phantoms, the creation methodology is reviewed. This includes the morphology-related operations for cup size and chest girth variation and the attribution of tissue composition and density.

V.1. Choice of the creation method

When investigating morphology-related operations, it should be highlighted that the applied geometry modifications were based on fixing a target volume for each structure and organ and then by realizing manual and/or automatic transformations using the Rhino 3D modeling software. However the shape and morphology of each organ had to be modeled in the supine position, i.e. the *in vivo* measurement position. The breast modeling was definitely the most delicate because of the variability of the breast size on the one hand and because of the consequent breast tissue weight addition required to realize cup size change on the other hand. Very little conclusive information was found regarding the anthropomorphic measurements that can be used to define breast shape in the supine position. The morphology modeling was hence done based on visual criteria to define the final model shape. In the aim of uniformity, the same method was used to create the various cup sizes which consisted on manually shifting the control vertices of the splines in the normal vector direction and then applying local inclinations to simulate breast natural falling on the chest in the supine position. The larger the cup size is, the more delicate the modeling can become. As a consequence, the realism of the created models can be debated. Indeed, some may consider the shifting operated in the normal vector direction to be somehow too strong and that the breasts would fall significantly more when the subject is lying back on the measurement table. However, at this stage all *in vivo* monitoring is done with female workers still wearing the bra and thus the created models represent rather well this situation. Moreover, all the pulmonary measurements at the AREVA NC installations are done with the person sitting upright on the chair that is tilted somewhat around 45° and thus the breast position on the chest is also different. All these considerations make the created models fairly realistic for *in vivo* counting studies, not to mention the major differences breast can have from one person to another considering age, musculature, origin and other parameters (Fabié et al. 2006).

V.2. Choice of tissue composition and density

Moreover, when investigating tissue composition and density attribution, the realism of the used method is reviewed. For the case of cup size variation, the recommendations by Turner and Dujon (2005) to define the tissue weight to be added/removed guarantee the realism of the target values. Nevertheless, the nature of the additional tissue can be debated since only adipose tissue was considered (no glandular tissue adding/removal was taken into account). For the operated chest girth variation, only adipose tissue growth was operated again to switch from a chest girth of 100 to a chest girth of 110 and 120. This may also be subject to questioning. However, the simplified hypothesis on the additional tissue composition eases the calculation of the mass proportion of each compound in the thoracic region and simplifies the assessment of the tissue composition and density to be assigned. Moreover, the main thoracic compounds (adipose tissue, muscle) and all internal organs have similar densities and more importantly similar energy-dependant mass attenuation coefficients ($\mu_{\text{adipose}} = 0.198 \text{ cm}^2/\text{g}$ and $\mu_{\text{muscle}} = 0.205 \text{ cm}^2/\text{g}$ while $\mu_{\text{breast}} = 0.201 \text{ cm}^2/\text{g}$ at 59 keV). As a consequence, the impact of the additional tissue nature on radiation interactions is negligible, especially with increasing photon energy.

V.3. Comparison to existing models

The developed library was finally compared to the models by Hegenbart et al. (2008). However, while Hegenbart et al. (2008) considered only a single chest girth with no variations in internal organ volume, different chest girths and internal organ volumes were considered in this work to cover a wider female population

To vary breasts cup size, Hegenbart et al. (2008) used in-house developed software, based on morphing algorithms, that translates the Mesh surfaces of the breasts in their normal vector direction. These phantoms were for women in the standing position with a 60° downward angle for all cup sizes. The breast weight of the smallest model (AA) was fixed to 500 g, matching that of the ICRP reference female phantom (ICRP 2002). Adipose tissue weight was then added to increase breasts size from one cup to another. The following adipose tissue weight increments were applied: 817 g (from cup size AA to cup size A), then 383 g (A to B), 197 g (B to C), 434 g (C to D), 460 g (D to E), 513 g (E to F), 551 g (F to G). However, publications available in plastic and reconstructive surgery (Regnault et al. 1972, Pechter 1998) suggest that using such weight increments for cup size variation is questionable. Indeed, in Turner and Dujon (2005) a constant weight adding is recommended for each cup size change and this is the approach followed here. In addition, in the publication of Ringberg et al. (2006), seven 105B female subjects were identified with a mean breast volume of about 1200 cm³ (i.e. 1172 grams) while Hegenbart et al. (2008) allocated 1317 grams for a 105A subject. Smith et al. (1986) considered 1189 cm³ (about 1162 grams) for a 100C subject and 954 cm³ (about 932 grams) for a 100B one. In the underwear industry, there is some understanding of bra size equivalence; for example, a 100C bra can be adjusted to fit a 105B woman since the breast volume is the same (Wood et al. 2008). These two breast sizes, 100C and 100B, are hence commonly considered equivalent to a 105B and a 105A subject, respectively. This means that there is a difference of at least 400 grams between breasts reported by Smith et al. (1986) and those designed by Hegenbart et al. (2008) using the morphing algorithm.

As a conclusion of this comparison, one can say that similar approaches were considered to vary the cup size since in both cases, the Mesh and NURBS control points were shifted in their normal vector direction. However, the construction of the models differs significantly in the used methods. Indeed, Hegenbart et al. (2008) operated the surface modifications and then attributed a cup size to the generated breast volumes. Whereas, in this work, targeted breast volumes were fixed based on recommendations from plastic and reconstructive surgery (Turner and Dujon 2005) and then the geometry was adjusted so that the required volume could fill in the created breasts. Moreover, the Hegenbart et al. (2008) models were generated for persons in the standing position adapted for whole body counting situations while in this study the generated models were representative of subjects in the supine positions and undergoing *in vivo* lung counting measurements.

Chapter 3

Numerical calibration of the AREVA NC *in vivo* monitoring installation

The developed library of female torso models is used to realize a numerical calibration of the AREVA NC *in vivo* monitoring installation. In this chapter, the methods and results of MC simulations are given and the morphology-induced variations of counting efficiency are put into equation.

I. Monte Carlo simulation of an *in vivo* measurement

Reproducing with MC simulations a realistic *in vivo* measurement requires a faithful definition of the contamination and an adequate positioning of the detectors. The OEDIPE software was hence used to prepare the MC simulations and generate the MCNPX input file.

I.1. Reproducing the *in vivo* measurement with OEDIPE

In this study, OEDIPE was used for its *in vivo* monitoring interface as the created library of female voxel phantoms was imported to the software. The modeling of the measurements requires the source specification, i.e. its nature, distribution and activity, and the detectors choice and positioning.

I.1.1. Choice and distribution of the source

OEDIPE allows a correct modeling of the source geometry. This includes the definition of punctual sources or the choice of a given radionuclide and its localization in a specific organ. OEDIPE also enables the definition of heterogeneous sources in both composition (a mixture of radionuclides) and distribution (in several organs). The choice of the radionuclide involved can be done from an existing database (that can be extended to a user-specific source) that includes the emission yields and energies.

In this study, OEDIPE was used to simulate a pulmonary contamination using 1 Bq of an artificial gamma source emitting 17 photons of energies ranging from 15 keV to 1.4 MeV (cf. Appendix B.1). This source represents the radionuclides most commonly used for the calibration of the AREVA NC *in vivo* measurement installations and was uniformly distributed in the lungs. For these simulations, however, the yield assigned to each photon was considered to be equal to one. This is particularly interesting since, in this case, all photons are simulated with the same importance regardless of their energy and true yield. This eases the definition of the source and the processing of the results as the total number of photons is uniformly distributed between all the 17 energy emissions. As a consequence, the resulting counting efficiency (given in counts/s/gamma) needs to be multiplied by the real emission yield (in gamma/Bq) to represent a realistic value (in counts/s/Bq) as obtained by measurements.

I.1.2. Choice and positioning of the detectors

Using OEDIPE, it is also possible to select a detector from a previously defined library containing MCNPX models of the available counting systems. The user has only to select the correct detector, specify the number of channels, the energy binning and the Gaussian Energy Broadening (GEB) factors and then position it to reproduce the *in vivo* measurement. The positioning of the detectors is one of the key points in the *in vivo* monitoring of workers as it

directly affect the counting efficiency and activity assessment a (Razafindralambo 1995). Thus detectors' positioning was considered here with extreme caution.

For these simulations, the counting system of the AREVA NC *in vivo* monitoring installation was used. This is a system of four-germanium-detectors commercialized by Canberra and used for the routine monitoring of the workers at the La Hague reprocessing plant. Such germanium detectors are dedicated for organ specific monitoring and low energy X and gamma emissions of nuclides most likely to be involved in an internal contamination in this particular workplace. An MCNPX version of these detectors was previously validated at LEDI (Lamart 2008) and was hence directly used for the MC simulations. This model faithfully reproduces the technical drawing of the detectors including the crystal dimensions and position and the available dead layers.

The AREVA NC existing system is totally dissociated giving the maximum freedom in the positioning of the 4 detectors and the routine positioning is set to maximize the count with various angulations and positions over the chest. However, for these simulations, the detectors were grouped in pairs (left-right) to simplify their positioning. These were put as close as possible to the skin while preventing any collision with breasts. However, as the breast size increases, the detectors should be shifted upwards. Nevertheless, detectors counting efficiency is highly affected by the distance to the organ as the radiation flux decreases inversely with the square of the distance (Podgorsak 2003). In order to homogenize detectors' positioning, and to exclusively visualize the drop in counting efficiency as cup size increases, the same distance to the skin was kept for a given chest girth and all cup sizes. This distance was fixed by first choosing the tilt and then by bringing the detectors as close as possible to the skin with the biggest cup size breasts i.e. E (85-90 chest girth models) or F (100, 110 and 120 chest girth models). For the 85 and 90 chest girth models, detectors were positioned at the clavicles level at a distance of 2 cm from the skin with a tilt of 35° along the head-to-foot axis to prevent any collision with the breasts. For the 100, 110 and 120 chest girth models, the distance to the skin was respectively 4, 5 and 8 cm with the same angulations. An example of the detector positioning is given in Figure 3.1. It should be noticed here that the tilt along the head-to-foot axis was privileged when compared to the distance to the skin as one could have simply changed the angulations instead of the distance to the skin. Nevertheless, it was considered here to be much easier to fix the tilt and then to vary the distance to guarantee the reproducibility and separate the morphology effect over the count from the positioning effect.

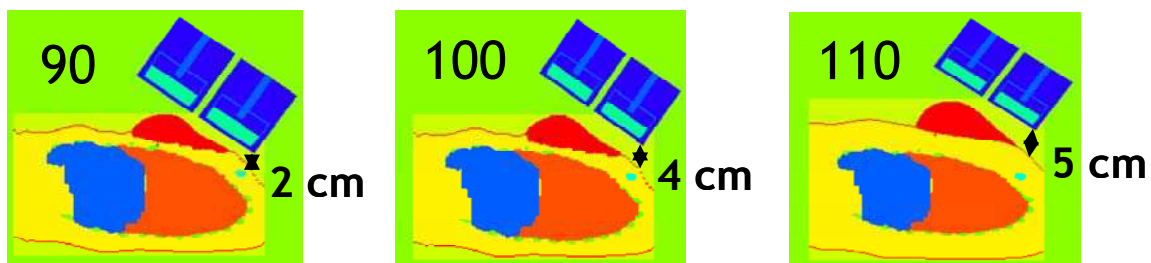


Figure 3.1. OEDIPE visualization of the detectors' positioning for phantoms of cup size C and a chest girth of 90, 100 and 110.

1.1.3. Generating the MCNPX input file

Using OEDIPE, the geometry of the phantom is written in the repeated structures format. The considered materials were taken from the ICRP 89 recommendations (ICRP 2002) and the MCNPX default cross sections were used. The artificial gamma radiation source was

distributed uniformly into the lungs as explained above. The number of simulated particles was chosen high enough (1E09) to guarantee a statistical relative error on the photoelectric peak below 1% at all photon energies. The tally required is the pulse height tally representing the number of counts collected in the detectors. Finally, no variance reduction techniques were used at this stage of the simulations to determine the calibration coefficients.

I.2. Simulated counting efficiency calculation

The MC tally results give the counting efficiency of the used detectors in counts/s/gamma for the energy of interest. It differs from the experimental measured spectrum which is deformed by the Gaussian Energy Broadening (GEB) factor. To correctly assess *in vivo* counting efficiency, the simulated spectrum needs to be processed.

I.2.1. From a simulated spectrum to a calibration curve

The MCNPX simulated tally represents the number of counts in the detectors normalized to the total number of starting particles. This is equivalent to the counting efficiency as defined by Equation 1.7 in the case where true yields are defined on the source card. However, the MCNPX output file must be processed to switch from a simulated spectrum (energy binning) to a calibration curve that represents counting efficiency values at different energies. This requires the calculation of the photoelectric peak at a certain energy from which we need to subtract the Compton contribution. Nevertheless, this can be time consuming and delicate depending on the number of tallies, the number of simulated photons (source emissions) and the spectrum itself (GEB parameters). Indeed, if different photons are simulated in the same file, the photoelectric peak of lower energy will be growing on the Compton continuum of the higher energy peaks cf. Figure 3.2. For such photons, both their own Compton continuum and that of all higher energy photons must be subtracted. To reduce this noisy contribution, no GEB was used in the simulations.

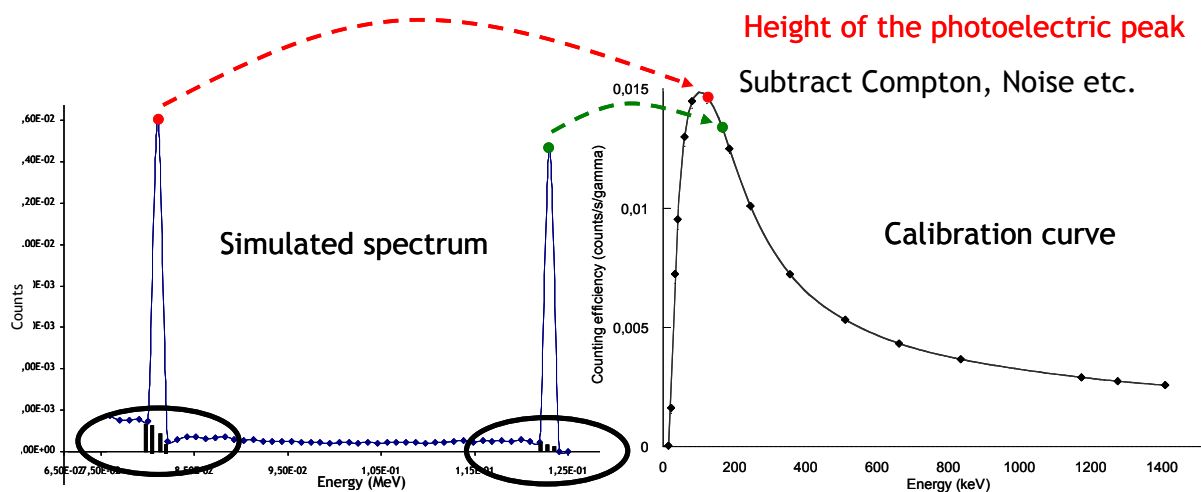


Figure 3.2. Schematic method to switch from a simulated spectrum to a calibration curve.

I.2.2. Uncertainty assessment

When calibrating a counting system, the uncertainty on counting efficiency can be as low as 5% (Doerfel et al. 2006). However, when applying these calibration coefficients to a routine measurement, the uncertainty on the assessed activity can be up to 50% (Razafindralambo 1995; Doerfel et al. 2006). Errors on the activity distribution within the body or on the subject positioning during *in vivo* measurement, commonly called Type B errors, are predominant in

uncertainty calculation. This uncertainty is assessed from the scattering factor (Doerfel et al. 2006). Nevertheless, voxel phantoms are more realistic when representing the human body. Simulations aim to reduce uncertainties, and particularly the Type B uncertainties on the phantom, and values of 5 to 10% can be considered satisfactory, particularly for low energy photons, when compared to the 50% uncertainty in activity assessment.

For MCNPX simulations, counting efficiency is assessed using a pulse height tally. For such a tally, results are acceptable only if the associated statistical relative error is less than 5%. Thus, the number of starting particles was carefully chosen in order to guarantee statistically reliable results for the lowest energy photons. However, the simulated counting efficiency value is calculated by considering the Compton bins surrounding the photoelectric peak. For these bins, the 5% simulation statistical relative error is not guaranteed. Thus, the error on the final counting efficiency can be assessed by using the following equation:

$$\sigma_{\varepsilon_{ff}} = \sqrt{(\sigma_{peak})^2 + (\sigma_{peak-1})^2 + (\sigma_{peak+1})^2} \quad \text{Equation 3.1}$$

where σ_{peak} is the uncertainty of the bin reproducing the photoelectric peak while σ_{peak-1} and σ_{peak+1} represent the uncertainty for the bins surrounding the peak and used for Compton subtraction. Each σ weights the MC statistical relative error with the number of counts (spectrum height) for each bin. For high energy photons (>100 keV), the Compton counts are negligible when compared to the photoelectric peak and thus the overall uncertainty is roughly equivalent to that of the photoelectric peak (no more than 5%). For low energy photons, however, a number of counts of the same order of magnitude can be observed for both the Compton and the photoelectric bins and thus high uncertainty values are obtained for such photons. Indeed, as the total number of particles only influences the photoelectric peak's uncertainty, the latter remains very high for Compton continuum bins regardless of the number of simulated particles. And thus, the overall uncertainty on the counting efficiency is degraded and should be assessed using Equation 3.1.

II. Numerical calibration using the developed female library and Monte Carlo simulations

The developed female library enables the correction of experimental calibration coefficients obtained using the Livermore male mannequin by accounting for the morphological differences between the male and female individuals. This section presents some of the MC simulation results and discusses the cup size and chest girth effects on counting efficiency. The simulation results for the 24 created phantoms of the library can be found in detail in Appendix B.2.

II.1. Cup size effect

To study the cup size effect on *in vivo* measurements, the simulated counting efficiencies for phantoms of the same chest girth were compared. Table 3.1 documents the Monte Carlo simulation results for the 85 chest girth with different cup sizes for the ^{238}U , ^{241}Am , ^{57}Co , ^{137}Cs and ^{60}Co radionuclides. These results show how the efficiency drops with increasing cup size. For example, the ^{238}U counting efficiency for the 85E model was roughly 85% lesser

than the value for the 85A model. For the ^{241}Am , ^{57}Co , ^{137}Cs and ^{60}Co these values were about 34%, 28%, 18% and 15% respectively. This can be explained since the increase in breast tissue results in greater attenuation of the photons emerging from the lungs. The lower the emitted photon energy is, the greater the attenuation becomes, and this results in a loss of counting efficiency. Figure 3.3 shows the counting efficiency variation with energy for the 90 chest girth and all created cup sizes.

Table 3.1. Counting efficiency and associated statistical error obtained with the MC simulations for the 85 chest girth and the different cup sizes for radionuclides of particular interest.

Radionuclide	Phantom	Counting efficiency (counts/s/gamma)	Simulation uncertainty (%)	Count relative to the A cup size
^{238}U 15.3 keV	85	A	1.10E-4	1
		B	4.50E-5	0.41
		C	3.38E-5	0.31
		D	2.45E-5	0.22
		E	1.72E-5	0.16
^{241}Am 59.5 keV	85	A	1.60E-2	1
		B	1.36E-2	0.85
		C	1.24E-2	0.77
		D	1.19E-2	0.74
		E	1.06E-2	0.66
^{57}Co 122.1 keV	85	A	1.76E-2	1
		B	1.54E-2	0.87
		C	1.44E-2	0.82
		D	1.38E-2	0.78
		E	1.26E-2	0.72
^{137}Cs 661.7 keV	85	A	4.85E-3	1
		B	4.48E-3	0.92
		C	4.31E-3	0.89
		D	4.23E-3	0.87
		E	3.98E-3	0.82
^{60}Co 1173.2 keV	85	A	3.14E-3	1
		B	2.96E-3	0.94
		C	2.88E-3	0.92
		D	2.83E-3	0.90
		E	2.68E-3	0.85

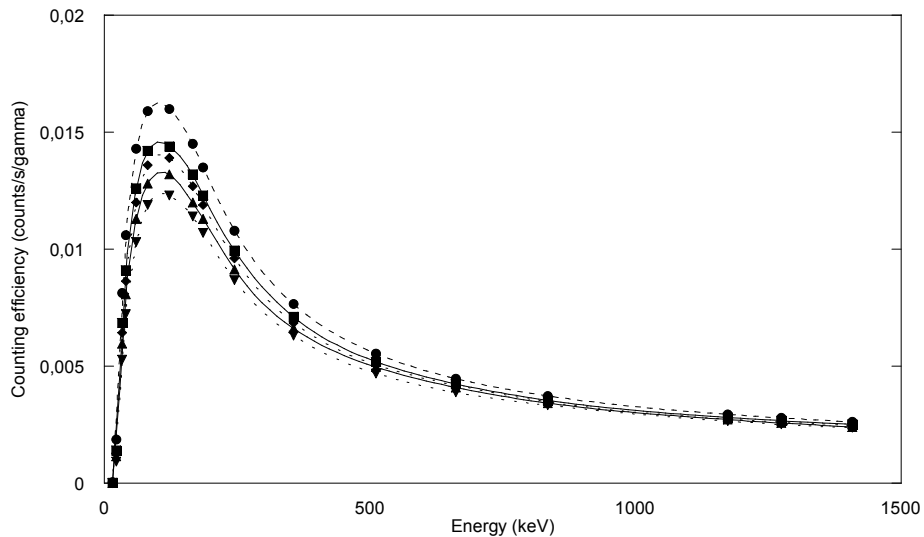


Figure 3.3. Counting efficiency (counts/s/gamma) variation with energy (keV) for the chest girth of 90 and all cup sizes: **A** (dots), **B** (squares), **C** (diamonds), **D** (triangles), **E** (inverted triangles).

The effect of breast shape on counting efficiency was also considered in this work. Thus different breast shapes were created representing the same tissue weight and composition but different positions over the bust (cf. Figure 3.4). In the particular case of big cup sizes, this study is justified since the exact positioning of the breast over the chest is quite uncertain. As shown in Table 3.2 the relative error or deviation from the count with the 90C3 phantom varies significantly for a given energy. For example, for the ^{238}U emissions at 15.31 keV, a difference ranging from -17.47% to 15.98% was observed, while for the ^{60}Co photons at 1.17 MeV this difference varied from -1.8% to 0.06%. This gives an order of magnitude of the uncertainty affecting the value of the efficiency variations presented here. The results of the 10 additional phantoms of the female library can be found in Appendix B.3.

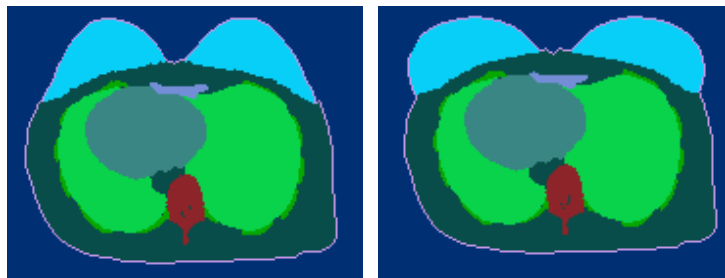


Figure 3.4. Example of two different breast shapes created to represent a female subject having a chest girth of 90 and a C cup size breast; visualization using OEDIPE.

Table 3.2. Counting efficiency and associated statistical error obtained with the MC simulations for the different breast morphologies of the 90C phantom and the radionuclides of particular interest.

Phantom	Radionuclide	Counting efficiency (counts/s/gamma)	Simulation uncertainty (%)	Relative difference (ref: 90 C3) (%)
90 C1	^{238}U (15.3 keV)	2.26E-5	0.94	15.98
	^{241}Am (59.5 keV)	1.15E-2	0.13	4.17
	^{57}Co (122.1 keV)	1.33E-2	0.86	4.31
	^{137}Cs (661.7 keV)	4.13E-3	0.78	1.43
	^{60}Co (1173.2 keV)	2.75E-3	0.78	0.06
90 C2	^{238}U (15.3 keV)	3.16E-5	0.80	-17.47
	^{241}Am (59.5 keV)	1.23E-2	0.63	-2.50
	^{57}Co (122.1 keV)	1.42E-2	0.83	-2.16
	^{137}Cs (661.7 keV)	4.22E-3	0.77	-0.71
	^{60}Co (1173.2 keV)	2.80E-3	0.77	-1.82
90 C3	^{238}U (15.3 keV)	2.69E-5	0.86	Ref.
	^{241}Am (59.5 keV)	1.20E-2	0.64	Ref.
	^{57}Co (122.1 keV)	1.39E-2	0.84	Ref.
	^{137}Cs (661.7 keV)	4.19E-3	0.77	Ref.
	^{60}Co (1173.2 keV)	2.75E-3	0.78	Ref.

II.2. Chest girth and internal organ volume effects

To study the chest girth and the internal organ volume effects on *in vivo* measurements, the simulated counting efficiencies for phantoms of the same cup size were next compared. Figure 3.5 represents the counting efficiency variation with energy for 5 phantoms of chest girth of 85 to 120 and a D cup size. Table 3.3 documents the Monte Carlo simulations results for all phantoms of cup size C but with different chest girths for radionuclides of interest.

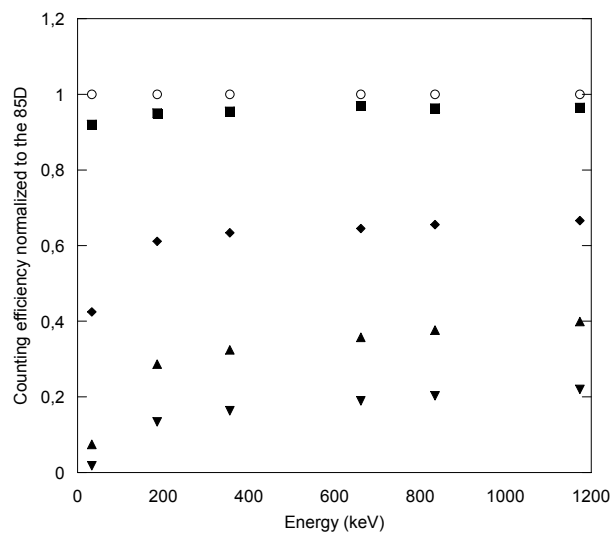


Figure 3.5. Counting efficiency (counts/s/gamma) variation with energy (keV) for the phantoms of cup size D and various chest girths (85-120) normalized to the 85 chest girth: **85** (dots), **90** (squares), **100** (diamonds), **110** (triangles), **120** (inverted triangles).

Table 3.3. Counting efficiency and associated statistical error obtained with the MC simulations for the C cup size and the 5 different chest girths; values given for the following radionuclides: ^{238}U , ^{241}Am , ^{57}Co , ^{137}Cs and ^{60}Co .

Phantom	Radionuclide	Counting efficiency (counts/s/gamma)	Simulation uncertainty (%)
85 C	^{238}U (15.3 keV)	3.38E-5	0.77
	^{241}Am (59.5 keV)	1.24E-2	0.63
	^{57}Co (122.1 keV)	1.44E-2	0.83
	^{137}Cs (661.7 keV)	4.31E-3	0.76
	^{60}Co (1173.2 keV)	2.88E-3	0.76
90 C	^{238}U (15.3 keV)	2.69E-5	0.86
	^{241}Am (59.5 keV)	1.20E-2	0.64
	^{57}Co (122.1 keV)	1.39E-2	0.84
	^{137}Cs (661.7 keV)	4.19E-3	0.77
	^{60}Co (1173.2 keV)	2.75E-3	0.78
100 C	^{238}U (15.3 keV)	9.97E-6	0.82
	^{109}Cd (22.2 keV)	6.86E-4	0.12
	^{241}Am (59.5 keV)	7.69E-3	0.16
	^{57}Co (122.1 keV)	9.15E-3	0.33
	^{137}Cs (661.7 keV)	2.88E-3	0.29
	^{60}Co (1173.2 keV)	1.99E-3	0.91
110 C	^{238}U (15.3 keV)	3.55E-7	3.75
	^{109}Cd (22.2 keV)	1.33E-4	0.27
	^{241}Am (59.5 keV)	3.22E-3	0.62
	^{57}Co (122.1 keV)	4.26E-3	1.75
	^{137}Cs (661.7 keV)	1.65E-3	1.62
	^{60}Co (1173.2 keV)	1.16E-3	1.57
120 C	^{238}U (15.3 keV)	1.55E-8	27.75
	^{109}Cd (22.2 keV)	2.53E-5	4.26
	^{241}Am (59.5 keV)	1.25E-3	2.45
	^{57}Co (122.1 keV)	1.81E-3	2.13
	^{137}Cs (661.7 keV)	8.63E-4	1.76
	^{60}Co (1173.2 keV)	6.53E-4	1.65

From these results, it is clear that counting efficiency decreases with increasing chest girth i.e. increasing extra-thoracic thickness. The important gap noticed between the 85-90 chest girths and the 100-110 and 120 ones can be explained as follows. The three biggest models have a lung volume significantly larger than the basic ones; detectors however “cover” the same original lung volume. Since a volumetric source distribution was simulated, the activity facing the detectors was smaller which means a lesser detection. The radionuclide distributions effect over lung counting efficiency has been properly studied by Kramer and Burns (1995) and confirms this finding. Furthermore, since an 85C model does not have the same breasts weight as a 100C one, breasts tissue adds up to chest wall thickness and results in additional attenuation of counting efficiency when compared to the values of the 85-90 models.

For the 85 and 90 models, the chest wall thickness (breasts + difference in thoracic thickness due to 2D contraction) was the only changing parameter between the two sets of phantoms. The most significant counting efficiency variation was obtained for the lowest energy, where a 1.25 fold decrease was noticed between the 85C and the 90C phantoms. For high energy photons (^{60}Co at 1.17 MeV) this attenuation factor was about 1.05 for the same phantoms and regardless of the cup size. This is explained by the fact that high energy photons suffer lower attenuations in the crossed tissues when compared to low energy photons.

For the 100, 110 and 120 chest girths, the same energy dependant attenuation effects were observed. For the ^{238}U emissions at 15.31 keV, the statistical error obtained with the maximum number of simulated particles was still unsatisfactory for the 110 and 120 chest girths. Thus we compare the simulation attenuation for the ^{109}Cd photons at 22.16 keV. The resulting attenuation was found to be about 5.1 times more important for the 110C than for the 100C and 5.2 times more for the 120C than for the 110C. This attenuation was about 3.9 times more important for the 110B than for the 100C and about 3.6 times more for the 120C and the 110D. These latter comparisons reveal clearly the effect of additional chest wall thickness, since the 110B phantom (respectively the 120C) was created from the 100C (resp. 110D) and thus have the same breast shape and weight (cf. step 3). For the high energy photons (^{60}Co 1.17 MeV), the attenuation is relatively constant with increasing cup size as it was observed for the smallest chest girths where factors of 1.7 and 3.1 were noticed for the 110C and 120C models when compared to the 100C phantom. Indeed, additional tissue thickness results in a cup size increase and induces a maximal variation of these factors for the 120F model when compared to the 120C of about 1.07%.

II.3. Comparison with published data

These simulation results were also compared to those of Hegenbart et al. (2008) who considered one chest girth (105) and 8 different cup sizes (AA to G). In their study, Hegenbart et al (2008) simulated a Phoswich, whole body, NaI-CsI counting system and three radionuclides: ^{241}Am , ^{137}Cs and ^{60}Co . They investigated how lung counting efficiency varied with breast size. Hegenbart et al. (2008) also found that detector efficiencies considerably decrease with increasing breast size and a difference of up to 50% was observed between models with cup size AA and those with cup size G for the ^{241}Am photons at 59.54 keV.

In both studies, efficiency variation with breast weight was found to exhibit the same trend for this same radionuclide. In Hegenbart et al. (2008), the efficiency loss was around 8% between the C cup size and D cup size for a difference in breast weight of 434 g. Moreover, the efficiency drop was 9% for the Hegenbart D-E (460 g) models and 19% and 13% respectively for the AA-A (817 g) and B-D (631 g) models. In our study, the breasts weight variation between the 100D and the 100E model (about 430 g) caused an efficiency drop of approximately 7%. Furthermore, the efficiency drop was 10% for our 90B-D (460 g) models and 20% and 12%, respectively, for our 120B-D (830 g) and 110B-C (630 g) models. To summarize, a similar attenuation is observed for the Am-241 photons at 59.54 keV when the same tissue increment is applied even though the two studies involve different counting systems, detector positions and phantoms. For high energy photons (^{137}Cs and ^{60}Co), however, efficiency does not decrease with the breast increment in the same way (>10% difference). This is presumably due to the different counting systems that were simulated.

As a conclusion of this comparison, one can say that despite the significant existing differences, particularly in breasts size, shape and the used detectors, similar tendencies were found regarding the decrease of counting efficiency with increasing cup size.

III. Parameterization of morphology-induced variations of counting efficiency

The morphology-induced variations of counting efficiency as a function of photon energy were next put into equation to enable a realistic estimate of detectors' counting efficiency for each monitored female subject. If such an equation can properly describe the variation of counting efficiency with morphology, it will enhance the realism and consistency of MC simulation results and give a physical explanation for the observed calculations. Moreover, this equation is of particular use for females with unusual body size and shape that are not represented in the created female torso library and for which the typical calibration coefficients require sensitive corrections.

III.1. Modeling the morphological effect

As observed from the previous simulations with the female torso library, cup size, chest girth and internal organ volume highly affect the count as efficiency values can decrease, by up to orders of magnitude, when these parameters change. To put into equation the efficiency variation with morphology, further investigations are required to assess the effect of each of the parameters alone.

III.1.1. Chest wall thickness effect

To identify the chest wall thickness effect, a review of the literature is done. The literature results were then confirmed by a series of simulations conducted with Mesh and NURBS phantoms of the same lung volume but various chest thicknesses.

- **Literature review**

To assess the activity in the lungs by *in vivo* spectrometry measurements, it is necessary to estimate or to measure the thickness of tissues overlying the lungs as these may cause severe attenuation of radiation. The effect of Chest Wall Thickness (CWT) on counting efficiency comes also from the decrease in the photon flux with the source-detector distance (Kramer and Capello 2005). Kruchten and Anderson (1990) distinguished between muscle and adipose tissues in the CWT. Kramer et al. (2000) have also compared the chest plate of typical calibration phantoms, the Livermore (Griffith et al. 1978) and the JAERI (Shirofani 1988), to a real person's chest wall and assessed the uncertainty on the activity estimate.

CWT is often estimated by biometric and empirical equations based on subject-specific data of weight and height (Fry and Sumerling 1980; Pierrat 2005) and even age (Sumerling and Quant 1982). However, as shown by Vickers (1996), such equations are site specific and thus

large errors can be introduced into the CWT estimate. Moreover, as observed by Kramer et al. (2001), the position of the person (seated vs supine) while measuring the CWT can highly influence the latter.

All these studies have confirmed the importance of CWT as one of the parameters most influencing the *in vivo* count and the results have highlighted the impact of CWT estimation and the inherent uncertainties when calculating the incorporated activity. Nevertheless, for these investigations, CWT was mainly studied for male workers although it is definitely greater and its variations can be more delicate to estimate when a female subject is involved.

- **Reproducing the CWT effect with simulations**

Experiments with the Livermore physical mannequin and the four physical overlay plates representing different chest wall thicknesses have shown an exponential counting efficiency decrease with tissue thickness. To prove that simulations reproduce the measured effects, a study was carried out with a voxelized version of the Livermore phantom. In this case however, numerical representations of 8 different plates, with a thickness ranging from 1.8 to 3.1 cm, were generated using the Rhino 3D modeling software.

First, a deformable core plate was created starting from a CT scan of the physical plate P1. Next, mesh offsets were used to vary the thicknesses of the plate and generate the 7 target models. The 8 different Mesh Livermore models were next voxelized in order to run MC calculations. The core chest plate was modeled separately and its composition was set to 100% muscle. Meanwhile, a 50-50% composition of muscular and adipose tissue was attributed to the remaining plates. The same homogeneous distribution of 1 Bq of ^{241}Am was simulated in the lungs volume and the AREVA NC germanium detectors positioned identically for the 8 phantoms.

The counting efficiency obtained with the MCNPX simulations reproduces the expected exponential attenuation as a consequence of the plate thickness variation (cf. Figure 3.6). Moreover, the exponential factor representing the mass attenuation coefficient, deduced from the exponential fit, agreed within a margin of 5% with the theoretical one recommended by the ICRU 44 (ICRU 1989) for such a tissue composition (0.2 cm^{-1}). This validates the simulation approach to reproduce the counting efficiency decrease with chest wall thickness.

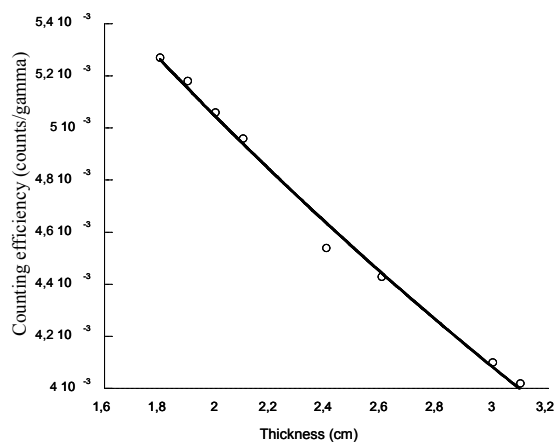


Figure 3.6. Counting efficiency (counts/gamma) variation with plate thickness (cm) for the Livermore mesh model. Linear fit calculated using Microsoft Excel 2008TM: $y=0.0077026*\exp(-0.2116x)$.

III.1.2. Internal organ volume effect

To identify the effect of internal organ volume, a second review of the literature was done followed by another series of MC simulations to validate the observations for lung counting studies.

- **Literature review**

As previously mentioned, *in vivo* lung counting systems are calibrated with an anthropometric phantom that has only one fixed lung size. However, people have widely varying lung size, volume and shape. As a result, a bias is introduced into the activity estimate because of the difference in lung volume between the physical phantom, used for calibration, and the subject being measured.

A previous study by Kramer and Capello (2005) investigated the effect of lung volume on counting efficiency using Monte Carlo simulations. In their study, Kramer and Capello (2005) constructed ellipsoidal cylinders to represent different lungs of sizes ranging from 0.935 L to 9.05 L. The MC simulations they conducted were for three different whole-body four-detector arrays of 50, 70 and 85 mm diameter and the energy range was from 17 keV to 1 MeV. The obtained result showed that counting efficiency increases with decreasing lung volume (cf. Figure 3.7). However, the authors found that there is no simple relationship between counting efficiency and lung volume. In Kramer and Capello (2005), three parameters were modified simultaneously: lung volume, detector position and chest wall thickness. This makes it difficult to clearly identify a simple relation.

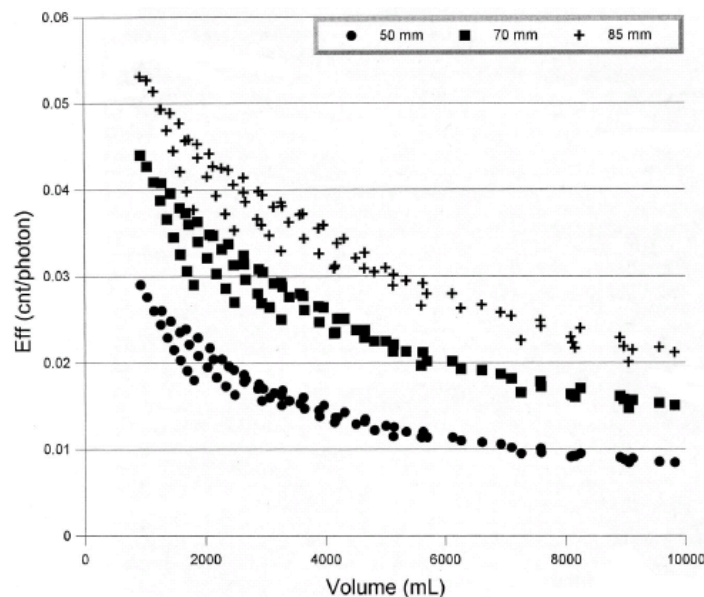


Figure 3.7. Counting efficiency of the three different detector arrays (50, 70 and 85 mm diameter) at 60 keV as a function of lung volume (Kramer and Capello 2005).

Nevertheless, the data given by Kramer and Capello (2005) seem to present, at least to a certain point, an inverse relation between the counting efficiency and the lung volume. Namely, Figure 3.7 reveals that there are families of curves, each belonging to a set where the ellipsoidal radii are fixed and the length of the lung is varied, which show a hyperbolic shape. Independently, and for a given family of curves, there seems to be a linear tendency

between counting efficiency and the inverse lung volume. Thus, we have investigated this trend using a realistic representation of the lungs, a different counting system and different counting positions. Particularly, a more systematic approach was adopted in which one parameter is varied at a time while keeping the others constant.

- **Reproducing the internal organ volume effect with simulations**

To create a realistic set of lungs, the CT scan of a male subject were used to create a male torso deformable model with the Mesh format following the method given in Chapter 2 Section I.2.1. The obtained deformable model was then dilated (or contracted) in the three directions using Rhino 3D. Factors of 1.05, 1.1 and 1.15 were used for both dilation and contraction to create 6 different thoracic models of various sizes. These operations, carried out on the chest wall itself and on the internal organs, induced lung volumetric variations up to 50% of the primary volume ($1.15^3 \sim 1.52$). Note that both the lung volume and chest wall thickness were modified with the operated 3D transformations. Thus, the study of the influence of both parameters on the count is possible to quantify and compare the two parameters most influencing the pulmonary *in vivo* count.

The seven models were then voxelized with the Binvox program and OEDIPE was again used to create the source and position the detectors. The simulations involved a photonic source of energy ranging from 20 keV to 1 MeV which was uniformly distributed it in the lung volume whereas, the considered detectors were germanium counters dedicated to *in vivo* pulmonary measurement. For all the simulations, these detectors were positioned 2 cm away from the skin at the level of the clavicles with no inclinations. This identical positioning guarantees the similarity of the 7 simulations and reduces the inter-variability of the simulations to only chest wall thickness and lung volume.

Figure 3.8 shows the simulated counting efficiency variation as a function of the source energy for the 7 different thoracic models. From the simulation results, one can conclude that counting efficiency decreases with increasing lung volume. This can be explained as follows: for isotropic dilations of the thorax and internal organs, source activity concentration decreases in the lungs resulting in significant loss of counting efficiency.

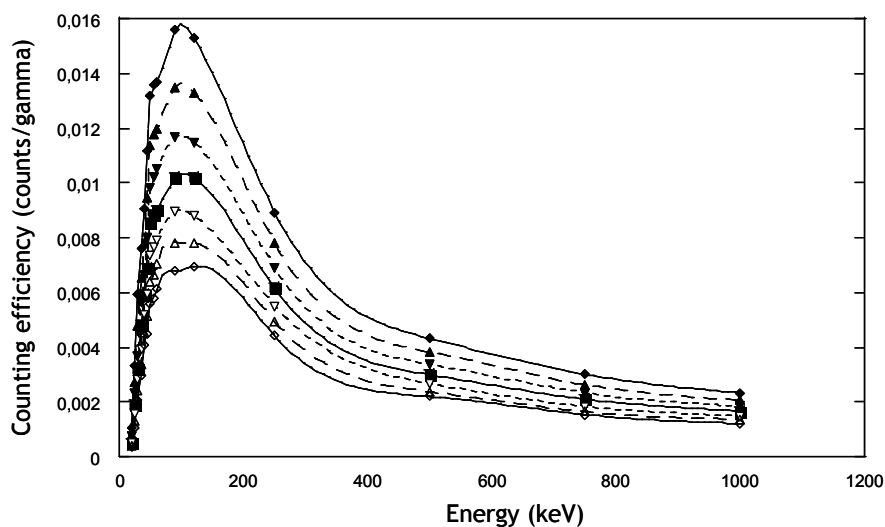


Figure 3.8. Counting efficiency (counts/gamma) variation with energy (keV) for the different Mesh models: 0.85 contracted (black diamonds), contracted (black triangles), 0.95 contracted (black inverted triangles), reference (black squares), 1.05 dilated (white inverted triangles), 1.1 dilated (white triangles), 1.15 dilated (white diamonds).

Figure 3.9 shows that counting efficiency linearly increases with the inverse of lung volume (loaded organ) over a broad energy scale. In other words, additional absorption due to supplementary tissue thickness has a poor or insignificant effect when compared to internal organs volume variation. This conclusion strongly depends on the construction hypothesis involving identical transformation of chest wall and internal organs (dilation/contraction). Although the anatomic realism of the uniform growth of chest wall and internal organ volume (same dilation coefficient) can be discussed, the observed relation gives at least a second indication concerning the effect of morphology on counting efficiency.

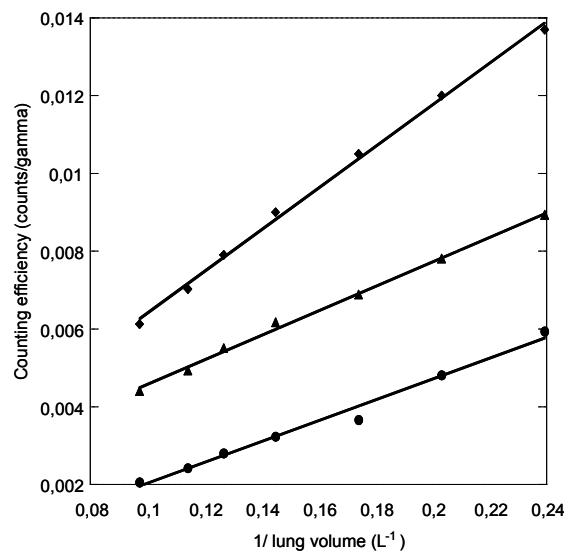


Figure 3.9. Counting efficiency (counts/gamma) variation with the inverse of lungs volume (L^{-1}) for photons of 30 keV (dots), 60 keV (diamonds) and 250 keV (triangles). Linear fit calculated using Microsoft Excel 2008TM: **30 keV**: $y = 0.0026807 x - 0.000649$, $R^2 = 0.98552$; **60 keV**: $y = 0.0053597 x + 0.00010445$, $R^2 = 0.99726$; **250 keV**: $y = 0.0031493 x + 0.00014296$, $R^2 = 0.99634$.

III.2. Development of a morphological equation

The changes in morphology, applied to create the series of phantoms of the developed female torso library were, for the most part, limited to variation in chest wall thickness, i.e. cup size variation, and a change in lung volume in the case of the three largest chest girths (100-110-120). For differences in chest wall thickness, a parameter was introduced to represent exponential radiation attenuation previously observed. This attenuation depends on the composition, density and thickness of all tissues penetrated by radiation when going throughout the body to the detectors. For differences in lung volume, a second parameter was used to simulate how counting efficiency varies with the loaded organ volume. As it was found in the previous section, counting efficiency varies inversely with lung volume if the activity is uniformly distributed in the volume. When considering a relative variation of counting efficiency from one subject to another, the first parameter represents the exponential attenuation with CWT variation while the second parameter is expected to represent the ratio of the reference lung volume to the new lung volume (a constant).

As a result of these considerations, the relationship between two counting efficiencies was simply written as:

$$\varepsilon_2(E) = \varepsilon_1(E)c_1e^{-c_2\mu(E)} \quad (\text{Equation 3.2})$$

where ε_1 represents the reference counting efficiency, ε_2 the unknown efficiency, E the photon energy, and c_1 and c_2 are the parameters that need to be calculated to fit the observed variation of counting efficiency with phantom morphology. The function $\mu(E)$ is the mass attenuation coefficient for ICRU-44 (ICRU 1989) adipose tissue (seven compounds) that was obtained using the online NIST-XCOM tool (Berger et al. 2005) for the relevant photon source. This simplified value of $\mu(E)$ was used here, since the three main structures responsible for additional attenuation (namely adipose tissue, muscular tissue and glandular tissue) have similar energy-dependant mass attenuation coefficients. This equation is correct for ideal geometries, where a uniform tissue growth is achieved, and is believed to hold in more complex cases. For example, expected tissue thickness due to given breast structures cannot be defined with precision. The parameter c_2 therefore represents a surrogate thickness describing the average attenuation of radiation.

This equation should provide a reasonably accurate estimate of counting efficiency for any female subject and would be particularly useful for a subject for whom no numerical model has yet been developed.

III.3. Validating the developed equation

The developed equation was first applied to reproduce the MC simulated efficiency curves. Next, it was tested against experimental data to fit the simulated curves and finally it was applied to published data.

III.3.1. Reproducing MC simulations with the developed equation

Equation 3.2 was applied to the simulated efficiency curves (ε_{phant}), taking the efficiency curve from the 85A model as the reference (ε_{ref}). The method was based on a linear

regression involving variables $Y = \ln\left(\frac{\varepsilon_{phant}}{\varepsilon_{ref}}\right)$ and $X = \mu(E)$, where

$$Y = \ln(c_1) - c_2X. \quad \text{Equation 3.3}$$

Once obtained, the parameters c_1 and c_2 were inserted into Equation 3.2 and the requested efficiency was calculated and compared to the MC values. The maximum difference between the MC efficiencies and those obtained from Equation 3.2 is a practical indicator of the validity of the proposed model and gives a local indication of the fit quality. A more accurate indication of the quality of the fit can be calculated using the following parameter:

$$\chi^2 = \frac{1}{N-n} \sum_{i=1}^N \left(\frac{\varepsilon_{MC} - \varepsilon_{MC}}{\varepsilon_{MC}} \right)^2 \quad \text{Equation 3.4}$$

where N is the number of data, n the number of varying parameters, ε_{cal} refers to efficiency values calculated using Equation 3.2 and ε_{MC} the efficiencies obtained with MC simulations. This chi-square-like parameter normalizes the difference between calculated values and the MC values using the MC data and gives a global indication of the fit quality (for the considered energy range). To obtain an acceptable error, this parameter should be inferior to

0.0025, which means that the calculated parameters c_1 and c_2 are only useful if the mean uncertainty of the calculated efficiency is below 5% ($100 * \sqrt{0.0025}$).

For the 85 and 90 (chest girth) models, the parameter c_1 was set to one, since the volume of the lungs was the same for all the phantoms in these series. Table 3.4 gives the parameter c_2 obtained with Equation 3.3 for the 85 and 90 chest girth phantoms, for all created cup sizes, with the associated R^2 and χ^2 . It also compares the MC and calculated counting efficiencies for the 85E phantom by using parameter c_2 and the 85A efficiency curve as the reference. For the 85E phantom, the estimated value of c_2 , representing the additional chest wall thickness, was around 1.87 g/cm². With this value, the highest relative error between the simulated and calculated counting efficiencies was about 6.4% and was observed for the lowest energy at 15 keV. Figure 3.10 shows the linear regression giving the $c_1 - c_2$ parameters for the 90 chest girth phantom simulations. Using these morphological coefficients, the highest difference (around 6%) was obtained for the 90E model at 15 keV.

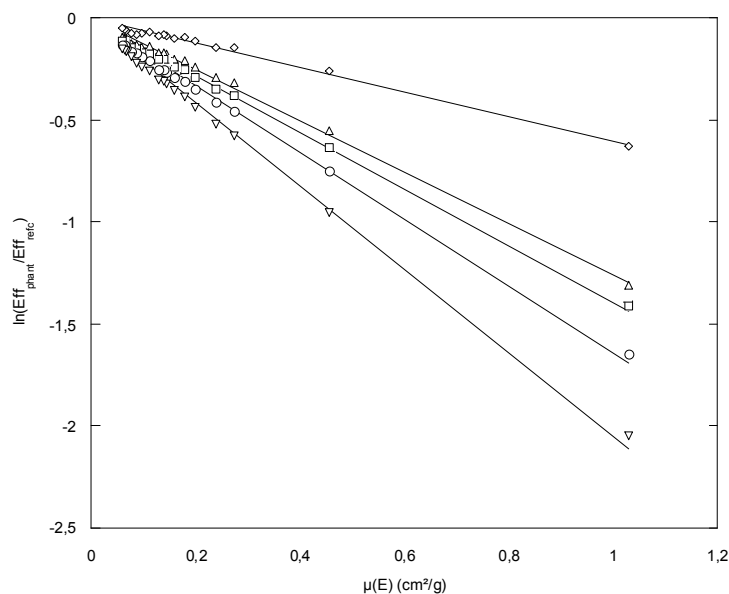


Figure 3.10. Linear regression giving the c_2 parameter for the 90 chest girth phantom; simulations normalized to the 85A phantom values. Linear fit calculated using Microsoft Excel 2008TM: **90A** (diamonds) $y = -0.6025x$, $R^2 = 0.9875$; **90B** (triangles) $y = -1.2576x$, $R^2 = 0.9964$; **90C** (squares) $y = -1.3966x$, $R^2 = 0.9943$; **90D** (circles) $y = -1.6433x$, $R^2 = 0.9936$; **90E** (inverted triangles) $y = -2.0526x$, $R^2 = 0.9944$.

Table 3.5 gives the c_1 and c_2 values for the three largest chest girth phantoms (cf. Equation 3.3) with their associated R^2 and χ^2 values. In addition, it compares the simulated and calculated counting efficiencies for the 120F phantom, using the c_1 and c_2 parameters and the 85A efficiency curve as the reference. Since the lung volume of the 100, 110 and 120 models was the same, but different from that of the 85 model, parameter c_1 had to be included. For the three largest chest girth phantoms, with various cup sizes from B to F, the MC and the calculated efficiencies did not differ by more than 5%.

Considering the small differences between calculated and MC efficiencies and the χ^2 values given in Tables 3.4 and 3.5, the model given by Equation (3.2) was validated with an accepted uncertainty of 5-10%. Figure 3.11 compares the simulated and calculated counting efficiency curves for the 85B, 90C, 100D, 110E and 120F models. The full comparison of the values

obtained with Equation 3.2 using the 85A simulation as the reference curve and the values of the 23 simulations are given in Appendix B.4.

Table 3.4. Values of the parameter c_2 for the 85 and 90 chest girths and associated R^2 and χ^2 (left). Comparison of the MC and calculated efficiencies for the 90E model at various energies (right).

phantom	c_2 (g/cm ²)	R^2	χ^2	Energy (keV)	MC efficiency (counts/s/ γ)	calculated efficiency (counts/s/ γ)	Diff. (%)	
85	B	0.86	0.9982	0.8E-4	15.31	1.72E-05	1.61E-05	6.4
	C	1.18	0.9967	2.5E-4	22.16	1.02E-03	1.04E-03	-1.4
	D	1.47	0.9995	0.6E-4	59.54	1.06E-02	1.10E-02	-4
	E	1.87	0.9928	13E-4	122.06	1.26E-02	1.31E-02	-3.8
90	A	0.60	0.9875	2.5E-4	185.72	1.10E-02	1.12E-02	-1.9
	B	1.26	0.9964	3.2E-4	356.01	6.46E-03	6.64E-03	-2.7
	C	1.40	0.9943	6E-4	661.66	3.98E-03	4.13E-03	-3.9
	D	1.64	0.9936	9.3E-4	1173.23	2.68E-03	2.78E-03	-3.6
	E	2.05	0.9944	13E-4	1408.01	2.40E-03	2.47E-03	-3.1

Table 3.5. Values of the parameters c_1 and c_2 for the 100, 110 and 120 chest girths and associated R^2 and χ^2 (left). Comparison of the MC and calculated efficiencies for the 120F model at various energies (right).

phantom	Parameters				Energy (keV)	MC efficiency (counts/s/ γ)	calculated efficiency (counts/s/ γ)	Diff. (%)	
	c_1	c_2 (g/cm ²)	R^2	χ^2					
100	B	0.73	1.63	0.9986	2E-4	22.16	1.28E-05	1.25E-05	2.4
	C	0.72	2.01	0.9997	1E-4	33.44	2.54E-04	2.47E-04	2.6
	D	0.70	2.51	0.9998	1E-4	40.12	4.42E-04	4.37E-04	1.1
	E	0.71	2.81	0.9996	1E-4	59.54	7.99E-04	8.15E-04	-2.
	F	0.66	3.17	0.987	7E-4	81	1.02E-03	1.06E-03	-3.5
110	B	0.53	4.31	0.9985	3E-4	122.06	1.22E-03	1.27E-03	-4.1
	C	0.52	4.87	0.9992	2E-4	165.86	1.25E-03	1.28E-03	-2.6
	D	0.51	5.65	0.9993	3E-4	244.7	1.08E-03	1.12E-03	-3
	E	0.50	5.91	0.9996	1E-4	356.01	8.93E-04	9.00E-04	-0.8
	F	0.49	6.20	0.9995	2E-4	511	7.42E-04	7.54E-04	-1.5
120	C	0.34	7.40	0.9994	4E-4	661.66	6.62E-04	6.68E-04	-0.9
	D	0.33	7.78	0.9996	3E-4	835.84	6.06E-04	5.99E-04	1.2
	E	0.31	8.11	0.9995	4E-4	1173.23	5.37E-04	5.18E-04	3.4
	F	0.29	8.86	0.9990	9E-4	1408.01	5.03E-04	4.81E-04	4.4

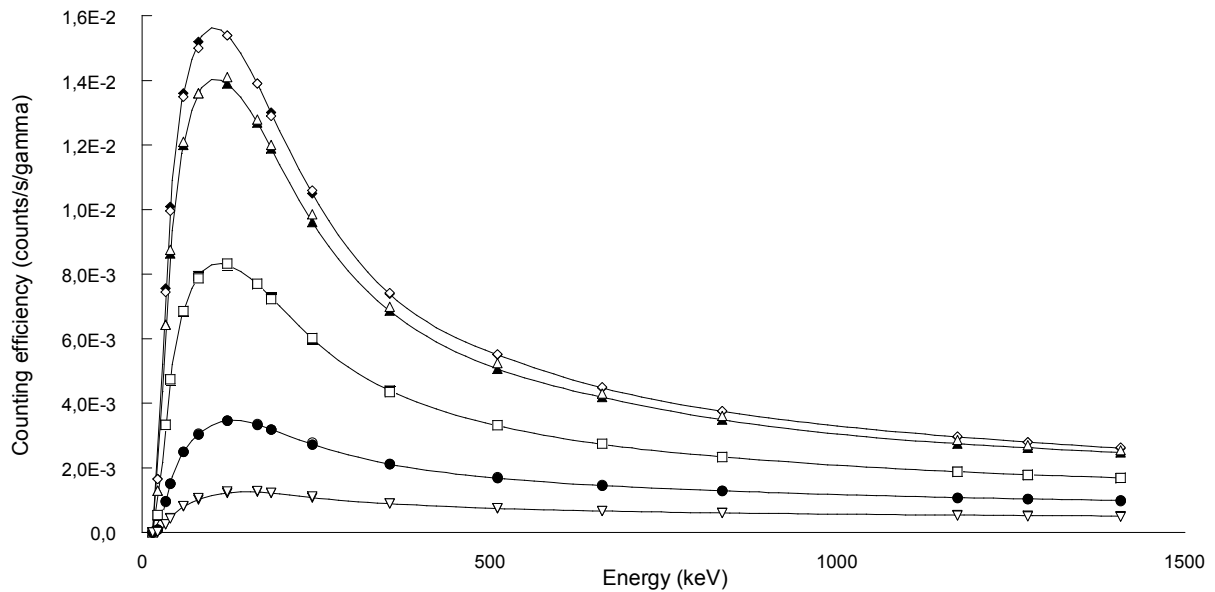


Figure 3.11. Counting efficiency (counts/s/gamma) variation with energy (keV): Comparison between MC simulated values (black symbols and solid lines) and the estimated ones (white symbols) for the models: 85B (diamonds), 90C (triangles), 100D (squares), 110E (dots) and 120F (inverted triangles). 85A being the reference for calculation.

III.3.2. Reproducing measurements with the developed equation

The model given by Equation 3.2 produced a rapid and reliable estimate of efficiency curves, which previously required time consuming MC calculations and specific voxel models. However, this equation remains of limited interest if it is not tested against experimental measurements. Indeed, the reference curve used by this equation is a simulation result that is rarely available for routine measurements optimization. It is thus of utmost importance to investigate if a calibration measurement can be used as the reference efficiency of Equation 3.2 to estimate the efficiencies of the 24 created models. This section first compares experimental calibration measurements to MC simulated efficiencies and then presents how Equation 3.2 was used to transform a Livermore calibration curve to an MC simulated curve.

- **Comparing a measured curve to a simulated curve**

The Livermore measurements taken at the AREVA NC reprocessing plant were used for this study. The medical department, responsible for the surveillance program at La Hague, provided measurement results obtained using the Livermore phantom associated with different plates (P0 to P4), with thicknesses ranging from 1.8 to 4.3 cm (P0 is the core plate). The monitoring system was the one previously described, for which MC efficiency curves were calculated. It was typically set as close as possible to the surface of the skin to cover at best the lungs. In routine measurements, the efficiency curve is interpolated by a polynomial

$$\text{relation of the form: } \ln(\varepsilon_{ff}) = \sum_{i=1}^6 (a_i \ln(E))^i, \quad \text{Equation 3.5}$$

where E is the Energy in keV, and ε_{ff} the counting efficiency in counts/s/gamma (Molnar et al. 2002). Table 3.6 lists the coefficients used here to calculate the experimental efficiency.

Table 3.6. Parameters of the sixth-order polynomial equation describing the counting efficiency variation with energy, measured for the Livermore phantom and the associated plates.

coefficient	P0 (1.8 cm)	P1 (2.4 cm)	P2 (2.8 cm)	P3 (3.5 cm)	P4 (4.3 cm)
a_6	-0.016	-0.025	-0.024	-0.024	-0.026
a_5	0.524	0.818	0.773	0.795	0.862
a_4	-6.967	-10.854	-10.276	-10.576	-11.546
a_3	48.904	75.865	72.013	74.281	81.671
a_2	-191.74	-95.28	-281.33	-291.03	-322.25
a_1	399.434	607.997	582.354	604.766	674.048
a_0	-345.43	-517.84	-499.57	-521.85	585.249

The measured calibration counting efficiencies were compared to MC simulation results for the 85A phantom. The 85A simulated efficiencies and those measured using plate P1 were almost equivalent, as shown in Table 3.7. The relative error was less than 5% for all energies higher than 59.54 keV. The noticeable difference observed between 22 and 40 keV can be explained by the materials used in the P0 and P1 plates. These materials were designed to reproduce the absorption of ^{238}U X rays, at around 15 keV, in a 100% muscle plate (case of plate P0) and a 50% adipose-50% muscle plate (case of plate P1) respectively (Griffith et al. 1978, Newton et al. 1985). At around 15 keV, and for energies above 100 keV, this combination of plates is expected to reproduce the absorption of gamma radiation in human tissues (with the correct adipose/muscle composition). The relative differences shown in Table 3.7 are acceptable since the tissue composition of the 85A model and the Livermore mannequin are quite different. This comparison indicates that the Livermore mannequin with plate P1 is similar to an 85A female subject when taking into account the different counting positions operated during the measurements and the simulations (cf. Section 2.2).

As a consequence, the Livermore P1 measurement can be directly used in Equation 3.1 with the $c_1 - c_2$ parameters of Tables 3.4. and 3.5 (obtained for the 85A simulation) to estimate the efficiency curve of each of the 24 models. In this case, however, the counting efficiency estimates of the 24 simulated models will show significant disagreement at the lowest energies since such differences exist between the 85A simulation and the P1 measurement (cf. Table 3.7). Meanwhile, at higher energies, and particularly starting from 59.54 keV, better counting efficiency estimates can be given. Indeed, differences up to 43% on the counting efficiency value were obtained for the 100F at 22 keV. Whereas, starting from the 59.54 keV this difference did not exceed 10% for all the 24 phantoms and all the 12 photon emissions. The full comparison of the counting efficiencies obtained with the Livermore plate P1 measurement as the reference curve of Equation 3.2 and the simulation values of the 24 female phantoms are given in detail in Appendix B.5.

Table 3.7. Comparison of simulated counting efficiencies for the 85A female model and measured values obtained for the Livermore with plate P1 and associated difference (relative error).

Energy (keV)	P1 measured efficiency (counts/s/ γ)	85A MC efficiency (counts/s/ γ)	Diff. (%)
15	1.21E-04	1.10E-04	-9.4
22	3.29E-03	2.43E-03	-34.9
33	1.16E-02	9.41E-03	-22.9
40	1.44E-02	1.22E-02	-18.1
59	1.72E-02	1.60E-02	-7.6
81	1.76E-02	1.75E-02	-0.5
122	1.68E-02	1.76E-02	4.7
165	1.51E-02	1.57E-02	4.1
185	1.42E-02	1.46E-02	2.4
245	1.17E-02	1.18E-02	0.3
356	8.36E-03	8.16E-03	-2.4
511	5.90E-03	5.99E-03	1.5
661	4.75E-03	4.85E-03	2.1
834	4.05E-03	4.03E-03	-0.6
1173	3.29E-03	3.14E-03	-4.7
1274	3.08E-03	2.95E-03	-4.3
1408	2.79E-03	2.76E-03	-0.9

- **Transforming a measured curve to a simulated one**

Another approach is to calculate the parameters c_1 - c_2 of Equation 3.2 taking the Livermore calibration data as the reference efficiency and the simulated 85A values as the unknown efficiency. The c_1 and c_2 obtained values are given in Table 3.8 along with the associated R^2 coefficients describing the linear regression quality. Negative c_2 values were obtained when the Livermore efficiency was smaller than that of the 85A phantom.

Table 3.8. Values of the c_1 and c_2 parameters for the different Livermore plates and associated determination coefficient obtained from linear regression.

Reference plate	c_1	c_2 (g/cm ²)	R^2
P0	0.96	1.19	0.964
P1	0.99	0.18	0.206
P2	1.05	-0.14	0.192
P3	1.20	-1.00	0.982
P4	1.30	-1.91	0.990

According to this table, the best fit for the 85A efficiency was obtained when the measurement from the 4.3-cm-thick Livermore P4 plate was used as the reference. This result could seem in contradiction with the previous one where the measurement with chest plate P1 was found to be close to 85A simulated curve. However, this observation can be explained as follows. The linear regression giving parameters c_1 and c_2 showed a poor capacity to reproduce the 85A data when starting from the Livermore plate P1 measured curve (cf. Figure 3.12). This is due to the large differences in efficiency values for energies between 22 and 40

keV as discussed above (cf. Table 3.7). Because of these differences, the linear fit is not parallel to the abscissa axis and the expected values ($c_1=1$ and $c_2=0$) were not obtained. The previously identified equivalence between the 85A simulation and the P1 measurement was thus not obtained. Meanwhile, the P4 plate count was significantly different from that of the 85A model. Nevertheless, this difference had the same order of magnitude for all energies so that a better linear regression (cf. Section 2.2 and Table 3.7) was obtained, as illustrated in Figure 3.12.

Using the c_1 and c_2 parameters determined for the P4 case, the 85A MC counting efficiency was reproduced with a maximum relative difference of 8.7% for the ^{152}Eu photon at 40 keV. Figure 3.13 compares the counting efficiency curves obtained by MC calculations and those calculated using the data of Tables 3.4 and 3.5 for the 85A, 90B, 100C, 110D and 120F models, taking the P4 efficiency as the reference. For these examples the maximum relative difference was less than 10%. The full comparison of the counting efficiencies obtained with the Livermore plate P4 measurement as the reference curve of Equation 3.2 and the simulation values of the 24 female phantoms are given in detail in Appendix B.6.

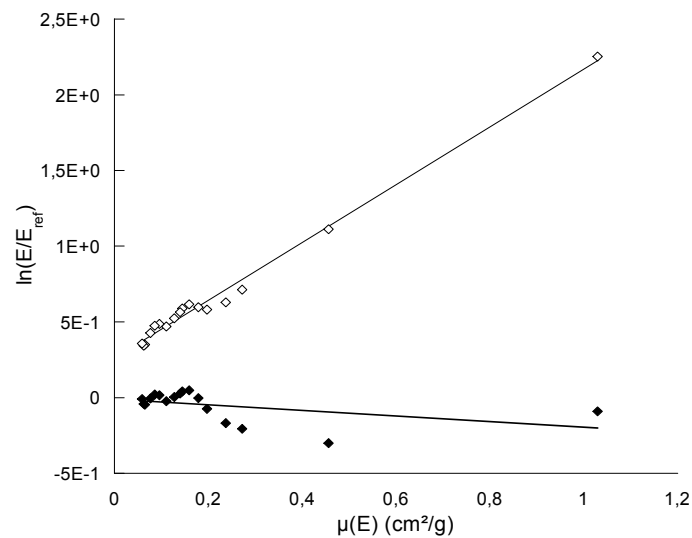


Figure 3.12. Variation of the natural logarithm of efficiency ratio as a function of the mass attenuation coefficient (cm^2/g) for plate P1 (black diamonds) and plate P4 (white diamonds).

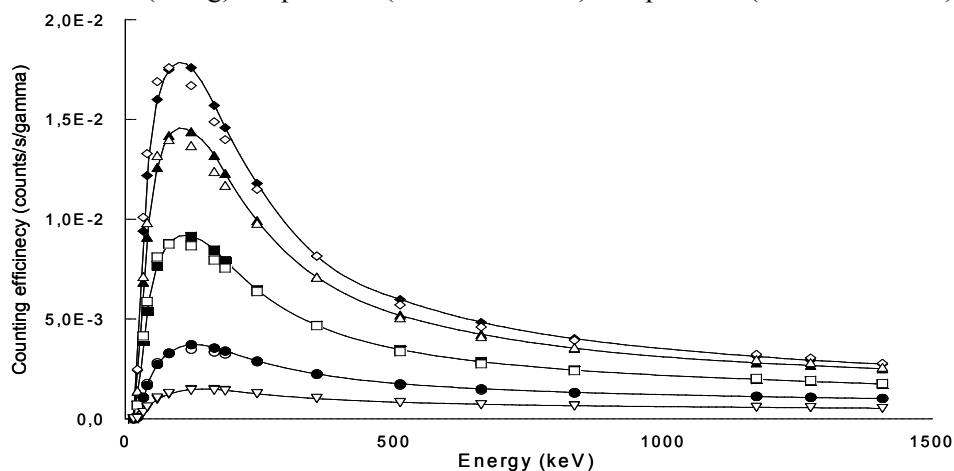


Figure 3.13. Variation of counting efficiency (counts/s/gamma) as a function of energy (keV): comparison between MC simulated values (black symbols and solid lines) and the calculated values (white symbols) for the 85A model (diamonds), 90B (triangles), 100C (squares), 110D (dots) and 120E (inverted triangles). The Livermore phantom with plate P4 is the calculation reference.

As a partial conclusion, the efficiency for an 85A female worker may be considered equivalent to the P1 calibration efficiency or the P4 calibration efficiency curve can be transformed to the 85A efficiency curve. Based on the data provided in Table 3.6, laboratory specific efficiency curves can be compared with those used in this paper. If an agreement is found, the correction efficiency for a given cup size and chest girth can be calculated from Tables 3.4 and 3.5. If not, the strategy employed here to transform the P4 efficiency into a female calibration curve should be adopted.

III.3.3. Reproducing published data with the developed equation

The equation developed in this work was also tested to reproduce the results obtained by Hegenbart et al. (2008). This section investigates to what extent the developed equation is capable of reproducing morphology-induced counting efficiency variations, even when the methods and simulation results are noticeably different from those in this study (different counting system, phantom creation hypothesis and methods).

Three main differences exist between the Hegenbart et al. (2008) models and those used here. First, while we used germanium (Ge) detectors; Hegenbart et al. (2008) used NaI-CsI Phoswich counting system for whole body measurements. Furthermore, Hegenbart et al. (2008) only provided efficiencies for 3 energy sources (Am-241, Cs-137, Co-60), which limits the significance of the fit giving c_1 and c_2 for Equation 3.2. Finally, the female mesh phantoms used by Hegenbart et al. (2008) represented different breast sizes (AA to G), but only one chest girth (105) and cup size variation was different from the one used in this study.

Despite all these differences, Equation 3.2 was applied to the Hegenbart et al. (2008) data taking their 105AA counting efficiency as the reference curve and using the adipose tissue mass attenuation coefficient defined in Section II.1. Table 3.9 gives the obtained c_1 and c_2 parameters and, for all cup sizes, compares the calculated and MC efficiencies at 59.54 keV. Using Equation 3.2 with the reported c_1 and c_2 values gave a good estimate of the counting efficiency for all cup sizes. The greatest difference between MC and calculated counting efficiency was about 3.5% for the 105F phantom at 661.66 keV. The results of using Equation 3.2 for the ^{137}Cs and ^{60}Co radionuclides and the Hegenbart et al. (2008) data are given in detail in Appendix B.7.

Table 3.9. Values of c_1 and c_2 parameters for all cup sizes (A to G) with the associated R^2 and χ^2 values (left). Comparison of published and calculated values of counting efficiency with the associated difference (%) for the Am-241 photons at 59.54 keV (right).

Cup	c_1	c_2 (g/cm ²)	R^2	χ^2	MC. Count. Eff. (counts/s/ γ)	Cal. Count. Eff. (counts/s/ γ)	Diff. (%)
A	0.86	0.31	0.9254	2E-4	2.260E-02	2.258E-02	0.1
B	0.80	0.46	0.9158	4E-4	2.030E-02	2.027E-02	0.2
C	0.78	0.61	0.9404	6E-4	1.920E-02	1.916E-02	0.2
D	0.72	0.67	0.9560	6E-4	1.768E-02	1.765E-02	0.2
E	0.69	0.89	0.9448	12E-4	1.610E-02	1.606E-02	0.3
F	0.64	0.94	0.9435	14E-4	1.488E-02	1.484E-02	0.3
G	0.62	1.06	0.9619	15E-4	1.390E-02	1.387E-02	0.3

To further investigate the efficiency of Equation 3.2 in reproducing the simulated data and the quality of parameters c_1 and c_2 , the reference efficiency curve of Equation 3.2 was changed from AA to A. Indeed, the first reference curve taken, i.e. that of the AA model, seemed to be of poor realism considering both the breast tissue weight (500 g) and the operated tissue weight adding per cup size change (Turner and Dujon 2005; Pechter 1998). Therefore, the A cup model was used as the reference curve since it was considered to have a more realistic value of breast weight (when compared to the AA cup), and the additional tissue weight required to pass from the A cup to other models seemed more appropriate (cf. Section 2.4).

The obtained results confirmed these considerations since a better fit (using Equation 3.3) was observed, improving thus the estimate of the morphological parameters c_1 and c_2 (cf. Figure 3.14). As a direct consequence, the efficiency estimate with Equation 3.2 was improved since the maximum relative error between simulated and estimated efficiency values was reduced from 3.5% to about 1% at 661.66 keV and the F-cup phantom. The results of using the A cup size counting efficiency as the reference values of Equation 3.2 and the comparison to the Hegenbart et al. (2008) simulated data are given in detail in Appendix B.8.

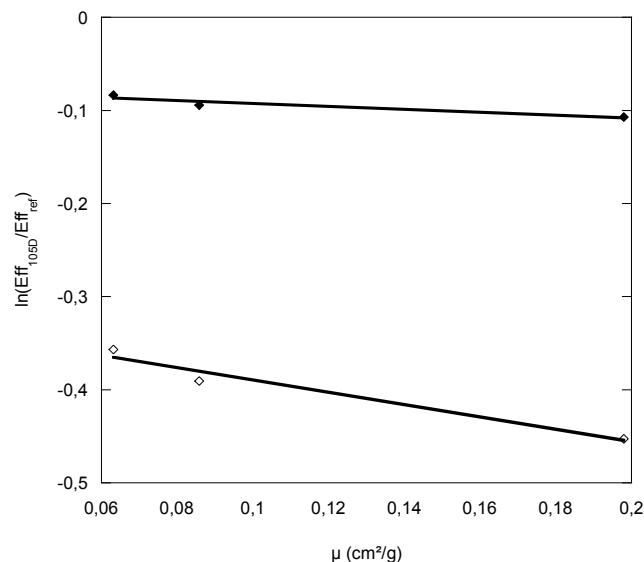


Figure 3.14. Variation of the natural logarithm of the ratio of the 105D efficiencies to the 105AA values (white diamonds) and those of the ratio of the 105D efficiencies to the 105A values (black diamonds) as a function of the mass attenuation coefficient (cm^2/g). Linear fit calculated using Microsoft Excel 2008TM: **105AA reference:** $y = x +$, $R^2=0.9$; **105A reference:** $y = x +$, $R^2=0.98$.

Hegenbart et al. (2008) also formulated an equation to represent how counting efficiency varies with breast weight and cup size. In the first case, a second order polynomial equation was found to reproduce the decrease in relative efficiency, while in the second case a linear equation with x to the power of -0.8 was determined (x in cm) for ^{241}Am simulations (-0.68 for ^{137}Cs and -0.62 for ^{60}Co). While the polynomial fits were shown to hold for the Hegenbart et al. (2008) models, here it was shown that Equation 3.2, based on physical considerations, also holds.

III.4. Study of the introduced parameters

Equation 3.2 uses the adipose tissue mass attenuation coefficient, which is tabulated and easily available, and two parameters (c_1 and c_2). This section focuses on the variation of these parameters with lung volume (c_1) and chest wall thickness (c_2), the main morphological factors involved. First we investigate these correlations for the MC simulated values, then for the Livermore measurements and finally for the data by Hegenbart et al. (2008).

III.4.1. C_1 correlation with lung volume

- **Simulated data**

In the female torso library created in this study, only phantoms with the biggest chest girth implicated a variation of the lung volume. For those models (100, 110 and 120 chest girth phantoms), c_1 is expected to be close to the ratio of the reference lung volume (2.3 L) to the modified lung volume (2.99 L). Since the three largest chest girths have the same lungs volume, they should have the same c_1 , regardless of cup size, and its value should be approximately 0.77 (2.3/2.99). Although it is true for the chest girth of 100 (cf. Table 3.5), this is far from being the case for the 110 and 120 phantoms (where c_1 is approximately 0.5 and 0.3 respectively).

However, for a given chest girth, c_1 is practically constant for all cup sizes. The c_1 values obtained for the 110 and 120 models can be explained since the detectors were not positioned in exactly the same way for all models, simply to prevent collisions between the breast and detectors. This changes the solid angle of the detectors covering the lungs, which implies that c_1 cannot give an exact representation of the lung volume ratio. Moreover, when linear regression is performed, c_1 and c_2 simply provide best estimates that can be used for data adjustment. Variations in lung volume, chest girth, cup size, and detector solid angle are necessarily aggregated in c_1 and c_2 .

- **Measured data**

For the Livermore measured data, no lung volume variation existed as the physical phantom contains only one set of loaded lungs. However, since the distance between the lungs and the detectors changed, as extra-thoracic plates were added, the solid angle of detection covering the lungs also changed. As a consequence, parameter c_1 was introduced to represent the loaded organ volume variation in the monitored region of the detectors due to the variation of the source-detector distance.

- **Published data**

Similarly to the Livermore case, there were no variations in the lung volume for the Hegenbart et al. (2008) models. However, Hegenbart et al. (2008) also operated a shift in the detectors positioning as cup size increased to maintain a 2 cm distance to the top of the breast. Therefore, the lung volume covered by the detector was changed and similarly parameter c_1 was introduced to represent this volumetric change. In these simulations, parameter c_1 was found to decrease with increasing cup size i.e. increase in the lung-detector distance (cf. Table 3.9).

III.4.2. c_2 correlation with chest wall thickness

Furthermore, we investigate the correlation of c_2 with CWT for all phantoms. This study is of particular interest for the female subjects since the CWT can be more delicate to estimate and the typical equations based on height, weight and age of male subjects remain of limited interest (Fry and Sumerling 1980; Pierrat 2005).

- **Simulated data**

For all chest girths, parameter c_2 is expected to represent an average thickness of absorption that describes the change in cup size. Since this absorption thickness cannot be defined with precision, the correlation between c_2 and the breast weight difference between the reference model (85A) and the considered model was studied. Figure 3.15 shows a linear variation of c_2 as a function of breast weight for all chest girths confirming the hypothesis on this parameter. The exact shape of the curve however, particularly the slope of the linear relation, clearly depends on chest girth.

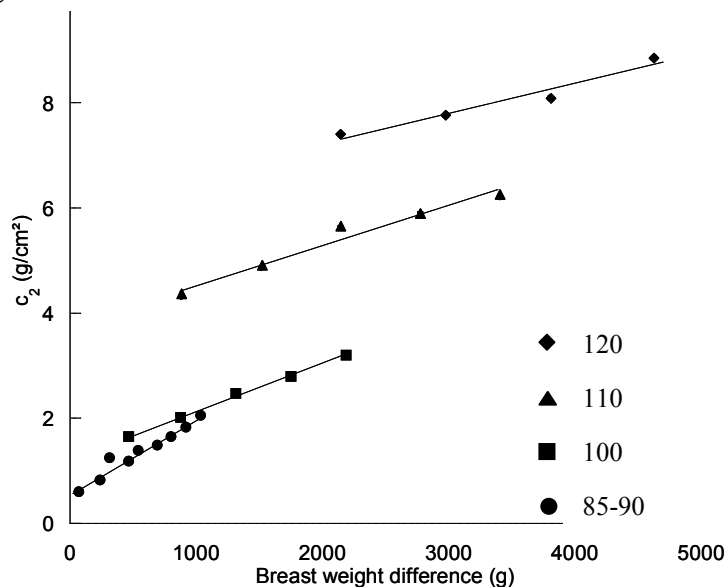


Figure 3.15. Variation of c_2 (g/cm²) as a function of breast weight difference (g) for chest girths from 85 to 90 (dots), 100 chest girth (squares), 110 chest girth (diamonds) and 120 chest girth (triangles). Linear fit calculated using Microsoft Excel 2008™: **85-90**: $y = 0.0016x + 0.4034$, $R^2 = 0.952$. **100**: $y = 0.0009x + 1.2424$, $R^2 = 0.994$. **110**: $y = 0.0008x + 3.7414$, $R^2 = 0.955$. **120**: $y = 0.0006x + 6.1098$, $R^2 = 0.961$.

- **Measured data**

As for the c_2 parameter obtained when transforming a Livermore calibration measurement to a MC simulated efficiency curve, the investigation showed a linear dependence with the plate thickness as expected (cf. Figure 3.16); giving a value of 0.992 for the determination coefficient (R^2). The c_2 values were taken from Table 3.9 while the CWT of each plate was represented on the x-axis.

- **Published data**

In the case of the data by Hegenbart et al. (2008), the calculated c_2 parameter showed an acceptable linear trend with the differences in breast weight (cf. Figure 3.17) which further validates the counting efficiency dependency with breast size and more generally with CWT.

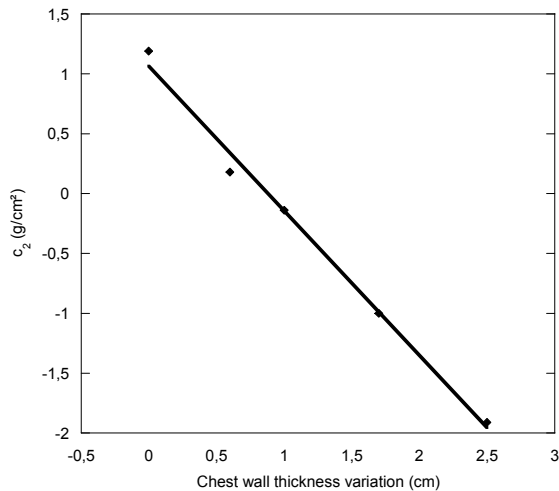


Figure 3.16. Variation of c_2 (g/cm²) as a function of chest wall thickness variation (cm) for the Livermore measured data and the 85A simulation as reference. Linear fit calculated using Microsoft Excel 2008TM: $y = -1.2084x + 1.0658$; $R^2 = 0.99217$.

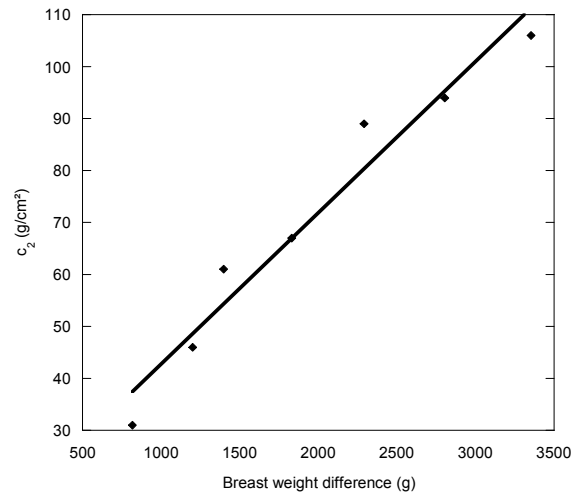


Figure 3.17. Variation of c_2 (g/cm²) as a function of breast weight difference (g) for the Hegenbart et al. (2008) data and the AA reference breasts. Linear fit calculated using Microsoft Excel 2008TM: $85-90$: $y = 0.029094x + 13.65$; $R^2 = 0.955$.

III.5. Generalizing the use of the developed equation

A practical method for the choice of parameters c_1 and c_2 was formulated to ease the use of the developed equation in order to give a reliable estimate of counting efficiency when a patient-equivalent phantom is unavailable. This involves the study of the correlation between these parameters. This was done using the MC simulation results for the phantoms of chest girth of 100, 110 and 120.

Figure 3.18, showing c_1 as a function of c_2 , reveals a linear relationship between both morphological parameters. This correlation is of particular interest since it can be used to calculate counting efficiency as a function of the female morphology. Indeed, when a good estimate of c_2 (i.e. cup size) is available, a realistic value can be calculated for c_1 (i.e. the variation in lung volume). For example, this equation could be used in the case of a 105D chest girth, which was not covered by a numerical model in this study. In the publication by Turner and Dujon (2005), the authors estimated that the additional weight increment required to represent a change of one cup size for a subject with a chest girth of 105 was the same as that for a chest girth of 110. By associating values in pairs, such as 105D/110C, 95C/100B or 115D/120C (Wood et al. 2008), the value c_2 from Table 3.5 can be estimated at 4.87 g/cm². This value can then be applied in the equation given in the caption of Figure 3.18 to give a c_1 value of about 0.52. Entering these parameters in Equation 3.2 for the 105 chest girth phantom gives a counting efficiency value of about 3.3E-03 counts/s/gamma for ²⁴¹Am photons at 59.54 keV. This counting efficiency value can be considered as reasonably correct, since it is less than that obtained for the 100D phantom (6.85E-03 counts/s/gamma), but

greater than that of the 110D model ($2.68E-03$ counts/s/gamma). The authors suggest using this rule for chest girth between 95 and 120. For chest girth between 80 and 90, the c_2 values in Table 3.4 are recommended, while the 85 values are recommended for a chest girth of 80.

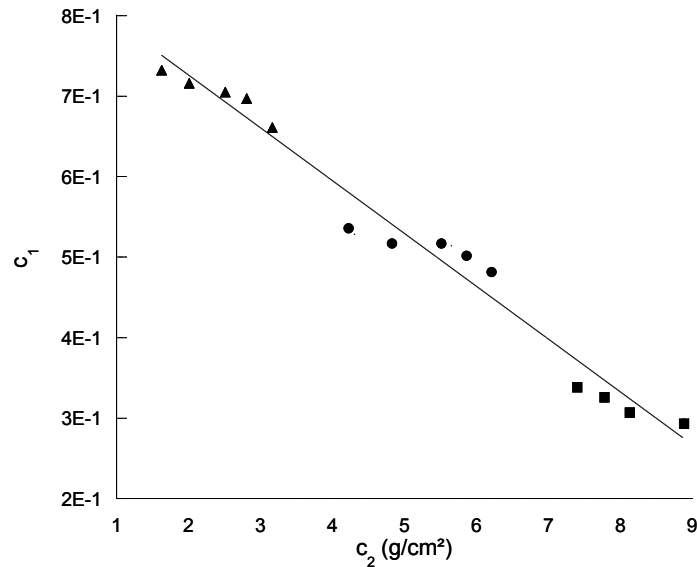


Figure 3.18. Variation of c_1 as a function of c_2 (g/cm²) for chest girths of 100 (triangles), 110 (dots) and 120 (squares), with all cup sizes represented. Linear fit calculated using Microsoft Excel 2008TM:
 $y = -0.0656 x + 0.8574$, $R^2=0.9728$.

As a conclusion, in order to use the developed equation the monitored subject's morphology and body size is studied to find the corresponding phantom in the developed library. If an equivalent model is found, the appropriate c_2 parameter can be taken from Tables 3.4 and 3.5 and directly used in Equation 3.2. Alternatively, parameter c_2 can be calculated using the equations given in the insets of Figures 3.15 or by simply examining the differences between the 85A model in this study and a given breast size, and apply the relative correction to the efficiency curve obtained with the Livermore-P1 or another phantom (JAERI phantom for example, Shirotani 1988). Once parameter c_2 is acquired, the Equation given in Figure 3.18 can be used to estimate parameter c_1 and then the counting efficiency based on Equation 3.2.

IV. Practical recommendations

A simple method was finally formulated to correct the typical calibration coefficients obtained with the Livermore male mannequin when monitoring a female subject. It consists in providing the adequate correction factors that should be used to divide the Livermore P1 measured calibration curve to account for additional radiation attenuation by breast. This way, the technician responsible of the monitoring program at La Hague can directly correct the activity estimate. Table 3.10 gives the correction factors for the germanium detectors of the AREVA NC *in vivo* monitoring installation and various female sizes. These include the 24 female phantoms developed in the library. This work however was extended to cover female subjects for whom no phantom exists in the library by using the developed equation.

Table 3.10. Conversion factors to correct the Livermore P1 measurement as a function of female size ($E_{ff} = E_{ff} \text{ Livermre} / \text{factor}$).

Size	Energy (keV)																	
	15	22	33	40	59	81	122	165	185	244	356	511	661	834	1173	1274	1408	
85	A	1.09	1.35	1.23	1.18	1.08	1.00	1.01	1.01	1.00	1.02	1.03	1.03	1.01	1.05	1.04	1.01	
	B	2.68	1.97	1.53	1.43	1.27	1.16	1.09	1.08	1.09	1.12	1.13	1.07	1.06	1.08	1.11	1.10	1.07
	C	3.57	2.33	1.72	1.60	1.39	1.26	1.17	1.15	1.16	1.17	1.18	1.12	1.10	1.11	1.14	1.13	1.09
	D	4.93	2.63	1.83	1.68	1.45	1.30	1.21	1.19	1.19	1.22	1.21	1.15	1.12	1.14	1.16	1.15	1.11
	E	7.01	3.21	2.09	1.90	1.62	1.45	1.33	1.29	1.29	1.31	1.29	1.23	1.19	1.20	1.22	1.20	1.16
90	A	2.05	1.75	1.42	1.36	1.21	1.10	1.05	1.04	1.06	1.09	1.09	1.06	1.06	1.08	1.11	1.10	1.06
	B	4.05	2.35	1.69	1.58	1.37	1.24	1.17	1.15	1.16	1.18	1.18	1.13	1.12	1.14	1.16	1.15	1.11
	C	4.49	2.54	1.80	1.67	1.44	1.30	1.21	1.19	1.19	1.22	1.22	1.16	1.13	1.16	1.19	1.17	1.13
	D	5.68	2.85	1.94	1.79	1.52	1.37	1.27	1.25	1.26	1.28	1.26	1.19	1.16	1.18	1.20	1.19	1.15
	E	8.51	3.49	2.19	1.99	1.67	1.48	1.36	1.32	1.33	1.35	1.33	1.25	1.22	1.21	1.23	1.22	1.17
95	A	5.31	3.03	2.09	1.89	1.68	1.62	1.58	1.56	1.56	1.54	1.52	1.49	1.48	1.46	1.41	1.40	1.38
	B	6.20	3.26	2.19	1.97	1.75	1.68	1.63	1.80	1.61	1.59	1.56	1.53	1.51	1.49	1.44	1.43	1.41
	C	8.06	3.71	2.39	2.13	1.87	1.78	1.73	1.70	1.69	1.67	1.63	1.60	1.57	1.55	1.50	1.48	1.46
	D	12.54	4.60	2.75	2.42	2.09	1.98	1.91	1.87	1.85	1.82	1.77	1.72	1.69	1.65	1.59	1.57	1.54
	E	21.50	5.99	3.28	2.84	2.41	2.26	2.15	2.09	2.07	2.02	1.95	1.88	1.84	1.79	1.72	1.69	1.66
100	B	8.16	3.80	2.56	2.35	2.01	1.81	1.68	1.65	1.66	1.68	1.69	1.60	1.56	1.58	1.60	1.59	1.54
	C	12.11	4.79	2.96	2.67	2.24	2.00	1.84	1.78	1.79	1.81	1.78	1.69	1.65	1.65	1.65	1.64	1.59
	D	20.38	6.17	3.47	3.05	2.51	2.22	2.03	1.96	1.95	1.96	1.90	1.78	1.74	1.73	1.75	1.72	1.65
	E	27.90	7.25	3.81	3.33	2.70	2.37	2.15	2.07	2.07	2.07	2.01	1.85	1.81	1.78	1.78	1.76	1.68
	F	41.56	9.20	4.51	3.87	3.09	2.71	2.44	2.33	2.31	2.28	2.19	2.00	1.95	1.90	1.87	1.87	1.79
	B	12.27	4.55	2.73	2.41	2.08	1.97	1.90	1.86	1.84	1.81	1.76	1.71	1.68	1.65	1.59	1.57	1.54
105	C	59.39	9.88	4.58	3.85	3.14	2.90	2.72	2.61	2.57	2.48	2.35	2.24	2.10	1.99	1.96	1.92	
	D	96.79	12.58	5.40	4.46	3.58	3.28	3.05	2.91	2.86	2.74	2.58	2.45	2.36	2.28	2.14	2.10	2.06
	E	185.5	17.40	6.72	5.44	4.27	3.87	3.55	3.36	3.30	3.14	2.93	2.76	2.64	2.53	2.37	2.33	2.27
	F	1052	41.78	12.24	9.41	6.96	6.12	5.46	5.06	4.92	4.60	4.19	3.85	3.63	3.44	3.16	3.09	3.00
	B	179.4	18.95	7.33	6.09	4.69	4.05	3.56	3.36	3.33	3.29	3.12	2.86	2.73	2.69	2.64	2.59	2.49
110	C	325.6	24.68	8.72	7.10	5.34	4.58	3.99	3.74	3.71	3.63	3.39	3.07	2.91	2.85	2.78	2.72	2.60
	D	741	35.43	10.78	8.57	6.27	5.31	4.50	4.22	4.17	4.02	3.71	3.34	3.13	3.02	2.92	2.84	2.72
	E	988	40.34	11.98	9.47	6.87	5.79	4.84	4.51	4.45	4.30	3.94	3.51	3.27	3.15	3.06	2.98	2.82
	F	1359	47.22	13.49	10.56	7.57	6.34	5.35	4.92	4.83	4.63	4.21	3.72	3.46	3.35	3.19	3.10	2.94
115	C	776	35.80	11.00	8.53	6.38	5.64	5.05	4.70	4.58	4.30	3.93	3.62	3.43	3.25	3.00	2.93	2.85
	D	2529	65.54	16.74	12.54	9.00	7.81	6.86	7.00	6.09	5.65	5.08	4.62	4.32	4.07	3.70	3.61	3.50
	E	3768	80.59	19.35	14.33	10.14	8.75	7.63	6.96	6.74	6.22	5.56	5.03	4.69	4.40	3.99	3.89	3.77
	F	14639	164.8	32.21	22.92	15.52	13.10	11.17	10.04	9.66	8.80	7.72	6.87	6.33	5.89	5.27	5.12	4.94
120	C	6744	122.2	26.38	19.69	13.59	11.19	9.23	8.34	8.15	7.74	6.94	6.05	5.57	5.33	5.04	4.91	4.65
	D	10277	147.9	30.22	22.30	15.18	12.42	10.17	9.13	8.89	8.40	7.42	6.43	5.90	5.60	5.28	5.13	4.87
	E	15369	176.3	34.90	25.60	17.27	14.06	11.37	10.15	9.85	9.21	8.13	6.99	6.35	6.01	5.59	5.43	5.11
	F	35571	256	45.60	32.66	21.52	17.23	13.76	12.07	11.67	10.82	9.36	7.94	7.17	6.69	6.12	5.88	5.54

V. Discussion and conclusion

This work used Mesh and NURBS 3D flexible formats to optimize the monitoring of female workers subject to internal contamination risks. Counting efficiency curves were calculated for a typical set of four-germanium-detectors used for *in vivo* measurements and a library of 24 female phantoms. The breast size influence over the counting efficiency was studied in detail for energies ranging from 15 keV to 1.4 MeV. Detectors' counting efficiency was found to decrease considerably with breast size and chest girth for low energy radionuclides, while it remains relatively constant for high energies. The breasts morphology has proven to be an important factor in low energy counting efficiency and thus detection limits are highly dependent on breast size and photon energy. Differences as high as 17% can be observed around 15 keV when comparing the counting efficiency values obtained for on particular breast size but different morphologies. This morphology effect is basically due to breast tissue deformation with gravity, particularly for women with large-size breasts monitored in the supine position, and provides an order of magnitude for the involved uncertainty due to the variation of morphology. This uncertainty should be comparable to the one due to errors on the source (nature and distribution) and to those on the positioning of the detectors. Nevertheless, these calculations provide typical efficiency correction factors that can be applied to optimize the lung monitoring of female workers.

A simple equation was next derived to establish a relationship between a given counting efficiency reference curve and any unknown efficiency value, taking into consideration differences in breasts size between subjects. This equation was used to obtain a reliable estimate of detector counting efficiency for any female subject, thereby avoiding time-consuming MC simulations. The developed equation was successfully tested on a library of female torsos and against experimental measurements and published data. The two parameters introduced in this equation depend on the morphology of the subject. MC results were explained using simple physical arguments and the parameters of the equation were linked to breast weight and lung volume. In addition to practical applications that may stem from the use of this equation, the given explanations for the MC results give confidence in the calculated efficiency correction. Even if no absolute rule can be given to calculate these parameters, orders of magnitude have been determined here and a method was suggested to obtain these parameters for a given counting system. This equation can also be useful even when different counting systems and methods are involved. For instance, similar equation could be determined by searching for one parameter that represents the exponential attenuation of radiation, another parameter representing the volume effect of the loaded organ and then establishing a comparison with the constants c_1 and c_2 given here.

To discuss the simulation results and the relevance of the developed equation, the work progress is reviewed. This includes the choice and distribution of the source, the positioning of the detectors and the introduced morphological parameters.

V.1. Choice and distribution of the source

In these simulations, an artificial source with 17 different photon emissions was used combining typical gamma radiations of the radionuclides most commonly used for the calibration of *in vivo* counting systems. It is thus necessary to compare the simulation results obtained with such a source with those obtained when simulating the natural emission spectrum of each radionuclide. Table 3.11 documents the MC simulation results for the ^{241}Am emissions at 59.54 keV and proves that no significant differences on counting efficiencies were obtained when considering the natural X and gamma emission spectrum of the source. However, this agreement was found to be directly related to the number of channels used. This can simply be explained by the fact that a better separation of the photoelectric peak (when subtracting the Compton continuum) becomes possible whenever the number of channels increases (cf. Table 3.11). This gives an idea on the uncertainty due to errors on the source nature.

Table 3.11. Comparison of simulated counting efficiencies obtained for the photons at 59.54 keV with the artificial 17 photon source and the natural Am-241 source; results for the ICRP female torso.

Natural Src.		Artificial Src.		Artificial Src.		Artificial Src.		
No GEB		1 NRJ.		17 NRJ.		Count. Eff.		
Count. Eff.		Count. Eff.		Count. Eff.		Count. Eff.		
(counts/s/ γ)		(counts/s/ γ)		(counts/s/ γ)		(counts/s/ γ)		
16384 ch	16384 ch	Diff. (%)	16384 ch	Diff. (%)	8192 ch	Diff. (%)	4096 ch	Diff. (%)
1.288E-2	1.289E-2	-0.15	1.288E-2	-0.01	1.292E-2	-0.3	1.305E-2	-1.3

Moreover, the effect of the source distribution on *in vivo* lung counting efficiency was investigated. The simulations carried out with the 24 models of the developed female library only considered uniform distribution of the activity in the lungs. However, it is legitimate to imagine inhomogeneous activity distribution in different lung compartments. Therefore, new simulations were done to alter the activity distribution within the lungs. To do this, the ICRP AF-RCP reference female was used since in this model the lungs are divided into four different compounds: lung left tissue, lung left blood, lung right tissue and lung right blood. With this phantom, two sets of simulations were done. At first, the source was distributed in the lungs following the volumetric proportion of each of the four compounds: 2.4% (lung left tissue), 42.6% (lung left blood), 1.7% (lung right tissue) and 53.3% (lung right blood). Next, a uniform distribution of the activity between the four compounds of the lungs was operated to compare the counting efficiency values to the first results. Figure 3.19 plots the MC simulation results and proves that significant differences on counting efficiencies (up to 40% at the lowest energy) can be obtained when considering an even slightly different activity distribution. This gives an order of magnitude on the uncertainty due to errors on the source distribution.

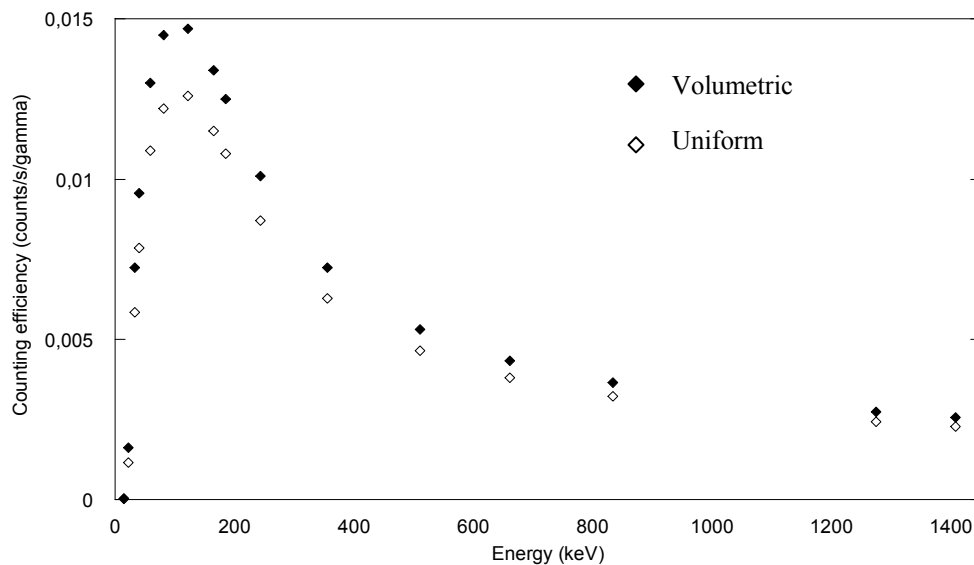


Figure 3.19. Counting efficiency (counts/s/gamma) variation with energy (keV) with the source distributed in the lung compounds (tissue/blood): (i) following the volumetric proportion of each compound (black diamonds), (ii) uniformly in the four compounds (white diamonds).

V.2. Alternative positioning of the detectors

When conducting MC simulations with the developed library of female phantoms, detectors were positioned facing the lungs and brought as close as possible to the skin while avoiding any collisions with the breast. For this reason, a tilt along the head-to-foot axis of 35° was operated on the four detectors as these were grouped in pairs (left and right). The 35° tilt was privileged, when compared to the distance to the skin, in order to guarantee the reproducibility of the detectors' positioning. Maintaining the same positioning from one simulation to another has also the advantage of eliminating the effect of detectors' positioning on the count and limiting it to the morphological variations between the phantoms.

However this positioning remains far from being similar to that operated by the AREVA NC medical department team responsible of *in vivo* monitoring. Indeed, when a female subject is monitored at the AREVA NC *in vivo* installations, the positioning is adapted to the female morphology and size and each detector is positioned alone to optimize its coverage of the lungs. Such personalized positioning surely gives better counting efficiency values than the conducted simulations but remains of limited interest should the morphological variations be studied.

The positioning operated during simulations remains however, faithful to the measurements' typical setup in such a matter. Indeed, the Livermore calibration phantom is composed of tissue equivalent plastic materials. However, the back of the phantom does not contain essential elements like the spine, the ribs and the shoulder blades. Therefore, the detectors should be placed on the frontal side and the closest to the chest. Nevertheless, for the female subjects, given that no physical calibration phantom exists, a numerical calibration was suggested here to correct the typical calibration curves. In this case, the detectors positioning in the back of the phantom is not only possible but should also be worthy of testing. The operator could hence hope to improve, up to orders of magnitude, the counting efficiency for medium and high energy photons as the detectors could sensitively be brought closer to the

body while for the low energy photons the significant mass attenuation coefficient of both the spine and the shoulder blades could be very severe.

For all these considerations, simulations were conducted with the detectors in the back of the ICRP AF-RCP phantom and also on its sides. Figure 3.20 presents the MC simulation results for the same source and compares the efficiency values obtained at different positions of the detectors. From this plot, it is clear that better counting efficiency values can be obtained, particularly at medium and high energies, when the positioning of the detectors is optimized. This result should also be taken into account when correcting the typical calibration coefficients obtained with Livermore male phantom and adapt it to the morphology of the monitored female worker. From this result, we suggest to investigate the possibility of developing not only a female torso phantom, but also to adjust the back of the Livermore phantom to the true tissue composition and densities and establish a new measurement protocol where the detectors would be set at the back of the subject to improve the counts.

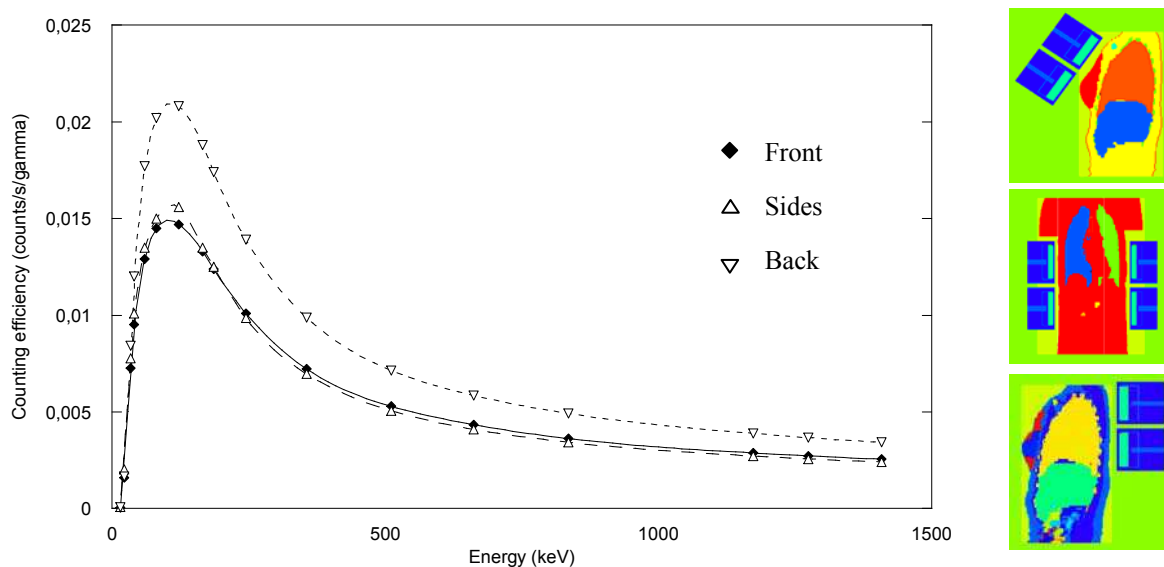


Figure 3.20. Counting efficiency (counts/s/gamma) variation with energy (keV) with the detectors positioned: (i) facing the breasts (black diamonds), (ii) at the sides (white triangles), (iii) in the back of the phantom (inverted triangles).

V.3. Improving the morphological equation

The developed equation has proven to give rapid and reliable estimate of counting efficiency variation with female morphology. The parameters of this equation were linked to breast weight and lung volume; these being the main morphological differences between the female phantoms of the developed library.

However, the calculation of the morphological parameters (c_1 and c_2) was done based on MC simulation results. Therefore, it would be of greater interest to consolidate the observed correlations with breast weight and lung volume based on measured data should these latter become available.

Moreover, the developed equation can be improved by adding a parameter to represent the effect of the source-detector distance. Indeed, as the radiation flux decreases inversely with the square of the distance (Podgorsak 2003), the detectors should be brought as close as

possible to the skin. However, to prevent any collisions with the breasts and to guarantee the reproducibility of the positioning and limit the differences between two simulations to female morphology only, this condition was not guaranteed in this study (cf. Section I.1.3). Furthermore, when conducting measurements with the Livermore phantom and different chest plates, this distance was also modified as it was the case for the simulations by Hegenbart et al. (2008). As a consequence, a new parameter could be added to represent the inverse-square law and further improve the efficiency of the equation when reproducing the morphology-induced variations of counting efficiency.

Chapter 4

Accelerating MC simulations using Variance Reduction techniques and geometry simplification operations

Optimizing the numerical calibration requires, in addition to realistic and personalized phantoms, rapid and reliable MC calculations. Hence, this chapter deals with accelerating MC simulations by using variance reduction techniques, by simplifying the phantom and by automating the MCNPX output file treatment.

This chapter is divided into 6 sections the first introducing the problem statement and objectives. The second section gives an overview of the Pulse Height Tally (PHT) and the available Variance Reduction (VR) methods for such a tally. In the third section, the used Variance reduction methods are presented with an overview of their functioning and the results of their application. The fourth section focuses on the geometry simplification operations to accelerate the simulations while in the fifth section, the MC output file treatment is automated through the development of a shell based script. Finally, a general conclusion summarizes the results and discusses the implementation of the retained methods for routine simulations of *in vivo* measurements.

I. In vivo simulation: problem statement, methods and objectives

The MC simulations have proven to be very efficient in reproducing *in vivo* measurements and realizing numerical calibration. However, simulations are time consuming depending on the complexity of the input file, particularly the phantom (morphology, tissue composition and density, size, etc.), the source (activity, energy, etc.) and the nature and number of the requested outputs (tally type, tally cell, etc.). Thus, calculations of several hours, days or even weeks were sometimes required to obtain statistically reliable MC results. To reduce the simulation time, VR methods and geometry simplification operations were tested with the following objectives:

- to reduce the simulation time but keep acceptable statistics,
- to maintain correct counting efficiency values (with respect to reference values obtained without VR and without geometry simplifications) and
- to find the methods that are easy to use.

The methods were tested with two voxel phantoms of different complexity: the Livermore voxelized model and the torso of the ICRP reference voxelized female whose differences are:

- number of structures: 5 for the Livermore against 67 for the ICRP female torso,
- tissue composition and densities: plastic equivalent tissue/organs for the Livermore and realistic densities for the ICRP female based on the ICRP 89 recommendations (ICRP 2002),
- number of voxels: 7.7 Millions for the Livermore and 2.2 Millions for the ICRP female and
- voxel dimensions: 8 mm³ for the Livermore and 15 mm³ for the ICRP female.

II. Overview of the MCNPX Pulse Height Tally

A brief summary of the PHT (tally f8) particularities is given first to improve the understanding of each of the VR methods and its functioning with such a tally.

II.1. General functioning of a PHT

Monte Carlo codes transport particles between events (collisions for example) that are separated in space and time. PHT is the MCNPX output quantity required to simulate the energy deposit spectrum. Unlike most energy-dependant tallies that score events at the energy of the projectile particle, PHT scores the number of events that deposit different amounts of energy and is thus directly dependent on the collective effects of several particles. This difference can be identified when representing the random walk of an MCNPX particle.

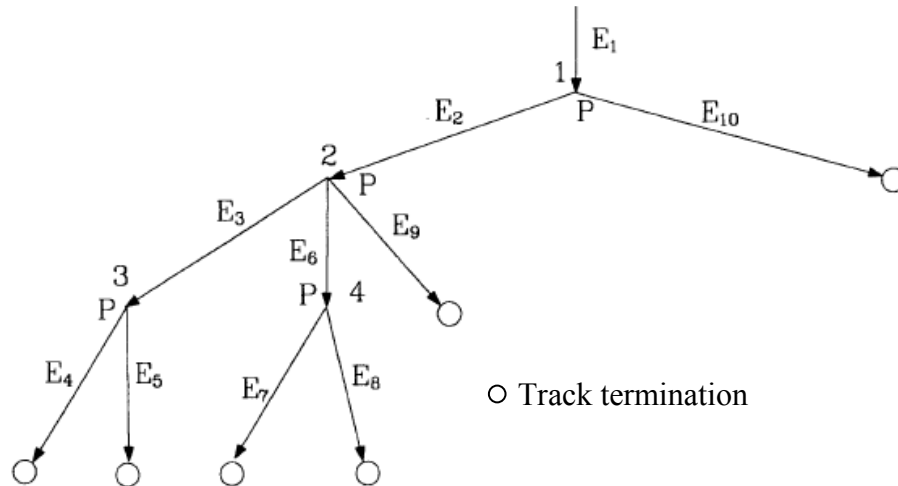


Figure 4.1. Representation of the analog random walk of an MCNPX particle (Booth 1992).

Figure 4.1 shows an analog random walk with four physical branch nodes. Each P represents a physical split of one particular physical branch node whereas each E_k is the energy the photon loses in the detector between the upper and lower nodes of the branch. For example, E_4 is the energy the left branch photon of node 3 loses in the detector between node 3 and the termination of the left branch. The current (tally F1) per bin or energy interval in this cell has two energy bins $EB_1=E_4+E_5$ and $EB_2=E_7+E_8$. On the contrary, a pulse height detector responds to the total energy lost (per source particle) in the detector by all photons in a history. And thus, the PHT has only one energy bin in this branch $EB=E_4+E_5+E_7+E_8$. In general, the PHT would account for the total energy lost by the incident particle that is $EB=E_1+\dots+E_{10}$. Thus, the pulse height tally cannot be made until the physical tree is complete. As a consequence, the simulation time of such a tally is sensitively higher than those tallies that consider individual particles.

II.2. Variance Reduction and PHT

As the PHT is sensitively different from typical MCNPX tallies, only few VR methods are compatible with such a tally. Therefore, this section presents first the aim of VR and the functioning of a PHT with VR. Next, the VR techniques available for PHT are summarized and examples of previous use of VR with PHT are given.

II.2.1. Variance Reduction aim

Generally, when conducting a MC simulation, the operator is interested in obtaining the smallest statistical relative error (R) in a given time (T). As shown in Equation 1.10 (cf. Chapter 1 Section III.1.3), in order to decrease R it is desirable to decrease the standard

deviation of the mean (S) and thus increase the number of histories (N). However, increasing N results in a longer simulation time. VR techniques were thus used to reduce the number of photons necessary to achieve the desired accuracy for a MC calculation. These methods increase the probability of each particle to contribute to the result and minimize thus the spread in the scores (Booth 1992). In consequence, the code spends more time simulating and following particles participating in the requested tally and saves time when not following those that are slightly or even not participating to the tally. Thus, either the result is obtained faster or the associated statistical relative error is reduced for an identical simulation time.

II.2.2. Functioning of a PHT with VR

Introducing VR methods that modify the sampling, as the splitting technique for example, makes the PHT tree even more difficult to handle as shown in Figure 4.2. Indeed, while physical splitting (P) generates two particles simultaneously, VR splitting (V) should be considered as an alternative and should take into account all the possible combinations of splitting. As a consequence, handling splitting in case of a PHT requires putting into bank the lost energy and the weight of each particle in order to reconstruct all the possible histories. Moreover, in standard non f8 MCNPX tallies, the tracks carry weights that multiply the tally when the track is tallied. For the f8 tally, it is the tree that tallies so that the weight is assigned to the tree. The tree, however, has a collective weight associated with all physical branches. If one track is terminated, whatever the reason, the branch weight is multiplied by 0. Thus, the whole tree is terminated because the tree is the product of all branch weight traced back to the source. As a consequence, some information may get lost with basic VR schemes such as track termination and the simulation results can be sensitively biased.

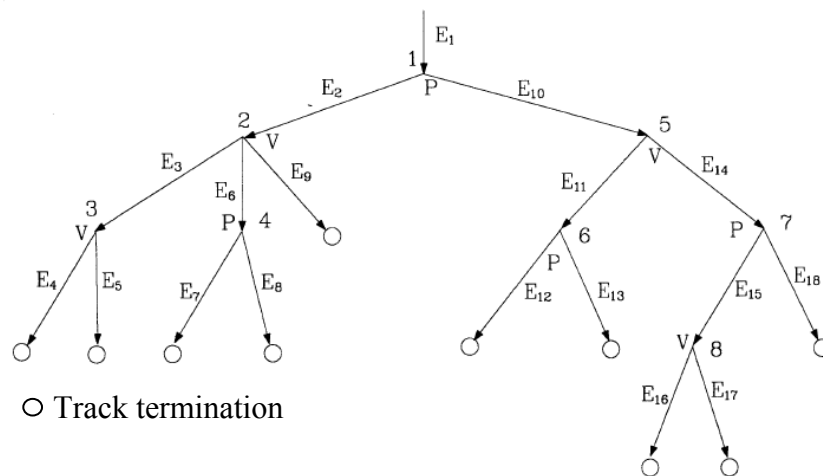


Figure 4.2. Representation of the random walk of an MCNPX particle with VR splitting (Hendricks and McKinney 2005).

II.3. The available VR methods for PHT

The PHT depends on the collection of particles and is therefore considered to be a non-Boltzmann tally. Several efforts were realized to apply VR techniques to non-Boltzmann tallies to make standard techniques, like splitting for example, compatible with such a tally (Haynor et al. 1991). The first introduced methods apply VR to the individual tracks and then analyze the effect on the collection of particles that are tallied. Three approaches for non-Boltzmann tallies were next developed to apply VR directly to the physical collections of

particles that tally. These include the deconvolution approach, the supertrack approach and the corrected single particle approach (Booth 1994).

For the particular case of PHTs, the MCNPX code developers have implemented a new recursion method based on the deconvolution approach (Booth 1992; Hendricks and McKinney 2005). Thanks to this new implementation, the entire PHT tree and all the associated information no longer need to be saved at every particle split. Moreover, with this new version, branches of the deconvolution tree can be terminated if the tree gets too large without killing the whole arborescent. Tree deconvolution remains however delicate and time consuming (Hendricks and McKinney 2005). The available VR techniques for PHT include Population Control Methods (PCM) such as geometry splitting and Russian roulette, energy splitting/roulette, weight cutoff and weight windows and Modified Sampling Methods (MSM) (Breismeister 2000) among which the exponential transform, implicit capture, forced collisions, source biasing, and neutron-induced photon production biasing.

II.4. Previous experience with VR and PHT

A previous study by Lamart (2008) has used VR techniques for two particular *in vivo* measurement situations and the MCNPX simulation of PHTs. Lamart (2008) investigated the effect of biokinetic distribution on counting efficiency and numerical calibrations. Lamart (2008) found poor efficiency values for sources situated away from the detectors. Therefore, variance reduction methods were considered to improve the simulation results. New techniques were hence developed in collaboration with J.S. Hendricks (MCNPX code developer at Los Alamos National Laboratory) to adapt VR to PHTs and the studied situations. The new methods aimed to bias the source emission direction towards a precise and well defined point (cf. Figure 4.3) or towards fictitious spheres surrounding the detectors (Lamart and Hendricks 2007). These were implemented in the local MCNPX 2.6c version of the code available at IRSN/LEDI.

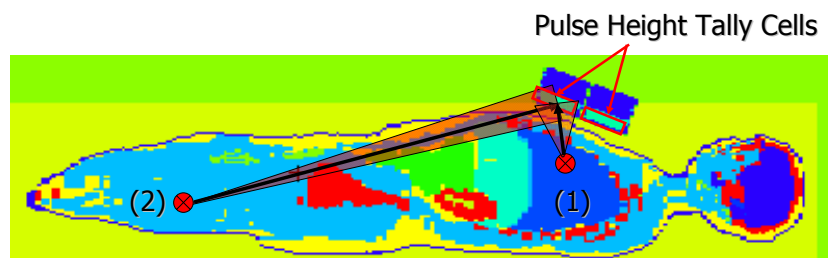


Figure 4.3. MCNPX plotter of a lung counting *in vivo* simulation with: (1) a point source located near the detectors and with small attenuation; (2) a point source located far from the detectors and suffering consequent attenuation (Lamart 2008).

The source emission biasing towards a point was used in the case of ^{241}Am distributed in lungs and for ^{60}Co in whole body. This method however did not give satisfactory results since the angle of the emission cone (defined by the emission direction basing vector) is fixed. This was explained by Lamart as follows. For point sources close to detectors, too many particles were biased towards the center of the detector and therefore do not hit the peripheral regions of the crystal. Whereas, for point sources located far from the detectors, this emission direction biasing method did not generate an efficient number of photons going in the right direction and with enough energy to get to the detectors.

Lamart next applied the source emission biasing towards fictitious spheres for the same contamination scenarios introduced above. Using this new technique, the total simulation time was reduced by a factor of about 6 in the case of a pulmonary measurement. Furthermore, the total simulation time factor in a whole body contamination varied from 12 to as high as 170 when using the biasing towards fictitious spheres (Lamart 2008). This time reduction factor of 170 was obtained to the detriment of the realism of the spectrum, and particularly the Compton and scattered compounds cf. Figure 4.4. When associated to weight windows, the time reduction factor was about 10 but the simulated spectrum showed a better agreement when compared to the reference analogue situation (without VR).

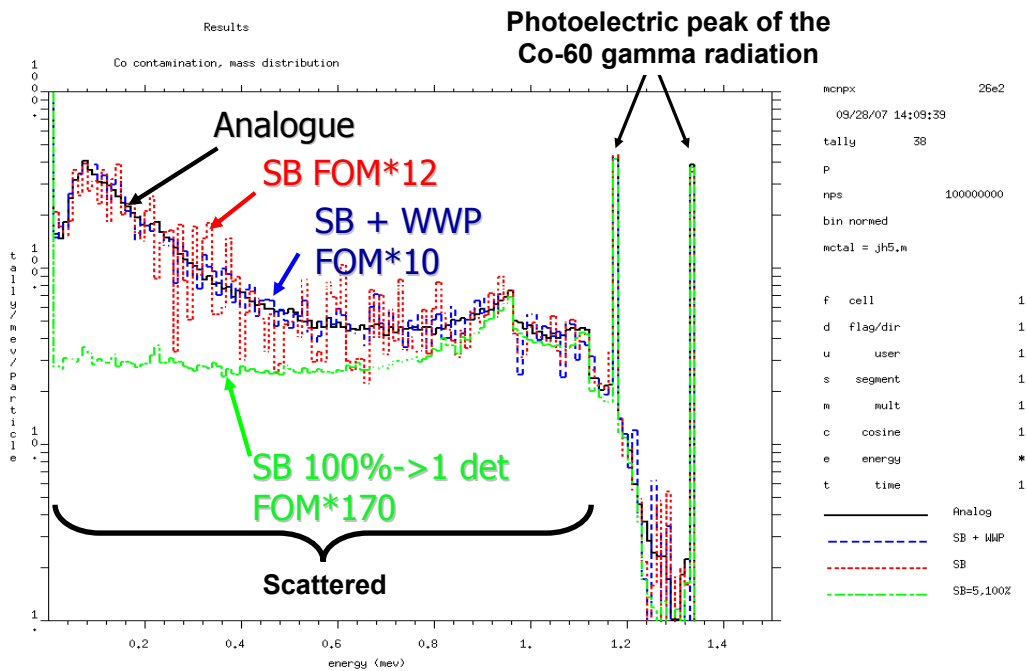


Figure 4.4 MCNPX plot of the energy spectrum obtained for different VR methods; (1) in black: analogue calculation; (2) in green: biasing at 100% probability towards a fictitious sphere around one detector; (3) in red: biasing towards a fictitious sphere around the four detectors; (4) in blue: biasing towards a fictitious sphere around the four detectors with weight windows (Lamart 2008).

III. Accelerating MC simulations with Variance Reduction techniques

The study by Lamart and Hendricks (2007) has proven that VR can improve the simulation of *in vivo* measurements. However, the introduced VR methods are of limited interest since they are only available in the MCNPX version modified by Hendricks.

Thus, classic VR methods available in almost all versions of the MCNPX code were considered here. The following paragraphs present the problem statement and introduce the available methods and their implementation for the particular case of *in vivo* measurements.

III.1. Problem identification

To identify the problem statement, a plot of counting efficiency variation with energy is studied. From Figure 4.5, it is clear that efficiency values are highly dependent on the source energy. Indeed, as detectors' counting efficiency represents the number of collected photons normalized to the total number of emitted photons, the energy and direction at which these are emitted directly affect the counting efficiency values. Poor efficiencies are obtained for low energy photons that suffer from high tissue attenuations. Meanwhile, satisfactory efficiency values are obtained for photons of medium energy whereas very high energy photons are too penetrative to be collected in the detectors and the efficiency drops again. The efficiency distribution with photon energy can thus be divided into 3 regions:

- Region #1: photons of less than 30 keV,
- Region #2: photons between 30 keV and 350 keV,
- Region #3: photons of more than 350 keV.

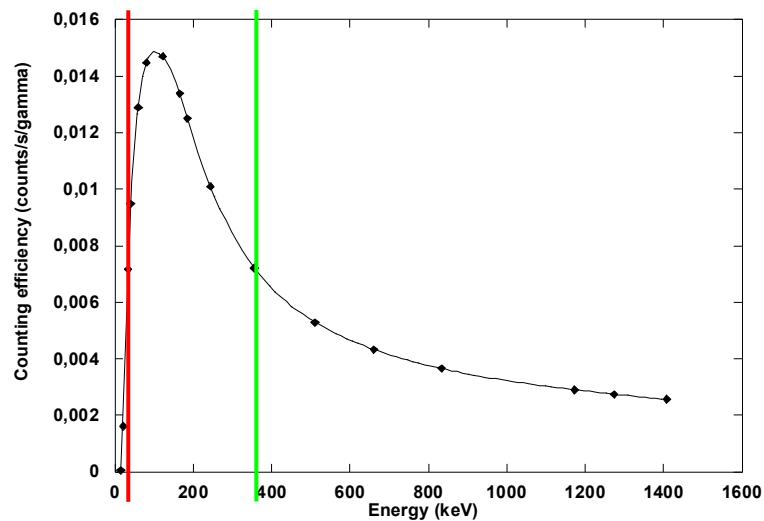


Figure 4.5. Variation of simulated counting efficiency (counts/gamma) with energy (keV) for the ICRP reference female.

Monte Carlo VR techniques were implemented to improve the results in each of the identified energy regions taking into account the physical reasons behind the low efficiency values.

III.2. Population control VR methods

The PCM are based on the use of particle splitting and Russian roulette to control the number of samples taken in various regions of the phase space. In important regions, many samples of low weight are tracked, while in unimportant regions few samples of high weight are tracked. A weight adjustment is made to ensure that the problem solution remains unbiased.

In this study, geometry splitting/roulette and weight windows were considered to improve the results and accelerate the simulations. For each of these methods, a general overview of their use and implementation is given for both the Livermore and the ICRP female torso phantoms.

III.2.1. IMP card: geometry splitting and Russian roulette

The cell importance method is commonly used to split the space into “interesting” and “less interesting” regions by the use of splitting and Russian roulette functions.

- **Generalities and functioning**

When a particle goes to a region of space that brings a sensitive contribution to the tally result, it is preferable not to lose this particle by absorption or by deviation after scattering. To decrease the probability of losing such a particle, it is possible to follow m particles instead of only one starting from a particular position in space. Thus, the probability of such particles to contribute to the tally is greater. In this case, the contribution of each daughter particle is divided by m to take into account the multiplying of the number of primary particles. This procedure is called splitting (cf. Figure 4.6).

Whereas, when a particle goes to a region of the space that brings very poor contribution to the tally result, it is preferable not to waste time transporting such a particle but to favor those going in the correct direction. Thus, a certain number of particles are eliminated with a probability $(1-p)$ while other particles survive with the probability p . If such particles make it to the tally region and contribute to the result, their contribution is divided by p to take into account the applied reduction of photon number (cf. Figure 4.6). This procedure is called Russian roulette (RR).

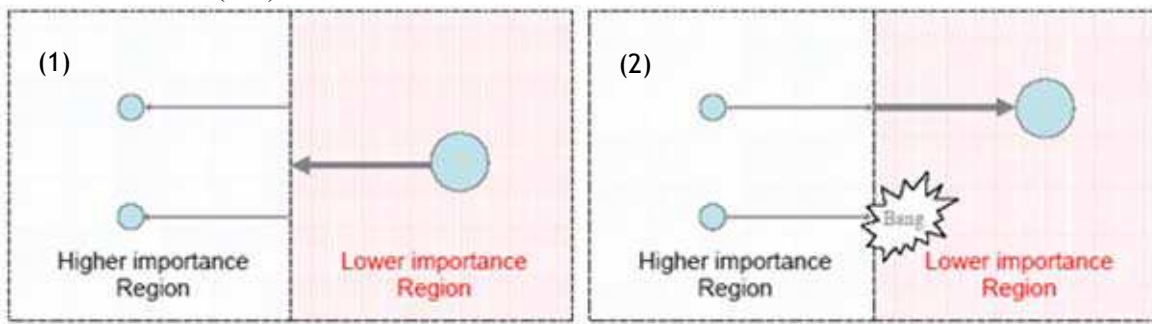


Figure 4.6. Principles of splitting (1) and Russian roulette (2) (Breismeister 2000).

In real simulations, the “interesting” and “less interesting” regions of the space are basically defined from the geometry cells. A given importance is associated to each cell and is used to propagate the particles. For example, a zero importance cell would mean that all particles entering this cell are killed. The becoming of a particle depends on the importance ratio between the entered and the exited cells. If this ratio is higher than one, i.e. a photon passes into a more “interesting” region, the primary particle is divided into as many daughter particles as the value of the ratio with the appropriate weight (original weight divided by the number of daughter particles). This conserves energy and improves the statistics in the region of greater interest. In the case where the ratio is less than 1, RR is played to fuse particles of identical energy and their weight is added. It should be noticed, however, that the ratio between two adjacent cells should be between 8 and 1/8.

- **Application to numerical calibration**

To improve the simulations of *in vivo* measurements with the cell importance card (IMP), a manual designation of the “interesting” and “less interesting” regions was operated. In these simulations, integer splitting/roulette was considered to simplify the cell importance choice. Appendix C.1 documents the list of cells present in the Livermore and ICRP female phantoms, their associated densities and corresponding materials.

For the Livermore simulations, the cell importance for the lung (source organ) was set to 1, the importance of residual tissue and bones was set to 3, the importance of chest wall plate

was set to 9 while it was set to 18 for the front dead layer of the detectors (cf. Figure 4.7). For the case of the female phantom, the same cell ratio was conserved as the breast organs replaced the extra-thoracic chest plate of the Livermore with a cell importance of 9. The cell importance parameters for all other body compounds were maintained. In a second time, different cell importance ratio were considered such as 1-3-9, 1-4-8 or even 1-4-16 to study the effect on counting efficiency estimate and on simulation time.

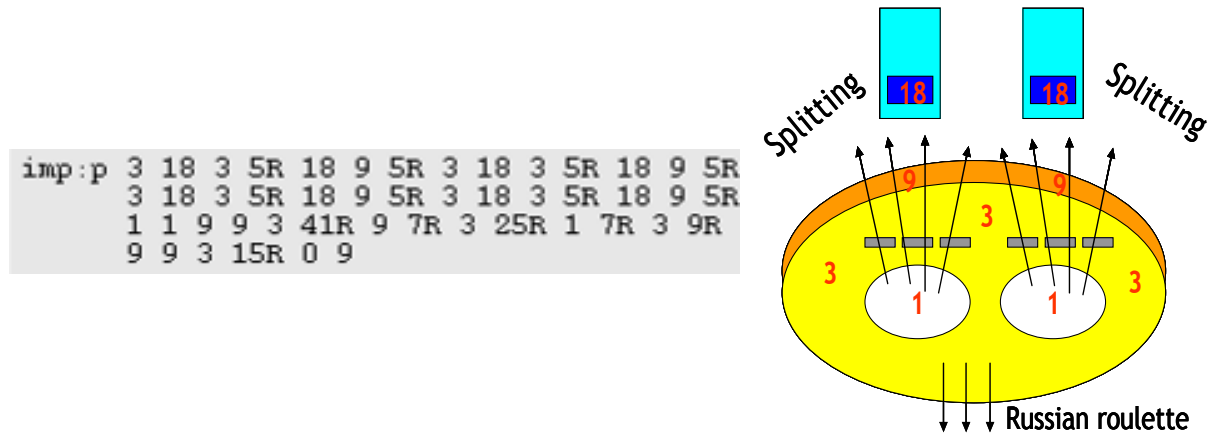


Figure 4.7. Input parameters of cell importance card (right) and schematic representation of the Livermore phantom (left).

III.2.2. WW card: weight windows to control weight fluctuations

Another method to control the number of samples is when using the Weight Window card (WW). This latter represents, up to a certain level, a more general and automatic method to use the splitting and RR functions when compared to cell importance card.

- **Generalities and functioning**

To make simulated particles equivalent to physical ones, a weight is associated to each MCNPX particle. This weight takes into account all the possible physical interactions of incident particles and materializes it to the simulated particle. For each new interaction, a new weight is calculated. The WW card controls the weight of the particles entering a given cell and helps keeping the weight dispersion within reasonable bounds throughout the problem.

An importance generator, the Weight Window Generator (WWG), is available to estimate optimal limits for a WW. Any particle having its weight beyond (respectively below) the WW bounds will suffer splitting (respectively Russian roulette) as illustrated in Figure 4.8. After splitting and RR, daughter particles' weight is automatically adjusted to guarantee the coherence of the result. The WWG requires the choice of the tally for which the VR is applied. The WWG estimates the importances of the space-energy regions of phase space specified by the user. The space-energy Weight Window Parameters (WWP) are then calculated inversely proportional to the importances. The generated WW is used for the calculations and its bounds are optimized when multiple iterations are run.

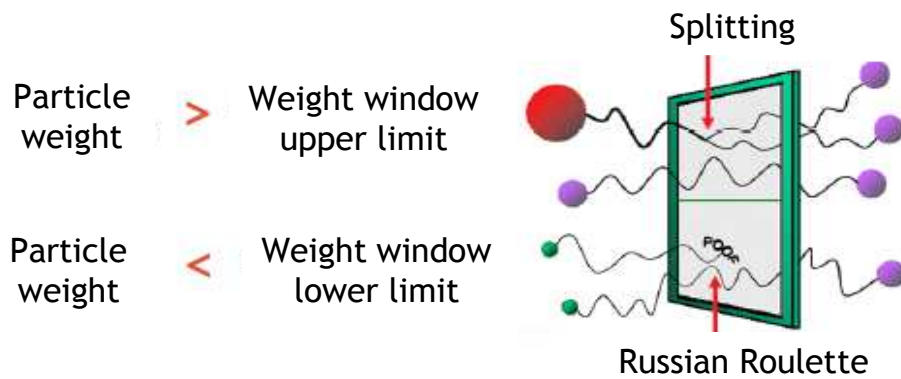


Figure 4.8. Weight window principles: particles are represented by spheres as their size is proportional to their statistical weight (Lamart 2008).

Two types of WWG are available to assess the WW bounds: cell-based or Mesh-based WWG. The cell-based generator estimates the average importance of a phase-space cell. If the cells are too large, the importance variation inside the cell will be large and the average importance will not represent the cell. Inadequate geometry specification also occurs with large importance differences between adjacent cells. If geometries are inadequately subdivided for importances, user-defined mesh-based weight windows should be used.

It should be noticed that WW do not act on the emitted particles from point sources but take effect at collisions and/or at the geometry surfaces depending on the user's choice. Finally, WW are very useful to control weight fluctuation of particles produced by other VR techniques and to prevent false convergence scenarios (cf. Section III.3.2 and Section III.3.4).

- **Application to numerical calibration**

For this particular application, Mesh-based WW were used to divide the importance regions of the phase space into rectangular or spherical mesh grids. Moreover, the WW control was activated only when the incident particle undergoes a collision and not when it crosses from one surface to another since the considered phantoms contain each more than 2 million voxel elements which would dramatically increase the simulation time. Multiple iterations of the simulations were conducted to generate the optimal weight windows.

Figure 4.9 presents a mesh-based rectangular weight window starting at (-55 -55 -55) and which subdivides the X axis to 15 slabs (2 from -55 to -17, 10 from -17 to 30 and 3 from 30 to 55) and similarly in the Y and Z axis. For this WW, the reference particle is taken at (1 -4.1 0) which is the center of the four detectors and its weight is of 1, as specified on the WWG card (last entry). The weight of all particles is thus compared to the weight of this reference point. The used WWP card indicates that the upper bound of the WW is set to 5 times the lower bound and each particle can undergo splitting or RR game only 3 times while its weight after RR would be twice the lower bound of the WW. These WWP define the optimal bounds found by Lamart and Hendricks (Lamart 2008) for the particular case of the PHT and the simulations of pulmonary *in vivo* measurements. Other WWP were also tested in this study to assess their effects on the counting efficiency value and on the simulation time. Figure 4.9 also represents the MCNPX plot of the rectangular WW.

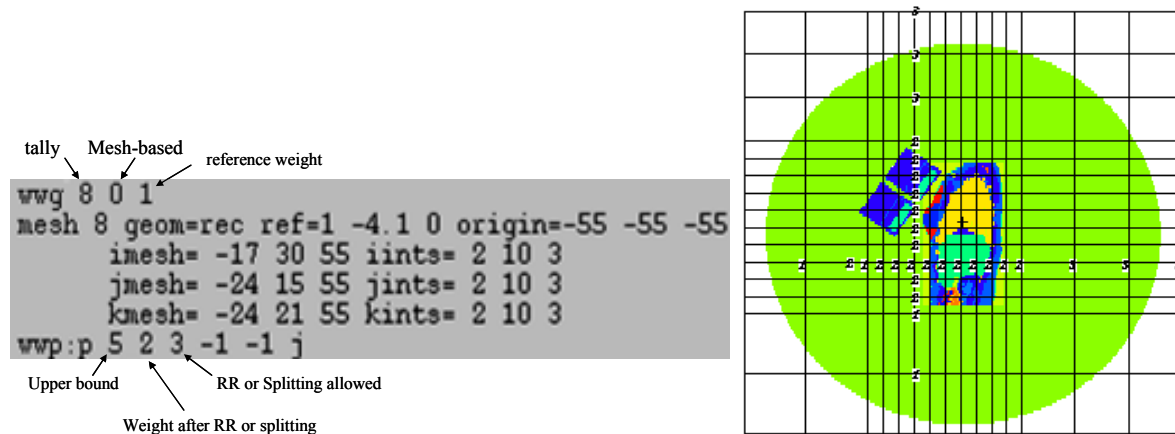


Figure 4.9. MCNPX code for a rectangular WW (left) and MCNPX plotter visualisation of the defined rectangular WW (right).

Figure 4.10 represents a snapshot of the MCNPX code used to define a mesh-based spherical WW starting at the center of the phantom (5.4775 0.295 -3.366) and which is subdivided in radius to 9 spheres (3 from 0 to 5, 4 from 5 to 20 and 2 from 20 to 55). In this case, jmesh and kmesh represents the phi and theta angles which were set at 360°. For this WW, the reference particle weight was also taken at (1 -4.1 0) and the used WWP card are identical to those of the rectangular WW. Figure 4.10 also represents the MCNPX plot of the spherical WW.

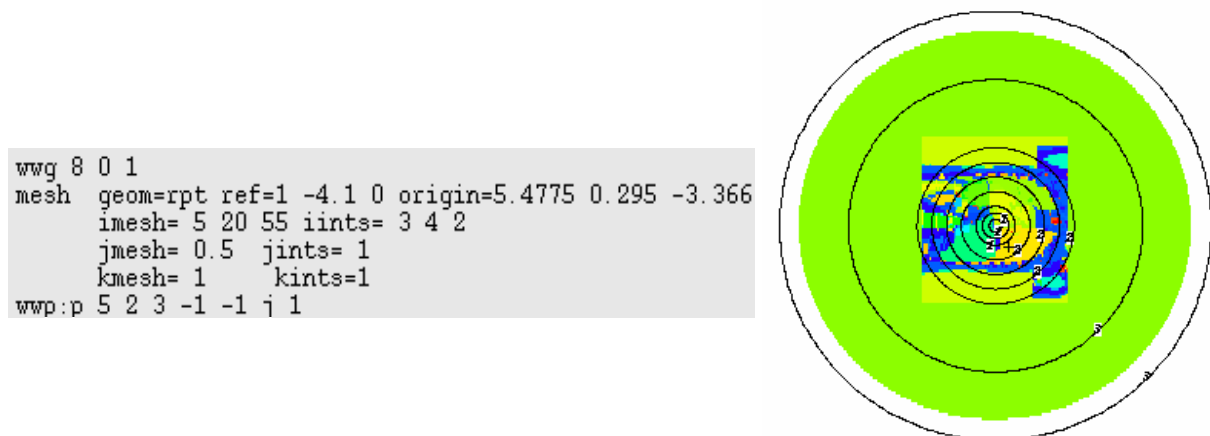


Figure 4.10. MCNPX code for a spherical WW (left) and MCNPX plotter visualisation of the defined spherical WW (right).

III.3. Modified Sampling Methods

The MSM considered in this study are the exponential transform, the forced collisions and the source biasing (both energy and direction) were considered. For each card, a general overview of their use and implementation is given for both the Livermore and ICRP female phantoms.

III.3.1. SB card: biasing the distribution of particles

Biasing the MCNPX sources is possible in any or all of the source definition parameters including the source positioning, energy, distribution, emission direction etc.

- **Generalities and functioning**

Each source parameter is defined by a Source Information (SI) card to which is associated a Source Probability (SP) function that represents its physical occurrence probability. The SB card inputs are identical to those of a SP card for an analytic source distribution.

The source biasing allows the production of more source particles in the more important regimes of each variable and automatically adjusts their weights. For example, one may start more tracks at high energies and in strategic directions in a shielding problem. To do so, a SB input card is added and associated to the source variable of interest and this new sampling frequency is applied. The corrected weight of the source particles in a particular bin is determined by the ratio of the actual frequency (defined on the SP card) divided by the new frequency (defined on the SB card). However this VR method needs to be considered with caution to ensure realistic results. Indeed, if the biased distribution is very different from the real one, the weight of the particles associated to the least emission probability is huge. If these particles come to participate to the tally results, they will have a huge contribution resulting in a false convergence situation.

Source biasing can be manually operated by specifying the new sampling frequency and also through certain built-in functions such as continuous exponential biasing.

- **Application to numerical calibration**

In this study, the SB technique was used to control the energy distribution of photon emissions. The artificial source that was originally used emitted an equal number of photons for the 17 simulated energies. Thus, for each energy, the number of photons was equal to the total NPS ($1E09$) divided by the number of photons (17) that is about $5.9E07$ photons. However, photons of region #1 have sensitively different counting efficiency values than those of region #2 and #3 (cf. Figure 4.5). As a consequence, the number of photons emitted in each region should not be identical. Moreover, the energy-dependant mass attenuation coefficient is sensitively higher at the lowest energies when compared to medium or high energy photons. Thus, the SB was introduced to send more photons at the lowest energies and consequently increase the probability of collecting such particles.

Different energy-dependant SB parameters were tested to reduce the number of photons of regions #2 and #3 and conserve the number in region #1 and particularly at 15 keV or even increase these latter. SB was first chosen considering the inverse variation of counting efficiency as a function of photon energy (cf. Figure 4.11). Next, the energy-dependent mass attenuation coefficient was considered for the choice of SB (cf. Figure 4.11). Figure 4.12 represents a snapshot of the MCNPX code used for each of the two retained SB combinations. In the first case, 29% (15/51) of the total number of starting particles were initiated at 15 keV. For the photons starting at 22 keV, 1.17 MeV, 1.27 MeV and 1.40 MeV the proportion was set to 7.3% while it was equal to 3.4% at all intermediate energies (between 30 and 885 keV). This situation is directly derived from the counting efficiency plot in Figure 4.5 and Figure 4.11 as efficiency drops both at the lowest and highest energies. In this case, the NPS was reduced to $2E08$, a value that guarantees a number of 15 keV photons identical to the original situation (29% of $2E08$ is equal to $5.9E07$). In the second SB combination, about 40% of the total NPS were associated with the 15 keV photons while the 20 keV photons' proportion was of 10% (SB 15/37.5 at 15 keV). In this case, the NPS was reduced from $1E9$ to $14.7E7$

particles. This SB setting was particularly tested with the forced collision card which increases the interactions probabilities in a given cell (here the detectors).

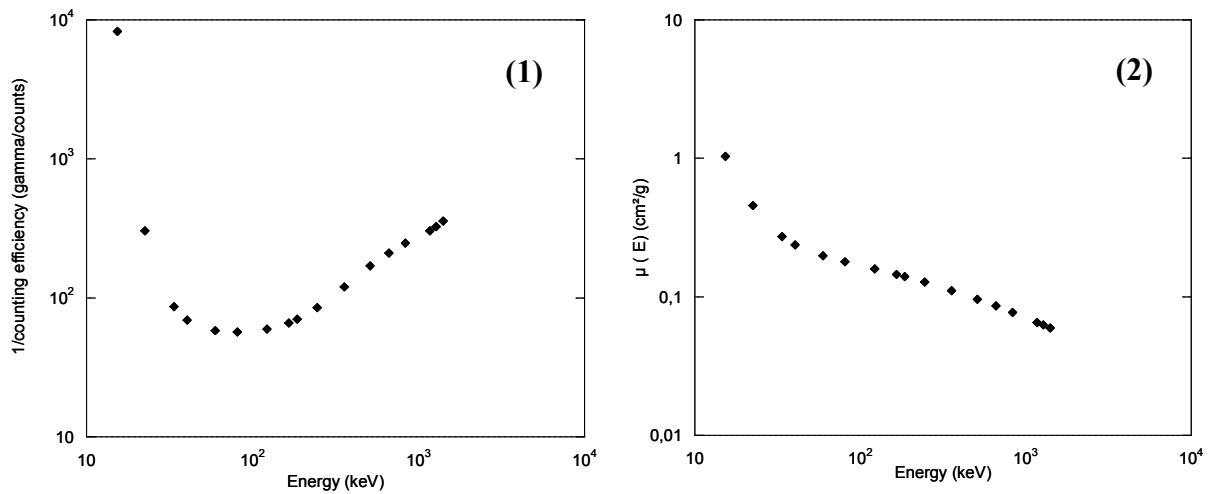


Figure 4.11. Comparison of the variation with photon energy of: (1) the inverse of counting efficiency and of (2) the germanium energy-dependant mass attenuation coefficient.

SI101	SP101	SB101	SI101	SP101	SB101
1	d	d	1	d	d
0.0153100	1	15	0.0153100	1	15
0.0221600	1	3.75	0.0221600	1	3.75
0.0334400	1	1.75	0.0334400	1	1.25
0.0401200	1	1.75	0.0401200	1	1.25
0.0595400	1	1.75	0.0595400	1	1.25
0.0810000	1	1.75	0.0810000	1	1.25
0.1220600	1	1.75	0.1220600	1	1.25
0.1658600	1	1.75	0.1658600	1	1.25
0.1857200	1	1.75	0.1857200	1	1.25
0.2447000	1	1.75	0.2447000	1	1.25
0.3560100	1	1.75	0.3560100	1	1.25
0.5110000	1	1.75	0.5110000	1	1.25
0.6616600	1	1.75	0.6616600	1	1.25
0.8348400	1	1.75	0.8348400	1	1.25
1.1732300	1	3.75	1.1732300	1	1.25
1.2745400	1	3.75	1.2745400	1	1.25
1.4080100	1	3.75	1.4080100	1	1.25

Figure 4.12. Two examples of the Source Biasing cards used to favor low energy photon emissions. In the first case (left), 15/51 photons start at 15 keV while in the second case (right) this proportion is equal to 15/37.5.

III.3.2. VEC card: biasing the emission direction

Since the emission direction is also one of the source definition entries, it can be biased with the SB card.

- **Generalities and functioning**

To bias the source emission direction, SB must be associated to a vector defining the emission direction to be favored. The user can bias particles in any arbitrary direction or combination of directions. The sampling can also be done from a user-defined density function or from available code-defined functions.

User-defined cone directional biasing can be invoked by specifying cone cosines on the Source Information card (SI), the true distribution on the Source Probability card (SP), and the user-defined biasing probabilities on the SB card. The cone vector is specified on the source definition card with the Vec card. Results remain coherent since the weight is

corrected with the ratio of SP to SB. Nevertheless, it should be noticed that for a small cone angulation and a high probability for particles being within the cone, the few source particles generated outside the cone will have a very high weight that can severely bias the tally. Thus, when using this card, one should pay careful attention to the weight fluctuations as they can cause false convergence.

Code-defined continuous exponential biasing can be invoked by specifying a negative prescription number (-31) on the first SB entry, which represents the type of biasing required, followed by an optional user-specified parameter (K). This latter defines the ratio of the weight of tracks starting in the biasing direction to the weight of tracks starting in the opposite direction. Thus, the direction of the source emissions is sampled from an exponential probability density function with a ratio of e^{-2K} (Breismeister 2000, Chapter 2 page 147).

In general, it is recommended to use continuous biasing because, in fixed cone biasing, the discontinuities of source track weight at the cone boundaries can cause false convergence. However, cone parameters, i.e. cone size and fraction of particles starting in the cone, can be optimized so that this technique would outperform continuous biasing. Unfortunately, the optimizing itself is time consuming (both human and computer).

- **Application to numerical calibration**

Since all particles going towards the back of the phantom have a very low, and even insignificant, probability to contribute to the counts, a cone directional biasing towards the detectors was first applied. For this work, particles going in the negative x plan direction were severely reduced to a probability of only 1E-6 (with a weight of 1E6) while for those going in the opposite direction, the probability was set to 1 (cf. Figure 4.13). Stronger directional biasing was also tested by using 80°, 60° and 40° cones which were directed towards the center of the four detectors. Figure 4.13 also represents the MCNPX plotter of the particles' tracks for a 180° cone directional biasing.

```
sdef x=d1 y=d2 z=d3 cell=d4 erg=fcell=d5 wgt=17 eff=1e-8
      vect=0 -1 0 dir=d7
SI1 -15 -14.8225
SP1 0 1
SI2 -10 -9.8225
SP2 0 1
SI3 -22 -21.516
SP3 0 1
SI7 -1 0 1
SP7 0 1 1
SB7 0 1e-6 1
```

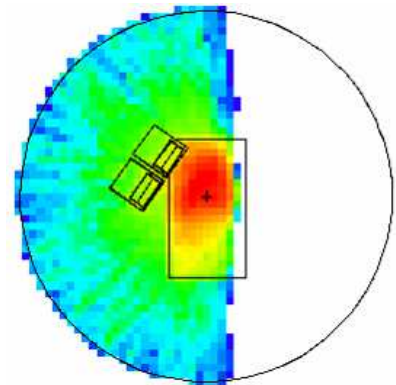


Figure 4.13. MCNPX command of the source Vec card for direction emission biasing (left) and visualization of the particles tracks with a 180° cone directional biasing (right).

Continuous exponential emission biasing was also tested by specifying a prescription number value of -31 on the first SB entry (Figure 4.14). As recommended by the MCNPX code developers, a K value equal to 1 was used in these simulations (Briesmeister 2000, Chapter 2 page 147). This value means that half the tracks start in a cone of 64° opening about the axis, and the weight of tracks at 64° is 0.762 times the unbiased weight of source particles. Figure 4.14 shows the particles' tracks for the continuous exponential directional biasing.

```
sdef x=d1 y=d2 z=d3 cell=d4 erg=fcell=d5 wgt=1 eff=1e-9
      vec=0 -1 0 dir=d7
SI1 -15 -14.8225
SP1 0 1
SI2 -10 -9.8225
SP2 0 1
SI3 -22 -21.516
SP3 0 1
SI7 -1 -0.17365 0 0.17365 1
SP7 -31 0
SB7 -31 1
```

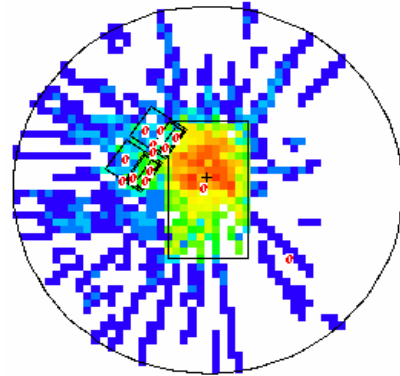


Figure 4.14. MCNPX command of the source Vec card for direction emission biasing (left) and visualization of the particles tracks with the continuous exponential biasing (right).

III.3.3. FCL card: forcing the collisions

The FC method is one of the MSM variance reduction schemes that increase the sampling of collisions in a specified cell. It was introduced in this work to improve the high energy photon interactions in the detectors and improve their statistics.

- **Generalities and functioning**

When a specified particle enters a region defined as the FC region, the incident particle splits into uncollided and collided particles. The uncollided particle passes through the current cell without collision whereas the collided particle is forced to collide within the specified cell.

To use the FCL card, the operator should define the Forced Collision Control (FCC) parameter which represents the collision probability in each MCNPX cell. The value of this parameter ranges from -1 to 1 where a null value means that no forced collision will occur. A negative value of the FCC parameter means that FCL is played for particles entering a given cell while a positive value indicates that detector contribution are made after the particles are split into collided and uncollided. It is recommended to use FCC values of 1 or -1 to keep the number of collided histories from getting too large unless a number of forced collision cells are adjacent to each other (Briesmeister 2000, Chapter 3 page 39).

- **Application to numerical calibration**

The use of such a card required the determination of the total number of cells in the problem (198 for the ICRP female torso against 74 for the Livermore) and the ones in which to force the collision (those of the detectors: 2, 17, 32 and 47). The FCL parameter was set to -1, which is equivalent to a 100% collision probability, for particles entering the detectors' cells, while default collision probabilities ("j" entry in the MCNPX code) were maintained in all other cells. Figure 4.15 shows the FCL card used for the ICRP female torso.

Moreover, to further study the impact of the FCC parameter on the number of total forced collisions, two values of the FCL parameters were also chosen and simulations were conducted for an FCC value of -0.8 and of -0.6.

```
FCL:p j -1 14j -1 14j -1 14j -1 151j
```

Figure 4.15. The FCL input parameters for the ICRP female phantom.

III.3.4. EXT card: increasing the mean free path

Low energy photons suffer high attenuation in body tissues and poorly contribute to the tally result. In order to increase their probability to reach the detectors, their penetration power can be increased thanks to the exponential transform (EXT) VR method.

- **Generalities and functioning**

The EXT allows particles to move in a preferred direction by artificially reducing the macroscopic cross section in the preferred direction and increasing the cross section in the opposite direction. The preferred direction can be specified on a VECT card along with the cosine of the angle between the preferred direction and the particle's direction.

To transport particles over long distances, the distance between collisions in a preferred direction is artificially increased and the weight is correspondingly artificially decreased. Because large weight fluctuations often result from this card, it is highly recommended to use the weight window with the exponential transform. The EXT card reduces variance by reducing the number of collisions.

EXT samples the distance to collision from a non-analog probability density function. Although many promising results are claimed for the exponential transform, one should remember that these results are usually obtained for one-dimensional geometries and quite often for energy-independent problems (Briesmeister 2000, Chapter 2 page 141). The use of EXT card requires the definition of the cells in which it should be applied, the length stretching parameter and the length stretching vector.

- **Application to numerical calibration**

The EXT card was used to help the photons pass through the body organs and compounds, mainly the bone structures, by increasing their mean free path. The rectangular weight windows were also used to control the weight fluctuations of particles generated by EXT.

To apply the EXT card, the cells in which the mean free path should be biased are defined. At first, the cells representing the bone structures available in both phantoms were selected alone (cf. Figure 4.16). In a next step, however, all torso organs were chosen as EXT cells and the mean free path was stretched to favor the penetration of the 15 keV photons. Finally, the front dead layer of the four detectors was also taken as an EXT cell since it was believed to prevent the 15 keV photons from reaching the detectors (cf. Figure 4.17).

The path length vector was chosen first to point out the center of the four detectors. In a second step, the path length stretching vector was shifted to the center of the upper pair of detectors as these were closer to the skin and suffer less attenuation by breasts (case of female phantom simulations).

Finally, the path length stretching parameter was studied. It was first set to 0.9 for both the Livermore and the female simulations as recommended by the MCNPX manual (Briesmeister 2000, Chapter 2 page 143). In a next step, the path stretching parameter was set to 0.6 and then to 0.3 to study its influence on the simulation result.

```
EXT:p 0 65R 0.9V2 0.9V2 0 0 0.9V2 0.9V2 0 0
Vect V2 27.8 17 29
```

Figure 4.16. EXT input parameters for the Livermore phantom when applied to the chest plate only.

```
EXT:p 0 7R 0.9V2 0 13R 0.9V2 0 13R 0.9V2 0 13R 0.9V2
      0 7R 0.9V2 9R 0 0
Vect V2 27.8 17 29
```

Figure 4.17. EXT input parameters for the Livermore phantom when applied to all internal organs and to the front dead layers of the used detectors.

III.4. Results of the VR methods

The MCNPX input files generated by OEDIPE were manually modified to include the different VR methods. The reference simulated efficiencies are given in Appendix C.2 for both the Livermore voxelized phantom and the ICRP female model. The simulation time for the Livermore phantom was of 10087 min while it was of 9141 min for the torso of the ICRP female. The statistical relative error was minimized at best while simulating $1E09$ particles.

To review the effect of each VR method, the simulation time, the counting efficiency values at the considered energy range and the associated uncertainties are assessed and compared to the reference values obtained without any VR.

III.4.1. IMP card effect

The first VR method that was used is the PCM cell importance card in which the user divides phase space into “interesting” and “less interesting” regions. For particles going towards the detectors, the cell importance ratio was increased and the number of particles also increased with the Splitting function. Therefore the total number of starting particles was reduced from $1E09$ to $1E08$ similarly to the IMP ratio (about 9 for all particles).

The MC results show that the simulation time was divided by 3 for both the Livermore voxelized model (4117 min) and the torso of the ICRP female (3075 min) when IMP was added. This time reduction factor is however disappointing since the total NPS was reduced by 10. Moreover, the simulation results indicate that using such a card can be more delicate when the number of cells increases. Indeed, the relative error in counting efficiency is much higher when comparing the Livermore model (74 cells, error about -1.6%) to the female phantom (198 cells, error about -12.2%) (cf. Appendix C.3). More adequate cell importance assigning can be found but remain, however, strictly based on essay-error tests. Indeed, the various combinations of cell importance ratios have shown that the difference to the reference efficiency values can drop from -12% to as low as -2.23% in the case of the female phantom when the importance is set to 1 for the lungs, 4 for the thoracic organs and 8 for the breasts and the front dead layer of the detectors. In this case, the simulation time was about 2340 min.

As a conclusion, one can say that the cell importance modification gave satisfying results as the simulation time was reduced by a factor of 3 with acceptable counting efficiency values. However, cell importance factors are totally operator dependent and the efficiency of such a card can be sensitively limited when the number of cells increases (case of the ICRP female).

III.4.2. WW card effect

In this study, Mesh-based WW were used to control automatically the number of samplings and to reduce the weight fluctuations of particles undergoing collisions.

First, rectangular mesh-based WW defined in Figure 4.10 were used. The obtained counting efficiency values were within 3% to the reference values at all energy range and both phantoms (cf. Appendix C.4). Meanwhile, the simulation time was increased by the use of rectangular WW for both phantoms. Next, spherical mesh-based WW defined in Figure 4.11 were used. For these WW, the counting efficiency values were within 1.8% to the reference values at all energy range and both phantoms (cf. Appendix C.4). However, the simulation time was slightly increased with spherical WW when compared to rectangular mesh-based WW. The difference in the simulation time is presumably due to the fact that the rectangular mesh tally was far more resolved than the spherical one. Hence, better WW were generated with the rectangular mesh tally and therefore MC simulations converge faster. Finally, it should be noticed that identical counting efficiency values were obtained using spherical or rectangular mesh-based WW once the multiple iterations had converged to the optimal WW.

Next, the effect on both the simulation time and the efficiency values of the parameters defining the WW bounds was investigated. For these simulations, the total number of starting particles (NPS) was set to $7.35E07$ photons to be sampled uniformly at the 17 energies defined on the source card. Table 4.1 gives the counting efficiency values at 15 keV and simulation time for the Livermore model and several WWP. From this table, it is clear that both counting efficiency and simulation time are highly dependent on the WWP. On the one hand, the best agreement on counting efficiency values was obtained with the weight window parameters recommended by Lamart (2008) since the error was about 0.4% for WW upper bound set to 5 and 1.5% when it was set to 3 while it was about 3% for an upper bound of 7. On the other hand, the smallest simulation time was obtained with the upper bound set to 7 since, in this case, WW are used a lower number of time. Similar results were observed for the female phantom which further confirms the choice of the optimal WWP for such a study. In the table below, the indicated simulation time does not take into account the time required to optimize the WW through multiple iterations and using an f6 tally type.

Table 4.1. Study of the impact of the WWP on the simulation time and on the counting efficiency values at 15 keV when spherical WW are used and the Livermore phantom.

WW Parameters					
5-2-3		7-2-3		3-2-3	
Count Eff. (counts/s/ γ)	Sim. time (min)	Count Eff. (counts/s/ γ)	Sim. time (min)	Count Eff. (counts/s/ γ)	Sim. time (min)
6.05E-05	2701	6.21E-05	1206	6.12E-05	4891

As a partial conclusion, it is clear that the Mesh-based WWs gave unsatisfactory results. These poor outcomes may be due to wrong or inappropriate use of the WW. Nonetheless, it appears that colleagues have obtained similar results and WW is also believed to be of limited interest for PHT. Finally, WW conflict with the main goal of this work since time consuming iterations are required to generate optimal WW from f6 tally.

III.4.3. SB card effect

Biassing the source aimed to favor low energy emissions in order to increase their number and consequently their potential in getting to the detectors and contributing to the tally.

First, the SB card was applied to mimic the inverse variation of counting efficiency as a function of energy (cf. Section 3.3.1) and to optimize the distribution of particles at emission energies. The simulation time was divided by a factor of 11 for the Livermore phantom (914 min) while it was reduced by 10.6 for the torso of the ICRP female (862 min). As for the counting efficiency values, the maximum difference when compared to the reference values obtained without VR were of -1% for the Livermore phantom (with an uncertainty of 8%) and of 8.7% for the ICRP female phantom (with an uncertainty of 13%). For higher energies, both the difference to the reference values and the uncertainties on counting efficiency did not exceed 1.5% (cf. Appendix C.5).

Next, the SB card was brought closer to the variation of the mass attenuation coefficient with energy. The resulting simulation time was reduced by a factor of about 16 for both phantoms. When compared to the reference efficiency values obtained without any VR, the Livermore voxelized phantom simulations showed an agreement within 2% when the same number of particles was simulated for the ^{238}U photons of 15 keV. For the female phantom, the maximum observed difference was about -3.5% for the same energy (cf. Appendix C.5).

Moreover, SB was used to double the number of particles of 15 keV with the second distribution of particles (SB 15/37.5 at 15 keV). In this case, the associated statistical relative error was reduced from 3% to 2% for the Livermore model and from 3.3% to 2.4% for the female phantom at that particular energy (cf. Appendix C.5). These observations confirm the efficiency of increasing the number of low-energy particles in order to improve the counting efficiency in Region #1 by using the SB card. The time reduction was again almost the same, about 5.4, regardless of the complexity of the phantom (Livermore vs. ICRP female phantom). However, the difference when compared to the reference value was higher at 15 keV for the female phantom (about 6%) which can be explained by the increase of the Compton and scattered radiation with increasing NPS. This is reflected in the efficiency value when the contribution of the Compton continuum is subtracted from the photoelectric peak (cf. Chapter 3 Section I.2.1).

As a conclusion, one can say that the SB card is easy to use for routine numerical calibrations and has a major impact on the simulation time reduction while maintaining correct counting efficiency values at the considered energy range. Indeed, the number of particles required to guarantee statistically reliable results at the lowest energies (15 keV in these simulations) can be easily and sensitively increased while reducing the total number of starting particles. Moreover, the choice of the SB artificial yields is suggested to be done taking into account the energy-dependent mass attenuation coefficient, a reliable and accessible reference value.

III.4.4. Vec card effect

Variance reduction methods were also introduced to bias the emission directions of the isotropic source distributed in the lungs in order to favor emissions towards the detectors.

First a user-defined cone directional biasing was used to favor emissions towards the detectors in a 180° angle. As the emission plane was cut in two (cf. Figure 4.13), the total number of photons was divided by 2 and a similar time gain factor was observed. The counting efficiency values remained in agreement with the reference ones (no VR) since acceptable differences (< 5%) were observed considering the uncertainty resulting from the Compton participation (cf. Appendix C.6).

Moreover, several cone directional biasing of smaller angulations (80°, 60° and 40° cone angles) were also tested to further increase the time reduction. However, these gave unsatisfactory results since the difference to the reference efficiency values at all energy range were about -20% for the 80° angulation, around -80% for the 60° angulation and as high as -160% for the 40° cone. This was presumably attributed to the huge weight (1E06) of particles going in the unfavored directions (cf. Section III.3.2). Therefore, the previously defined mesh-based rectangular WW were added to limit the weight fluctuations and test the efficiency of this method. For both phantoms, however, this method brought poor results as the error on counting efficiency remained sensitively above 10% at the considered energy range.

In a second time, the continuous exponential biasing was introduced to modify the emission directions. However, the simulation results were unacceptable as the counting efficiency values were in total disagreement with the reference values (error about -90%) for both phantoms at the considered energy range (cf. Appendix C.6). Moreover, the use of mesh-based rectangular WW to limit the weight fluctuations did not give satisfying results since the error remained as high as -80%. Therefore, the continuous exponential biasing was rejected.

As a conclusion, using the VEC card as a mean to bias the emission direction is a method easy to use and to implement in routine. Even though small angulations did not work, the fixed cone directional biasing remains efficient and reliable and is recommended to at least halve the number of starting particles and save time with a 180° cone biasing. The continuous exponential biasing was not retained as poorer results were obtained. The work done by Lamart and Hendriks (2007) has proven that emissions' directional biasing can give satisfying results when the right options are available. Fictitious spheres surrounding the detectors could therefore be used if these are implemented in the new versions of the MCNPX code.

III.4.5. FCL card effect

The FCL card was used to increase the interaction probability of high energy photons in detectors' active cells.

At first, the collision probability was set to -1 meaning that each particle entering the designed FCL region will collide. The result of using such a MSM method was a decrease in the statistical relative error of high energy photons. For example, for the photons of 1.4 MeV, the statistical relative error dropped from 0.28% (Ref) to 0.19% (FCL) for the Livermore phantom and from 0.26% (Ref) to 0.18% (FCL) for the female phantom. However, the simulation time reduction with FCL was almost null. Moreover, the maximum difference observed for high energy photons between the reference efficiencies and the new one with FCL, was about -0.4% for the Livermore phantom and the ¹⁵²Eu photons of 1.4 MeV. For the female phantom and the same gamma radiation, this difference was around 0.3% (cf. Appendix C.7).

Next, the collision probability (FCC) was changed to -0.8 and -0.6 to identify its impact on both the number of collisions in the active cells of the detectors and on the statistical relative error of high energy photons. The study of the variation in the number of forced collisions as a function of the FCC parameter showed that the total number of collisions decreases with decreasing FCC (cf. Table 4.2). Meanwhile, the statistical relative error increased with the FCC parameters' decrease (cf. Table 4.3) further confirming the obtained results.

Table 4.2. Number of collisions obtained for three different FCC values and the ICRP female torso phantom.

FCC value	-1	-0.8	-0.6
Number of collisions	3.7E+06	2.9E+06	2.2E+06

Table 4.3. Statistical relative error (%) obtained for three different FCC values and the ICRP female torso phantom.

Energy (keV)	FCC value		
	-1	-0.8	-0.6
1173.23	0.59	0.66	0.77
1274.54	0.60	0.68	0.78
1408.01	0.61	0.69	0.80

As a conclusion, one can say that the FCL method is easy to use for routine numerical calibrations in order to improve the statistics of high energy photons as the only required entry is the cell number in which to force the collision. However, this card showed poor simulation time reduction factors and remains of limited interest as the highest photon energy considered in this study was of only 1.4 MeV.

III.4.6. EXT card effect

To increase the penetration probability of the lowest energy photons, the total cross section (absorption and scattering) of the materials with the highest attenuation coefficients (bones, torso organs and front dead layers) was changed with the EXT card.

First, the path stretching vector was directed towards the geometric center of the four detectors with a path stretching factor of 0.9 and EXT was applied for bone structures only. In this case, the counting efficiencies were in good agreement with reference values at all energy range (cf. Appendix C.8) with a difference of -4% for the Livermore simulations and the 15 keV photons (-1.2% for the ICRP female torso at the same energy). Moreover, the simulation time was divided by 12.8 for the Livermore (789 min) and by 4.4 for the female phantom (1445 min). Next, EXT was applied for all thoracic organs of the phantoms (cf. Appendix C.8). In this case, the efficiency improved as the difference at 15 keV dropped to 2% for the Livermore simulations and to -0.2% for the female model. Meanwhile, the simulation time was reduced by a factor 12.4 for the Livermore phantom (815 min) and 4.3 for the female model (1473 min). Finally, EXT was applied for body organs and for the front dead layer of the detectors, in this case the efficiency did not change much and the difference to the reference value was about 1.8% at 15 keV and the Livermore phantom (cf. Appendix C.8). Meanwhile, the simulation time was reduced by a factor 12.3 for the Livermore phantom (820 min) and 4.5 for the female model (1419 min).

Next, the EXT path stretching vectors was directed towards the geometric center of the upper pair of detectors with EXT applied for all organs and the front dead layer. This was considered to be particularly interesting for the female phantoms as the upper pair of detectors suffers lesser attenuation by breasts. The counting efficiency values were within 1.2% to the reference values while the statistical relative error was slightly improved at 15 keV (cf. Appendix C.8). Meanwhile, the simulation time did not vary much with the path stretching vector (858 min for the Livermore phantom and 1480 min for the female model). Finally, the path stretching factor was changed from 0.9 to 0.6 first and then to 0.3. In this case, the parameter of interest is the simulated counting rate which represents the height of the photoelectric peak along with the associated statistical relative error. The results came in disagreement with the expected values as little effect was observed when changing the path stretching factor from 0.9 to 0.6 or even to 0.3 (cf. Appendix C.8). Moreover, the simulation time also surprisingly increased; for the female model for example, it was about 1508 min for a path stretching factor of 0.6 and 1505 min when the path stretching factor was set to 0.3.

As a conclusion, the EXT card was successfully introduced to modify the interactions' cross sections and to increase the mean free path of particles. The use of such a method brings an answer to low energy photons as it increases their probability of penetrating through body organs and getting to the detectors. However, this card was found to be difficult to use in routine and to suffer from many limits; the first being the simulation time increase due to the need of adapted WW. In addition, the leak of effect of the path stretching factor and the statistical behaviour of the code remain unclear. In some cases indeed, the code failed to pass the 10 statistical checks, with a warning message indicating that the FOM has a trend during the last half of the problem, which required reducing the NPS and restarting the simulations.

III.4.7. Combining different VR cards

To verify that the successful VR methods are compatible with one another and that they could be used together to further accelerate the simulations, different combinations of VR cards were done. The study also includes the counting efficiency value to make sure that the error on the efficiency estimate due to each VR alone does not add up when combining more than one VR. Finally, the aim was to investigate if the weaknesses coming from a particular VR method can be resolved by the use of another card. Hereafter, a “*” was added to refer to the combinations of VR methods; for example, FCL* is the combination of SB and FCL.

As the source biasing is one of the oldest VR schemes available for PHT we have tested it in combination with other VR cards. In all the following simulations, the SB distribution used was that in which 40% (15/37.5) of the emissions were starting at 15 keV.

- **SB and FCL (FCL*)**

First, SB was combined with FCL with a particular focus on the high energy photons. The NPS used was identical to that of the SB card alone i.e. 14.7E07 particles.

The simulation time reduction while adding the FCL card was again null. Nevertheless, FCL improved the high energy photons statistics by forcing interactions in the detectors. For example, for the ¹⁵²Eu photons of 1.4 MeV, the statistical relative error dropped from 0.1% (SB) to 0.07% (SB+FCL) for the Livermore phantom and from 0.9% (SB) to 0.6% (SB+FCL) for the female phantom. Moreover, when comparing the results in Appendix C.7 with those in

Appendix C.9, it is clear that the maximum difference observed on the counting efficiency values for high energy photons was reduced for both phantoms when using the FCL card.

As a conclusion, these two cards can be used together to slightly improve the simulation uncertainty at the highest energies.

- **SB, FCL and VEC (VEC^{*})**

Then user-defined cone directional biasing Vec was added to the SB and FCL cards to study the effect of the three easiest methods to implement in routine numerical simulations.

The results show that the simulation time was divided by about 20 for both phantoms. Moreover, the counting efficiency agreement to the reference values remained below 1.5% starting from 22 keV and within 10% for the 15 keV photons (cf. Appendix C.9). The number of simulated particles was reduced to 7.35E07 photons (half the NPS with SB card alone) most of which (40%) are starting at 15 keV.

This combination clearly highlights the advantage of VR methods when reducing the simulation time and maintaining reliable numerical calibrations.

- **SB, FCL, Vec and IMP (IMP^{*})**

First, the Cell importance card was combined with the SB alone and then with the SB, FCL and Vec (IMP^{*}). The NPS was first maintained at 7.35E07 photons and then it was reduced to 3E07. The cell importance ratio that was used here was the first one i.e. a value of 1 for the lungs, 3 for internal organs, 9 for chest wall plate/breasts and 18 for the front dead layer (cf. Section III.2.1).

The simulation time for the Livermore phantom was divided by 5.5 for the SB-IMP combination (1823 min) and by 6.3 when combined also to FCL and Vec (1593 min). For the female model, the simulation time reduction factors were respectively about 6.9 and 7.3 for SB-IMP (1329 min) and IMP^{*} (1250 min). When comparing these simulation time to the ones obtained for VEC^{*}, it is clear that the cell importance card has increased the simulation time. Moreover, this combination of cards did not concur with the expected results as efficiency values did not improve with the adding of the cell IMP card (cf. Appendix C.9). Indeed, when investigating the error on counting efficiency, it was noticed that the latter increased from 3.8% (VEC^{*}) to about 10.7% (IMP^{*}) at 15 keV and the female model. Meanwhile, the associated statistical relative error decreased from 3% (VEC^{*}) to about 2.3% (IMP^{*}). Furthermore, when the NPS was set at 3E07, and for the female phantom, the difference in counting efficiency increased to as high as 17.6% at 15 keV with a statistical error of 3.5% and a simulation time of 507 min (against 462 min for VEC^{*}).

To conclude, this combination was found to be of limited interest since the directional biasing with VEC is already favouring the particles going towards the detectors while SB and FCL are respectively increasing the number of “interesting” particles and forcing collisions in the detectors. Hence, IMP seems not to be bringing sustainable improvements to the results.

Finally, EXT and WW were combined with VEC^{*} to test the effect of such combinations on counting efficiency although the simulation time increases with the necessary iterations to

generate WW. In these cases, results showed that counting efficiency remains in good agreement with the reference values as the maximum difference observed at 15 keV was only of about -3.6% for the female model (cf. Appendix C.9). WW iterations remain however unaffordable.

III.5. VR methods discussion

VR methods were introduced in this work to reduce the simulation time or to improve the statistics, to maintain correct counting efficiency values and to find those methods that are easy to implement for routine numerical calibrations. Therefore, the discussion focuses on these parameters obtained for the combinations of VR cards.

III.5.1. Simulation time

In most situations, the simulation time was reduced with the use of VR methods. This results from the combination of two effects. The first effect is inherent to the method itself which saves time by killing particles unlikely to participate in the tally for example (case of the Cell Importance card). While the second effect comes from the fact that using a particular VR method, the number of starting particles required to have statistically reliable results at a given energy can be reduced, this is typically the case of the SB card. In this case, the VR acts indirectly on the simulation time by controlling the NPS. Thus, to discuss the obtained time reduction factors, the NPS should be taken into account along with the functioning of each method. The NPS was carefully chosen to maintain the statistical uncertainties within tolerance (5%). Table 4.4 documents the number of simulated particles for the combination of VR considered in this study and gives the time reduction factor obtained for each phantom.

Table 4.4. Number of simulated particles for the applied VR techniques to save time and guarantee reliable MC values.

VR method		SB	FCL*	VEC*	IMP*
NPS		14.7E07	14.7E07	7.35E07	7.35E07
Time reduction factor	Livermore	11	10.7	20.3	6.3
	ICRP female	10.6	10.6	19.8	7.3

From this table, it is clear that VR methods brought a positive contribution as they reduced the simulation time. This table also shows that, despite the sensitive differences existing between the two phantoms (in terms of the number of structures, the voxel number and size) similar time reduction factors were obtained. As a matter of fact, it was found that the simulation time was more affected by the number of voxels rather than by the number of structures. This conclusion was taken as the simulations were faster for the ICRP female torso which contained only 2.2 Millions of voxels but 67 structures in comparison to the Livermore voxelized model which contained 7 Million voxels but only 5 structures. As a conclusion, VR methods were found to work similarly for these two phantoms and to efficiently reduce the simulation time while maintaining good agreements with the reference situations and should work in a similar manner for any other phantom.

Moreover, the linear variation of the simulation time with NPS was investigated. For the VEC card for example, the time reduction factor was in agreement with the expected value, i.e.

13.6, representing the NPS ratio of the reference simulation (1E09) and the new simulation (7.35E07). For some other cards, this trend was not as expected. Indeed, in the case of the SB card for example, the NPS was reduced by a factor of 5 but the resulting simulation time reduction factor was about 10. This result can be simply explained by the fact that high energy photons are followed for a longer time, when compared to those at the lowest energies, and reducing their number gives additional time gain. The opposite effect was observed for the Cell Importance card for which the NPS was reduced by a factor of 10 while the simulation time reduction was of 3 only. This result is due to inherent splitting and RR operations that can sensitively alter the number of photons to be followed. The simulation time was unaffected (or poorly affected) in the case of the FCL. Meanwhile, the WW and EXT cards increased the simulation time especially when considering the necessary iterations.

III.5.2. Statistical relative error

The second objective was to improve the statistical relative error at the considered photon energy range. This requires an increase in the number of histories that tally at a particular energy since $R^2 \sim 1/N$ (cf. Section II.2.1). Table 4.5 documents the statistical relative errors for the photoelectric peaks of the ^{238}U photons at 15 keV obtained with the combined VR methods. This table also indicates that the statistical relative error on photoelectric peak is acceptable (<5%) and that the uncertainty values are mainly due to Compton compounds.

For the particular case of the SB card, it was noticed that the 15 keV statistical relative error increased when the number of photons of higher energies was reduced (from 1.2% in the reference situation to about 3% for the SB simulations and both phantoms). This was the case even when the NPS was doubled at 15 keV (statistical error about 2% for both phantoms) and was believed to be due to cascade effects of photons of high energies emitting daughter particles at 15 keV. Meanwhile, the FCL method improved the high energy photon statistics.

Table 4.5. Statistical relative error on the photoelectric peak at 15 keV obtained for the applied VR techniques and both phantoms.

Phantom	Statistical relative error at 15 keV (%)					
	Ref.	SB	FCL*	VEC*	EXT*	IMP*
Livermore	1.9	2.96	2.63	2.60	2.75	2.01
ICRP female	1.2	3.31	2.95	3.03	3.06	2.34

III.5.3. Counting efficiency values and uncertainties

To discuss the counting efficiency values and the differences when compared to reference values obtained without VR, one should start considering the uncertainties. It should be noticed here that no GEB was used for these simulation. This has the advantage of reducing the statistical uncertainty per energy bin as the Gaussian Energy Brodening function distributes the impulses on multiple channels which decreases the MC precision.

For the simulation results given in Appendix C.2 to C.9, high uncertainties were obtained (using Equation 3.2) at the lowest energies and particularly at 15 keV. These uncertainties do not reflect the quality of the result for the simulated photopeak as the statistical relative error is degraded by the Compton continuum. Indeed, the error on the photoelectric peak did not

exceed the 5% limit (cf. Table 4.5) above which the tally results are no longer trustworthy (Briesmeister 2000, Chapter 1 page 7). However, the errors on the Compton and scattered part of the spectrum cannot be easily mastered just by increasing the total NPS. Nevertheless, it has been decided to account for the Compton error when determining the efficiency uncertainty to be conservative. It is thus very difficult to draw conclusions from the simulation results when a difference to the reference efficiency value is below 1% but the associated uncertainty is as high as 10%. Fortunately, this is limited to the 15 keV photons which are the most difficult to assess. For all the 16 energy emissions of higher energy, the uncertainty remained within 2% and the error on counting efficiency was of the same order of magnitude. Figure 4.18 shows the counting efficiency values at 15 and 59 keV comparing VR results to reference values along with the associated error bars due to uncertainties.

Meanwhile, it should be noticed that measurements uncertainties for the 15 keV peak are often as high as 50% (Razafindralambo 1995). These include errors in the calibration itself (source activity), measurement uncertainties (detector positioning) and also errors from the differences between the calibration phantom and the measured subject. Therefore, a 10% error value was finally chosen to be the limit of acceptable difference on the counting efficiency due to the uncertainty resulting from the Compton continuum. In this case, most VR cards were within the acceptable range of counting efficiency difference for the considered energy range except the IMP and IMP* simulations for the female phantom.

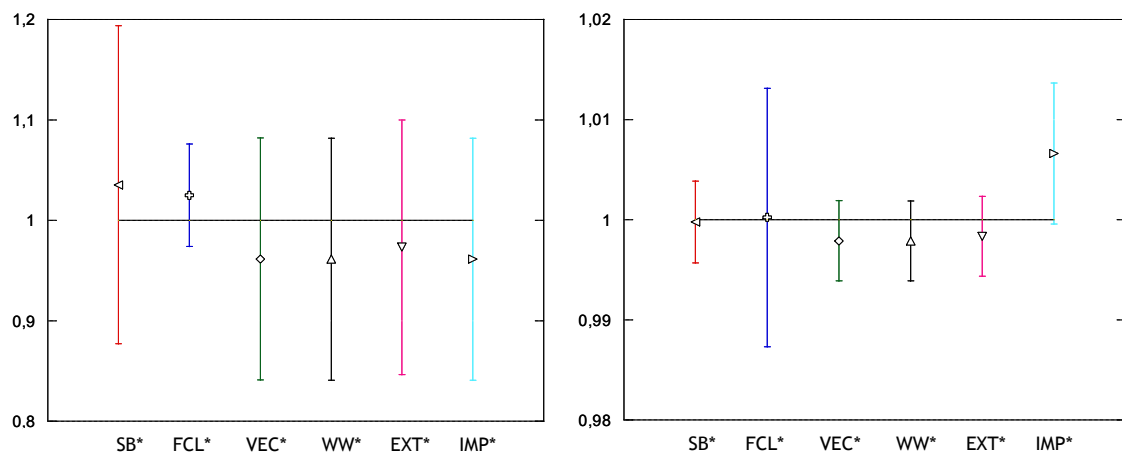


Figure 4.18. Counting efficiency ratio of the values obtained with the VR methods to the reference values obtained without VR and associated uncertainties; results at 15 keV (left) and 59.5 keV (right) and the ICRP female phantom.

III.5.4. Implementation for routine use

VR methods have proven to be an efficient tool to reduce the simulation time and efficiently assess the detectors' counting efficiency of the typical germanium counting system considered in this study. The obtained results ensure that variance reduction techniques are improving the sampling of the particles that tally. The SB, FCL and Vec cards have shown to be of simple use and implementation. For these cards, little information is required such as the cell number in which to apply FCL or the direction to be favoured. Meanwhile WW, Cell IMP and EXT were considered to be more complex and require a strong experience and understanding of the VR functioning. Therefore, it is only recommended to use the first three cards for routine numerical calibrations. Moreover, the combination of different VR methods has proved that those latter are working cooperatively; that is, one is not destructively interfering with another and the use of SB, FCL and VEC together was also recommended.

IV. Accelerating MC simulations with geometry simplification operations

In addition to using VR techniques, we have considered simplifying the geometry of the phantom to accelerate the MC simulations. The operated geometry simplifications include the adding of void plans and reducing the number of voxels in each phantom.

IV.1. Void plans

IV.1.1. Generalities and functioning

When conducting MC simulations, the user defines a typical sphere of work inside of which all particles are transported and followed until complete absorption in matter (cf. Figure 4.19 left). However, this can be time consuming depending on the size of the sphere of work, on the number of propagated particles and on the objects present within the sphere. To avoid such time consuming transport of particles, void plans were added in the sphere of work to kill any particle going through such a plan in any undesired direction. These void plans were put in a manner to surround the phantom and the detectors' region (cf. Figure 4.19 right) and kill the particles unlikely to participate to the count (i.e. particles entering the white space on the figure).

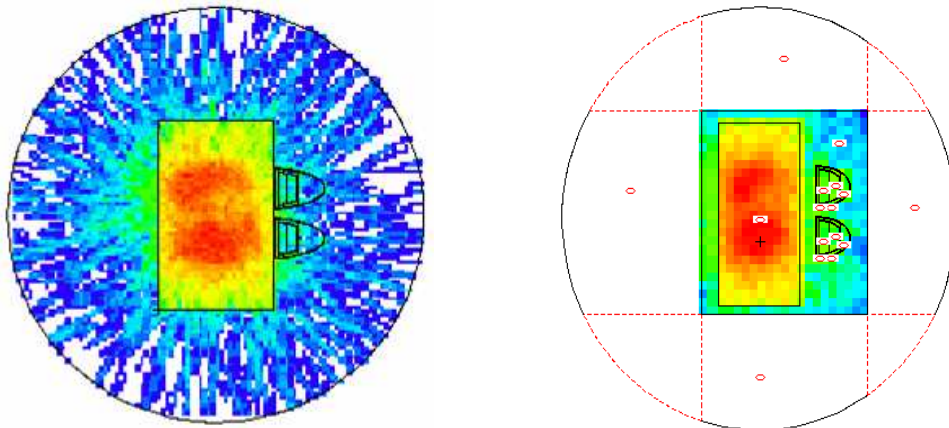


Figure 4.19. MCNPX plotter of a typical sphere of work inside of which the transport of particles is followed (right) and introduced void plans kill particles going in undesired directions (right).

IV.1.2. Application to the numerical calibration

First, void plans were used alone to run the simulations with an NPS value of $1\text{E}+09$. The simulation time reduction obtained was equal to 1.23 for the Livermore simulations and 1.27 for the ICRP female torso simulations. As for the counting efficiency values, the comparison of the reference values obtained without VR and those obtained while adding the Void plan showed a maximum relative error below 1% for both phantoms at all energy range (cf. Appendix C.10).

Next, void plans were used in combination with VR methods and particularly the SB, FCL and Vec cards (the user defined cone biasing). The simulation time reduction obtained thanks to the void plans was also of the same order of magnitude for both phantoms (around 1.22 for the Livermore and 1.28 for the ICRP female). As for the counting efficiency, the values were

in agreement with the reference one with a maximum relative error of -6.23% for the Livermore and of -1.49% for the female phantom (cf. Appendix C.10).

As a conclusion, one can say that void plans are easy to use and to implement in routine and give satisfying time reduction factors although VR methods are far more efficient in reducing the simulation time. The combination of void plans with VR methods is also possible and also gives acceptable results. Nevertheless, the use of such plans should be considered with caution as no scattering whatsoever is accounted for with this method while it could be sensitively non-negligible. Indeed, when conducting a real measurement, the walls of the measurement chamber, the table/chair on which the monitored subject is seated, the mechanics supporting the detectors and any other object present in the chamber can scatter radiation back to the detectors and contribute to the result. These are not accounted for when including the void plans which may result in an underestimation of the contamination activity. It should be noticed however, that many other factors, particularly the detectors positioning, are responsible for higher uncertainties and errors on the activity estimate that can be far more important than accounting for the scattering contribution.

IV.2. Phantom geometry simplification

IV.2.1. Voxel grid reduction

To further accelerate the MC simulations, we have considered simplifying the phantom by reducing the total number of voxels. This was done by using the IDL rebin function that resizes a vector or array to user-specific dimensions. By default, rebin will interpolate the value of the resulting voxel from the values of the fused voxels. When the same color is present (cf. Figure 4.20. left), the fusion will result in a voxel equal to the size of all fused voxels and with the same color; otherwise, a new color will be created (cf. Figure 4.20. right).



Figure 4.20. Schematic visualization of the rebin functioning when two adjacent voxels with similar (left) and different (right) colors are fused together.

Nevertheless, this interpolation becomes problematic for all boundary voxels. Indeed, if the voxel fusion results in a new color, the MCNPX code would fail to run the simulation as no materials were defined for this new color i.e. structure. To avoid such an error, the interpolation can be stopped by adding the “/sample” option to the rebin function. In this case, the fused voxel will be colored following the first voxel of smaller index i.e. the one on the left (yellow in this case).

For small structures, this forced color assignment can result in a difference in the organ volume. For example, in the case of one particular rib, a certain number of voxels situated on the left side of the structure (Figure 4.21. voxels #1) will be lost as such voxels become part of the soft tissue structure (in orange). Meanwhile, another number of voxels situated on the right side of the ribs (Figure 4.21. voxels #2) will be gained. As the total number of voxels exchanging colors is rarely the same, the final ribs will have different volume when compared to the primary one. For the biggest organs, the number of voxel exchanging colors is roughly balanced and thus the rebin fusion will have insignificant impact on the final organ volume.

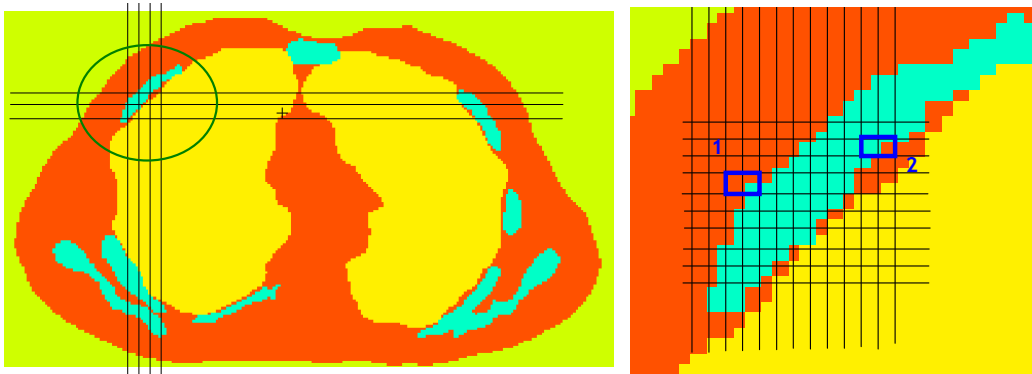


Figure 4.21. Errors on the organ volume caused by the rebin voxel fusion.

Rebin only operates integer voxel fractions while the IDL “congrid” function enables also non-integer array resizing. For this reason, a layer of air-equivalent voxels was added each time it was required to enable the use of the rebin function.

In this study, the rebin function was used with the “/sample” option to reduce the matrix size from 256x256x256 to 128x128x128 for the Livermore phantom and from 77x299x137 to 77x150x69 for the torso of the ICRP reference female. The IDL procedure that was used to reduce the voxel grid dimensions is given in Appendix C.11. The operated phantom resizing did not, however, involve any changes in the tissue composition and density.

IV.2.2. Validation of the simplified phantom

Since the rebin function resulted in the creation of a new phantom, a comparison with the initial model was required to validate the resized model. The validation involves the comparison of the created volumes.

- **Case of the Livermore phantom**

The volumes of the resized organs for the Livermore voxelized phantom and the reference organ volumes are equivalent as the maximum observed deviation is below 1% (cf. Table 4.6). This validates the operated voxel grid resizing i.e. phantom’s geometry simplification.

Table 4.6. Comparison of the reference organ volumes and the resized phantom and associated relative error.

organ	Reference volume (cm ³)	Resized volume (cm ³)	Difference (%)
Lungs	4150.42	4147.33	0.07
Bone	1543.11	1546.56	-0.22
Soft tissue	26738.69	26790.53	-0.19
Plate P1	1088.10	1092.54	-0.41

- **Case of the ICRP female torso phantom**

Similarly, when considering the volumetric comparison of the resized torso of the ICRP voxelized female with the original model, the agreement was found to be within 1% (cf. Table 4.7) for the main structures/organs of the female torso. Higher errors were however observed

for the smallest organs as expected (up to 12% for the cortical compound of the sternum). More details relative to the volumetric comparison can be found in Appendix C.12.

Table 4.7. Comparison of the reference organ volumes with the resized phantom and associated relative error.

organ	Initial volume (cm ³)	Resized volume (cm ³)	Difference (%)
Lungs	2301.06	2303.82	-0.12
Breasts	511.88	511.70	0.04
Ribs	321.14	321.88	-0.23
Heart	587.16	586.05	0.19
Liver	1333.33	1332.64	0.05

IV.2.3. Application to the numerical calibration

Once the resized phantoms were validated, they could be used to realize a numerical calibration of the AREVA NC germanium counting system.

First, the resized phantoms were used without including any VR methods and the NPS was set to 1E09 (reference situation). Reducing the number of voxels with rebin resulted in a simulation time gain of 2; i.e. of the same order of magnitude as the voxel number reduction. The counting efficiency values also remained in good agreement (difference < 3%) with the reference values for all energy but the 15 keV photons and the Livermore phantom (cf. Appendix C.13). These results indicate that resizing the phantom to reduce the voxel grids gives sensitive simulation time reduction factors.

Next, the resized phantoms were used in combination with VR methods such as SB, FCL and Vec cards. In this case, for the Livermore voxelized phantom the simulation time was of about 252 min and for the ICRP female torso of about 231 min with a total gain of about 40 when compared to reference simulations obtained without VR and with the initial voxelized phantoms. Appendix C.13 documents the simulation results which indicate that resizing the phantom is coherent with VR methods and further accelerates the simulations. Indeed, the counting efficiency was within the 5% difference to the reference values for both phantoms and all simulated photons starting from 20 keV.

As a conclusion, one can say that the use of the rebin function to reduce the total number of voxels is easy to use and to implement in routine and gives a satisfying time reduction. Nevertheless, the use of such method has a major limitation since the voxel dimension can be sensitively increased and thus the resolution could be severely lost.

V. Accelerating MC output file treatment

Reducing the simulation time with VR methods and with the geometry simplification operations gave satisfying results. However, transforming the PHT (f8) results into a calibration curve requires a manual processing of the MCNPX output files that can sometimes

become delicate and time consuming (cf. Chapter 3 Section I.2.1). Therefore, a script was developed using the Unix/Linux bash utilities to ease and accelerate the MC output file treatment.

V.1. Development of a Unix/Linux shell script

V.1.1. Objective

This script aims at plotting the numerical calibration curve by assessing the height of the photoelectric peak from which the Compton contribution must be subtracted (cf. Chapter 3 Section I.2.1). The processing can be time consuming and delicate depending on the number of tallies, the number of simulated photons (source emissions) and the spectrum itself (GEB parameters). This script uses basic bash/shell utilities and functions to process any MCNPX output file and plot the calibration curve.

V.1.2. Functioning

There are two main sections in the script the first dealing with the input requests and the second one searching the MCNPX output section for the simulation result and treating it to extract the counting efficiency values and plotting the calibration curve.

• Input file section

The input section treatment consists of identifying first the source and particularly its weight, distribution, emissions energy and yield. This section also includes the identification of the number of requested tallies, the energy range and the number of bins of each tally and finally, the total number of simulated particles (cf. Figure 4.22.). The script writes these inputs in a “txt” file to summarize the requested values of the MCNPX file run.

• Output file section

The developed script searches the output section of the MCNPX file to find the energy line for each simulated photon and the associated statistical relative error. This is done for each requested tally. Then, the script extracts the values surrounding the photoelectric peak that stand for the Compton continuum and their associated statistical error. Next, the code subtracts from the photoelectric peak the contribution of the Compton continuum and assesses the uncertainty on the simulated counting efficiency (cf. Chapter 3 Section I.1.2). Finally, the script writes these MCNPX output values along with the counting efficiency values (corrected from noise) in the previously defined “txt” file.

V.1.3. Polynomial equation

To further simplify the use of the MCNPX numerical calibration curves, the counting efficiency variation with energy was put into equation. This is commonly done in routine since the efficiency curve can be interpolated by a polynomial relation of the form:

$$\ln(\varepsilon_{ff}) = \sum_{i=1}^6 (a_i \ln(E))^i, \text{ where } E \text{ is the Energy in keV, and } \varepsilon_{ff} \text{ the counting efficiency in}$$

counts/s/gamma (Molnar et al. 2002). The script was thus upgraded to plot directly the simulated calibration curve and extract the coefficients of the polynomial equation. These coefficients are also written in the “txt” file. The polynomial interpolation is also validated by comparing the simulated counting efficiency values with the ones given by the equation. The

script also offers the user the possibility of plotting the calibration curve along with the polynomial equation and these are systematically saved in a “png” file that can be easily read by most image viewing/processing software.

```

mode p
sdef x=d1 y=d2 z=d3 cell=d4 erg=fcell=d5 wgt=17 eff=1e-9
      vec=0 -1 0 dir=d7
SI1  -15 -14,8225
SP1  0 1
SI2  -10 -9,8225
SP2  0 1
SI3  -22 -21,516
SP3  0 1
SI7  -1 0 1
SP7  -31 0
SB7  -31 1
c Nombre total de photons emis dans chaque organe :
# SI4      SP4      DS5
  l      d      s
(1495<1003<1002)  0,02428  11
(1505<1003<1002)  0,42557  12
(1515<1003<1002)  0,01733  13
(1525<1003<1002)  0,53282  14
c Nombre total de photons emis par chaque radioelement dans un organe donne :
c lung_left_blood
# SI11     SP11
  s      d
  101    0,02428
c lung_left_tissue
# SI12     SP12
  s      d
  101    0,42557
c lung_right_blood
# SI13     SP13
  s      d
  101    0,01733
c lung_right_tissue
# SI14     SP14
  s      d
  101    0,53282
c Energie et nombre de photons emis par radioelement :
c Am-241
# SI101    SP101
  l      d
0,0153100  1
0,0221600  1
0,0334400  1
0,0401200  1
0,0595400  1
0,0810000  1
0,1220600  1
0,1558600  1
0,1857200  1
0,2447000  1
0,3560100  1
0,5110000  1
0,6616600  1
0,8348400  1
1,1732300  1
1,2745400  1
1,4080100  1
f18:p (2 17 32 47)
e18 0 1e-5 5e-3 16382i 1,41
ft18 GEB 0 0 0
CUT:p 2j 0 0
pps 73529411
PHYS:n 100 1 1

```

1: source weight

2: source distribution (here lungs)

3: energy of photons and yields

4: requested tally and energy parameters

5: number of simulated particles

Figure 4.22. Example of an MCNPX input file and highlighted steps of the inputs identified by the script.

V.2. Script use and validation

The developed script was generalized to cover at best all possible situations including the input of a punctual source, different organ sources and various distributions, multiple output tallies and other relevant input parameters. The use of such a script was however maintained as simple as possible and different messages are printed at each stage of the MCNPX file processing to make the code user-friendly and indicate the advances of the processing.

The following command is necessary to run the code:

./GetEfficiency MC_output; where GetEfficiency is the executable script developed in this work and MC_output is the simulation result file to be processed.

Below is a printscreen of the “txt” file generated by the script (Figure 4.23) along with a plot of the comparison between the simulated counting efficiencies and the polynomial equation developed by the script (Figure 4.24).

Input request		Output evaluation			Efficiency value		Equation validation	
Req_NRJ	Y	Sim_NRJ	Effic_counts	S.R.E.	Counting_Eff.	C_Eff_Uncert.	Eqt_Eff_val	R.E.
0,0153100	1	1,5384E-02	1,15107E-04	0,0122	0,000045211500	0,046124491056	0,0000456106	-0,88
0,0221600	1	2,2220E-02	1,70474E-03	0,0032	0,001595005000	0,003629248274	0,0015570956	2,38
0,0334400	1	3,3500E-02	7,37533E-03	0,0015	0,007109900500	0,001612692645	0,0071956227	-1,20
0,0401200	1	4,0165E-02	9,70391E-03	0,0013	0,009439764000	0,001373414969	0,0096206469	-1,91
0,0595400	1	5,9564E-02	1,31797E-02	0,0011	0,012884903000	0,001151802495	0,0129500259	-0,50
0,0810000	1	8,1013E-02	1,46974E-02	0,0011	0,014466463500	0,001134118307	0,0141945065	1,88
0,1220600	1	1,2212E-01	1,48410E-02	0,0011	0,014697477500	0,001120803559	0,0143964770	2,05
0,1658600	1	1,6587E-01	1,35213E-02	0,0011	0,013432254000	0,001114876358	0,0132139477	1,63
0,1857200	1	1,8578E-01	1,25750E-02	0,0012	0,012512278500	0,001211664063	0,0124918095	0,17
0,2447000	1	2,4474E-01	1,01260E-02	0,0013	0,010092399500	0,001308610674	0,0103254307	-2,30
0,3560100	1	3,5609E-01	7,24600E-03	0,0015	0,007229918000	0,001506813661	0,0072825641	-0,72
0,5110000	1	5,1102E-01	5,33103E-03	0,0018	0,005321510000	0,001806389358	0,0051174690	3,84
0,6616600	1	6,6168E-01	4,33728E-03	0,0020	0,004332137500	0,002004699351	0,0041454359	4,31
0,8348400	1	8,3489E-01	3,66930E-03	0,0022	0,003665475000	0,002204490825	0,0035773844	2,41
1,1732300	1	1,1733E+00	2,91008E-03	0,0024	0,002907504500	0,002404278583	0,0029122110	-0,16
1,2745400	1	1,2746E+00	2,75500E-03	0,0025	0,002754269000	0,002501318694	0,0027100709	1,61
1,4080100	1	1,4080E+00	2,57536E-03	0,0026	0,002575343000	0,002600033920	0,0024167995	6,16

Polynomial equation parameters		
cst = -575,396	+/- 24,4	(4,24%)
x1 = 672,207	+/- 32,53	(4,839%)
x2 = -328,282	+/- 17,66	(5,381%)
x3 = 84,9064	+/- 5,005	(5,895%)
x4 = -12,2337	+/- 0,7813	(6,386%)
x5 = 0,929127	+/- 0,06378	(6,864%)
x6 = -0,0290325	+/- 0,002129	(7,334%)

Figure 4.23. Visualization of the “txt” output file of the script summarizing the requested inputs, the simulated outputs, the processed counting efficiency values and the polynomial equation parameters as well as validation for the ICRP female reference simulation.

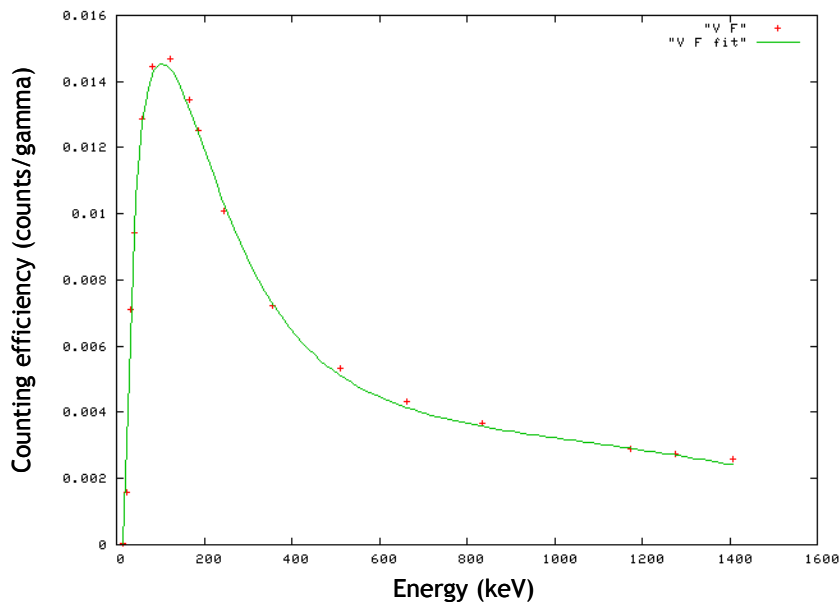


Figure 4.24. Visualization of the “png” script output file representing the counting efficiency (counts/gamma) variation with energy (keV) and comparing the simulated values (red) to those given by the polynomial equation (green) for the ICRP female reference simulation.

The values given in the “txt” file presented in Figure 4.23 represent correctly the requested inputs (i.e. number of requested energies and associated yields) in the column called “Input request”. The second column, “Output evaluation”, gives the MCNPX values extracted at the tally lines corresponding to the simulated photon energies. Moreover, the counting efficiency values and associated uncertainties are automatically calculated by the code and saved in the “Efficiency value” column. From Figure 4.24, it is clear that the polynomial equation, calculated by the script, reproduces very well the simulated counting efficiency values and the highest difference (relative error) was observed at 1.4 MeV and was about 6.2% (cf. Figure 4.23 column “Equation Validation”). Therefore, the parameters of the polynomial equation presented in Figure 4.23 are validated and with them the whole script is also validated.

This script was used to plot the counting efficiency curves for all the previous simulations involving VR methods and/or phantom geometry simplifications.

VI. Discussion and conclusion

MC simulations were used here to assess counting efficiency calibration curves. This chapter looked for the most available and easy to use VR techniques to speed up the calculations while maintaining unbiased results. The work also included some geometry operations to simplify the phantom and the development of a shell-based script to automatically plot the calibration curve from the MCNPX output files.

The main results are summarized first and then the statistical analyses are given and discussed while finally an example is given where VR methods are put into benefit to enhance the counting efficiency calculation.

VI.1. A one hour calibration process

The applied variance reduction techniques were the source biasing, the emission direction biasing, the forced collision, mesh-based weight windows associated to exponential transform and the cell importance card. The methods were tested on two different phantoms: the Livermore voxel model and the torso of the ICRP reference female in order to study the efficiency of each VR technique when considering different number of structures and voxels. The used VR cards enabled a final time reduction by a factor of about 20 for both phantoms. The obtained counting efficiency values agreed with the reference values (obtained without VR) since the observed differences remained within 5-10% for the 15 keV photons and around 1% for photons of higher energy. The VR also improved the MC statistics, particularly for high energy photons with the FCL card. The obtained results confirmed that the efficiency of each VR techniques depends mainly on the energy of the simulated particles. The obtained results also showed that simulation time depends on the number of voxels rather than on the number of organs. Indeed, for a simple phantom like the Livermore model, with only 5 different structures, the simulation time reduction was equal to the one obtained with the female complex phantom with 67 structures. As a future step, new VR techniques can be tested such as the DXTRAN spheres for deterministic transport of particles or the RDUM card for emission direction biasing towards a fictitious sphere covering the detectors, should these techniques become available for the pulse height tally in the latest versions of the code.

Simple geometry operations were next conducted and combined to VR methods to further improve the results. This included adding void plans and reducing the total number of voxels in the phantom. The results showed a time reduction factor of 1.3 with the void plans and a factor of 2 for the voxel reducing operations.

To further reduce the MC simulation time, a parallel version of the code was used on 32 processors at the same time. This nearly reduced the total simulation time by a factor of 20 that adds up to the previous time gain for the SB-FCL-VEC simulation.

Before conducting this work, a whole week was required to run the simulations and plot a typical calibration curve; for the ICRP female for example, the simulation time was of 9141.29 min that is 6.3 days. The simulation time was successfully reduced to about one hour thanks to parallel calculations, VR methods, geometry simplification operations and the developed script for MCNPX output file treatment.

VI.2. Statistical checks and FOM analyses

At the end of each MCNPX output file, 10 statistical checks are made on the Tally Fluctuation Charts (TFC) to provide the user with information about the statistical behavior of the result.

For all the conducted MC simulations, the 10 statistical checks were studied to provide additional confidence in the tally results. These however, were not always fulfilled for the operated simulations that included VR methods and different NPS. Indeed, for the cell IMP card for example, since the IMP parameters were multiplied by 9 (or even 18), the NPS was first decreased by the same factor (10). However, in this case the simulations failed to pass the 10 statistical checks with the female phantom. Therefore, the NPS decrease was limited to a factor of 3 which gave satisfactory results (cf. Section III.4.1). Divergent observations were obtained with the WW card when used alone and also for the EXT* simulations. In these cases, the message error was often indicating that the tally was converging starting from a certain number of samples and that there is no need to start as many particles as it was done. This was being traduced by the fact that some parameters, such as the mean or the FOM for example, were tending to remain constant during the last half of the problem. For these simulations, the total number of starting particles was thus reduced and simulations were restarted.

The Figure Of Merit (FOM) is one of the key indicators of the tally reliability (cf. Chapter 1 Section III.2.3). FOM is often used to optimize the efficiency of the Monte Carlo calculation with variance reduction (selecting the method with the largest FOM). Thus, the FOM values obtained with the combination of VR methods were investigated.

Table 4.8 documents the FOM values obtained with the reference simulations and when combining the different VR techniques for both phantoms. From this table, it is clear that FOM can be significantly increased indicating an optimal use of VR methods (case of VEC*) but it can be sensitively decreased meaning a non-optimal use of VR techniques (case of EXT*). However, as recalled by Booth (1985), the FOM is an estimate of the calculational efficiency but it is not the only piece of summary information. Sometimes, VR methods bring

the desired effect; for example the “tracks entering” numbers are greater with the Cell IMP card but the FOM drops. Thus, FOM should be examined with care keeping into mind that the ultimate goal remains the use of VR to improve the sampling. In this study, the key parameter that was retained to study the efficiency of a VR method was the simulation time and the counting efficiency value which was checked to remain within a 5% interval from the reference values obtained without VR at the considered energy range.

Table 4.8. The FOM value obtained for the applied VR techniques and both phantoms.

Phantom	VR method				
	REF	SB	FCL*	VEC*	IMP*
Livermore	4392	3897	3860	6377	1601
ICRP female	7143	6258	6201	10153	2523

VI.3. Enhancing efficiency calculation with VR methods

For the previously conducted simulations with the library of female torsos, no VR methods were used. In some cases, particularly the big female morphologies, of chest girth 110 and 120 for example, no counting efficiency values were given for the lowest photon energies (15 keV). Indeed, the statistical relative error at such energy remained exceeding the 5% acceptable limit for the pulse height tally (Briesmeister 2000, Chapter 1 page 7) no matter how high the NPS became (2E09 maximum value).

To solve this problem, VR methods were introduced to get statistically reliable results at 15 keV. The used cards include the cone directional biasing towards the detectors with Vec, the EXT applied to all body compounds and detectors’ front dead layer. Weight fluctuations were again controlled by a mesh-based rectangular weight window generated and optimized with an f6 tally. Table 4.9 documents the simulation results for the 110 chest girth phantoms giving both the counting efficiency and the statistical relative error at 15 keV. This table represents a successful and basic use of VR methods when a direct estimate of the counting efficiency is unavailable because of the geometry of the phantom.

Table 4.9. Counting efficiency values and associated statistical relative error obtained for the 110 chest girth phantoms and the combination of Vec, EXT and WW VR cards.

Phantom	110B	110C	110D	110E	110F
Counting efficiency (counts/s/ γ)	6.26E-07	3.79E-07	2.04E-07	1.65E-07	1.38E-07
Stat. R. E. (%)	0.34	0.4	0.57	0.65	0.74

Chapter 5

Activity mapping using in vivo spectrometry measurements and MC simulations

In vivo measurements are usually carried out under the hypothesis of a known activity distribution inside the body. However, for complex contaminations and wounds, it is difficult to estimate a posteriori the activity distribution only by using spectrometry measurements. The case of an old or a chronic contamination is also challenging especially if followed by a new or an acute contamination. Monte Carlo simulation tools were thus introduced to assess the activity distribution when combined with *in vivo* measurements.

This chapter is divided into five main sections. The first section introduces the problem and the available tools and describes the developed method to assess the activity mapping. The second section discusses the feasibility of the separation method through the use of the Livermore physical phantom. In the third section, the Monte Carlo tools are introduced to generalize the method for any contaminated worker. The fourth section proves the effectiveness of the method for two different counting systems and various radioactive organs while the last section discusses the method and the main improvements that can be done.

I. Management of complex contaminations

In vivo measurements are commonly used to assess the incorporated radionuclides and to estimate the activity distribution following an internal contamination. However, the method fails to give satisfying results in the case of complex contaminations where the incorporation date is not precisely known. These complex cases include also the scenarios where a mixture of radionuclides of different type and solubility are incorporated with different intake routes. For old contamination scenarios and for wounds, spectrometry analyses can also be of limited efficiency when investigating the activity distribution.

A new method that combines *in vivo* spectrometry analyses with Monte Carlo simulations was thus introduced. This method uses the definition of experimental counting efficiency and the linearity of *in vivo* measurements to determine the activity mapping. Meanwhile, Monte Carlo simulations provide the contribution coefficients of each organ to the count, i.e. counting efficiency, essential to separate the counts for the detector at a precise position.

I.1. Activity distribution in complex scenarios

To obtain a realistic distribution of the internal contamination, a whole body counting can first be considered to determine the incorporated radionuclides from the measured spectrum. Next, ICRP biokinetic models are used to determine the most important retention organs for each of the incorporated radionuclides. Finally, organ-specific *in vivo* measurements are done with the most appropriate counting system fitting the energy of the radionuclides.

However, biokinetic models are far from being person-specific and are regularly updated. Moreover, when multiple routes of intake are involved (inhalation and wound routes for example), the main difficulty lies in the fact that the proportion of each route of intake is not known a priori. This proportion influences directly the biokinetic distribution of the radionuclides and should also be assessed from the measurement results. Finally, during *in*

in vivo spectrometry, the collected number of counts integrates the radiation emerging from all contaminated organs.

To correctly establish the activity distribution in each contaminated organ, it is thus necessary to separate the contribution of each organ from the experimental counting rate. For a thoracic measurement for example, it is necessary to determine the proportion of counts coming from the lungs and the proportion coming from bones and from the liver or any other contaminated organ in the monitored region (cf. Figure 5.1). This is done by determining the counting efficiency coefficients for each contaminated organs and a given detector positioning. Therefore, it is extremely difficult to determine the activity present in each of these structures separately just by using *in vivo* measurements.

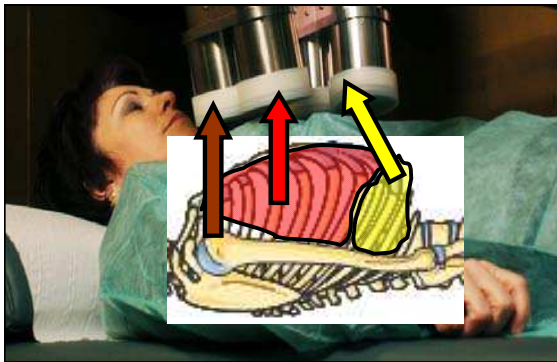


Figure 5.1. Visualization of a typical *in vivo* pulmonary measurement and schematic representation of the possible organ sources which contribute to the detectors' count.

I.2. Separation method

Typically, to determine the activity within a contaminated organ, the *in vivo* experimental counting rate (counts/s) is directly used since it is related to the activity of the organ (Bq) through the following relation:

$$\tau_{\text{exp}} = y_i \cdot A \cdot \varepsilon \quad \text{Equation 5.1}$$

where ε is the counting efficiency (counts/s/ γ) and y_i the yield of the considered energy line (γ /nuclear disintegration). Counting efficiency is directly dependent on the characteristics of the detector and on its positioning and represents the contribution of the organ to the count. This contribution is never equal to 1 (100%) since not all particles emitted from the source are collected in the detectors.

However, when several organs are contaminated, the experimental counting rate accounts for the total number of emissions detected by the counting system and should thus be written as follows:

$$\tau_{\text{exp}} = y_i \sum_{\text{organ}} A_{\text{organ}} \cdot \varepsilon_{\text{organ}}^{\text{detector position}} \quad \text{Equation 5.2}$$

In this case, a separation of the contribution of each organ is mandatory.

Two organs loaded at the same time, for example two lungs, will be considered. In this case, the total number of counts collected in the detector at a given position (left) is equal to the sum of counts for each lung loaded alone.

$$\tau_{left} = \tau_{left}^{right.lung} + \tau_{right}^{left.lung} \quad \text{Equation 5.3}$$

The experimental counting rate can also be written as the product of the counting efficiency and the activity of the organ which can be written as follows:

$$\tau_{left} = y_i (\epsilon_{left}^{right.lung} \times A^{right.lung} + \epsilon_{right}^{left.lung} \times A^{left.lung}) \quad \text{Equation 5.4}$$

These measurements give the values for the experimental counting rate (left matrix) and the counting efficiency which accounts for the contribution of each organ to the count (middle matrix). Using also the counts from the right detector, a system of two equations is obtained:

$$\begin{pmatrix} \tau_{exp}^{det.pos.1} \\ \tau_{exp}^{det.pos.2} \end{pmatrix} = \begin{pmatrix} \epsilon_{right.lung}^{det.pos.1} & \epsilon_{left.lung}^{det.pos.1} \\ \epsilon_{right.lung}^{det.pos.2} & \epsilon_{left.lung}^{det.pos.2} \end{pmatrix} \times \begin{pmatrix} A_{right.lung} \\ A_{left.lung} \end{pmatrix} \quad \text{Equation 5.5}$$

By inverting the system given above, the activity in each organ can be estimated from the matrix product below:

$$\begin{pmatrix} \epsilon_{right.lung}^{det.pos.1} & \epsilon_{left.lung}^{det.pos.1} \\ \epsilon_{right.lung}^{det.pos.2} & \epsilon_{left.lung}^{det.pos.2} \end{pmatrix}^{-1} \times \begin{pmatrix} \tau_{exp}^{det.pos.1} \\ \tau_{exp}^{det.pos.2} \end{pmatrix} = \begin{pmatrix} A_{right.lung} \\ A_{left.lung} \end{pmatrix} \quad \text{Equation 5.6}$$

This system highlights the importance of assessing the contribution of each organ to the count (the counting efficiency matrix) in order to determine the activity in each lung. To determine this matrix, Monte Carlo simulations were introduced since it is impossible to isolate each contaminated organ in the body of the victim and count it alone.

This separation method remains mathematically correct whatever the number of contaminated organs, provided the number of necessary measurements exists. However, the higher the number of loaded organs is, the greater the number of required measurements and consequently the higher the measurement time. Furthermore, it should be noticed that the method is based on the a priori hypothesis regarding the number of sources present in the monitored region. If the number of potentially contaminated organs is wrong, this method will fail to give a correct activity distribution. For this method to work, it is thus essential to first identify the plausible retention organs and to consider all the possible distribution scenarios using biokinetic models.

I.3. Tools

The developed method enables the assessment of the activity distribution through the use of biokinetic models, the choice and positioning of an appropriate counting system, the use of a physical phantom loaded with radioactive organs and Monte Carlo simulations.

I.3.1. ICRP biokinetic models

Incorporated radionuclides are transferred throughout body organs and tissues following biokinetic mechanisms. The radionuclide retention is highly dependent on the organ's

metabolism and the similarity of the radionuclide to a natural element usually taken up by the organ from the blood. For example, ^{241}Am is preferably retained by the liver and the skeleton whereas ^{137}Cs is homogeneously distributed in the organism (ICRP 1995; Legget et al. 2003). Specific models are recommended by ICRP to describe the movement of radionuclides in the site of entry following incorporation. These allow predicting, from a given intake, the retention of activity in organs and the excretion in urine and feces as functions of time. In this work, biokinetic models are essential as they give a fairly realistic and rational idea on the activity distribution within the organism. Figure 5.2 presents the retention organ of americium following inhalation where most of the activity is retained in the lungs the first ten days following incorporation while the liver and bones represent the long-term retention organs.

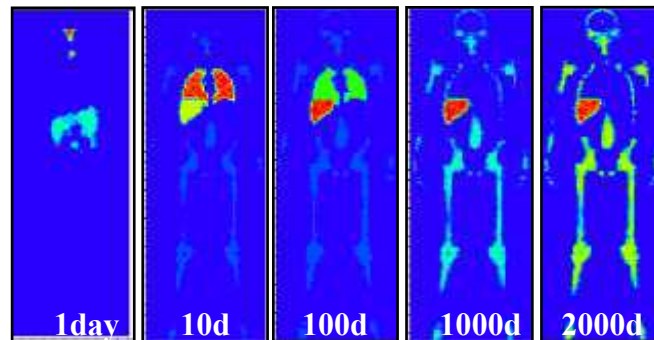


Figure 5.2. ^{241}Am biokinetics and retention organs days after a contamination by inhalation (Lamart 2008).

I.3.2. Counting system and positioning

Spectrometry detectors are based on scintillation and ionization phenomena. The counting system must be chosen according to the energy of the emitted X and gamma radiations. Thallium-doped sodium iodide scintillation crystals are often used to detect high energy photon emitters such as ^{137}Cs and ^{60}Co while detectors with germanium or silicon semiconductor crystals are more appropriate for low energy emissions of actinides such as ^{241}Am .

For the measurements conducted in this study, the LOAX germanium counting system available at IRSN, the four-germanium array available at CIEMAT and the high purity germanium detector of KIT were involved (cf. Figure 5.3). Moreover, the positioning of the counting system was done to maximize the count and cover at best the contaminated region.



Figure 5.3. Photos of the three different germanium counting systems used for this study: IRSN's LOAX (left), CIEMAT's 4-LEGe (middle) and KIT's HPGe (right).

I.3.3. Physical phantom and radioactive sources

For this study, the Livermore male-equivalent torso phantom was considered with the core torso chest plate (Griffith et al. 1978, Newton et al. 1984). The lungs and liver are the source organs in which the activity is uniformly distributed. The available radioactive organs include ^{241}Am and ^{152}Eu radionuclides. In addition, point sources of ^{241}Am and ^{152}Eu were also introduced in the torso of the Livermore for a more extensive study of the method.

I.3.4. Monte Carlo calculation tools

The Monte Carlo MCNPX code was used to simulate the experimental *in vivo* measurements and to help determine the activity distribution. For these simulations, a voxelized model of the Livermore phantom was built from CT scan images of the physical mannequin. The used detectors were also modeled using MCNPX to correctly reproduce the *in vivo* counting experiments with MC calculations. This was done by reproducing the exact technical drawing of the detector compounds as indicated by the manufacturer.

I.4. Work plan and investigation limits

The effectiveness of the method in determining the activity mapping was tested through:

- A feasibility study using measurements with the Livermore phantom to realize a physical separation of the contributions and validation of the method,
- Running Monte Carlo simulations of the Livermore experiments to validate this tool as a mean to determine the organ contributions when measurements are impossible,
- Generalizing the use of the method for different counting systems, various counting configurations and different number of loaded organs.

In addition, the work included a study of the method's limits. The examined parameters of influence were the detector positioning, the a priori distribution hypothesis and the presence of a perturbation point source simulating, for example, a contaminated lymphatic node or an old contamination.

I.4.1. Detector positioning

In this study, organ-specific *in vivo* spectrometry measurements were considered with the detectors aligned to cover at best the monitored organ and brought as close as possible to the skin to maximize the counts. This positioning significantly reduces the contributions of other organs to the count but does not eliminate them which explains the need for separating the counts. Nevertheless, the external anatomical frame, used to localize the contaminated organ, may sometimes be inappropriate or badly chosen. In this case, it is difficult to reproduce the exact position with MC simulations. Therefore, the effect of a bad detector positioning on the activity mapping was investigated.

I.4.2. Biokinetic distribution

The a priori hypothesis on the activity distribution, based on biokinetic models, is also a major parameter influencing the activity mapping. Indeed, to correctly use this method, the number of contaminated organs must be precisely determined as it is equal to the number of required measurements. If two organs are supposedly loaded with activity then two

measurements at two different counting positions are necessary. Therefore, the effect of a false hypothesis on the number of presumably loaded organs was investigated by either considering an overestimation of the number of loaded structures or an underestimation.

I.4.3. Presence of a perturbation source

This investigation aims at accounting for the presence of an old contamination or considering the contamination of a lymphatic node. Indeed, in these cases, the count may be significantly biased and correction steps should thus be considered. To simulate these scenarios, a point source was added in the Livermore phantom at different positions and its effect on activity mapping was studied.

II. Feasibility study using the Livermore phantom

To study the feasibility of the separation method, the Livermore calibration phantom was used to physically assess the contribution of each organ to the experimental count. In this case, the user loads inside the mannequin one radioactive lung at a time and then runs a third measurement with both lungs together. This way, it is possible to experimentally assess the efficiency matrix, i.e. contributions, which is essential to determine the activity mapping.

II.1. Method validation with measurements

To validate the consistency of the mathematical separation method, experiments were done considering the Livermore phantom and the americium lungs. The activity on the measurement date of the right lung was of 34.62 kBq, while it was of 25.73 kBq for the left lung. In this case, a total of six measurements are required at two different detector positions to obtain a system of two equations with two unknowns, these being the activities of each of the lungs. The estimated activities were compared to the true ones through the assessment of the relative bias (%) defined as follows: $B_r = 100 \times \frac{(A_{true} - A_{est})}{A_{true}}$ where A_{true} represents the true activity of the lungs and A_{est} the estimated activity given by the method.

Table 5.1 documents the experimental counting rate obtained with different configurations of loaded lungs considering the LOAX counting system positioned at 2 cm away from the skin and a measurement time of 45 min. From this table, it is clear that the linearity is respected and that the measurement conditions were faithfully reproduced from one experiment to another; that is the exact same positioning of the detectors and the source. Indeed, for the detector positioned over the right lung, the counting rate when both lungs were loaded together (97.84) is roughly equal to the sum of counts for each lung loaded alone (91.04+4.46=95.50) within 2.4%. This is also the case for the detector positioned over the left lung with a difference of -0.8%. Moreover, it should be noticed that the operated detector positioning limits sensitively the contributions. Indeed, when the detector is over the right lung, 93% of the counts are coming from the right lung. In the case of a detector positioning over the left lung, the latter contributes to about 78% of the counts although the right lung is more active.

Table 5.1. Experimental counting rate (counts/s) of the LOAX detector obtained for the Livermore phantom and different configurations of loaded americium lungs.

Loaded lung		Right & Left	Right	Left
Detector positioning	Right	97.84	91.04	4.46
	Left	45.86	10.57	35.65

From the data in Table 5.1, the contribution of each organ when loaded alone, i.e. counting efficiency (counts/s/Bq), is first calculated by dividing the experimental counting rate by the activity. Next, Equation 5.5 is written as follows:

$$\begin{pmatrix} 97.84 \\ 45.86 \end{pmatrix} = \begin{pmatrix} 2.63E-03 & 1.73E-04 \\ 3.05E-04 & 1.39E-03 \end{pmatrix} \times \begin{pmatrix} Act_{Right\ Lung} \\ Act_{Left\ Lung} \end{pmatrix}$$

To estimate the activity, this system is inverted and the matrix product is done (cf. Section I.2). In this case, the activity in the right lung was estimated to be about 35.54 kBq while in the left lung it was estimated at 25.26 kBq. These estimates were within -2.7% and 1.8% respectively when compared to the real activity present in the used lungs. This validates the method and demonstrates the feasibility of the separation.

II.2. Parameters investigation

II.2.1. Effect of the detector positioning

To study the importance of the choice and positioning of the detector and its effect on the activity estimation, the LOAX was shifted first over the liver and then over the heart. This positioning is unsuitable for the contamination present in the lungs and the method should clearly reveal an error in the activity estimate.

Table 5.2 documents the experimental counting rate obtained when the counting system was positioned over the heart and liver. Before estimating the activity distribution, the linearity was again verified to validate the reproducibility of the positioning. It was found here that small errors occurred while repositioning the detector or even the lungs as the linearity was guaranteed within 5.2%. However, this error remains reasonable and within the uncertainties on the detectors positioning which can be as high as 9% (Razafindralambo 1995). These measurements can thus be used to give a fairly good estimate of the activity distribution.

Table 5.2. Experimental counting rate (counts/s) obtained for the Livermore phantom and different configurations of loaded Americium lungs with the LOAX detector positioned over the heart and liver.

Loaded lung		Right & Left	Right	Left
Detector positioning	Heart	29.95	25.21	3.18
	Liver	7.02	6.39	0.34

From the data in Table 5.2, Equation 5.5 can be written as follows:

$$\begin{pmatrix} 29.95 \\ 7.02 \end{pmatrix} = \begin{pmatrix} 7.28E-04 & 1.24E-04 \\ 1.85E-04 & 1.32E-05 \end{pmatrix} \times \begin{pmatrix} Act_{Right\ Lung} \\ Act_{Left\ Lung} \end{pmatrix}$$

Similarly, by inverting the system and realizing a simple matrix product the activity in each lung can be estimated. In this case, the activity in the right lung was found to be of about 35.78 kBq while in the left lung it was estimated at 31.38 kBq. This time, the relative bias on the activity estimates was as high as -22% for the left lung. This difference highlights the importance of the operated detector positioning when considering the activity mapping. Nevertheless, the result is somehow disappointing as it shows that it would have been difficult to give a strong and accurate conclusion if the activity in the lungs was really unknown. A negative activity value in one of the lungs or an activity difference between the lungs of orders of magnitudes would have been more decisive results.

II.2.2. Effect of the contamination hypothesis

The method used here to estimate the incorporated activity is totally based on ICRP recommendations giving a general idea on the activity distribution from biokinetic models. However, if these pre-established hypotheses are incorrect, the activity mapping becomes in total disagreement with the true distribution. Here, the method was tested to make sure such crucial errors cannot occur without being noticed and clearly identified.

- **Underestimating the activity distribution**

For the first scenario, let us imagine that one organ is considered to be loaded (hypothesis) while two are actually contaminated. In this case, only one measurement is required to use the equation and estimate the activity.

Let us say the hypothesis is that only the right lung is contaminated. In this case, Equation 5.5 can be written as follows: $(97.84) = (2.63E-03) \times (Act_{Right\ Lung})$

This gives an activity of 37.2 kBq for the right lung with an overestimation of about 7.5%.

Now, let us consider that only the left lung is contaminated and in this case Equation 5.5 becomes: $(45.86) = (3.05E-04) \times (Act_{Left\ Lung})$

This gives an activity of 33.1 kBq for the left lung with an overestimation of about 28.6%.

Considering the operated detector positioning that limit sensitively the contribution of each lung to the total count at a given position (cf. Section II.2.1), it is very difficult in this case to conclude that an error on the activity distribution hypothesis was done.

- **Overestimating the activity distribution**

For the second scenario, let's imagine that both organs are considered to be loaded (hypothesis) while only one is actually contaminated. In this case, two measurements are required to use the equation and estimate the activity.

For the case where the actual contamination was in the right lung only, Equation 5.5 and data from Table 5.1 give the following relation:

$$\begin{pmatrix} 91.04 \\ 10.57 \end{pmatrix} = \begin{pmatrix} 2.63E-03 & 1.73E-04 \\ 3.05E-04 & 1.39E-03 \end{pmatrix} \times \begin{pmatrix} Act_{Right\ Lung} \\ Act_{Left\ Lung} \end{pmatrix}$$

This gives an activity of 34.6 kBq in the right lung while the activity in the left one is almost null. This clearly indicates that the hypothesis on the activity distribution is erroneous.

The same investigation was conducted but this time considering the actual contamination to be in the right lung only. Equation 5.5 and data from Table 5.1 give the following relation:

$$\begin{pmatrix} 4.46 \\ 35.56 \end{pmatrix} = \begin{pmatrix} 2.63E-03 & 1.73E-04 \\ 3.05E-04 & 1.39E-03 \end{pmatrix} \times \begin{pmatrix} Act_{Right\ Lung} \\ Act_{Left\ Lung} \end{pmatrix}$$

This system gives an almost null activity for the right lung which also clearly indicates that the hypothesis on the activity distribution is erroneous and that this organ is not contaminated.

II.2.3. Effect of a perturbation point source

To further investigate the effectiveness of the method when determining the activity distribution, a point source of 41.7 kBq was added in the phantom to bias the measurement. This point source can represent an old contamination or even a contaminated lymph node that was not considered in the contamination hypothesis.

• Measurement biasing

Two different positions of the point source were considered. In the first case, the perturbation point source was inserted in the Livermore phantom at the level of the heart to significantly bias the measurements (cf. Table 5.3). In the second case, however, the point source was shifted away from the detectors towards the liver (cf. Table 5.4).

Table 5.3. Experimental counting rate of the LOAX detector obtained for the Livermore phantom and different configurations of loaded americium lungs by adding a perturbation point source at the level of the heart.

Loaded lung		Right & Left	Right	Left	Punct. Src. heart
Detector positioning	Right	116.92	109.99	23.74	22.57
	Left	52.78	17.27	42.00	6.99
	Heart	45.79	19.92	43.85	16.27
	Liver	11.33	11.83	5.33	4.98

Table 5.4. Experimental counting rate of the LOAX detector obtained for the Livermore phantom and different configurations of loaded americium lungs by adding a point source at the level of the liver.

Loaded lung		Right & Left	Right	Left	Punct. Src. liver
Detector positioning	Right	96.65	93.17	6.81	2.15
	Left	46.07	10.91	36.79	0.49
	Heart	35.09	9.17	31.05	5.75
	Liver	24.97	25.3	19.57	18.20

- **Lung activity estimate biasing**

For the case when the point source was positioned at the level of the heart, Equation 5.5 and data from Table 5.3 give the following relation:

$$\begin{pmatrix} 116.92 \\ 52.78 \end{pmatrix} = \begin{pmatrix} 2.63E-03 & 1.73E-04 \\ 3.05E-04 & 1.39E-03 \end{pmatrix} \times \begin{pmatrix} Act_{Right\ Lung} \\ Act_{Left\ Lung} \end{pmatrix}$$

This system gives an activity of 42.57 kBq in the right lung while the activity in the left one is about 28.7 kBq. This indicates that the perturbation source has significantly biased the interpretation of measurements since the relative error on the right lung activity was about -23% (against -2.7% in the previous situation without the point source). Nevertheless, this result is also disappointing since it is difficult to clearly identify the presence of such a perturbation source. Indeed, the system does not conclude to abnormal results, such as a negative activity in one organ for example, which makes it difficult to say if the estimated activity distribution is correct or not.

For the case where the point source was positioned at the level of the liver, Equation 5.5 and data from Table 5.4 give the following relation:

$$\begin{pmatrix} 96.65 \\ 46.07 \end{pmatrix} = \begin{pmatrix} 2.63E-03 & 1.73E-04 \\ 3.05E-04 & 1.39E-03 \end{pmatrix} \times \begin{pmatrix} Act_{Right\ Lung} \\ Act_{Left\ Lung} \end{pmatrix}$$

This gives an activity of 35.07 kBq in the right lung while the activity in the left one is 25.51 kBq according to this system. The activity estimates remain within -1.3% for the right lung and 0.8% for the left lung from the true lung activities. From this result, it is difficult to even notice the presence of such a perturbation source since the latter did not significantly bias the measurement as it is located far away from the detector.

- **Activity estimation of the perturbation source**

To estimate the activity of the perturbation source, a system of three equations with three unknown variables is defined. The experimental measurement obtained when the detector was positioned over the point source was thus added to the previous matrix to get the necessary three dimensional system.

First, for the case when the point source was positioned at the level of the heart, Equation 5.5 and data from Table 5.3 give the following relation:

$$\begin{pmatrix} 116.92 \\ 52.78 \\ 45.79 \end{pmatrix} = \begin{pmatrix} 2.63E-03 & 1.73E-04 & 5.42E-04 \\ 3.05E-04 & 1.39E-03 & 1.68E-04 \\ 7.28E-04 & 1.24E-04 & 3.90E-04 \end{pmatrix} \times \begin{pmatrix} Act_{Right\ Lung} \\ Act_{Left\ Lung} \\ Act_{Pct.\ Src.\ Heart} \end{pmatrix}$$

This system gives an activity of 32.95 kBq in the right lung, 25.03 kBq in the left lung and around 47.88 kBq in the point source. The relative bias is thus about 4.8% on the right lung, 2.7% on the left lung activity and -27.3% for the point source.

Next, when the point source was positioned at the level of the liver, Equation 5.5 and data from Table 5.4 give the following relation:

$$\begin{pmatrix} 96.65 \\ 46.07 \\ 24.97 \end{pmatrix} = \begin{pmatrix} 2.63E-03 & 1.73E-04 & 5.15E-05 \\ 3.05E-04 & 1.39E-03 & 1.16E-05 \\ 7.28E-04 & 1.24E-04 & 4.37E-04 \end{pmatrix} \times \begin{pmatrix} Act_{Right\ Lung} \\ Act_{Left\ Lung} \\ Act_{Pct.\ Src.\ Liver} \end{pmatrix}$$

In this case, the activity in the right lung is estimated to be about 34.26 kBq, 25.34 kBq in the left lung and around 41.93 kBq in the point source. Meanwhile, the relative bias on the activity estimate is thus about 1 % on the right lung, 1.5% on the left lung activity and -11.5% for the point source.

Finally, the effect of detectors' positioning on activity estimation in the lungs and the perturbation point source was studied. In this case, the investigation focuses on determining if an operated bad detector positioning would be certainly noticeable. For example, the activity was estimated while using the data measured when the detector was positioned over the liver while the point source was set at the level of the heart. In this case, Equation 5.5 and the values from Table 5.3 give the following system:

$$\begin{pmatrix} 96.65 \\ 46.07 \\ 24.97 \end{pmatrix} = \begin{pmatrix} 2.63E-03 & 1.73E-04 & 5.42E-04 \\ 3.05E-04 & 1.39E-03 & 1.68E-04 \\ 7.28E-04 & 1.24E-04 & 3.90E-04 \end{pmatrix} \times \begin{pmatrix} Act_{Right\ Lung} \\ Act_{Left\ Lung} \\ Act_{Pct.\ Src.\ Liver} \end{pmatrix}$$

From this system, a negative activity is estimated in the right lung which definitely proves the importance of detectors' setup and positioning to monitor at best the contaminated organs.

As a partial conclusion, it was noticed that the activity estimate was biased by the presence of the perturbation point source. Nonetheless, the results remain insufficient since it was very difficult to conclude of the presence of such a point source. Moreover, determining the activity of the point source was delicate and the positioning of the detector facing the perturbation source has proven to be crucial. Therefore, we recommend conducting systematically 4 to 5 measurements with different detector positioning to correctly handle such situations.

III. Method validation with MC simulations

When determining the activity distribution for a contaminated worker, the physical separation of each organ's contribution is impossible. Monte Carlo simulations were thus introduced to estimate the contribution of each organ and to determine the activity mapping.

Before extrapolating to a worker, the MC simulation results were validated through a comparison between the calculated contributions and the experimental ones obtained with the Livermore measurements. The steps include a faithful reproduction of the conducted *in vivo* measurements and the calculation of the organ-contribution matrix for each considered detector positioning.

III.1. Reproducing *in vivo* measurements

Monte Carlo simulations of the experimental *in vivo* measurements were carried out with a voxelized model of the Livermore phantom, created from CT scan images of the mannequin, and with a validated model of the detectors.

To correctly apply the separation method, the experimental detector positioning must be correctly reproduced in the MC calculations. Therefore, the various reference points of the shielded measurement chamber were carefully used to determine the exact position of the detector facing the phantom. During these experiments, the Livermore phantom was positioned over a graph paper on which the outline of the mannequin is marked (cf. Figure 5.5). The basis of the MCNPX model of the phantom was aligned with the origin of the used graph paper. The LOAX detector was first positioned over the right lung at (16.3; 25.9; 21) and then over the left lung at (31.3; 25.9; 21). This identical detector positioning was next used for MC simulations since no detector inclinations and tilts were operated (cf. Figure 5.4).

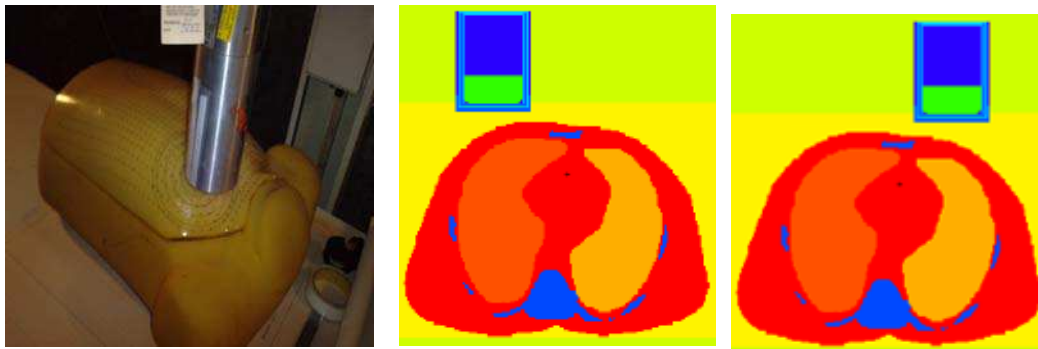


Figure 5.4. Visualization of the LOAX experimental positioning (left) and of the MCNPX simulated one (right).

For each detector positioning, simulations were conducted by loading each lung alone since only the matrix of organ contributions was required. The simulation results give the number of counts collected in the detectors and normalized per starting particles, i.e. the counting efficiency in counts/ γ . This efficiency should be multiplied by the yield to obtain the efficiency in counts/Bq to be used directly in the system. The total number of starting particles was chosen so that the statistical relative error remains always below 1%. Table 5.5 documents the simulation results for the considered detector positioning and loaded lungs. The data given in this table replaces the contribution matrix obtained with the physical separation of the counts since simulations are the only mean available when estimating the contamination of a worker.

Table 5.5. Simulated counting efficiencies (counts/Bq) for the considered detector positioning and the two configurations of loaded Americium lungs.

Loaded lung		Right	Left
Detector positioning	Right	2.73E-03	1.96E-04
	Left	5.17E-04	1.38E-03

III.2. Activity estimation from simulations

From the data in Table 5.1 and the simulation results of Table 5.5, Equation 5.5 can be written as follows:

$$\begin{pmatrix} 97.84 \\ 45.86 \end{pmatrix} = \begin{pmatrix} 2.73E-03 & 1.96E-04 \\ 5.17E-04 & 1.38E-03 \end{pmatrix} \times \begin{pmatrix} Act_{Right\ Lung} \\ Act_{Left\ Lung} \end{pmatrix}$$

This system gives an activity of 34.38 kBq in the right lung and of about 20.35 kBq in the left lung. The relative bias is thus about 0.7% on the right lung activity while it is as high as 20.6% on the left lung activity.

The observed relative bias on activity estimate is mainly due to cross fire situations when the detector is not aligned with the loaded lung. In this case, simulations are overestimating the count up to a factor of 1.7 (i.e. 70%) for the left lung positioning of the detector and the right loaded lung configuration (5.17E-04 against 3.05E-04 for measurements cf. Section II.1). This error can have two origins: a shift in the detector positioning and/or an error in the detector modeling. The effect of each of these two parameters was thus investigated to improve the agreement between simulations and measurements.

III.2.1. Optimizing the detector positioning

To study the effect of detector positioning on cross fire counting efficiency, several simulations were run while varying each of the coordinates. For this case, ± 5 mm shifts were progressively tested in each direction (X = right to left side of the phantom, Y = back to front of the phantom and Z = head to feet). First, shifts in the Y direction were considered alone since this was the only parameter that was modified to bring the detectors away from the phantom when exchanging the contaminated lungs. A slight error could have been done while repositioning the detectors at the primary settings. Nevertheless, the simulation results did not concur with the measurements when only the Y direction was considered and shifts in the X and Z directions were found to be necessary. Table 5.6 documents the simulated efficiency values and the difference between the measurement results for various detector positions.

Table 5.6. Effect of the errors in the detector positioning on the simulated counting efficiency for cross fire situations.

Coordinates			Right Lung loaded		Coordinates			Left Lung loaded	
X	Y	Z	Efficiency (counts/Bq)	Diff. (%)	X	Y	Z	Efficiency (counts/Bq)	Diff. (%)
31.3	26.4	21	5.27E-04	-72.46	16.3	26.4	21	1.99E-04	-14.87
31.3	26.9	21	5.41E-04	-77.21	16.3	26.9	21	1.97E-04	-13.58
31.3	25.9	20.5	4.77E-04	-56.27	16.3	25.9	20.5	2.03E-04	-17.11
31.3	25.9	21.5	5.03E-04	-64.76	16.3	25.9	21.5	1.87E-04	-8.20
31.8	25.9	21	4.74E-04	-55.32	15.8	25.9	21	1.83E-04	-5.36
32.3	25.9	21	4.29E-04	-40.50	15.3	25.9	21	1.76E-04	-1.47

These results prove the simulations to be directly related to the operated detector positioning with the left-right direction being the major parameter influencing the cross fire counts. For

the detector over the right lung and left lung cross fire situation, small shifts in the X (-0.8 cm) and Y (+0.25 cm) directions reduced the difference on the efficiency value to -1.35%. However, for the left lung positioning, the primary relative bias was as high as -70% thus leading to higher operated shifts. Indeed, to bring the agreement to within -1.9%, a shift of 2.5 cm in the X direction and of 1 cm in the Z direction was necessary.

As a partial conclusion, errors of few millimeters on the detector positioning can be considered reasonable and may be made unintentionally during experiments. However, higher errors involving several centimeters of shift from the original position are totally unacceptable. For this reason, reviewing the detector model seems necessary to try to explain the observed differences between simulations and measurements for cross fire situations.

III.2.2. Improving the MCNPX model of detectors

In order to further improve the agreement between simulations and measurements, the thickness of the side dead layer was modified. As the thickness increases, lesser particles would get to the active cells of the detector and fewer counts would thus be collected in the case of cross fire situations when the detector is not aligned with the contaminated organ.

The side dead layer thickness in the primary model of the LOAX detector was of 1 μm , this latter was increased to 5, 10, 20 and 25 μm . Table 5.7 documents the simulated efficiency values and the difference between the measurement results for various side dead layer thicknesses and cross fire situations. This table indicates that the thickness of the side dead layer has limited effect on the counts. Indeed, an increase of the side dead layer thickness by a factor 25 decreases the efficiency by about 3%. It seems thus that the efficiency drop is due to a decrease in the crystal volume rather than a decrease in the cross fire contributions. In addition, the aluminum cap surrounding the detectors is apparently sufficient to stop most cross fire photons from getting to the crystal at the considered americium energy. This suggests that additional parameters, such as tangent counts for example, should also be taken into account. It is hence most likely necessary to adapt the front dead layer thickness not only for direct measurements but also for cross fire counts. To further improve the detector modeling, new measurements are thus required with the use of point sources located off axis to account for cross fire counts. However, this work was not fulfilled since the detector went out of service and the available time after repair was insufficient for a complete remodeling.

Table 5.7. Effect of an increase in the side dead layer thickness on the simulated counting efficiency for cross fire situations.

Side dead layer thickness (μm)	Right Lung + Left detector		Left Lung + Right detector	
	Efficiency (counts/Bq)	Diff. (%)	Efficiency (counts/Bq)	Diff. (%)
1	3.21E-04	-5.26	1.83E-04	-5.50
5	3.19E-04	-4.43	1.82E-04	-5.15
10	3.16E-04	-3.56	1.80E-04	-4.15
20	3.14E-04	-2.80	1.80E-04	-3.75
25	3.12E-04	-2.26	1.79E-04	-3.34

Nevertheless, the simulation results were considered when using the 25 μm thickness side dead layer and shifted detectors set at (15.8; 26.15; 21) and at (33.8; 25.9; 21.5). In this case, the activity estimate using MC results were again within 5% to the true values.

As a partial conclusion, one can say that the separation method also works when Monte Carlo calculations are used if the experimental measurements are faithfully reproduced and the detectors' model valid. The positioning of the detectors remains the primary parameter affecting the simulation. Nevertheless, it was found that a review of the detector modeling can sometimes be necessary to correctly account for cross fire situations.

IV. Applying the method for different counting systems

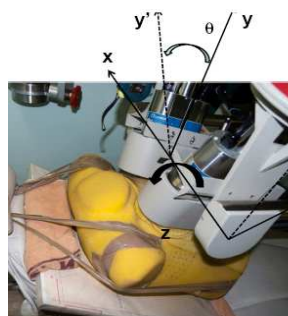
To test the effectiveness of the method in determining the activity distribution, different counting systems with various loaded organs and radionuclides were considered. First, a study using the CIEMAT counting system (Lopez-Ponte and Bravo 2000) with americium and europium lungs was done. In a second study, the KIT system was used with americium lungs and a radioactive liver. This section summarizes the experiments and introduces the main results.

IV.1. Feasibility study with the CIEMAT counting system

IV.1.1. Tools and methods: phantom, source and detectors

For these experiments, the IRSN Livermore phantom was used with CIEMAT lungs containing both americium and europium. Here, we give the results for europium lungs only since americium has been used in the previous set of experiments. The europium activity, on the measurement date, was of 5.02 kBq for the right lung and of 3.59 kBq for the left lung. Because of these low activities, the measurement time was set to one hour to guarantee statistically acceptable results for the 121 keV photons.

The counting system is a four-germanium-detectors system dedicated for *in vivo* lung counting studies. In this system, detectors are grouped in pairs and inserted in a lead shielding to minimize the noise contributions to the count. The Livermore was positioned to represent a person seated upright with a 45% tilted chair. To get closer to real measurements, the counting system was tilted in the head-to-foot and left-to-right directions to maximize the counting and approach the measurement procedure followed at CIEMAT (cf. Figure 5.5).



Tilts	Det. #1 & #2	Det. #3 & #4
XX'	0°	0°
YY'	17°	-15°
ZZ'	12°	14°

Figure 5.5. Visualization and designation of the detectors and their positioning with various angulations to cover at best the lungs.

As the counting system includes an array of four germanium detectors, a single measurement provides four different counting spectra at four positions. In addition, three spectra consisting of the sum of counts of the four detectors and the counts of the left (Det. #1 and #2) and right (Det. #3 and #4) pairs are also given. Therefore, each measurement can be interpreted with as high as 7 different experimental counting rates. As a consequence, multiple estimates of the activity distribution can be given from one measurement.

IV.1.2. Measurement data and linearity check

Table 5.8 documents the experimental counting rate obtained for three configurations of loaded lungs. Meanwhile, Table 5.9 resumes the results of the linearity check which represent, to a certain point, the limits of the activity estimate. Indeed, the minimum error on the activity estimate using this measurement data cannot be less than the error on the linearity. The good linearity values of Table 5.9 indicate that detectors were correctly repositioned at the original setup after exchanging the lungs.

Table 5.8. Experimental counting rate (counts/s) obtained for the CIEMAT four-germanium counting system and different sets of loaded lungs.

Loaded organ		Left & Right lungs	Left lung	Right lung
Experimental counting rate	Sum four detectors	23.94	8.67	15.49
	Sum left pair	14.31	2.04	12.00
	Sum right pair	10.38	6.63	3.54
	Detector 1	7.62	1.16	6.36
	Detector 2	6.17	0.79	5.44
	Detector 3	5.92	3.91	1.78
	Detector 4	4.37	2.82	1.66

Table 5.9. Linearity check for the CIEMAT system and the operated detector positioning.

Detector	Sum four det.	Sum left pair	Sum right pair	Det. #1	Det. #2	Det. #3	Det. #4
Linearity error (%)	-0.96	1.88	2.02	1.38	-0.92	3.92	-2.55

IV.1.3. Activity estimation from measurements

To create a system of two equations with two unknown activity values, two experimental counting rates at two different detector positions are required. Equation 5.5 used with the data from Table 5.8 gives multiple possibilities to estimate the activity.

First, using the experimental counts from each pair of detectors, the system is as follows:

$$\begin{pmatrix} 14.31 \\ 10.38 \end{pmatrix} = \begin{pmatrix} 2.39E-03 & 5.68E-04 \\ 7.04E-04 & 1.85E-03 \end{pmatrix} \times \begin{pmatrix} Act_{Right\ Lung} \\ Act_{Left\ Lung} \end{pmatrix}$$

This gives an activity in the right lung of about 5.11 kBq and in the left one about 3.67 kBq. These values are within -2.2% from the true values validating the separation method for the CIEMAT counting system. It should be noticed that the error on the activity estimate is, as expected, of the same order of magnitude as the error on the linearity of the measurements.

Table 5.10 documents the activity estimation results when different experimental measurements with several detector positions are used. These results prove that, for the method to work, detector positioning should be carefully chosen. Indeed, from this table, it is clear that crucial errors, up to 75%, can be made when estimating the activity distribution if the detectors positioning is not adapted to the actual location of the contamination. In this case, the contribution of one organ is dominant when compared to others and thus the method fails to give satisfying activity estimates for the organs having the lowest contributions.

Table 5.10. Activity estimates and differences to reference values for various combinations of detectors' counts.

Detectors combination	Act. Right Lung (kBq)	Diff. (%)	Act. Left Lung (kBq)	Diff. (%)
Det. #1 – Det. #2	4.43	11.8	6.25	-74.1
Det. #1 – Det. #3	5.05	-0.6	3.80	-5.6
Det. #1 – Det. #4	5.15	-2.7	3.40	5.5
Det. #2 – Det. #3	4.92	2.0	3.84	-6.9
Det. #2 – Det. #4	4.99	0.5	3.46	3.6
Det. #3 – Det. #4	1.26	74.9	5.03	-40.1

IV.1.4. Activity estimation from Monte Carlo simulations

- **Reproducing the experiments and detectors setup**

MC simulations were used to estimate the contribution of each organ to the count. To correctly do this, the experimental setup was faithfully reproduced. In this particular study, both the detectors and phantom were tilted to reproduce the typical *in vivo* measurement protocol used at CIEMAT. This setup is far more complex than the previous one (realized at IRSN) and requires careful angular calculation and definition using the MCNPX translation card. Moreover, to faithfully reproduce the measurements, the detector modeling was reviewed. Indeed, the used detectors are mounted within a lead shielding which sensitively reduces cross fire contribution. However, the existing model was given without the shielding. The latter was thus modeled with MCNPX. Figure 5.6 represents the MCNPX translation card with a visual of the lower pair of detectors realized using the MCNPX plotter.

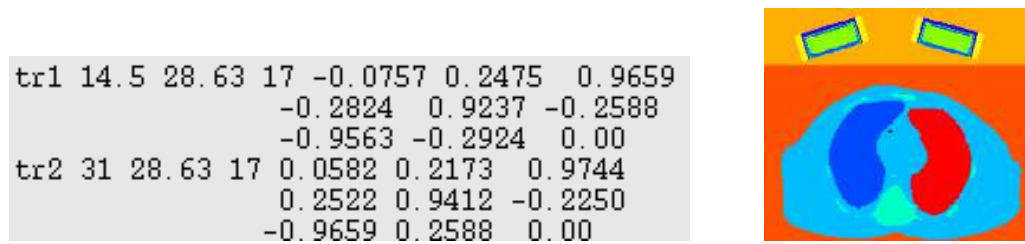


Figure 5.6. MCNPX translation card and visualization of the lower pair positioning (shielding in yellow).

Table 5.11 documents the simulation results obtained for each of the four germanium detectors and europium lungs. This table clearly indicates that sensitive positioning errors were done when reproducing the measurement conditions. This calls into question the method used to determine the experimental positioning although strong effort was done to correctly assess the coordinates and tilts of each detector. This is mainly due to the fact that positioning measurements were taken with reference to the shielded chamber and not the phantom itself.

Table 5.11. Simulated counting efficiency for the CIEMAT detectors and difference to reference values.

	Detector #1		Detector #2		Detector #3		Detector #4	
	Efficiency (counts/Bq)	Diff. (%)	Efficiency (counts/Bq)	Diff. (%)	Efficiency (counts/Bq)	Diff. (%)	Efficiency (counts/Bq)	Diff. (%)
Right lung	1.38E-03	-8.7	1.18E-03	-8.9	4.72E-04	-33.1	3.56E-04	-7.7
Left lung	1.83E-04	43.2	1.02E-04	53.5	9.63E-04	11.3	5.06E-04	35.6

• Activity calculation and comparison to real a one

The experimental counting rates are used to give the overall counts of the detectors while MC simulations give the contribution of each loaded organ. Considering again the count of the right and left pairs of detectors, the system can be written as follows:

$$\begin{pmatrix} 14.31 \\ 10.38 \end{pmatrix} = \begin{pmatrix} 2.56E-03 & 2.85E-04 \\ 8.28E-04 & 1.47E-03 \end{pmatrix} \times \begin{pmatrix} Act_{Right\ Lung} \\ Act_{Left\ Lung} \end{pmatrix}$$

This gives an activity in the right lung of about 5.13 kBq and in the left one about 4.17 kBq. These values implicate a relative bias of about -16% for the left lung activity estimate. When comparing the simulation results in Table 5.11 to the measured values of Table 5.8, substantial differences are noticed. Indeed, the error is not only due to cross fire contributions but also to direct situations where the detector is aligned with the loaded organ. Thus, detectors' positioning should be improved to optimize the activity distribution assessment.

• Detector positioning improvement

To render the simulations more realistic, the work focused on repositioning the detectors to improve the correspondence between simulations and measurements. Considering the data in Table 5.11, detectors #1 and #2 are found to have similar differences to the measurement results. This indicates that an adjustment in the detector positioning should similarly affect the two detectors and contribute to improve the agreement between simulations and measurements. However, for detectors #3 and #4, the error is not equally balanced between

the two detectors. This indicates that a probable error on the operated tilt was done along with the positioning mismatch. Therefore, to study the effect of detector positioning on counting efficiency, shifts in each of the three directions were first operated and then small variations in the tilts were tested (in the head-to-feet and left-to-right directions).

Appendix D.1 documents the simulated efficiency values of the four detectors and the differences to measurements. These results prove the complexity of the used detector positioning and the errors inherent to the method used to record the experimental positions. Besides, it was noticed that when a positioning improved the agreement for the right lung configuration, the results were far from being acceptable when the left lung was used alone (and vice-versa). Thus, detector positioning was fixed for each configuration independently to guarantee an agreement between simulations and measurements within 5%. For the left pair (detector #1 and #2) and the right lung configuration, retrieving the detectors by 0.5 cm (in the Y direction) was enough. In this case, the final positioning was (14.5; 29.13; 17) and the original tilts were maintained (17° in the head-to-feet direction and 12° in the left-to-right direction). However, for the right pair (detectors #3 and #4) and the right lung configuration, the final positioning was set at (32.5; 28.63; 15) and the tilts were (19°; -15°). Meanwhile, for the left lung configuration, detectors #1 and #2 were set at (18.5; 28.63; 13) with the original tilts (17°; 12°); whereas detectors #3 and #4 were finally positioned at (34.5; 27.13; 15) and the original tilts were maintained (14°; -15°).

With this improved positioning of detectors, the measurement results and Equation 5.3, the right and left lung activity estimates were within 3.7% to the true values using detectors 2 and 4 data. This partially validates Monte Carlo calculations as a tool to determine the contribution of each contaminated organ to the count. However, since the detector positioning required sensitive reconsiderations, no further simulations of the CIEMAT measurements were considered. Meanwhile, it should be noticed that the available CIEMAT model of detectors did not include any side dead layer. Nevertheless, the adding of a side dead layer was considered to remain of limited interest because of the shielding surrounding the detectors and no detector modeling corrections were undertaken for these experiments.

To conclude, the detector positioning used in this study is the routine *in vivo* positioning protocol used at CIEMAT and maximizes the counts since detectors cover at best the lungs. Nevertheless, this positioning revealed to be very complex and difficult to reproduce using MC simulations. Therefore, it is preferable to use simple and easy to reproduce detector positioning whenever it is necessary to use the developed method with MC simulations in order to determine the activity distribution. In addition, measurement uncertainties including those on the source activity and measurement statistics should also be considered with caution when comparing simulation results to measurement.

IV.1.5. Investigating the effect of a perturbation source

Next, a 30.5 kBq ^{152}Eu point source was added to bias the count and to study the effect of such a perturbation on the activity mapping. For each detector positioning, 3 measurements were done with different configurations of loaded lungs and a perturbation point source.

- **Measurements with a perturbation point source**

At first, the point source was positioned on the left side of the phantom at the level of the liver relatively away from the detectors (cf. Figure 5.7). This positioning was operated because of the huge activity of the perturbation source (30.5 kBq) when compared to the activity of the lungs (no more than 9 kBq for both lungs together). It was believed here that such a positioning would bias the result while remaining roughly acceptable; that is a contribution of no more than 30% to the count.



Figure 5.7. Operated positioning of the ^{152}Eu point source on the left and right side of the phantom at the level of the liver.

Table 5.12 gives the experimental counting rates obtained with the point source and different combinations of radioactive lungs. A simple comparison with the data of Table 5.8 gives the effect of the perturbation source and its contribution to the counts. For example, when the left lung was loaded alone, the point source brought about 48% of the counts collected in detector #4 which was set directly over this lung.

Table 5.12. Experimental counting rate (counts/s) obtained for the CIEMAT four-germanium counting system and different sets of loaded lungs with the adding of the point source on the left side of the phantom.

Loaded organ		Left & Right lungs + Pt. Src.	Left lung + Pt. Src.	Right lung + Pt. Src.
Experimental counting rate	Sum four detectors	29.45	13.45	20.79
	Sum left pair	15.23	3.09	13.19
	Sum right pair	14.00	10.37	7.22
	Detector 1	7.91	1.49	6.77
	Detector 2	7.08	1.62	6.34
	Detector 3	6.79	5.12	2.82
	Detector 4	7.17	5.44	4.35

In a second step, the source was shifted to the right side of the phantom and maintained at the level of the liver (cf. Figure 5.8). Similarly, Table 5.13 gives the experimental counting rates and indicates the effect of the perturbation source with the new positioning and its relative contribution to the counts.

Table 5.13. Experimental counting rate (counts/s) obtained for the CIEMAT four-germanium counting system and different sets of loaded lungs with the adding of the point source on the right side of the phantom.

Loaded Organ		Left & Right lungs + Pt. Src.	Left lung + Pt. Src.	Right lung + Pt. Src.
Experimental counting rate	Sum four detectors	29.16	13.64	19.67
	Sum left pair	17.31	5.81	15.15
	Sum right pair	11.45	8.30	4.51
	Detector 1	9.11	2.59	7.61
	Detector 2	8.52	3.15	7.35
	Detector 3	6.38	4.31	2.07
	Detector 4	5.15	3.77	2.64

- **Activity estimate with the perturbation source**

From the data of the left (Det. #1 and #2) and right (Det. #3 and #4) pairs of detectors given in Table 5.12, Equation 5.5 can be written as follows:

$$\begin{pmatrix} 15.23 \\ 14.00 \end{pmatrix} = \begin{pmatrix} 2.39E-03 & 5.68E-04 \\ 7.04E-04 & 1.85E-03 \end{pmatrix} \times \begin{pmatrix} Act_{Right\ Lung} \\ Act_{Left\ Lung} \end{pmatrix}$$

This system gives an activity of 5.03 kBq in the right lung and of about 2.34 kBq in the left lung. The relative bias is thus about -0.25% on the right lung activity while it is as high as 34.8% on the left lung activity. In this case, the point source was positioned at the left side of the phantom and therefore the main biasing came for the left lung. Table 5.14 documents the activity estimation results for the different combinations of detectors with the perturbation point source positioned at the left side of the phantom. The similar method was followed to determine the impact of a change in the point source positioning on the activity estimate. Table 5.15 documents these results and clearly indicates that the activity estimate was mainly biased for the lung located on the same side of the point source.

Finally, the point source activity estimate was investigated. The obtained results show that negative activity values can be obtained for the point source when using detectors 2 and 4 (lower pairs) which are highly biased by the presence of such perturbation source.

Table 5.14. Impact of different possible combinations of detectors on the activity estimates and on their differences to the reference values when a point source was added on the left side of the phantom.

Detectors combination	Act. Right Lung (kBq)	Diff. (%)	Act. Left Lung (kBq)	Diff. (%)
Det. #1 – Det. #2	7.49	-49.25	-5.29	247.22
Det. #1 – Det. #3	5.00	0.32	2.80	22.22

Det. #1 – Det. #4	5.35	-6.53	1.68	53.32
Det. #2 – Det. #3	4.55	9.41	2.98	17.21
Det. #2 – Det. #4	4.92	1.92	1.92	46.57
Det. #3 – Det. #4	-1.95	103.88	4.85	-34.92

Table 5.15. Impact of different possible combinations of detectors on the activity estimates and on their differences to the reference values when a point source was added on the right side of the phantom.

Detectors combination	Act. Right Lung (kBq)	Diff. (%)	Act. Left Lung (kBq)	Diff. (%)
Det. #1+2 – Det. #3+4	3.89	22.57	3.45	4.09
Det. #1 – Det. #2	6.77	-34.90	-1.6	144.53
Det. #1 – Det. #3	4.16	17.02	3.88	-7.93
Det. #1 – Det. #4	4.83	3.80	2.48	30.89
Det. #2 – Det. #3	3.32	33.77	4.17	-15.98
Det. #2 – Det. #4	4.12	17.97	2.84	20.96
Det. #3 – Det. #4	-2.56	150.97	6.19	-72.29

As both experiments realized at IRSN and CIEMAT failed to give satisfying estimates of the perturbation point source activities, one can wonder if this method would still hold when the number of loaded organs increases. Although point sources were glued to the phantom, these could be slightly shifted when repositioning the torso compounds of the Livermore. Thus, it was difficult to make sure that this was not happening and the doubts were increased and even founded when considering the poor linearity of the results obtained each time a point source was introduced (cf. Tables 5.12 and 5.13).

IV.1.6. Activity estimate from other energy lines

The used CIEMAT lungs were loaded with americium and europium at the same time. Therefore, the americium X and gamma emissions were also used to test the effectiveness of the method in determining the activity distribution. These lungs enable a direct and clear comparison of the activity estimates when using different energy lines since for each detector positioning, the acquired counts contained both americium and europium spectra. Appendix D.2 documents the experimental counting rate (counts/s) obtained for the americium lungs. In this case, the determined activity values were in closer agreement when compared to the europium lungs. Indeed, the best activity estimates with europium were within 4% (when using the counts of Det. #2 and #4) while for americium the best estimate was within 1.3% (when using the counts of Det. #1 and #4). This is mainly due to the sensitive activity difference between the americium and europium lungs (42 against 9 kBq respectively) which involve higher statistics and thus lesser uncertainties.

IV.2. Feasibility study with the KIT counting system

The method was next tested to ensure its functioning for the counting system of the Karlsruhe Institute for Technology with a different protocol and one additional loaded organ. In this case, if the method works with three loaded organs then it will be considered to hold for as many organs as necessary.

IV.2.1. Tools and methods: phantom, source and detectors

The Livermore phantom was also used in this study with a set of americium lungs of 49 kBq and 36 kBq for the right and left lung respectively and a liver of 85 kBq. Moreover, a point source of 37.6 kBq was added to bias the measurements and quantify the impact on the activity estimate. A voxelized model of the Livermore phantom with its various organs is available for MC simulations.

Furthermore, a high purity germanium counting system was used for these measurements. The positioning of the detectors was carefully studied to find the most appropriate positions for an optimal separation of the contribution of each organ. Consequently, the distributions of the particle tracks were simulated for each organ loaded alone using a Mesh-based MCNPX tally calculation. Then, the tracks were plotted using the ParaView (<http://www.paraview.org/>) data analysis and visualization platform. The positioning of the detector was chosen so that the number of particles coming from each organ was fixed. For example, the detector was aligned over the liver in order to have 80% of the photons coming from this organ, 15% coming from the right lung and 5% only from the left lung (Figure 5.8). Similar operations were made to choose an accurate and appropriate positioning for the detector when facing the right and left lungs. Finally, a MCNPX model of the used detector previously validated (Marzocchi et al. 2010) was used for this study.

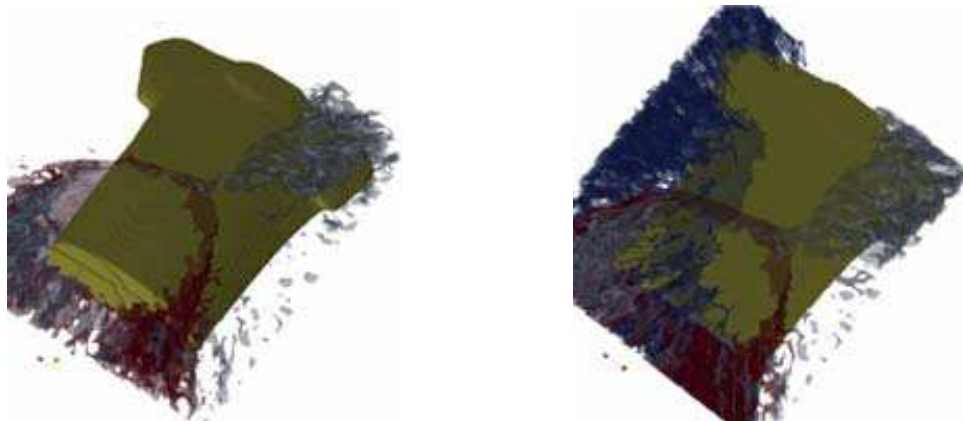


Figure 5.8. Plot of particles tracks with the ParaView software representing different organ contribution curves: Left: Liver and right lung with 80-15% proportion; Right: Liver, right lung and left lung with 80-15-5% proportion.

IV.2.2. Measurement data and linearity check

Table 5.16 documents the experimental counting rate (counts/s) obtained for the three configurations of loaded lungs. The linearity check was again conducted before using this measurement data to estimate the activity distribution.

Table 5.16. Experimental counting rate (counts/s) obtained at KIT for different detector positioning and various organ configurations.

Loaded organ		Liver, Right Lung and Left lung	Liver	Right Lung	Left Lung
Detector positioning	Liver	182.42	150.59	28.18	2.72
	Right	147.05	28.68	108.55	11.15
	Left	85.50	15.46	21.39	50.48

The linearity was guaranteed within 3% (cf. Table 5.17) indicating that small errors have occurred while repositioning the detectors. These errors remain negligible and the measurements were used to obtain the activity distribution.

Table 5.17. Linearity check for the KIT system and the operated detector positioning.

Detector positioning	Liver	Right lung	Left Lung
Linearity error (%)	0.51	-0.90	-2.14

IV.2.3. Activity estimation from measurements

From the data in Table 5.16, Equation 5.5 can be written as follows:

$$\begin{pmatrix} 182.42 \\ 147.05 \\ 85.50 \end{pmatrix} = \begin{pmatrix} 1.77E-03 & 5.75E-04 & 7.57E-05 \\ 3.37E-04 & 2.22E-03 & 3.10E-04 \\ 1.82E-04 & 4.36E-04 & 1.40E-03 \end{pmatrix} \times \begin{pmatrix} Act_{Liver} \\ Act_{Right Lung} \\ Act_{Left Lung} \end{pmatrix}$$

This system gives an activity of 85.75 kBq for the liver with an error of -0.9% when compared to the actual activity present in the liver. Meanwhile, for the right lung, the activity is estimated to be about 48.46 kBq (difference of 1.1% to the true value) and for the left lung 34.76 kBq (difference of 3.4% to the true value).

These results clearly indicate the successful application of this method when considering a different counting system, positioning and a different set of contaminated organs with various activities and contributions. As the method was demonstrated to work with two and three organs, it is expected here that it would also hold for situations involving even a higher number of contaminated organs.

IV.2.4. Activity estimation from Monte Carlo simulations

MC simulations were again used to estimate the contributions of each organ by reproducing the experimental setup. In this particular study, the positioning of the detector over the phantom was recorded using devoted position sensors available in the shielded chamber. This should significantly improve the precision when taking the positioning and would contribute to obtain better results. Table 5.18 documents the simulated contributions for the KIT system.

Table 5.18. Simulated counting efficiencies (counts/Bq) obtained at KIT for different detector positioning and various organ configurations.

Loaded organ		Liver	Right Lung	Left Lung
Detector positioning	Liver	1.57E-03	4.28E-04	2.36E-05
	Right	2.88E-04	1.85E-03	2.47E-04
	Left	1.51E-04	3.30E-04	1.20E-03

From the experimental data in Table 5.16, the simulation results presented in Table 5.18 and Equation 5.5, the liver activity was estimated to be about 99.67 kBq. The activity of the right lung was found to be about 58.27 kBq while the left lung contained 42.68 kBq. These involve differences to the reference values of about -17.25% for the liver, -18.93% for the right lung and -18.56% for the left lung.

Although a sophisticated system was used to locate the detector over the phantom, sensitive differences were observed when comparing the measured contribution matrix to the simulated one and not only for cross fire situations but also for direct simulations (source-detector aligned). This was extremely disappointing and indicates a necessary to reinvestigate the effect on counting efficiency of both the MCNPX model of the detector and its positioning.

- **Improving the detector positioning**

In the case of the KIT measurements, a simplified detector positioning was operated with no inclinations or tilts. Therefore, the work focused on repositioning the detectors to improve the correspondence between simulations and measurements by operating multiple shifts in each of the directions.

Appendix D.3 documents the simulated efficiency values of the detector at the different tested positions and the differences when compared to measurements. In this case, it was shown that shifts of 3 to 6 cm were sometimes necessary to bring the agreements to within 5%. Such changes remain unrealistic and unacceptable and question the validity of the detector model.

- **Improving the detector model**

The simulation disagreement with measurements revokes the validity of the used detector model although the latter was reviewed and upgraded using a CT scan of the detector compounds. Therefore, point source experiments with eccentric detector positioning were considered and measurements were done. In this case, the source-detector distance was set at 15 cm and the point source was shifted up to 25 cm off axis. Then, the same experiments were simulated with the detector model and calculated efficiencies were compared to the measured values. The first results show that the side dead layer thickness should be increased from 0.6 to 1 mm to guarantee a relative bias within 2% for cross fire simulations. Further investigations are necessary to fully explain the observed differences. Indeed, different source-detector distance should be considered and the point source validated model should also be tested for the phantom before considering a validation (Bremaud 2011).

IV.2.5. Investigating the effect of a perturbation source

A perturbation source was next added to bias the measurement and study its effect on activity determination. This perturbation source was positioned on the basis of the heart (cf. Figure

5.9) to simulate a contaminated lymphatic node which was not taken into account when considering the hypothesis on activity distribution. This positioning was chosen again using the ParaView platform (<http://www.paraview.org/>). The MC Mesh tally track simulation helped assessing the point for which each organ equally contributes to the count (33% of the total counts). When the perturbation source was positioned at this particular point, it equally biases the measurements for any detector positioning. Table 5.19 documents the experimental counting rate (counts/s) obtained for the three configurations of loaded lungs when the point source was added.



Figure 5.9. Positioning of the point perturbation source operated at KIT. Left: simulated tracks to determine the position for which there is an equal contribution of each organ; Right: positioning within the Livermore phantom.

Table 5.19. Experimental counting rate (counts/s) obtained at KIT for various organ configurations when the point source was added.

Loaded organ		Liver, Right Lung, and Left lung	Liver	Right Lung	Left Lung
Detector positioning	Liver	189.03	154.61	31.27	9.24
	Right	150.67	34.08	116.19	16.51
	Left	92.02	22.03	27.45	56.88

From this table and using Equation 5.5, the liver activity was estimated to be about 89.1 kBq while for the right lung it was found to be about 49 kBq and about 38.8 kBq for the left lung. These activity estimates involve differences to the reference values of about -4.9% for the liver, below -0.1% on the right lung and about -7.8% for the left lung. The point source activity is comparable to the ones of the used lungs and was thus expected to lead to far more conclusive results. Moreover, the point source was carefully positioned so that it significantly biases the results for the operated detector positioning but this was not fulfilled either. Indeed, Table 5.19 indicates that the introduced point source induced only a 3.5% increase in the number of counts per second for the liver detector positioning. This increase was about 7.6% for the left lung, and only 2% for the right lung. This explains the small effect on the right lung and liver activity estimates and the more sensitive effect on the left lung activity estimate. The positioning of the source was incorrect since it did not equally bias the counts.

IV.2.6. Alternative detector positioning

In the previous studies, detectors' positioning was changed to simulate an erroneous setup and study its effect on the count. In this case however, a second detector was used simultaneously while realizing experiments and an alternative positioning was operated with the detector set on the side of the phantom (cf. Figure 5.10). The detector was hence positioned facing the

loaded organ on the right side of the phantom within few centimeters from the skin first near the liver then near the right lung and finally on the left side of the phantom facing the left lung. Table 5.21 documents the experimental counting rate (counts/s) obtained for the three configurations of loaded lungs and the second detector.



Figure 5.10. Detectors positioning operated at KIT.

Table 5.20. Experimental counting rate (counts/s) obtained at KIT for the new detector positioning and the various configurations of loaded organs.

Loaded organ	Liver, Right Lung, and Left lung	Liver	Right Lung	Left Lung	
Detector positioning	Liver	255.94	187.03	70.44	2.13
	Right	177.94	46.68	126.58	7.10
	Left	80.25	15.98	5.33	58.62

From this table and Equation 5.5, the system giving the activity distribution can be written as:

$$\begin{pmatrix} 255.94 \\ 177.94 \\ 80.25 \end{pmatrix} = \begin{pmatrix} 2.38E-03 & 1.54E-03 & 7.49E-05 \\ 5.49E-04 & 2.58E-03 & 1.97E-04 \\ 1.88E-04 & 1.09E-04 & 1.63E-03 \end{pmatrix} \times \begin{pmatrix} Act_{Liver} \\ Act_{Right Lung} \\ Act_{Left Lung} \end{pmatrix}$$

In this case, the liver activity is estimated to be about 82.8 kBq while for the right lung it is of 48.5 kBq and for the left lung about 36.5 kBq. These involve differences to the reference values of about 2.6% for the liver, 1% on the right lung and -1.3% for the left lung. These values are of the same order of magnitude as those obtained with the previous detector positioning. This indicates that both counting configurations were adapted for the measurements as each detector positioned on top or on the side of the phantom was covering at best the monitored organ and collecting with a good efficiency the emitted radiation.

V. Discussion and Conclusion

This study proved that *in vivo* spectrometry measurements, when combined to MC simulations, is an efficient tool to determine the activity distribution within the body. This is particularly important in the case of complex contaminations and wounds where little information on the intake is available.

To determine the activity distribution inside the body, the developed method uses the mathematical equation relating the experimental count to the activity through the counting efficiency coefficient. This coefficient represents the contribution of each potentially contaminated organ to the count for a given detector positioning. When monitoring a nuclear worker, however, it is impossible to isolate a given organ and to determine the emitted radiation. This is where Monte Carlo simulations come into play to calculate the contribution coefficients.

The feasibility of the method was first experimentally tested using the Livermore phantom that enables a physical separation. The obtained results showed the effectiveness of the method in determining the activity distribution with errors below 5%. Next, the Monte Carlo simulations were used to reproduce the Livermore measurements and validate the calculations as a tool for determining the activity distribution. In this case, the modeling of the detector and its exact positioning over the phantom were found to require additional care. Indeed, the simulation results often showed differences, up to 20%, on the activity estimates. After the correction steps, the simulation results were sensitively improved as the relative bias dropped to within 5%. Finally, the method was tested for different counting systems, different radioactive elements and up to three simultaneously contaminated organs. The obtained results further prove the effectiveness of the method regardless of the measurement protocols. It must be noted that the larger differences on the activity estimates remain of the same order of magnitude as uncertainties usually found for low-energy *in vivo* measurements. A more detailed study on the conditioning of the matrix system, used to assess the activity, could provide more insights into the uncertainty and confidence intervals for the assessed activities.

Moreover, the measurement conditions were investigated by including a study of the impact of a bad detector positioning on the activity estimate, the effect of a perturbation source and also an error on the activity distribution hypothesis based on biokinetic models. Nevertheless, some improvements remain necessary especially concerning the measurements, the choice and positioning of the detector and that of the perturbation source.

V.1. Measurements and MC simulations

For the measurements, special care should be taken into account when exchanging the radioactive organs to guarantee the linearity of the experimental counting rate. Indeed, this check represents to a certain point the lower limit of the error on the activity estimate. Moreover, the positioning of the detector over the phantom or the contaminated worker should be carefully recorded. The use of concrete and reliable anatomical references could sensitively improve the reproducibility of the measurement conditions when running MC simulations.

For the simulations, an accurate reproduction of the measurement conditions and particularly of the detector positioning is essential. The simulation results, in the three cases of this study, have clearly highlighted the impact of the detector positioning on activity estimates since shifts of few centimeters (<3 cm) were equivalent to relative bias of up to 70% on the simulation results (when compared to measurements). Moreover, the modeling of the detector should be carefully revised. Indeed, the use of point sources when characterizing the detector remains insufficient when considering only direct shots and no cross fire situations. Furthermore, a study conducted at LEDI has shown that a detector model with a perfect match

for point sources, i.e. simulation result within 1% of the measurements at the considered energy range, is not always adequate for phantoms (Bremaud 2011). This means that detector modeling can be complex since the user should definitely find a compromise between point source and phantom measurements.

V.2. Choice of the detector and positioning

When adapted experimental measurements are available, the developed method demonstrated a good effectiveness in determining the activity distribution following an internal contamination. The number of measurements, however, should be equal to the number of monitored organs. To reduce the uncertainties due to errors on detector positioning, it would be even better to use several counting configurations to process the results of several experiments. Indeed, the higher the counting statistics were, the better the activity estimates agreed with the true values and thus the method became more efficient.

Moreover, the operated detector positioning in the conducted measurement experiments reproduced typical *in vivo* pulmonary measurement protocols and configurations. However, the exam protocol is expected to be improved by looking for detector positions enabling a better separation of organs' contribution. The use of Monte Carlo simulations to study the track-distribution of the particles for each source organ represents a promising solution. Indeed, plotting the tracks with ParaView (case of the experiments at KIT) gave a fairly realistic idea on the particle flux outside the phantom. This helped positioning the detector in order to obtain a well-defined contribution proportion for each organ. This method could be systematically used to find the optimal detector positioning whenever an accurate activity distribution should be assessed.

Finally, the use of a reduced-size detector enabling the mapping of a region of interest should be considered for wounds for example. Indeed, with the use of X-ray Passivated Implanted Planar Silicon detectors (X-PIPS) for example, a very limited noise contribution is registered and a focalized measurement with high resolution can be done. This would definitely improve the activity estimate within the monitored region since close detector-source spacing is operated with this type of detector (Broggio et al. 2009).

V.3. Choice of the point source positioning

When introducing a point perturbation source inside the phantom, its positioning should be carefully selected. Indeed, the positioning of the point source should be done taking into account its activity and strength when compared to the activity of the other loaded organs. Moreover, a more realistic positioning should be operated if the point source is intended to represent a contaminated lymphatic node. Besides, it should always be kept in mind that point sources cannot faithfully reproduce any contamination since the extent of the contaminated volume is not represented. The volume of the source in the monitored region remains indeed of significant relevance to represent at least the effect of an activity concentration. Finally, it is very difficult to make schematic assumptions on the location of the lymph nodes in the MC model of the phantom. Moreover, local measurements using germanium detectors have proven that the source-detector distance is a major parameter affecting the MC representation of such point sources (Bremaud 2011; Gualdrini et al. 2000).

Chapter 6

Synthesis, Discussion and Perspectives

I. Synthesis

I.1. Treatment chain for numerical calibration

The nuclear industry is witnessing an increase in the community of female workers for whom an adapted monitoring is required. As a matter of fact, the *in vivo* measurement installations are typically calibrated using a male physical phantom. Monte Carlo simulations have proved to efficiently improve the calibrations by the mean of voxelized numerical phantoms created from medical images. However, voxel grids are rigid structures that are very difficult to deform in order to modify the geometry and the body shape. Mesh and NURBS 3D modeling techniques were introduced here to create realistic and deformable phantoms in order to optimize the monitoring of female workers.

A library of 24 female torso models representing the most common female morphologies was developed using the Rhino 3D modeling software. Starting from the new ICRP adult female reference computational phantom, a deformable torso core model was designed using Mesh and NURBS representations. The core model was then deformed to realize the morphological variations. The work focused on changing cup size, chest girth and internal organ volume to study their effect on *in vivo* lung counting measurements. To realize cup size change, the recommendations by Turner and Dujon (2005) were followed to establish the target weight of each cup size depending on the chest girth. The method consisted in deforming the NURBS breast surfaces using the control vertices of the Splines. For internal organ resizing, autopsy data (Clairand et al. 2000) was used to link internal organ volume to the total height of the subject. All the operated size modifications in chest girth and in breast size involved adipose tissue addition. The library was also compared to existing models (Hegenbart et al. 2008) which were also created using BREP representations and the Rhino 3D modeling tools.

The developed library was next used to realize the numerical calibration of the AREVA NC *in vivo* counting installation. The simulated efficiencies for each model were compared to typical counting efficiency values obtained with the Livermore male physical phantom and correction coefficients were deduced to account for the additional radiation attenuation due to breasts. The obtained results showed that errors up to 80% on the activity estimate, and consequently on the dose calculation, were introduced at 15 keV when using the typical Livermore-based calibration coefficients. The higher the energy is, the lower the error on the calibration coefficients becomes since attenuation decreases with increasing photon energy.

Next, counting efficiency variation with energy and morphology was put into equation to enable a reliable estimate of the morphological dependence of lung counting efficiency for *in vivo* female monitoring studies. The developed equation takes into account the difference in the loaded organ volume and in the chest wall thickness to define the morphological effect. This equation uses also the energy-dependent mass attenuation coefficient of adipose tissue and was tested against simulated data, measured data and published results. Starting from a measured Livermore male curve, indications were given to calculate the calibration coefficients of any female subject. The equation was applied for the AREVA NC *in vivo* counting installation and a table was given which defines the correction coefficients to be used each time a female subject is monitored depending on its cup size and chest girth.

Furthermore, to optimize the numerical calibration, the work's main focus was to accelerate Monte Carlo calculations by the mean of variance reduction techniques, geometry simplification operations and by the development of a Unix/Linux script to automatically process the MC output file. Several variance reduction methods were tested on two voxelized phantoms representing respectively the Livermore model and the torso of the ICRP reference female (a more complex model with a higher number of structures). The study focused on improving the simulation time and on reducing the statistical relative error while maintaining unbiased results (when compared to values obtained without variance reduction). The source biasing -of both emission probabilities and directions- and the forced collision methods were found to give satisfying results, since the simulation time was sensitively decreased, and to be easy to use for routing numerical calibrations. Moreover, the combination of these cards proved that they are working cooperatively and a total time reduction factor of about 16 was obtained. Other methods like weight windows, cell importance and exponential transport were found to be more delicate for a routing usage and showed poor results when investigating the simulation time reduction. Finally, it was noticed that the methods worked similarly for both phantoms regardless of the existing differences related to the number of structures, the number of voxels and the voxel dimension. Geometry simplification operations included adding void plans and reducing the total number of voxels in each phantom. These also reduced the simulation time by a factor of about 2 but were recommended to be used with caution as the scatter contribution and the voxel resolution are lost with these geometrical modifications. Finally, a script using the Unix/Linux bash tools was developed to automatically transform the Monte Carlo tally results into a calibration curve and give a 6th order polynomial equation defining the counting efficiency variation with energy.

1.2. Management of complex contaminations

In vivo measurements are often done under the hypothesis of a known activity distribution. However, the problem arises for wounds or complex contaminations where several radionuclides can be incorporated for which very little information on the nature, size and solubility type are available. For such situations, determining the activity distribution remains delicate. The work focused thus, on developing a method for the activity mapping using both *in vivo* measurements and Monte Carlo simulations.

The developed method is a three step process where first a whole body *in vivo* counting is done and the measured spectrum is analyzed to identify the incorporated radionuclides and determine the primary and the long-term retention organs using biokinetic models. The second step involves the choice of the most adapted counting system according to the energy of the radionuclides and the positioning of the detector to cover at best the retention organs or tissue. The final step includes the *in vivo* measurements and the use of Monte Carlo simulations to separate the contribution of contaminated structures. From *in vivo* measurements, the experimental counting rate is obtained. This rate is equal to the sum of counts emitted from several source organs in the monitored region and collected in the detector. The contribution of each organ to the experimental count is provided by MC simulations.

The method was first tested and validated using experiments with the Livermore phantom, americium lungs and a LOAX germanium detector. Experimental measurements with such a phantom make the physical separation of the contribution of each organ possible. Indeed,

when for a real subject it is impossible to isolate a given organ and measure it alone, this is feasible using the Livermore phantom. From the measurements, it was observed that the developed method for activity mapping holds since activity estimates were within a few percent ($< 5\%$) from the reference values. The effect of detector positioning was highlighted through the study as the best activity estimates were obtained for the positions maximizing the count. Moreover, the method has proven to be accurate even when perturbation point sources, representing an old contamination or a lymphatic node for example, are available. Finally, the activity distribution hypotheses were also investigated and the results have shown that errors on the hypotheses can be identified and handled correctly by the developed method.

For the case of a contaminated subject, however, MC simulations are needed to assess the contribution of each organ alone by calculating the counting efficiency. These simulations require a realistic modeling of the experimental measurements including the phantom/subject, the source, the detectors and their positioning. The experimental counting rate and the MC simulated contributions are then used to estimate the activity distribution. The obtained results have proven the method to work with calculated efficiencies. Nevertheless, Monte Carlo simulations were strongly dependent on the model of detectors and on their positioning. Indeed, a slight error in the detector modeling has proven to cause errors on the activity estimate beyond 5-10%. Meanwhile, an error on the detector positioning can be more severe and induce errors on the activity estimates of over 20-30%. The detector modeling was reviewed for cross fire situations as the contributions of each organ were overestimated with simulations each time the loaded organ and the detector were not aligned.

Finally, the method was tested with different counting systems and different radioactive sources including europium and americium lungs and americium liver. The obtained results prove that the method successfully estimates the activity distribution in three loaded organs at the same time and for several radionuclides. To conclude, the mathematical separation of activity distribution works well in real time experiments and can be useful for the case of complex contaminations.

II. Discussion and improvements

II.1. Library of female phantoms and numerical calibration

In this work, two protocols were developed to generate deformable anthropomorphic phantoms by extracting organ contours from medical images or from a voxelized phantom. The library development requires the use of the Rhino 3D modeling software to create Mesh and NURBS geometries and the Binvox program for voxelization. The automatic contour extraction from a voxel model, using a home made IDL routine, saves consequent time and effort when compared to manual segmentation of medical images. However, improvements remain necessary to smooth the surfaces for example and to correct organ intersections if any. Moreover, using Binvox requires multiple iterations depending on the number of available structures that need to be separately voxelized (while ignoring the others). To accelerate this process, an MS-DOS script was developed to automatically run Binvox with the correct parameters for the ignore function. As for organ deformation, new tools based on artificial

intelligence are being tested (cf. Section III.2). Future work will focus on further automating these processes and ultimately on designing a new module in the OEDIPE software to implement the new phantom creation protocol.

The developed library of female phantoms was built starting from a deformable torso core model that was created from the ICRP reference adult female. However, in the designed models, only organs most influencing the *in vivo* counting simulations were modeled using Mesh and NURBS geometries. These include the ribs, sternum, shoulder blades, spine, heart, lungs, liver, breasts and skin. However, for a wider use of the developed library in internal and external dosimetry studies, it is desirable to add some other organs such as the thyroid gland, the stomach, the kidneys etc. In addition, the conducted simulations involved a lung contamination study where all the activity was retained in the lungs. This is rarely the case in real situations where radionuclides are distributed within different retention organs depending on their biokinetics. It is thus, also necessary to account for the radionuclide's distribution by simulating the activity spread inside the phantom.

To modify the size and shape of the core model in order to create the library of female phantoms, the method consisted in fixing a final target volume for each structure and organ and then realizing morphology transformations using the Rhino 3D modeling software. However, the shape of each organ was modeled based on visual criteria to operate morphological variations. For breasts, the modeling became more delicate with increasing cup size due to the falling of breasts over chest in supine position. Moreover breasts can differ significantly from one person to another considering age, musculature, origin and other parameters (Fabié et al. 2006). Thus, improvements can be made on the breast modeling and new morphologies and sizes can be created to cover a wider female population. For example, CT scan images of female patients could be used to create realistic breast shapes which could then be adjusted to the chest of any model from the library. Besides, morphing algorithms and software used in 3D animations and graphic design, such as MakeHuman (<http://www.makehuman.org/>) or Autodesk (www.autodesk.fr/), could also be implemented to improve the breast modeling in supine positions. Nevertheless, this library represents at least a mean to correct the typical calibration coefficients obtained with the male Livermore physical phantom. Finally, the added tissue to realize cup size and chest girth increase was considered to be of adipose nature only which can be debated. However, since the main thoracic compounds (adipose tissue, muscle) and all internal organs have similar energy-dependent mass attenuation coefficients, the impact of the additional tissue on radiation interaction with matter remains negligible. Besides, the simplified mass attenuation coefficient eases the tissue composition and density definition for all organs and structures and has commonly been used in similar works (Cassola et al. 2010).

To run the MC calculations, the developed phantoms were voxelized using the Binvox program. This step can be time-consuming depending on the classification algorithm and on the voxel resolution. However, voxels remain the only format accepted by MCNPX. It would be of prime interest to upgrade the MCNPX code by enabling particles transport with Mesh and NURBS representations and skipping the voxelization process. Nevertheless, even if other Monte Carlo codes (Geant 4, Penlope etc.) can handle such representations, the calculation speed and efficiency is sensitively less than with voxel geometries. This is inherent to the particles tracking process which is based on situating the particle inside or outside the volume of interest. A new approach for the MC transport of particles in non-voxel geometries seems necessary to accelerate simulations for Mesh and NURBS formats.

Finally, the morphological dependency of counting efficiency was put into equation by modeling the effect of both chest wall thickness (exponential attenuation of radiation) and of the loaded organ volume (inverse proportion). This equation was able to reproduce the simulation results and indications were given to transform a Livermore measured curve into that of any female. Improvements are however necessary as the equation relates a Livermore P1 plate measurement to an 85A female subject. Nevertheless, the operated detectors' positioning should be taken into account to represent the effect of the source-detector distance since radiation flux decreases inversely with the square of the distance (Podgorsak 2003). Furthermore, the equation was given for the AREVA NC *in vivo* counting installation and should be adapted before being used for another counting system.

II.2. Variance reduction techniques for *in vivo* simulations

Variance reduction techniques were introduced in this work to reduce the Monte Carlo simulation time while maintaining acceptable statistical relative errors. These include typical methods implemented in the MCNPX source code such as the source emissions' biasing, the weight windows, the forced collision cards and several others. The high attenuation of low energy photons is the main issue for such *in vivo* simulations. The obtained results showed that some of these methods work properly with two different phantoms.

However, the tally results were not always in good agreement with the predicted results. Indeed, for the cell card for example, although the importance ratio defining the splitting was increased up to 10, the total number of particles required for the same statistical relative error did not vary accordingly. Furthermore, the figure of merit gave some disappointing results for methods such as the exponential transform. Such methods were basically designed for point source neutron simulations and energy-independent studies and should be adapted for studies involving photons of different energies.

Besides, thanks to the introduction of these VR cards, it was possible to obtain statistically reliable results for the 15 keV photons with the biggest female morphologies. This was not the case in the prior simulations as such low energy photons were severely attenuated by the phantom organs and structures.

The work done on applying variance reduction methods for *in vivo* numerical calibrations should be deepened for other activity distributions. Moreover, methods such as the DXTRAN spheres, available in the MCNPX 6.0 version of the code, should give outstanding results and further accelerate the simulations. This was not done since the US authorities did not grant non US citizens an access to the latest versions of the MCNPX code.

Finally, variance reduction methods should also be implemented in the OEDIPE software with a user-friendly interface and sufficient indications enabling a simple, direct and optimal use of the most adapted techniques for a given situation.

II.3. Contamination mapping procedure

In this work, a method was developed to estimate the incorporated activity and its distribution inside the body as well as handle post accidental situations using *in vivo* measurements and Monte Carlo calculations.

Thanks to Monte Carlo simulations, it is possible to assess the contribution of each organ to an experimental measurement. This is essential when determining the activity distribution inside the body of the monitored subject. Indeed, since it is simply impossible to isolate each potentially contaminated organ and measure it alone, determining its contribution to the total count helps determining the activity mapping.

However, to correctly simulate the contributions of each organ, a thorough Monte Carlo representation of the *in vivo* experiments is necessary. This involves a correct modeling of subject's anatomy through the creation and use of person-specific voxelized phantom. In addition, a faithful modeling of the used counting system and a precise positioning of the latter are mandatory. Nevertheless, generating a personalized voxel model of the monitored subject is extremely delicate and time-consuming. Furthermore, experimental positioning of the counting system is subject to high uncertainties (Razafindralambo 1995) and is difficult to reproduce with MC simulations especially when different tilts of the counting system are operated. When realizing *in vivo* measurements, extreme caution and care should be given when taking the overall positions of the detector facing the subject. Finally, the MC model of detectors should respond identically to the used counting system which involves correct modeling of the active cells, gaps, shieldings and other relevant parameters.

To solve the positioning problem, it is suggested to use sensors positioned not only in the measurement chamber but also on the subject's chest to correctly locate the detector facing the monitored organ. Moreover, to improve detector modeling, a CT scan of the detector could bring sufficient indications on the size and arrangement of the main compounds and elements inside the aluminum cap. A direct comparison with the technical drawing may identify any manufacturing errors. Furthermore, the traditional protocol followed for detector modeling could need some upgrades. Indeed, point source measurements aligned with the detector remain insufficient to reproduce cross fire situations. It would thus be useful to systematically accomplish new measurements with point sources situated off axis when compared to the detector. Besides, the study by Bremaud (2011) has proven that a validated model of detector for point source experiments is not automatically correct for phantom measurements. Therefore, additional experiments with physical phantoms should be accomplished to further validate the detector modeling. Finally, detector manufacturers often suggest a method to improve the detector modeling by modifying successively the gap between the front surface of the crystal and the window, the crystal diameter and thickness, and the side and back dead-layer thickness. For characterizations going down to 10 keV, the front dead layer could also be adjusted. These recommendations should be taken into account to efficiently adjust the detector model.

III. Perspectives

In vivo monitoring remains of little use since counting installations are extremely expensive and require well-trained and qualified personnel. This makes *in vivo* measurements of limited interest and even inaccessible for a wide community of nuclear workers. This is particularly the case of hospital personnel working in the nuclear medicine departments which is only monitored using *in vitro* monitoring programs. However, *in vivo* measurements have proven to be more efficient when detecting accidental incorporations especially for radioactive elements of a short half life. Thus, to render this technique available for these workers, mobile *in vivo* measurement units initially developed for interventions in nuclear crisis situations were considered. A numerical calibration of a mobile unit was considered in this work involving the modeling of the detectors and the use of numerical phantoms of various body size and morphology.

Moreover, until today, internal and external dosimetry studies are based on the use of recommended values obtained for a reference individual. However, this reference individual is far from representing the entire human population with its dissimilarities and specificity. Errors and uncertainties are systematically introduced when using the reference individual data despite the dosimetry challenges and precision requirements. Thus, several research groups have been working on the development of libraries of adult male, female and even pediatric phantoms to offer more appropriate, personalized and realistic human representations (Johnson et al. 2009; Na et al. 2010). In this framework, the female library developed here was considered for a more general use in emergency situations through the development of a case-based reasoning platform which looks for the most similar phantom and adapts it to fit, at best, the morphology of the victim.

III.1. Numerical calibration of a mobile *in vivo* unit

IRSN has been recently asked to provide its expertise to monitor hospital workers from several nuclear medicine departments. However, the calibration process of the detectors is again limited by the use of physical phantoms and fixed activity distributions. The know-how and tools developed in this PhD were therefore used to realize a numerical calibration of this counting system using voxelized phantoms and biokinetic distributions.

An MCNPX model of the detector was first upgraded and validated through the use of experimental measurements with point sources and the IGOR phantom. Monte Carlo simulations were then operated using a library of whole body male phantoms of different size and shape. Realistic activity distributions were operated in these phantoms for the most commonly used radionuclides in nuclear medicine medical departments.

III.1.1. The IRSN *in vivo* mobile unit

To fulfill its mission of intervention and monitoring in the case of major nuclear catastrophes or crises, IRSN has developed a series of mobile *in vivo* measurement units (LMA) (cf. Figure 6.1.). These include light and heavy trucks with a capacity of over 50 simultaneous *in vivo* examinations. These mobile units have also been implemented to make *in vivo* monitoring techniques available for nuclear medicine hospital departments.



Figure 6.1. Photos of the IRSN LMA *in vivo* mobile unit and of the two installed germanium detectors.

Measurement campaigns have been conducted at national hospitals and particularly for workers in nuclear medicine and imaging departments (Poitiers, Angers etc.). Several internal contaminations were identified with these measurements where *in vitro* bioassay analyses were usually “clean” (unless samples were measured on the same day). Most contaminations involved radiopharmaceuticals such as Technetium 99m, Thallium 201 and Iodine 131. These further confirmed the advantage of using *in vivo* measurements to improve the monitoring of workers handling radioactive materials and subject to internal contamination accidents.

III.1.2. MCNPX modeling of the *in vivo* mobile unit detectors

The IRSN LMA *in vivo* mobile unit consists of two broad energy germanium detectors for which the Canberra MCNPX model was acquired. This model was upgraded by adding the shielding surrounding each detector.

To validate the available MCNPX model of detectors, experimental measurements were achieved with several X and gamma point sources, including ^{241}Am , ^{57}Co , ^{51}Cr , ^{85}Sr , ^{137}Cs , ^{88}Y and ^{60}Co covering a wide energy range (21 keV to 1.33 MeV). The experiments were simulated using the MCNPX model of detectors and efficiency values were compared to the measurement results. Next, the IGOR bricks were mounted to represent a 70 kg subject and 142 cylindrical sources of ^{57}Co , ^{60}Co , ^{137}Cs and ^{133}Ba were used corresponding to a homogeneous whole body contamination (cf. Figure 6.2). To simulate the IGOR experiments, a MCNPX model of the phantom was developed and the same source distribution and detector positioning was faithfully reproduced.



Figure 6.2. Visualization of the experimental measurements done with point sources (left) and with the IGOR phantom (right).

At first, the observed differences between experiments and simulations with point sources showed a necessity to review the detector modeling (errors $>10\%$). To improve detector modeling, the work focused on changing the front dead layer thickness, modifying the crystal size and particularly its radius and thickness and also the positioning of the crystal inside the detector cap. With the upgraded model of detectors, the measured and simulated counting efficiencies agreed within 10% at the considered energy range for point sources. As for the IGOR simulations, the obtained results further validate the upgraded model of detectors since the differences on counting efficiency remained within 5% at the considered energy range.

III.1.3. Numerical calibration using a whole body male library

A numerical calibration of the mobile *in vivo* counting system was realized using a library of male phantoms representing the most common male morphologies (Broggio et al. 2010). The work includes modeling the activity distribution starting from biokinetic recommendations and simulating the morphological effect on counting efficiency.

Indeed, the calibration of counting systems is directly dependent on the activity distribution (Kramer and Burns 1995). Thus, biokinetic models were used (Legget et al. 2003; ICRP 1995) to reproduce the activity distribution of ^{137}Cs and $^{99\text{m}}\text{Tc}$ inside the body (cf. Figure 6.3).

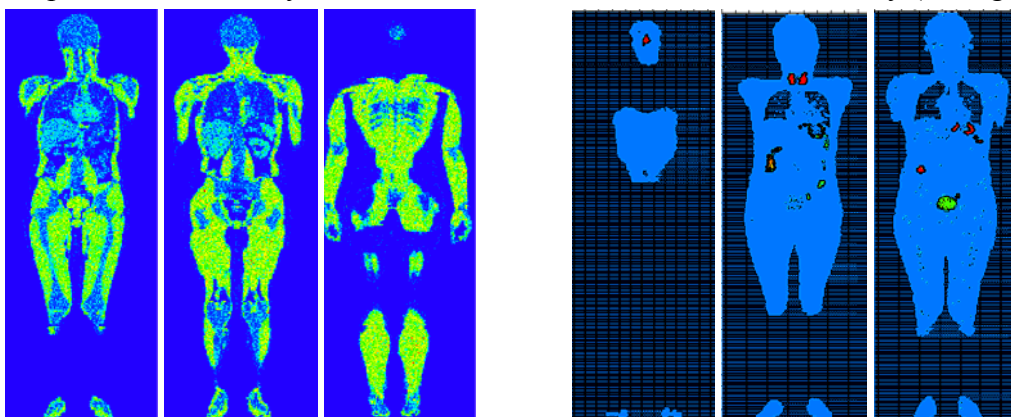


Figure 6.3. MCNPX visualization of the activity distributions in the ICRP male reference phantom for the ^{137}Cs (left) and $^{99\text{m}}\text{Tc}$ (right). (red = 95% activity, blue = 5% activity).

Moreover, to study the effect of body size and shape on counting efficiency, ten different voxelized male of various heights (1.62 m to 2 m) and weights (50.8 kg to 110.3 kg) were considered. Figure 6.4 gives the ^{137}Cs counting efficiency simulated values (green) and shows examples of the used phantoms of different body height, weight and morphology. Similar results were obtained for the $^{99\text{m}}\text{Tc}$.

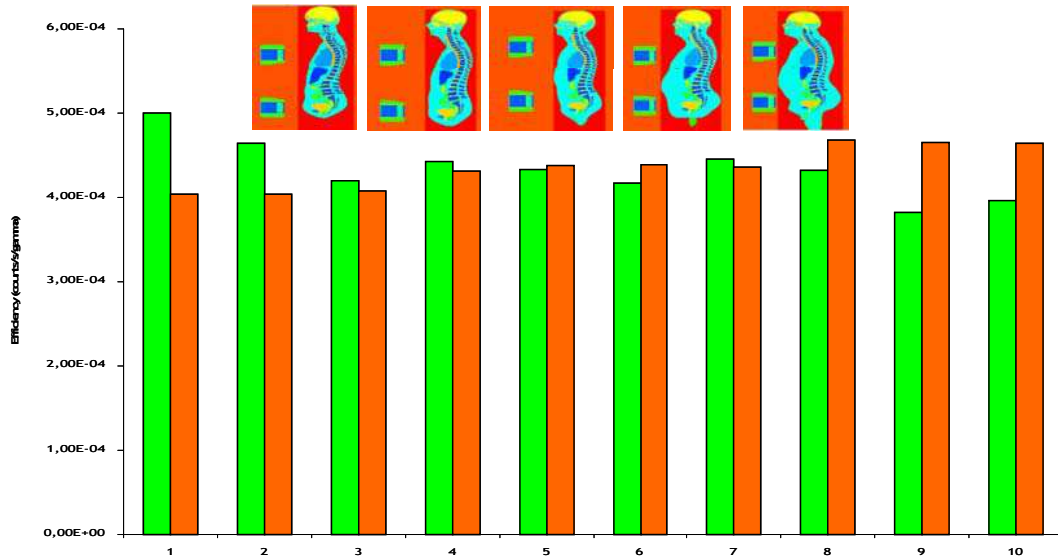


Figure 6.4. MCNPX counting efficiency (counts/s/gamma) values for the ten phantoms. Inset: Example of several phantoms representing adult male individuals of different height and weight.

Future work will focus on finding parametric equations based on external parameters of height and weight that enable a correct and rapid estimate of the counting efficiency variation with morphology. As a first step, efficiency correlations with subject's height have been identified and a practical parameter was defined to directly determine the efficiency of any individual just multiplying by the actual height of the subject. When using this parameter, the previous simulations results were correctly reproduced (Figure 6.4 orange values). Further investigations remain however necessary to improve the agreement between simulation results and the developed equation which ultimately should be related to the typical calibration coefficients obtained with the IGOR male physical calibration phantom.

III.1.4. Conclusion

Thanks to the development of mobile *in vivo* units, IRSN provides now its expertise to monitor hospital workers from several nuclear medicine departments. The MCNPX modeling of the counting system installed in this mobile unit enables the improvement of *in vivo* spectrometry analyses through the use of numerical calibrations. The effect on counting efficiency of both phantom morphology and activity distribution following biokinetic models were investigated through the use of voxelized phantoms. The results indicate that the counts are directly affected by both the activity distribution and the morphology of the subject.

Calibrations using the developed female library will soon be done to improve the monitoring of female workers undergoing *in vivo* measurements using the LMA. Moreover, the developed method enabling the assessment of the activity distribution could be tested and validated for the counting system of the mobile unit. Thus, a better estimate of the activity mapping can be provided when monitoring workers with internal contamination risks using this particular counting system.

III.2. A CBR-Based platform for dosimetry in emergency situations

III.2.1. Aim and methods

In the case of accidental exposure to radiation, it is necessary to establish as soon as possible a dosimetry evaluation for each victim. In most cases, this evaluation is based on available 3D voxel phantoms. However, even when medical images are available, the specific phantom of the victim is not always accessible since its construction is delicate and time-consuming. In emergency cases, such time and effort are unaffordable. Moreover, medical images are avoided to prevent any additional exposure to radiation. Thus, existing models are used even if their characteristics are far from the biometrical data of the victim. However, the dosimetry assessment accuracy is highly dependent on the similarity of the phantom and the victim. Hence, a new approach based on Case-Based Reasoning (CBR) and Artificial Neural Networks (ANN) was considered to assist the physician in choosing the best fitting phantom from the existing and available models and to adapt the latter to the victim.

The EquiVox platform was developed in collaboration with “Université de Franche Comté” to optimize the dosimetry in emergency situations using the developed female torso phantoms (Bopp et al. 2009, Henriet et al. 2010). EquiVox first uses the CBR method to solve new problems based on similar past problem solutions and then adapts the selected phantom to the victim, with ANN tools, and stores the victim equivalent phantom in the case-base database for future reuse (Makovicka et al. 2009).

III.2.2. Case-Based reasoning principles

The central unit of the CBR-cycle is the case-base database that contains the available solutions. At the beginning of the cycle, the new case or problem is formulated by defining the comparison criteria (Mille 1999). Given a target problem, the most similar case(s) in the case-base database is retrieved then (re)used to attempt to solve the problem, this step includes the adaptation of the case-base retrieved model(s). Next the new solution is tested and, if necessary, revised. Finally, the model is retained if successfully adapted and the resulting experience stored in the case-base for future reuse (cf. Figure 6.5).

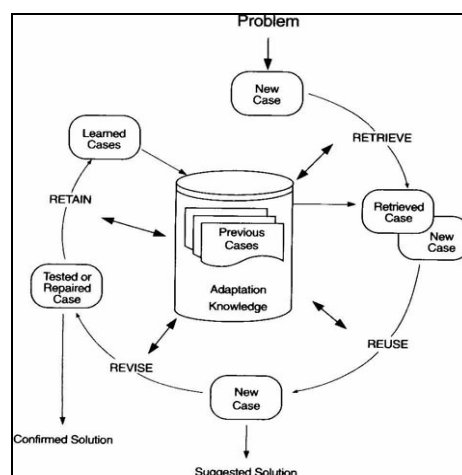


Figure 6.5. The CBR cycle: problem definition (new case), retrieve (most similar case from the database), reuse (previous solution), revise (adaptation) and retain (storage in the CBR database).

Selecting the most similar phantom with CBR includes the calculation of a similarity index, which defines the correspondence between the victim and the phantom, and of a confidence index, which associates an error to the retrieved solution. The higher the number of “informed” descriptors is, the better the convergence towards the “correct” solution. The similarity calculation was done using the K-nearest neighbor algorithm (Bremner et al. 2005) that allows a weight application to stress on the importance of some parameters, gender for example, when compared to others, smoker/non smoker for example.

III.2.3. Artificial neuronal network methods

Once a matching case is retrieved with CBR, the system adapts the solution to the needs of the current case. Adaptation looks for prominent differences between the retrieved case and the current case and then applies formulas or rules that take those differences into account when suggesting a solution. ANN tools were used here to adapt organ geometries and volumes. An ANN is a mathematical or computational model that tries to simulate the structure and/or functional aspects of biological neural networks. It is an adaptive system that changes its structure based on external or internal information that flows through the network during the learning phase (Drew and Monson 2000).

There are many learning algorithms available depending on the ANN type and its intended application, the backpropagation is the most frequently used learning algorithm (Drew and Monson 2000). Backpropagation attempts to minimize the least mean square difference over the entire training set. The ANN output is thus compared with the true output, and the error is backpropagated through the network, altering the weights of the connections to reduce the least mean square error (the best fit with the data). This is repeated until the error is minimized (a tolerated error is set during the learning phase). The more the available models are, the better the ANN convergence to the correct solution.

III.2.4. Preliminary results of the platform

- **The retrieval phase validation**

A set of 80 female subjects was randomly selected from the CAESAR database (<http://store.sae.org/caesar/>) and the available descriptors were inserted into the EquiVox platform to find the most similar phantom between the 24 models available in the developed library. In 85% of the cases (28 times), EquiVox was able to find for the 80 new cases the exact model when the latter existed in the library. However, in 5 cases, EquiVox did not find the correct case-base model although it existed. These 5 cases in which EquiVox missed the correct solution are the result of the influence of each informed descriptor (age, height, weight, etc.). Moreover, in the 47 cases where the exact model was unavailable in the database, EquiVox retrieved the case-base model having the closest morphology.

Figure 6.6 shows the EquiVox graphical interface representing a random CAESER female (pink area) compared to two case-base models (blue area): the 85A phantom (left) and the 120F phantom (right). The better the areas are merged, the more similar the case-base model is to the victim (new case). This is the case of the 85A model for which the morphology reasonably matches with that of the CAESER female. Indeed, the similarity index computed

for this phantom was equal to 0.765 meaning that the considered CAESER female and the case-base 85A model correspond up to 76.5 % considering the available descriptors. The confidence index, equivalent to an uncertainty calculation, was found to be equal to 0.8 and suggests that the obtained similarity can be trusted (Farah et al. 2011).

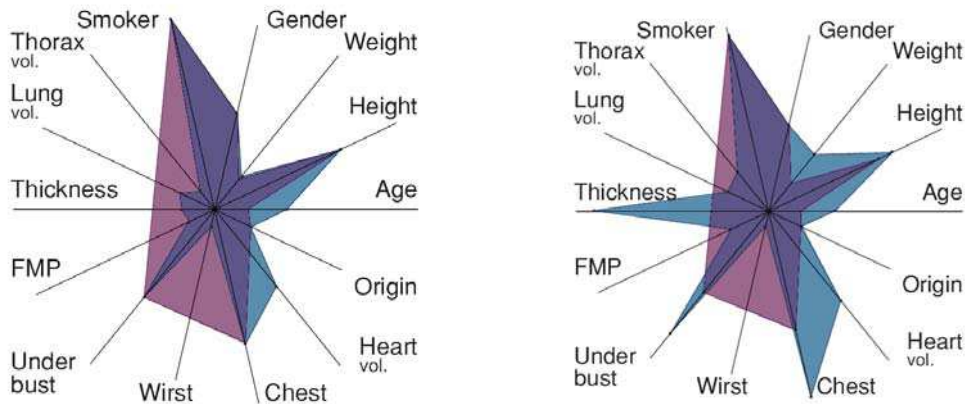


Figure 6.6. The EquiVox graphical comparison of the CAESER female with case-base model 85A (left) and model 120F (right).

- **The adaptation phase validation**

ANN tools were used here to adapt the lungs of the case-base most similar model to those of the victim in order to perform more realistic and personalized dosimetry. To validate the ANN adaptation process, eight phantoms of various lung volumes were developed using the Rhino 3D modeling software and following the recommendations by Clairand et al. (2000). One of the lung models was selected and considered to be the unknown lung volume of the victim that needs to be determined with EquiVox. The case-base phantoms are the seven remaining lung models for which the ANN learns the position of well defined characteristic points. The unknown lung was changed eight times to determine the efficiency of the ANN algorithm in reconstructing the lung volume when starting from different lung size and morphology.

The ANN adaptation process starts with a learning phase for which the algorithm is trained to generate lungs starting from the characteristic points. Three different learning configurations have been used here to study the efficiency of the ANN algorithm when learning separately or together the 3 coordinates (x, y and z) of each point defining the lung surface. The results are very convenient as the overall error on the lung volume remained within 1%. Moreover, the key point in using such ANN tools is its speed. Indeed, once the ANN training is finalized, it was able to estimate the positioning of 2400 points in just tens of milliseconds using a very common Dual Core 2.1 GHz processor (Laurent et al. 2010).

III.2.5. Conclusion

The EquiVox platform was developed to be used in emergency cases where a rapid but reliable decision is required to choose the best model reproducing the actual situation. The choice is done using the CBR approach based on previous similar experiences feedback. EquiVox helps the experts to choose the most adapted model thanks to the computations of similarity and confidence indices. The similarity index defines the equivalence between the new case and a previous one available in the case-base and the confidence index highlights

the uncertainty in the similarity calculation. At this stage of our work, the adaptation phase is being designed and the ANN tools implemented to the Equivox platform with very encouraging preliminary results. In perspective, the adaptation will be extended to all organs using the same ANN algorithm and future work will also focus on enriching the case-base database with new phantoms.

General conclusion

In the case of accidental internal contaminations, *in vivo* gamma spectrometry measurements represent a very efficient and direct method to determine the incorporated radionuclides and to estimate their activity. However, the calibration process of *in vivo* counting installations is based on the use physical calibration phantoms of limited anatomical realism. To optimize the monitoring with *in vivo* measurements, numerical calibrations using anthropomorphic phantoms and Monte Carlo simulations were carried out. This worked focused on improving the monitoring of female workers, for whom no physical calibration phantom is available.

This study started with the development of a library of 24 different female torso phantoms, using deformable Mesh and NURBS geometries, based on plastic surgery recommendations, autopsy data and clothing standards and representing the most common female body types and morphologies. Using the developed library, a numerical calibration of the AREVA NC *in vivo* counting system was achieved. The work has quantified the effect of breast size and chest girth on counting efficiency and enabled to provide correction factors for measurements based on the Livermore physical male phantom. Next, the morphology-induced variations of counting efficiency as a function of female morphology were put into equation. Thanks to the use of such an equation, practical recommendations were given to correct the typical calibration coefficients for any female worker. This equation, based on simple physical considerations to properly describe the variation of counting efficiency with morphology, further supports the realism and the coherence of the MC simulation results.

The next chain in the numerical calibration process involved the work on accelerating Monte Carlo calculations with the use of variance reduction techniques and geometry simplification operations. When combining the source biasing, the emission direction biasing and the forced collision cards, the simulation time was divided by 20. These cards did not bias the results since the maximum difference on counting efficiency, when compared to reference values obtained without VR, did not exceed 5% at all energies. The use of void plans and the voxel fusion geometry simplification operations also decreased the simulation time by a factor of 1.3 and 2 respectively. Meanwhile, combining VR, geometry simplification operations and parallel calculations made a MC numerical calculation feasible within 1-2 hours while it first took a whole week. Finally, a script was developed using Unix/Linux to automatically treat the MCNPX output file and plot the counting efficiency variation with energy.

The study next focused on improving the post-accidental estimation of activity distribution for complex or old internal contaminations. The developed method uses *in vivo* spectrometry measurements coupled with Monte Carlo simulations to determine the activity mapping. The unknown activity is directly derived from the experimental counting rate by using the simulated counting efficiencies which represent the contributions of a given contaminated organ to the count of a detector at a given position. A feasibility study with the Livermore phantom was first done to validate the method. Next, MC tools were used to reproduce the Livermore experiments and to confirm simulations as a correct mean to determine the organ contributions. Further investigations were done to validate the method for different counting systems, different detector positioning, various radionuclides with different energies and several contaminated organs. The reliability of the method was also tested by investigating the effect on activity mapping of a perturbation source and of errors in biokinetic distributions.

Finally, to go towards a more realistic and personalized dosimetry in emergency situations, a platform based on the case-based reasoning principles and the artificial neural network tools was also developed in collaboration with the Université de Franche Comté. This platform looks, among the models of the developed female library, for the phantom most similar to the victim. Next, it adapts the model to the victim to enable a personalized dosimetry study by accounting for the particular morphology, body type and characteristics of the victim.

Future step will include the adding of several radiation-sensitive internal organs to the models and making the developed library available to all users who wish to use it for dosimetry studies or any other application. The OEDIPE software could also be upgraded by the adding of a new module to implement the new phantom creation protocol and the different variance reduction methods that have been successfully tested for pulse height tallies. Finally, the effort to use case-based reasoning principles and artificial neural network tools in internal dosimetry should be pursued and also expanded to other radiation safety studies.

References:

Agostinelli S., Allison J., Amako K., Apostolakis J., Araujo H., Arce P., et al. Geant4: a Simulation Toolkit. *Nucl. Instrum. Meth.* **506**(3): 250-303; 2003.

Badal A., Kyprianou I., Badano A. and Sempau J. Monte Carlo simulation of a realistic anatomical phantom described by triangle meshes: application to prostate brachytherapy imaging. *Radiotherapy and Oncology* **86**: 99-103; 2008.

Baumgart B. Winged-Edge Polyhedron Representation for Computer Vision. *National Computer Conference*; 1975. <http://www.baumgart.org/winged-edge/winged-edge.html>

Behr M., Arnoux P.J., Serre T., Bidal S., Kang H.S., Thollon L., Cavallero C., Kayvantash K. and Brunet C. A human model for road safety: from geometrical acquisition to model validation with radios. *Computer methods in biomechanics and biomedical engineering* **6**(4): 263-273; 2003.

Berger C.D. and Lane B.H. Biometric estimate of chest wall thickness of females. *Health Phys.* **49**(3): 419-24; 1985.

Berger M. J., Hubbell J.H., Seltzer S.M., Chang J., Coursey J.S., Sukumar R. and Zucker D.S. XCOM: Photon Cross Section Database National Institute of Standards and Technology; 2005. <http://physics.nist.gov/xcom>

Bhattacharyya M.H., Breistenstein B.D., Métivier H., Muggenburg B.A., Stradling G.N. and Volf V. Traitement de la contamination interne accidentelle des travailleurs. *Ouvrage IPSN*; 1995.

Bolch W.E., Eckerman K.F., Sgouros G. and Thomas S.R. MIRD pamphlet No. 21: a generalized schema for radiopharmaceutical dosimetry--standardization of nomenclature. *J. Nucl. Med.* **50**(3): 477-84; 2009.

Booth T E. A sample problem for variance reduction in MCNP. *LA-10363-M8 UC-32*; 1985.

Booth T.E. Monte Carlo Variance Reduction Approaches for Non-Boltzmann Tallies. *LA-12433 UC-910*; 1992.

Booth T.E. A Monte Carlo Variance Reduction Approach for Non-Boltzmann Tallies. *Nucl. Sc. Eng.* **116**(2): 113-124; 1994.

Bopp M., Henriot J., Makovicka L., Morello B. and Broggio D. A new CBR-Based application for voxelized phantom creation: REEPH. *Proceedings of Singaporean-French IPAL Symposium.*; 2009.

Borisov N., Franck D., de Carlan L. and Laval L. A new graphical user interface for fast construction of computation phantoms and MCNP calculations: application to calibration of in vivo measurement systems. *Health Phys.* **83**(2): 272-279; 2002.

Boulet B., Bouvier-Capely C., Cote G., Poriel L. and Cossonnet C. Selective extraction of Pu(IV) by a calix[6]arene bearing hydroxamic groups. Application to bioassays. *J. Alloys and Compounds.* **444-445**: 526-528; 2007.

Bouvier-Capély C., Ritt J., Baglan N. and Cossonnet C. Potentialities of mass spectrometry (ICP-MS) for actinides determination in urine. *Appl. Radiat. Isot.* **60**(5): 629-633; 2004.

Braid I.C. Designing with Volumes. *Ph.D. Thesis, University of Cambridge, England*; 1973.

Bremaud M. Modélisation du système de mesure du laboratoire mobile d'anthroporadiométrie et étalonnage numérique à partir d'une famille de fantômes voxelisés masculins. *Rapport de stage, Université Claude Bernard Lyon I*; 2011.

Bremner D., Demaine E., Erickson J., Iacono J., Langerman S., Morin P. and Toussaint G. Output-Sensitive Algorithms for Computing Nearest-Neighbour Decision Boundaries. *Discrete Comput. Geom.* **33**(4): 593-604; 2005.

Briesmeister J.F. (Editor). MCNP-A general Monte Carlo N-particle transport code. Los Alamos National Laboratory, *LA-13709-M Version 4C*; 2000.

Broggio D., Janeczko J., Lamart S., Blanchardon E., Borisov N., Molokanov A., Yatsenko V. and Franck D. New method based on Monte Carlo calculation and voxelized phantoms for realistic internal dosimetry: application to a complex and old actinide contamination. *Nuclear Technology* **168**(3): 824-831; 2009.

Broggio D., Beurrier J., Farah J. and Franck D. Construction of an extended library of full body male voxel models: rationale and preliminary results. *Proceedings of the SNA+MC2010 conference*; 2010.

Brown T.P., Ringrose C., Hyland R.E., Cole A.A. and Brotherton T.M. A method of assessing female breast morphometry and its clinical application. *Br. Jr. Plast. Surg.* **52**(5): 355-359; 1999.

Caon M., Bibbo G. and Pattison J.E. An EGS4-ready tomographic computational model of a 14-year-old female torso for calculating organ doses from CT examinations. *Phys. Med. Biol.* **44**(9): 2213-2225; 1999.

de Carlan L., Aubineau-Lanièce I., Borissov N., Jourdain J.R., Jeanbourquin D., Le Guen B. and Franck D. Application of new imaging and calculation techniques for the activity and dose assessment in the case of a Ru-106 contaminated wound. *Radiat. Prot. Dosim.* **105**(1-4): 219-224; 2003.

de Carlan L., Roch P., Blanchardon E., Franck D. Application of voxel phantoms in whole-body counting for the validation of calibration phantoms and the assessment of uncertainties. *Radiat. Prot. Dosim.* **125**(1-4): 477-482; 2007.

Cassola V.F., De Melo Lima V.J., Kramer R., Khoury H.J. FASH and MASH: female and male adult human phantoms based on polygon mesh surfaces: I Development and the anatomy. *Phys. Med. Biol.* **55**(1): 133-162; 2010.

Chiavassa S. Développement d'un outil dosimétrique personnalisé pour la radioprotection en contamination interne et la radiothérapie vectorisée en médecine nucléaire. *Mémoire de Thèse, Université Paul Sabatier*; 2005.

Christ A., Kainz W., Hahn E.G., Honegger K., Zefferer M., Neufeld E., Rascher W., Janka R., Bautz R., Chen J., Kiefer B., Schmitt P., Hollenbach H.P., Shen J., Oberle M., Szczerba D., Kam A., Guag J.W. and Kuster N. The Virtual Family development of surface-based anatomical models of two adults and two children for dosimetric simulations. *Phys. Med. Biol.* **55**(2): 23-38; 2010.

Clairand I. Développement de nouveaux modèles physiques dédiés à la dosimétrie interne par l'utilisation du code de Monte Carlo EGS. *Mémoire de hèse, Université Paul Sabatier, Toulouse*; 1999.

Clairand I., Bouchet L.G., Ricard M., Durigon M., Di Paola M., Aubert B. Improvement of internal dose calculations using mathematical models of different adult heights. *Phys. Med. Biol.* **45**(10): 2771-2785; 2000.

Code du Travail. Code du Travail, quatrième partie - santé et sécurité au travail, livre IV - prévention de certains risques d'exposition, titre V - préventions des risques d'exposition aux rayonnements ionisants, section 3 - valeurs limites d'exposition, article R4451-12; 2008.

Courageot E., Huet C., Clairand I., Bottollier-Depois J.F. and Gourmelon P. Numerical dosimetric reconstruction of radiological accident in South America on April 2009. *Radiat. Prot. Dosim.* doi:10.1093/rpd/ncq338; 2010.

Cristy M. Mathematical phantoms representing children of various ages for use in estimates of internal dose. *U.S. Nuclear Regulatory Commission Rep., NUREG/CR-1159, Also Oak Ridge National Laboratory Rep., ORNL/NUREG/TM-367*; 1980.

Davesne E. Optimisation des programmes de surveillance de la contamination interne par l'étude des incertitudes liées à l'évaluation dosimétrique. *Mémoire de Thèse, Université Paris-Sud 11*; 2010.

DeLand F.H. and North W.A. Relationship between liver size and body size. *Radiology.* **91**(6): 1195–1198; 1968.

Dimbylow P.J. The development of realistic voxel phantoms for electromagnetic field dosimetry. *Proc. Int. Workshop on Voxel Phantom Development. Chilton, UK: National Radiological Protection Board*; 1995.

Dimbylow P.J. Development of the female voxel phantom, Naomi, and its application to calculations of induced current densities and electric fields from applied low frequency magnetic and electric fields. *Phys. Med. Biol.* **50**(6): 1047-1070; 2005.

Doerfel H., Andrasi A., Bailey M., Berkovski V., Blanchardon E., Castellani C.M., Hurtgen C., LeGuen B., Malatova I., Marsh J., Stather J. General guidelines for the estimation of Committed Effective Dose from incorporation monitoring data. *Project IDEAS-EU Contract No. FIKR-CT2001-00160*; 2006.

Drew J. P and Monson J.R.T. Artificial Neural Networks. *Surgery* **127**(1): 3-11; 2000.

Eckerman K.F., Leggett R. W., Cristy M., Nelson C.B., Ryman J.C., Sjoreen A.L. and Ward R.C. User's Guide to the DCAL System. *ORNL/TM-2001/190*; 2006.

Ecole Joliot Curie, 2006: Berger J.-F., Baeten P., Bauge E., Jurado B., Boudard A., Billard I., Varraine F., Billebaud A., David S., Nifenecker H. and Protassov K. Le cycle électronucléaire : de la fission aux nouvelles filières.

<http://www.cenbg.in2p3.fr/heberge/EcoleJoliotCurie/coursJC/Joliotcurie2006.pdf>

European Committee for Standardization (CEN). Size designation of clothes: -part 1. Terms, definitions and body measurement procedure EN 13402-1 (ISO 3635:1981 modified); 2001.

European Committee for Standardization (CEN). Size designation of clothes: -part 2. Primary and secondary dimensions EN 13402-2; 2002.

European Committee for Standardization (CEN). Size designation of clothes: -part 3. Measurements and intervals EN 13402-3; 2004.

Fabié A., Delay E., Chavoïn J.P., Soulhiard F. and Seguin P. Plastic surgery application in artistic studies of breast cosmetic. *Ann. Chir. Plast. Esthet.* **51**(2):142-150 ; 2006.

Farah J., Henriët J., Broggio D., Laurent R., Fontaine E., Chebel-Morello B., Sauget M., Salomon M., Makovicka L. and Franck D. Development of a new CBR-Based platform for human contamination emergency situations. *Radiat. Prot. Dosim.* **144**(1-4): 564-570; 2011.

Fish H.L.J. and Snyder W.S. Distribution of dose in the body from as source of gamma rays distributed uniformly in an organ. *ORNL-4168, Oak Ridge, TN: Oak Ridge National Laboratory*, 1967.

Franck D., de Carlan L., Berard P., Dousse C., Pihet P., Razafindralambo N. and Soulie R. Les mesures anthroporadiométriques dans les basses énergies : évolution technologique et bases des recherches actuelles. *Radioprotection* **32**(5): 685-696; 1997.

Franck D., Borissov N., de Carlan L., Pierrat N., Genicot J.L. and Etherington G. Application of Monte Carlo calculations to calibration of anthropomorphic phantoms used for activity assessment of actinides in lungs. *Rad. Prot. Dos.* **105**(1-4): 403-408; 2003.

Franck D., de Carlan L., Pierrat N., Broggio D. and Lamart S. OEDIPE: a new graphical user interface for fast construction of numerical phantoms and MCNP calculations. *Radiat. Prot. Dos.* **127**(1-4): 262-265; 2007.

Fry F.A. and Sumerling T. Measurement of chest wall thickness for assessment of plutonium in human lungs. *Health Phys.* **39**(1): 89-92; 1980.

Gibbs S.J., Pujol A., Chen T.S., Malcolm A.W. and James A.E. Patient risk from interproximal radiography. *Oral Surg. Oral Med. Oral Pathol.* **58**(3): 347-354; 1984.

Griffith R.V., Dean P.N., Anderson A.L. and Fisher J.C. Fabrication of a tissue-equivalent torso phantom for intercalibration of in-vivo transuranic-nuclide counting facilities. *Symp. Adv. Radiat. Prot. Monit.* (Stockholm, Sweden); 1978.

Gualdrini G., Battisti P., Biagini R., De Felice P., Fazio A. and Ferrari P. Development and characterisation of a head calibration phantom for in vivo measurements of actinides. *Appl. Radiat. Isot.* **53**(1-2): 387-393; 2000.

Haynor D.R., Harrison R.L. and Lewellen T.K. The use of importance sampling techniques to improve the efficiency of photon tracking in emission tomography simulations. *Med. Phys.* **18**(5): 990-1001; 1991.

Hegenbart L., Na Y. H., Zhang J. Y., Urban M. and Xu X. G. A Monte Carlo study of lung counting efficiency for female workers of different breast sizes using deformable phantoms. *Phys Med. Biol.* **53**(19): 5527-5538; 2008.

Hendricks J.S. MCNPX, Version 2.5e. Los Alamos National Laboratory Report, *LA-UR-04-0569*; 2004.

Hendricks J. and McKinney G.W. Pulse-height tallyies with variance reduction. American Nuclear society topical meeting in Monte Carlo, Chattanooga, TN. *LA-UR-05-2806*; 2005.

Henriet J., Farah J., Chebel-Morello B., Bopp M., Broggio D. and Makovicka L. Feasibility study of a new platform based on the Case-Based Reasoning principles to efficiently search and store voxel phantoms. *Radioprotection* **45**(1): 67-82; 2010.

Heymsfield S.B., Gallagher D., Mayer L., Beetsch J., Pietrobelli A. Scaling of human body composition to stature: New insights into body mass index. *Am. J. Clin. Nut.* **86**(1): 82-91; 2007.

Hurtgen C. and Cossonnet C. OMINEX Work Package 3, Uncertainties on bioassay measurements, Scientific Report *SCK•CEN - BLG-935 SCK•CEN (Mol) BLG-935*; 2003.

International Commission on Radiological Protection Publication 30. Report of the Task Group on Reference Man; 1975. (Oxford: Pergamon)

International Commission on Radiological Protection Publication 54. Individual monitoring for intakes of radionuclides by workers: design and interpretation. *Ann. ICRP* **19**(1-3); 1988. (Pergamon Press, Oxford).

International Commission on Radiological Protection Publication 71. Age-dependent doses to member of the public from intake of radionuclides: Part 4 Inhalation dose coefficients. *Ann. ICRP* **25**(3-4); 1995. (Oxford: Elsevier Science Ltd)

International Commission on Radiological Protection Publication 78. Individual monitoring for internal exposure of workers. *Ann. ICRP* **27**(3/4); 1997. (Oxford: Elsevier Science Ltd)

International Commission on Radiological Protection. CD-ROM Version 2.01: The ICRP database of dose coefficients: workers and members of the public: An extension of ICRP publications 68 and 72; 1998.

International Commission on Radiological Protection Publication 89. Basic anatomical and physiological data for use in radiological protection: Reference values. *Ann. ICRP* **32**(3-4); 2002. (New York: Elsevier).

International Commission on Radiological Protection Publication 103. The 2007 Recommendations of the International Commission on Radiological Protection. *Ann. ICRP* **37**(2-4); 2007. (Oxford: Elsevier)

International Commission on Radiological Protection Publication 107. Nuclear Decay Data for Dosimetric Calculations. *Ann. ICRP* **38**(3); 2008. (Oxford: Elsevier)

International Commission on Radiological Protection Publication 110. Adult reference computational phantoms. *Ann. ICRP* **39**(2); 2009. (Oxford: Elsevier)

International Commission on Radiation Units and Measurements. Tissues Substitutes in Radiation Dosimetry and Measurements. *ICRU Report 44*; 1989.

International Commission on Radiation Units and Measurements. Phantoms and Computational Models in Therapy, Diagnosis and Protection. *ICRU Report 48*; 1992. (Bethesda, MD: ICRU)

International Commission on Radiation Units and Measurements. Fundamental quantities and units for ionizing radiation. *ICRU Report 60*; 1998. (Bethesda, MD: ICRU)

International Organization for Standardization. Determination of the characteristic limits (decision threshold, detection limit and limits of the confidence interval) for measurements of ionizing radiation -- Fundamentals and application. *ISO 11929*; 2010.

Johnson P.B., Whalen S.R., Wayson M., Juneja B., Lee C. and Bolch W.E. Hybrid patient-dependent phantoms covering statistical distributions of body morphometry in the u.s. adult and pediatric population. *Proceedings of the IEEE* **97**(12): 2060-2075; 2009.

Jones D.G. A realistic anthropomorphic phantom for calculating organ doses arising from external photon irradiation. *Radiat. Prot. Dosim.* **72**(1): 21-29; 1997.

Kawrakow I. and Rogers D.W.O. The EGSnrc Code System: Monte Carlo Simulation of Electron and Photon Transport. *NRCC Report PIRS-701*; 2001.

Kinase S., Zankl M., Kuwabara J., Sato K., Noguchi H., Funabiki J. and Saito K. Evaluation of specific absorbed fractions in voxel phantoms using Monte Carlo simulation. *Radiat. Prot. Dosim.* **105**(1-4): 557-563; 2003.

Kovtun A.N., Firsanov V.B., Fominykh V.I. and Isaakyan G.A. Metrological parameters of the unified calibration whole-body phantom with gamma-emitting radionuclides. *Radiat. Prot. Dosim.* **89**(3-4): 239-242; 2000.

Kramer G.H. and Burns L. C. Effect of radionuclide distributions on lung counting efficiency. *Radiat. Prot. Dosim.* **61**(1-3): 145-7; 1995.

Kramer G.H., Crowley P. and Burns L.C. The uncertainty in the activity estimate from a lung count due to the variability in chest wall thickness profile. *Health Phys.* **78**(6): 739-743; 2000.

Kramer G.H., Hauck B.M and Allen S.A. Chest Wall Thickness measurements and the dosimetric implications for male workers in the Uranium Industry. *Health Phys.* **80**(1): 74-80; 2001.

Kramer G.H., Burns L.C. and Thind K.S. Monte Carlo simulations: A useful tool to extend in vivo calibrations and explore alternative approaches. *Rad. Prot. Dos.* **105**(1-4): 553-556; 2003a.

Kramer G.H and Capello K. Effect of lung volume on counting efficiency: a Monte Carlo investigation. *Health Phys.* **88**(4): 357-363; 2005.

Kramer R., Zankl M., Williams G., Drexler G. The calculation of dose from external photon exposures using reference human phantoms and Monte Carlo methods: Part I. The male (Adam) and female (Eva) adult mathematical phantoms. *GSF-report-S-885*; 1982.

Kramer R, Vieira J.W., Khoury H.J., Lima F.R.A. and Fuelle D. All about MAX: a male adult voxel phantom for Monte Carlo calculations in radiation protection dosimetry. *Phys Med Biol.* **48**(10): 1239-1262; 2003b.

Kramer R, Khoury H.J., Vieira J.W., Loureiro E.C.M., Lima V.J.M., Lima F.R.A. and Hoff G. All about FAX: a Female Adult voXel phantom for Monte Carlo calculation in radiation protection dosimetry. *Phys. Med. Biol.* **49**(23): 5203-5216; 2004.

Kruchten D.A. and Anderson A.L. Improved ultrasonic measurement techniques applied to assay of Pu and other transuranics in lung. *Health Phys.* **59**(1): 117-123; 1990.

Kuzmin D. A Guide to Numerical Methods for Transport Equations. Friedrich-Alexander-Universitat, Erlangen-Nurnberg; 2010. <http://www.mathematik.uni-dortmund.de/~kuzmin/Transport.pdf>

de La Grandmaison G.L., Clairand I., Durigon M. Organ weight in 684 adult autopsies: New tables for a Caucasoid population *Forensic Science International*, **119**(2): 149-154; 2001.

Lamart S. and Hendricks J.S. A Human Voxel Phantom Distributed Source Monte Carlo Solution. *Transactions on Nuclear Science, American Nuclear Society 2007 winter meeting* **97**: 456-457; 2007.

Lamart S. Etude de l'influence de la biocinétique des radionucléides sur la mesure anthroporadiométrique à l'aide de fantômes numériques voxelisés. *Mémoire de Thèse, Université Paris-Sud 11*; 2008.

Lataillade J.J., Doucet C., Bey E., Carsin H., Huet C., Clairand I., Bottollier-Depois J.F., Chapel A., Ernou I., Gourven M., Boutin L., Hayden A., Carcamo C., Buglova E., Joussemet M., de Revel T. and Gourmelon P. New approach to radiation burn treatment by dosimetry-guided surgery combined with autologous mesenchymal stem cell therapy. *Regen. Med.* **2**(5): 785-794; 2007.

Lathrop K.D. and Carlson B.G. Discrete Ordinates Angular Quadrature of the Neutron Transport Equation. *Los Alamos Scientific Laboratory LA-3186*; 1965.

Laurent R., Henriot J., Salomon M., Sauget M., Nguyen F., Gschwind R., Makovicka L. Utilisation d'un réseau de neurones artificiels pour la simulation des mouvements pulmonaires. *Cancer/Radiothérapie* **15**(2): 123-129; 2010.

Lee H.Y., Hong K., Kim E.A. Measurement protocol of women's nude breasts using a 3D scanning technique. *Appl. Ergonom.* **35**(4): 353-9; 2004.

Lee C., Lee C. and Bolch W.E. Age-dependent organ and effective dose coefficients for external photons: A comparison of stylized and voxel-based paediatric phantoms. *Phys. Med. Biol.* **51**(18): 4663-4688; 2006a.

Lee C., Lee C., Park S.-H. and Lee J.-K. Development of the two Korean adult tomographic computational phantoms for organ dosimetry. *Medical Phys.* **33**(2): 380-390; 2006b.

- Lee C., Lee C., Lodwick D. and Bolch W.E. NURBS-based 3-d anthropomorphic computational phantoms for radiation dosimetry applications. *Radiat. Prot. Dosim.* **127**(1-4): 227-232; 2007a.
- Lee C., Lodwick D., Hasenauer D., Williams J.L., Lee C. and Bolch W.E. Hybrid computational phantoms of the male and female newborn patient: NURBS-based whole-body models. *Phys. Med. Biol.* **52**(12): 3309-3333; 2007b.
- Lee C., Kaufman K., Hasenauer-Pafundi D., and Bolch W.E. An Algorithm for Lymphatic Node Placement in Hybrid Computational Phantoms. *Proceedings of the IEEE.* **97**(12) : 2098-2108; 2009.
- Legget R.W., Williams L.R., Meloc D.R. and Lipsztein J.L. A physiologically based biokinetic model for cesium in the human body. *The Science of the Total Environment* **317**(1-3): 235-255; 2003.
- Lemosquet A., de Carlan L., Clairand I. and Aubineau-Lanière I. Fantômes numériques anthropomorphes appliqués à la dosimétrie des rayonnements ionisants : état de l'art. *Rapport IRSN - SDOS/2002-004*; 2002.
- Lemosquet A., de Carlan L. and Clairand I. Voxel anthropomorphic phantoms: review of models used for ionising radiation dosimetry. *Radioprotection* **38**(4): 509-528; 2003.
- LeVeque R. Finite Volume Methods for Hyperbolic Problems. *Cambridge University Press*; 2002.
- Lopez-Ponte M.A. and Bravo T.N. A low energy germanium detector system for lung counting at the WBC facility of CIEMAT. *Radiat. Prot. Dosim.* **89**(3-4): 221-227; 2000.
- Lopez-Ponte M.A. and Navarro T. Sensitivity of a low energy Ge detector system for in vivo monitoring in the framework of ICRP 78 applications. *Radiat. Prot. Dosim.* **105**(1-4): 477-482; 2003.
- Lopez-Ponte M.A., Broggio D., Capello K., Cardenas-Mendez E., El-Faramawy N., Franck D., James A.C., Kramer G.H., Lacerenza G., Lynch T.P., Navarro J.F., Navarro T., Perez B., Rühm W., Tolmachev S.Y. and E. Weitzenegger. Eurados intercomparison on measurements and Monte Carlo modeling for the assessment of americium in a USTUR leg phantom. *Radiat. Prot. Dosim.* **144**(1-4): 295-299; 2011.
- Loughry C.W., Sheffer D.B, Price T.E. Einsporn R.L., Bartfai R.G., Morek W.M. and Meli N.M. Breast volume measurement of 598 women using biostereometric analysis. *Ann. Plast. Surg.* **22**(5): 380-385; 1989.
- Ludwig J. Normal weights and measurements. In Current Methods of Autopsy Practice. ed. Ludwig, J. pp. 315-347. Philadelphia: W.B. Saunders and Co; 1972.
- Makovicka L., Vasseur A., Sauget M., Martin E., Gschwind R., Henriot J., Salomon M. Avenir des nouveaux concepts des calculs dosimétriques basés sur les méthodes de Monte Carlo. *Radioprotection.* **44**(1), 77-88; 2009.
- Marzocchi O., Breustedt B. and Urban M. Characterisation, modelling and optimisation of the model of a HPGe detector with the aid of point sources. *Appl. Radiat. Isot.* **68**(7-8): 1438-1440; 2010.

Métivier H. Toxiques nucléaires (sous la direction de P. Galle) 2^{ème} édition, Editions Masson, Paris; 1997.

Métivier H. Radioprotection et ingénierie nucléaire; 2006. (Les Ulis: EDP Sciences)

Metropolis N. and Ulam S. The Monte Carlo Method. *Journal of the American Statistical Association*. **44**(247): 335-341; 1949.

Mille A. Tutorial CBR : Etat de l'art de raisonnement à partir de cas, Plate-forme AFIA'99, Palaiseau, France (1999).

Molnar G.L., Révay Z. and Belgya T. Wide energy range efficiency calibration method for Ge detectors. *Nucl. Instrum. Meth.* **489**(1-3): 140-159; 2002.

Na Y.H., Zhang B., Zhang J., Caracappa P.F. and Xu X.G. Deformable adult human phantoms for radiation protection dosimetry: Anthropometric data representing size distributions of adult worker populations and software algorithms. *Phys. Med. Biol.* **55** (13): 3789-3811; 2010.

Nelson W.R., Hirayama H., Rogers D.W.O. The EGS4 Code System; 1985.

<http://www.slac.stanford.edu/pubs/slacreports/slac-r-265.html>

Newton D., Wells A.C., Mizushita S., Toohey R.E., Sha J.Y., Jones R., Jefferies S.J., Palmer H.E., Rieksts G.A., Anderson A.L. and Campbell G.W. The Livermore phantom as a calibration standard in the assessment of plutonium in lungs IN Proc. Assessment of Radioactive Contamination in Man, Paris, 19-23 november 1984, organized by IAEA in co-operation with WHO; 1984.

Nooruddin F. and Turk G. Simplification and Repair of Polygonal Models Using Volumetric Techniques. *IEEE Trans. Vis. Comput. Graphics.* **9**(2): 191-205; 2003.

Padilla L., Lee C., Milner R., Shahlaee A. and Bolch W.E. Canine Anatomic Phantom for Preclinical Dosimetry in Internal Emitter Therapy. *J. Nucl. Med.* **49**(3): 446-452; 2008.

Park S., Lee J.K. and Lee C. Development of a Korean adult male computational phantom for internal dosimetry calculation. *Radiat. Prot. Dosim.* **121**(3): 257-264; 2006.

Pechter E.A. A new method for determining bra size and predicting postaugmentation breast size. *Plast. Reconstr. Surg.* **102**(4): 1259-1265; 1998.

Pelowitz D.B. (ed). MCNPX User's manual version 2.5.0. Los Alamos National Laboratory Report LA-CP-05-0369; 2005.

Petoussi-Hens N., Jacob P., Zankl M. and Saito K. Organ doses for fetuses, babies, children and adults from environmental gamma-rays. *Radiat. Prot. Dosim.* **37**(1): 31-41; 1991.

Petoussi-Hens N. and Zankl M. Voxel anthropomorphic models as a tool for internal dosimetry. *Radiat. Prot. Dosim.* **79**(1-4): 415-418; 1998.

Pierrat N. Application des fantômes numériques voxélisés associés au code Monte Carlo MCNP à la mesure in vivo réaliste des actinides dans les poumons et les plaies contaminées. *Mémoire de Thèse, Université Paris-Sud 11*; 2005.

Podgorsak B. Review of Radiation Oncology Physics: A Handbook for Teachers and Students Editor: *Ervin International Atomic Energy Agency*, pp: 138-139, 2003.

Pretorius P. H., Xia W., King M.A., Tsui B.M., Pan T.S. and Villegas B.J. Evaluation of right and left ventricular volume and ejection fraction using a mathematical cardiac torso phantom. *J. Nucl. Med.* **38**(10):1528-1535; 1997.

Razafindralambo N. Limite de détection de la spectrométrie X pour l'anthroporadiométrie pulmonaire du plutonium : Analyse et perspectives de développement. *Mémoire de Thèse, Université Paul Sabatier*; 1995.

Regnault P., Baker T.J., Gleason M.C., Gordon H.L., Grossman A.R., Lewis J.R., Waters W.R. and Williams J.E. Clinical trial and evaluation of a proposed new inflatable mammary prosthesis. *Plast. Reconst. Surg.* **50**(3): 220-226; 1972.

Ringberg A., Bageman E., Rose C., Ingvar C., Jernstrom H. Of breast and cup size: Reply to a prospective study of breast size and premenopausal breast cancer incidence. *Int. J. Cancer* **119**(9): 2242-2243; 2006.

Roger M. Méthodes de Monte-Carlo. Cours du CEA/Saclay Service de Physique de l'Etat Condensé; 2008.

Sachse F.B., Werner C.D., Meyer-Waarden K. and Dössel O. Development of a human body model for numerical calculation of electrical fields. *Comput. Med. Imaging Graph.* **24**(3): 165-171; 2000.

Salvat F., Fernández-Varea J.M. and Sempau J. PENELOPE-2006: A Code System for Monte Carlo Simulation of Electron and Photon Transport. Workshop Proceedings Barcelona, Spain 4-7 July 2006. <http://www.nea.fr/html/science/pubs/2006/nea6222-penelope.pdf>

Saito K., Wittmann A., Koga S., Ida Y., Kamei T., Funabiki J. and Zankl M. Construction of a computed tomographic phantom for a japanese male adult and dose calculation system. *Radiat. Environ. Biophys.* **40**(1): 69-76; 2001.

Sato K., Noguchi H., Emoto Koga Y. and Saito K. Japanese adult male voxel phantom constructed on the basis of CT-images. *Radiat. Prot. Dosim.* **123**(3): 337-344; 2007.

Schlagbauer M. Calibration and uncertainty budget analyses for a whole body counter in scan geometry using physical and numerical phantoms. *PhD thesis, Graz University of Technology*; 2006.

Segars W.P. Development of a new dynamic NURBS-based cardiac-torso (NCAT) phantom. *PhD thesis, The University of North Carolina*; 2001.

Segars W.P., Lalush D.S. and Tsui B.M.W. Modeling respiratory mechanics in the MCAT and spline-based MCAT phantoms. *IEEE Trans. Nucl. Sci.* **48**(1): 89-97; 2001.

Segars W.P., Tsui B.M.W., Frey E.C., Johnson W.A. and Berr S.S. Development of a 4D Digital Mouse Phantom for Molecular Imaging Research. *Mol. Imaging Biol.* **6**(3): 149-159; 2004.

Shi C. and Xu X.G. Development of a 30-week-pregnant female tomographic model from computed tomography (CT) images for Monte Carlo organ dose calculations. *Med. Phys.* **31**(9): 2491-2497; 2004.

Shirovani T. Realistic Torso Phantom for Calibration on in vivo Transuranic-nuclide Counting Facilities. *J. Nucl. Sci. Technol.* **25**(11): 875-883; 1988.

Sigurdson L.J. and Kirkland S.A. Breast volume determination in breast hypertrophy: an accurate method using two anthropomorphic measurements. *Plast. Reconst. Surg.* **118**(2): 313-320; 2006.

Smith D.J.Jr., Palin W.E.Jr., Katch V.L., Bennett J.E. Breast volume and anthropomorphic measurements: Normal values. *Plast. Reconst. Surg.* **78**(3): 331-335; 1986.

Snyder W.S., Ford M.R., Warner G.G. and Fisher H.L. Estimates of absorbed fractions for monoenergetic photon sources uniformly distributed in various organs of a heterogeneous phantom. *Medical Internal Radiation Dose Committee pamphlet n°5 revised*; 1978.

Spitzer V.M. and Whitlock D.G. The visible human dataset: The anatomical platform for human simulation. *The Anatomical Record* **253**(2): 49-57; 1998. (doi: 10.1002/(SICI)1097-0185(199804)253:2<49::AID-AR8>3.0.CO;2-9)

Stabin M., Watson E., Cristy M., Ryman J., Eckerman K., Davis J., Marshall D. and Gehlen K. Mathematical models and specific absorbed fractions of photon energy in the nonpregnant adult female and at the end of each trimester of pregnancy. *Report No ORNL/TM-12907 Oak Ridge National Laboratory, Oak Ridge, TN, USA*; 1995.

Stabin M. and Siegel J. Physical models and dose factors for use in internal dose assessment. *Health Phys.* **85**(3): 294-310; 2003.

Staton R.J., Lee C., Lee C., Williams M.D., Hintenlang D.E., Arreola M.M., Williams J.L. and Bolch W.E. Organ and effective doses in newborn patients during helical multislice computed tomography examination. *Phys. Med. Biol.* **51**(20): 5151-5166; 2006.

Stroud I. Bounded representation modeling techniques. ISBN 978-1-84628-312-3; 2006. (London: Springer-Verlag)

Sumerling T.J and Quant S.P. Measurement of the human anterior chest wall by ultrasound and estimates of chest wall thickness for use in determination of transuranic nuclides in the lung. *Radiat. Prot. Dosim.* **3**(4): 203-210; 1982.

Taranenko V. and Xu X.G. Fluence to absorbed foetal dose conversion coefficients for photons in 50 keV—10 GeV calculated using RPI-P model. *Radiat. Prot. Dosim.* **131**(2): 159-166; 2008.

Tsui B.M.W., Terry J.A. and Gullberg G.T. Evaluation of cardiac cone-beam single-photon emission computed tomography using observer performance experiments and receiver operating characteristic analysis. *Invest. Radiol.* **28**(12): 1101-1012; 1993.

- Tsui B.M.W., Zhao X.D., Gregoriou G. K., Lalush D.S., Frey E.C., Johnston R.E. and McCartney W.H. Quantitative cardiac SPECT reconstruction with reduced image degradation due to patient anatomy. *Nucl. Sci. IEEE Trans.* **41**(2): 2838-2844; 1994.
- Turner A.J. and Dujon D.G. Predicting cup size after reduction mammoplasty. *Br. Jr. Plast. Surg.* **58**(3): 290-298; 2005.
- Usuda K., Kono K., Dote T., Shimizu H., Tominaga M., Koizumi C., Nakase E., Toshina Y., Iwai J., Kawasaki T. and Akashi M. Log-normal distribution of the trace element data results from a mixture of stochastic input and deterministic internal dynamics. *Biol. Trace Elem. Res.* **86**(1): 45-54; 2002.
- Vandeput J.J. and Nelissen M. Considerations on Anthropometric Measurements of the Female Breast. *Aesth. Plast. Surg.* **26**(5): 348-355; 2002.
- Veit R., Zankl M., Petoussi N., Mannweiler E., Williams G. and Drexler G. Tomographic anthropomorphic models, Part I: Construction technique and description of models of an 8-week-old baby and a 7-year-old child. GSF Report 3/89 GSF-National Research Center for Environment and Health, Neuherberg, Germany; 1989.
- Vickers L.R. The gender specific chest wall thickness prediction equations for routine measurements of ^{239}Pu and ^{241}Am within the lungs using HPGe detectors. *Health Phys.* **70**(3), 346-357; 1996.
- Wainwright P. Thermal effects of radiation from cellular telephones. *Phys. Med. Biol.* **45**(8): 2363-2372; 2000.
- Warren R. Thompson D., del Frate C., Cordell M., Highnam R., Tromans C., Warsi I., Ding J., Sala E., Estrella F., Solomonides A.E., Odeh M., McClatchey R., Bazzocchi M., Amendolia S.R. and Brady M. A comparison of some anthropometric parameters between an Italian and a UK population “proof of principle” of a European project using MammoGrid. *Clin Radiol.* **62**(11): 1052-60; 2007.
- Williams G., Zankl M., Abmayr W., Veit R. and Drexler G. The calculation of dose from external photon exposures using reference and realistic human phantoms and Monte Carlo methods. *Phys. Med. Biol.* **31**(4): 449-452; 1986.
- Wood K., Cameron M. and Fitzgerald K. Breast size, bra fit and thoracic pain in young women: a correlational study. *Chiropr. Osteopat.* **16**(1); 2008. doi:10.1186/1746-1340-16-1
- Xu X.G., Chao T. C. and Bozkurt A. VIP-MAN: an image-based whole- body adult male model constructed from color photographs of the visible human project for multi-particle Monte Carlo calculations. *Health Phys.* **78**(5), 476-486; 2000.
- Xu X.G. and Shi C. Preliminary development of a 4D anatomical model for Monte Carlo simulations, in Monte Carlo 2005 Topical Meeting. The Monte Carlo Method: Versatility Unbounded in a Dynamic Computing World, Chattanooga, TN, April 17-21, 2005.
- Xu X.G., Su H. and Bushart S. The EPRI EDE calculator – A software package for assessing effective dose equivalent from hot particles on the skin. *Health Phys.* **91**(4): 373-378; 2006.

Xu X.G., Taranenko V., Zhang J. and Shi C. A boundary-representation method for designing whole-body radiation dosimetry models: pregnant females at the ends of three gestational periods - RPI-P3, -P6 and -P9. *Phys. Med. Biol.* **52**(23): 7023-7044; 2007.

Xu X.G., Zhang J.Y. and Na Y.H. Preliminary data for mesh-based deformable phantom development: is it possible to design person-specific phantoms on-demand? *ICRS-11 and RPSD 2008. Callaway Gardens; Pine Mountain, GA, USA*; 2008.

Xu X.G. and Eckerman K.F. Handbook of anatomical models for radiation dosimetry; 2009. (Boca Raton, FL: Taylor & Francis)

Young V.L., Nemecek J.R., Nemecek D.A. The efficacy of breast augmentation: breast size increase, patient satisfaction, and psychological effects. *Plast. Reconst. Sur.* **94**(7): 958-969; 1994.

Zaidi H. and Xu X.G. Computational Anthropomorphic Models of the Human anatomy: The Path to Realistic Monte Carlo Modeling in Radiological Sciences. *Annu. Rev. Biomed. Eng.* **9**: 471-500; 2007.

Zankl M., Veit R., Williams G., Schneider K., Fendel H., Petoussi N. and Drexler G. The construction of computer tomographic phantoms and their application in radiology and radiation protection. *Radiat. Environ. Biophys.* **27**(2): 153-164; 1988.

Zankl M. and Wittmann A. The adult male voxel model 'Golem' segmented from whole-body CT patient data. *Radiat. Environ. Biophys.* **40**(2): 153-162 ; 2001.

Zhang B., Ma J., Liu L. and Cheng J. CNMAN: a Chinese adult male voxel phantom constructed from color photographs of a visible anatomical data set. *Radiat. Prot. Dosim.* **124**(2): 130-136; 2007.

Zhang J., Xu X.G., Shi C. and Fuss M. Development of a geometry-based respiratory motion-simulating patient model for radiation treatment dosimetry. *J. Appl. Clin. Med. Phys.* **9**(1): 16-28; 2008.

Zhang J., Na Y.H., Caracappa P.F. and Xu X.G. RPI-AM and RPI-AF, a pair of mesh-based, size-adjustable adult male and female computational phantoms using ICRP-89 parameters and their calculations for organ doses from monoenergetic photon beams. *Phys. Med. Biol.* **54** (19): 5885-5908; 2009.

Zubal I.G., Harrell C.R., Smith E.O., Rattner Z., Gindi G. and Hoffer P.B. Computerized three-dimensional segmented human anatomy. *Med. Phys.* **21**(2): 299-302; 1994.

List of publications

Farah J., Broggio D. and Franck D. Creation and use of adjustable 3D phantoms: application for the lung monitoring of female workers. *Health Phys.* **99**(5): 649–661; 2010.

Farah J., Broggio D. and Franck D. Female workers and in vivo lung monitoring: a simple model for morphological dependency of counting efficiency curves. *Phys. Med. Biol.* **55**(23): 7377-7395; 2010.

Farah J., Broggio D., Franck D. Utilisation des fantômes de type NURBS pour l'étude des facteurs morphologiques influent sur l'anthroporadiamétrie pulmonaire. *Proceedings Journées SFRP code de calcul en radioprotection, radiophysique et dosimétrie*. March 2010.

Farah J., Broggio D. and Franck D. Morphological dependence of lung counting efficiency for female workers. *Proceedings of the 3rd European IRPA conference*, June 2010.

<http://www.irpa2010europe.com/proceedings/S08/S08-04.pdf>

Farah J., Broggio D. and Franck D. Examples of Mesh and NURBS modeling for in vivo lung counting studies. *Radiat. Prot. Dosim.* **144**(1-4): 344-348; 2011.

Farah J., Henriet J., Broggio D., Laurent R., Fontaine E., Chebel-Morello B., Sauget M., Salomon M., Makovicka L. and D. Franck. Development of a new CBR-Based platform for human contamination emergency situations. *Radiat. Prot. Dosim.* **144**(1-4): 564-570; 2011.

Farah J., Broggio D. and Franck D. Nouvelle méthode de surveillance des travailleuses du nucléaire par anthroporadiamétrie : utilisation des calculs Monte Carlo associés aux fantômes déformables de type Mesh et NURBS. *Radioprotection* **46**(2): 209-233; 2011.

Farah J., Leone D., Marzocchi O., Navarro J.F., Perez B., Lucena E., Lopez-Ponte M.A., Breustedt B., Broggio D. and Franck D. Contamination mapping with in vivo measurements and Monte Carlo calculations. *Proceedings of the 17th International conference on Medical Physics. Special Issue of the Brazilian Journal of Medical Physics* **5**(1): 76; 2011.

Farah J., Broggio D. and Franck D. Efficient calculation of in vivo efficiency curves using Variance Reduction techniques. *Progress in Nuclear Science and Technology*, Accepted June 2011.

Farah J., Marzocchi O., Leone D., Broggio D., Breustedt B. and Franck D. Post accidental estimation of activity distribution using gamma spectrometry measurements and Monte Carlo calculations. *In progress*.

Henriet J., Farah J., Chebel-Morello B., Bopp M., Broggio D. and Makovicka L. Feasibility study of a new platform based on the Case-Based Reasoning principles to efficiently search and store voxel phantoms. *Radioprotection* **45**(1): 67-82; 2010.

Henriet J., Fontaine E., Bouhelal H., Farah J., Laurent R., Salomon M., Chebel-Morello B., Broggio D., Sauget M., Franck D., Makovicka L. Using an artificial neural network to adapt cases retrieved by a case-based reasoning. *Submitted Expert Syst.*

Broggio D., Beurrier J., Bremaud M., Desbrée A., Farah J., Huet C. and Franck D. Construction of an extended library of adult male 3D models: rationale and results. *Phys. Med. Biol. Accepted*, October 2011.

List of oral presentations

Farah J., Broggio D., Franck D. Utilisation des fantômes Mesh et NURBS pour l'étude des facteurs morphologiques influent sur l'anthroporadiamétrie pulmonaire. *26èmes Journées des Laboratoires Associés de Radiophysique et de Dosimétrie (LARD), Lausanne, Switzerland, 4-5 November 2009.*

Farah J., Broggio D., Franck D. Creation and use of adjustable phantoms: application for the lung monitoring of female nuclear workers. *Individual Monitoring of Ionizing Radiation (IM2010), 52nd Annual Meeting, Athens, Greece, 8-12 March 2010.*

Farah J., Broggio D., Franck D. Utilisation des fantômes de type NURBS pour l'étude des facteurs morphologiques influent sur l'anthroporadiamétrie pulmonaire. *Journées SFRP sur les codes de calcul en radioprotection, radiophysique et dosimétrie, Sochaux, France, 28-29 April 2010.*

Farah J., Broggio D., Franck D. Morphological dependence of lung counting efficiency for female workers. *3rd European IRPA Conference, Helsinki, Finland, 14-18 June 2010.*

Farah J., Broggio D., Franck D. Efficient Calculation of in vivo Efficiency curves. *The Joint International conference on the 7th Supercomputing in Nuclear Application and the 3rd Monte Carlo (SNA-MC2010), Tokyo, Japan, 17-21 October 2010.* Nominated "Student Award Finalist".

Farah J., Leone D., Marzocchi O., Navarro J.F., Perez B., Lucena E., Lopez-Ponte M.A., Breustedt B., Broggio D. and Franck D. Contamination mapping with in vivo measurements and Monte Carlo calculations. *18th International conference on Medical Physics, Porto Alegre, Brazil, 17-20 April 2011.*

Farah J., Broggio D., Franck D. Cartographie de l'activité incorporée en cas de contaminations complexes par l'utilisation des simulations Monte Carlo. *8^{ème} Congrès National de la SFRP, Tours, France, 21-23 June 2011.*

Farah J., Broggio D., Beurrier J. and Franck D. Nouvelle generation de fantômes 3D flexibles : application en dosimétrie interne. *8^{ème} Congrès National de la SFRP, Tours, France, 21-23 June 2011.* Nominated candidate of the French Society of Radiation Protection (SFRP) for the "Young Scientist Award" at the *13th International Congress of the International Radiation Protection Association (IRPA2012); Glasgow, United Kingdom, 13-18 May 2012.*

Appendix

Appendix A.1. IDL routine used to extract organ contours from the ICRP reference phantom.

```

pro Voxels_To_VRML
;; number of voxels of each dimension and voxel size
l_nNbPixels_X=fix(299) & Vx=0.1775
l_nNbPixels_Y=fix(137) & Vy=0.1775
l_nNbPixels_Z=fix(77) & Vz=0.4840
l_bytarrFantCol=BYTARR(l_nNbPixels_Z, l_nNbPixels_X, l_nNbPixels_Y)
;; reading the input file
l_dir="T:\SDI\LEDI_FAR\Jad FARAH\OEDIPE_Regina\dossier\Cipr\ETUDE-Cipr-1\fantseg\"
l_File='Thorax-reg-seg.seg'
l_path=l_dir+l_File
openr, lun, l_path, /GET_LUN
readu, lun, l_bytarrFantCol
free_lun, lun
;; defining the output file
l_outFile='JFRegina_'+strtrim(string(fix(keep_color)),2)+'-heart.wrl'
l_save=l_dir+l_outFile
;; ***** isolating the organ (color) of interest *****
keep_color=56b
ind_KEEP=where(l_bytarrFantCol EQ keep_color)
l_bytarrFantCol=0b*l_bytarrFantCol
l_bytarrFantCol[ind_KEEP]=1b
;; ***** MESHING *****
SHADE_VOLUME, l_bytarrFantCol, 0b, v, p, /low, $
                    Xrange=[0, l_nNbPixels_Z-1], Yrange=[0, l_nNbPixels_X-1], Zrange=[0,
l_nNbPixels_y-1], /verbose
SCALE3, Xrange=[0, l_nNbPixels_Z-1], Yrange=[0, l_nNbPixels_X-1], Zrange=[0, l_nNbPixels_y-
1]
TV, POLYSHADE(v, p, /T3D)
;; ***** Generating the string matrix of vertices *****
S=size(v, /dimensions)
N_vertex=S[1]
v(0,*)=Vz*v(0,*)
v(1,*)=Vy*v(1,*)
v(2,*)=Vx*v(2,*)
StrArrV=strarr(3, N_vertex)
StrArrV(0:2,*)=string(v)
StrArrV(2,0:N_vertex-2)=StrArrV(2,0:N_vertex-2)+' '+string(10b)
StrArrV(2,N_vertex-1)=StrArrV(2,N_vertex-1) +string(10b)
;; ***** Generating the string matrix of connectivities *****
;; number of faces of each polygon
temp=ulonarr(n_elements(p)) ; saving the connectivities in p (we noticed that sometimes 3, 4 or even
5 points were connected. So, when meshing, we should dissociate those of 4 and 5 to create triangles)
tempPos=ulonarr(n_elements(p)) ; saving the associated positions in p
ctr=0UL ; parameter that will count the number of 3, 4, 5 linked summits
i=0UL ; loop on p
while i LE n_elements(p)-1 do begin
    tempPos(ctr)=ulong(i+p(i)+1) ; position of 3 / 4 ; we add the position of the first "next" summit
    temp(ctr)=p(i) ; 3 or 4
    i=ulong(i+p(i)+1) ; jump to the next 3 / 4

```

```

ctr=ctr+1UL
endwhile
ind=where(temp NE 0UL)
ArrNbre_points=ulonarr(n_elements(ind))
ArrNbre_points=temp(ind)
ind=where(tempPos NE 0UL, nc)
Pos=[0UL, tempPos[ind[0:nc-2]]] ; nc-2 because the last element in tempPos is of p +1 size
ind_3=where(ArrNbre_points EQ 3UL, nc3)
ind_4=where(ArrNbre_points EQ 4UL, nc4)
ind_5=where(ArrNbre_points EQ 5UL, nc5)
N_connect=ulong(nc4*2 + nc3+ nc5*3)
print, N_connect
print, ArrNbre_points[uniq( ArrNbre_points, sort( ArrNbre_points))]
Mat_connect=ulonarr(3,N_connect)
ctr=0UL
for i=0UL,n_elements(Pos)-1 do begin
  if p(Pos(i)) EQ 3 then begin
    Mat_connect(*,ctr)=p(Pos(i)+1:Pos(i)+3)
    ctr=ctr+1
  endif else begin
    if p(Pos(i)) EQ 4 then begin
      Mat_connect(*,ctr)=p(Pos(i)+1:Pos(i)+3)
      Mat_connect(*,ctr+1)=[p(Pos(i)+3),p(Pos(i)+4),p(Pos(i)+1)]
      ctr=ctr+2
    endif else begin
      Mat_connect(*,ctr)=p(Pos(i)+1:Pos(i)+3)
      Mat_connect(*,ctr+1)=[p(Pos(i)+3),p(Pos(i)+4),p(Pos(i)+5)]
      Mat_connect(*,ctr+2)=[p(Pos(i)+5),p(Pos(i)+1),p(Pos(i)+3)]
      ctr=ctr+3
    endif
  endif
endfor
:: ***** writing the string matrix of connectivities in the Rhino input format
StrMatConnect=strarr(4, N_connect)
StrMatConnect[0:2,*]=string(Mat_Connect)
StrMatConnect[3,0:N_connect-2]='-1,'+string(10b)
StrMatConnect[3,N_connect-1]='-1'+string(10b)
StrMatConnect[0:2,*]=string(StrMatConnect[0:2,*])
StrMatConnect[0:2,*]=StrMatConnect[0:2,*]+' '
:: ***** Generating the string matrix of normal vectors *****
MatNorm=fltarr(size(Mat_connect, /dimensions))
for i=ulong(0), N_connect-1 do begin
  uu=V(*,Mat_Connect(1,i))-V(*,Mat_Connect(0,i))
  vv=V(*,Mat_Connect(2,i))-V(*,Mat_Connect(0,i))
  w=crossp(uu,vv)/norm(crossp(uu,vv),/double,lnorm=2)
  MatNorm(*,i)=w
endif
StrArrNorm=strarr(3,N_connect)
StrArrNorm(0:2,*)=string(MatNorm)
StrArrNorm(2,0:N_connect-2)=StrArrNorm(2,0:N_connect-2)+''+string(10b)
StrArrNorm(2,N_connect-1)=StrArrNorm(2,N_connect-1)+string(10b)
:: ***** Writing of the final VRML file *****
N_cut=3;
Entete='#VRML V2.0 utf8'+string(10b)+$
'Background {''+string(10b)+$

```

```

'skyColor [ 0.627451 0.627451 0.627451 ]'+string(10b)+$
}' +string(10b)+$
'Shape { # triangle mesh'+string(10b)+$
  'appearance Appearance {' +string(10b)+$
    'material      Material {' +string(10b)+$
      'ambientIntensity 0' +string(10b)+$
      'diffuseColor   1 1 1'+string(10b)+$
      'specularColor  0 0 0'+string(10b)+$
      'emissiveColor  0 0 0'+string(10b)+$
      'shininess     1'+string(10b)+$
      'transparency  0'+string(10b)+$
    }'+string(10b)+$
  } # appearance'+string(10b)+$
  'geometry IndexedFaceSet { # triangle mesh'+string(10b)+$
    'ccw TRUE'+string(10b)+$
    'convex TRUE'+string(10b)+$
    'solid FALSE'+string(10b)+$
    'coordIndex ['
openw,lun,l_save, /GET_LUN
writeu,lun,Entete
writeu,lun,strcompress(strtrim(StrMatConnect))
writeu,lun, ']' +string(10b)+'coord Coordinate { point ['
writeu,lun,strcompress(strtrim(StrArrV))
writeu,lun, ']' +string(10b)+'normal Normal { vector ['
writeu,lun,strcompress(strtrim(StrArrNorm))
writeu, lun,']}' +string(10b)+' } # geometry'+string(10b)+'}' # triangle mesh'
free_lun, lun
; ***** PLOT *****
oModel = OBJ_NEW('IDLgrModel') ; Initialize model for display.
vertex=v
; Initialize polygon and polyline outline to contain
; the mesh of the octahedron.
oPolygon = OBJ_NEW('IDLgrPolygon', vertex, $
  POLYGONS = Mat_connect, SHADING = 1, $
  COLOR = [0, 255, 0])
oPolyline = OBJ_NEW('IDLgrPolyline', vertex, $
  POLYLINES = Mat_connect, COLOR = [1, 1, 1])
oModel->Add, oPolyline
; Rotate model for better initial perspective.
oModel->Rotate, [-1, 0, 1], 22.5
; Display model.
XOBJVIEW, oModel, /BLOCK, SCALE = 1, $
  TITLE = 'Regina VRML'
end

```

Appendix A.2. IDL routine used to correct phantom intersections.

```

pro phantom_intersections_correction
; ***** reading organ matrix and assigning a color *****
N=256 ;number of voxels i.e. matrix dimension
Input_Dir='D:\Travail_sur_Regina\Regina_NURBS-Volume\';path to the voxel matrixes
Mat_cxt=read_binary(Input_Dir+'cxt.raw',Data_dims=[N,N,N])
Mat_cxt=Mat_cxt < 5b ; assign to the chest wall thickness the color 5
Mat_sternum=read_binary(Input_Dir+'sternum.raw',Data_dims=[N,N,N])
Mat_sternum=Mat_sternum < 10b ;assign to the sternum the color 10
Mat_scapulae = read_binary(Input_Dir+'scapulae.raw',Data_dims=[N,N,N])
Mat_scapulae = Mat_scapulae < 20b ;assign to the scapulae the color 20
Mat_ribs=read_binary(Input_Dir+'ribs.raw',Data_dims=[N,N,N])
Mat_ribs=Mat_ribs < 30b ;assign to the ribs the color 30
Mat_spine=read_binary(Input_Dir+'spine.raw',Data_dims=[N,N,N])
Mat_spine=Mat_spine < 40b ;assign to the spine the color 40
Mat_b_left=read_binary(Input_Dir+'breast_left.raw',Data_dims=[N,N,N])
Mat_b_left=Mat_b_left<50b ;assign to the left breast the color 50
Mat_b_right=read_binary(Input_Dir+'breast_right.raw',Data_dims=[N,N,N])
Mat_b_right=Mat_b_right < 50b ;assign to the right breast the color 50
Mat_l_left=read_binary(Input_Dir+'lung_left.raw',Data_dims=[N,N,N])
Mat_l_left =Mat_l_left < 60b ;assign to the left lung the color 60
Mat_l_right=read_binary(Input_Dir+'lung_right.raw',Data_dims=[N,N,N])
Mat_l_right=Mat_l_right < 60b ;assign to the right lung the color 60
Mat_heart=read_binary(Input_Dir+'heart.raw',Data_dims=[N,N,N])
Mat_heart=Mat_heart < 70b ;assign to the heart the color 70
Mat_liver=read_binary(Input_Dir+'liver.raw',Data_dims=[N,N,N])
Mat_liver=Mat_liver < 80b ;assign to the liver the color 80
; ***** start adding matrix and correct intersections *****
Mat_totale= Mat_cxt+ Mat_sternum          ; adding the sternum
Mat_totale = Mat_totale < 10b          ; replace the intersection by sternum

Mat_totale= Mat_totale + Mat_scapulae      ; adding the scapulae
errors_scapulae=where(Mat_totale gt 20b, count_errors_scapulae)
print, 'error scapulae intersection', count_errors_scapulae
Mat_totale = Mat_totale < 20b          ; replace the intersection by scapulae

Mat_totale= Mat_totale + Mat_ribs          ; adding the ribs
errors_ribs=where(Mat_totale gt 30b, count_errors_ribs)
print, 'error ribs intersection', count_errors_ribs
Mat_totale = Mat_totale < 30b          ; replace the intersection by ribs

Mat_totale= Mat_totale + Mat_spine         ; adding the spine
errors_spine=where(Mat_totale gt 40b, count_errors_spine)
print, 'error spine intersection', count_errors_spine
Mat_totale = Mat_totale < 40b          ; replace the intersection by spine

Mat_totale= Mat_totale + Mat_b_left + Mat_b_right ; adding the breasts
errors_breasts=where(Mat_totale gt 50b, count_errors_breast)
print, 'error breast intersection', count_errors_breast
Mat_totale = Mat_totale < 50b          ; replace the intersection by breasts

Mat_totale= Mat_totale + Mat_l_left + Mat_l_right ; adding the lungs
errors_lungs=where(Mat_totale gt 60b, count_errors_lungs)

```

```

print, 'error lungs intersection', count_errors_lungs
Mat_totale = Mat_totale < 60b ; replace the intersection by lungs

Mat_totale= Mat_totale + Mat_heart ; adding the heart
errors_heart=where(Mat_totale gt 70b, count_errors_heart)
print, 'error heart intersection', count_errors_heart
Mat_totale = Mat_totale < 70b ; replace the intersection by heart

Mat_totale= Mat_totale + Mat_heart ; adding the liver adding the liver
errors_liver=where(Mat_totale gt 80b, count_errors_liver)
print, 'error liver intersection', count_errors_liver
Mat_totale = Mat_totale < 80b ; replace the intersection by liver
; ***** calculating the total number of intersections *****
tot_nb_errors=count_errors_scapulae+count_errors_spine+count_errors_ribs+count_errors_breasts+co
unt_errors_lungs+count_errors_liver+count_errors_heart
print, 'total nb of errors=', tot_nb_errors
; ***** plotting the phantom *****
for i=0,100 do begin
tvsc1, Mat_totale(i,*,*)
wait, 0.1
endfor
ivolume, Mat_totale
stop
; ***** generating the .col file for OEDIPE *****
openw, lun, 'T:\SDI\LEDI_FAR\Jad FARAH\OEDIPE_Regina\dossier\Cipr\ETUDE-Cipr-1\fantcol\
ICRP_female.col', /get_lun
writetu, lun, Mat_totale
free_lun, lun
print, 'file .col written'
Entete='UNDEFINED'+string(10b)+$
'COULEUR'+string(10b)+$
'ICRP_female'+string(10b)+$;attention, change the name
'Cipr'+string(10b)+$
'ETUDE-Cipr-1'+string(10b)+$
' 256'+string(10b)+$
' 256'+string(10b)+$
' 256'+string(10b)+$
' 0.1907'+string(10b)+$ ;attention, change the elementary voxel size
' 0.1907'+string(10b)+$
' 0.1907'+string(10b)+$
' 8'+string(10b)+$
' 0.000000'+string(10b)+$
' 0.000000'+string(10b)+$
'cm'+string(10b)+$
' 0'+string(10b)+$
' 0'+string(10b)+$
' 10'+string(10b)+$ ;attention, change the number of colors in the phantom
' 0 5 10 20 30 40 50 60 70 80' ; attention, specify the available colors in the phantom
openw, lun, 'T:\SDI\LEDI_FAR\Jad FARAH\OEDIPE_Regina\dossier\Cipr\ETUDE-Cipr-1\fantcol\
ICRP_female.col.ref', /get_lun
writetu, lun, Entete
free_lun, lun
print, 'file .col.ref written'
end

```

Appendix A.3. IDL routine used to add the skin.

PRO Add_Skin

```

; loading the phantom :
l_strPath="T:\SDI\LEDI_FAR\Jad FARAH\OEDIPE_Regina\dossier\Cipr\ETUDE-Cipr-1\fantcol\"
l_strFantColFile = DIALOG_PICKFILE ( PATH = l_strPath, TITLE = "Select the file .col of the
input phantom: ", /READ) ; phantom matrix
l_strFantColRefFile = DIALOG_PICKFILE ( PATH = l_strPath, TITLE = "Select the file .col.ref of
this phantom: ", /READ) ; phantom colors
; Reading the phantom parameters and colors (from file .col.ref):
l_nNbLinesFichREF = FILE_LINES (l_strFantColRefFile)
l_strarrParamFantCol =strarr(l_nNbLinesFichREF)
openr, lun, l_strFantColRefFile, /GET_LUN
readf, lun, l_strarrParamFantCol
free_lun, lun
PRINT, "
PRINT, "input file .col.ref : ", l_strFantColRefFile
PRINT, "Parametres and colors of input file .col.ref : "
HELP, l_strarrParamFantCol
PRINT, l_strarrParamFantCol
PRINT, "
; Reading the voxel grid dimensions and elementary voxel size
l_nNbPixels_X=fix(l_strarrParamFantCol(6)) ; the X dimension is written at line number 6 of the
.col.ref file
l_nNbPixels_Y=fix(l_strarrParamFantCol(7)) ; the Y dimension is written at line number 7 of the
.col.ref file
l_nNbPixels_Z=fix(l_strarrParamFantCol(5)) ; the Z dimension is written at line number 5 of the
.col.ref file
lfltResol_X=float(l_strarrParamFantCol(8)) ; the voxel resolution in the X direction is written at line
number 8 of the .col.ref file
lfltResol_Y=float(l_strarrParamFantCol(9)) ; the voxel resolution in the Y direction is written at line
number 9 of the .col.ref file
lfltResol_Z=float(l_strarrParamFantCol(10)) ; the voxel resolution in the Z direction is written at line
number 10 of the .col.ref file
PRINT, " "
print, 'Nx : ', l_nNbPixels_X, 'Ny : ', l_nNbPixels_Y, 'Nz : ', l_nNbPixels_Z
PRINT, 'dx : ', lfltResol_X, 'dy : ', lfltResol_Y, 'dz : ', lfltResol_Z
; Choice of the number of voxels to be added (here one voxel layer):
READ, l_nNbVoxelsX, PROMPT='Entrer the number of voxels to be colored in the X direction: '
READ, l_nNbVoxelsY, PROMPT='Entrer the number of voxels to be colored in the Y direction: '
READ, l_nNbVoxelsZ, PROMPT='Entrer the number of voxels to be colored in the Z direction: '
; ***** Adding voxels based on the operator designations: *****
; Opening and reading the file .col :
l_bytarrFantCol=BYTARR(l_nNbPixels_Z, l_nNbPixels_X, l_nNbPixels_Y)
openr, lun, l_strFantColFile, /GET_LUN
readu, lun, l_bytarrFantCol
free_lun, lun
; Getting the color equivalent to the air material :
l_intarrNumColor = STRSPLIT(STRCOMPRESS(l_strarrParamFantCol(18)), /EXTRACT)
PRINT, "Number of colors : ", l_intarrNumColor
HELP, l_intarrNumColor
; Color of the skin to be added :
l_strInfo = STRING(l_intarrNumColor)

```

```

Result = DIALOG_MESSAGE(l_strInfo, /INFO, TITLE = Table of the color numbers :)
l_nColor=0
READ, l_nColor, PROMPT='Enter a new color number: '
l_intarrNumColor = [l_intarrNumColor, l_nColor]
PRINT, 'New Table of the color numbers: '
PRINT, l_intarrNumColor
; Incrementing the number of colors in the .col.ref file :
l_nNbColors = N_ELEMENTS(l_intarrNumColor)
l_strarrParamFantCol(17) = ' ' + STRCOMPRESS(STRING(l_nNbColors))
l_strarrParamFantCol(18) = STRCOMPRESS(l_strarrParamFantCol(18) + STRING(l_nColor))
; specifying the phantom region in which the voxels should be added:
print, 'Choose your Region Of Interest'
READ, l_nXmin, PROMPT='Entrer the startup slice of the phantom in the X direction: '
READ, l_nXmax, PROMPT='Entrer the final slice of the phantom in the X direction: '
READ, l_nYmin, PROMPT='Entrer the startup slice of the phantom in the Y direction: '
READ, l_nYmax, PROMPT='Entrer the final slice of the phantom in the Y direction: '
READ, l_nZmin, PROMPT='Entrer the startup slice of the phantom in the Z direction: '
READ, l_nZmax, PROMPT='Entrer the final slice of the phantom in the Z direction: '
; ***** Starting from Y min and upwords and replacing the first encountered air voxel
by a skin voxel: *****
print, 'Adding voxels in the Y direction'
FOR K = l_nZmin, l_nZmax DO BEGIN
  FOR i = l_nXmin, l_nXmax DO BEGIN
    j = l_nYmin
    WHILE l_bytarrFantCol (k, i, j) NE l_intarrNumColor(0) DO BEGIN
      j++
    ENDWHILE
    IF j NE l_nYmax THEN $
    if l_bytarrFantCol (k,i,j-1) NE l_nColor then $
    l_bytarrFantCol (k,i,j) = l_nColor
  ENDFOR
ENDFOR
; ***** Starting from X min and upwords and replacing the first encountered air voxel
by a skin voxel: *****
print, ' Adding voxels in the X direction'
  l_nXmin = 0
  l_nXmax = 255
  FOR K = l_nZmin, l_nZmax DO BEGIN
    FOR j = l_nYmin, l_nYmax DO BEGIN
      i = l_nXmin
      WHILE l_bytarrFantCol (k, i, j) NE l_intarrNumColor(0) DO BEGIN
        i++
      ENDWHILE
      IF i NE l_nXmin THEN if l_bytarrFantCol (k, i-1, j) NE l_nColor then l_bytarrFantCol (k, i, j)
      = l_nColor
    ENDFOR
  ENDFOR
; ***** Starting from Z min and upwords and replacing the first encountered air voxel
by a skin voxel: *****
print, 'Adding voxels in the Z direction'
FOR i = l_nXmin, l_nXmax DO BEGIN
  FOR j = l_nYmin, l_nYmax DO BEGIN
    k = l_nZmin
    WHILE l_bytarrFantCol (k, i, j) NE l_intarrNumColor(0) DO BEGIN
      K++

```

```
        ENDWHILE
        IF k NE l_nZmax THEN
        if l_bytarrFantCol (k-1, i, j) NE l_nColor then
        l_bytarrFantCol (k, i, j) = l_nColor
        ENDFOR
    ENDFOR
; ***** Writing the modified phantom: *****
    l_strOUTPUTFantCol = DIALOG_PICKFILE ( PATH = l_strPath, TITLE = 'Indicate the name of
the output file :', $
/WRITE, /OVERWRITE_PROMPT)
PRINT, "Output file .col.ref : ", l_strOUTPUTFantCol+'.col.ref'
l_strREFSortie = "
for i=0,N_ELEMENTS (l_strarrParamFantCol) - 1 do
    IF i EQ 0 THEN l_strREFSortie = STRING(l_strarrParamFantCol(i)) $
    ELSE l_strREFSortie = l_strREFSortie + STRING(13b)+STRING(10b)
+STRING(l_strarrParamFantCol(i))
    openw,lun,l_strOUTPUTFantCol+'.col.ref', /GET_LUN
    printf, lun, l_strREFSortie
    FREE_LUN, lun
    openw,lun,l_strOUTPUTFantCol+'.col', /GET_LUN
    writeu,lun,l_bytarrFantCol
    FREE_LUN, lun
END
ENDFOR
```


Appendix B.1. MC artificial source defined using OEDIPE and used for the simulations.

Table 1. Energy and yield of gamma rays used for the simulation, according to Mini Table de radionucléides (Laboratoire National Henri Becquerel, EDP science 2007).

Radioactive Element	Emission energy (X or Gamma) keV	True yield (%)
²³⁸ U	15	7.9
¹⁰⁹ Cd	22	54.7
¹³⁹ Ce	33	41.2
¹⁵² Eu	40	37.7
²⁴¹ Am	59	35.8
¹³³ Ba	81	32.9
⁵⁷ Co	122	85.5
¹³⁹ Ce	165	79.9
²³⁵ U	185	57.2
¹⁵² Eu	244	7.6
¹³³ Ba	356	62.1
²² Na	511	178.0
¹³⁷ Cs	661	85.0
⁵⁴ Mn	834	100.0
⁶⁰ Co	1173	99.8
²² Na	1274	99.9
¹⁵² Eu	1408	20.8

Appendix B.2. MC simulation results of the library of female workers.

Table 1. Simulated counting efficiency values for phantoms with a chest girth of 85.

Energy	Counting efficiency (counts/s/gamma) for each phantom				
	85A	85B	85C	85D	85E
15	1.10E-04	4.50E-05	3.38E-05	2.45E-05	1.72E-05
22	2.43E-03	1.67E-03	1.41E-03	1.25E-03	1.02E-03
33	9.41E-03	7.57E-03	6.73E-03	6.32E-03	5.52E-03
40	1.22E-02	1.01E-02	9.05E-03	8.58E-03	7.61E-03
59	1.60E-02	1.36E-02	1.24E-02	1.19E-02	1.06E-02
81	1.75E-02	1.52E-02	1.40E-02	1.35E-02	1.21E-02
122	1.76E-02	1.54E-02	1.44E-02	1.38E-02	1.26E-02
165	1.57E-02	1.39E-02	1.31E-02	1.27E-02	1.17E-02
185	1.46E-02	1.30E-02	1.22E-02	1.19E-02	1.10E-02
244	1.18E-02	1.05E-02	9.99E-03	9.64E-03	8.94E-03
356	8.16E-03	7.39E-03	7.08E-03	6.93E-03	6.46E-03
511	5.99E-03	5.51E-03	5.27E-03	5.13E-03	4.81E-03
661	4.85E-03	4.48E-03	4.31E-03	4.23E-03	3.98E-03
834	4.03E-03	3.75E-03	3.65E-03	3.56E-03	3.38E-03
1173	3.14E-03	2.96E-03	2.88E-03	2.83E-03	2.68E-03
1274	2.95E-03	2.80E-03	2.71E-03	2.68E-03	2.56E-03
1408	2.76E-03	2.61E-03	2.56E-03	2.52E-03	2.40E-03

Table 2. Simulated counting efficiency values for phantoms of chest girth of 90.

Energy	Counting efficiency (counts/s/gamma) for each phantom				
	90A	90B	90C	90D	90E
15	5.89E-05	2.99E-05	2.69E-05	2.13E-05	1.42E-05
22	1.88E-03	1.40E-03	1.29E-03	1.15E-03	9.41E-04
33	8.13E-03	6.86E-03	6.44E-03	5.97E-03	5.29E-03
40	1.06E-02	9.11E-03	8.64E-03	8.08E-03	7.24E-03
59	1.43E-02	1.26E-02	1.20E-02	1.13E-02	1.03E-02
81	1.59E-02	1.42E-02	1.36E-02	1.28E-02	1.19E-02
122	1.60E-02	1.44E-02	1.39E-02	1.32E-02	1.23E-02
165	1.45E-02	1.32E-02	1.27E-02	1.20E-02	1.14E-02
185	1.35E-02	1.23E-02	1.19E-02	1.13E-02	1.07E-02
244	1.08E-02	9.94E-03	9.61E-03	9.15E-03	8.68E-03
356	7.66E-03	7.11E-03	6.87E-03	6.62E-03	6.31E-03
511	5.55E-03	5.20E-03	5.07E-03	4.97E-03	4.70E-03
661	4.48E-03	4.25E-03	4.19E-03	4.10E-03	3.89E-03
834	3.74E-03	3.55E-03	3.49E-03	3.43E-03	3.34E-03
1173	2.95E-03	2.82E-03	2.75E-03	2.73E-03	2.66E-03
1274	2.80E-03	2.68E-03	2.62E-03	2.58E-03	2.52E-03
1408	2.63E-03	2.52E-03	2.47E-03	2.42E-03	2.38E-03

Table 3. Simulated counting efficiency values for phantoms of hest girth of 100.

Energy	Counting efficiency (counts/s/gamma) for each phantom				
	100B	100C	100D	100E	100F
15	1.48E-05	9.97E-06	5.93E-06	4.33E-06	2.91E-06
22	8.66E-04	6.86E-04	5.32E-04	4.53E-04	3.57E-04
33	4.52E-03	3.90E-03	3.34E-03	3.03E-03	2.56E-03
40	6.15E-03	5.41E-03	4.73E-03	4.33E-03	3.73E-03
59	8.57E-03	7.69E-03	6.85E-03	6.38E-03	5.56E-03
81	9.71E-03	8.80E-03	7.94E-03	7.42E-03	6.50E-03
122	1.00E-02	9.15E-03	8.28E-03	7.81E-03	6.89E-03
165	9.16E-03	8.47E-03	7.69E-03	7.27E-03	6.47E-03
185	8.57E-03	7.94E-03	7.28E-03	6.87E-03	6.14E-03
244	6.97E-03	6.47E-03	6.00E-03	5.68E-03	5.15E-03
356	4.94E-03	4.70E-03	4.40E-03	4.15E-03	3.82E-03
511	3.69E-03	3.48E-03	3.31E-03	3.19E-03	2.95E-03
661	3.04E-03	2.88E-03	2.73E-03	2.63E-03	2.44E-03
834	2.56E-03	2.45E-03	2.34E-03	2.27E-03	2.13E-03
1173	2.06E-03	1.99E-03	1.88E-03	1.84E-03	1.76E-03
1274	1.94E-03	1.88E-03	1.79E-03	1.75E-03	1.65E-03
1408	1.81E-03	1.76E-03	1.69E-03	1.66E-03	1.56E-03

Table 4. Simulated counting efficiency values for phantoms of hest girth of 110.

Energy	Counting efficiency (counts/s/gamma) for each phantom				
	110B	110C	110D	110E	110F
22	1.73E-04	1.33E-04	9.27E-05	8.14E-05	6.96E-05
33	1.58E-03	1.33E-03	1.07E-03	9.65E-04	8.57E-04
40	2.37E-03	2.03E-03	1.68E-03	1.52E-03	1.37E-03
59	3.67E-03	3.22E-03	2.74E-03	2.50E-03	2.27E-03
81	4.35E-03	3.85E-03	3.32E-03	3.04E-03	2.78E-03
122	4.72E-03	4.21E-03	3.73E-03	3.47E-03	3.14E-03
165	4.48E-03	4.03E-03	3.57E-03	3.34E-03	3.07E-03
185	4.26E-03	3.83E-03	3.41E-03	3.19E-03	2.94E-03
244	3.57E-03	3.24E-03	2.92E-03	2.73E-03	2.53E-03
356	2.68E-03	2.47E-03	2.26E-03	2.12E-03	1.99E-03
511	2.06E-03	1.92E-03	1.77E-03	1.68E-03	1.58E-03
661	1.74E-03	1.63E-03	1.52E-03	1.45E-03	1.37E-03
834	1.51E-03	1.42E-03	1.34E-03	1.29E-03	1.21E-03
1173	1.24E-03	1.18E-03	1.13E-03	1.07E-03	1.03E-03
1274	1.19E-03	1.13E-03	1.08E-03	1.03E-03	9.95E-04
1408	1.12E-03	1.07E-03	1.03E-03	9.90E-04	9.49E-04

Table 5. Simulated counting efficiency values for phantoms of hest girth of 120.

Energy	Counting efficiency (counts/s/gamma) for each phantom			
	120C	120D	120E	120F
22	2.69E-05	2.22E-05	1.86E-05	1.28E-05
33	4.38E-04	3.83E-04	3.31E-04	2.54E-04
40	7.33E-04	6.47E-04	5.64E-04	4.42E-04
59	1.27E-03	1.13E-03	9.96E-04	7.99E-04
81	1.57E-03	1.42E-03	1.25E-03	1.02E-03
122	1.82E-03	1.65E-03	1.48E-03	1.22E-03
165	1.81E-03	1.65E-03	1.49E-03	1.25E-03
185	1.74E-03	1.60E-03	1.44E-03	1.22E-03
244	1.52E-03	1.40E-03	1.27E-03	1.08E-03
356	1.20E-03	1.13E-03	1.03E-03	8.93E-04
511	9.75E-04	9.18E-04	8.44E-04	7.42E-04
661	8.52E-04	8.04E-04	7.47E-04	6.62E-04
834	7.60E-04	7.23E-04	6.74E-04	6.06E-04
1173	6.52E-04	6.22E-04	5.88E-04	5.37E-04
1274	6.28E-04	6.00E-04	5.67E-04	5.23E-04
1408	6.00E-04	5.73E-04	5.46E-04	5.03E-04

Appendix B.3. Counting efficiency variation with breast morphology.

Table 1. Chest girth of 100 and cup size E and F.

Energy (keV)	100E (#1)		100E (#2)		100E (#3)		100F (#1)		100F (#2)		100F (#3)	
	Counting efficiency (counts/s/ γ)	Stat. R. E. (%)	Counting efficiency (counts/s/ γ)	Stat. R. E. (%)	Counting efficiency (counts/s/ γ)	Stat. R. E. (%)	Counting efficiency (counts/s/ γ)	Stat. R. E. (%)	Counting efficiency (counts/s/ γ)	Stat. R. E. (%)	Counting efficiency (counts/s/ γ)	Stat. R. E. (%)
15	4.33E-06	1.5	1.52E-05	2.9	5.84E-06	4.7	2.91E-06	1.9	9.85E-06	3.6	9.37E-06	3.7
22	4.53E-04	0.5	8.15E-04	2.3	5.34E-04	2.9	3.57E-04	0.5	6.57E-04	2.6	6.62E-04	2.6
33	3.03E-03	0.6	4.47E-03	2.4	3.41E-03	2.8	2.56E-03	0.6	3.78E-03	2.6	3.79E-03	2.6
40	4.33E-03	0.5	6.61E-03	2.7	4.62E-03	3.1	3.73E-03	0.6	5.08E-03	2.9	5.15E-03	2.9
59	6.38E-03	0.5	8.60E-03	2.9	6.80E-03	3.2	5.56E-03	0.6	7.42E-03	3.1	7.36E-03	3.1
81	7.42E-03	1.2	9.79E-03	2.8	8.11E-03	3.0	6.50E-03	0.6	8.60E-03	3.0	8.55E-03	3.0
122	7.81E-03	0.7	1.01E-02	2.8	8.44E-03	3.0	6.89E-03	0.7	9.08E-03	2.9	9.00E-03	2.9
165	7.27E-03	0.5	8.98E-03	2.9	7.96E-03	3.0	6.47E-03	0.7	8.40E-03	3.0	8.38E-03	3.0
185	6.87E-03	0.5	8.47E-03	2.9	7.54E-03	3.1	6.14E-03	0.7	7.87E-03	3.1	8.02E-03	3.0
244	5.68E-03	0.5	6.99E-03	2.8	6.14E-03	2.9	5.15E-03	0.7	6.29E-03	2.9	6.36E-03	2.9
356	4.15E-03	0.7	5.22E-03	2.7	4.45E-03	2.9	3.82E-03	0.8	4.57E-03	2.8	4.59E-03	2.8
511	3.19E-03	0.6	3.87E-03	2.8	3.36E-03	3.0	2.95E-03	1.1	3.44E-03	3.0	3.48E-03	3.0
661	2.63E-03	0.6	3.12E-03	2.8	2.73E-03	3.0	2.44E-03	0.7	2.81E-03	3.0	2.85E-03	3.0
834	2.27E-03	0.7	2.60E-03	2.8	2.27E-03	3.0	2.13E-03	1.0	2.32E-03	3.0	2.35E-03	3.0
1173	1.84E-03	0.7	2.09E-03	2.8	1.85E-03	3.0	1.76E-03	2.3	1.97E-03	2.9	1.93E-03	2.9
1274	1.75E-03	0.8	1.93E-03	2.8	1.82E-03	2.9	1.65E-03	0.9	1.87E-03	2.8	1.84E-03	2.9
1408	1.66E-03	0.6	1.83E-03	2.8	1.69E-03	2.9	1.56E-03	0.8	1.76E-03	2.9	1.74E-03	2.9

Table 2. Chest girth of 110 and cup size B, E and F.

Energy (keV)	110B (#1)		110B (#2)		110E (#1)		110E (#2)		110F (#1)		110F (#2)		110F (#3)	
	Counting efficiency (counts/s/ γ)	Stat. R. E. (%)	Counting efficiency (counts/s/ γ)	Stat. R. E. (%)	Counting efficiency (counts/s/ γ)	Stat. R. E. (%)	Counting efficiency (counts/s/ γ)	Stat. R. E. (%)	Counting efficiency (counts/s/ γ)	Stat. R. E. (%)	Counting efficiency (counts/s/ γ)	Stat. R. E. (%)	Counting efficiency (counts/s/ γ)	Stat R. E. (%)
22	1.73E-04	0.2	1.46E-04	2.2	8.14E-05	0.4	9.18E-05	2.8	6.96E-05	0.4	7.21E-05	3.2	5.79E-05	3.6
33	1.58E-03	0.1	1.42E-03	1.8	9.65E-04	0.1	9.98E-04	2.1	8.57E-04	0.2	8.74E-04	2.3	7.61E-04	2.4
40	2.37E-03	0.2	2.17E-03	1.9	1.52E-03	0.3	1.56E-03	2.2	1.37E-03	0.3	1.38E-03	2.3	1.20E-03	2.5
59	3.67E-03	0.2	3.44E-03	1.9	2.50E-03	0.3	2.57E-03	2.2	2.27E-03	0.3	2.28E-03	2.3	1.95E-03	2.5
81	4.35E-03	0.2	4.12E-03	1.8	3.04E-03	0.3	3.11E-03	2.0	2.78E-03	0.3	2.76E-03	2.2	2.38E-03	2.3
122	4.72E-03	0.2	4.48E-03	1.7	3.47E-03	0.9	3.58E-03	1.9	3.14E-03	0.3	3.16E-03	2.0	2.75E-03	2.2
165	4.48E-03	0.2	4.25E-03	1.7	3.34E-03	0.9	3.39E-03	1.9	3.07E-03	0.3	3.07E-03	2.0	2.71E-03	2.2
185	4.26E-03	0.2	4.05E-03	1.8	3.19E-03	0.9	3.24E-03	2.0	2.94E-03	0.3	2.93E-03	2.1	2.61E-03	2.2
244	3.57E-03	0.2	3.43E-03	1.6	2.73E-03	0.2	2.79E-03	1.8	2.53E-03	0.2	2.57E-03	1.9	2.28E-03	2.0
356	2.68E-03	0.3	2.55E-03	1.6	2.12E-03	0.3	2.09E-03	1.7	1.99E-03	0.3	1.96E-03	1.8	1.75E-03	1.9
511	2.06E-03	0.3	1.96E-03	1.6	1.68E-03	0.3	1.71E-03	1.8	1.58E-03	0.3	1.60E-03	1.8	1.38E-03	2.0
661	1.74E-03	0.3	1.66E-03	1.6	1.45E-03	0.3	1.50E-03	1.7	1.37E-03	0.3	1.42E-03	1.7	1.21E-03	1.9
834	1.51E-03	0.3	1.45E-03	1.6	1.29E-03	0.3	1.30E-03	1.6	1.21E-03	0.3	1.25E-03	1.7	1.07E-03	1.8
1173	1.24E-03	0.3	1.21E-03	1.5	1.07E-03	0.3	1.09E-03	1.6	1.03E-03	0.3	1.08E-03	1.6	9.42E-04	1.7
1274	1.19E-03	0.3	1.14E-03	1.5	1.03E-03	0.3	1.05E-03	1.6	9.95E-04	0.3	1.02E-03	1.6	9.07E-04	1.7
1408	1.12E-03	0.2	1.08E-03	1.5	9.90E-04	0.3	1.01E-03	1.6	9.49E-04	0.3	9.74E-04	1.6	8.74E-04	1.7

Table 3. Chest girth of 120 and cup size D, E and F.

Energy (keV)	120D (#1)		120D (#2)		120D (#3)		120E (#1)		120E (#2)		120F (#1)		120F (#2)	
	Counting efficiency (counts/s/ γ)	Stat. R. E. (%)	Counting efficiency (counts/s/ γ)	Stat. R. E. (%)	Counting efficiency (counts/s/ γ)	Stat. R. E. (%)	Counting efficiency (counts/s/ γ)	Stat. R. E. (%)	Counting efficiency (counts/s/ γ)	Stat. R. E. (%)	Counting efficiency (counts/s/ γ)	Stat. R. E. (%)	Counting efficiency (counts/s/ γ)	Stat. R. E. (%)
22	2.22E-05	0.7	2.01E-05	4.8	1.77E-05	4.8	1.86E-05	0.7	1.27E-05	4.4	1.28E-05	0.7	1.17E-05	0.6
33	3.83E-04	0.2	3.84E-04	2.7	3.46E-04	2.8	3.31E-04	0.2	2.70E-04	3.2	2.54E-04	0.3	2.33E-04	3.5
40	6.47E-04	0.4	6.27E-04	3.4	5.84E-04	3.6	5.64E-04	0.4	4.62E-04	4.0	4.42E-04	0.5	4.15E-04	4.2
59	1.13E-03	0.4	1.09E-03	2.6	1.01E-03	2.7	9.96E-04	0.5	8.27E-04	3.0	7.99E-04	0.5	7.49E-04	3.2
81	1.42E-03	0.4	1.35E-03	2.4	1.28E-03	2.5	1.25E-03	0.4	1.05E-03	2.8	1.02E-03	0.4	9.62E-04	0.7
122	1.65E-03	0.4	1.59E-03	2.3	1.50E-03	2.3	1.48E-03	0.4	1.21E-03	0.6	1.22E-03	0.4	1.11E-03	2.7
165	1.65E-03	0.4	1.59E-03	2.2	1.51E-03	2.3	1.49E-03	0.4	1.27E-03	2.5	1.25E-03	0.4	1.15E-03	2.6
185	1.60E-03	0.4	1.55E-03	2.2	1.49E-03	2.3	1.44E-03	0.4	1.27E-03	2.5	1.22E-03	0.4	1.13E-03	2.6
244	1.40E-03	0.3	1.35E-03	2.1	1.28E-03	2.1	1.27E-03	0.3	1.11E-03	2.3	1.08E-03	0.4	1.02E-03	2.4
356	1.13E-03	0.4	1.12E-03	1.9	1.04E-03	1.9	1.03E-03	0.4	9.17E-04	2.1	8.93E-04	0.4	8.38E-04	2.2
511	9.18E-04	0.4	9.28E-04	1.9	8.56E-04	2.0	8.44E-04	0.4	7.71E-04	2.1	7.42E-04	0.4	7.09E-04	2.2
661	8.04E-04	0.4	8.05E-04	1.8	7.56E-04	1.9	7.47E-04	0.4	6.87E-04	2.0	6.62E-04	0.4	6.30E-04	2.1
834	7.23E-04	0.4	7.13E-04	1.8	6.80E-04	1.8	6.74E-04	0.4	6.28E-04	1.9	6.06E-04	0.4	5.80E-04	1.9
1173	6.22E-04	0.4	6.38E-04	1.7	6.00E-04	1.7	5.88E-04	0.4	5.53E-04	1.8	5.37E-04	0.4	5.19E-04	1.9
1274	6.00E-04	0.4	6.02E-04	1.6	5.77E-04	1.7	5.67E-04	0.4	5.25E-04	1.8	5.23E-04	0.4	5.08E-04	1.8
1408	5.73E-04	0.4	5.81E-04	1.6	5.59E-04	1.7	5.46E-04	0.4	5.08E-04	1.7	5.03E-04	0.4	4.93E-04	1.8

Appendix B.4. Counting efficiency values obtained using the 85A simulation and Equation 3.2.

Table 1. Counting efficiency values estimated using Equation (3.2), starting from the 85A simulated curve, for the phantoms of chest girth of 85 and differences to the reference simulated values.

Energy (keV)	85B		85C		85D		85E	
	Counting efficiency (counts/s/ γ)	Stat. R. E. (%)	Counting efficiency (counts/s/ γ)	Stat. R. E. (%)	Counting efficiency (counts/s/ γ)	Stat. R. E. (%)	Counting efficiency (counts/s/ γ)	Stat. R. E. (%)
15	4.57E-05	-1.5	3.28E-05	3.0	2.44E-05	0.5	1.61E-05	6.4
22	1.65E-03	1.4	1.42E-03	-0.7	1.25E-03	0.5	1.04E-03	-1.4
33	7.45E-03	1.7	6.82E-03	-1.3	6.30E-03	0.2	5.65E-03	-2.3
40	9.96E-03	1.0	9.23E-03	-2.0	8.62E-03	-0.4	7.83E-03	-3.0
59	1.35E-02	0.6	1.27E-02	-2.3	1.20E-02	-0.7	1.10E-02	-4.0
81	1.50E-02	1.2	1.42E-02	-1.3	1.35E-02	0.4	1.25E-02	-3.5
122	1.54E-02	0.1	1.46E-02	-1.8	1.40E-02	-0.9	1.31E-02	-3.8
165	1.39E-02	0.4	1.32E-02	-1.0	1.27E-02	-0.04	1.20E-02	-2.4
185	1.29E-02	0.5	1.23E-02	-0.8	1.19E-02	0.3	1.12E-02	-1.9
244	1.06E-02	-0.5	1.01E-02	-1.4	9.76E-03	-1.2	9.27E-03	-3.8
356	7.42E-03	-0.4	7.16E-03	-1.1	6.94E-03	-0.1	6.64E-03	-2.7
511	5.52E-03	-0.1	5.35E-03	-1.5	5.20E-03	-1.4	5.01E-03	-4.0
661	4.51E-03	-0.6	4.38E-03	-1.8	4.27E-03	-1.1	4.13E-03	-3.9
834	3.77E-03	-0.5	3.68E-03	-0.8	3.59E-03	-0.9	3.49E-03	-3.1
1173	2.97E-03	-0.2	2.91E-03	-0.8	2.85E-03	-0.9	2.78E-03	-3.6
1274	2.80E-03	-0.03	2.74E-03	-1.1	2.69E-03	-0.5	2.63E-03	-2.6
1408	2.63E-03	-0.5	2.58E-03	-0.5	2.53E-03	-0.7	2.47E-03	-3.1

Table 2. Counting efficiency values estimated using Equation (3.2), starting from the 85A simulated curve, for the phantoms of chest girth of 90 and differences to the reference simulated values.

Energy (keV)	90A		90B		90C		90D		90E	
	Counting efficiency (counts/s/ γ)	R. E. (%)	Counting efficiency (counts/s/ γ)	R. E. (%)	Counting efficiency (counts/s/ γ)	R. E. (%)	Counting efficiency (counts/s/ γ)	R. E. (%)	Counting efficiency (counts/s/ γ)	R. E. (%)
15	5.93E-05	-0.7	3.02E-05	-1.2	2.62E-05	2.7	2.03E-05	4.5	1.33E-05	6.1
22	1.85E-03	1.7	1.37E-03	2.0	1.29E-03	0.5	1.15E-03	0.2	9.53E-04	-1.3
33	7.98E-03	1.9	6.67E-03	2.6	6.43E-03	0.2	6.01E-03	-0.6	5.37E-03	-1.6
40	1.06E-02	0.1	9.06E-03	0.6	8.76E-03	-1.4	8.26E-03	-2.3	7.50E-03	-3.5
59	1.42E-02	0.5	1.25E-02	0.9	1.21E-02	-1.3	1.15E-02	-2.3	1.06E-02	-3.3
81	1.57E-02	1.3	1.40E-02	1.6	1.36E-02	-0.5	1.31E-02	-1.7	1.21E-02	-2.0
122	1.60E-02	-0.3	1.44E-02	-0.3	1.41E-02	-1.6	1.36E-02	-2.7	1.27E-02	-3.1
165	1.44E-02	0.4	1.31E-02	0.4	1.28E-02	-1.1	1.24E-02	-2.8	1.17E-02	-2.4
185	1.34E-02	0.6	1.22E-02	0.5	1.20E-02	-0.6	1.16E-02	-2.4	1.09E-02	-2.4
244	1.09E-02	-0.9	1.00E-02	-0.9	9.85E-03	-2.4	9.54E-03	-4.2	9.06E-03	-4.4
356	7.63E-03	0.3	7.10E-03	0.2	6.99E-03	-1.8	6.80E-03	-2.8	6.50E-03	-3.1
511	5.65E-03	-1.9	5.31E-03	-2.1	5.24E-03	-3.3	5.11E-03	-2.9	4.92E-03	-4.6
661	4.60E-03	-2.7	4.35E-03	-2.5	4.30E-03	-2.8	4.21E-03	-2.7	4.07E-03	-4.4
834	3.84E-03	-2.7	3.65E-03	-2.8	3.61E-03	-3.5	3.55E-03	-3.4	3.44E-03	-2.7
1173	3.02E-03	-2.2	2.89E-03	-2.5	2.87E-03	-4.2	2.82E-03	-3.4	2.74E-03	-3.1
1274	2.84E-03	-1.7	2.73E-03	-1.9	2.70E-03	-3.2	2.66E-03	-3.1	2.60E-03	-2.9
1408	2.67E-03	-1.4	2.56E-03	-1.6	2.54E-03	-2.9	2.51E-03	-3.4	2.45E-03	-2.6

Table 3. Counting efficiency values estimated using Equation (3.2), starting from the 85A simulated curve, for the phantoms of chest girth of 100 and differences to the reference simulated values.

Energy (keV)	100B		100C		100D		100E		100F	
	Counting efficiency (counts/s/ γ)	R. E. (%)	Counting efficiency (counts/s/ γ)	R. E. (%)	Counting efficiency (counts/s/ γ)	R. E. (%)	Counting efficiency (counts/s/ γ)	R. E. (%)	Counting efficiency (counts/s/ γ)	R. E. (%)
15	1.51E-05	-2.0	9.94E-06	0.3	5.87E-06	1.0	4.25E-06	1.8	2.79E-06	3.9
22	8.47E-04	2.2	6.95E-04	-1.3	5.45E-04	-2.4	4.70E-04	-3.6	3.78E-04	-6.0
33	4.42E-03	2.4	3.89E-03	0.4	3.34E-03	-0.2	3.04E-03	-0.4	2.62E-03	-2.2
40	6.07E-03	1.3	5.42E-03	-0.1	4.74E-03	-0.2	4.36E-03	-0.6	3.80E-03	-2.0
59	8.48E-03	1.1	7.68E-03	0.0	6.86E-03	-0.1	6.39E-03	-0.1	5.65E-03	-1.6
81	9.58E-03	1.3	8.75E-03	0.6	7.88E-03	0.7	7.38E-03	0.5	6.57E-03	-1.1
122	9.96E-03	0.5	9.16E-03	-0.2	8.33E-03	-0.7	7.86E-03	-0.6	7.04E-03	-2.2
165	9.09E-03	0.8	8.41E-03	0.8	7.70E-03	-0.1	7.29E-03	-0.2	6.57E-03	-1.4
185	8.49E-03	1.0	7.87E-03	1.0	7.22E-03	0.8	6.85E-03	0.3	6.18E-03	-0.6
244	7.00E-03	-0.5	6.52E-03	-0.7	6.02E-03	-0.3	5.73E-03	-0.8	5.19E-03	-0.9
356	4.99E-03	-1.0	4.67E-03	0.6	4.35E-03	0.9	4.17E-03	-0.3	3.80E-03	0.6
511	3.75E-03	-1.6	3.53E-03	-1.5	3.32E-03	-0.1	3.19E-03	0.0	2.92E-03	1.1
661	3.09E-03	-1.4	2.92E-03	-1.4	2.75E-03	-0.9	2.66E-03	-1.1	2.44E-03	-0.2
834	2.60E-03	-1.7	2.47E-03	-0.8	2.34E-03	-0.1	2.26E-03	0.7	2.08E-03	2.2
1173	2.07E-03	-0.5	1.97E-03	1.1	1.88E-03	0.2	1.82E-03	1.3	1.69E-03	4.2
1274	1.95E-03	-0.6	1.86E-03	0.8	1.78E-03	0.8	1.73E-03	1.6	1.60E-03	3.0
1408	1.84E-03	-1.5	1.76E-03	0.1	1.68E-03	0.6	1.63E-03	1.7	1.51E-03	2.9

Table 4. Counting efficiency values estimated using Equation (3.2), starting from the 85A simulated curve, for the phantoms of chest girth of 110 and differences to the reference simulated values.

Energy (keV)	110B		110C		110D		110E		110F	
	Counting efficiency (counts/s/ γ)	R. E. (%)	Counting efficiency (counts/s/ γ)	R. E. (%)	Counting efficiency (counts/s/ γ)	R. E. (%)	Counting efficiency (counts/s/ γ)	R. E. (%)	Counting efficiency (counts/s/ γ)	R. E. (%)
22	1.80E-04	-3.7	1.37E-04	-2.7	9.45E-05	-1.9	8.22E-05	-1.0	6.94E-05	0.2
33	1.53E-03	2.8	1.29E-03	2.5	1.03E-03	3.7	9.43E-04	2.3	8.40E-04	2.0
40	2.32E-03	2.2	1.99E-03	2.0	1.63E-03	2.9	1.51E-03	1.2	1.36E-03	0.8
59	3.60E-03	1.7	3.17E-03	1.7	2.68E-03	2.2	2.50E-03	0.3	2.27E-03	-0.1
81	4.28E-03	1.5	3.81E-03	1.1	3.27E-03	1.3	3.06E-03	-0.6	2.80E-03	-0.8
122	4.70E-03	0.5	4.22E-03	-0.3	3.69E-03	1.3	3.47E-03	0.1	3.19E-03	-1.8
165	4.45E-03	0.7	4.03E-03	0.1	3.56E-03	0.4	3.36E-03	-0.4	3.10E-03	-1.3
185	4.21E-03	1.1	3.82E-03	0.3	3.39E-03	0.6	3.20E-03	-0.3	2.97E-03	-0.9
244	3.59E-03	-0.6	3.28E-03	-1.3	2.93E-03	-0.6	2.78E-03	-1.9	2.58E-03	-2.1
356	2.68E-03	0.3	2.47E-03	0.0	2.24E-03	0.7	2.13E-03	-0.4	1.99E-03	-0.2
511	2.09E-03	-1.6	1.95E-03	-1.3	1.79E-03	-1.2	1.71E-03	-1.6	1.60E-03	-1.1
661	1.77E-03	-1.8	1.66E-03	-1.6	1.53E-03	-1.1	1.47E-03	-1.1	1.38E-03	-0.6
834	1.53E-03	-1.3	1.43E-03	-0.8	1.34E-03	0.3	1.28E-03	0.2	1.21E-03	-0.3
1173	1.25E-03	-0.8	1.18E-03	-0.1	1.11E-03	1.1	1.07E-03	0.1	1.02E-03	1.5
1274	1.19E-03	-0.4	1.13E-03	0.3	1.06E-03	1.8	1.03E-03	0.9	9.72E-04	2.3
1408	1.13E-03	-0.8	1.07E-03	0.0	1.01E-03	1.1	9.79E-04	1.1	9.28E-04	2.2

Table 5. Counting efficiency values estimated using Equation (3.2), starting from the 85A simulated curve, for the phantoms of chest girth of 120 and differences to the reference simulated values.

Energy (keV)	120C		120D		120E		120F	
	Counting efficiency (counts/s/ γ)	Stat. R. E. (%)	Counting efficiency (counts/s/ γ)	Stat. R. E. (%)	Counting efficiency (counts/s/ γ)	Stat. R. E. (%)	Counting efficiency (counts/s/ γ)	Stat. R. E. (%)
22	2.79E-05	-3.8	2.28E-05	-2.5	1.87E-05	-0.1	1.25E-05	2.4
33	4.20E-04	4.1	3.68E-04	3.7	3.21E-04	3.3	2.47E-04	2.6
40	7.07E-04	3.5	6.28E-04	3.0	5.53E-04	2.0	4.37E-04	1.1
59	1.24E-03	1.6	1.12E-03	1.0	1.00E-03	-0.5	8.15E-04	-2.0
81	1.57E-03	0.2	1.43E-03	-0.6	1.28E-03	-2.1	1.06E-03	-3.5
122	1.83E-03	-0.6	1.67E-03	-1.4	1.51E-03	-2.4	1.27E-03	-4.1
165	1.81E-03	-0.1	1.67E-03	-0.8	1.51E-03	-1.8	1.28E-03	-2.6
185	1.74E-03	0.1	1.60E-03	-0.4	1.46E-03	-1.1	1.24E-03	-2.0
244	1.54E-03	-1.4	1.42E-03	-2.0	1.30E-03	-2.1	1.12E-03	-3.0
356	1.21E-03	-0.4	1.13E-03	-0.1	1.03E-03	-0.5	9.00E-04	-0.8
511	9.91E-04	-1.6	9.29E-04	-1.2	8.57E-04	-1.5	7.54E-04	-1.5
661	8.65E-04	-1.5	8.14E-04	-1.3	7.53E-04	-0.9	6.68E-04	-0.9
834	7.66E-04	-0.8	7.23E-04	0.0	6.71E-04	0.4	5.99E-04	1.2
1173	6.52E-04	0.0	6.18E-04	0.6	5.76E-04	2.1	5.18E-04	3.5
1274	6.25E-04	0.4	5.93E-04	1.0	5.54E-04	2.5	4.99E-04	4.6
1408	5.99E-04	0.0	5.70E-04	0.5	5.32E-04	2.6	4.81E-04	4.4

Appendix B.5. Counting efficiency values obtained using the Livermore P1 measurement and Equation 3.2.

Table 1. Results for the phantoms of chest girth of 85 and differences to the reference simulated values.

Energy (keV)	85A		85B		85C		85D		85E	
	Counting efficiency (counts/s/ γ)	R. E. (%)	Counting efficiency (counts/s/ γ)	R. E. (%)	Counting efficiency (counts/s/ γ)	R. E. (%)	Counting efficiency (counts/s/ γ)	R. E. (%)	Counting efficiency (counts/s/ γ)	R. E. (%)
15	1.21E-04	-9.4	5.00E-05	-11.1	3.59E-05	-6.1	2.66E-05	-8.8	1.77E-05	-2.4
22	3.29E-03	-34.9	2.22E-03	-33.0	1.92E-03	-35.9	1.68E-03	-34.3	1.40E-03	-36.8
33	1.16E-02	-22.9	9.15E-03	-20.9	8.38E-03	-24.6	7.75E-03	-22.7	6.95E-03	-25.8
40	1.44E-02	-18.1	1.18E-02	-17.0	1.09E-02	-20.5	1.02E-02	-18.6	9.26E-03	-21.7
59	1.72E-02	-7.6	1.45E-02	-6.9	1.36E-02	-10.0	1.29E-02	-8.3	1.19E-02	-11.9
81	1.76E-02	-0.5	1.51E-02	0.7	1.43E-02	-1.8	1.35E-02	-0.1	1.26E-02	-4.0
122	1.68E-02	4.7	1.47E-02	4.8	1.39E-02	3.0	1.33E-02	3.8	1.25E-02	1.1
165	1.51E-02	4.1	1.33E-02	4.4	1.27E-02	3.1	1.22E-02	4.0	1.15E-02	1.8
185	1.42E-02	2.4	1.26E-02	2.9	1.20E-02	1.7	1.16E-02	2.8	1.09E-02	0.6
244	1.17E-02	0.3	1.05E-02	-0.2	1.01E-02	-1.0	9.73E-03	-0.8	9.24E-03	-3.4
356	8.36E-03	-2.4	7.60E-03	-2.9	7.34E-03	-3.6	7.11E-03	-2.5	6.80E-03	-5.2
511	5.90E-03	1.5	5.43E-03	1.4	5.27E-03	0.1	5.12E-03	0.2	4.93E-03	-2.4
661	4.75E-03	2.1	4.41E-03	1.5	4.29E-03	0.4	4.18E-03	1.1	4.04E-03	-1.7
834	4.05E-03	-0.6	3.79E-03	-1.1	3.70E-03	-1.4	3.62E-03	-1.5	3.51E-03	-3.7
1173	3.29E-03	-4.7	3.11E-03	-4.9	3.04E-03	-5.5	2.99E-03	-5.6	2.91E-03	-8.4
1274	3.08E-03	-4.3	2.92E-03	-4.3	2.86E-03	-5.4	2.81E-03	-4.8	2.74E-03	-7.0
1408	2.79E-03	-0.9	2.65E-03	-1.4	2.60E-03	-1.4	2.56E-03	-1.7	2.50E-03	-4.0

Table 2. Counting efficiency values estimated using Equation (3.2), starting from the Livermore P1 measured, for the phantoms of chest girth of 90 and differences to the reference simulated values.

Energy (keV)	90A		90B		90C		90D		90E	
	Counting efficiency (counts/s/ γ)	R. E. (%)	Counting efficiency (counts/s/ γ)	R. E. (%)	Counting efficiency (counts/s/ γ)	R. E. (%)	Counting efficiency (counts/s/ γ)	R. E. (%)	Counting efficiency (counts/s/ γ)	R. E. (%)
15	6.49E-05	-10.2	3.31E-05	-10.8	2.87E-05	-6.4	2.22E-05	-4.5	1.46E-05	-2.8
22	2.49E-03	-32.7	1.85E-03	-32.2	1.74E-03	-34.3	1.55E-03	-34.6	1.29E-03	-36.7
33	9.81E-03	-20.7	8.20E-03	-19.7	7.90E-03	-22.6	7.38E-03	-23.7	6.60E-03	-24.9
40	1.25E-02	-18.0	1.07E-02	-17.4	1.04E-02	-19.8	9.76E-03	-20.9	8.86E-03	-22.3
59	1.53E-02	-7.1	1.34E-02	-6.6	1.30E-02	-8.9	1.24E-02	-10.0	1.15E-02	-11.1
81	1.58E-02	0.9	1.41E-02	1.1	1.37E-02	-1.0	1.31E-02	-2.2	1.22E-02	-2.5
122	1.53E-02	4.4	1.37E-02	4.5	1.34E-02	3.2	1.29E-02	2.2	1.21E-02	1.8
165	1.38E-02	4.4	1.26E-02	4.4	1.23E-02	3.0	1.19E-02	1.3	1.12E-02	1.7
185	1.31E-02	3.0	1.19E-02	3.0	1.17E-02	1.9	1.13E-02	0.1	1.07E-02	0.1
244	1.09E-02	-0.5	9.99E-03	-0.5	9.81E-03	-2.1	9.51E-03	-3.9	9.02E-03	-4.0
356	7.82E-03	-2.1	7.27E-03	-2.3	7.16E-03	-4.3	6.97E-03	-5.3	6.66E-03	-5.6
511	5.57E-03	-0.3	5.23E-03	-0.6	5.16E-03	-1.8	5.04E-03	-1.3	4.84E-03	-3.0
661	4.51E-03	-0.5	4.26E-03	-0.3	4.21E-03	-0.6	4.12E-03	-0.5	3.98E-03	-2.2
834	3.87E-03	-3.4	3.68E-03	-3.5	3.64E-03	-4.1	3.57E-03	-4.0	3.46E-03	-3.4
1173	3.16E-03	-7.0	3.03E-03	-7.3	3.00E-03	-9.1	2.95E-03	-8.2	2.87E-03	-7.9
1274	2.97E-03	-6.0	2.85E-03	-6.3	2.82E-03	-7.6	2.78E-03	-7.6	2.71E-03	-7.3
1408	2.69E-03	-2.4	2.59E-03	-2.6	2.57E-03	-3.9	2.53E-03	-4.4	2.47E-03	-3.6

Table 3. Counting efficiency values estimated using Equation (3.2), starting from the Livermore P1 measured, for the phantoms of chest girth of 100 and differences to the reference simulated values.

Energy (keV)	100B		100C		100D		100E		100F	
	Counting efficiency (counts/s/ γ)	R. E. (%)	Counting efficiency (counts/s/ γ)	R. E. (%)	Counting efficiency (counts/s/ γ)	R. E. (%)	Counting efficiency (counts/s/ γ)	R. E. (%)	Counting efficiency (counts/s/ γ)	R. E. (%)
15	1.65E-05	-11.6	1.09E-05	-9.0	6.42E-06	-8.3	4.65E-06	-7.5	3.06E-06	-5.2
22	1.14E-03	-32.0	9.37E-04	-36.6	7.36E-04	-38.2	6.34E-04	-39.9	5.11E-04	-43.1
33	5.43E-03	-20.0	4.78E-03	-22.5	4.11E-03	-23.2	3.74E-03	-23.4	3.22E-03	-25.7
40	7.17E-03	-16.6	6.40E-03	-18.3	5.60E-03	-18.4	5.15E-03	-18.9	4.49E-03	-20.5
59	9.12E-03	-6.4	8.27E-03	-7.5	7.38E-03	-7.7	6.87E-03	-7.7	6.07E-03	-9.3
81	9.63E-03	0.8	8.79E-03	0.1	7.92E-03	0.2	7.42E-03	0.0	6.60E-03	-1.6
122	9.49E-03	5.2	8.73E-03	4.6	7.94E-03	4.1	7.49E-03	4.2	6.71E-03	2.7
165	8.72E-03	4.8	8.06E-03	4.8	7.39E-03	4.0	6.99E-03	3.9	6.30E-03	2.7
185	8.28E-03	3.4	7.67E-03	3.4	7.05E-03	3.2	6.68E-03	2.7	6.03E-03	1.9
244	6.98E-03	-0.1	6.49E-03	-0.3	6.00E-03	0.0	5.71E-03	-0.5	5.17E-03	-0.5
356	5.11E-03	-3.4	4.79E-03	-1.9	4.46E-03	-1.5	4.27E-03	-2.7	3.89E-03	-1.8
511	3.69E-03	0.0	3.48E-03	0.1	3.27E-03	1.4	3.14E-03	1.5	2.88E-03	2.6
661	3.02E-03	0.8	2.86E-03	0.8	2.70E-03	1.2	2.60E-03	1.1	2.39E-03	1.9
834	2.62E-03	-2.3	2.48E-03	-1.4	2.35E-03	-0.7	2.27E-03	0.0	2.10E-03	1.5
1173	2.16E-03	-5.1	2.06E-03	-3.5	1.97E-03	-4.5	1.91E-03	-3.4	1.77E-03	-0.3
1274	2.04E-03	-5.0	1.94E-03	-3.4	1.85E-03	-3.4	1.80E-03	-2.7	1.67E-03	-1.2
1408	1.85E-03	-2.42	1.77E-03	-0.8	1.69E-03	-0.3	1.65E-03	0.8	1.53E-03	2.0

Table 4. Counting efficiency values estimated using Equation (3.2), starting from the Livermore P1 measured, for the phantoms of chest girth of 110 and differences to the reference simulated values.

Energy (keV)	110B		110C		110D		110E		110F	
	Counting efficiency (counts/s/ γ)	R. E. (%)	Counting efficiency (counts/s/ γ)	R. E. (%)	Counting efficiency (counts/s/ γ)	R. E. (%)	Counting efficiency (counts/s/ γ)	R. E. (%)	Counting efficiency (counts/s/ γ)	R. E. (%)
22	2.43E-04	-40.0	1.85E-04	-38.6	1.27E-04	-37.5	1.11E-04	-36.3	9.37E-05	-34.6
33	1.89E-03	-19.5	1.59E-03	-19.9	1.27E-03	-18.3	1.16E-03	-20.1	1.03E-03	-20.5
40	2.74E-03	-15.6	2.35E-03	-15.8	1.93E-03	-14.7	1.78E-03	-16.8	1.60E-03	-17.2
59	3.87E-03	-5.7	3.41E-03	-5.7	2.89E-03	-5.2	2.69E-03	-7.3	2.45E-03	-7.7
81	4.31E-03	1.0	3.82E-03	0.6	3.29E-03	0.8	3.08E-03	-1.1	2.82E-03	-1.3
122	4.47E-03	5.2	4.02E-03	4.5	3.51E-03	6.0	3.30E-03	4.8	3.04E-03	3.0
165	4.27E-03	4.8	3.86E-03	4.2	3.41E-03	4.4	3.22E-03	3.6	2.98E-03	2.8
185	4.11E-03	3.6	3.73E-03	2.7	3.31E-03	3.0	3.13E-03	2.2	2.89E-03	1.6
244	3.57E-03	-0.3	3.27E-03	-0.9	2.92E-03	-0.3	2.77E-03	-1.5	2.58E-03	-1.7
356	2.74E-03	-2.1	2.53E-03	-2.4	2.29E-03	-1.7	2.18E-03	-2.8	2.04E-03	-2.6
511	2.06E-03	0.0	1.92E-03	0.2	1.76E-03	0.4	1.68E-03	-0.1	1.58E-03	0.5
661	1.73E-03	0.4	1.62E-03	0.5	1.50E-03	1.0	1.44E-03	1.0	1.35E-03	1.5
834	1.54E-03	-1.9	1.44E-03	-1.4	1.35E-03	-0.3	1.29E-03	-0.4	1.22E-03	-0.9
1173	1.31E-03	-5.5	1.24E-03	-4.8	1.17E-03	-3.5	1.12E-03	-4.5	1.06E-03	-3.1
1274	1.24E-03	-4.7	1.18E-03	-4.0	1.11E-03	-2.5	1.07E-03	-3.4	1.01E-03	-1.9
1408	1.14E-03	-1.8	1.08E-03	-0.9	1.02E-03	0.2	9.88E-04	0.2	9.37E-04	1.3

Table 5. Counting efficiency values estimated using Equation (3.2), starting from the Livermore P1 measured, for the phantoms of chest girth of 120 and differences to the reference simulated values.

Energy (keV)	120C		120D		120E		120F	
	Counting efficiency (counts/s/ γ)	Stat. R. E. (%)	Counting efficiency (counts/s/ γ)	Stat. R. E. (%)	Counting efficiency (counts/s/ γ)	Stat. R. E. (%)	Counting efficiency (counts/s/ γ)	Stat. R. E. (%)
22	3.77E-05	-40.1	3.07E-05	-38.3	2.52E-05	-35.1	1.69E-05	-31.7
33	5.17E-04	-17.9	4.53E-04	-18.3	3.94E-04	-18.9	3.04E-04	-19.7
40	8.36E-04	-14.0	7.42E-04	-14.6	6.53E-04	-15.8	5.17E-04	-16.9
59	1.34E-03	-5.8	1.21E-03	-6.5	1.08E-03	-8.1	8.77E-04	-9.8
81	1.58E-03	-0.3	1.43E-03	-1.1	1.29E-03	-2.6	1.06E-03	-4.0
122	1.74E-03	4.1	1.60E-03	3.4	1.44E-03	2.4	1.21E-03	0.9
165	1.74E-03	3.9	1.60E-03	3.3	1.45E-03	2.4	1.23E-03	1.5
185	1.70E-03	2.6	1.56E-03	2.1	1.42E-03	1.4	1.21E-03	0.5
244	1.53E-03	-1.1	1.42E-03	-1.6	1.30E-03	-1.7	1.11E-03	-2.6
356	1.24E-03	-2.8	1.15E-03	-2.5	1.06E-03	-3.0	9.22E-04	-3.2
511	9.75E-04	0.0	9.14E-04	0.4	8.43E-04	0.0	7.42E-04	0.1
661	8.46E-04	0.6	7.96E-04	0.9	7.37E-04	1.3	6.54E-04	1.3
834	7.71E-04	-1.4	7.27E-04	-0.6	6.75E-04	-0.2	6.03E-04	0.6
1173	6.82E-04	-4.7	6.47E-04	-4.0	6.03E-04	-2.5	5.43E-04	-1.1
1274	6.52E-04	-3.9	6.19E-04	-3.2	5.77E-04	-1.7	5.21E-04	0.5
1408	6.05E-04	-0.9	5.75E-04	-0.4	5.37E-04	1.7	4.85E-04	3.6

Appendix B.6. Counting efficiency values obtained using the Livermore P4 measurement and Equation 3.2.

Table 1. Counting efficiency values estimated using Equation (3.2), starting from the Livermore P4 measured curve, for the phantoms of chest girth of 85 and differences to the reference simulated values.

Energy (keV)	85A		85B		85C		85D		85E	
	Counting efficiency (counts/s/ γ)	R. E. (%)	Counting efficiency (counts/s/ γ)	R. E. (%)	Counting efficiency (counts/s/ γ)	R. E. (%)	Counting efficiency (counts/s/ γ)	R. E. (%)	Counting efficiency (counts/s/ γ)	R. E. (%)
15	1.07E-04	2.8	4.44E-05	1.3	3.18E-05	5.8	2.37E-05	3.3	1.57E-05	9.1
22	2.48E-03	-2.1	1.68E-03	-0.6	1.45E-03	-2.8	1.27E-03	-1.6	1.06E-03	-3.5
33	1.01E-02	-7.0	7.96E-03	-5.2	7.29E-03	-8.4	6.74E-03	-6.7	6.04E-03	-9.5
40	1.33E-02	-8.7	1.08E-02	-7.7	1.00E-02	-10.9	9.37E-03	-9.1	8.52E-03	-12.0
59	1.69E-02	-5.7	1.43E-02	-5.1	1.34E-02	-8.1	1.26E-02	-6.4	1.17E-02	-9.9
81	1.76E-02	-0.3	1.51E-02	1.0	1.42E-02	-1.5	1.35E-02	0.2	1.26E-02	-3.7
122	1.67E-02	5.2	1.46E-02	5.3	1.38E-02	3.5	1.32E-02	4.3	1.24E-02	1.6
165	1.49E-02	5.2	1.32E-02	5.6	1.26E-02	4.2	1.20E-02	5.1	1.14E-02	2.9
185	1.40E-02	3.8	1.24E-02	4.2	1.19E-02	3.0	1.14E-02	4.1	1.08E-02	1.9
244	1.15E-02	2.1	1.03E-02	1.6	9.91E-03	0.8	9.55E-03	1.0	9.07E-03	-1.6
356	8.16E-03	0.1	7.42E-03	-0.4	7.16E-03	-1.1	6.93E-03	0.0	6.63E-03	-2.6
511	5.73E-03	4.3	5.28E-03	4.2	5.12E-03	2.9	4.98E-03	3.0	4.79E-03	0.5
661	4.61E-03	5.0	4.28E-03	4.4	4.16E-03	3.3	4.06E-03	4.0	3.92E-03	1.3
834	3.94E-03	2.1	3.69E-03	1.7	3.60E-03	1.3	3.52E-03	1.2	3.41E-03	-0.9
1173	3.24E-03	-3.4	3.07E-03	-3.6	3.00E-03	-4.2	2.95E-03	-4.3	2.87E-03	-7.1
1274	3.06E-03	-3.7	2.90E-03	-3.8	2.84E-03	-4.8	2.79E-03	-4.2	2.72E-03	-6.4
1408	2.80E-03	-1.4	2.66E-03	-2.0	2.61E-03	-1.9	2.57E-03	-2.2	2.51E-03	-4.6

Table 2. Counting efficiency values estimated using Equation (3.2), starting from the Livermore P4 measured, for the phantoms of chest girth of 90 and differences to the reference simulated values.

Energy (keV)	90A		90B		90C		90D		90E	
	Counting efficiency (counts/s/ γ)	R. E. (%)	Counting efficiency (counts/s/ γ)	R. E. (%)	Counting efficiency (counts/s/ γ)	R. E. (%)	Counting efficiency (counts/s/ γ)	R. E. (%)	Counting efficiency (counts/s/ γ)	R. E. (%)
15	5.77E-05	2.2	2.94E-05	1.6	2.55E-05	5.5	1.97E-05	7.2	1.30E-05	8.7
22	1.89E-03	-0.4	1.40E-03	0.0	1.31E-03	-1.6	1.17E-03	-1.8	9.72E-04	-3.4
33	8.54E-03	-5.0	7.14E-03	-4.1	6.87E-03	-6.7	6.42E-03	-7.7	5.75E-03	-8.7
40	1.15E-02	-8.6	9.85E-03	-8.1	9.53E-03	-10.3	8.98E-03	-11.3	8.15E-03	-12.5
59	1.50E-02	-5.2	1.32E-02	-4.8	1.28E-02	-7.0	1.22E-02	-8.1	1.13E-02	-9.2
81	1.58E-02	1.1	1.40E-02	1.4	1.37E-02	-0.8	1.31E-02	-2.0	1.22E-02	-2.3
122	1.52E-02	4.9	1.37E-02	5.0	1.34E-02	3.7	1.29E-02	2.7	1.21E-02	2.3
165	1.37E-02	5.6	1.24E-02	5.6	1.22E-02	4.2	1.17E-02	2.5	1.11E-02	2.9
185	1.29E-02	4.3	1.17E-02	4.3	1.15E-02	3.2	1.11E-02	1.5	1.05E-02	1.4
244	1.07E-02	1.3	9.81E-03	1.3	9.64E-03	-0.3	9.34E-03	-2.0	8.86E-03	-2.1
356	7.63E-03	0.3	7.10E-03	0.2	6.99E-03	-1.7	6.80E-03	-2.7	6.50E-03	-3.0
511	5.41E-03	2.5	5.08E-03	2.3	5.01E-03	1.1	4.89E-03	1.5	4.71E-03	-0.1
661	4.37E-03	2.4	4.13E-03	2.7	4.09E-03	2.4	4.00E-03	2.4	3.86E-03	0.8
834	3.76E-03	-0.6	3.58E-03	-0.6	3.54E-03	-1.3	3.47E-03	-1.2	3.36E-03	-0.5
1173	3.12E-03	-5.7	2.99E-03	-5.9	2.96E-03	-7.7	2.91E-03	-6.8	2.84E-03	-6.6
1274	2.95E-03	-5.5	2.83E-03	-5.7	2.81E-03	-7.0	2.76E-03	-7.0	2.69E-03	-6.7
1408	2.71E-03	-2.9	2.60E-03	-3.1	2.58E-03	-4.4	2.54E-03	-4.9	2.48E-03	-4.1

Table 3. Counting efficiency values estimated using Equation (3.2), starting from the Livermore P4 measured, for the phantoms of chest girth of 100 and differences to the reference simulated values.

Energy (keV)	100B		100C		100D		100E		100F	
	Counting efficiency (counts/s/ γ)	R. E. (%)	Counting efficiency (counts/s/ γ)	R. E. (%)	Counting efficiency (counts/s/ γ)	R. E. (%)	Counting efficiency (counts/s/ γ)	R. E. (%)	Counting efficiency (counts/s/ γ)	R. E. (%)
15	1.47E-05	0.9	9.66E-06	3.2	5.70E-06	3.8	4.13E-06	4.5	2.72E-06	6.6
22	8.64E-04	0.2	7.09E-04	-3.3	5.56E-04	-4.5	4.79E-04	-5.8	3.86E-04	-8.2
33	4.72E-03	-4.4	4.16E-03	-6.6	3.57E-03	-7.2	3.26E-03	-7.4	2.80E-03	-9.4
40	6.60E-03	-7.3	5.89E-03	-8.9	5.15E-03	-9.0	4.74E-03	-9.4	4.13E-03	-10.9
59	8.96E-03	-4.6	8.12E-03	-5.7	7.25E-03	-5.8	6.75E-03	-5.9	5.97E-03	-7.4
81	9.61E-03	1.0	8.77E-03	0.3	7.90E-03	0.5	7.40E-03	0.2	6.59E-03	-1.4
122	9.44E-03	5.6	8.68E-03	5.1	7.90E-03	4.6	7.45E-03	4.7	6.67E-03	3.2
165	8.62E-03	5.9	7.97E-03	5.9	7.30E-03	5.1	6.91E-03	5.0	6.23E-03	3.8
185	8.17E-03	4.8	7.57E-03	4.7	6.95E-03	4.6	6.59E-03	4.1	5.95E-03	3.2
244	6.85E-03	1.7	6.38E-03	1.5	5.89E-03	1.8	5.61E-03	1.3	5.08E-03	1.3
356	4.99E-03	-0.9	4.67E-03	0.6	4.35E-03	1.0	4.16E-03	-0.2	3.80E-03	0.6
511	3.59E-03	2.8	3.38E-03	2.9	3.17E-03	4.2	3.05E-03	4.3	2.80E-03	5.3
661	2.93E-03	3.7	2.77E-03	3.7	2.62E-03	4.1	2.52E-03	4.0	2.32E-03	4.8
834	2.54E-03	0.5	2.42E-03	1.4	2.29E-03	2.0	2.21E-03	2.8	2.04E-03	4.2
1173	2.14E-03	-3.8	2.04E-03	-2.2	1.94E-03	-3.2	1.88E-03	-2.1	1.74E-03	0.9
1274	2.02E-03	-4.4	1.93E-03	-2.9	1.84E-03	-2.9	1.79E-03	-2.1	1.66E-03	-0.6
1408	1.86E-03	-2.9	1.78E-03	-1.3	1.70E-03	-0.8	1.65E-03	0.3	1.54E-03	1.5

Table 4. Counting efficiency values estimated using Equation (3.2), starting from the Livermore P4 measured, for the phantoms of chest girth of 110 and differences to the reference simulated values.

Energy (keV)	110B		110C		110D		110E		110F	
	Counting efficiency (counts/s/ γ)	R. E. (%)	Counting efficiency (counts/s/ γ)	R. E. (%)	Counting efficiency (counts/s/ γ)	R. E. (%)	Counting efficiency (counts/s/ γ)	R. E. (%)	Counting efficiency (counts/s/ γ)	R. E. (%)
22	1.83E-04	-5.9	1.40E-04	-4.9	9.64E-05	-4.0	8.39E-05	-3.1	7.08E-05	-1.8
33	1.64E-03	-4.0	1.38E-03	-4.3	1.10E-03	-3.0	1.01E-03	-4.5	8.98E-04	-4.8
40	2.52E-03	-6.4	2.17E-03	-6.5	1.78E-03	-5.5	1.64E-03	-7.5	1.47E-03	-7.8
59	3.81E-03	-3.9	3.35E-03	-3.9	2.84E-03	-3.4	2.64E-03	-5.4	2.40E-03	-5.8
81	4.30E-03	1.2	3.82E-03	0.8	3.28E-03	1.1	3.07E-03	-0.9	2.81E-03	-1.1
122	4.45E-03	5.7	4.00E-03	4.9	3.49E-03	6.5	3.28E-03	5.3	3.02E-03	3.5
165	4.22E-03	5.9	3.82E-03	5.3	3.37E-03	5.5	3.18E-03	4.8	2.94E-03	4.0
185	4.05E-03	4.9	3.68E-03	4.0	3.26E-03	4.3	3.08E-03	3.5	2.85E-03	2.9
244	3.51E-03	1.5	3.21E-03	0.9	2.87E-03	1.5	2.72E-03	0.3	2.53E-03	0.1
356	2.67E-03	0.4	2.47E-03	0.1	2.24E-03	0.7	2.13E-03	-0.3	1.99E-03	-0.1
511	2.00E-03	2.8	1.86E-03	3.0	1.71E-03	3.2	1.63E-03	2.7	1.53E-03	3.2
661	1.68E-03	3.3	1.57E-03	3.4	1.46E-03	3.9	1.40E-03	3.9	1.31E-03	4.4
834	1.49E-03	0.8	1.40E-03	1.4	1.31E-03	2.4	1.26E-03	2.3	1.19E-03	1.8
1173	1.29E-03	-4.1	1.22E-03	-3.5	1.15E-03	-2.2	1.11E-03	-3.2	1.05E-03	-1.9
1274	1.24E-03	-4.1	1.17E-03	-3.4	1.10E-03	-1.9	1.06E-03	-2.8	1.01E-03	-1.3
1408	1.15E-03	-2.3	1.09E-03	-1.4	1.03E-03	-0.3	9.93E-04	-0.3	9.41E-04	0.8

Table 5. Counting efficiency values estimated using Equation (3.2), starting from the Livermore P4 measured, for the phantoms of chest girth of 120 and differences to the reference simulated values.

Energy (keV)	120C		120D		120E		120F	
	Counting efficiency (counts/s/ γ)	Stat. R. E. (%)	Counting efficiency (counts/s/ γ)	Stat. R. E. (%)	Counting efficiency (counts/s/ γ)	Stat. R. E. (%)	Counting efficiency (counts/s/ γ)	Stat. R. E. (%)
22	2.85E-05	-6.0	2.32E-05	-4.6	1.90E-05	-2.2	1.28E-05	0.4
33	4.50E-04	-2.6	3.94E-04	-3.0	3.43E-04	-3.5	2.64E-04	-4.1
40	7.69E-04	-4.9	6.83E-04	-5.5	6.01E-04	-6.6	4.75E-04	-7.6
59	1.32E-03	-4.0	1.19E-03	-4.7	1.06E-03	-6.2	8.62E-04	-7.9
81	1.57E-03	0.0	1.43E-03	-0.8	1.28E-03	-2.4	1.06E-03	-3.7
122	1.73E-03	4.6	1.59E-03	3.9	1.43E-03	2.9	1.20E-03	1.4
165	1.72E-03	5.0	1.58E-03	4.4	1.43E-03	3.5	1.22E-03	2.7
185	1.67E-03	3.9	1.54E-03	3.4	1.40E-03	2.7	1.19E-03	1.9
244	1.51E-03	0.7	1.39E-03	0.2	1.27E-03	0.1	1.09E-03	-0.8
356	1.21E-03	-0.3	1.13E-03	0.0	1.03E-03	-0.5	9.00E-04	-0.7
511	9.48E-04	2.8	8.89E-04	3.2	8.20E-04	2.8	7.21E-04	2.9
661	8.22E-04	3.6	7.73E-04	3.8	7.16E-04	4.2	6.34E-04	4.2
834	7.50E-04	1.3	7.08E-04	2.1	6.57E-04	2.5	5.86E-04	3.3
1173	6.74E-04	-3.4	6.39E-04	-2.7	5.95E-04	-1.2	5.36E-04	0.2
1274	6.48E-04	-3.3	6.16E-04	-2.6	5.74E-04	-1.2	5.18E-04	1.0
1408	6.08E-04	-1.4	5.78E-04	-0.9	5.40E-04	1.2	4.88E-04	3.1

Appendix B.7. Counting efficiency values obtained using the AA cup simulation and Equation 3.2.

Table 1. Comparison of published and calculated values of counting efficiency with the associated difference (%) for the Cs-137 photons at 661.66 keV.

Phantom	MC. Count. Eff. (counts/s/ γ)	Cal. Count. Eff. (counts/s/ γ)	Diff. (%)
A	2.22E-02	2.23E-02	-0.66
B	2.02E-02	2.04E-02	-1.07
C	1.94E-02	1.96E-02	-1.17
105 D	1.80E-02	1.82E-02	-1.11
E	1.67E-02	1.70E-02	-1.66
F	1.55E-02	1.58E-02	-1.78
G	1.47E-02	1.49E-02	-1.62

Table 2. Comparison of published and calculated values of counting efficiency with the associated difference (%) for the Co-60 photons at 1173.23 keV.

Phantom	MC. Count. Eff. (counts/s/ γ)	Cal. Count. Eff. (counts/s/ γ)	Diff. (%)
A	1.87E-02	1.85E-02	1.16
B	1.72E-02	1.69E-02	1.83
C	1.66E-02	1.62E-02	2.21
105 D	1.54E-02	1.51E-02	2.26
E	1.45E-02	1.40E-02	3.16
F	1.35E-02	1.30E-02	3.35
G	1.28E-02	1.24E-02	3.47

Appendix B.8. Counting efficiency values obtained using the A cup simulations and Equation 3.2.

Table 1. Values of c_1 and c_2 parameters for all cup sizes (B to G) with the associated R^2 and χ^2 values (left).

Phantom	c_1	c_2 (g/cm ²)	R^2	χ^2	
105	B	0.93	0.16	0.9046	2.7E-05
	C	0.90	0.30	0.9595	4.0E-05
	D	0.84	0.36	0.9800	2.8E-05
	E	0.80	0.58	0.9595	1.5E-04
	F	0.74	0.63	0.9571	1.9E-04
	G	0.71	0.75	0.9777	1.3E-04

Table 3. Comparison of published and calculated values of counting efficiency with the associated difference (%) for the Cs-137 photons at 661.66 keV (right).

Phantom	MC. Count. Eff. (counts/s/ γ)	Cal. Count. Eff. (counts/s/ γ)	Diff. (%)	
105	B	2.02E-02	2.03E-02	-0.40
	C	1.94E-02	1.95E-02	-0.49
	D	1.80E-02	1.81E-02	-0.40
	E	1.67E-02	1.69E-02	-0.94
	F	1.55E-02	1.57E-02	-1.04
	G	1.47E-02	1.48E-02	-0.88

Table 2. Comparison of published and calculated values of counting efficiency with the associated difference (%) for the Am-241 photons at 59.54 keV (right).

Phantom	MC. Count. Eff. (counts/s/ γ)	Cal. Count. Eff. (counts/s/ γ)	Diff. (%)	
105	B	2.030E-02	2.03E-02	0.07
	C	1.920E-02	1.92E-02	0.08
	D	1.768E-02	1.77E-02	0.07
	E	1.610E-02	1.61E-02	0.16
	F	1.488E-02	1.49E-02	0.18
	G	1.390E-02	1.39E-02	0.15

Table 4. Comparison of published and calculated values of counting efficiency with the associated difference (%) for the Co-60 photons at 1173.23 keV (right).

Phantom	MC. Count. Eff. (counts/s/ γ)	Cal. Count. Eff. (counts/s/ γ)	Diff. (%)	
105	B	1.72E-02	1.71E-02	0.33
	C	1.66E-02	1.65E-02	0.40
	D	1.54E-02	1.53E-02	0.34
	E	1.45E-02	1.44E-02	0.77
	F	1.35E-02	1.34E-02	0.87
	G	1.28E-02	1.27E-02	0.73

Appendix C.1 List of cell, densities and corresponding materials in the used phantoms

• Case of the Livermore phantom

Cell	density	Material	Cell	density	Material
1	2.70	\$Al	38	2.70	\$Al
2	5.32	\$Ge	39	5.32	\$Ge
3	1.25	\$CEpoxy_EndCap	40	1.00E-08	\$Air_Dry_LowP
4	11.4	\$Pb	41	1.00E-08	\$Air_Dry_LowP
5	2.70	\$Al	42	1.00E-08	\$Air_Dry_LowP
6	2.70	\$Al	43	1.00E-08	\$Air_Dry_LowP
7	2.70	\$Al	44	1.00E-08	\$Air_Dry_LowP
8	2.70	\$Al	45	1.00E-08	\$Air_Dry_LowP
9	5.32	\$Ge	46	2.70	\$Al
10	1E-08	\$Air_Dry_LowP	47	5.32	\$Ge
11	1E-08	\$Air_Dry_LowP	48	1.25	\$CEpoxy_EndCap
12	1E-08	\$Air_Dry_LowP	49	11.4	\$Pb
13	1E-08	\$Air_Dry_LowP	50	2.70	\$Al
14	1E-08	\$Air_Dry_LowP	51	2.70	\$Al
15	1E-08	\$Air_Dry_LowP	52	2.70	\$Al
16	2.70	\$Al	53	2.70	\$Al
17	5.32	\$Ge	54	5.32	\$Ge
18	1.25	\$CEpoxy_EndCap	55	1.00E-08	\$Air_Dry_LowP
19	11.4	\$Pb	56	1.00E-08	\$Air_Dry_LowP
20	2.70	\$Al	57	1.00E-08	\$Air_Dry_LowP
21	2.70	\$Al	58	1.00E-08	\$Air_Dry_LowP
22	2.70	\$Al	59	1.00E-08	\$Air_Dry_LowP
23	2.70	\$Al	60	1.00E-08	\$Air_Dry_LowP
24	5.32	\$Ge	1002	-	\$rpp_phantom
25	1.00E-08	\$Air_Dry_LowP	1003	-	\$repeated_struct
26	1.00E-08	\$Air_Dry_LowP	1004	1.21E-03	\$air
27	1.00E-08	\$Air_Dry_LowP	1005	1.21E-03	\$air
28	1.00E-08	\$Air_Dry_LowP	1014	1.03	\$tissu_equiv_plastic
29	1.00E-08	\$Air_Dry_LowP	1015	1.03	\$tissu_equiv_plastic
30	1.00E-08	\$Air_Dry_LowP	1024	1.03	\$bone_equiv_plastic
31	2.70	\$Al	1025	1.03	\$bone_equiv_plastic
32	5.32	\$Ge	1034	1.03	\$lungs_equiv_plastic
33	1.25	\$CEpoxy_EndCap	1035	1.03	\$lungs_equiv_plastic
34	11.4	\$Pb	1044	1.03	\$plate50%_equiv_plastic
35	2.70	\$Al	1045	1.03	\$plate50%_equiv_plastic
36	2.70	\$Al	10000	0.00	\$ void_outside_world
37	2.70	\$Al	10001	1.20E-03	\$air_sphere of work

- **Case of the ICRP phantom**

Cell	density	Material	Cell	density	Material
1	2.70	\$Al	1185	1.17	\$lumar_spine_spongiosa
2	5.32	\$Ge	1194	1.92	\$sternum_cortical
3	1.25	\$CEpoxy_EndCap	1195	1.92	\$sternum_cortical
4	11.4	\$Pb	1204	1.08	\$sternum_spongiosa
5	2.70	\$Al	1205	1.08	\$sternum_spongiosa
6	2.70	\$Al	1214	1.10	\$cartilage_trunk
7	2.70	\$Al	1215	1.10	\$cartilage_trunk
8	2.70	\$Al	1224	0.95	\$breast_left_adiposetissue
9	5.32	\$Ge	1225	0.95	\$breast_left_adiposetissue
10	1E-08	\$Air_Dry_LowP	1234	1.02	\$breast_left_glandular_tissue
11	1E-08	\$Air_Dry_LowP	1235	1.02	\$breast_left_glandular_tissue
12	1E-08	\$Air_Dry_LowP	1244	0.95	\$breast_right_adiposetissue
13	1E-08	\$Air_Dry_LowP	1245	0.95	\$breast_right_adiposetissue
14	1E-08	\$Air_Dry_LowP	1254	1.02	\$breast_right_glandular_tissue
15	1E-08	\$Air_Dry_LowP	1255	1.02	\$breast_right_glandular_tissue
16	2.70	\$Al	1264	1.03	\$gall_bladder_wall
17	5.32	\$Ge	1265	1.03	\$gall_bladder_wall
18	1.25	\$CEpoxy_EndCap	1274	1.03	\$gall_bladder_contents
19	11.4	\$Pb	1275	1.03	\$gall_bladder_contents
20	2.70	\$Al	1284	1.04	\$stomach_wall
21	2.70	\$Al	1285	1.04	\$stomach_wall
22	2.70	\$Al	1294	1.04	\$stomach_contents
23	2.70	\$Al	1295	1.04	\$stomach_contents
24	5.32	\$Ge	1304	1.04	\$small_intestine_wall
25	1.00E-08	\$Air_Dry_LowP	1305	1.04	\$small_intestine_wall
26	1.00E-08	\$Air_Dry_LowP	1314	1.04	\$small_intestine_contents
27	1.00E-08	\$Air_Dry_LowP	1315	1.04	\$small_intestine_contents
28	1.00E-08	\$Air_Dry_LowP	1324	1.04	\$ascending_colon_wall
29	1.00E-08	\$Air_Dry_LowP	1325	1.04	\$ascending_colon_wall
30	1.00E-08	\$Air_Dry_LowP	1334	1.04	\$ascending_colon_contents
31	2.70	\$Al	1335	1.04	\$ascending_colon_contents
32	5.32	\$Ge	1344	1.04	\$transverse_colon_wall_right
33	1.25	\$CEpoxy_EndCap	1345	1.04	\$transverse_colon_wall_right
34	11.4	\$Pb	1354	1.04	\$transverse_colon_cont_right
35	2.70	\$Al	1355	1.04	\$transverse_colon_cont_right
36	2.70	\$Al	1364	1.04	\$transverse_colon_wall_left
37	2.70	\$Al	1365	1.04	\$transverse_colon_wall_left
38	2.70	\$Al	1374	1.04	\$transverse_colon_cont_left
39	5.32	\$Ge	1375	1.04	\$transverse_colon_cont_left
40	1.00E-08	\$Air_Dry_LowP	1384	1.04	\$descending_colon_wall
41	1.00E-08	\$Air_Dry_LowP	1385	1.04	\$descending_colon_wall
42	1.00E-08	\$Air_Dry_LowP	1394	1.04	\$descending_colon_contents

43	1.00E-08	\$Air_Dry_LowP	1395	1.04	\$descending_colon_contents
44	1.00E-08	\$Air_Dry_LowP	1404	1.05	\$heart_wall
45	1.00E-08	\$Air_Dry_LowP	1405	1.05	\$heart_wall
46	2.70	\$Al	1414	1.06	\$heart_contents
47	5.32	\$Ge	1415	1.06	\$heart_contents
48	1.25	\$CEpoxy_EndCap	1424	1.05	\$kidney_left_cortex
49	11.4	\$Pb	1425	1.05	\$kidney_left_cortex
50	2.70	\$Al	1434	1.05	\$kidney_left_medulla
51	2.70	\$Al	1435	1.05	\$kidney_left_medulla
52	2.70	\$Al	1444	1.05	\$kidney_left_pelvis
53	2.70	\$Al	1445	1.05	\$kidney_left_pelvis
54	5.32	\$Ge	1454	1.05	\$kidney_right_cortex
55	1.00E-08	\$Air_Dry_LowP	1455	1.05	\$kidney_right_cortex
56	1.00E-08	\$Air_Dry_LowP	1464	1.05	\$kidney_right_medulla
57	1.00E-08	\$Air_Dry_LowP	1465	1.05	\$kidney_right_medulla
58	1.00E-08	\$Air_Dry_LowP	1474	1.05	\$kidney_right_pelvis
59	1.00E-08	\$Air_Dry_LowP	1475	1.05	\$kidney_right_pelvis
60	1.00E-08	\$Air_Dry_LowP	1484	1.05	\$liver
1002	-	\$rpp_phantom	1485	1.05	\$liver
1003	-	\$repeated_struct	1494	1.06	\$lung_left_blood
1004	1.21E-03	\$air	1495	1.06	\$lung_left_blood
1005	1.21E-03	\$air	1504	0.385	\$lung_left_tissue
1014	1.03	\$adrenal_left	1505	0.385	\$lung_left_tissue
1015	1.03	\$adrenal_left	1514	1.06	\$lung_right_blood
1024	1.03	\$adrenal_right	1515	1.06	\$lung_right_blood
1025	1.03	\$adrenal_right	1524	0.385	\$lung_right_tissue
1034	1.03	\$trachea	1525	0.385	\$lung_right_tissue
1035	1.03	\$trachea	1534	1.03	\$lymph_nodes_thor_airways
1044	1.03	\$bronchi	1535	1.03	\$lymph_nodes_thor_airways
1045	1.03	\$bronchi	1544	1.03	\$lymph_nodes_trunk
1054	1.06	\$blood_vessels_trunk	1545	1.03	\$lymph_nodes_trunk
1055	1.06	\$blood_vessels_trunk	1554	1.05	\$muscle_trunk
1064	1.92	\$humeri_upperhalf_cort	1555	1.05	\$muscle_trunk
1065	1.92	\$humeri_upperhalf_cort	1564	1.03	\$oesophagus
1074	1.18	\$humeri_upperhalf_spong	1565	1.03	\$oesophagus
1075	1.18	\$humeri_upperhalf_spong	1574	1.05	\$pancreas
1084	0.98	\$humeri_upperhalf_medu	1575	1.05	\$pancreas
1085	0.98	\$humeri_upperhalf_medu	1584	1.09	\$skin_trunk
1094	1.92	\$clavicles_cortical	1585	1.09	\$skin_trunk
1095	1.92	\$clavicles_cortical	1594	1.03	\$spinal_cord
1104	1.19	\$clavicles_spongiosa	1595	1.03	\$spinal_cord
1105	1.19	\$clavicles_spongiosa	1604	1.04	\$spleen
1114	1.92	\$ribs_cortical	1605	1.04	\$spleen
1115	1.92	\$ribs_cortical	1614	1.03	\$thymus

1124	1.09	\$ribs_spongiosa	1615	1.03	\$thymus
1125	1.09	\$ribs_spongiosa	1624	1.04	\$thyroid
1134	1.92	\$scapulae_cortical	1625	1.04	\$thyroid
1135	1.92	\$scapulae_cortical	1634	1.03	\$ureter_left
1144	1.13	\$scapulae_spongiosa	1635	1.03	\$ureter_left
1145	1.13	\$scapulae_spongiosa	1644	1.03	\$ureter_right
1154	1.92	\$thoracic_spine_cortical	1645	1.03	\$ureter_right
1155	1.92	\$thoracic_spine_cortical	1654	1.21E-03	\$air_inside_body
1164	1.08	\$thoracic_spine_spong	1655	1.21E-03	\$air_inside_body
1165	1.08	\$thoracic_spine_spong	1664	0.95	\$residual_tissue_trunk
1174	1.92	\$lumbar_spine_cortical	1665	0.95	\$residual_tissue_trunk
1175	1.92	\$lumbar_spine_cortical	10000	0.00	\$ void_outside_world
1184	1.17	\$lumbar_spine_spongiosa	10001	1.20E-03	\$air_sphere of work

Appendix C.2. Reference MC simulation results without VR methods.

- **Case of the Livermore phantom**

Table 1. MC reference simulated counting rates, associated statistical relative error, counting efficiency value and associated uncertainty.

Energy (keV)	Simulated counting rate (counts)	Statistical Relative Error (%)	Counting efficiency (counts/s/ γ)	Uncertainty (%)
15	1.21E-04	1.90	6.03E-05	3.37
22	1.62E-03	0.32	1.53E-03	0.36
33	6.43E-03	0.16	6.22E-03	0.17
40	8.54E-03	0.14	8.32E-03	0.15
59	1.17E-02	0.12	1.15E-02	0.13
81	1.31E-02	0.11	1.29E-02	0.11
122	1.32E-02	0.11	1.31E-02	0.11
165	1.19E-02	0.12	1.18E-02	0.12
185	1.10E-02	0.12	1.10E-02	0.12
244	8.79E-03	0.14	8.76E-03	0.14
356	6.20E-03	0.17	6.19E-03	0.17
511	4.48E-03	0.19	4.47E-03	0.19
661	3.63E-03	0.22	3.62E-03	0.22
834	3.06E-03	0.24	3.06E-03	0.24
1173	2.40E-03	0.27	2.40E-03	0.27
1274	2.27E-03	0.27	2.27E-03	0.27
1408	2.12E-03	0.28	2.12E-03	0.28

- **Case of the ICRP female torso phantom**

Table 2. MC reference simulated counting rates, associated statistical relative error, counting efficiency value and associated uncertainty.

Energy (keV)	Simulated counting rate (counts)	Statistical Relative Error (%)	Counting efficiency (counts/s/ γ)	Uncertainty (%)
15	1.15E-04	1.20	4.52E-05	4.61
22	1.70E-03	0.32	1.60E-03	0.36
33	7.38E-03	0.15	7.11E-03	0.16
40	9.70E-03	0.13	9.44E-03	0.14
59	1.32E-02	0.11	1.29E-02	0.12
81	1.47E-02	0.11	1.45E-02	0.11
122	1.48E-02	0.11	1.47E-02	0.11
165	1.35E-02	0.11	1.34E-02	0.11
185	1.26E-02	0.12	1.25E-02	0.12
244	1.01E-02	0.13	1.01E-02	0.13
356	7.25E-03	0.15	7.25E-03	0.15
511	5.33E-03	0.18	5.32E-03	0.18
661	4.34E-03	0.20	4.33E-03	0.20
834	3.67E-03	0.22	3.67E-03	0.22
1173	2.91E-03	0.24	2.91E-03	0.24
1274	2.76E-03	0.25	2.75E-03	0.25
1408	2.58E-03	0.26	2.58E-03	0.26

Appendix C.3. MC simulation results for the Cell IMP card.

- **Case of the Livermore phantom**

Table 1. Counting efficiency values, associated relative error and uncertainty obtained with the cell importance card with the parameters 1, 3, 9 and 18.

Energy (keV)	Simulated counting rate (counts)	Statistical Relative Error (%)	Counting efficiency (counts/s/ γ)	Uncertainty (%)	Difference (%)
15	1.24E-04	2.52	6.13E-05	8.00	-1.62
22	1.61E-03	0.76	1.51E-03	0.85	1.01
33	6.43E-03	0.44	6.21E-03	0.47	0.18
40	8.54E-03	0.40	8.32E-03	0.42	-0.04
59	1.17E-02	0.35	1.15E-02	0.36	0.03
81	1.31E-02	0.34	1.29E-02	0.35	0.23
122	1.33E-02	0.33	1.31E-02	0.34	-0.37
165	1.19E-02	0.33	1.18E-02	0.33	-0.15
185	1.10E-02	0.33	1.10E-02	0.33	-0.01
244	8.77E-03	0.33	8.74E-03	0.33	0.24
356	6.21E-03	0.33	6.20E-03	0.33	-0.19
511	4.52E-03	0.33	4.51E-03	0.33	-0.82
661	3.65E-03	0.34	3.64E-03	0.34	-0.48
834	3.07E-03	0.34	3.06E-03	0.34	-0.06
1173	2.40E-03	0.35	2.40E-03	0.35	0.02
1274	2.28E-03	0.36	2.28E-03	0.36	-0.71
1408	2.12E-03	0.36	2.12E-03	0.36	0.11

- **Case of the ICRP female torso phantom**

Table 2. Counting efficiency values, associated relative error and uncertainty obtained with the cell importance card with the parameters 1, 3, 9 and 18.

Energy (keV)	Simulated counting rate (counts)	Statistical Relative Error (%)	Counting efficiency (counts/s/ γ)	Uncertainty (%)	Difference (%)
15	1.21E-04	2.67	5.07E-05	9.92	-12.20
22	1.69E-03	0.71	1.58E-03	0.81	0.72
33	7.36E-03	0.40	7.10E-03	0.43	0.16
40	9.73E-03	0.36	9.46E-03	0.38	-0.25
59	1.31E-02	0.32	1.28E-02	0.33	0.67
81	1.47E-02	0.31	1.45E-02	0.32	-0.11
122	1.48E-02	0.30	1.47E-02	0.30	0.06
165	1.36E-02	0.30	1.35E-02	0.30	-0.70
185	1.26E-02	0.30	1.25E-02	0.30	-0.28
244	1.01E-02	0.30	1.01E-02	0.30	-0.08
356	7.24E-03	0.30	7.22E-03	0.30	0.10
511	5.33E-03	0.30	5.33E-03	0.30	-0.07
661	4.34E-03	0.31	4.34E-03	0.31	-0.17
834	3.64E-03	0.32	3.63E-03	0.32	0.84
1173	2.90E-03	0.32	2.89E-03	0.32	0.52
1274	2.75E-03	0.33	2.75E-03	0.33	0.23
1408	2.57E-03	0.33	2.57E-03	0.33	0.36

Table 3. Counting efficiency values, associated uncertainty and difference to reference values obtained for the ICRP female and for various cell importance entries.

Energy	Cell IMP parameters					
	1-4-8			1-4-16		
	Count Eff. (counts/s/ γ)	Unc. (%)	Diff. (%)	Count Eff. (counts/s/ γ)	Unc. (%)	Diff. (%)
15	4.62E-05	12.31	-2.23	4.01E-05	15.26	11.24
22	1.59E-03	1.03	0.33	1.59E-03	1.04	0.11
33	7.12E-03	0.54	-0.15	7.13E-03	0.56	-0.33
40	9.42E-03	0.49	0.25	9.41E-03	0.51	0.36
59	1.28E-02	0.44	0.64	1.28E-02	0.46	0.65
81	1.45E-02	0.42	-0.04	1.45E-02	0.43	-0.13
122	1.46E-02	0.41	0.40	1.47E-02	0.43	0.00
165	1.35E-02	0.40	-0.79	1.35E-02	0.41	-0.34
185	1.26E-02	0.40	-0.30	1.26E-02	0.41	-0.52
244	1.01E-02	0.41	-0.39	1.01E-02	0.41	-0.35
356	7.20E-03	0.43	0.43	7.24E-03	0.42	-0.10
511	5.31E-03	0.45	0.18	5.32E-03	0.42	0.11
661	4.33E-03	0.47	-0.04	4.33E-03	0.44	0.09
834	3.65E-03	0.49	0.38	3.64E-03	0.45	0.56
1173	2.88E-03	0.52	0.92	2.87E-03	0.47	1.16
1274	2.75E-03	0.52	0.27	2.74E-03	0.46	0.58
1408	2.56E-03	0.53	0.67	2.56E-03	0.47	0.56

Appendix C.4. MC simulation results for the WW card.

- **Case of the Livermore phantom**

Table 1. Counting efficiency values, associated uncertainty and the difference to the reference simulation obtained with the mesh-based rectangular WW.

Energy (keV)	Simulated counting rate (counts)	Statistical Relative Error (%=)	Counting efficiency (counts/s/ γ)	Uncertainty (%)	Difference (%)
15	1.19E-04	4.40	6.21E-05	11.84	-2.95
22	1.60E-03	1.20	1.51E-03	1.35	1.29
33	6.42E-03	0.60	6.20E-03	0.64	0.34
40	8.42E-03	0.52	8.19E-03	0.55	1.49
59	1.18E-02	0.44	1.15E-02	0.46	-0.43
81	1.31E-02	0.42	1.29E-02	0.43	-0.46
122	1.32E-02	0.42	1.31E-02	0.43	-0.24
165	1.18E-02	0.44	1.17E-02	0.45	0.51
185	1.11E-02	0.46	1.11E-02	0.46	-0.66
244	8.84E-03	0.51	8.81E-03	0.51	-0.60
356	6.23E-03	0.61	6.21E-03	0.61	-0.42
511	4.51E-03	0.72	4.50E-03	0.72	-0.60
661	3.65E-03	0.80	3.65E-03	0.80	-0.69
834	3.07E-03	0.87	3.07E-03	0.87	-0.24
1173	2.40E-03	0.98	2.39E-03	0.98	0.21
1274	2.27E-03	1.01	2.27E-03	1.01	-0.25
1408	2.13E-03	1.04	2.13E-03	1.04	-0.14

Table 2. Counting efficiency values, associated uncertainty and the difference to the reference simulation obtained with the mesh-based spherical WW.

Energy (keV)	Simulated counting rate (counts)	Statistical Relative Error (%)	Counting efficiency (counts/s/ γ)	Uncertainty (%)	Difference (%)
15	1.22E-04	2.36	6.05E-05	6.52	-0.41
22	1.61E-03	0.75	1.52E-03	0.83	0.72
33	6.42E-03	0.42	6.21E-03	0.44	0.19
40	8.51E-03	0.37	8.28E-03	0.39	0.40
59	1.18E-02	0.33	1.15E-02	0.34	-0.39
81	1.31E-02	0.32	1.29E-02	0.33	-0.27
122	1.33E-02	0.32	1.31E-02	0.32	-0.44
165	1.19E-02	0.32	1.18E-02	0.32	0.05
185	1.10E-02	0.33	1.10E-02	0.33	0.10
244	8.80E-03	0.35	8.77E-03	0.35	-0.10
356	6.21E-03	0.38	6.20E-03	0.38	-0.14
511	4.51E-03	0.43	4.50E-03	0.43	-0.61
661	3.65E-03	0.46	3.64E-03	0.46	-0.51
834	3.07E-03	0.49	3.07E-03	0.49	-0.18
1173	2.40E-03	0.54	2.40E-03	0.54	0.10
1274	2.26E-03	0.55	2.26E-03	0.55	0.22
1408	2.13E-03	0.56	2.13E-03	0.56	-0.23

- **Case of the ICRP female torso phantom**

Table 3. Counting efficiency values, associated uncertainty and the difference to the reference simulation obtained with the mesh-based rectangular WW.

Energy (keV)	Simulated counting rate (counts)	Statistical Relative Error (%)	Counting efficiency (counts/s/ γ)	Uncertainty (%)	Difference (%)
15	1.20E-04	4.39	4.48E-05	17.62	0.85
22	1.71E-03	1.16	1.60E-03	1.32	-0.07
33	7.28E-03	0.56	7.01E-03	0.60	1.38
40	9.68E-03	0.49	9.42E-03	0.52	0.24
59	1.32E-02	0.42	1.29E-02	0.44	0.09
81	1.47E-02	0.40	1.45E-02	0.41	-0.09
122	1.49E-02	0.39	1.48E-02	0.40	-0.40
165	1.36E-02	0.41	1.35E-02	0.42	-0.41
185	1.26E-02	0.43	1.25E-02	0.43	-0.14
244	1.01E-02	0.48	1.01E-02	0.48	-0.02
356	7.23E-03	0.57	7.21E-03	0.57	0.26
511	5.27E-03	0.66	5.26E-03	0.66	1.21
661	4.36E-03	0.73	4.35E-03	0.73	-0.46
834	3.66E-03	0.79	3.66E-03	0.79	0.18
1173	2.89E-03	0.89	2.89E-03	0.89	0.76
1274	2.77E-03	0.91	2.77E-03	0.91	-0.47
1408	2.57E-03	0.95	2.57E-03	0.95	0.04

Table 4. Counting efficiency values, associated uncertainty and the difference to the reference simulation obtained with the mesh-based spherical WW.

Energy (keV)	Simulated counting rate (counts)	Statistical Relative Error (%)	Counting efficiency (counts/s/ γ)	Uncertainty (%)	Difference (%)
15	1.15E-04	2.37	4.54E-05	8.73	-0.36
22	1.70E-03	0.71	1.59E-03	0.79	0.42
33	7.41E-03	0.38	7.13E-03	0.40	-0.28
40	9.73E-03	0.34	9.47E-03	0.35	-0.33
59	1.32E-02	0.30	1.29E-02	0.31	0.08
81	1.47E-02	0.29	1.45E-02	0.30	0.08
122	1.49E-02	0.29	1.48E-02	0.29	-0.44
165	1.36E-02	0.29	1.35E-02	0.29	-0.68
185	1.26E-02	0.30	1.26E-02	0.30	-0.32
244	1.02E-02	0.32	1.01E-02	0.32	-0.54
356	7.27E-03	0.35	7.25E-03	0.35	-0.31
511	5.29E-03	0.39	5.28E-03	0.39	0.73
661	4.35E-03	0.41	4.35E-03	0.41	-0.33
834	3.64E-03	0.44	3.64E-03	0.44	0.67
1173	2.86E-03	0.49	2.86E-03	0.49	1.79
1274	2.76E-03	0.49	2.76E-03	0.49	-0.09
1408	2.57E-03	0.51	2.57E-03	0.51	0.38

Appendix C.5. MC simulation results for the SB card.

- **Case of the Livermore phantom**

Table 1. Counting efficiency values, associated uncertainty and the difference to the reference simulation obtained with the SB card simulation (15/51 starting at 15 keV, NPS 2e8).

Energy (keV)	Simulated counting rate (counts)	Statistical Relative Error (%)	Counting efficiency (counts/s/ γ)	Uncertainty (%)	Difference (%)
15	1.23E-04	2.43	6.10E-05	8.25	-1.12
22	1.62E-03	0.66	1.53E-03	0.76	-0.38
33	6.46E-03	0.47	6.24E-03	0.50	-0.29
40	8.48E-03	0.41	8.26E-03	0.43	0.73
59	1.18E-02	0.35	1.15E-02	0.37	-0.02
81	1.31E-02	0.33	1.29E-02	0.34	-0.39
122	1.33E-02	0.33	1.32E-02	0.34	-0.81
165	1.19E-02	0.35	1.18E-02	0.35	-0.27
185	1.11E-02	0.36	1.10E-02	0.36	-0.42
244	8.74E-03	0.41	8.71E-03	0.41	0.59
356	6.17E-03	0.49	6.16E-03	0.49	0.46
511	4.47E-03	0.57	4.47E-03	0.57	0.17
661	3.62E-03	0.63	3.62E-03	0.63	0.20
834	3.03E-03	0.69	3.03E-03	0.69	1.06
1173	2.39E-03	0.53	2.39E-03	0.53	0.42
1274	2.29E-03	0.55	2.29E-03	0.55	-0.95
1408	2.14E-03	0.56	2.14E-03	0.56	-0.65

Table 2. Counting efficiency values and associated relative error obtained with the second SB card simulation (15/37.5 starting at 15 keV) when the NPS was reduced in regions #2 and #3 and maintained at 15 keV.

Energy (keV)	Simulated counting rate (counts)	Statistical Relative Error (%)	Counting efficiency (counts/s/ γ)	Uncertainty (%)	Difference (%)
15	1.19E-04	2.96	5.92E-05	10.18	1.90
22	1.62E-03	0.67	1.53E-03	0.80	0.00
33	6.43E-03	0.56	6.22E-03	0.60	-0.07
40	8.56E-03	0.49	8.34E-03	0.52	-0.26
59	1.18E-02	0.42	1.15E-02	0.44	0.03
81	1.31E-02	0.39	1.29E-02	0.40	-0.05
122	1.32E-02	0.39	1.31E-02	0.40	-0.06
165	1.18E-02	0.42	1.17E-02	0.43	0.59
185	1.10E-02	0.43	1.10E-02	0.43	0.22
244	8.74E-03	0.48	8.71E-03	0.48	0.55
356	6.18E-03	0.57	6.16E-03	0.57	0.41
511	4.54E-03	0.67	4.53E-03	0.67	-1.28
661	3.66E-03	0.75	3.66E-03	0.75	-0.97
834	3.09E-03	0.81	3.09E-03	0.81	-0.88
1173	2.39E-03	0.92	2.38E-03	0.92	0.63
1274	2.30E-03	0.94	2.30E-03	0.94	-1.39
1408	2.14E-03	0.98	2.14E-03	0.98	-0.66

Table 3. Counting efficiency values, associated uncertainty and the difference to the reference simulation obtained with the second SB card simulation and doubled NPS.

Energy (keV)	Simulated counting rate (counts)	Statistical Relative Error (%)	Counting efficiency (counts/s/ γ)	Uncertainty (%)	Difference (%)
15	1.20E-04	2.07	5.93E-05	7.22	1.68
22	1.62E-03	0.47	1.52E-03	0.56	0.22
33	6.45E-03	0.40	6.24E-03	0.43	-0.32
40	8.55E-03	0.35	8.33E-03	0.37	-0.19
59	1.17E-02	0.29	1.15E-02	0.30	0.11
81	1.31E-02	0.28	1.29E-02	0.29	-0.31
122	1.32E-02	0.28	1.31E-02	0.29	-0.08
165	1.18E-02	0.29	1.17E-02	0.29	0.44
185	1.10E-02	0.30	1.09E-02	0.30	0.46
244	8.74E-03	0.34	8.71E-03	0.34	0.57
356	6.20E-03	0.41	6.19E-03	0.41	0.01
511	4.55E-03	0.47	4.55E-03	0.47	-1.62
661	3.64E-03	0.53	3.63E-03	0.53	-0.27
834	3.05E-03	0.58	3.05E-03	0.58	0.50
1173	2.39E-03	0.65	2.39E-03	0.65	0.29
1274	2.28E-03	0.67	2.28E-03	0.67	-0.71
1408	2.15E-03	0.69	2.15E-03	0.69	-1.15

- **Case of the ICRP female torso phantom**

Table 4. Counting efficiency values, associated uncertainty and the difference to the reference simulation obtained with the SB card simulation (15/51 starting at 15 keV, NPS 2e8).

Energy (keV)	Simulated counting rate (counts)	Statistical Relative Error (%)	Counting efficiency (counts/s/ γ)	Uncertainty (%)	Difference (%)
15	1.15E-04	2.72	4.13E-05	13.08	8.70
22	1.71E-03	0.64	1.60E-03	0.75	-0.15
33	7.37E-03	0.44	7.11E-03	0.47	-0.03
40	9.73E-03	0.39	9.46E-03	0.41	-0.27
59	1.32E-02	0.33	1.30E-02	0.34	-0.56
81	1.47E-02	0.31	1.44E-02	0.32	0.21
122	1.49E-02	0.31	1.47E-02	0.32	-0.12
165	1.34E-02	0.33	1.33E-02	0.33	0.90
185	1.25E-02	0.34	1.24E-02	0.34	0.52
244	1.01E-02	0.38	1.01E-02	0.38	-0.13
356	7.27E-03	0.45	7.26E-03	0.45	-0.41
511	5.31E-03	0.52	5.30E-03	0.52	0.41
661	4.37E-03	0.58	4.36E-03	0.58	-0.68
834	3.61E-03	0.64	3.60E-03	0.64	1.74
1173	2.92E-03	0.48	2.92E-03	0.48	-0.48
1274	2.75E-03	0.50	2.74E-03	0.50	0.35
1408	2.57E-03	0.51	2.57E-03	0.51	0.35

Table 5. Counting efficiency values and associated relative error obtained with the second SB card simulation (15/37.5 starting at 15 keV) when the NPS was reduced in regions #2 and #3 and maintained at 15 keV.

Energy (keV)	Simulated counting rate (counts)	Statistical Relative Error (%)	Counting efficiency (counts/s/ γ)	Uncertainty (%)	Difference (%)
15	1.18E-04	3.31	4.68E-05	14.13	-3.53
22	1.69E-03	0.66	1.59E-03	0.79	0.54
33	7.41E-03	0.52	7.14E-03	0.56	-0.47
40	9.65E-03	0.46	9.38E-03	0.49	0.64
59	1.32E-02	0.39	1.29E-02	0.41	0.02
81	1.47E-02	0.37	1.45E-02	0.38	-0.01
122	1.50E-02	0.37	1.48E-02	0.38	-0.89
165	1.36E-02	0.39	1.35E-02	0.40	-0.29
185	1.26E-02	0.40	1.26E-02	0.40	-0.54
244	1.01E-02	0.45	1.01E-02	0.45	-0.17
356	7.16E-03	0.53	7.14E-03	0.53	1.18
511	5.33E-03	0.62	5.33E-03	0.62	-0.08
661	4.33E-03	0.69	4.33E-03	0.69	0.13
834	3.66E-03	0.75	3.66E-03	0.75	0.16
1173	2.89E-03	0.84	2.89E-03	0.84	0.65
1274	2.79E-03	0.86	2.79E-03	0.86	-1.14
1408	2.57E-03	0.89	2.57E-03	0.89	0.32

Table 6. Counting efficiency values, associated uncertainty and the difference to the reference simulation obtained with the second SB card simulation and doubled NPS.

Energy (keV)	Simulated counting rate (counts)	Statistical Relative Error (%)	Counting efficiency (counts/s/ γ)	Uncertainty (%)	Difference (%)
15	1.14E-04	2.37	4.25E-05	10.92	5.96
22	1.70E-03	0.46	1.59E-03	0.56	0.23
33	7.38E-03	0.37	7.11E-03	0.40	-0.07
40	9.72E-03	0.32	9.45E-03	0.34	-0.14
59	1.31E-02	0.28	1.28E-02	0.29	0.27
81	1.47E-02	0.26	1.44E-02	0.27	0.14
122	1.49E-02	0.26	1.48E-02	0.27	-0.52
165	1.35E-02	0.27	1.34E-02	0.27	-0.10
185	1.25E-02	0.29	1.25E-02	0.29	0.26
244	1.02E-02	0.32	1.01E-02	0.32	-0.48
356	7.20E-03	0.38	7.18E-03	0.38	0.65
511	5.32E-03	0.44	5.31E-03	0.44	0.13
661	4.36E-03	0.48	4.35E-03	0.48	-0.50
834	3.69E-03	0.53	3.68E-03	0.53	-0.45
1173	2.90E-03	0.59	2.90E-03	0.59	0.27
1274	2.76E-03	0.61	2.76E-03	0.61	-0.12
1408	2.56E-03	0.63	2.56E-03	0.63	0.58

Appendix C.6. MC simulation results for the Vec card.

- **Case of the Livermore phantom**

Table 1. Counting efficiency values, associated uncertainties and differences to the reference values obtained for the user-defined cone directional biasing (VEC).

Energy (keV)	Simulated counting rate (counts)	Statistical Relative Error (%)	Counting efficiency (counts/s/ γ)	Uncertainty (%)	Difference (%)
15	1.14E-04	1.22	6.32E-05	3.03	-4.88
22	1.61E-03	0.33	1.53E-03	0.36	-0.12
33	6.40E-03	0.16	6.23E-03	0.17	-0.17
40	8.50E-03	0.14	8.33E-03	0.15	-0.17
59	1.17E-02	0.12	1.15E-02	0.12	0.06
81	1.30E-02	0.11	1.29E-02	0.11	-0.17
122	1.32E-02	0.11	1.31E-02	0.11	0.05
165	1.18E-02	0.12	1.18E-02	0.12	0.00
185	1.10E-02	0.12	1.09E-02	0.12	0.39
244	8.75E-03	0.14	8.73E-03	0.14	0.34
356	6.19E-03	0.17	6.17E-03	0.17	0.20
511	4.50E-03	0.19	4.49E-03	0.19	-0.34
661	3.64E-03	0.22	3.63E-03	0.22	-0.25
834	3.05E-03	0.24	3.05E-03	0.24	0.40
1173	2.41E-03	0.27	2.40E-03	0.27	-0.23
1274	2.28E-03	0.27	2.28E-03	0.27	-0.52
1408	2.13E-03	0.28	2.13E-03	0.28	-0.06

Table 2. Counting efficiency values, associated uncertainties and differences to the reference values obtained for the continuous exponential direction biasing (SB -31 1).

Energy (keV)	Simulated counting rate (counts)	Statistical Relative Error (%)	Counting efficiency (counts/s/ γ)	Uncertainty (%)	Difference (%)
15	2.20E-04	3.24	1.30E-04	7.42	-115.36
22	3.06E-03	0.87	2.91E-03	0.96	-90.86
33	1.19E-02	0.44	1.16E-02	0.46	-87.17
40	1.60E-02	0.38	1.56E-02	0.40	-88.03
59	2.19E-02	0.32	2.16E-02	0.33	-87.71
81	2.42E-02	0.31	2.40E-02	0.32	-86.07
122	2.46E-02	0.31	2.44E-02	0.31	-86.75
165	2.22E-02	0.32	2.21E-02	0.32	-87.30
185	2.05E-02	0.34	2.04E-02	0.34	-86.01
244	1.62E-02	0.38	1.61E-02	0.38	-84.06
356	1.15E-02	0.45	1.15E-02	0.45	-85.53
511	8.29E-03	0.53	8.28E-03	0.53	-85.09
661	6.74E-03	0.59	6.73E-03	0.59	-85.82
834	5.67E-03	0.64	5.66E-03	0.64	-84.91
1173	4.46E-03	0.72	4.45E-03	0.72	-85.57
1274	4.14E-03	0.75	4.14E-03	0.75	-82.78
1408	3.95E-03	0.76	3.95E-03	0.76	-85.93

- **Case of the ICRP female torso phantom**

Table 3. Counting efficiency values, associated uncertainties and differences to the reference values obtained for the user-defined cone directional biasing (VEC).

Energy (keV)	Simulated counting rate (counts)	Statistical Relative Error (%)	Counting efficiency (counts/s/ γ)	Uncertainty (%)	Difference (%)
15	1.04E-04	1.28	4.44E-05	4.37	1.79
22	1.70E-03	0.32	1.60E-03	0.36	-0.53
33	7.31E-03	0.15	7.09E-03	0.16	0.21
40	9.67E-03	0.13	9.46E-03	0.14	-0.25
59	1.31E-02	0.11	1.29E-02	0.11	0.06
81	1.46E-02	0.11	1.45E-02	0.11	0.07
122	1.48E-02	0.11	1.47E-02	0.11	0.04
165	1.35E-02	0.11	1.34E-02	0.11	0.32
185	1.26E-02	0.12	1.25E-02	0.12	-0.09
244	1.01E-02	0.13	1.01E-02	0.13	-0.07
356	7.28E-03	0.15	7.26E-03	0.15	-0.44
511	5.33E-03	0.18	5.33E-03	0.18	-0.08
661	4.34E-03	0.20	4.33E-03	0.20	0.01
834	3.67E-03	0.22	3.67E-03	0.22	-0.04
1173	2.90E-03	0.24	2.89E-03	0.24	0.51
1274	2.74E-03	0.25	2.73E-03	0.25	0.72
1408	2.58E-03	0.26	2.58E-03	0.26	-0.22

Table 4. Counting efficiency values, associated uncertainties and differences to the reference values obtained for the continuous exponential direction biasing (SB -31 1).

Energy (keV)	Simulated counting rate (counts)	Statistical Relative Error (%)	Counting efficiency (counts/s/ γ)	Uncertainty (%)	Difference (%)
15	1.73E-04	2.58	8.83E-05	7.14	-95.24
22	3.07E-03	0.61	2.91E-03	0.68	-82.35
33	1.33E-02	0.30	1.29E-02	0.31	-81.97
40	1.74E-02	0.26	1.71E-02	0.27	-81.44
59	2.36E-02	0.22	2.34E-02	0.23	-81.25
81	2.65E-02	0.21	2.62E-02	0.21	-81.38
122	2.68E-02	0.21	2.67E-02	0.21	-81.36
165	2.45E-02	0.22	2.44E-02	0.22	-81.33
185	2.29E-02	0.22	2.28E-02	0.22	-82.19
244	1.85E-02	0.25	1.85E-02	0.25	-82.83
356	1.32E-02	0.30	1.32E-02	0.30	-81.95
511	9.67E-03	0.35	9.65E-03	0.35	-81.38
661	7.80E-03	0.38	7.79E-03	0.38	-79.90
834	6.64E-03	0.42	6.63E-03	0.42	-80.96
1173	5.28E-03	0.47	5.28E-03	0.47	-81.60
1274	4.98E-03	0.48	4.98E-03	0.48	-80.77
1408	4.69E-03	0.50	4.69E-03	0.50	-81.95

Appendix C.7. MC simulation results for the FCL card.

- **Case of the Livermore phantom**

Table 1. Counting efficiency values and associated uncertainties obtained with the FCL card and difference to reference values obtained without VR.

Energy (keV)	Simulated counting rate (counts)	Statistical Relative Error (%)	Counting efficiency (counts/s/ γ)	Uncertainty (%)	Difference (%)
15	1.22E-04	1.12	5.98E-05	3.15	0.85
22	1.62E-03	0.32	1.53E-03	0.36	0.01
33	6.43E-03	0.16	6.22E-03	0.17	-0.01
40	8.54E-03	0.14	8.32E-03	0.15	0.00
59	1.17E-02	0.12	1.15E-02	0.13	0.01
81	1.31E-02	0.11	1.29E-02	0.11	0.02
122	1.32E-02	0.11	1.31E-02	0.11	0.00
165	1.19E-02	0.11	1.18E-02	0.11	0.00
185	1.10E-02	0.11	1.10E-02	0.11	0.08
244	8.79E-03	0.12	8.76E-03	0.12	0.00
356	6.20E-03	0.14	6.19E-03	0.14	-0.01
511	4.49E-03	0.15	4.48E-03	0.15	-0.08
661	3.64E-03	0.17	3.63E-03	0.17	-0.21
834	3.06E-03	0.17	3.05E-03	0.17	0.23
1173	2.40E-03	0.19	2.40E-03	0.19	-0.05
1274	2.27E-03	0.19	2.27E-03	0.19	-0.21
1408	2.13E-03	0.19	2.13E-03	0.19	-0.36

- **Case of the ICRP female torso phantom**

Table 2. Counting efficiency values and associated uncertainties obtained with the FCL card and difference to reference values obtained without VR.

Energy (keV)	Simulated counting rate (counts)	Statistical Relative Error (%)	Counting efficiency (counts/s/ γ)	Uncertainty (%)	Difference (%)
15	1.16E-04	1.13	4.55E-05	4.16	-0.74
22	1.71E-03	0.31	1.60E-03	0.35	-0.08
33	7.38E-03	0.15	7.11E-03	0.16	-0.03
40	9.70E-03	0.13	9.44E-03	0.14	-0.01
59	1.32E-02	0.11	1.29E-02	0.12	0.00
81	1.47E-02	0.11	1.45E-02	0.11	0.00
122	1.48E-02	0.10	1.47E-02	0.10	-0.01
165	1.35E-02	0.11	1.34E-02	0.11	0.03
185	1.26E-02	0.11	1.25E-02	0.11	0.09
244	1.01E-02	0.11	1.01E-02	0.11	-0.11
356	7.26E-03	0.13	7.24E-03	0.13	-0.13
511	5.34E-03	0.14	5.33E-03	0.14	-0.13
661	4.34E-03	0.15	4.34E-03	0.15	-0.11
834	3.66E-03	0.16	3.66E-03	0.16	0.14
1173	2.90E-03	0.17	2.90E-03	0.17	0.18
1274	2.74E-03	0.17	2.74E-03	0.17	0.52
1408	2.57E-03	0.18	2.57E-03	0.18	0.30

Appendix C.8. MC simulation results for the EXT card.

- **Case of the Livermore phantom**

Table 1. Counting efficiency values, associated uncertainties and difference to reference values obtained with the combination of mesh-based rectangular WW and EXT used for the bone structures of the phantom (NPS 7.35E07).

Energy (keV)	Simulated counting rate (counts)	Statistical Relative Error (%)	Counting efficiency (counts/s/ γ)	Uncertainty (%)	Difference (%)
15	1.18E-04	4.57	6.27E-05	11.79	-4.04
22	1.61E-03	1.17	1.51E-03	1.32	0.97
33	6.41E-03	0.58	6.20E-03	0.62	0.36
40	8.42E-03	0.51	8.19E-03	0.54	1.50
59	1.18E-02	0.43	1.15E-02	0.45	-0.55
81	1.32E-02	0.41	1.29E-02	0.42	-0.51
122	1.32E-02	0.41	1.31E-02	0.42	-0.16
165	1.18E-02	0.44	1.17E-02	0.45	0.55
185	1.11E-02	0.45	1.10E-02	0.45	-0.58
244	8.82E-03	0.51	8.80E-03	0.51	-0.41
356	6.22E-03	0.60	6.20E-03	0.60	-0.28
511	4.51E-03	0.71	4.50E-03	0.71	-0.64
661	3.65E-03	0.79	3.65E-03	0.79	-0.73
834	3.07E-03	0.86	3.07E-03	0.86	-0.25
1173	2.40E-03	0.97	2.40E-03	0.97	0.10
1274	2.27E-03	1.00	2.27E-03	1.00	-0.17
1408	2.13E-03	1.04	2.13E-03	1.04	-0.15

Table 2. Counting efficiency values, associated uncertainties and difference to reference values obtained with the combination of mesh-based rectangular WW and EXT used for the phantom body compounds (NPS 7.35E07).

Energy (keV)	Simulated counting rate (counts)	Statistical Relative Error (%)	Counting efficiency (counts/s/ γ)	Uncertainty (%)	Difference (%)
15	1.22E-04	4.18	5.91E-05	18.23	2.02
22	1.63E-03	0.92	1.52E-03	1.56	0.55
33	6.39E-03	0.41	6.17E-03	0.61	0.85
40	8.48E-03	0.37	8.25E-03	0.65	0.85
59	1.18E-02	0.35	1.15E-02	0.44	-0.29
81	1.31E-02	0.32	1.29E-02	0.35	-0.07
122	1.32E-02	0.33	1.31E-02	0.35	-0.30
165	1.18E-02	0.35	1.18E-02	0.36	0.26
185	1.11E-02	0.36	1.10E-02	0.37	-0.12
244	8.79E-03	0.41	8.76E-03	0.42	0.07
356	6.21E-03	0.50	6.20E-03	0.50	-0.15
511	4.49E-03	0.60	4.48E-03	0.61	-0.16
661	3.66E-03	0.68	3.66E-03	0.68	-0.98
834	3.07E-03	0.76	3.07E-03	0.76	-0.25
1173	2.39E-03	0.87	2.39E-03	0.87	0.57
1274	2.27E-03	0.89	2.27E-03	0.89	-0.31
1408	2.13E-03	0.93	2.13E-03	0.93	-0.12

Table 3. Counting efficiency values, associated uncertainties and difference to reference values obtained with the combination of mesh-based rectangular WW and EXT used for both the phantom body compounds and the front dead layer of the detectors (NPS 7.35E07).

Energy (keV)	Simulated counting rate (counts)	Statistical Relative Error (%)	Counting efficiency (counts/s/ γ)	Uncertainty (%)	Difference (%)
15	1.22E-04	4.17	5.92E-05	18.19	1.79
22	1.62E-03	0.68	1.51E-03	1.42	1.25
33	6.39E-03	0.41	6.17E-03	0.61	0.86
40	8.48E-03	0.37	8.25E-03	0.65	0.83
59	1.18E-02	0.35	1.15E-02	0.44	-0.29
81	1.31E-02	0.32	1.29E-02	0.35	-0.07
122	1.32E-02	0.33	1.31E-02	0.35	-0.30
165	1.18E-02	0.35	1.18E-02	0.36	0.25
185	1.11E-02	0.36	1.10E-02	0.37	-0.12
244	8.79E-03	0.41	8.76E-03	0.42	0.07
356	6.21E-03	0.50	6.20E-03	0.50	-0.15
511	4.49E-03	0.60	4.48E-03	0.61	-0.14
661	3.66E-03	0.68	3.66E-03	0.68	-0.99
834	3.07E-03	0.76	3.07E-03	0.76	-0.25
1173	2.39E-03	0.87	2.39E-03	0.87	0.57
1274	2.27E-03	0.89	2.27E-03	0.89	-0.31
1408	2.13E-03	0.93	2.13E-03	0.93	-0.12

Table 4. Counting efficiency values, associated uncertainties and difference to reference values obtained with the combination of mesh-based rectangular WW and EXT used with the path stretching vector pointing out the center of the upper pair of detectors (NPS 7.35E07).

Energy (keV)	Simulated counting rate (counts)	Statistical Relative Error (%)	Counting efficiency (counts/s/ γ)	Uncertainty (%)	Difference (%)
15	1.22E-04	3.88	6.17E-05	15.65	-2.32
22	1.62E-03	0.69	1.52E-03	0.96	0.57
33	6.38E-03	0.42	6.16E-03	0.59	0.90
40	8.48E-03	0.39	8.25E-03	0.68	0.76
59	1.18E-02	0.34	1.15E-02	0.39	-0.10
81	1.31E-02	0.32	1.29E-02	0.34	-0.13
122	1.32E-02	0.33	1.31E-02	0.35	-0.20
165	1.18E-02	0.35	1.18E-02	0.36	0.20
185	1.11E-02	0.36	1.10E-02	0.38	-0.12
244	8.79E-03	0.41	8.76E-03	0.42	-0.02
356	6.21E-03	0.50	6.19E-03	0.50	-0.12
511	4.49E-03	0.61	4.49E-03	0.61	-0.26
661	3.67E-03	0.68	3.66E-03	0.68	-1.08
834	3.07E-03	0.76	3.07E-03	0.76	-0.32
1173	2.39E-03	0.87	2.38E-03	0.87	0.67
1274	2.27E-03	0.90	2.27E-03	0.90	-0.26
1408	2.13E-03	0.93	2.13E-03	0.93	-0.11

Table 5. Counting efficiency values, associated uncertainties and difference to reference values obtained with the combination of mesh-based rectangular WW and EXT used with the path stretching vector pointing out the center of the upper pair of detectors with a path stretching factor of 0.6 (NPS 7.35E07).

Energy (keV)	Simulated counting rate (counts)	Statistical Relative Error (%)	Counting efficiency (counts/s/ γ)	Uncertainty (%)	Difference (%)
15	1.19E-04	3.39	5.81E-05	11.88	3.72
22	1.62E-03	0.79	1.52E-03	0.94	0.34
33	6.40E-03	0.46	6.18E-03	0.50	0.58
40	8.45E-03	0.41	8.24E-03	0.44	0.90
59	1.18E-02	0.36	1.15E-02	0.38	-0.39
81	1.31E-02	0.35	1.29E-02	0.37	-0.35
122	1.32E-02	0.35	1.31E-02	0.36	-0.14
165	1.18E-02	0.37	1.18E-02	0.38	0.20
185	1.11E-02	0.39	1.11E-02	0.40	-0.66
244	8.81E-03	0.44	8.78E-03	0.44	-0.19
356	6.22E-03	0.53	6.21E-03	0.53	-0.34
511	4.50E-03	0.64	4.49E-03	0.64	-0.32
661	3.67E-03	0.71	3.66E-03	0.71	-1.14
834	3.08E-03	0.79	3.07E-03	0.79	-0.37
1173	2.39E-03	0.90	2.39E-03	0.90	0.42
1274	2.27E-03	0.93	2.27E-03	0.93	-0.30
1408	2.13E-03	0.96	2.13E-03	0.96	-0.06

Table 6. Counting efficiency values, associated uncertainties and difference to reference values obtained with the combination of mesh-based rectangular WW and EXT used with the path stretching vector pointing out the center of the upper pair of detectors with a path stretching factor of 0.3 (NPS 7.35E07).

Energy (keV)	Simulated counting rate (counts)	Statistical Relative Error (%)	Counting efficiency (counts/s/ γ)	Uncertainty (%)	Difference (%)
15	1.16E-04	3.67	6.05E-05	10.79	-0.33
22	1.63E-03	0.95	1.53E-03	1.09	-0.26
33	6.40E-03	0.52	6.18E-03	0.56	0.60
40	8.44E-03	0.46	8.22E-03	0.49	1.19
59	1.18E-02	0.40	1.15E-02	0.42	-0.43
81	1.31E-02	0.38	1.29E-02	0.39	-0.46
122	1.32E-02	0.38	1.31E-02	0.39	-0.11
165	1.18E-02	0.41	1.18E-02	0.42	0.23
185	1.11E-02	0.42	1.11E-02	0.42	-0.69
244	8.83E-03	0.47	8.80E-03	0.47	-0.43
356	6.21E-03	0.57	6.20E-03	0.57	-0.19
511	4.50E-03	0.67	4.49E-03	0.67	-0.43
661	3.66E-03	0.75	3.65E-03	0.75	-0.86
834	3.07E-03	0.82	3.07E-03	0.82	-0.24
1173	2.39E-03	0.94	2.38E-03	0.94	0.68
1274	2.28E-03	0.97	2.28E-03	0.97	-0.47
1408	2.13E-03	1.00	2.13E-03	1.00	-0.14

- **Case of the ICRP female torso phantom**

Table 7. Counting efficiency values, associated uncertainties and difference to reference values obtained with the combination of mesh-based rectangular WW and EXT used for the bone structures of the phantom (NPS 7.35E07).

Energy (keV)	Simulated counting rate (counts)	Statistical Relative Error (%)	Counting efficiency (counts/s/ γ)	Uncertainty (%)	Difference (%)
15	1.17E-04	2.54	4.58E-05	9.07	-1.23
22	1.70E-03	0.75	1.58E-03	0.83	0.66
33	7.33E-03	0.41	7.06E-03	0.43	0.72
40	9.72E-03	0.37	9.46E-03	0.39	-0.18
59	1.32E-02	0.33	1.29E-02	0.34	0.07
81	1.47E-02	0.32	1.45E-02	0.33	-0.34
122	1.49E-02	0.31	1.48E-02	0.31	-0.45
165	1.36E-02	0.31	1.35E-02	0.31	-0.63
185	1.26E-02	0.32	1.26E-02	0.32	-0.38
244	1.02E-02	0.33	1.01E-02	0.33	-0.36
356	7.26E-03	0.37	7.24E-03	0.37	-0.18
511	5.30E-03	0.40	5.29E-03	0.40	0.55
661	4.35E-03	0.42	4.34E-03	0.42	-0.24
834	3.64E-03	0.44	3.64E-03	0.44	0.68
1173	2.88E-03	0.48	2.88E-03	0.48	0.92
1274	2.75E-03	0.48	2.75E-03	0.48	0.23
1408	2.56E-03	0.49	2.56E-03	0.49	0.60

Table 8. Counting efficiency values, associated uncertainties and difference to reference values obtained with the combination of mesh-based rectangular WW and EXT used for the phantom body compounds (NPS 7.35E07).

Energy (keV)	Simulated counting rate (counts)	Statistical Relative Error (%)	Counting efficiency (counts/s/ γ)	Uncertainty (%)	Difference (%)
15	1.16E-04	2.27	4.53E-05	9.25	-0.21
22	1.71E-03	0.67	1.60E-03	0.75	-0.14
33	7.34E-03	0.38	7.08E-03	0.40	0.46
40	9.70E-03	0.35	9.43E-03	0.37	0.05
59	1.32E-02	0.31	1.29E-02	0.32	0.00
81	1.48E-02	0.30	1.45E-02	0.31	-0.43
122	1.49E-02	0.30	1.48E-02	0.31	-0.38
165	1.36E-02	0.30	1.35E-02	0.30	-0.49
185	1.26E-02	0.30	1.25E-02	0.30	-0.16
244	1.02E-02	0.32	1.01E-02	0.32	-0.28
356	7.27E-03	0.35	7.25E-03	0.35	-0.31
511	5.32E-03	0.38	5.31E-03	0.38	0.26
661	4.33E-03	0.40	4.33E-03	0.40	0.15
834	3.64E-03	0.43	3.64E-03	0.43	0.82
1173	2.87E-03	0.46	2.87E-03	0.46	1.30
1274	2.76E-03	0.47	2.76E-03	0.47	-0.20
1408	2.56E-03	0.48	2.56E-03	0.48	0.58

Table 9. Counting efficiency values, associated uncertainties and difference to reference values obtained with the combination of mesh-based rectangular WW and EXT used for both the phantom body compounds and the front dead layer of the detectors (NPS 7.35E07).

Energy (keV)	Simulated counting rate (counts)	Statistical Relative Error (%)	Counting efficiency (counts/s/ γ)	Uncertainty (%)	Difference (%)
15	1.17E-04	2.55	4.57E-05	9.25	-1.01
22	1.70E-03	0.75	1.59E-03	0.83	0.49
33	7.32E-03	0.41	7.06E-03	0.44	0.75
40	9.72E-03	0.37	9.46E-03	0.39	-0.19
59	1.32E-02	0.33	1.29E-02	0.34	0.04
81	1.47E-02	0.32	1.45E-02	0.33	-0.35
122	1.49E-02	0.31	1.48E-02	0.31	-0.46
165	1.36E-02	0.31	1.35E-02	0.31	-0.63
185	1.26E-02	0.32	1.26E-02	0.32	-0.40
244	1.02E-02	0.33	1.01E-02	0.33	-0.37
356	7.26E-03	0.37	7.24E-03	0.37	-0.19
511	5.30E-03	0.40	5.29E-03	0.40	0.52
661	4.35E-03	0.42	4.34E-03	0.42	-0.24
834	3.65E-03	0.44	3.64E-03	0.44	0.66
1173	2.88E-03	0.48	2.88E-03	0.48	0.91
1274	2.75E-03	0.48	2.75E-03	0.48	0.24
1408	2.56E-03	0.49	2.56E-03	0.49	0.62

Table 10. Counting efficiency values, associated uncertainties and difference to reference values obtained with the combination of mesh-based rectangular WW and EXT used with the path stretching vector pointing out the center of the upper pair of detectors (NPS 7.35E07).

Energy (keV)	Simulated counting rate (counts)	Statistical Relative Error (%)	Counting efficiency (counts/s/ γ)	Uncertainty (%)	Difference (%)
15	1.18E-04	2.27	4.52E-05	9.54	0.09
22	1.71E-03	0.66	1.60E-03	0.74	0.00
33	7.34E-03	0.38	7.07E-03	0.40	0.53
40	9.70E-03	0.34	9.44E-03	0.36	-0.03
59	1.32E-02	0.31	1.29E-02	0.32	-0.02
81	1.48E-02	0.30	1.45E-02	0.31	-0.50
122	1.49E-02	0.30	1.48E-02	0.31	-0.37
165	1.36E-02	0.30	1.35E-02	0.30	-0.39
185	1.26E-02	0.30	1.25E-02	0.30	-0.29
244	1.02E-02	0.32	1.01E-02	0.32	-0.24
356	7.27E-03	0.35	7.26E-03	0.35	-0.39
511	5.32E-03	0.38	5.31E-03	0.38	0.21
661	4.34E-03	0.40	4.33E-03	0.40	-0.05
834	3.64E-03	0.43	3.63E-03	0.43	0.85
1173	2.88E-03	0.46	2.87E-03	0.46	1.15
1274	2.76E-03	0.47	2.76E-03	0.47	-0.31
1408	2.56E-03	0.48	2.56E-03	0.48	0.69

Table 11. Counting efficiency values, associated uncertainties and difference to reference values obtained with the combination of mesh-based rectangular WW and EXT used with the path stretching vector pointing out the center of the upper pair of detectors with a path stretching factor of 0.6 (NPS 7.35E07).

Energy (keV)	Simulated counting rate (counts)	Statistical Relative Error (%)	Counting efficiency (counts/s/ γ)	Uncertainty (%)	Difference (%)
15	1.17E-04	2.24	4.61E-05	8.59	-2.06
22	1.70E-03	0.67	1.59E-03	0.75	0.40
33	7.34E-03	0.39	7.07E-03	0.41	0.50
40	9.71E-03	0.35	9.45E-03	0.36	-0.12
59	1.32E-02	0.32	1.29E-02	0.33	0.03
81	1.48E-02	0.30	1.45E-02	0.31	-0.46
122	1.49E-02	0.30	1.48E-02	0.30	-0.50
165	1.36E-02	0.30	1.35E-02	0.30	-0.45
185	1.26E-02	0.31	1.25E-02	0.31	-0.19
244	1.02E-02	0.32	1.01E-02	0.32	-0.40
356	7.25E-03	0.35	7.24E-03	0.35	-0.10
511	5.30E-03	0.39	5.29E-03	0.39	0.54
661	4.36E-03	0.41	4.36E-03	0.41	-0.61
834	3.64E-03	0.43	3.64E-03	0.43	0.70
1173	2.89E-03	0.47	2.89E-03	0.47	0.72
1274	2.76E-03	0.47	2.76E-03	0.47	-0.20
1408	2.56E-03	0.48	2.56E-03	0.48	0.42

Table 12. Counting efficiency values, associated uncertainties and difference to reference values obtained with the combination of mesh-based rectangular WW and EXT used with the path stretching vector pointing out the center of the upper pair of detectors with a path stretching factor of 0.3 (NPS 7.35E07).

Energy (keV)	Simulated counting rate (counts)	Statistical Relative Error (%)	Counting efficiency (counts/s/ γ)	Uncertainty (%)	Difference (%)
15	1.19E-04	2.29	4.73E-05	8.45	-4.57
22	1.72E-03	0.70	1.60E-03	0.78	-0.61
33	7.33E-03	0.40	7.07E-03	0.42	0.54
40	9.72E-03	0.36	9.46E-03	0.38	-0.25
59	1.32E-02	0.32	1.29E-02	0.33	-0.03
81	1.48E-02	0.31	1.45E-02	0.32	-0.43
122	1.49E-02	0.31	1.48E-02	0.31	-0.55
165	1.36E-02	0.31	1.35E-02	0.31	-0.62
185	1.26E-02	0.31	1.25E-02	0.31	-0.23
244	1.02E-02	0.33	1.01E-02	0.33	-0.54
356	7.25E-03	0.36	7.24E-03	0.36	-0.08
511	5.32E-03	0.39	5.31E-03	0.39	0.28
661	4.35E-03	0.41	4.34E-03	0.41	-0.27
834	3.65E-03	0.44	3.64E-03	0.44	0.63
1173	2.89E-03	0.47	2.88E-03	0.47	0.83
1274	2.76E-03	0.48	2.76E-03	0.48	-0.14
1408	2.57E-03	0.49	2.57E-03	0.49	0.07

Appendix C.9. MC simulation results of combined Variance Reduction methods.

- **Case of the Livermore phantom**

Table 1. Counting efficiency values and associated uncertainties obtained with the combination of SB and FCL cards. The differences to reference values prove the successful combination of these two VR cards.

Energy (keV)	Simulated counting rate (counts)	Statistical Relative Error (%)	Counting efficiency (counts/s/ γ)	Uncertainty (%)	Difference (%)
15	1.23E-04	2.63	6.25E-05	8.70	-3.57
22	1.62E-03	0.66	1.53E-03	0.77	-0.23
33	6.43E-03	0.56	6.22E-03	0.60	0.02
40	8.56E-03	0.49	8.33E-03	0.52	-0.22
59	1.18E-02	0.42	1.15E-02	0.44	-0.11
81	1.31E-02	0.39	1.29E-02	0.40	-0.03
122	1.32E-02	0.39	1.31E-02	0.40	0.15
165	1.18E-02	0.39	1.18E-02	0.39	0.29
185	1.10E-02	0.40	1.09E-02	0.40	0.34
244	8.69E-03	0.43	8.66E-03	0.43	1.14
356	6.16E-03	0.48	6.14E-03	0.48	0.71
511	4.55E-03	0.53	4.55E-03	0.53	-1.62
661	3.62E-03	0.57	3.62E-03	0.57	0.20
834	3.08E-03	0.60	3.08E-03	0.60	-0.52
1173	2.42E-03	0.64	2.42E-03	0.64	-0.96
1274	2.29E-03	0.65	2.29E-03	0.65	-1.06
1408	2.14E-03	0.66	2.14E-03	0.66	-0.87

Table 2. Counting efficiency values and associated uncertainties obtained with the combination of SB, FCL and Vec cards. The differences to reference values prove the successful combination of these three VR cards.

Energy (keV)	Simulated counting rate (counts)	Statistical Relative Error (%)	Counting efficiency (counts/s/ γ)	Uncertainty (%)	Difference (%)
15	1.13E-04	2.60	6.34E-05	7.65	-5.19
22	1.59E-03	0.67	1.51E-03	0.77	0.97
33	6.44E-03	0.56	6.28E-03	0.59	-1.04
40	8.55E-03	0.49	8.38E-03	0.51	-0.73
59	1.17E-02	0.42	1.15E-02	0.43	-0.33
81	1.31E-02	0.39	1.30E-02	0.40	-0.62
122	1.31E-02	0.39	1.30E-02	0.40	0.60
165	1.18E-02	0.39	1.17E-02	0.39	0.32
185	1.10E-02	0.40	1.09E-02	0.40	0.33
244	8.81E-03	0.42	8.79E-03	0.42	-0.34
356	6.17E-03	0.48	6.15E-03	0.48	0.52
511	4.50E-03	0.53	4.49E-03	0.53	-0.38
661	3.64E-03	0.57	3.64E-03	0.57	-0.43
834	3.06E-03	0.60	3.05E-03	0.60	0.25
1173	2.41E-03	0.64	2.40E-03	0.64	-0.22
1274	2.29E-03	0.65	2.29E-03	0.65	-1.08
1408	2.13E-03	0.66	2.13E-03	0.66	-0.14

Table 3. Counting efficiency values and associated uncertainties obtained with the combination of EXT, mesh-based rectangular WW, Vec, FCL and SB cards. The differences to reference values prove the successful combination of these five VR cards.

Energy (keV)	Simulated counting rate (counts)	Statistical Relative Error (%)	Counting efficiency (counts/s/ γ)	Uncertainty (%)	Difference (%)
15	1.09E-04	2.75	5.97E-05	10.47	1.00
22	1.60E-03	0.38	1.53E-03	0.55	0.12
33	6.40E-03	0.37	6.23E-03	0.44	-0.21
40	8.54E-03	0.33	8.38E-03	0.39	-0.73
59	1.17E-02	0.31	1.15E-02	0.34	-0.46
81	1.30E-02	0.30	1.29E-02	0.33	-0.07
122	1.31E-02	0.29	1.30E-02	0.31	0.41
165	1.18E-02	0.31	1.17E-02	0.32	0.34
185	1.10E-02	0.31	1.09E-02	0.31	0.59
244	8.80E-03	0.34	8.78E-03	0.34	-0.20
356	6.16E-03	0.39	6.15E-03	0.39	0.68
511	4.48E-03	0.44	4.47E-03	0.44	0.00
661	3.64E-03	0.48	3.63E-03	0.48	-0.24
834	3.06E-03	0.52	3.06E-03	0.52	0.01
1173	2.41E-03	0.56	2.41E-03	0.56	-0.45
1274	2.29E-03	0.57	2.29E-03	0.57	-1.21
1408	2.13E-03	0.59	2.13E-03	0.59	-0.23

Table 4. Counting efficiency values and associated uncertainties obtained with the combination of the Cell Importance card with SB. The differences to reference values prove the successful combination of these two VR cards. (Cell IMP parameters 1-3-9-18).

Energy (keV)	Simulated counting rate (counts)	Statistical Relative Error (%)	Counting efficiency (counts/s/ γ)	Uncertainty (%)	Difference (%)
15	1.25E-04	3.25	6.47E-05	10.61	-7.24
22	1.64E-03	0.72	1.54E-03	0.86	-0.91
33	6.41E-03	0.68	6.19E-03	0.72	0.43
40	8.65E-03	0.61	8.42E-03	0.64	-1.27
59	1.18E-02	0.55	1.16E-02	0.57	-0.70
81	1.31E-02	0.52	1.29E-02	0.53	0.10
122	1.32E-02	0.51	1.31E-02	0.52	-0.36
165	1.19E-02	0.50	1.18E-02	0.51	-0.22
185	1.10E-02	0.50	1.10E-02	0.50	0.12
244	8.74E-03	0.50	8.71E-03	0.50	0.62
356	6.14E-03	0.51	6.13E-03	0.51	0.90
511	4.51E-03	0.51	4.51E-03	0.51	-0.68
661	3.62E-03	0.52	3.62E-03	0.52	0.17
834	3.07E-03	0.53	3.07E-03	0.53	-0.28
1173	2.42E-03	0.55	2.42E-03	0.55	-0.69
1274	2.29E-03	0.55	2.29E-03	0.55	-1.08
1408	2.11E-03	0.56	2.11E-03	0.56	0.83

Table 5. Counting efficiency values and associated uncertainties obtained with the combination of the Cell Importance card with Vec, FCL and SB cards. The differences to reference values prove the successful combination of these four VR cards. (Cell IMP parameters 1-3-9-18).

Energy (keV)	Simulated counting rate (counts)	Statistical Relative Error (%)	Counting efficiency (counts/s/ γ)	Uncertainty (%)	Difference (%)
15	1.14E-04	3.48	6.07E-05	11.50	-0.65
22	1.60E-03	0.94	1.52E-03	1.07	0.37
33	6.45E-03	0.93	6.28E-03	0.97	-1.02
40	8.60E-03	0.83	8.42E-03	0.86	-1.20
59	1.17E-02	0.74	1.15E-02	0.76	-0.55
81	1.31E-02	0.71	1.30E-02	0.72	-0.98
122	1.31E-02	0.70	1.30E-02	0.71	0.23
165	1.19E-02	0.68	1.18E-02	0.69	-0.35
185	1.09E-02	0.68	1.09E-02	0.68	1.10
244	8.84E-03	0.68	8.82E-03	0.68	-0.66
356	6.20E-03	0.67	6.18E-03	0.67	0.06
511	4.51E-03	0.67	4.51E-03	0.67	-0.73
661	3.66E-03	0.67	3.65E-03	0.67	-0.86
834	3.07E-03	0.67	3.06E-03	0.67	-0.08
1173	2.41E-03	0.67	2.41E-03	0.67	-0.25
1274	2.26E-03	0.67	2.26E-03	0.67	0.26
1408	2.12E-03	0.67	2.12E-03	0.67	0.25

- **Case of the ICRP female torso phantom**

Table 6. Counting efficiency values and associated uncertainties obtained with the combination of SB and FCL cards. The differences to reference values prove the successful combination of these two VR cards.

Energy (keV)	Simulated counting rate (counts)	Statistical Relative Error (%)	Counting efficiency (counts/s/ γ)	Uncertainty (%)	Difference (%)
15	1.17E-04	2.95	4.63E-05	4.98	-2.51
22	1.69E-03	0.65	1.58E-03	0.16	0.88
33	7.41E-03	0.52	7.14E-03	0.71	-0.41
40	9.66E-03	0.46	9.39E-03	0.94	0.58
59	1.32E-02	0.39	1.29E-02	1.29	-0.02
81	1.47E-02	0.37	1.45E-02	1.45	-0.08
122	1.50E-02	0.36	1.48E-02	1.48	-0.78
165	1.35E-02	0.37	1.34E-02	1.34	-0.01
185	1.26E-02	0.37	1.26E-02	1.26	-0.56
244	1.01E-02	0.40	1.01E-02	1.01	0.07
356	7.20E-03	0.45	7.18E-03	0.72	0.63
511	5.32E-03	0.49	5.31E-03	0.53	0.15
661	4.34E-03	0.53	4.34E-03	0.43	-0.10
834	3.67E-03	0.56	3.66E-03	0.37	0.11
1173	2.89E-03	0.59	2.89E-03	0.29	0.68
1274	2.76E-03	0.60	2.76E-03	0.28	-0.05
1408	2.57E-03	0.61	2.57E-03	0.26	0.20

Table 7. Counting efficiency values and associated uncertainties obtained with the combination of SB, FCL and Vec cards. The differences to reference values prove the successful combination of these three VR cards.

Energy (keV)	Simulated counting rate (counts)	Statistical Relative Error (%)	Counting efficiency (counts/s/ γ)	Uncertainty (%)	Difference (%)
15	1.06E-04	3.03	4.35E-05	12.53	3.84
22	1.68E-03	0.65	1.58E-03	0.76	0.81
33	7.38E-03	0.52	7.16E-03	0.55	-0.75
40	9.72E-03	0.46	9.51E-03	0.48	-0.78
59	1.31E-02	0.39	1.29E-02	0.40	0.21
81	1.47E-02	0.37	1.45E-02	0.38	-0.20
122	1.47E-02	0.36	1.46E-02	0.37	0.73
165	1.35E-02	0.37	1.34E-02	0.37	-0.03
185	1.26E-02	0.37	1.25E-02	0.37	-0.13
244	1.02E-02	0.40	1.02E-02	0.40	-0.73
356	7.30E-03	0.44	7.29E-03	0.44	-0.78
511	5.34E-03	0.49	5.33E-03	0.49	-0.23
661	4.32E-03	0.53	4.31E-03	0.53	0.45
834	3.66E-03	0.56	3.65E-03	0.56	0.32
1173	2.91E-03	0.59	2.91E-03	0.59	0.04
1274	2.74E-03	0.60	2.74E-03	0.60	0.52
1408	2.57E-03	0.61	2.57E-03	0.61	0.15

Table 8. Counting efficiency values and associated uncertainties obtained with the combination of EXT, mesh-based rectangular WW, Vec, FCL and SB cards. The differences to reference values prove the successful combination of these five VR cards.

Energy (keV)	Simulated counting rate (counts)	Statistical Relative Error	Counting efficiency (counts/s/ γ)	Uncertainty (%)	Difference (%)
15	1.07E-04	3.06	4.40E-05	13.02	2.66
22	1.68E-03	0.65	1.58E-03	0.78	1.13
33	7.37E-03	0.52	7.16E-03	0.55	-0.68
40	9.72E-03	0.45	9.52E-03	0.47	-0.83
59	1.31E-02	0.39	1.29E-02	0.40	0.16
81	1.46E-02	0.37	1.45E-02	0.38	-0.18
122	1.47E-02	0.36	1.46E-02	0.37	0.67
165	1.35E-02	0.36	1.34E-02	0.36	-0.08
185	1.26E-02	0.37	1.25E-02	0.37	-0.18
244	1.02E-02	0.39	1.02E-02	0.39	-0.71
356	7.31E-03	0.44	7.29E-03	0.44	-0.88
511	5.34E-03	0.49	5.33E-03	0.49	-0.23
661	4.32E-03	0.53	4.31E-03	0.53	0.48
834	3.66E-03	0.56	3.65E-03	0.56	0.29
1173	2.91E-03	0.59	2.91E-03	0.59	-0.05
1274	2.74E-03	0.60	2.74E-03	0.60	0.46
1408	2.57E-03	0.61	2.57E-03	0.61	0.13

Table 9. Counting efficiency values and associated uncertainties obtained with the combination of the Cell Importance card with SB. The differences to reference values prove the successful combination of these two VR cards. (Cell IMP parameters 1-3-9-18).

Energy (keV)	Simulated counting rate (counts)	Statistical Relative Error	Counting efficiency (counts/s/ γ)	Uncertainty (%)	Difference (%)
15	1.13E-04	3.39	4.33E-05	15.47	4.13
22	1.71E-03	0.67	1.60E-03	0.81	0.81
33	7.45E-03	0.61	7.18E-03	0.65	0.65
40	9.67E-03	0.56	9.40E-03	0.59	0.59
59	1.33E-02	0.50	1.30E-02	0.52	0.52
81	1.47E-02	0.48	1.44E-02	0.49	0.49
122	1.49E-02	0.47	1.48E-02	0.48	0.48
165	1.35E-02	0.47	1.34E-02	0.48	0.27
185	1.26E-02	0.46	1.26E-02	0.46	-0.41
244	1.01E-02	0.46	1.01E-02	0.46	-0.18
356	7.24E-03	0.47	7.22E-03	0.47	0.08
511	5.28E-03	0.47	5.27E-03	0.47	1.04
661	4.29E-03	0.48	4.29E-03	0.48	1.02
834	3.65E-03	0.49	3.64E-03	0.49	0.56
1173	2.91E-03	0.50	2.90E-03	0.50	0.13
1274	2.75E-03	0.51	2.75E-03	0.51	0.03
1408	2.56E-03	0.51	2.56E-03	0.51	0.68

Table 10. Counting efficiency values and associated uncertainties obtained with the combination of the Cell Importance card with Vec, FCL and SB cards. The differences to reference values prove the successful combination of these four VR cards. (Cell IMP parameters 1-3-9-18).

Energy (keV)	Simulated counting rate (counts)	Statistical Relative Error	Counting efficiency (counts/s/ γ)	Uncertainty (%)	Difference (%)
15	9.94E-05	2.34	4.0363E-05	10.62	10.72
22	1.69E-03	0.46	0.00158118	0.56	0.87
33	7.38E-03	0.44	0.00717255	0.46	-0.88
40	9.70E-03	0.39	0.00949347	0.40	-0.57
59	1.30E-02	0.36	0.01283322	0.37	0.40
81	1.46E-02	0.34	0.0144588	0.35	0.05
122	1.47E-02	0.33	0.01458647	0.33	0.76
165	1.35E-02	0.33	0.01339976	0.33	0.24
185	1.26E-02	0.33	0.01257672	0.33	-0.52
244	1.02E-02	0.32	0.01017168	0.32	-0.79
356	7.29E-03	0.32	0.00727482	0.32	-0.62
511	5.34E-03	0.32	0.00532757	0.32	-0.11
661	4.36E-03	0.32	0.00435452	0.32	-0.52
834	3.65E-03	0.32	0.00364569	0.32	0.54
1173	2.91E-03	0.32	0.00290278	0.32	0.16
1274	2.72E-03	0.32	0.0027204	0.32	1.23
1408	2.58E-03	0.32	0.00258138	0.32	-0.23

Appendix C.10. MC simulation results for geometry simplification operations using void plans.

Table 1. Counting efficiency values, associated uncertainties and difference to reference values obtained when simplifying the geometry with Void plans.

Phantom	Livermore			ICRP female			
	Energy	Count Eff. (counts/s/ γ)	Diff. (%)	Unc. (%)	Count Eff. (counts/s/ γ)	Diff. (%)	Unc. (%)
15		6.03E-05	0.03	3.37	4.51E-05	0.28	4.62
22		1.53E-03	0.00	0.36	1.59E-03	0.33	0.36
33		6.22E-03	0.00	0.17	7.15E-03	-0.61	0.16
40		8.32E-03	0.00	0.15	9.45E-03	-0.06	0.14
59		1.15E-02	0.00	0.13	1.29E-02	-0.24	0.12
81		1.29E-02	0.00	0.11	1.44E-02	0.22	0.11
122		1.31E-02	0.00	0.11	1.47E-02	-0.11	0.11
165		1.18E-02	0.00	0.12	1.34E-02	0.00	0.11
185		1.10E-02	0.00	0.12	1.25E-02	0.00	0.12
244		8.76E-03	0.00	0.14	1.01E-02	0.00	0.13
356		6.19E-03	0.00	0.17	7.23E-03	-0.04	0.15
511		4.47E-03	0.00	0.19	5.32E-03	-0.01	0.18
661		3.62E-03	0.00	0.22	4.33E-03	0.00	0.20
834		3.06E-03	0.00	0.24	3.67E-03	0.00	0.22
1173		2.40E-03	0.00	0.27	2.91E-03	0.02	0.24
1274		2.27E-03	0.00	0.27	2.75E-03	-0.01	0.25
1408		2.12E-03	0.00	0.28	2.58E-03	0.00	0.26

Table 2. Counting efficiency values, associated uncertainties and difference to reference values obtained for the combination of Void plans with SB, FCL and Vec VR cards.

Phantom	Livermore			ICRP female		
	Count Eff. (counts/s/ γ)	Diff. (%)	Unc. (%)	Count Eff. (counts/s/ γ)	Diff. (%)	Unc. (%)
15	6.41E-05	-6.23	7.82	4.59E-05	-1.49	11.85
22	1.53E-03	-0.30	0.76	1.58E-03	1.17	0.76
33	6.31E-03	-1.41	0.59	7.21E-03	-1.40	0.55
40	8.43E-03	-1.39	0.51	9.52E-03	-0.90	0.48
59	1.15E-02	-0.07	0.43	1.29E-02	0.02	0.40
81	1.29E-02	-0.48	0.40	1.45E-02	0.05	0.38
122	1.30E-02	0.60	0.40	1.46E-02	0.58	0.37
165	1.17E-02	0.33	0.39	1.34E-02	0.00	0.37
185	1.10E-02	0.27	0.40	1.25E-02	-0.13	0.37
244	8.79E-03	-0.35	0.42	1.02E-02	-0.74	0.40
356	6.16E-03	0.46	0.48	7.28E-03	-0.75	0.44
511	4.48E-03	-0.16	0.53	5.33E-03	-0.18	0.49
661	3.64E-03	-0.42	0.57	4.31E-03	0.46	0.53
834	3.05E-03	0.26	0.60	3.65E-03	0.30	0.56
1173	2.40E-03	-0.22	0.64	2.91E-03	0.02	0.59
1274	2.29E-03	-1.08	0.65	2.74E-03	0.53	0.60
1408	2.13E-03	-0.14	0.66	2.57E-03	0.15	0.61

Appendix C.11. IDL routine used for simplifying the phantom geometry.

```

pro simplify_phant_rebin
; input file loaction
l_dir="D:\"
l_File='ICRP_female.seg'
l_path=l_dir+l_File
; input file size
l_bytarrFantCol=BYTARR(77, 299, 137)
; reading the input file
openr, lun, l_path, /GET_LUN
readu, lun, l_bytarrFantCol
free_lun, lun
help, l_bytarrFantCol
; intermediary grids
Mplus1=BYTARR(77, 300, 137)
Mplus2=BYTARR(77, 300, 138)
Mplus1[*,0:298,*]=l_bytarrFantCol[*,*,*]
Mplus1[*,299,*]=0b*l_bytarrFantCol[*,0,*]
Mplus2[*,*,0:136]=Mplus1[*,*,*]
Mplus2[*,*,137]=0b*Mplus1[*,*,0]
; voxel fusion with rebin
mat_modif2=rebin(Mplus2, 77, 150, 69, /sample)
;the option /sample guarentees that no interpolations will be applied
; output file creation
openw, lun, 'D:\ICRP_female_simplified.seg', /get_lun
writeu, lun, mat_modif2
free_lun, lun
print, 'file .col written'
Entete='UNDEFINED'+string(10b)+$
'COULEUR'+string(10b)+$
' ICRP_female_simplified'+string(10b)+$;attention à modifier le nom
'ICRP'+string(10b)+$
'ETUDE-ICRP-1'+string(10b)+$
' 77'+string(10b)+$
' 150'+string(10b)+$
' 69'+string(10b)+$
' 0.484'+string(10b)+$
' 0.355'+string(10b)+$
' 0.355'+string(10b)+$
' 8'+string(10b)+$
' 0.000000'+string(10b)+$
' 0.000000'+string(10b)+$
'cm'+string(10b)+$
' 0'+string(10b)+$
' 0'+string(10b)+$
' 11'+string(10b)+$ ;attention aux couleurs présentes dans le fantôme
' 0 5 10 20 38 50 65 81 93 110 135'+$
' 142 186 182 145 185 143 183 184 147
146 187' ;attention a rajouter la couleur supplémentaire si nécessaire

openw, lun, 'D:\ ICRP_female_simplified.seg.ref', /get_lun
writeu, lun, Entete
free_lun, lun
print, 'file .col.ref written'

```

```
;validating the created volume
ind_1=where(l_bytarrFantCol EQ 5, count_5)
print, "old soft tissue volume", count_5*0.1754^3
ind_1=where(mat_modif2 EQ 5, count_5)
print, "new soft tissue volume", count_5*0.3508^3
ind_10=where(l_bytarrFantCol EQ 10, count_10)
print, "old sternum volume", count_10*0.1754^3
ind_10=where(mat_modif2 EQ 10, count_10)
print, " new sternum volume", count_10*0.3508^3
ind_20=where(l_bytarrFantCol EQ 20, count_20)
print, "old scapulae volume", count_20*0.1754^3
ind_20=where(mat_modif2 EQ 20, count_20)
print, " new scapulae volume", count_20*0.3508^3
ind_30=where(l_bytarrFantCol EQ 30, count_30)
print, "old ribs volume ", count_30*0.1754^3
ind_30=where(mat_modif2 EQ 30, count_30)
print, "new ribs volume", count_30*0.3508^3
ind_40=where(l_bytarrFantCol EQ 40, count_40)
print, "old spine volume", count_40*0.1754^3
ind_40=where(mat_modif2 EQ 40, count_40)
print, "new spine volume", count_40*0.3508^3
ind_50=where(l_bytarrFantCol EQ 50, count_5)
print, "old breast volume", count_50*0.1754^3
ind_50=where(mat_modif2 EQ 50, count_50)
print, "new breast volume", count_50*0.3508^3
ind_60=where(l_bytarrFantCol EQ 60, count_60)
print, "old lung volume", count_60*0.1754^3
ind_60=where(mat_modif2 EQ 60, count_60)
print, "new lung volume", count_60*0.3508^3
ind_70=where(l_bytarrFantCol EQ 70, count_70)
print, "old heart volume", count_70*0.1754^3
ind_70=where(mat_modif2 EQ 70, count_70)
print, "new heart volume", count_70*0.3508^3
ind_80=where(l_bytarrFantCol EQ 80, count_80)
print, "old liver volume", count_80*0.1754^3
ind_80=where(mat_modif2 EQ 80, count_5)
print, "new liver volume", count_80*0.3508^3
ind_90=where(l_bytarrFantCol EQ 90, count_90)
print, "old skin volume", count_90*0.1754^3
ind_90=where(mat_modif2 EQ 90, count_90)
print, "new skin volume", count_90*0.3508^3
end
```

Appendix C.12. Validation of the new ICRP phantom after voxel fusion with Rebin.

Table 1. Volume comparison of the ICRP female torso structures between the reference values and the new values obtained with the rebin function when simplifying the phantom geometry.

Structure ICRP female	Ref. Nb voxel	Rebin Nb. voxel	Ref. volume (mL)	Rebin volume (mL)	Diff (%)
Adrenal, left	365	91	5.57	5.55	0.27
Adrenal, right	463	117	7.06	7.14	-1.08
Trachea	393	100	5.99	6.10	-1.78
Bronchi	553	143	8.43	8.72	-3.44
Blood vessels, head	0	0	0.00	0.00	
Blood vessels, trunk	9812	2448	149.62	149.32	0.20
Humeri, upper half, cortical	1899	492	28.96	30.01	-3.63
Humeri, upper half, spongiosa	5839	1448	89.04	88.32	0.80
Humeri, upper half, medullary cavity	474	123	7.23	7.50	-3.80
Clavicles, cortical	800	192	12.20	11.71	4.00
Clavicles, spongiosa	1515	384	23.10	23.42	-1.39
Ribs, cortical	5523	1371	84.22	83.63	0.71
Ribs, spongiosa	15537	3906	236.92	238.25	-0.56
Scapulae, cortical	3487	862	53.17	52.58	1.12
Scapulae, spongiosa	4472	1124	68.19	68.56	-0.54
Thoracic spine, cortical	6960	1756	106.13	107.11	-0.92
Thoracic spine, spongiosa	15283	3804	233.05	232.03	0.44
Lumbar spine, cortical	3058	791	46.63	48.25	-3.47
Lumbar spine, spongiosa	7944	1969	121.14	120.10	0.86
Sternum, cortical	57	16	0.87	0.98	-12.28
Sternum, spongiosa	2890	717	44.07	43.73	0.76
Cartilage, trunk	8875	2182	135.34	133.09	1.66
Breast, left, adipose tissue	10355	2605	157.90	158.89	-0.63
Breast, left, glandular tissue	6429	1600	98.04	97.59	0.45
Breast, right, adipose tissue	10355	2576	157.90	157.13	0.49
Breast, right, glandular tissue	6429	1608	98.04	98.08	-0.05
Gall bladder wall	652	157	9.94	9.58	3.68
Gall bladder contents	2913	730	44.42	44.53	-0.24
Stomach wall	8828	2212	134.62	134.92	-0.23
Stomach contents	14503	3633	221.16	221.60	-0.20
Small intestine wall	15293	3826	233.20	233.37	-0.07
Small intestine contents	10304	2571	157.13	156.82	0.19
Ascending colon wall	1261	317	19.23	19.34	-0.56
Ascending colon contents	1103	274	16.82	16.71	0.63
Transverse colon wall, right	570	143	8.69	8.72	-0.35

Transverse colon contents, right	657	165	10.02	10.06	-0.46
Transverse colon wall, left	251	62	3.83	3.78	1.20
Transverse colon contents, left	68	18	1.04	1.10	-5.88
Descending colon wall	418	102	6.37	6.22	2.39
Descending colon contents	194	49	2.96	2.99	-1.03
Heart wall	15614	3894	238.10	237.52	0.24
Heart contents (blood)	22891	5714	349.07	348.53	0.15
Kidney, left, cortex	6535	1655	99.65	100.95	-1.30
Kidney, left, medulla	2334	578	35.59	35.26	0.94
Kidney, left, pelvis	467	117	7.12	7.14	-0.21
Kidney, right, cortex	5488	1373	83.69	83.75	-0.07
Kidney, right, medulla	1960	489	29.89	29.83	0.20
Kidney, right, pelvis	392	96	5.98	5.86	2.04
Liver	87437	21848	1333.33	1332.64	0.05
Lung, left, blood	3664	934	55.87	56.97	-1.97
Lung, left, tissue	64218	16090	979.26	981.43	-0.22
Lung, right, blood	2615	661	39.88	40.32	-1.11
Lung, right, tissue	80402	20085	1226.05	1225.11	0.08
Lymphatic nodes, thoracic airways	215	54	3.28	3.29	-0.47
Lymphatic nodes, trunk	2207	539	33.65	32.88	2.31
Muscle, trunk	252890	63275	3856.33	3859.53	-0.08
Oesophagus	1896	477	28.91	29.10	-0.63
Pancreas	7495	1878	114.29	114.55	-0.23
Residual tissue, trunk	333338	83342	5083.08	5083.54	-0.01
Skin, trunk	33296	8129	507.73	495.84	2.34
Spinal cord	771	191	11.76	11.65	0.91
Spleen	8197	2055	125.00	125.35	-0.28
Thymus	1273	324	19.41	19.76	-1.81
Thyroid	723	184	11.03	11.22	-1.80
Ureter, left	143	35	2.18	2.13	2.10
Ureter, right	163	40	2.49	2.44	1.84
Air inside body	897	224	13.68	13.66	0.11

Appendix C.13. MC simulation results for geometry simplification operations using the rebin function.

Table 1. Counting efficiency values, associated uncertainties and difference to reference values obtained when resizing the phantoms with the rebin function.

Phantom	Livermore			ICRP female			
	Energy	Count Eff. (counts/s/ γ)	Diff. (%)	Unc. (%)	Count Eff. (counts/s/ γ)	Diff. (%)	Unc. (%)
15		6.70E-05	-11.05	3.11	4.56E-05	-0.96	4.57
22		1.57E-03	-2.82	0.36	1.58E-03	1.10	0.36
33		6.32E-03	-1.67	0.17	7.06E-03	0.70	0.16
40		8.45E-03	-1.57	0.15	9.39E-03	0.54	0.14
59		1.16E-02	-1.03	0.13	1.28E-02	0.71	0.12
81		1.30E-02	-1.04	0.11	1.44E-02	0.67	0.11
122		1.32E-02	-1.18	0.11	1.46E-02	0.69	0.11
165		1.19E-02	-1.25	0.12	1.33E-02	0.84	0.11
185		1.11E-02	-1.10	0.12	1.24E-02	0.77	0.12
244		8.87E-03	-1.20	0.14	1.00E-02	0.48	0.13
356		6.25E-03	-1.03	0.16	7.20E-03	0.45	0.15
511		4.54E-03	-1.51	0.19	5.29E-03	0.52	0.18
661		3.68E-03	-1.49	0.21	4.28E-03	1.12	0.20
834		3.10E-03	-1.13	0.23	3.63E-03	0.88	0.22
1173		2.43E-03	-1.23	0.26	2.87E-03	1.18	0.24
1274		2.31E-03	-1.94	0.27	2.72E-03	1.15	0.25
1408		2.15E-03	-1.09	0.28	2.55E-03	1.00	0.26

Table 2. Counting efficiency values, associated uncertainties and difference to reference values obtained for the resized phantoms and the combination of SB, FCL and Vec VR cards.

Phantom	Livermore			ICRP female		
	Energy	Count Eff. (counts/s/ γ)	Diff. (%)	Unc. (%)	Count Eff. (counts/s/ γ)	Diff. (%)
15	6.20E-05	-2.85	7.95	4.30E-05	4.91	12.09
22	1.56E-03	-2.13	0.75	1.56E-03	1.91	0.76
33	6.38E-03	-2.63	0.59	7.08E-03	0.48	0.56
40	8.52E-03	-2.44	0.50	9.45E-03	-0.16	0.48
59	1.17E-02	-1.85	0.42	1.28E-02	1.02	0.41
81	1.31E-02	-1.43	0.40	1.44E-02	0.58	0.38
122	1.32E-02	-0.91	0.38	1.45E-02	1.05	0.37
165	1.19E-02	-0.98	0.39	1.33E-02	0.79	0.37
185	1.10E-02	-0.19	0.40	1.24E-02	0.55	0.37
244	8.85E-03	-1.07	0.42	1.00E-02	0.89	0.40
356	6.25E-03	-1.08	0.47	7.18E-03	0.75	0.45
511	4.54E-03	-1.54	0.53	5.28E-03	0.80	0.50
661	3.67E-03	-1.34	0.57	4.24E-03	2.09	0.53
834	3.08E-03	-0.53	0.60	3.62E-03	1.37	0.56
1173	2.47E-03	-2.91	0.64	2.90E-03	0.18	0.59
1274	2.31E-03	-2.00	0.65	2.70E-03	1.88	0.61
1408	2.14E-03	-0.70	0.66	2.56E-03	0.65	0.61

Appendix D.1. Effect of detector positioning on counting efficiency for the CIEMAT measurements

Table 1. Effect of the errors in detector positioning on simulated counting efficiency for detectors 1 and 2.

Coordinates			Left Lung + Detector #1		Left Lung + Detector #2		Right Lung + Detector #1		Right Lung + Detector #2	
X	Y	Z	Efficiency (counts/s/ γ)	Diff. (%)	Efficiency (counts/s/ γ)	Diff. (%)	Efficiency (counts/s/ γ)	Diff. (%)	Efficiency (counts/s/ γ)	Diff. (%)
14.5	28.63	16.5	1.85E-04	42.26	1.07E-04	51.33	1.35E-03	-6.22	1.20E-03	-10.84
14.5	28.63	17.5	1.80E-04	43.95	9.83E-05	55.23	1.42E-03	-12.18	1.16E-03	-6.79
14.5	28.13	17	1.83E-04	43.01	1.02E-04	53.46	1.45E-03	-14.74	1.25E-03	-15.39
14.5	29.13	17	1.83E-04	43.12	1.03E-04	53.16	1.32E-03	-3.84	1.12E-03	-3.04
15	28.63	17	1.95E-04	39.39	1.07E-04	51.07	1.40E-03	-10.50	1.20E-03	-10.40
15.5	28.63	17	2.07E-04	35.55	1.12E-04	49.21	1.42E-03	-11.81	1.20E-03	-11.13
13.5	28.63	17	1.64E-04	48.93	9.42E-05	57.09	1.34E-03	-5.58	1.15E-03	-5.92
12.5	28.63	17	1.49E-04	53.65	8.79E-05	59.96	1.28E-03	-0.82	1.11E-03	-2.20

Table 3. Effect of errors in detector tilts on simulated counting efficiency for the left lung loaded alone.

Tilt ($^{\circ}$)		Detector #1		Detector #2		Tilt ($^{\circ}$)		Detector #3		Detector #4	
YY'	ZZ'	Efficiency (counts/s/ γ)	Diff. (%)	Efficiency (counts/s/ γ)	Diff. (%)	YY'	ZZ'	Efficiency (counts/s/ γ)	Diff. (%)	Efficiency (counts/s/ γ)	Diff. (%)
+5	0	1.90E-04	40.97	1.05E-04	52.18	+5	0	9.51E-04	12.48	5.05E-04	35.69
-5	0	1.74E-04	45.88	9.90E-05	54.91	-5	0	9.71E-04	10.57	5.05E-04	35.75
0	+5	1.84E-04	42.81	1.06E-04	51.72	0	+5	8.35E-04	23.09	2.95E-04	62.49
0	-5	1.80E-04	44.00	9.90E-05	54.91	0	-5	9.62E-04	11.40	4.75E-04	39.56

Table 3. Effect of the errors in detector positioning on simulated counting efficiency for detectors 3 and 4.

Coordinates			Left Lung + Detector #3		Left Lung + Detector #4		Right Lung + Detector #3		Right Lung + Detector #4	
X	Y	Z	Efficiency (counts/s/ γ)	Diff. (%)	Efficiency (counts/s/ γ)	Diff. (%)	Efficiency (counts/s/ γ)	Diff. (%)	Efficiency (counts/s/ γ)	Diff. (%)
31	28.63	16.5	9.56E-04	11.98	5.33E-04	32.21	4.69E-04	-32.30	3.65E-04	-10.24
31	28.63	17.5	9.67E-04	10.96	4.78E-04	39.17	4.75E-04	-33.78	3.43E-04	-3.55
31	28.13	17	1.03E-03	5.61	5.28E-04	32.81	4.72E-04	-33.12	3.49E-04	-5.57
31	29.13	17	9.07E-04	16.52	4.84E-04	38.34	4.72E-04	-33.02	3.58E-04	-8.32
30	28.63	17	9.30E-04	14.37	4.75E-04	39.57	5.47E-04	-54.29	4.14E-04	-25.16
30.5	28.63	17	9.48E-04	12.70	4.90E-04	37.60	5.09E-04	-43.57	3.83E-04	-15.79
32	28.63	17	9.80E-04	9.81	5.31E-04	32.37	4.10E-04	-15.47	3.03E-04	8.41
33	28.63	17	9.82E-04	9.55	5.56E-04	29.25	3.53E-04	0.37	2.59E-04	21.68

Table 4. Effect of errors in detector tilts on simulated counting efficiency for the right lung loaded alone.

Tilt ($^{\circ}$)		Detector #1		Detector #2		Tilt ($^{\circ}$)		Detector #3		Detector #4	
YY'	ZZ'	Efficiency (counts/s/ γ)	Diff. (%)	Efficiency (counts/s/ γ)	Diff. (%)	YY'	ZZ'	Efficiency (counts/s/ γ)	Diff. (%)	Efficiency (counts/s/ γ)	Diff. (%)
+5	0	1.38E-03	-8.64	1.18E-03	-9.16	+5	0	4.91E-04	-38.50	3.59E-04	-8.54
-5	0	1.38E-03	-9.09	1.18E-03	-8.90	-5	0	4.50E-04	-27.01	3.46E-04	-4.62
0	+5	1.37E-03	-7.94	1.30E-03	-20.34	0	+5	4.12E-04	-16.09	2.46E-04	25.57
0	-5	1.39E-03	-9.67	1.07E-03	1.23	0	-5	4.75E-04	-33.94	3.44E-04	-3.96

Appendix D.2. CIEMAT measurement results for the americium lungs

The used CIEMAT lungs were loaded with americium and europium at the same time. It is thus natural to test the method with americium also. In this case however, the lungs were more active than europium that has a half life of 13.5 years (against 432 years for americium). Namely, the right lung americium activity was of 25.21 kBq and the left one was of 17.7 kBq on the measurement date. Table 1 documents the measurement results for the 60 keV americium energy line.

Table 1. Experimental counting rate (counts/s) obtained for the CIEMAT four-germanium counting system with americium lungs.

Loaded Organ		Left & Right lungs	Left lung	Right lung
Experimental counting rate	Sum four detectors	145.64	50.58	93.37
	Sum left pair	88.91	10.38	75.74
	Sum right pair	60.46	41.79	18.97
	Detector 1	48.38	6.19	41.70
	Detector 2	39.18	4.14	34.20
	Detector 3	35.90	24.85	9.86
	Detector 4	24.41	15.76	8.37

Before estimating the activity distribution, the linearity test was performed to check if the positioning of the detectors and of the lungs was identical from one measurement to another. This should be true since the linearity was obtained for the europium 122 keV emission. Table 2 documents the results and proves the reproducibility of the measurement.

Table 2. Linearity check for the CIEMAT system and the operated detector positioning.

Detector	Sum four det.	Sum left pair	Sum right pair	Det. #1	Det. #2	Det. #3	Det. #4
Linearity error (%)	1.16	3.14	-0.50	1.02	2.15	3.32	1.16

From the data in Table 1 and Equation 5.3, the activity distribution was assessed for the different configurations of detectors (cf. Table 3). For americium lungs, better statistics of the counts were obtained considering the activity difference when compared to europium experiments. As a direct consequence, better activity estimates were obtained when using the americium experimental data.

Table 3. Impact of the different possible combinations of detectors on the activity estimates and on their differences to the reference values.

Detectors combination	Act. Right Lung (kBq)	Diff. (%)	Act. Left Lung (kBq)	Diff. (%)
Det. #1+2 – Det. #3+4	26.22	-4.0	17.25	2.6
Det. #1 – Det. #2	27.25	-8.1	9.46	46.6
Det. #1 – Det. #3	25.33	-0.5	18.51	-4.6
Det. #1 – Det. #4	25.46	-1.0	17.93	-1.3
Det. #2 – Det. #3	25.71	-2.0	18.41	-4.0
Det. #2 – Det. #4	25.81	-2.4	17.79	-0.5
Det. #3 – Det. #4	19.58	22.3	20.12	-13.7

Appendix D.3. Effect of detector positioning on counting efficiency for the KIT measurements

To make the simulated counting efficiency correspond to the measurement values, shifts in the X (left-right), Y (back-top) and Z (head-feet) directions were tested. Tables below represent the simulation results obtained for different configurations of loaded organ and detector positioning. The positioning was modified to obtain a difference below 5% for each configuration of loaded organ. The results prove however, that it was impossible to obtain a good agreement for the three detector positions at the same time. When the agreement was acceptable for the direct measurement, the considered detector positioning failed to give satisfying results for cross fire situations and vice versa.

Table 1. Counting efficiency simulated values and differences to measurements obtained when the left lung was loaded with activity.

Coordinates			Src. LL. +		Src. LL. +		Src. LL. +	
Shifts (cm)			Det. Liv		Det. RL		Det. LL	
X	Y	Z	Efficiency (counts/s/γ)	Difference (%)	Efficiency (counts/s/γ)	Difference (%)	Efficiency (counts/s/γ)	Difference (%)
0	0	-3	3.74E-05	51	2.76E-04	11	1.21E-03	14
0	0	3	1.49E-05	80	1.89E-04	39	1.06E-03	24
-3	0	0	1.97E-05	74	1.64E-04	47	1.16E-03	17
3	0	0	3.44E-05	55	3.87E-04	-25	1.11E-03	21
0	-2	0	1.82E-05	76	2.38E-04	23	1.52E-03	-9
0	2	0	2.84E-05	63	2.45E-04	21	9.69E-04	31
0	-1	0	2.36E-05	69	2.42E-04	22	1.35E-03	4
6	-1	-3	7.80E-05	-3	6.74E-04	-118	9.60E-04	32
3	0	3	2.02E-05	73	2.99E-04	4	1.02E-03	21

Table 2. Counting efficiency simulated values and differences to measurements obtained when the right lung was loaded with activity.

Coordinates			Src. RL. +		Src. RL. +		Src. RL. +	
Shifts (cm)			Det. Liv		Det. RL.		Det. LL.	
X	Y	Z	Efficiency (counts/s/γ)	Difference (%)	Efficiency (counts/s/γ)	Difference (%)	Efficiency (counts/s/γ)	Difference (%)
0	0	-3	6.95E-04	-21	1.55E-03	30	3.33E-04	24
0	0	3	2.56E-04	56	2.00E-03	10	3.02E-04	31
-3	0	0	4.67E-04	19	1.64E-03	26	5.48E-04	-25
3	0	0	3.69E-04	36	1.82E-03	18	1.99E-04	54
0	-2	0	4.08E-04	29	2.32E-03	-5	2.83E-04	35
0	2	0	4.32E-04	25	1.51E-03	32	3.52E-04	19
3	2	-3	5.85E-04	-2	1.29E-03	42	2.35E-04	46
-3	0	6	1.87E-04	68	1.78E-03	20	4.49E-04	-3

Table 3. Counting efficiency simulated values and differences to measurements obtained when the liver was loaded with activity.

Coordinates			Src. Liver +		Src. Liver +		Src. Liver +	
Shifts (cm)			Det. Liv.		Det. RL.		Det. LL.	
X	Y	Z	Efficiency (counts/s/ γ)	Difference (%)	Efficiency (counts/s/ γ)	Difference (%)	Efficiency (counts/s/ γ)	Difference (%)
0	0	-3	1.51E-03	15	1.91E-04	43	1.06E-04	42
0	0	3	1.44E-03	19	4.49E-04	-33	2.40E-04	-32
-3	0	0	1.29E-03	27	2.71E-04	20	2.04E-04	-12
3	0	0	1.78E-03	1	2.91E-04	14	1.14E-04	37
0	-2	0	1.93E-03	-9	2.50E-04	26	1.16E-04	36
0	2	0	1.29E-03	27	3.19E-04	5	1.85E-04	-2

Résumé

Afin d'optimiser la surveillance des travailleuses du nucléaire par anthroporadiométrie, il est nécessaire de corriger les coefficients d'étalonnage obtenus à l'aide du fantôme physique masculin Livermore. Pour ce faire, des étalonnages numériques basés sur l'utilisation des calculs Monte Carlo associés à des fantômes numériques ont été utilisés. De tels étalonnages nécessitent d'une part le développement de fantômes représentatifs des tailles et des morphologies les plus communes et d'autre part des simulations Monte Carlo rapides et fiables. Une bibliothèque de fantômes thoraciques féminins a ainsi été développée en ajustant la masse des organes internes et de la poitrine suivant la taille et les recommandations de la chirurgie plastique. Par la suite, la bibliothèque a été utilisée pour étalonner le système de comptage du Secteur d'Analyses Médicales d'AREVA NC La Hague. De plus, une équation décrivant la variation de l'efficacité de comptage en fonction de l'énergie et de la morphologie a été développée. Enfin, des recommandations ont été données pour corriger les coefficients d'étalonnage du personnel féminin en fonction de la taille et de la poitrine. Enfin, pour accélérer les simulations, des méthodes de réduction de variance ainsi que des opérations de simplification de la géométrie ont été considérées.

Par ailleurs, pour l'étude des cas de contamination complexes, il est proposé de remonter à la cartographie d'activité en associant aux mesures anthroporadiométriques le calcul Monte Carlo. La méthode développée consiste à réaliser plusieurs mesures spectrométriques avec différents positionnements des détecteurs. Ensuite, il s'agit de séparer la contribution de chaque organe contaminé au comptage grâce au calcul Monte Carlo. L'ensemble des mesures réalisées au LEDI, au CIEMAT et au KIT ont démontré l'intérêt de cette méthode et l'apport des simulations Monte Carlo pour une analyse plus précise des mesures *in vivo*, permettant ainsi de déterminer la répartition de l'activité à la suite d'une contamination interne.

Mots-clés : surveillance anthroporadiométrique, étalonnages numériques, fantômes déformables, réduction de variance, répartition d'activité.